TECHNISCHE UNIVERSITÄT MÜNCHEN

Department of Chemistry and Catalysis Research Center
Chair of Technical Electrochemistry

Degradation Mechanisms of High-Energy Electrode Materials for Lithium-Ion Batteries

Roland Jung

Vollständiger Abdruck der von der Fakultät für Chemie der Technischen Universität München zur Erlangung des akademischen Grades eines

Doktors der Naturwissenschaften (Dr. rer. nat.)

genehmigten Dissertation.

Vorsitzender:	Prof. Dr. Thomas Fässler
Prüfer der Dissertation:	1. Prof. Dr. Hubert A. Gasteiger
	2. Prof. Dr. Tom Nilges
	3. Prof. Dr. Jeff Dahn

Diese Dissertation wurde am 17.10.2018 bei der Technischen Universität München eingereicht und durch die Fakultät für Chemie am 05.12.2018 angenommen.

Acknowledgement

First of all, I want to express my deepest gratitude to my PhD adviser Prof. Hubert Gasteiger. It was a great honor working with and learning from you. Thank you very much for your support, very inspiring scientific discussions and the outstanding environment you created at the Chair of Technical Electrochemistry. I also want to address my greatest gratitude to my mentors Dr. Christoph Stinner and Dr. Filippo Maglia. I feel honored working with you, your invaluable support and effort greatly improved this Thesis. I am looking forward to our coming projects.

Special thanks go to all group members at the Chair of Technical Electrochemistry at Technical University Munich for your outstanding collegiality, the great scientific discussions and the awesome working atmosphere. I also would like to greatly acknowledge my former colleague Dr. Michael Metzger for your support and our great collaborations. Additionally, I want to thank Fabian Linsenmann, Robert Morasch and Philipp Strobl for your great and passionate work in the course of your Master's Thesis and Research internships. It was a lot of fun working with you. Furthermore, I thank all members of the EA-46 department at BMW for your support and all the scientific discussions. I especially thank Dr. Odysseas Paschos for all your help and support.

I would like to thank Dr. Peter Lamp for trusting me to work as PhD student as part of your Rudolf-Diesel Fellowship. Thank you very much for your support over the past years. I always feel very inspired seeing what you built up over the last years at BMW and I am looking forward to our future projects. Thank you also for recruiting me to your group in the course of my internship at BMW back in 2013.

I would like to thank Dr. Holger Hain for supervising my internship at BMW and I also greatly would like to acknowledge the supervisors of my Master's Thesis Dr. Cyril Marino and Dr. Nikolaos Tsiouvaras. All of you inspired me to battery research and taught me a lot of electrochemistry and thereby laid the fundament for this PhD thesis. It was a great pleasure working with you.

Special thanks go to Prof. Yang Shao-Horn for inviting me to join your group at Massachusetts Institute of Technology for several months. It was a great honor and I definitely will not forget this awesome experience. I also want to thank all your group members for the great hospitality and the very inspiring working atmosphere. I would like to

greatly acknowledge our collaboration partners Prof. Moniek Tromp from the University of Amsterdam (Netherlands) and Prof. Thomas Fässler from Technical University Munich for the great and successful collaboration. Many thanks go to all members of the BMW Focus Group for all the very interesting meetings, your input and all the inspiring scientific discussions we had during the past years.

I also would like to greatly acknowledge BMW and TUM-IAS for the financial support of this work. I also thank the German Academic Exchange Service (DAAD) for the conference travel grant to the 231st ECS meeting in New Orleans (USA).

Last but not least, I want to express my deepest gratitude to my family and my girlfriend. Without your continuous support over the past years this PhD thesis would not have been possible. Thank you very much!

Abstract

Li-ion battery materials are subject to a large variety of aging mechanisms. In this PhD thesis, various degradation phenomena are investigated in dependence of the applied voltage limits, the temperature, or the composition of the electrolyte. It is a primary target to understand the root causes of cathode or anode active material aging from a fundamental point of view in order to evaluate their long-term stability. The focus of this thesis lies on the so-called nickel rich NMCs ($LiNi_xMn_yCo_zO_2$ with $x >> y, z$ and $x+y+z=1$), one of the most promising classes of cathode materials. In particular, NMC materials with different transition metal compositions are analyzed at various cut-off voltages and temperatures to test and understand the stability limits of these materials. As one major result, we describe the release of reactive oxygen from the NMC lattice that leads to cathode material degradation and chemical oxidation of the electrolyte. This kind of electrolyte oxidation mechanism will be critically differentiated from the electrochemical oxidation pathway. It is shown that the onset of oxygen release correlates with the cycling stability of NMC, providing clear evidence that oxygen release is a severe aging mechanism which leads to rapid capacity decay.

Furthermore, the degradation of nickel rich NMC811 ($LiNi_{0.8}Mn_{0.1}Co_{0.1}O_2$) upon storage at ambient air is analyzed. It will be shown that the surface decomposes, forming nickel carbonate species with minor amounts of hydroxides and crystal water, which detrimentally affect the cycling performance of the material by a growing impedance. Another important aging mechanism occurring due to the interaction of cathode and anode is also investigated, viz, the dissolution of transition metals from NMC and its deposition on a graphite anode. We compare metal dissolution from NMC111 ($LiNi_{0.33}Mn_{0.33}Co_{0.33}O_2$) and NMC622 ($LiNi_{0.6}Mn_{0.2}Co_{0.2}O_2$) and investigate the oxidation states of the deposited metals as well as analyze their impact on NMC-graphite cells. The deposition of all three transition metals leads to the same effect, namely the chemical decomposition of the anode SEI, yet with manganese causing the fastest SEI degradation. Reconstruction of the SEI ultimately leads to loss of cycleable lithium as primary cause of capacity fade.

Finally, degradation mechanisms occurring on silicon electrodes are investigated. It will be shown that the consumption of electrolyte is a very severe effect which has to be accounted for when silicon electrodes are to be applied in future Li-ion batteries. Furthermore, we have examined the fundamental degradation mechanisms of silicon on a particle as well as on an electrode level to better understand the fundamental causes of capacity fading.

Kurzfassung

Li-Ionen Akkumulatoren sind einer großen Bandbreite von Alterungsmechanismen ausgesetzt. In dieser Arbeit untersuchen wir verschiedene Zersetzungsmechanismen in Abhängigkeit der Spannungslimits, der Temperatur, oder der Elektrolytzusammensetzung. Primäres Ziel ist es ein grundlegendes Verständnis der Aktivmaterialalterung zu entwickeln, um daraus die Langzeitstabilität von Kathoden- oder Anodenmaterial beurteilen zu können. Dabei liegt der Fokus auf den so genannten nickelreichen NMCs, einer der vielversprechendsten Kathodenmaterialklasse. Wir untersuchen NMC Materialien mit unterschiedlicher Übergangsmetallzusammensetzung hinsichtlich ihres Stabilitätslimits bei verschiedenen Abschaltspannungen und Temperaturen. Ein zentrales Ergebnis dieser Arbeit ist die Beschreibung der Sauerstofffreisetzung aus der NMC Kristallstruktur, wobei der Sauerstoff in hochreaktiver Form freigesetzt wird, was zur chemischen Elektrolytoxidation führt, die klar von der elektrochemischen Elektrolytoxidation zu unterscheiden ist. Weiterhin korrelieren wir das Einsetzen der Sauerstofffreisetzung mit der Zyklisierungsstabilität von NMC und beweisen, dass die Sauerstofffreisetzung ein schwerwiegender Alterungsmechanismus ist, der zu schnellem Kapazitätsverlust führt.

Darüber hinaus untersuchen wir die Stabilität von nickelreichem NMC811 ($LiNi_{0.8}Mn_{0.1}Co_{0.1}O_2$) bei Kontakt mit Luft. Die Zersetzung der Oberfläche unter Bildung von Nickelcarbonatspezies mit geringem Anteil an Hydroxid und Kristallwasser führen zu einer Verschlechterung der Zyklisierungsstabilität aufgrund wachsender Impedanzen. Ein weiterer Alterungsmechanismus, der durch die Wechselwirkung zwischen Kathode und Anode auftritt, nämlich die Auflösung von Übergangsmetallen aus dem Kathodenmaterial und die anschließende Abscheidung dieser auf der Anode, wird ebenfalls analysiert. Wir vergleichen die Übergangsmetallauflösung aus NMC111 ($LiNi_{0.33}Mn_{0.33}Co_{0.33}O_2$) und NMC622 ($LiNi_{0.6}Mn_{0.2}Co_{0.2}O_2$) und untersuchen die Oxidationszustände der abgeschiedenen Metalle sowie deren Einfluss auf NMC-Graphit Zellen. Die Abscheidung aller drei Übergangsmetalle führt zur chemischen Zersetzung der Anoden SEI, wobei Mangan die schnellste Zersetzung bedingt. Der Wiederaufbau der SEI führt zum Verlust von zyklisierbarem Lithium, was zugleich der Hauptmechanismus des Kapazitätsverlusts ist.

Abschließend untersuchen wir Zersetzungsmechanismen von Silizium Elektroden und zeigen, dass der Elektrolytverbrauch ein zentraler Effekt ist, der bei der Zellauslegung berücksichtigt werden muss, wenn Siliziumelektroden in zukünftigen Li-Ionen Akkumulatoren eingesetzt

werden. Weiterhin analysieren wir in einer grundlegenden Studie die Zersetzung von Silizium auf Partikelebene als auch auf Elektrodenebene, um die Gründe des Kapazitätsverlustes zu verstehen.

Table of Contents

List of Acronyms

CEI	cathode electrolyte interphase
EC	ethylene carbonate
EV	electric vehicle
EXAFS	extended X-ray absorption fine structure
FEC	fluoroethylene carbonate
GC	gas chromatography
IR	infrared
LCO	lithium cobalt oxide ($LiCoO_2$)
LCP	lithium cobalt phosphate ($LiCoPO_4$)
LEDC	lithium ethylene dicarbonate
LFP	lithium iron phosphate ($LiFePO_4$)
LMO	lithium manganese oxide ($LiMn_2O_4$)
LNCO	lithium nickel cobalt oxide ($LiNi_xCo_yO_2$)
LNMO	lithium nickel manganese oxide, high-voltage spinel ($LiNi_{0.5}Mn_{1.5}O_4$)
LNO	lithium nickel oxide ($LiNiO_2$)
LTO	lithium titanate ($Li_4Ti_5O_{12}$)
NCA	lithium nickel cobalt aluminum oxide ($LiNi_xCo_yAl_zO_2$)
NMC	lithium nickel manganese cobalt oxide ($LiNi_xMn_yCo_zO_2$)
NMR	nuclear magnetic resonance
OEMS	on-line electrochemical mass spectrometry
PC	propylene carbonate
PCTFE	polychlorotrifluoroethylene
PTFE	polytetrafluoroethylene
SEI	solid electrolyte interphase
XANES	X-ray absorption near edge structure
XAS	X-ray absorption spectroscopy
XPS	X-ray photoelectron spectroscopy

1. Introduction

In the year 1991, Sony revolutionized the battery market by launching the first large-scale commercial Li-ion battery cell production. With a volumetric energy density of 200 Wh/L and a specific energy of 80 Wh/kg, it was already comparable to the state-of-the-art nickel metal hydride batteries and many improvements were about to develop.[1-3] A comparison of the gravimetric and volumetric energies as well as the operating voltages of various battery types are listed in Table 1.1. While the lead acid, nickel-cadmium, and nickel metal hydride cells were already well developed, Li-ion battery cells drastically improved since 1991 (fourth row in Table 1.1) and they are targeted to reach volumetric and specific energies of ≥800 Wh/L and ≥300 Wh/kg by 2025 (last row in Table 1.1).[4, 5] Nowadays, essentially all portable electronic devices like laptops and cell phones use Li-ion batteries. Recently, they have also been used as energy supply for the powertrain of electric vehicles (EVs), with essentially all car manufacturers having electric cars in their fleet.

Table 1.1 Specific energy and energy density of different commercially available secondary battery cells.[1, 2, 4-6] The specific energy of the first generation and today's Li-ion batteries are the specifications of the first Sony cell[1] and today's BMW i3 cells, respectively.[6]

Battery type	Specific energy [Wh/kg]	Energy density [Wh/L]	Voltage [V]	Reference
Lead acid	30–40	100	2	2
Nickel-Cadmium	50	150	1.35	2
Nickel metal hydride	80	250	1.35	2
Lithium ion (first generation)	80	200	~3.7	1
Lithium ion (today)	174	357	~3.8	6
Lithium ion (target)	≥300	≥800	~3.8	4, 5

Today's strive for higher energy densities is strongly driven by the desire to more widely use electric drivetrains powered by Li-ion batteries as alternative to the combustion engines in automobiles. The realization of electromobility in form of a substantial penetration of EVs into the mass market is mostly depending on two factors, namely the cost of EVs compared to conventional vehicles with a combustion engine as well as the available driving range of the EV.[7] The cost per kWh of a Li-ion battery has already dropped since its first commercialization by a factor of ten and is predicted to decrease even further.[5, 8-10] The driving range of an EV depends on the total energy of the battery pack and the energy

consumption per driven mile. The latter is determined by the vehicle weight, the assumed drive-cycle, and the vehicle performance characteristics.[9] To make EVs available to the mass market, Andre et al. and Blomgren defined driving ranges ≥300 miles and ≥200 miles, respectively, as a key requirement.[5, 11] Today's BMW i3 vehicle (94 Ah version) has a 33 kWh battery (27.2 kWh useable) and a driving range of 114–125 miles depending on the applied drive-cycle.[11, 12] This gives an energy requirement of ~22–24 kWh/100 miles similar to the values reported previously in the literature.[9, 10, 12, 13] Therefore, driving ranges of 200–300 miles require battery packs with useable energies of roughly 44–66 kWh. According to the current battery price of ~250 $/kWh,[9] this translates into costs of 11,000–16,500 $ per vehicle, which is too high for an average mid-size car accessible to the mass market. If the projected battery cost targets of ~125 $/kWh[9, 10] will be met, the battery prices will be cut by one half to 5,500–8,250 $, which eventually may render EVs competitive to vehicles with a combustion engine. Yet, to reach this battery cost target, advanced Li-ion battery technology including Si-anodes and high-capacity cathodes needs to become available[9, 10] fulfilling at the same time the high requirements with respect to safety and lifetime[4, 5] of the Li-ion battery in automotive applications.

1.1 The Working Principle of a Lithium-Ion Battery

In Figure 1-1 the most important components of a Li-ion battery are depicted. The hearts of every battery cell are the electrode materials which primarily govern the overall energy. On the one hand, the electrode with the higher lithiation potential is the positive electrode (right side in Figure 1-1), by convention in Li-ion battery research also called the cathode. On the other hand, the electrode with the lower lithiation potential is the negative electrode (left side in Figure 1-1), by convention called the anode. In state-of-the-art Li-ion batteries, the cathode is typically a layered oxide with the general formula $LiMO_2$ (M = Ni, Co, Mn, Al) and the anode consists of graphite. Further details on the different electrode materials will be presented in the sections 1.2, 2.1, and 2.2. The cathode is typically coated onto an aluminum current collector, whereas for the anode a copper current collector is used. The current collectors are thin foils with optimized thicknesses of 8-12 µm.[4]

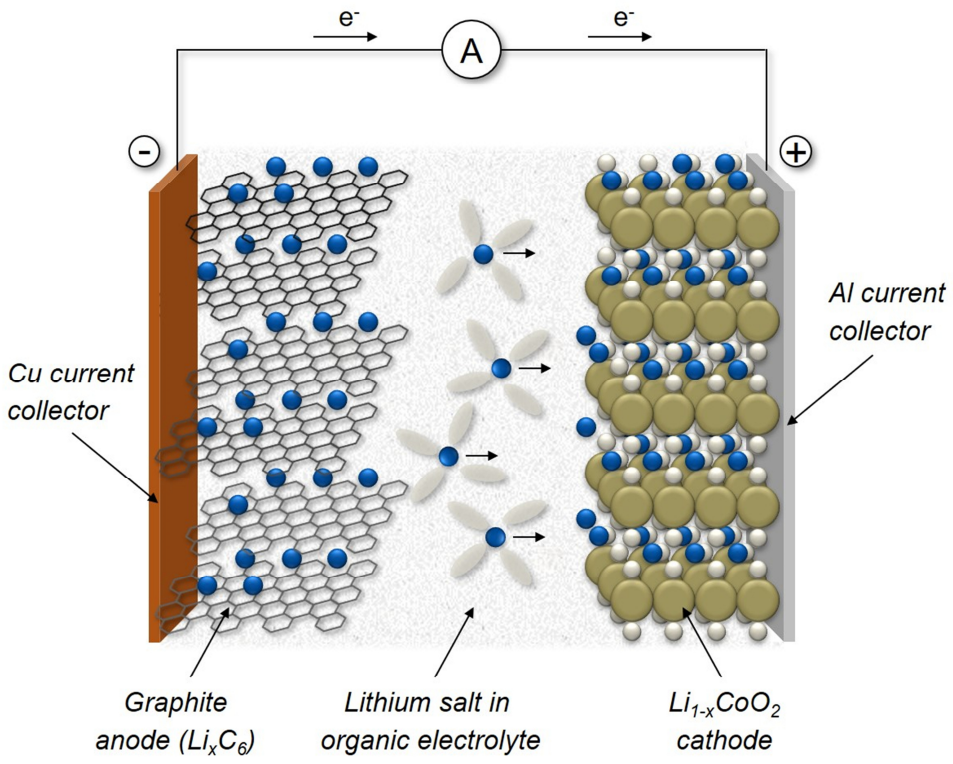

Figure 1-1 Schematic illustration of the basic components as well as the working principle of a Li-ion battery. The figure is reproduced from Reference 14 with permission from the author.

To avoid a mechanical contact between the two electrodes, i.e., a short circuit, a polyolefin separator with a typical thickness of 12-25 µm is placed in between the electrodes.[4, 11] The pores of the separator and the electrodes are filled with the electrolyte, which typically consists of $LiPF_6$ as conducting salt dissolved in alkyl carbonate solvents (grey ellipses in Figure 1-1).[15] During the charge process of the Li-ion battery, Li^+-ions are deintercalated from the $LiMO_2$ cathode and become dissolved in the electrolyte. In this process the host lattice is oxidized and electrons are transported via the external circuit to the anode reducing the graphite host structure. Simultaneously, Li^+-ions from the electrolyte are intercalated in between the layers of the graphite anode. The general equation of the Li-ion cell can be written as:

$$LiMO_2 + C_6 \rightleftharpoons Li_{1-x}MO_2 + Li_xC_6 \qquad (1.1)$$

In equation (1.1) the forward reaction is the charge and the backward reaction is the discharge reaction of the Li-ion cell. The specific capacity of the active material is the amount of charge or Li-ions transferred per mass of active material and is defined for the cathode and the anode as $c_+ = \frac{n \cdot F}{M_{CAM}}$ and $c_- = \frac{n \cdot F}{M_{AAM}}$, respectively. In these equations n, F, M_{CAM}, and M_{AAM} are the number of transferred electrons, the Faraday constant, the molar mass of the cathode active material, and the molar mass of the anode active material, respectively. The specific capacity is typically given in mAh/g. In a perfectly balanced cell the specific capacity based on the masses of both active materials is calculated as $c_\pm = \frac{c_+ \cdot c_-}{c_+ + c_-}$.

The specific energy $E_\pm$ of a battery cell based exclusively on the masses of the active materials is the product of $c_\pm$ and the difference of the average operating voltages measured vs. Li/Li^+ of the cathode V_+ and the anode V_-, which are defined as $V = \frac{\int V_{Li} \cdot dQ}{Q_{total}}$:

$$E_\pm = c_\pm \cdot (V_+ - V_-) = c_\pm \cdot \Delta V \qquad (1.2)$$

According to equation (1.2) the potential difference for Li-ion intercalation/deintercalation between cathode and anode should in an ideal case be as large as possible to achieve a high cell potential and accordingly a high cell energy.

1.2 The Journey to Increasing Energy Densities

Figure 1-2 shows a summary of the specific capacity of various anode (left panel) and cathode (right panel) active materials plotted versus the average operating voltage, the two parameters which determine the energy of a Li-ion battery cell. The symbols in Figure 1-2a indicate how lithium is stored in the respective anode material, i.e., by intercalation, alloy formation, or in metallic form. The differently shaded regions in Figure 1-2b mark the groups of so-called 3 V, 4 V, and 5 V cathode materials. The symbols indicate the structure of the specific cathode material, i.e., layered, spinel, or olivine. In the following the development as well as advantages and disadvantages of the materials in Figure 1-2 will be described. The aging mechanisms associated with the anode and cathode active materials will be described in section 2.2.

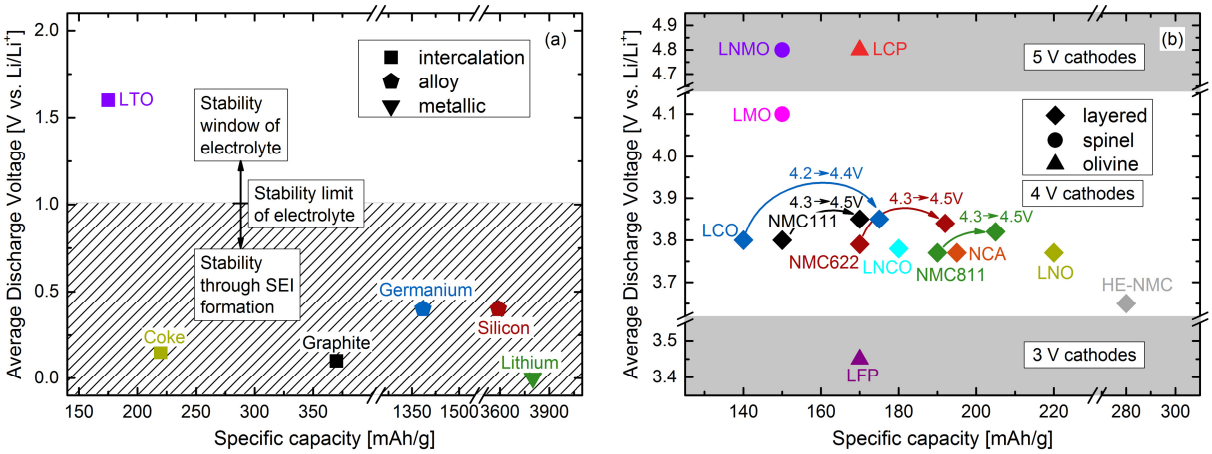

Figure 1-2 (a) Average discharge voltage vs. Li/Li^+ plotted versus specific capacity of several anode materials. Squares indicate intercalation, pentagons alloy, and triangles metallic anodes. The specific capacity of coke is the one of the anode in the first commercial Li-ion battery. (b) Average discharge voltage vs Li/Li^+ plotted versus specific capacity of several cathode materials. Diamonds indicate layered, dots spinel, and triangles olivine structured active materials. The arrows indicate the possible improvements achieved by increasing the upper cut-off potentials.

Among all elements in the periodic table lithium is the lightest metal and has one of the lowest standard reduction potentials, which makes it in theory the ideal anode material. As a consequence, in 1973, Stanley Whittingham was the first to propose a rechargeable battery composed of a lithium metal anode and a titanium disulfide (TiS_2) cathode, which can reversibly intercalate lithium ions forming $LiTiS_2$ and is operated at a potential around 2 V vs. the lithium metal anode potential.[16-18] In an attempt to increase the operating voltage, it were Goodenough and coworkers who focused on oxides instead of the sulfides,[19] which resulted in 1980 in the seminal work by Mizushima et al., in which $LiCoO_2$ (LCO) was described as

cathode material operating at average potentials slightly below 4 V vs. Li/Li^+ (see blue diamond in Figure 1-2b).[20] In this publication the family of the layered oxides was described, a material class which until today is the most promising cathode material class and will also be primarily investigated in this PhD thesis. For a long time, the use of metallic lithium hampered the mass commercialization of lithium batteries,[19] because of various challenges which could not be overcome until today: In particular, the very low standard reduction potential of lithium makes it chemically reactive with any electrolyte. Even though in many non-aqueous electrolytes a surface passivation layer is formed preventing corrosion of the bulk lithium,[19] repeated lithium plating and stripping exposes continuously fresh metal surface to the electrolyte leading to ongoing electrolyte consumption. Furthermore, non-uniform lithium plating results in the formation of dendrites, which may not only cause a total cell failure by short circuiting the two electrodes, but also displays a serious safety threat due to possible local overheating.[19] The latter eventually may cause unexpected cell explosions preventing the safe use of batteries with a lithium anode and conventional liquid electrolytes.[11]

A way to avoid the use of a metallic lithium anode is to use intercalation compounds not only for the cathode but also for the anode. This idea of a battery in which Li-ions are reversibly intercalated between two different host materials came from Michel Armand.[11, 21] Graphite was known to intercalate Li-ions at a potential very close to the lithium metal potential, yet a major issue was electrolyte solvent reduction and co-intercalation causing exfoliation of the graphite layers.[11, 22, 23] Yoshino et al. were the first to report a Li-ion battery composed of an LCO cathode and a petroleum coke anode system in a patent from 1987.[24] Petroleum coke is more stable against solvent co-intercalation, yet delivers lower capacities than graphite (see yellow square Figure 1-2a).[25] This finding was confirmed by Dahn and coworkers in 1990.[26] As a result, the first commercially available Li-ion battery from Sony was based on the LCO/C system.[1, 11] The upper cut-off voltage of the cell was 4.1 V and the carbon anode had a capacity of 220 mAh/g.[1]

In the work by Fong, von Sacken, and Dahn, the beneficial effect of the addition of ethylene carbonate (EC) to the at that time state-of-the-art propylene carbonate (PC) based electrolyte was described.[26] Since EC does not co-intercalate into the layered graphite structure thereby avoiding graphite exfoliation,[26] this finding allowed the use of graphite as anode material in Li-ion batteries. Graphite anodes have a significantly larger specific capacity of 372 mAh/g compared to petroleum coke and are much safer than lithium anodes. Furthermore, the voltage

for lithium intercalation is only ~0.1 V above the metallic lithium potential yielding a high energy density. This low lithium intercalation potential of course also renders the graphite electrode surface to be reactive towards the electrolyte. However, in contrast to the repeated lithium plating and stripping on a metallic lithium anode, for graphite anodes no fresh surface is created during cycling. Therefore, for electrolytes containing EC,[26] a stable interface forms in the very first cycle between the graphite electrode and the electrolyte, which remains stable over a wide range of cycle numbers. This interface is the so-called solid electrolyte interphase (SEI) and was already introduced in 1979 by Peled.[27] It will be discussed in further detail in section 2.2.

Nowadays, graphite is used in essentially all Li-Ion batteries as anode material because of its comparably high specific capacity and the very low lithiation potential. The only anode active material candidate which has the potential to at least partially replace graphite in the anode is silicon (Si) due to its almost ten times higher specific capacity (~3600 mAh/g for the $Li_{15}Si_4$ phase[28]) at only roughly 0.3 V higher potential (see Figure 1-2a).[8, 28-32] In fact, nowadays small amounts of Si are already added to the negative electrode.[11] Its extremely high capacity enables a significant increase of the total anode capacity even when only low amounts of Si are added.[11] Furthermore, its high natural abundance and comparably low cost make silicon a very attractive anode material. However, due to huge volume changes occurring upon lithiation/delithiation of silicon particles the cycling stability of silicon electrodes is still unsatisfactory.[29, 30, 33-38] The large volume changes also arise when germanium electrodes are used, which analogously form a $Li_{15}Ge_4$ (specific capacity: ~1400 mAh/g[39]) phase upon lithiation. Despite its two orders of magnitude higher Li ion diffusivity compared to silicon,[40] the high cost of germanium makes an application of germanium in anodes very unlikely.

Besides the state-of-the-art graphite anode, another material offering good cycling stability is $Li_4Ti_5O_{12}$ (LTO), which can be reversibly lithiated to form $Li_7Ti_5O_{12}$. Yet, with a theoretical specific capacity of only ~175 mAh/g and an operating potential of ~1.6 V vs. Li/Li^+, Li-ion batteries with an LTO anode result in significantly lower energy densities compared to the ones using graphite, which makes them inadequate to be used in EVs. Nevertheless, because of its higher (de)lithiation potential, it is operated within the stability window of the electrolyte (see Figure 1-2a). Together with the only very low volume changes during lithiation/delithiation, it yields a long lifetime and good safety properties.[4, 41] When applied as nanopowder, it furthermore gives an excellent rate capability and low-temperature stability.[42]

In contrast to the anode material development, the cathode material development progressed in several steps. After the discovery of LCO in 1980,[20] it were Thackeray and Goodenough who discovered the lithium manganese oxide spinel ($LiMn_2O_4$, LMO) in 1983,[43] and thereby described the class of the spinels as potential cathode material. LMO operates in average at a slightly higher potential than LCO, and due to the use of manganese instead of cobalt it is cheaper than LCO. However, it delivers significantly lower specific capacities than the advanced layered oxides (with a theoretical capacity of 148 mAh/g, it will only deliver ~120-130 mAh/g_{LMO} in a full-cell with a graphite anode, because of the losses during SEI formation). Furthermore the presence of instable Mn^{3+} in LMO causes poorer electrochemical performance, at part due to Mn dissolution from the cathode and subsequent deposition on the anode.[44-48] The issues related to transition metal dissolution/deposition will be discussed later on in this PhD thesis.

In 1997, Amine et al. synthesized for the first time $LiNi_{0.5}Mn_{1.5}O_4$ (LNMO), also referred to as high-voltage spinel because it is operated at ~4.7 V vs. Li/Li^+ and belongs to the so-called 5 V cathode materials (see Figure 1-2b).[49] A few months later, the suitability of LNMO as cathode material was confirmed by Dahn and coworkers.[50] This material contains manganese in the more stable Mn^{4+}-state instead of Mn^{3+}, yet its specific capacity (147 mAh/g theoretical capacity, which yields ~120 mAh/g in an LNMO-graphite cell[51]) is still lower than in the layered oxides, and the very high operating voltage of LNMO is suspected to lead to electrolyte decomposition, especially at elevated temperatures.

Also in 1997, Padhi et al. synthesized $LiFePO_4$ (LFP) for the first time – a third class of cathode materials with olivine structure.[52] Due to its rather low operating potential of ~3.4 V vs. Li/Li^+ and its generally lower tap density,[11] it delivers lower energy densities than the before mentioned materials (see Figure 1-2b). However, due to its good power characteristics, thermal stability and long lifetime, it is widely used in power tools, hybrid electric vehicles, or for grid-scale storage applications.[42] Besides LFP, Padhi et al. also synthesized the structural derivatives $LiCoPO_4$ (LCP) and $LiNiPO_4$ (LNP), yet could not extract lithium from their structure.[52] In 2000, Amine et al. were the first to report electrochemical delithiation of LCP.[53] With an operating potential of ~4.8 V and a theoretical specific capacity of 170 mAh/g (orange triangle in Figure 1-2b), it exceeds a specific energy of 800 Wh/kg, which is well above the target specific energy of 750 Wh/kg on a material level required to reach ~300 Wh/kg on a cell level.[5] However, significantly lower practically accessible specific

capacities as well as structural instabilities causing a poor lifetime of LCP, hinder the usage of LCP as cathode material in commercial Li-ion batteries.[53-56]

Currently amongst the three different material classes, the layered oxides are most widely used and are considered as the most promising ones for automotive applications.[5, 10] From the estimated annual cathode active material production of 117 kt in 2015, 89 kt belong to the class of layered oxides.[11] Essentially all layered oxide cathodes belong to the class of the 4 V cathode materials (see Figure 1-2b). A common characteristic is the fact that their practically accessible specific capacity is significantly lower than the theoretical one of ~275 mAh/g. The first generation of LCO developed by Goodenough allowed only the extraction of roughly half of the lithium amount, yielding a practical capacity of ~140 mAh/g (blue diamond in Figure 1-2b). The reason for this limit were structural distortions leading to the transformation of the initial O3 structure (ABCABC stacking sequence of the oxygen layers) to a O1 structure (ABAB stacking) occurring at higher degrees of delithiation,[19, 57] as well as irreversible structural changes including the loss of oxygen from the lattice.[58-61] In the early 1990's, the Dahn lab worked extensively on applying the isostructural $LiNiO_2$ (LNO, yellow diamond in Figure 1-2b) as cathode material because of its significantly higher accessible specific capacity of >200 mAh/g compared to LCO.[62, 63] However, difficulties in synthesizing LNO in a well-ordered structure (alternating Li and Ni slabs in between the oxygen layers),[64-66] irreversible phase transitions occurring during charge-discharge cycling,[67] poor temperature stability in the charged state[68, 69] as well as its extremely high sensitivity towards surface impurities upon exposure to the ambient hindered the usage of LNO as cathode material.

$LiMnO_2$ (layered LMO) was also considered as cheaper alternative to LCO and LNO.[70] However, in contrast to LCO and LNO, it does not form the layered structure upon high temperature synthesis.[71-73] Instead, only more complicated synthesis routes like cation exchange[74, 75] or hydrothermal synthesis[76] yield the layered structure. Additionally, poor electrochemical cycling stability was reported for layered LMO due to its structural instability.[77, 78] Also substituting some of the Mn for Co or Ni did not yield the hoped for improvements with respect to the structural stability and electrochemical performance.[70]

Instead, mixing Co and Ni into the layered oxide structure to yield LNCO significantly stabilized the structure and its electrochemistry, as was reported for the first time by Delmas et al. in 1992.[79] The improved structural stability of $LiNi_{0.85}Co_{0.15}O_2$ (LNCO, bright blue diamond in Figure 1-2b) yielded higher capacities of ~180 mAh/g compared to LCO and superior cycling stability over LNO.[80] In contrast to LCO, LNCO does not undergo the O3 to

O1 phase transition resulting in the higher accessible capacity.[58, 61] Yet, in contrast to LCO based cells, the cell impedance of LNCO cells was found to increase with cycling,[19] which was ascribed to the diffusion of nickel into the lithium layer hindering the lithium ion transport within the layered structure,[19, 81, 82] a problem which is considered to be in part responsible for capacity degradation in any Ni-containing layered oxides, especially in the Ni-rich layered oxides.[83]

Besides mixing LCO and LNO to a solid solution yielding LNCO, also doping with $LiAlO_2$ was investigated as ab initio calculations suggested that the latter has an intercalation potential of 5 V vs. Li/Li^+.[84] Even though pure $LiAlO_2$ is electrochemically inactive,[85] it was investigated as part of a solid solution with LCO, LNO, or LNCO.[85-90] Substitution of Al to the latter yields $LiNi_xCo_yAl_zO_2$ (NCA) with $LiNi_{0.8}Co_{0.15}Al_{0.05}O_2$ being its most prominent representative delivering capacities of up to 200 mAh/g.[91] This material is already well developed and is used for instance in today's Tesla Model S.[5, 11] Yet, similar to the very Ni-rich NMCs, which will be discussed in the next paragraph, it suffers from a rather low thermal stability.[92-94]

In 1999, Liu et al. substituted the Ni in LNO simultaneously by Co and Mn and thereby reported for the first time the class of NMC cathodes.[95] Interestingly, coming from LNO they substituted a maximum of 50% of the Ni and therefore reported the Ni-rich subcategory of the NMC materials class, which nowadays probably comprises the most promising cathode materials for EVs. Their aging mechanisms are the primary topic of this PhD thesis. In particular, Liu et al. reported $LiNi_{0.5}Mn_{0.3}Co_{0.2}O_2$ (NMC532), $LiNi_{0.6}Mn_{0.2}Co_{0.2}O_2$ (NMC622, red diamond in Figure 1-2b), and $LiNi_{0.7}Mn_{0.1}Co_{0.2}O_2$ (NMC712). NMC materials with lower Ni-content were reported in 2001 simultaneously by the groups of Jeff Dahn and Yoshinari Makimura.[96, 97] Lu et al. derived the NMC from LCO by substituting Co^{3+} by equal amounts of Ni^{2+} and Mn^{4+}.[96] In particular, they synthesized $LiNi_{0.25}Mn_{0.25}Co_{0.5}O_2$ and $LiNi_{0.375}Mn_{0.375}Co_{0.25}O_2$. Similarly, Ohzuku et al. used equal contents of Ni, Mn, and Co to yield $LiNi_{1/3}Mn_{1/3}Co_{1/3}O_2$ (NMC111, black diamond in Figure 1-2b), which is until today one of the most common representatives of the NMC materials class.[97] In the report by Lu et al., the good thermal stability of NMCs with rather low Ni-content was already pointed out.[96] This is primarily due to the introduction of significant amounts of Mn into the layered oxide structure which yields improved temperature stability.[98-100] However, new challenges like electromobility require the energy density of Li-ion batteries to be improved, and nowadays the bottleneck is the cathode active material, whose specific capacities must be improved to

meet the energy density targets for EVs. That is the reason why research focuses on improving Ni-rich NMCs with rather low Mn-contents, because with rising nickel content the accessible specific capacity for a given cell cut-off potential is increased.[99, 101] For instance, at a cut-off voltage of 4.3 V vs. Li/Li^+ and a 0.1 C-rate, NMC811 (green diamond in Figure 1-2b) has a reversible capacity of ~190 mAh/g compared to ~150 mAh/g for NMC111.[99, 101] However, with rising Ni-content the synthesis of the NMC materials becomes more difficult[102] and only lower calcination temperatures are possible,[99] which may result in higher amounts of surface impurities which in turn lead to gassing and worse cycling performance. Additionally, a lower decomposition temperature of the layered oxides with growing Ni-content may also cause safety issues. These kind of problems have to be accounted for when Ni-rich NMCs replace state-of-the-art cathode materials. Some of the reasons which may cause the poorer stability of Ni-rich NMCs will be reviewed in greater detail in section 2.2 and in the studies presented in section 3.1. The most common NMCs used nowadays are NMC111 and NMC532.[11] NMC111, for example, is the cathode material used in today's BMW i3 EV (94 Ah version).

To improve the stability of the layered oxides, in the early 2000's several researchers focused on the stabilization of the LCO surface by coating it with Al_2O_3, ZrO_2, or TiO_2. These modifications significantly improved the cycling stability and also allowed charging the material to higher upper cut-off voltages (see blue arrow in Figure 1-2).[19, 103-107] These surface coating approaches are also pursued to stabilize the NMC surface especially of the Ni-rich NMCs to improve their cycling stability and enable higher cut-off potentials (black, red, and green arrows in Figure 1-2).[108-113] Nowadays, layered oxides with a maximum Ni content of 80-85%, e.g., NMC811 or NCA, are targeted to be accessible for large scale applications within the next years. Even higher Ni contents may be difficult to realize due to the poor safety characteristics as well as the problems occurring when the material becomes more and more similar to LNO with all its difficulties described above. In order to achieve higher capacities than in NMC811, core-shell as well as gradient materials have been developed.[114-121] The development of these materials was primarily pioneered by Yang Kook-Sun and Khalil Amine at Argonne National Laboratory. The general idea behind these novel materials is to achieve high capacities by a very Ni-rich core ($\geq$ 85% Ni)[116, 118, 121] and a reduced Ni content on the surface to improve the stability of the material. In an ideal case, this yields the cycling stability of low Ni-content NMCs but the capacity of high Ni-content NMCs. In fact, it was already shown that the cycling stability of gradient materials is similar to standard NMCs with the overall composition of the outer composition of the gradient material, yet due

to the Ni-rich core higher capacities are achieved.[115, 117, 118] Furthermore, the stabilizing effect of higher Mn-contents in the surface-near regions was also shown to render the material thermally more stable.[115, 117, 118]

Another potential material for high energy Li-ion batteries is the class of Li-rich layered oxides in which Li occupies besides the Li slabs also parts of the transition metal slabs. This materials class is capable to deliver reversible capacities larger than 250 mAh/g and was simultaneously discovered by the groups of Michael Thackeray[122] and Jeff Dahn[123]. This materials class is at an earlier development state compared to the Ni-rich NMCs, and besides a high irreversible capacity loss in the very first cycle and still unsatisfactory cycling stability, a further issue is its characteristic voltage fading behavior over the course of cycling causing a loss of energy and power.[11, 124]

Retrospectively, one might say that on the journey of cathode material development, LCO was initially proven to be superior over LNO. Later on, the derivatives from LNO with high Ni-content showed improved characteristics, yet NMCs with rather low Ni-content were preferred. Finally, nowadays research focusses on the Ni-rich NMCs and moves in terms of the Ni-content very close to LNO, where the journey began in the early 1990's. This strive to higher Ni-contents is on the one hand driven by the higher accessible capacities and energies but on the other hand also by the need to minimize the Co-contents due to resource constraints and highly problematic mining conditions. Since the early 1990's the understanding on the issues related to the layered oxides have grown drastically, which enables a much more precise tailoring of the material properties and raises the hope that almost 30 years of research experience enable the successful application of the very Ni-rich compounds. To summarize this section, some of the most important milestones in Li-ion battery research, particularly with respect to cathode active materials development and stabilization, starting in the 1970's until the 2000's are collected in Figure 1-3. It is perhaps still too difficult to name the innovations and findings which most strongly influenced the battery community within the last 10-15 years, and some more years will probably have to pass before this can be done.

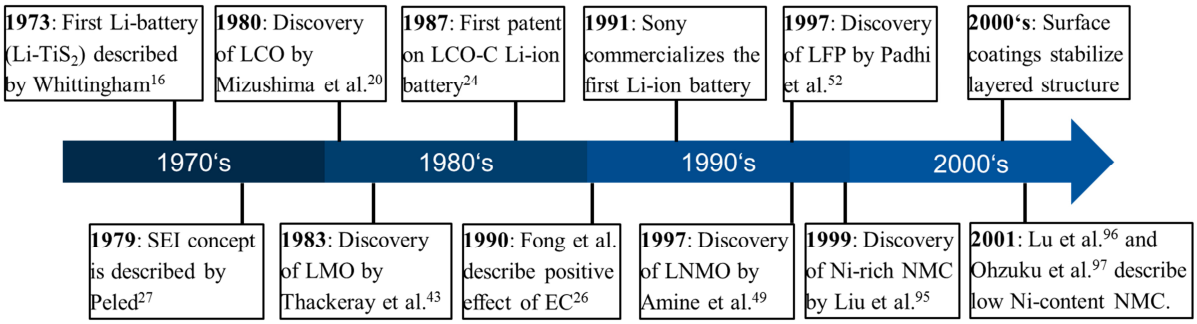

Figure 1-3 Some of the most important milestones in Li-ion battery research between 1970 and 2001, particularly with respect to cathode active materials development and stabilization.

2. Materials and Methods

2.1 Crystal Structure and Properties of $LiNi_xMn_yCo_zO_2$ (NMC)

The layered oxides LCO, LNO, NCA, and NMC crystallize in the trigonal system with the space group $R\bar{3}m$ (no. 166). Along the c-axis, Li and M (M = Ni, Mn, Co, Al) occupy alternating layers in between the oxide layers to give a layer sequence of O-Li-O-M- (Figure 2-1). In case M is a mixture of more than just one element, e.g., in NMC, the metals form a solid solution in the M layer. The lattice may alternatively be described by a cubic close-packed system of the oxide anions with the stacking sequence ABCABC, in which the octahedral voids are occupied in an ordered way by Li and M. This structure is also referred to as O3-structure, because the Li-ions occupy the octahedral interstices and there are three MO_2 sheets per unit cell.[19]

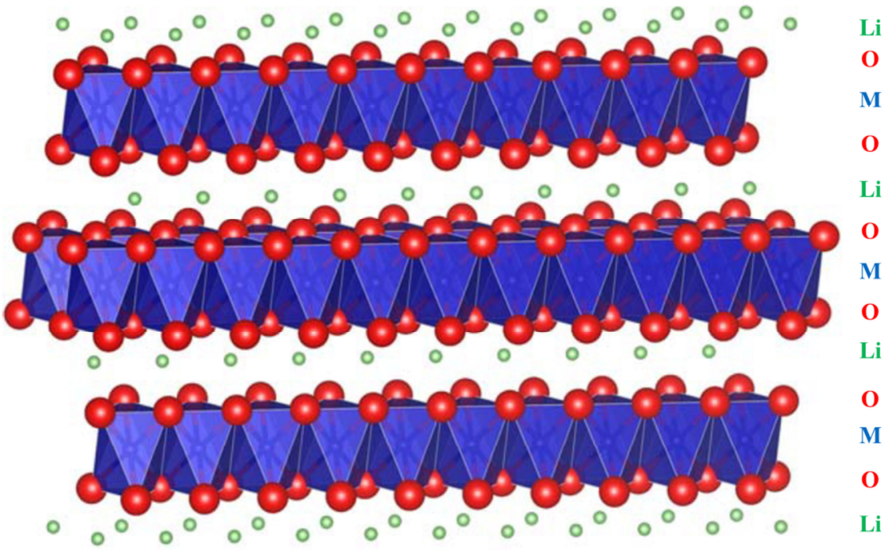

Figure 2-1 Crystal structure of layered oxides with the general formula $LiMO_2$. The structure is composed of alternating layers of lithium (Li, green) and transition metals (M, blue), which are separated by oxygen (O, red) layers. The figure was published in the Journal of the Electrochemical Society as open access article distributed under the terms of the Creative Commons Attribution Non-Commercial No Derivatives 4.0 License.[70]

NMC is typically synthesized by using $NiSO_4$, $MnSO_4$ and $CoSO_4$ as precursors and coprecipitating them in aqueous solution with NaOH to yield $(Ni,Mn,Co)(OH)_2$.[99] Subsequent calcination with Li_2CO_3 or LiOH yields the NMC structure. The metal composition is determined by the ratio of the transition metal precursors. The used calcination temperature depends on the nickel content and decreases with increasing nickel content, which is one of the reasons why the Ni-rich compounds are more challenging to synthesize at a good quality.

At low to moderate nickel contents the calcination can be performed under air, whereas high nickel contents do not allow the presence of CO_2 due to the formation of carbonates on the surface so that they are typically calcined in CO_2-free synthetic air or pure oxygen atmosphere.[102] This also does not allow the use of Li_2CO_3, as it decomposes during calcination under formation of CO_2. Furthermore, with growing nickel content the NMCs are more prone to cation mixing (see section 2.2),[83, 99] which detrimentally affects the lithium ion diffusion during charge/discharge of the material. To limit cation mixing, the Li-precursor can be added in an excess amount, however, this may yield higher amounts of residual lithium compounds on the surface of the NMC.[99]

Figure 2-2 shows typical SEM micrographs of NMC with (a) 1700-fold and (b) 13000-fold magnifications. The particles depicted in Figure 2-2 are secondary particles with diameters on the order of ~5-10 µm, which consist of sintered primary particles of ~100-200 nm diameter.

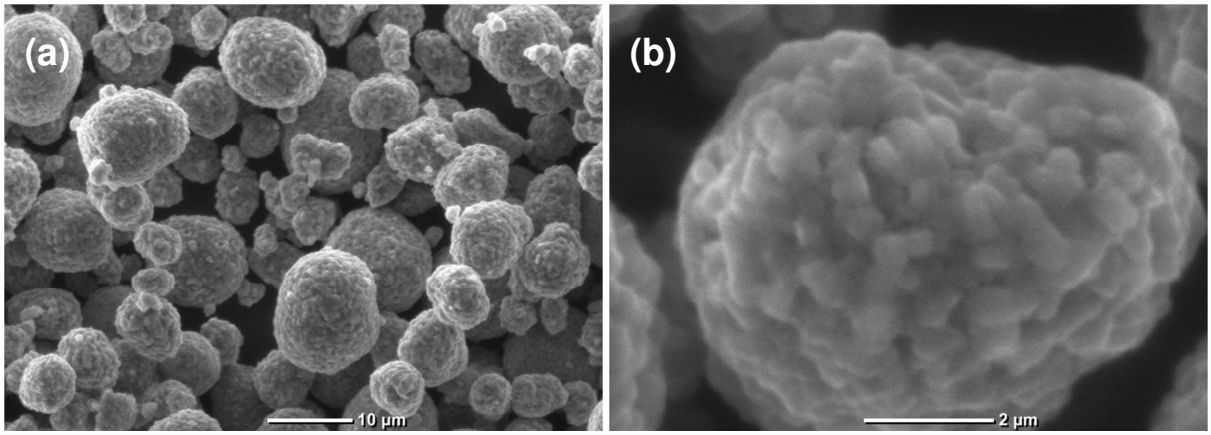

Figure 2-2 Typical SEM micrographs of NMC622. The particles are nearly spherical with diameters of 3-13 µm. Magnifications are (a) 1700× and (b) 13000×.

As a rule of thumb, higher specific capacities but lower thermal stabilities are obtained for NMCs with increasing Ni content. Co improves the rate capability and capacity but increases the cost of the material, while Mn renders the material more stable and cheaper but reduces the specific capacity and electrical as well as ionic conductivity. The theoretical specific capacities of all NMCs are very similar with ~275 mAh/g due to the very similar molar masses of Ni, Mn, and Co. However the practically accessible capacity at a given upper cut-off potential increases with the nickel content. For instance, at a cut-off voltage of 4.3 V vs. Li/Li^+ and a 1C-rate, NMC111 has a reversible capacity of ~140 mAh/g, which can be increased to ~160 mAh/g and ~175 mAh/g for NMC622 and NMC811, respectively.[101] Additionally, the electronic conductivity increases from ~5×10^{-8} S/cm to ~2×10^{-5} S/cm as the nickel content is increased from NMC111 to NMC811.[99] The Li-diffusivity increases for the

same materials from ~10^{-11} cm²/s to ~10^{-9} cm²/s.[99] Therefore, besides the higher accessible specific capacity within a given voltage window for Ni-rich NMCs the improved electronic conductivity and Li-diffusivity may also yield improved rate capabilities. However, with rising Ni-content several researchers reported faster cell aging,[83, 99, 101, 125] and a thermally less stable structure.[94, 98-100]

2.2 Aging Mechanisms in a Lithium-Ion Battery

Capacity fading in a Li-ion battery during cyclic aging is mainly due to irreversible side reactions occurring on the anode or the cathode. Figure 2-3 depicts some of the most important processes which lead to aging of a Li-ion battery. On the anode this includes impedance growth, lithium plating, and loss of cycleable lithium due to SEI formation and its subsequent cracking/growth. In case silicon anodes are used additionally particle cracking and electrical contact loss of some particles may contribute to capacity fading. On the cathode this includes cation mixing, transition metal dissolution, electrochemical electrolyte oxidation, as well as surface transformations including the release of reactive oxygen into the electrolyte inducing chemical electrolyte oxidation. Additionally, the products formed upon electrolyte oxidation and dissolved transition metals may diffuse to the anode and become reduced there, causing additional side reactions. This interaction between cathode and anode is referred to as cross-talk.[126, 127] In the following, these aging mechanisms will be discussed in greater detail.

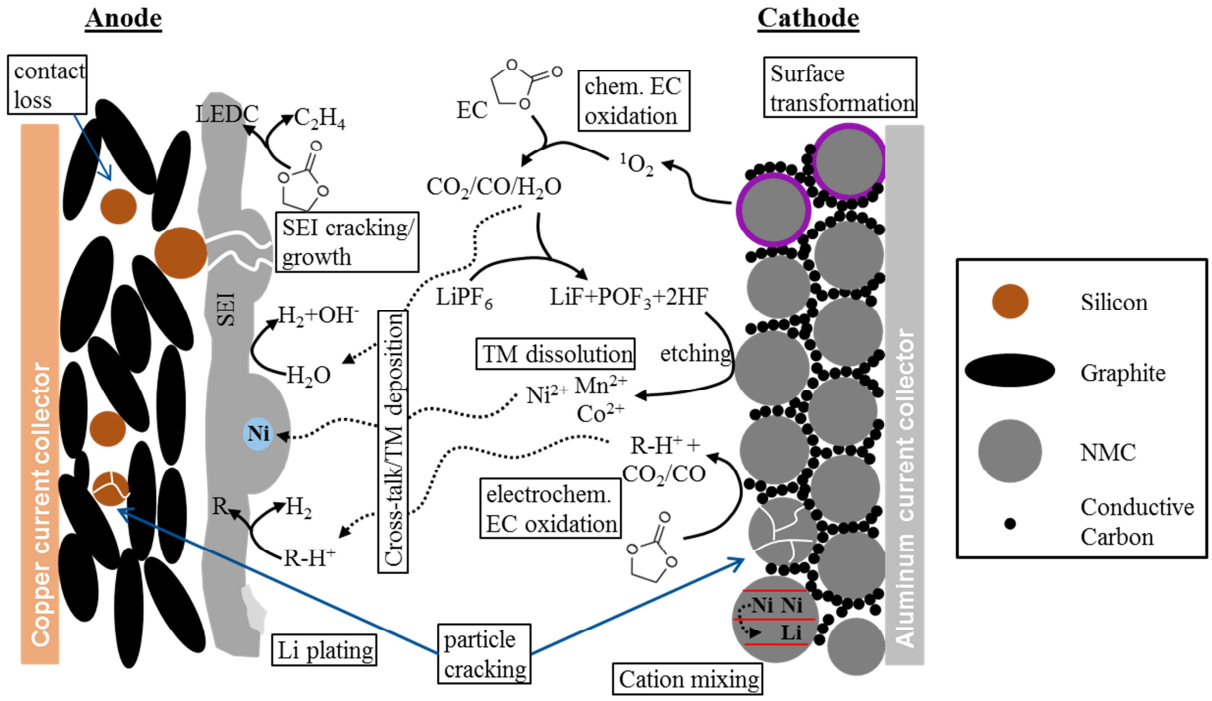

Figure 2-3. Schematic illustration of the most important aging mechanism occurring in a Li-ion battery.

Capacity fading caused by graphite and silicon anodes arises primarily from the formation and growth of the SEI. Due to the very low lithium intercalation potential of 0.1 – 0.5 V vs. Li/Li^+ which is below the reductive stability limit of the electrolyte, an SEI is formed. This protective layer passivates the electrode and prevents the electrolyte from further reduction

during extended cycling. It consists of electrolyte reduction products like LiF, Li_2CO_3 and lithium ethylene dicarbonate (LEDC).[36, 128, 129] The formation of these compounds binds Li-ions irreversibly, so that they cannot be used during charge/discharge cycling anymore. The SEI is typically between 10-100 nm thick, permeable for lithium ions but electronically insulating.[22] The latter property avoids the continuous electrolyte reduction on the anode (passivation). Consequently, stable cycling of a Li-ion battery with a graphite and/or silicon anode operating below the reduction potential of any commonly used non-aqueous electrolyte solvent is only possible because of the metastable state caused by the SEI layer.

To keep the loss of cycleable lithium during SEI formation (within the first cycle) as small as possible, an optimum balancing between the anode capacity and the cathode capacity is required. A too high ratio of anode to cathode capacity causes large irreversible lithium losses in the first cycle, whereas too small anode to cathode ratios will cause Li-plating on the anode if not all of the Li-ions extracted from the cathode can be intercalated into the anode. One peculiarity when NMC-graphite cells are used is that both the graphite anode as well as the NMC cathode have an irreversible capacity loss. In particular, not all the lithium which is deintercalated from the NMC cathode in the first charge cycle can be reintercalated during discharge due to kinetic limitations.[130-132] This first-cycle irreversible capacity loss of NMC is very similar in magnitude compared to the SEI formation on conventional graphite anodes, so that hardly any "additional" Li is lost in the SEI on the graphite. Ideally, once the SEI is formed it is stable during the complete lifetime of the Li-ion cell. However, as a consequence of small volume changes of ~10%[31] between C_6 (fully discharged state of graphite) and LiC_6 (fully charged state), the SEI slowly cracks during extended charge/discharge cycling which is repaired at the cost of additional loss of lithium ions. This phenomenon is very pronounced when the anode contains silicon,[29, 30] which changes its volume by roughly 300% between the fully lithiated and delithiated state.[28, 31, 133] The accompanied consumption of electrolyte will be discussed in the studies presented in sections 3.3.1 and 3.3.2. Furthermore, SEI decomposition (e.g., LEDC $\rightarrow$ $Li_2CO_3 + C_2H_4$) and dissolution, especially at elevated temperatures, cause further lithium loss over time. These processes are the primary causes for capacity loss for Li-ion batteries with well-developed cathodes and anodes.[132, 134, 135] To minimize the loss of cycleable lithium, a stable SEI is desired over a very long time and many cycles. This may be achieved by the use of appropriate electrolyte additives which improve the stability of the SEI.[30, 136-139] Upon reduction these additive molecules form a more stable SEI layer on the graphite anode than the standard electrolyte components and thereby significantly improve the lifetime of a Li-ion battery. Yet, in some cases the improved SEI

stability comes at the expense of an increased anode impedance. Extensive SEI formation which is especially present on silicon electrodes may also cause a clogging of the pores in the electrode leading to increased impedance due to hindered Li-ion transport. Also particle cracking and particle degradation mechanisms may lead to increasing impedances and capacity losses due to the loss of electrical contact between the particles.[29]

As the lithiation of graphite is very close to the metallic lithium potential, especially at high charging rates or low temperatures, another phenomenon may occur, viz., the plating of metallic lithium on the graphite anode.[134, 140-144] Lithium plating may occur on the graphite surface due to the formation of a steep Li^+ ion concentration gradient throughout the thickness of the electrode. In this case, the graphite anode is inhomogeneously charged and in order to intercalate Li^+ into graphite at low Li^+ ion concentration (close to the current collector), the potential of the electrode must be lowered because the Nernst potential shifts to a lower value. If this shift in the Nernst potential is significantly strong, the electrode potential drops below the lithium plating potential in the region close to the separator where the Li^+ ion concentration is high so that lithium plating occurs at the interface of the anode and the separator. Alternatively, high impedances, e.g., caused by thick SEIs, lead to high overpotentials at high rates, so that Li plating may become thermodynamically possible. This is based on the assumption that the additional SEI resistance does affect the lithium intercalation, but not the lithium plating reaction. In this case, Li plating can occur in the absence of Li^+ concentration gradients in the electrode and is not restricted to the region close to the separator. Even though some of the plated lithium may dissolve in the subsequent discharge, the plated lithium is chemically reactive towards the electrolyte and SEI formation on its surface leads to a loss of cycleable lithium. Alternatively, the plated lithium may form dendrites which eventually shorten the two electrodes or it loses the contact to the graphite electrode to form so-called dead lithium, which is lost for charge/discharge cycling.[142, 145]

The aging mechanisms from the cathode material vary for the different cathode active materials. As in this PhD Thesis the focus lies primarily on NMC cathodes, some of the relevant degradation phenomena for layered oxides will be described in this section. In Figure 2-4 the voltage versus specific capacity of an NMC111-graphite cell is plotted including the respective half-cell potentials of NMC111 and graphite versus a Li-reference electrode. As already described above, the voltage profile of the graphite anode is already very close to the metallic lithium potential and therefore close to the optimum value for an anode. In contrast, the layered NMC111 cathode has a sloped voltage profile, hence, an increase of the upper cut-

off voltage results not only in an increase of the mean cell voltage but also in an increasing specific capacity. Therefore, according to equation (1.2) it has a two-fold effect on the energy density of the Li-ion battery. Even though charging the cell to high cell potentials around 5 V would maximize the energy density, this is prohibited by the fast cell aging at high upper cut-off potentials, ascribed to several aging mechanisms: Particle cracking,[121, 146] inherent material instability reported for various layered oxides at very high states of charge,[99, 101, 147-151] transition metal dissolution,[132, 152-155] and electrolyte decomposition.[51, 101, 147, 156, 157] The investigation of some root causes of this accelerated cell degradation will be analyzed within this PhD thesis (section 3.1).

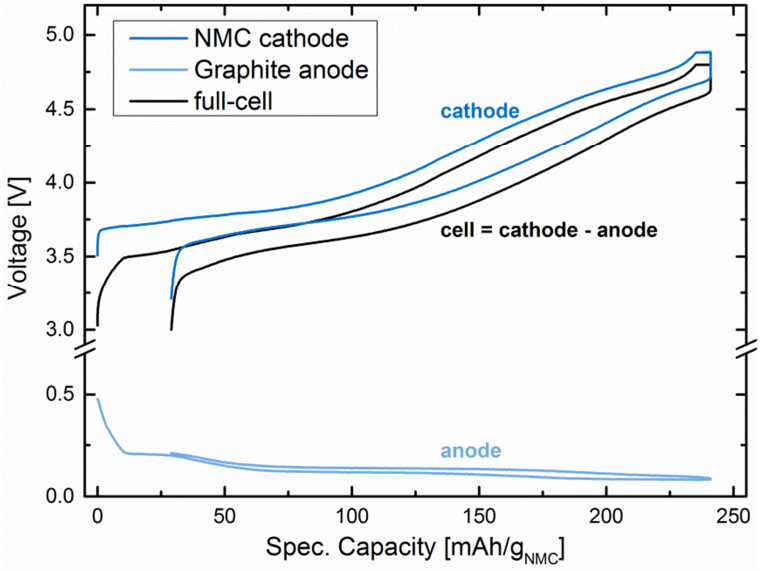

Figure 2-4 Voltage profile of the first cycle of an NMC111-graphite cell (black) in LP57 electrolyte (1 M $LiPF_6$ in EC:EMC 3:7) including the respective half-cell potentials of the NMC111 cathode (dark blue) and the graphite anode (bright blue). The half-cell potentials are measured using a Li-reference electrode. The areal capacity ratio of anode to cathode is 1.2 based on the reversible capacities of the active materials. Charge and discharge are performed at a 0.1 C-rate. During charge at 4.8 V, a CV-step with a current cut-off of 0.05 C is applied.

The volume of NMC changes only slightly during charge/discharge cycling (~5% for NMC811 cycled to 4.3 V vs. Li/Li^+ [158] and <2% for NMC111 at 4.5 V vs. Li/Li^+ [158, 159]). However, these repeated volume changes in every single cycle may still cause micro cracking of the secondary particles especially for the Ni-rich compounds.[121, 146] On the one hand, this may deteriorate the electrical contact between the primary particles, and on the other hand, it increases the surface area which consequently may accelerate side reactions like chemical electrolyte decomposition processes[101, 147, 160-162] or electrochemical electrolyte oxidation.[147] Some of these processes will be discussed in more detail later on in this section as well as in the sections 3.1.2-3.1.4.

When the upper cut-off voltage of a cell containing NMC is increased, more Li is removed from the layered structure. This may accelerate the diffusion of transition metals into the less and less filled Li slabs. This so-called cation mixing will cause capacity fading due to increased impedance, as the transition metals significantly hinder the Li diffusion pathways within the NMC material.[83] The tendency for diffusion into the Li slabs decreases in the order Ni > Co > Mn.[83] Therefore, this aging mechanism is more pronounced in Ni-rich NMCs. Due to the low diffusion tendency of manganese, its presence is supposed to stabilize the layered NMC structure.

The diffusion of transition metals from the octahedral voids of the transition metal slab into the octahedral voids of the Li slabs occurs via the neighboring tetrahedral voids.[98, 163, 164] This diffusion is simultaneously the first step to an even more severe structural change. In particular, the diffusion of transition metals into the Li slab may be followed by Li or additional transition metal diffusion into the tetrahedral voids of the Li slab, yielding a disordered spinel structure that may further transform into a rock-salt type structure. In our recent works (sections 3.1.2 and 3.1.4) on NMC111, NMC622, and NMC811, we show that under battery operating temperatures (<60 °C) the formation of spinel and/or rock-salt phases occurs under release of reactive oxygen from the layered NMC structure once ~80% of the lithium is removed from the NMC structure.[101, 165] As will be shown in the results section (3.1.1 – 3.1.4), the release of oxygen occurs primarily from the particle surface.[101] Additionally, the onset of oxygen release directly correlates with a significant drop in the cycling stability,[101] which in part has its origin in the severe impedance growth upon the phase transformation on the surface,[101, 148-151, 166] as the disordered spinel and rock-salt phases have a significantly reduced Li-ion conductivity. In other words, to allow for a stable cycling, the upper cut-off voltage of the battery cell has to be kept below the onset potential for oxygen release.

The structural transformation of the layered structure to spinel or rock-salt phases under release of lattice oxygen was previously also shown to occur when the layered oxides are charged and afterwards heated up to temperatures >170°C.[94, 98-100] In these experiments the structural decomposition is a bulk effect, whereas under battery operating conditions the phase transformation is limited to the particle surface due to limited solid state diffusion of oxygen. Even though temperatures >170°C are well above normal battery operation these findings clearly demonstrate that the layered structure is thermodynamically not stable when it is delithiated and in the absence of kinetic barriers will decompose exothermically to spinel

and rock-salt type phases.[94, 98-100] In fact, these experiments became very useful to investigate the safety of the cathode material, because in the case of uncontrolled heating of the cell, the release of oxygen gives additional 'fuel' to further propagate the heat generation, causing the so-called thermal runaway.

As will be presented in sections 3.1.1–3.1.4, oxygen release not only results in the decomposition of the particle surface, but also leads to the oxidation of the electrolyte and therefore is very harmful for the long-term durability of a Li-ion battery.[101, 147] As it was hypothesized in our work and proven very recently,[167] at least some part of the oxygen is released as singlet oxygen which is very reactive towards the electrolyte leading to a *chemical* oxidation of the electrolyte.[101, 147, 168] In contrast to the *electrochemical* electrolyte oxidation, the *chemical* pathway has a distinct onset and has to be avoided to prevent NMC particle degradation and electrolyte breakdown.[101, 147, 168] As a matter of fact, today's batteries typically limit the end-of-charge voltage to ~4.2 V.[11] Yet, at this potential a significant portion of the theoretical capacity of layered oxides remains unused (Figure 2-4). Therefore, in an attempt to increase the end-of-charge voltage to obtain higher capacities one has to be careful to stay below the threshold voltage for oxygen release, which sets in for all NMCs once ~80% of the lithium ions are removed from the layered structure.[101, 165, 167] This SOC limit is reached for Ni-rich NMCs at lower potentials, which minimizes the impact of *electrochemical* electrolyte oxidation at high voltages. As *electrochemical* electrolyte oxidation does not have a distinct onset potential but increases exponentially with the potential even low amounts of electrolyte oxidation per cycle may accumulate to substantial amounts over a long time.[147] The dependency of the *chemical* and *electrochemical* electrolyte oxidation pathways on the potential as well as active material surface will be discussed in detail in the studies presented in sections 3.1.2 and 3.1.3. The electrolyte oxidation products may form a resistive film on the cathode surface, the so-called cathode electrolyte interface (CEI), which eventually may cause impedance growth.[169-174] As the CEI layer is believed to be rather thin its presence was debated for a long time and current research progress indicates that impedance growth on the cathode material may primarily stem from the surface transformation of the layered oxide structure to spinel and/or rock-salt type phases.[101, 148-151, 166]

During *chemical* and *electrochemical* electrolyte oxidation the decomposition products may further diffuse to the anode and react/deposit there, causing gas evolution or a decomposition of the SEI layer.[101, 126, 127, 175, 176] This cross contamination is referred to as cross-talk between cathode and anode.[126, 127, 175] During electrolyte decomposition, the formation of protic species

like H_2O, ROH, H^+, etc. is very likely,[101, 175, 177, 178] which subsequently cause among other reactions the decomposition of the $LiPF_6$ conducting salt according to the following reactions:[179-182]

$$\mathbf{LiPF_6 + H_2O \rightarrow LiF + POF_3 + 2\ HF} \quad (2.1)$$

$$\mathbf{LiPF_6 + H^+ \rightarrow Li^+ + PF_5 + HF} \quad (2.2)$$

Besides the formation of potentially corrosive POF_3 and PF_5 gas, the formation of HF will promote the etching of the cathode material leading to the dissolution of transition metals into the electrolyte, which is known as another severe aging mechanism.[132, 152-155] Subsequent diffusion of the transition metals to and deposition on the graphite anode leads to the loss of active lithium as a consequence of additional SEI formation. This phenomenon will be discussed in greater detail in the studies presented in the sections 3.2.1 and 3.2.2.

2.3 Used Experimental Techniques

In the studies presented in section 3, a large variety of experimental techniques were used to characterize and analyze the degradation phenomena occurring on the different materials. Electrochemical charge/discharge cycling was performed to characterize the used materials. The experiments were either done in a half-cell set-up with a metallic lithium counter electrode, in which case the lithium inventory is quasi infinite so that observed capacity fading may be accounted to material or electrolyte degradation, or in a full-cell set-up in which case the cathode material defines the lithium inventory. In the latter case capacity fading may also be ascribed to the loss of cycleable lithium, typically associated with continuous SEI formation on the anode (see section 2.2 for further details). For full-cell cycling, Swagelok® T-cells were typically used. A schematical drawing as well as a photograph are depicted in Figure 2-5. It consists of the working and counter electrode, separated by a glassfiber or polyolefin separator soaked with electrolyte. The electrodes are contacted with stainless steel bars (marked as Anode and Cathode). The electrode stack is compressed by a spring, applying a compression of ~1–2 bar. One advantage of a T-cell is that it allows the optional use of a reference electrode, typically a small piece of lithium metal that has a stable potential which does not shift over time, which is also contacted with a stainless steel bar (marked as Reference). The latter is essential to independently monitor the half-cell potential of the working and counter electrode and to deconvolute the aging mechanisms associated with the cathode and the anode. For example, during a battery cell degradation a reference electrode helps to distinguish if it is due to aging of the anode and/or the cathode. Furthermore, independently monitoring the potential profiles of anode and cathode gives insights into the evolution of the polarization over several cycle numbers for each electrode.

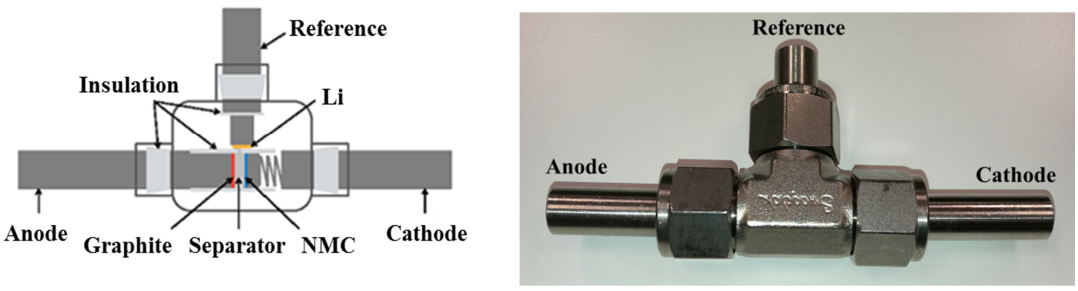

Figure 2-5 Schematical drawing and photograph of a 3-electrode Swagelok® T-cell.

One major drawback of Swagelok® T-cells is the fact that the electrolyte amount which is placed between anode and cathode is undefined to a certain extent, since this cell design contains hollow space outside the electrodes an the separator, into which the electrolyte can flow. An alternative set-up are coin-cells: While we have not been able to build them with a reference electrode, the electrolyte volume between anode and cathode can be defined rather precisely due to the compact design, which is shown in Figure 2-6. It is therefore very useful when the focus lies on electrolyte decomposition and consumption, as presented in the studies in sections 3.3.1 and 3.3.2.

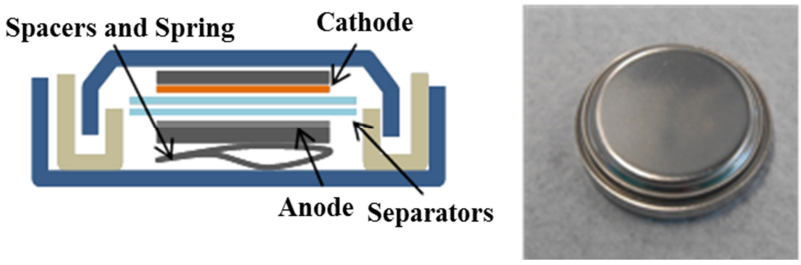

Figure 2-6 Schematical drawing and photograph of a coin cell.

In the work presented in the sections 3.1.1–3.1.4, the most insightful technique was On-Line Electrochemical Mass Spectrometry (OEMS). The set-up was developed at the Chair of Technical Electrochemistry at Technical University Munich, and is depicted schematically in Figure 2-7. It was described in detail in previous publications.[42, 183]

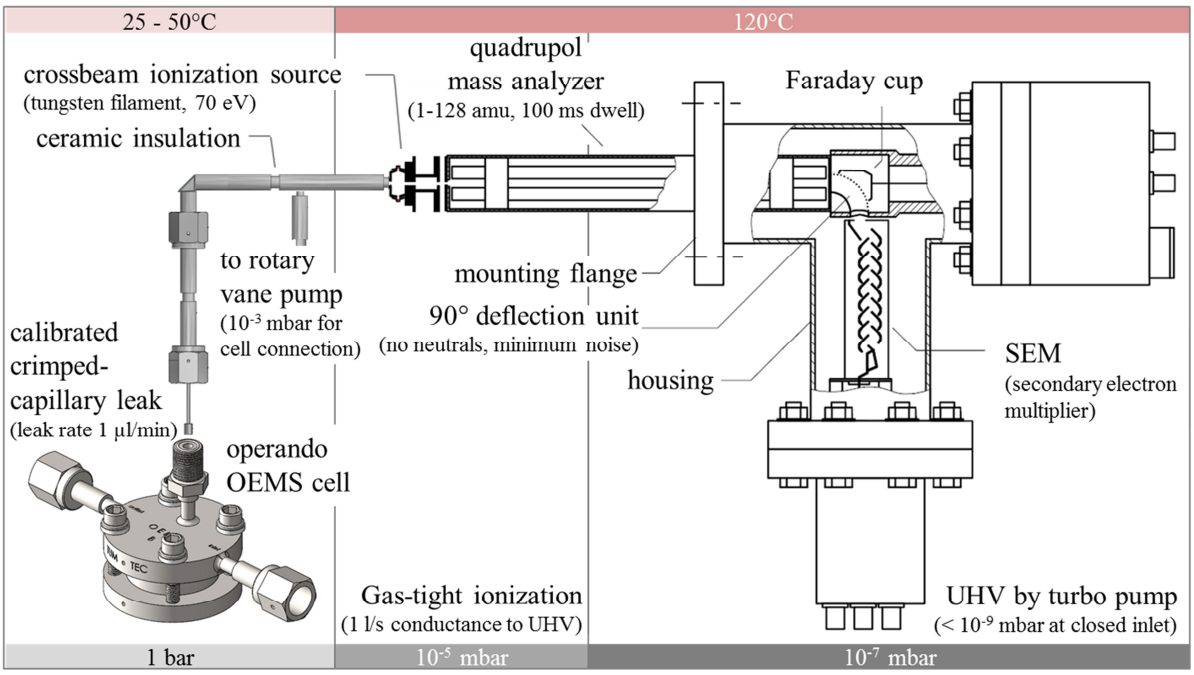

Figure 2-7 Schematic illustration of the OEMS set-up. The figure is adapted with minor changes from Reference 42 with permission from the author.

In brief, the set-up consists of a sealed OEMS cell, which is connected via a capillary with a calibrated leak of ~1 µL/min to the mass spectrometer system. OEMS is an operando technique which is used to measure the gas evolution and consumption during cell operation. Quantification of O_2, CO_2, CO, C_2H_4, and H_2 was done by flushing the OEMS cell at the end of the measurement with a calibration gas containing 2000 ppm of the gases in argon and measuring the response of the respective signals in the mass spectrometer. In this PhD thesis (sections 3.1.1–3.1.4), OEMS is primarily used to detect the oxygen release from Li- and Mn-rich NMC (section 3.1.1) and from stoichiometric NMCs with various Ni:Mn:Co ratios (sections 3.1.2–3.1.4). It aided to significantly advance the fundamental understanding of the degradation processes occurring in NMC materials. Furthermore, it was essential to understand the interdependency between the oxygen release and the CO_2 and CO evolution in a Li-ion battery which ultimately led to an improved understanding of the *chemical* electrolyte oxidation mechanism, clearly different from the *electrochemical* electrolyte oxidation pathway (section 3.1.3). OEMS can also be used to analyze the gas formation due to electrolyte reduction during SEI formation. In particular, in the study presented in section 3.3.1, it was used to determine the ratio of fluoroethylene carbonate (FEC) to ethylene carbonate (EC) reduction on a silicon-carbon composite electrode.

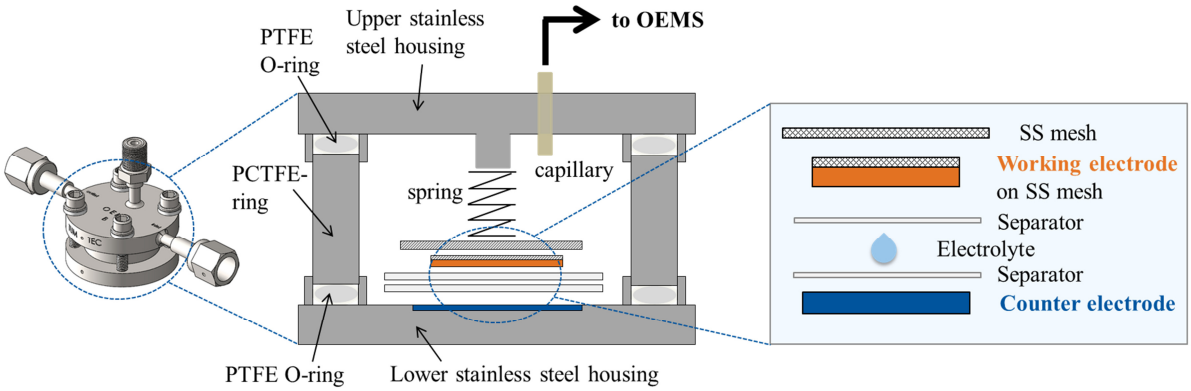

Figure 2-8 Schematical illustration of the OEMS cell.

More details of the OEMS cell which is depicted in the lower left corner of Figure 2-7 are shown schematically in Figure 2-8. The cell consists of the upper and lower part of the stainless steel housing, with the upper part being on the potential of the working electrode and the lower one on the counter electrode potential. To avoid a short circuit between the housing and to have the housing parts at a constant distance, the upper and lower housing is connected with a PCTFE (polychlorotrifluoroethylene) spacer. Between the housing parts and the PCTFE spacer a PTFE (polytetrafluoroethylene, Teflon) O-ring is placed which seals the cell via its plastic deformation. The capillary which connects the cell with the mass spectrometer system is passed through the upper housing part. With a cell volume of ~9.5 mL and a capillary leak of ~1 µL/min this set-up allows for measurement times of ~40 h with still acceptable changes to the cell pressure.

For cell assembly, the counter electrode (either metallic lithium, graphite, or LFP) is placed on top of the lower housing part (see blue rectangle in Figure 2-8). Afterwards, the separators containing most of the electrolyte are added and then the working electrode is placed on top. One peculiarity is that the working electrode is coated on a porous substrate to allow for a fast diffusion of the evolved gases to the head space of the OEMS cell, thereby improving the time and voltage resolution of the OEMS experiment.[183, 184] Typically, the porous substrate is a stainless steel mesh (see Figure 2-8), yet also a direct coating onto the separator or carbon fiber paper is possible. Finally, another stainless steel mesh is placed on top of the working electrode and the electrode stack is compressed with a spring (see middle panel of see Figure 2-8). To compare gas evolution occurring from different active materials or electrodes with different mass loadings, normalization of the gas evolution to the surface area of the active material is very convenient. This also allows an estimation of the expected gas evolution occurring in larger format cells with much higher active material amounts than those used in

the rather small OEMS cell. To determine the specific surface areas of the various investigated materials, nitrogen adsorption according to the theory developed by Brunauer, Emmett and Teller was applied to obtain the so-called BET surface area.

In the studies with a focus on silicon electrodes (sections 3.3.1 and 3.3.2) electrolyte consumption is a very severe effect due to the instability of the formed SEI caused by the large volume changes of the silicon particles during lithiation and delithiation. The consumption of the electrolyte additive FEC was investigated and quantified by liquid state ^{19}F-NMR spectroscopy. Fluorine is a mononuclidic element with ^{19}F being the only stable isotope with a spin of ½ and a natural abundance of 100%. This, coupled with the high gyromagnetic ratio makes the ^{19}F nucleus very NMR-sensitive. In the absence of a magnetic field, the spin states +½ and -½ are degenerated. Once a fluorine containing molecule is placed in a magnetic field, the energy levels of the two spin states separate. The difference in energy between the levels is dependent on the gyromagnetic ratio and the effective magnetic field, which differs for various chemical environments and can therefore be used to differentiate between fluorine species in different molecules. In sections 3.3.1 and 3.3.2 we analyzed the electrolyte after cell cycling with the only fluorine containing compounds being FEC and the PF_6^- anions. As the decomposition of $LiPF_6$ is negligible compared to the FEC consumption, we used the peak corresponding to PF_6^- as internal standard to measure the consumption of FEC. Besides this, NMR can also be used to observe changes to the electrolyte or to determine the purity of an electrolyte by extending the analysis to further nuclei like ^{1}H, ^{31}P, or ^{13}C. For example, ^{1}H and ^{13}C-NMR spectra were used to detect, identify, and quantify impurities before and after distillation of ^{13}C-labelled EC, which could not be delivered in the required purity (section 3.1.4).

In the study presented in section 3.1.5, we studied the formation of surface species on NMC811 upon storage at ambient air. For this, Raman spectroscopy and X-ray photoelectron spectroscopy (XPS) were employed to detect and identify surface species. In Raman spectroscopy, vibrational modes which cause a change in the polarizability of a molecule or solid are Raman active and can be analyzed. This is in contrast to infrared (IR) spectroscopy which also analyzes vibrations, however, for a vibrational mode to be IR-active a change in the dipole moment is required. XPS is a very surface sensitive technique and probes the material until a depth of 3-5 nm due to the very limited mean free path of the photoelectrons.[185] Knowing the energy of the incident X-ray beam and analyzing the kinetic energy of the photoelectrons, one obtains the binding energy of the electron which is very

characteristic for every element. Slight shifts in the binding energies are caused by different oxidation states or a change in the chemical environment of an element, which provides further insights to characterize the surface of a material. With the aid of Raman spectroscopy and XPS we found the formation of carbonate species on the surface of NMC811 during storage at ambient air. To quantify these species, hydrochloric acid was added to the sample and the evolved CO_2 according to equation (2.3) was quantified by the use of gas chromatography (GC).

$$\mathbf{CO_3^{2-} + 2\,HCl \rightarrow CO_2 + 2\,H_2O + 2\,Cl^-} \quad (2.3)$$

In GC a gas mixture is separated into its single components by a flow of the gas mixture through a column with a carrier gas (argon in our studies). As various gases differ in their interaction with the column, their retention times, i.e., the time required for a specific gas to flow through the column, are different so that they reach the detector – placed at the end of the column – at different points in time. Quantification of the detected gases is accomplished by calibrating the system with defined gas concentrations in the carrier gas and measuring the response of the detector.

In the studies presented in section 3.2, operando X-ray absorption spectroscopy (XAS) was used to measure transition metal dissolution from NMC and its subsequent deposition on a graphite anode as well as to determine the oxidation states of the precipitates. In XAS one may distinguish between the so-called X-ray absorption near edge structure (XANES) and the extended X-ray absorption fine structure (EXAFS). The latter contains information on the chemical environment of the measured species. In particular, number and distance to the neighboring atoms may be determined. In contrast, the XANES region contains information on the amount of the measured species which is linked to the intensity of the absorption edge – also referred to as edge jump – and the oxidation state of the examined species which is linked to the edge position on the energy axis. Quantification of deposited transition metals was done by first establishing a calibration curve from measurements of the edge jump of the transition metals dissolved at different concentrations. Oxidation state determination was done by comparing the edge position to compounds with a known oxidation state. All measurements were performed operando in a cell which was jointly developed at the Chair of Technical Electrochemistry at Technical University Munich and the van't Hoff Institute for Molecular Sciences at University of Amsterdam. The cell design is schematically illustrated in Figure 2-9 and was described in detail in previous publications.[145, 186]

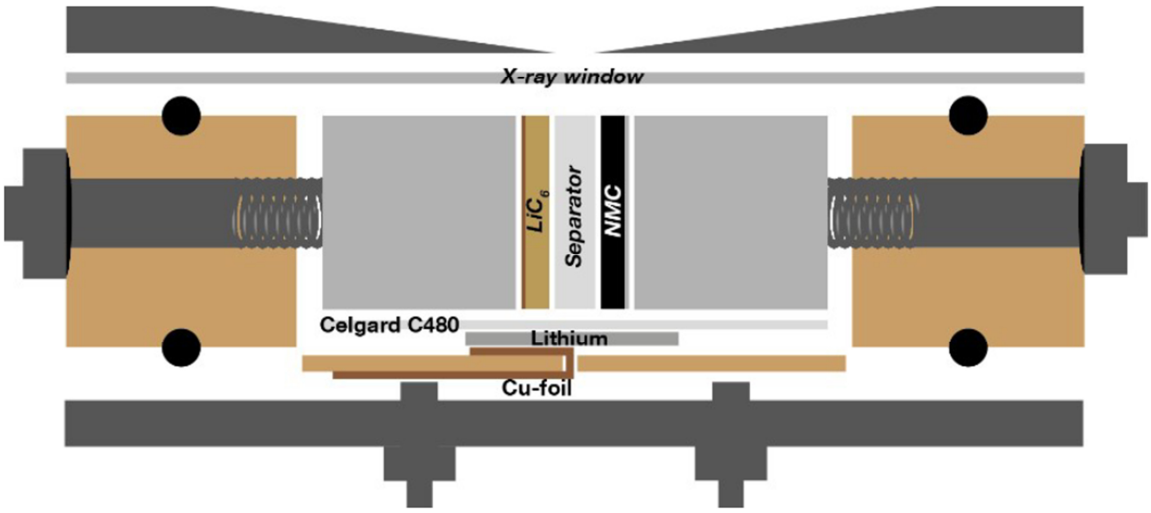

Figure 2-9 Schematic illustration of the operando XAS cell. The scheme is reproduced from Reference 152 with permission from The Royal Society of Chemistry.

In brief, the cell consists of the electrode stack (anode, separator, and cathode) with a square geometry of 1 cm × 1 cm size which is compressed by two springs pressing on an aluminum (cathode) and copper (anode) cube. The electrode stack is aligned perpendicularly to the X-ray window. To seal the cell against ambient air and simultaneously to be as transparent as possible to the X-rays, an aluminized Kapton window (100 nm Al on 12 µm Kapton) was used. The focused X-ray beam hits the sample at a 45° angle and is set to a width of 100 or 140 µm, thereby probing a thickness in the electrode plane of ~140 and ~200 µm, respectively. The length of the beam was adjusted to 1000 µm. The used graphite electrode thickness was always larger than the probed thickness to enable an exclusive focus on the graphite electrode. A lithium reference electrode can be optionally added to the cell to measure the potentials of anode and cathode independent of each other.[152]

3. Results

In the following sections all the published and unpublished work comprising this PhD thesis will be presented. The publications and manuscripts are topically grouped into three different main sections: i) section 3.1 contains the work performed on the degradation phenomena of cathode active materials; ii) in section 3.2, studies on aging mechanisms involving the interaction between cathode and anode will be presented; and iii) section 3.3 comprises publications with a focus on anode materials.

3.1 Degradation Phenomena of Cathode Materials

Section 3.1 contains all the work related to cathode active material aging. All of the five studies are implemented in their final published versions to this PhD thesis.

In all the cathode material aging studies, the focus lies on layered oxides with the general formula $Li_{1+x}M_{1-x}O_2$ (M = Ni, Mn, Co) as the cathode active material. In section 3.1.1, a study on the release of lattice oxygen from Li- and Mn-rich NMC (also referred to as HE-NMC, $x > 0$) will be presented.[168] There, we critically discuss the impact of oxygen release on the bulk and surface structure of the HE-NMC material and its link to the distinct first-cycle activation plateau at ~4.5 V vs. Li/Li^+.[168] In section 3.1.2, a study on the oxygen release from stoichiometric NMC materials with $x = 0$ is shown. In contrast to HE-NMC, the presence of oxygen release from stoichiometric NMCs was debated for a long time and was not clearly shown until very recently. We analyze and compare the occurrence of oxygen release from NMC111, NMC622, and NMC811 and discuss its impact on *chemical* electrolyte oxidation and cycling stability of NMC-graphite cells.[101] As an extension to the findings on *chemical* electrolyte oxidation, a study in which we compare the *chemical* versus the *electrochemical* pathway of electrolyte oxidation will be described in section 3.1.3. In particular, we present the potential dependence of electrolyte oxidation on various materials and discuss their origins.[147] In section 3.1.4, the temperature dependence of oxygen release from NMC622 as well as the impact of temperature on the cycling performance of NMC-graphite cells is investigated.[165] Finally, in section 3.1.5, degradation phenomena occurring on NMC811 upon storage at ambient air are shown.[187]

3.1.1 The Role of Oxygen Release from Li- and Mn-Rich Layered Oxides during the First Cycles Investigated by On-Line Electrochemical Mass Spectrometry

In this section the article "The Role of Oxygen Release from Li- and Mn-Rich Layered Oxides during the First Cycles Investigated by On-Line Electrochemical Mass Spectrometry" will be presented. The research work was primarily conducted by Benjamin Strehle, who is also the first author of the publication. The paper was published in the *Journal of the Electrochemical Society* on January 5, 2017 as open access article distributed under the terms of the Creative Commons Attribution Non-Commercial No Derivatives 4.0 License.[168] The permanent web-link to the publication is http://jes.ecsdl.org/content/164/2/A400 and the DOI is 10.1149/2.1001702jes.

In the study we use On-Line Electrochemical Mass Spectrometry (OEMS) to quantify the evolved gases during the first two cycles of the Li- and Mn-rich layered oxide $Li_{1.17}[Ni_{0.22}Mn_{0.66}Co_{0.12}]_{0.83}O_2$ (HE-NMC), which alternatively can be described as two-phase material with the nominal composition $0.42\ Li_2MnO_3 \cdot 0.58\ Li[Ni_{0.38}Co_{0.21}Mn_{0.41}]O_2$.[168] We critically discuss the common hypothesis that it is the activation of the Li_2MnO_3 phase[188, 189] at the activation plateau around ~4.5 V vs. Li/Li^+ which causes the previously observed oxygen release[190-192] via the reaction $Li_2MnO_3 \rightarrow 2\ Li^+ + MnO_2 + 0.5\ O_2$ that has been hypothesized to lead to a restructuring of the bulk material[193, 194]. We show that oxygen release from the oxide lattice actually sets in at ~4.6 V vs. Li/Li^+ and therefore right after the activation plateau at ~4.5 V vs. Li/Li^+, contradicting the previous interpretation. Furthermore, quantification of the evolved O_2 and CO_2 amounts shows that even if all the oxygen bound in CO_2 would stem from the NMC bulk lattice, this amount could still only account for ~20% of the expected oxygen amounts based on the equation above for the hypothesized Li_2MnO_3 activation. Based on these findings we propose that oxygen release is limited to the surface-near region of the HE-NMC due to the limited diffusivity of the oxide anion at room temperature, and that there is a change in the bulk properties due to the formation of Li vacancies in the transition metal layer, yet the layered structure is maintained in the bulk. Therefore, we present a model in which the surface of the layered HE-NMC is transformed to a spinel-like phase with a layered bulk structure. As the oxygen content decreases from the layered oxide to the spinel, the release of oxygen from any layered oxide structure can be described by $Li_xM_yO_2 \rightarrow \frac{x+y}{3}\ Li_{3-\frac{3y}{x+y}}M_{\frac{3y}{x+y}}O_4 + \frac{3-2(x+y)}{3}\ O_2$. Based on the remaining lithium

content x at the onset of O_2 evolution and on the metal stoichiometry y in the HE-NMC structure, one can calculate the theoretically possible amount of oxygen evolution, which may be compared to the gas amounts observed in the OEMS. Setting their ratio equal to the volume of the particle divided by the volume of the shell, one may calculate the oxygen depleted layer thickness. For the HE-NMC used in this work, this yields a layer thickness of 2-3 nm, which is in excellent agreement with previous (S)TEM studies and which was confirmed by recent TEM measurements on the same material.[195-198]

Author Contributions

Benjamin Strehle designed and performed the OEMS experiments. Karin Kleiner built the cells to analyze the voltage profiles and dq/dV curves. Roland Jung and Benjamin Strehle worked on the phase-transformation model and calculated the oxygen depleted layer thicknesses. Benjamin Strehle, Karin Kleiner, Hubert Gasteiger, and Michele Piana wrote the manuscript. All authors discussed the results and commented on the manuscript.

The Role of Oxygen Release from Li- and Mn-Rich Layered Oxides during the First Cycles Investigated by On-Line Electrochemical Mass Spectrometry

Benjamin Strehle,[a,*,z] Karin Kleiner,[a,*] Roland Jung,[a,*] Frederick Chesneau,[b] Manuel Mendez,[b] Hubert A. Gasteiger,[a,] and Michele Piana[a,***]**

[a]*Chair of Technical Electrochemistry, Department of Chemistry and Catalysis Research Center, Technische Universität München, D-85748 Garching, Germany*
[b]*BASF SE, GCN/EE - M311, D-67056 Ludwigshafen, Germany*

In the present work, the extent and the role of oxygen release during the first charge of lithium- and manganese-rich $Li_{1.17}[Ni_{0.22}Co_{0.12}Mn_{0.66}]_{0.83}O_2$ (also referred to as HE-NCM) was investigated with on-line electrochemical mass spectrometry (OEMS). HE-NCM shows a unique voltage plateau at around 4.5 V in the first charge, which is often attributed to a decomposition reaction of the Li-rich component Li_2MnO_3. For this so-called "activation", it has been hypothesized that the electrochemically inactive Li_2MnO_3 would convert into MnO_2 while lattice oxide ions are oxidized and released as O_2 (or even CO_2) from the host structure. However, qualitative and quantitative examination of the O_2 and CO_2 evolution during the first charge shows that the onset of both reactions is above the 4.5 V voltage plateau and that the amount of released oxygen is an order of magnitude too low to be consistent with the commonly assumed Li_2MnO_3 activation. Instead, the amount of released oxygen can be correlated to a structural rearrangement of the active material which occurs at the end of the first charge. In this process, oxygen depletion from the HE-NCM host structure leads to the formation of a spinel-like phase. This phase transformation is restricted to the near-surface region of the HE-NCM particles due to the poor mobility of oxide ions within the bulk. From the evolved amount of O_2 and CO_2, the thickness of the spinel-like surface layer was estimated to be on the order of ≈2–3 nm, in excellent agreement with previously reported (S)TEM data.

Manuscript submitted September 8, 2016; revised manuscript received November 21, 2016. Published January 5, 2017.

Since the discovery of the positive electrode material $LiCoO_2$ and its commercialization in the Li-ion technology by Sony in 1991,[1] analogous layered oxides ($LiMeO_2$, Me = Ni, Co, Mn, Al, etc.) were studied, aiming at higher intrinsic specific capacity, energy, stability, and lower costs.[2–7] Among others, $Li[Ni_{1/3}Co_{1/3}Mn_{1/3}]O_2$ (NCM-111) showed very interesting performances in terms of specific capacity and stability.[8,9] Recently, materials characterized by an increase of exploitable Li^+ charge drew a lot of attention.[10,11] These so-called Li-rich compounds result from the substitution of part of the transition metal ions by Li^+, in a structural arrangement closely related to the layered structure.[11–14]

Li_2MnO_3 (or $Li[Li_{1/3}Mn_{2/3}]O_2$) is the simplest structure in this category and crystallizes in the monoclinic system (space group *C2/m*), while the common $LiMeO_2$-based layered structures crystallize in the hexagonal system (space group *R-3m*).[11,13,14] The two structures are very close to each other despite this difference in symmetry, related simply to the Li^+ ordering in the transition metal sites. This similarity is evident in the structure of the Li-rich NCM $Li_{1+x}Me_{1-x}O_2$ (Me = Ni, Co, Mn), also referred to as high-energy NCM (HE-NCM), where the hexagonal symmetry of the layered structure is broken by the superstructure of Li^+ in the transition metal sites, shown by the superlattice reflections in the diffractograms.[15,16] This similarity makes the Li_2MnO_3 crystalline domains difficult to detect, for which typically the notation $x\ Li_2MnO_3 \bullet (1\text{-}x)\ LiMeO_2$ has been used.[14,17,18]

The higher lithium content of the HE-NCM material results in an increase in specific capacity and energy. Peculiar to this material is that the amount of lithium ions that can be deintercalated is higher than the possible increase in the valence of the transition metals. This was initially rationalized by the formation of an oxygen-deficient layered oxide throughout the bulk of the material, formed by oxygen loss during the first activation cycle.[19,20] Accordingly, subsequent on-line mass spectrometry studies demonstrated the evolution of O_2 during the first charge.[21–23] The observed oxygen release was commonly attributed to Li_2MnO_3 activation and assigned to a unique plateau in the first charge of HE-NCM.[24,25] In the proposed process, lattice O^{2-} anions are oxidized to O_2 and removed from the oxide bulk structure, while the initially inactive manganese becomes electrochemically active after the first activation charge. However, very recently, an alternative view has been proposed, namely the direct involvement of lattice oxide ions by oxygen redox in the reversible charge/discharge reaction.[26,27]

The present paper will critically discuss the extent and the role of oxygen release from the HE-NCM host structure during the first activation charge. By means of quantitative on-line electrochemical mass spectrometry (OEMS) analysis of the amount of evolved oxygen and the onset potential of oxygen evolution it can be clearly shown that the O_2 release does not take place during the 4.5 V plateau in the first charge (the so-called "activation"). Instead, we provide evidence that the O_2 release occurs due to a structural rearrangement, consistent with the formation of a spinel-like surface layer observed in several (S)TEM studies.[28–30] This hypothesis is in good agreement with the amount of oxygen observed in our study, which in turn would be too low for the previously proposed Li_2MnO_3 activation.[17,24]

Experimental

All experiments were conducted with $Li_{1.17}[Ni_{0.22}Co_{0.12}Mn_{0.66}]_{0.83}O_2$ (further on referred to as HE-NCM; BET >>1 $m^2\ g^{-1}$, BASF SE, Germany), which can also be written as $0.42\ Li_2MnO_3 \bullet 0.58\ Li[Ni_{0.38}Co_{0.21}Mn_{0.41}]O_2$. HE-NCM inks were prepared by mixing 96 wt% of HE-NCM, 2 wt% of Super C65 conductive carbon (Timcal, Switzerland), and 2 wt% of polyvinylidene fluoride binder (PVDF, Kynar HSV 900, Arkema, France) with *N*-methyl-2-pyrrolidone (NMP, anhydrous, 99.5%, Sigma-Aldrich, Germany) in a planetary orbital mixer (Thinky, USA) in several steps. In the case of standard electrodes for tests in Swagelok T-cells, the ink was coated onto an aluminum foil using a doctor blade at a wet-film thickness of 50 μm. For the OEMS measurements conducted in a specially designed cell,[31] the ink was coated on a steel mesh (SS316, aperture 26 μm, wire diameter 25 μm, The Mesh Company Ltd, UK) in order to allow access of the

*Electrochemical Society Student Member.
**Electrochemical Society Fellow.
***Electrochemical Society Member.
[z]E-mail: benjamin.strehle@tum.de

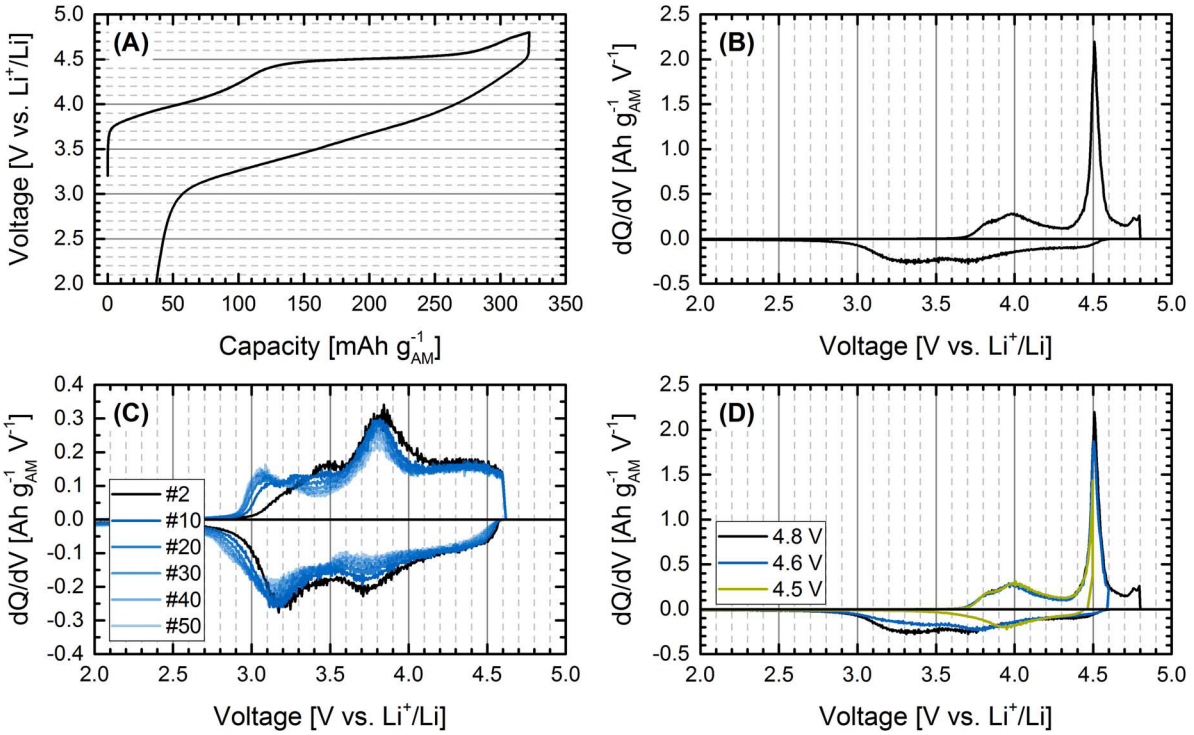

Figure 1. First cycle of HE-NCM (A) and the corresponding differential capacity (dQ/dV) plot (B). Panel C shows the differential capacity of the subsequent cycles. In panel D, the dQ/dV plot of the first cycle is shown for different upper voltage cutoffs, illustrating its influence on the discharge peaks. HE-NCM was cycled vs. metallic Li at a C-rate of C/10 and 25°C. In panel A-C, the first cycle was performed between 4.8 V and 2.0 V, while the upper cutoff voltage was 4.6 V for the subsequent cycles.

evolved gases to the capillary leading to the mass spectrometer.[32] The electrodes were punched out (loading/diameter: ≈4 mg_{AM} cm^{-2}/10 mm for T-cells and ≈10 mg_{AM} cm^{-2}/15 mm for OEMS cells), pressed for 20 s with 2.5 tons, and dried overnight at 120°C under dynamic vacuum. Swagelok T-cells were built using two glass fiber separators (glass microfiber filter, 691, VWR, Germany) and 120 µL LP57 electrolyte (1 M $LiPF_6$ in EC:EMC 3:7 by weight, <20 ppm H_2O, BASF SE). In contrast, OEMS cells were built using two porous polyolefin separators (H2013, Celgard, USA) and 100 µL LP57. Metallic lithium foil (thickness 0.45 mm, 99.9%, Rockwood Lithium, USA) was used as counter-electrode for all cells (diameter: 11 mm for T-cells and 17 mm for OEMS cells), except in one OEMS experiment, where a partially charged (delithiated) LFP counter-electrode with an areal capacity of 3.5 mAh cm^{-2} was used (from Custom Cells Itzehoe GmbH, Germany), which was charged at C/5 by 3.0 mAh cm^{-2}, corresponding to ca. $Li_{0.14}FePO_4$. Prior to cycling, the head space of the OEMS cells was purged for 2 min with argon to remove any gas traces from the glove box atmosphere. A 4 h OCV step was applied prior to starting the experiments. Conversion of the mass spectrometer currents to concentrations was done for O_2 and CO_2, using a calibration gas containing 2000 ppm of each gas in Ar (Westfalen AG, Germany). C-rates are defined based on a specific capacity of 300 mAh $g^{-1}{}_{AM}$ (AM ≡ cathode active material, HE-NCM in our case).

Results and Discussion

Electrochemical characterization.—HE-NCM shows a unique activation cycle with a plateau around 4.5 V in the first charge to 4.8 V (Figure 1A), yielding an overall capacity of ca. 320 mAh $g^{-1}{}_{AM}$, which is close to the theoretical capacity of the material of ca. 360 mAh $g^{-1}{}_{AM}$ (if one were to assume that all lithium could be extracted, based on $Li_{1.17}[Ni_{0.22}Co_{0.12}Mn_{0.66}]_{0.83}O_2$ with a molar mass of 86.8 g mol^{-1}). This can be seen more clearly in the differential capacity (dQ/dV) plot of the first charge/discharge cycle (Figure 1B), in which the activation plateau corresponds to a large peak at 4.5 V (HE-NCM vs. Li^+/Li). The presence of this peak is only observed in the first charge but not in the following cycles (Figure 1C). Depending on the voltage cutoff (before, on, or after the activation plateau), additional peaks appear at ca. 3.2 V and 3.7 V in the subsequent discharge cycles and at 3.0 V in the charge cycles (Figure 1C). The higher the end-of-charge voltage during the first activation cycle, the more pronounced are the additional peaks in the dQ/dV plot (Figure 1D). Apart from the electrochemical characterization, XRD patterns of the pristine material and after the first cycle are shown in the Supporting Information. The weak reflections between 9 and 12° are consistent with a two-phase rhombohedral-monoclinic system,[33] which clearly assign the material to the class of Li- and Mn-rich layered oxides (see Section 1 of the Supporting Information).

Li_2MnO_3 activation.—In the past, most authors have ascribed the origin of this so-called activation to the removal of oxygen from the bulk structure, leading to an oxygen-deficient bulk material.[17,19–21,24,25,34] Some of them attributed the activation of HE-NCM to the formation of delithiated MnO_2 according to Eq. 1,[17,24] which can be reversibly lithiated in the following discharge:

$$Li_2MnO_3 \rightarrow 2\,Li^+ + 2\,e^- + MnO_2 + 1/2\,O_2 \uparrow \quad [1]$$

If following Eq. 1, the quantitative activation of Li_2MnO_3 in our material with the composition 0.42 Li_2MnO_3 • 0.58 $Li[Ni_{0.38}Co_{0.21}Mn_{0.41}]O_2$ (molar mass 104.8 g mol^{-1}) would lead to the release of ca. 2000 μmol_{O_2} $g^{-1}{}_{AM}$, corresponding to ca. 17% of all oxygen atoms in HE-NCM (calculation given in Section 2 of the Supporting Information). This requires transport of oxygen anions from the bulk of the material to the surface during activation, from where it could be released as molecular oxygen.

Gas evolution during first charge.—Figure 2 shows OEMS data obtained while charging HE-NCM vs. metallic Li at C/20 up to 4.8 V. Following the first constant current step (CC), one cell was held at open circuit voltage (OCV, black curve in Figure 2A) for 10 h, while

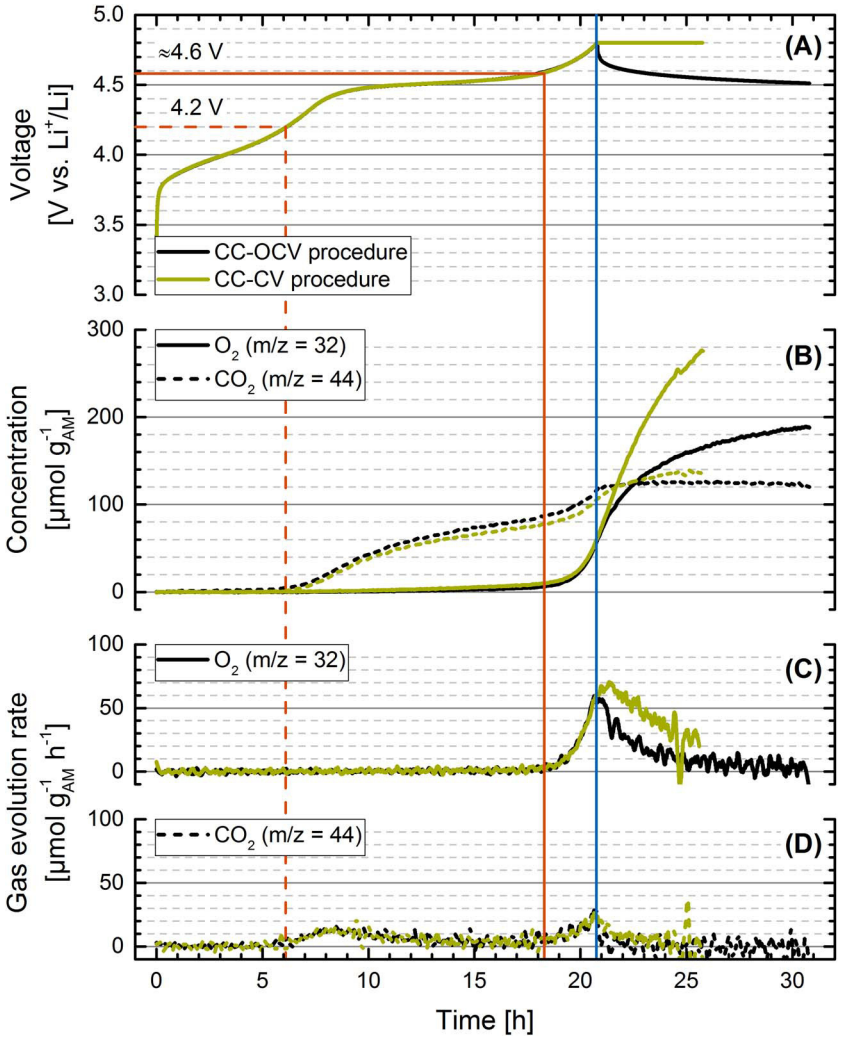

Figure 2. OEMS measurement of the first charge of HE-NCM vs. metallic Li to 4.8 V at C/20 and 25°C, followed by either an OCV step for 10 h (black curves) or a CV hold at 4.8 V for 5 h (green curves). Panel A shows the voltage curve vs. time (note that the curves are superimposed up to the upper cutoff voltage, i.e., up to ca. 21 h). Panel B illustrates the evolved amount of O_2 (solid curves) and CO_2 (dashed curves) in units of µmol g^{-1}_{AM}, whereas the O_2 and CO_2 evolution rates in units of µmol g^{-1}_{AM} h^{-1} are shown in the panels C and D, respectively. The dashed red lines indicate the initial onset potential of CO_2 evolution; the solid red lines indicate the onset potential of O_2 evolution (as well as the second onset potential for CO_2 evolution); the solid blue line marks the end of the CC charge at the cutoff voltage of 4.8 V.

another cell was held at 4.8 V in a constant voltage step (CV, green curve in Figure 2A) for 5 h, recording continuously the O_2 and CO_2 evolution in both cases (accumulated O_2 and CO_2 signals are shown in Figure 2B, while the evolution rates of O_2 and CO_2 are shown in Figure 2C and Figure 2D, respectively).

Starting with the CC-OCV experiment (black lines in Figure 2), the CO_2 evolution begins at 4.2 V (before the plateau), followed by a second increase at ≈4.6 V (after the plateau), which coincides with the onset potential for O_2 evolution. While the CO_2 release stops at the beginning of the OCV step, interestingly, the O_2 evolution goes on and does not complete within the measurement time. Let us first examine the evolution of CO_2. In agreement with Metzger et al.,[35] we attribute the initial CO_2 evolution starting at 4.2 V (marked by the dashed red lines in Figure 2) to the decomposition of carbonate impurities on the surface of the HE-NCM particles. The 4.2 V onset potential agrees with the Li_2CO_3 oxidation potential reported in the literature,[25,36,37] whereby essentially one CO_2 molecule per Li_2CO_3 is produced.[37] This first CO_2 evolution process continues up to a potential of ≈4.6 V (marked by the solid red lines in Figure 2), beyond which a second increase of the CO_2 evolution is observed. Note that the first process gradually levels off during the plateau, consistent with the consumption of an impurity which is only present in limited quantities. Up to ≈4.6 V, ≈80 μmol_{CO_2} g^{-1}_{AM} are evolved (Figure 2B), which for a 1:1 stoichiometric ratio between oxidized Li_2CO_3 and evolved CO_2 would correspond to a Li_2CO_3 content of ≈0.6 wt% (from: 80 μmol_{CO_2} g^{-1}_{AM} · 74 $g_{Li_2CO_3}$ $mol^{-1}_{Li_2CO_3}$). The calculated amount of Li_2CO_3 is to be expected on the HE-NCM particles (particularly in view of its rather high BET surface area[23]). This interpretation of the CO_2 signal is at variance with the mechanism proposed by Streich et al.[23] and by Luo et al.,[27] who concluded that the entire amount of CO_2 evolved during the initial charging of HE-NCM materials (i.e., including the CO_2 evolved between ≈4.2 and ≈4.6 V in their experiments) would originate from the attack of reactive oxygen species (e.g., superoxide radicals) released from the HE-NCM lattice on the electrolyte solvents. As evidence, Luo et al. noted the detection of $C^{16/18}O_2$ from their partially ^{18}O-labeled active material, but since their isotopic labeling process (heating the synthesized material in $^{18}O_2$-containing gas at 800°C) would also lead to the labeling of carbonate species, the formation of $C^{16/18}O_2$ can equally well be explained by the electrooxidation of Li_2CO_3 surface impurities. The latter are typically present in layered oxide materials.[38–40] However, the detection of $C^{16/18}O_2$ during the entire charging curve shows that the anodic oxidation of the electrolyte (without any involvement of the active material), which would release solely $C^{16/16}O_2$ in the experiment by Luo et al., is of minor importance for this class of materials. Thus, while we disagree with the interpretation by Streich et al.[23] and by Luo et al.[27] that the evolved CO_2 below ≈4.6 V originates from the reaction of the electrolyte with released lattice oxygen, we do believe that the second increase of the CO_2 evolution rate above 4.6 V, which coincides with the onset of O_2 evolution, is indeed caused by this reaction.

Next we will examine the O_2 evolution during the CC-OCV procedure. During the initial sloping region and during the high voltage plateau, i.e., at potentials below ≈4.6 V and a charge capacity of ≈280 mAh g^{-1}_{AM}, only minute amounts of O_2 are observed (less than 10 μmol_{O_2} g^{-1}_{AM}). This number could account for only

≈1 mAh g^{-1}_{AM} (assuming 4 electrons/O_2) and would thus be negligible compared to the overall charge capacity of ≈280 mAh g^{-1}_{AM}. Therefore, since the lattice oxygen evolution happens only after the plateau at 4.5 V, it cannot be correlated to the Li_2MnO_3 activation according to Eq. 1, as was done in some of the literature.[17,24] Only at potentials above ≈4.6 V, substantial O_2 evolution is observed, reaching a total amount of ≈60 μmol_{O_2} g^{-1}_{AM} once the positive voltage cutoff of 4.8 V is reached (see solid blue line in Figure 2). At this point, the charge capacity amounts to ≈310 mAh g^{-1}_{AM}, of which only ≈6.4 mAh g^{-1}_{AM} can be ascribed to the detected amount of O_2. The O_2 data may be compared to the study by Streich et al.,[23] who obtained 29 μmol_{O_2} g^{-1}_{AM} at a cutoff potential of 4.7 V, in excellent agreement with the ≈25 μmol_{O_2} g^{-1}_{AM} which we recorded at 4.7 V (Figure 2B). While the O_2 evolution rate (Figure 2C) is at its maximum at the positive voltage cutoff of 4.8 V, O_2 evolution continues even during the subsequent OCV period at a rate which decreases with decreasing potential. After 10 h of OCV, the potential decays to ≈4.5 V, at which point the total amount of O_2 approaches a value of ≈200 μmol_{O_2} g^{-1}_{AM} and the O_2 evolution gradually stops. Consequently, the total amount of evolved O_2 during the CC-OCV procedure amounts to only 10% of what would be predicted on the basis of Eq. 1 (i.e., of 2000 μmol_{O_2} g^{-1}_{AM}; see Section 2 of the Supporting Information). Note that the amount of O_2 dissolved in the electrolyte accounts to ca. 0.1% of the overall O_2 and is thus negligible compared to the gas phase which is detected by OEMS (calculation given in Section 3 of the Supporting Information). Even if we were to assume that all of the evolved CO_2 (≈120 μmol_{CO_2} g^{-1}_{AM}) would derive from the oxidation of the electrolyte by released lattice oxygen, as was suggested by Luo et al. (assuming the formation of 1 mol of CO_2 from 1 mol of released O_2),[27] only ≈16% of the evolved O_2 predicted by Eq. 1 would be released during the CC-OCV procedure. More likely, however, only ≈40 μmol_{CO_2} g^{-1}_{AM} derive from electrolyte oxidation by lattice oxygen (based on the above argument that CO_2 formed up to 4.6 V is due to Li_2CO_3 oxidation), so that the maximum amount of released oxygen (≈240 μmol g^{-1}_{AM}) amounts to ≈12% of what would be predicted by Eq. 1.

One remaining unresolved phenomenon in the CC-OCV data in Figure 2 is the fact that the CO_2 evolution stops very shortly after entering the OCV step (best seen by the CO_2 trace in Figure 2B), despite the fact that the amount of O_2 still increases by a factor of ≈3 (see O_2 trace in Figure 2B). This is clearly inconsistent with the above assumption that released lattice oxygen attacks the electrolyte solvents leading to CO_2 formation. As it seems to be required that charge passes the external circuit, one could hypothesize an (independent) oxidation step of the electrolyte which would be suppressed during OCV. Furthermore, as the released lattice oxygen species is not known, the absent CO_2 evolution might be explained by assuming that the oxidation of the electrolyte is largely triggered by superoxide radicals ($O_2^{\bullet-}$) rather than by molecular oxygen, which was proposed previously for alkyl carbonate-based electrolytes[41,42] as well as for the photo-assisted oxidation of organic dyes in aerated solutions.[43] At cathode potentials significantly above 3 V, superoxide radicals could only be formed by O_2 reduction at the lithium anode, where it might proceed as long as lithium is deposited (i.e., as long as a fresh lithium is being plated). Under this assumption, superoxide radicals to decompose the alkyl carbonates to CO_2 would be present during the CC step, but could not be supplied anymore during the OCV period. This will be discussed further when examining the gas evolution during the CC-CV charge.

Layered-to-spinel transformation.—Let us now summarize our observations so far: (i) almost no O_2 from the HE-NCM host structure is released during the activation plateau, (ii) the total amount of evolved gases is roughly one order of magnitude lower than what would be predicted based on Eq. 1, and (iii) the O_2 evolution continues during OCV, i.e., when no charge is passed. This provides strong evidence that the evolved O_2 is not related to the bulk oxidation of the Li_2MnO_3 phase according to Eq. 1. In contrast, the negligible amount of O_2 and the probably largely Li_2CO_3-derived CO_2 accumulated by the end of the voltage plateau (i.e., just below 4.6 V) suggests that the following oxygen release is associated with a structural rearrangement of the surface of the HE-NCM material, rather than being related to the electrochemically driven process described traditionally by Eq. 1. Such reactions are well-known from structurally related layered oxides and describe the chemical decomposition of Li_xMeO_2 into a spinel-like structure with the composition M'_3O_4 (M' = Me+Li), shown in Eq. 2.[44–46] This phase transformation is consistent with the observed phase reported in several (S)TEM studies from Li- and Mn-rich layered oxides (an overview is provided in Section 4 of the Supporting Information).[28–30,47–50] As the transition metal content in Li-rich materials is smaller than that for common layered oxides, the reaction is given in the generalized form for $Li_xMe_yO_2$. Especially in the case of Ni-rich materials,[51–55] the oxygen depletion of the near-surface region is a continuously ongoing process during cycling and/or at elevated temperatures, leading via the spinel structure to a rock-salt structure with the composition M'O (M' = Me+Li), described in Eq. 3.[44,45] The restriction of these reactions to the near-surface region can be rationalized by the low O^{2-} anion mobility within the bulk material at/near room temperature.

$$Li_xMe_yO_2 \rightarrow \frac{x+y}{3} Li_{3-\frac{3y}{x+y}} Me_{\frac{3y}{x+y}} O_4 + \frac{3-2(x+y)}{3} O_2 \uparrow, \quad \text{where } x \ll 1 \text{ and } y \leq 1 \qquad [2]$$

$$Li_xMe_yO_2 \rightarrow \frac{x+y}{3} Li_{3-\frac{3y}{x+y}} Me_{\frac{3y}{x+y}} O_4 + \frac{3-2(x+y)}{3} O_2 \uparrow$$
$$\rightarrow (x+y) Li_{1-\frac{y}{x+y}} Me_{\frac{y}{x+y}} O + \frac{2-(x+y)}{2} O_2 \uparrow \qquad [3]$$

In summary, Equations 2 and 3 present an alternative view to Eq. 1 of the oxygen evolution mechanism for HE-NCM materials during activation, assuming that oxygen is released by the conversion of a layered oxide into a spinel (or rock-salt) structure at high potentials. This picture would be by analogy with thermally induced phase transformations observed for charged layered oxide materials.[44–46,53]

In the second experiment shown in Figure 2, a C/20 activation charge to 4.8 V and then continued with a constant voltage step for 5 h was performed (see green curves). Up to the positive cutoff potential of 4.8 V, the voltage and gas evolution responses are identical with the foregoing experiment (compare green vs. black curves). The O_2 evolution rate during the 4.8 V hold period is substantially larger than during OCV (see black vs. green solid curves in Figure 2C), so that the total amount of evolved oxygen is larger at the end of the CV step (≈280 μmol_{O_2} g^{-1}_{AM} after 5 h CV compared to ≈200 μmol_{O_2} g^{-1}_{AM} after 10 h OCV, see Figure 2B). This seems to be at variance with our above assumption that the diffusion of O^{2-} anions within the bulk structure would limit the growth of the oxygen-depleted surface layer, i.e., that it would restrict the release of molecular oxygen to the near-surface region. However, since lithium deintercalation continues during the CV step (amounting to ≈20 mAh g^{-1}_{AM}), the oxide material becomes even more unstable, so that it is not unreasonable to assume that this would lead either to a slightly increased O^{2-} diffusion and/or a further conversion of the spinel layer to a rock-salt structure (Eq. 3). Both effects would be accompanied by further O_2 release. As the O_2 evolution rate during the CV step diminishes in a similar way than during OCV, we think that the oxygen depletion is still limited to the external part of the particles and does not affect the core of the particles. Note that Equation 2 and 3 describe the formation of the spinel (metal/oxygen ratio 3:4) and rock-salt structure (metal/oxygen ratio 1:1) with an ideal stoichiometry. However, it is also possible to reach stoichiometries in between in which the metal to oxygen ratio differs from the ideal case. Contrary to the CC-OCV experiment, the CO_2 evolution continues at low rate during most of the CV step, which would be consistent with an oxidation step of the alkyl carbonates or the continuous formation of superoxide radicals during lithium plating on the anode.

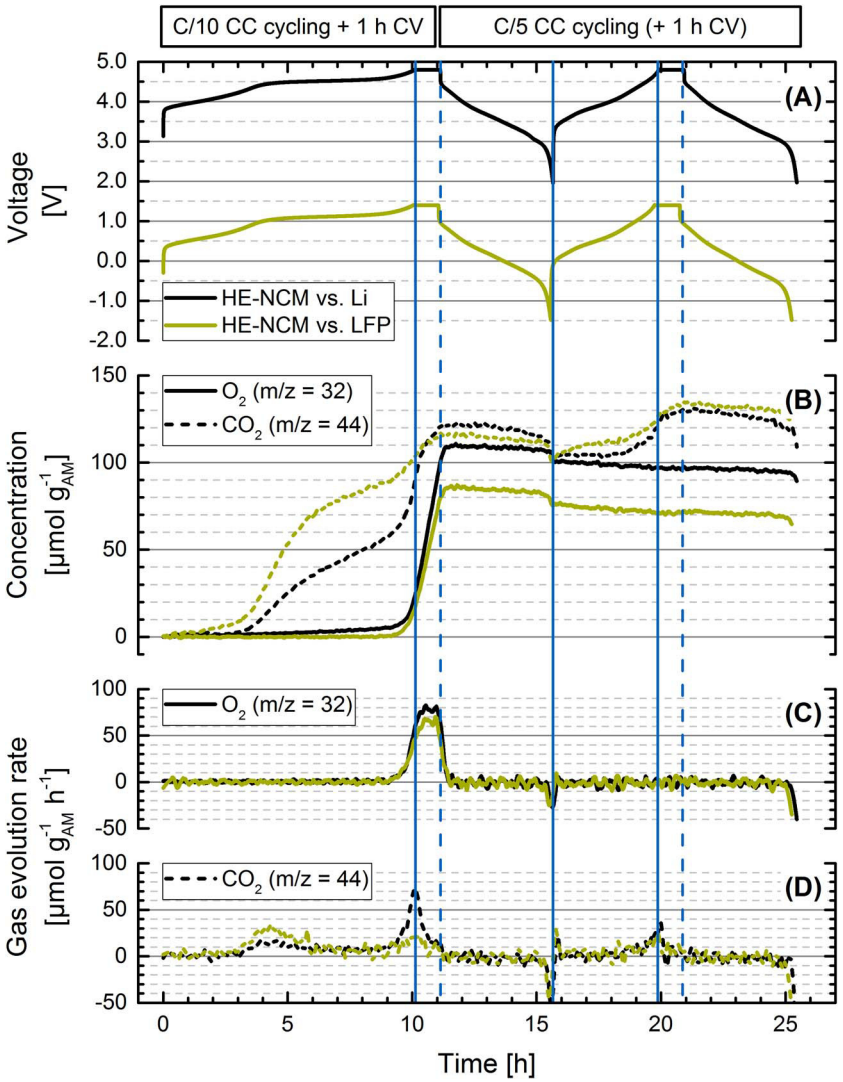

Figure 3. HE-NCM vs. Li (black curves) and HE-NCM vs. LFP (green curves), cycled at C/10 in the first charge and at C/5 in the subsequent discharge as well as the second cycle. Both measurements were performed at 25°C in the potential range of 2.0–4.8 V vs. Li^+/Li for the HE-NMC working-electrode, including a CV step of 1 h at the end of each CC charge. Panel A shows the voltage curves vs. time. Panel B illustrates the evolved amount of O_2 (solid curves) and CO_2 (dashed curves) in units of µmol g^{-1}_{AM}, whereas the O_2 and CO_2 evolution rates in units of µmol g^{-1}_{AM} h^{-1} are shown in the panels C and D, respectively. The blue solid lines indicate the end of the CC steps; the dotted blue lines show the end of the CV steps.

Gas evolution during the first two cycles.—After having examined the first activation charge, we now investigate whether O_2 release from the HE-NCM host structure also occurs in the second cycle or not (Figure 3). Therefore, using first the same electrode configuration as was used in Figure 2 (viz., HE-NCM vs. Li), we performed a C/10 charge to 4.8 V completed with a CV step of 1 h and followed by a C/5 discharge to 2.0 V, with a subsequent second cycle at C/5 (see black curves in Figure 3). Once the upper cutoff voltage is reached in this first charge at C/10, the amounts of evolved O_2 and CO_2 are lower than what we had observed at C/20 (≈25 µmol$_{O_2}$ g^{-1}_{AM} and ≈90 µmol$_{CO_2}$ g^{-1}_{AM} at C/10 vs. ≈60 µmol$_{O_2}$ g^{-1}_{AM} and ≈105 µmol$_{CO_2}$ g^{-1}_{AM} at C/20), which we ascribe to the slow kinetics of lattice oxygen release. However, at the end of the subsequent 1 h hold at 4.8 V, the amounts of evolved O_2 and CO_2 are essentially identical for first cycle activation at either C/10 or C/20 (≈110 µmol$_{O_2}$ g^{-1}_{AM} and ≈120 µmol$_{CO_2}$ g^{-1}_{AM} at C/10 + 1 h CV vs. ≈125 µmol$_{O_2}$ g^{-1}_{AM} and ≈120 µmol$_{CO_2}$ g^{-1}_{AM} at C/20 + 1 h CV). It is noteworthy that the O_2 evolution immediately stops upon switching from the CV step in the first cycle, during which O_2 is still being evolved, to the first discharge step. The rapidly vanishing O_2 evolution rate (Figure 3C) demonstrates that there is no delay between the O_2 evolution from the HE-NCM material and its detection in the OEMS. As the near-surface region is lithiated and thus stabilized first during discharge, the abrupt end of the O_2 evolution also shows that it must originate from the external part of the particles. Very surprising is the observation that there is no O_2 evolution during the second charge, even though the overall amount of evolved O_2 after the first charge at C/10 and 1 h hold at 4.8 V (≈110 µmol$_{O_2}$ g^{-1}_{AM}) is less than what was measured in the previous experiments with a C/20 charge and 5 h hold at 4.8 V (≈280 µmol$_{O_2}$ g^{-1}_{AM}). Consequently, any formed spinel-like surface layer in the former case should be thinner and further O_2 evolution in the second charge would be expected, contrary to what we and others[23] have observed. In order to explain this discrepancy, we hypothesize that the initially formed surface layer is modified during the first discharge, thereby preventing further oxygen release in subsequent charges. In addition, the change in the HE-NCM bulk structure upon the initial release of almost all of its lithium ions during activation (320 mAh g^{-1}_{AM} in the first charge vs. a theoretical maximum of ca. 360 mAh g^{-1}_{AM}) leads to different bulk thermodynamic properties, which might affect the oxygen release. Note that the overall capacity during the second charge decreases to ca. 275 mAh g^{-1}_{AM}. The OEMS measurement shows also a slight decrease in the O_2 and CO_2 signals once the potential decreases below 3.0 V at the end of discharge, which can be attributed to the formation of Li_2O_2 and Li_2CO_3 on the HE-NCM surface.[25,56] This newly formed Li_2CO_3 can then be oxidized in a subsequent charge, which we believe is the reason for the observed CO_2 evolution in the second charge, starting again at 4.2 V. This was already proposed previously.[56]

In order to ensure that no gaseous products are consumed on the Li counter-electrode, the same cycling procedure was applied to HE-NCM but using partially delithiated LFP as counter-electrode (green curves in Figure 3; see also in the experimental part). Neither O_2 nor CO_2 are expected to be reduced at the LFP potential.[57] Its potential was monitored in a T-cell with a Li reference-electrode to

Table I. Estimation of the molar fraction and thickness of the spinel-like surface layer for *Model A* (lattice oxygen-derived CO_2 only above ≈4.6 V) and *Model B* (CO_2 evolved prior to O_2 evolution at ≈4.6 V also due to the reaction with lattice oxygen), based on the gas evolution for the HE-NCM/Li cell data in Figure 3 (black lines). For CO_2, we assume that both oxygen atoms come from the lattice O^{2-} anions, as suggested by Luo et al.[27] The capacity is also derived from the gas evolution, assuming that four electrons are exchanged per gas molecule. For details see Section 5 and 6 of the Supporting Information.

		Model A (≥4.6 V)		*Model B* (≥4.2 V)	
Gas evolution	n [μmol g^{-1}_{AM}]	O_2	110	O_2	110
		CO_2	60	CO_2	120
Capacity ($4e^-/O_2$ & CO_2)	C_{spec} [mAh g^{-1}_{AM}]	18		25	
Fraction of spinel phase	x_{spinel} [mol.%]	5.7		7.7	
Spinel-like surface layer thickness	t_{spinel} [nm]	2.1		2.9	

determine the voltage cutoffs in the HE-NCM/LFP full-cell for the OEMS measurement (−1.45 V and 1.40 V selected as cell potential for the lower and upper voltage cutoffs). That the chosen cutoffs are reasonably comparable can be deduced from the close similarity of the charge/discharge curve features for the HE-NCM/Li and the HE-NCM/LFP cells (compare black and green curve in Figure 3A). The amount of evolved O_2 after the first cycle is slightly lower for the HE-NCM/LFP cell compared to the HE-NCM/Li cell (≈85 μmol_{O_2} g^{-1}_{AM} vs. ≈110 μmol_{O_2} g^{-1}_{AM}, respectively), but this might be due to small but finite differences in the upper voltage hold value. Regarding the CO_2 evolution, there are clear differences prior to the onset of O_2 evolution (reaching ≈90 μmol_{CO_2} g^{-1}_{AM} for HE-NCM/LFP vs. ≈60 μmol_{CO_2} g^{-1}_{AM} for HE-NCM/Li), which might be due to an inhomogeneous distribution of carbonate impurities among different electrodes. Overall, however, the differences in total gas evolution are not very large, so that any possible "cross-talk" effects between anode and cathode are either negligible or very similar.

Thickness of the spinel-like surface layer.—Assuming that the detected O_2 as well as the associated CO_2 obtained from Figure 3 derives from the formation of a near-surface spinel layer and not from the removal of oxygen from the bulk of the material, we will now estimate its thickness. The latter can be calculated by taking into account the amount of oxygen atoms which are released from the HE-NCM host structure according to Eq. 2. To perform this calculation, we will use two different models. *Model A*: We only consider the amount of gases evolved at a voltage higher than 4.6 V, i.e., once the onset of O_2 evolution is observed, which, without doubt, will derive from HE-NCM lattice oxygen. *Model B*: As some authors assume that the CO_2 observed prior to O_2 evolution (i.e., between 4.2 V and 4.6 V) originates from electrolyte oxidation by reaction with released lattice oxygen,[23,27] we will also provide an estimate for the near-surface layer thickness using the overall gas evolution (i.e., including the CO_2 evolution starting at 4.2 V), even though we believe that it is more likely due to the electrooxidation of Li_2CO_3 impurities. These two models will now be applied to the HE-NCM/Li cell data shown in Figure 3 (black lines). The formation of a spinel structure (M'_3O_4, M' = Me+Li) at 4.6 V, corresponding to a charge capacity of ≈275 mAh g^{-1}_{AM} at C/10, can be written as follows (see Supporting Information for more details):

$$Li_{0.28}Me_{0.83}O_2 \rightarrow 0.37\ Li_{0.76}Me_{2.24}O_4 + 0.26\ O_2 \uparrow \quad [4]$$

Comparing the results in Table I, the difference between the two models is less than 1 nm which is reasonably small compared to the estimated average HE-NCM particle radius of ≈110 nm (see Section 6 of the Supporting Information) and based on the approximations used for this calculation. Nevertheless, the estimated thickness of ≈2–3 nm for the spinel-like phase is in excellent agreement with recent (S)TEM results, which propose also a 2–3 nm thick surface layer formed during the first cycle.[28–30] As already mentioned in the discussion of Figure 2, it is not possible to determine whether the transformation of the near-surface region stops at the spinel structure (as described in Eq. 2) and to what extent it may proceed all the way to the rock-salt structure (as described in Eq. 3). In the latter case, the estimated thickness of the near-surface layer would be smaller by a factor of ca. 2. The overall maximum estimated capacity of ≈25 mAh g^{-1}_{AM} is five times lower than the capacity provided by HE-NCM during the plateau. However, the gas evolution does not occur during the plateau but mostly after plateau at potentials of 4.6 V and above, proceeding even if HE-NCM is hold at open circuit potential after the first charge.

Conclusions

In the present work, we show the gas evolution of HE-NCM during the first two cycles using OEMS. The gas evolution can be divided into a CO_2 evolution starting at 4.2 V and ending before 4.6 V, followed by a second CO_2 production starting at 4.6 V after the activation plateau and coinciding with the onset of the evolution of O_2. In agreement with the literature[25,35,37,56] and according to the use of a Li excess in HE-NCM synthesis, we attribute the CO_2 evolution at low voltages mainly to the electrooxidation of Li_2CO_3 impurities, while the O_2 and CO_2 evolution at voltages higher than 4.6 V are both attributed to oxygen evolved from the HE-NCM lattice. We exclude any possible gas consumption on the Li counter-electrode by comparing the results obtained with LFP as counter-electrode. The maximum recorded gas evolution due to lattice oxygen upon extended potential hold at 4.8 V (see CC-CV experiment in Figure 2), ≈420 μmol g^{-1}_{AM} (assuming that CO_2 evolution at low potentials is due to electrolyte oxidation by released lattice oxygen) or ≈340 μmol g^{-1}_{AM} (assuming that CO_2 evolution at low potentials is due to the oxidation of Li_2CO_3 impurities), is, in any case, at least 5-fold lower than what would be expected for the so-called Li_2MnO_3 activation (2000 μmol g^{-1}_{AM}) assumed in the literature.[17,24] This led us to propose an alternative reaction to the Li_2MnO_3 activation, namely, the formation of a spinel-like near-surface structure analogous to the known structural rearrangements in layered oxides. From the amount of evolved gases, we estimated the thickness of such a spinel-like surface layer on the HE-NCM particles to be on the order of ≈2–3 nm, in excellent agreement with previously observed (S)TEM data.[28–30]

Acknowledgments

The authors gratefully acknowledge BASF SE for financial support of this research through the framework of its Scientific Network on Electrochemistry and Batteries. R.J. thanks BMW AG for funding.

References

1. K. Mizushima, P. C. Jones, P. J. Wiseman, and J. B. Goodenough, *Mater. Res. Bull.*, **15**, 783 (1980).
2. C. Delmas and I. Saadoune, *Solid State Ionics*, **53–56**, 370 (1992).
3. T. Ohzuku, A. Ueda, and M. Kouguchi, *J. Electrochem. Soc.*, **142**, 4033 (1995).
4. T. Ohzuku and Y. Makimura, *Chem. Lett.*, **30**, 744 (2001).
5. J. S. Weaving, F. Coowar, D. A. Teagle, J. Cullen, V. Dass, P. Bindin, R. Green, and W. J. Macklin, *J. Power Sources*, **97–98**, 733 (2001).
6. Z. Lu, D. D. MacNeil, and J. R. Dahn, *Electrochem. Solid-State Lett.*, **4**, A200 (2001).
7. F. Zhou, X. Zhao, and J. R. Dahn, *J. Electrochem. Soc.*, **156**, A343 (2009).
8. I. Belharouak, Y.-K. Sun, J. Liu, and K. Amine, *J. Power Sources*, **123**, 247 (2003).
9. J. Choi and A. Manthiram, *J. Electrochem. Soc.*, **152**, A1714 (2005).
10. Z. Lu and J. R. Dahn, *J. Electrochem. Soc.*, **149**, A1454 (2002).
11. Z. Lu, L. Y. Beaulieu, R. A. Donaberger, C. L. Thomas, and J. R. Dahn, *J. Electrochem. Soc.*, **149**, A778 (2002).

12. Y. S. Meng, G. Ceder, C. P. Grey, W. S. Yoon, M. Jiang, J. Bréger, and Y. Shao-Horn, *Chem. Mater.*, **17**, 2386 (2005).
13. N. Tran, L. Croguennec, C. Labrugère, C. Jordy, P. Biensan, and C. Delmas, *J. Electrochem. Soc.*, **153**, A261 (2006).
14. M. M. Thackeray, S.-H. Kang, C. S. Johnson, J. T. Vaughey, R. Benedek, and S. A. Hackney, *J. Mater. Chem.*, **17**, 3112 (2007).
15. J. Bréger, M. Jiang, N. Dupré, Y. S. Meng, Y. Shao-Horn, G. Ceder, and C. P. Grey, *J. Solid State Chem.*, **178**, 2575 (2005).
16. K. A. Jarvis, Z. Deng, L. F. Allard, A. Manthiram, and P. J. Ferreira, *Chem. Mater.*, **23**, 3614 (2011).
17. J.-S. Kim, C. S. Johnson, J. T. Vaughey, M. M. Thackeray, S. A. Hackney, W. Yoon, and C. P. Grey, *Chem. Mater.*, **16**, 1996 (2004).
18. M. M. Thackeray, C. S. Johnson, J. T. Vaughey, N. Li, and S. A. Hackney, *J. Mater. Chem.*, **15**, 2257 (2005).
19. Z. Lu and J. R. Dahn, *J. Electrochem. Soc.*, **149**, A815 (2002).
20. N. Tran, L. Croguennec, M. Ménétrier, F. Weill, P. Biensan, C. Jordy, and C. Delmas, *Chem. Mater.*, **20**, 4815 (2008).
21. A. R. Armstrong, M. Holzapfel, P. Novák, C. S. Johnson, S.-H. Kang, M. M. Thackeray, and P. G. Bruce, *J. Am. Chem. Soc.*, **128**, 8694 (2006).
22. F. La Mantia, F. Rosciano, N. Tran, and P. Novák, *J. Appl. Electrochem.*, **38**, 893 (2008).
23. D. Streich, A. Guéguen, M. Mendez, F. Chesneau, P. Novák, and E. J. Berg, *J. Electrochem. Soc.*, **163**, A964 (2016).
24. H. Yu, H. Kim, Y. Wang, P. He, D. Asakura, Y. Nakamura, and H. Zhou, *Phys. Chem. Chem. Phys.*, **14**, 6584 (2012).
25. N. Yabuuchi, K. Yoshii, S.-T. Myung, I. Nakai, and S. Komaba, *J. Am. Chem. Soc.*, **133**, 4404 (2011).
26. H. Koga, L. Croguennec, M. Ménétrier, P. Mannessiez, F. Weill, C. Delmas, and S. Belin, *J. Phys. Chem. C*, **118**, 5700 (2014).
27. K. Luo, M. R. Roberts, R. Hao, N. Guerrini, D. M. Pickup, Y.-S. Liu, K. Edström, J. Guo, A. V. Chadwick, L. C. Duda, and P. G. Bruce, *Nat. Chem.*, **8**, 684 (2016).
28. A. Boulineau, L. Simonin, J.-F. Colin, E. Canévet, L. Daniel, and S. Patoux, *Chem. Mater.*, **24**, 3558 (2012).
29. A. Boulineau, L. Simonin, J.-F. Colin, C. Bourbon, and S. Patoux, *Nano Lett.*, **13**, 3857 (2013).
30. C. Genevois, H. Koga, L. Croguennec, M. Ménétrier, C. Delmas, and F. Weill, *J. Phys. Chem. C*, **119**, 75 (2015).
31. S. Meini, M. Piana, N. Tsiouvaras, A. Garsuch, and H. A. Gasteiger, *Electrochem. Solid-State Lett.*, **15**, A45 (2012).
32. N. Tsiouvaras, S. Meini, I. Buchberger, and H. A. Gasteiger, *J. Electrochem. Soc.*, **160**, A471 (2013).
33. F. Amalraj, M. Talianker, B. Markovsky, D. Sharon, L. Burlaka, G. Shafir, E. Zinigrad, O. Haik, D. Aurbach, J. Lampert, M. Schulz-Dobrick, and A. Garsuch, *J. Electrochem. Soc.*, **160**, A324 (2012).
34. J. R. Croy, K. G. Gallagher, M. Balasubramanian, Z. Chen, Y. Ren, D. Kim, S.-H. Kang, D. W. Dees, and M. M. Thackeray, *J. Phys. Chem. C*, **117**, 6525 (2013).
35. M. Metzger, B. Strehle, S. Solchenbach, and H. A. Gasteiger, *J. Electrochem. Soc.*, **163**, A798 (2016).
36. B. D. McCloskey, D. S. Bethune, R. M. Shelby, G. Girishkumar, and A. C. Luntz, *J. Phys. Chem. Lett.*, **2**, 1161 (2011).
37. S. Meini, N. Tsiouvaras, K. U. Schwenke, M. Piana, H. Beyer, L. Lange, and H. A. Gasteiger, *Phys. Chem. Chem. Phys.*, **15**, 11478 (2013).
38. K. Matsumoto, R. Kuzuo, K. Takeya, and A. Yamanaka, *J. Power Sources*, **81–82**, 558 (1999).
39. N. Mijung, Y. Lee, and J. Cho, *J. Electrochem. Soc.*, **153**, A935 (2006).
40. S.-W. Lee, H. Kim, M.-S. Kim, H.-C. Youn, K. Kang, B.-W. Cho, K. C. Roh, and K.-B. Kim, *J. Power Sources*, **315**, 261 (2016).
41. S. A. Freunberger, Y. Chen, Z. Peng, J. M. Griffin, L. J. Hardwick, F. Bardé, P. Novák, and P. G. Bruce, *J. Am. Chem. Soc.*, **133**, 8040 (2011).
42. V. S. Bryantsev, V. Giordani, W. Walker, M. Blanco, S. Zecevic, K. Sasaki, J. Uddin, D. Addison, and G. V. Chase, *J. Phys. Chem. A*, **115**, 12399 (2011).
43. M. Stylidi, D. I. Kondarides, and X. E. Verykios, *Appl. Catal. B Environ.*, **47**, 189 (2004).
44. N. Yabuuchi, Y.-T. Kim, H. H. Li, and Y. Shao-Horn, *Chem. Mater.*, **20**, 4936 (2008).
45. S.-M. Bak, K.-W. Nam, W. Chang, X. Yu, E. Hu, S. Hwang, E. A. Stach, K.-B. Kim, K. Y. Chung, and X.-Q. Yang, *Chem. Mater.*, **25**, 337 (2013).
46. S.-M. Bak, E. Hu, Y. Zhou, X. Yu, S. D. Senanayake, S.-J. Cho, K.-B. Kim, K. Y. Chung, X.-Q. Yang, and K.-W. Nam, *ACS Appl. Mater. Interfaces*, **6**, 22594 (2014).
47. A. K. Shukla, Q. M. Ramasse, C. Ophus, H. Duncan, F. Hage, and G. Chen, *Nat. Commun.*, **6**, 8711 (2015).
48. B. Qiu, M. Zhang, L. Wu, J. Wang, Y. Xia, D. Qian, H. Liu, S. Hy, Y. Chen, K. An, Y. Zhu, Z. Liu, and Y. S. Meng, *Nat. Commun.*, **7**, 12108 (2016).
49. H. Koga, L. Croguennec, P. Mannessiez, M. Ménétrier, F. Weill, L. Bourgeois, M. Duttine, E. Suard, and C. Delmas, *J. Phys. Chem. C*, **116**, 13497 (2015).
50. P. Yan, A. Nie, J. Zheng, Y. Zhou, D. Lu, X. Zhang, R. Xu, I. Belharouak, X. Zu, J. Xiao, K. Amine, J. Liu, F. Gao, R. Shahbazian-Yassar, J.-G. Zhang, and C.-M. Wang, *Nano Lett.*, **15**, 514 (2015).
51. D. P. Abraham, R. D. Twesten, M. Balasubramanian, I. Petrov, J. McBreen, and K. Amine, *Electrochem. Commun.*, **4**, 620 (2002).
52. S. Muto, Y. Sasano, K. Tatsumi, T. Sasaki, K. Horibuchi, Y. Takeuchi, and Y. Ukyo, *J. Electrochem. Soc.*, **156**, A371 (2009).
53. L. Wu, K.-W. Nam, X. Wang, Y. Zhou, J.-C. Zheng, X.-Q. Yang, and Y. Zhu, *Chem. Mater.*, **23**, 3953 (2011).
54. S.-K. Jung, H. Gwon, J. Hong, K.-Y. Park, D.-H. Seo, H. Kim, J. Hyun, W. Yang, and K. Kang, *Adv. Energy Mater.*, **4**, 1300787 (2014).
55. R. Jung, M. Metzger, F. Maglia, C. Stinner, and H. A. Gasteiger, Manuscript in preparation.
56. J. Hong, H. D. Lim, M. Lee, S. W. Kim, H. Kim, S. T. Oh, G. C. Chung, and K. Kang, *Chem. Mater.*, **24**, 2692 (2012).
57. A. Guéguen, D. Streich, M. He, M. Mendez, F. F. Chesneau, P. Novák, and E. J. Berg, *J. Electrochem. Soc.*, **163**, A1095 (2016).

Supporting Information for

The Role of Oxygen Release from Li- and Mn-Rich Layered Oxides During the First Cycles Investigated by On-Line Electrochemical Mass Spectrometry

Benjamin Strehle,[a,*,z] Karin Kleiner,[a,*] Roland Jung,[a,*] Frederick Chesneau,[b] Manuel Mendez,[b] Hubert A. Gasteiger,[a,**] and Michele Piana[a,***]

[a] *Chair of Technical Electrochemistry, Department of Chemistry and Catalysis Research Center, Technische Universität München, D-85748 Garching, Germany*

[b] *BASF SE, GCN/EE – M311, D-67056 Ludwigshafen, Germany*

* Electrochemical Society Student Member.
** Electrochemical Society Fellow.
*** Electrochemical Society Active Member.
[z] E-mail: benjamin.strehle@tum.de

1) XRD of the pristine material and after the first cycle

Figure S1 shows the XRD patterns of the pristine material and of an electrode after the first cycle. The weak reflections between 9 and 12° arise from the Li^+ ordering in the transition metal plane and are a clear indication for Li- and Mn-rich layered oxide materials. The bulk structure of the material is maintained after the first activation cycle.

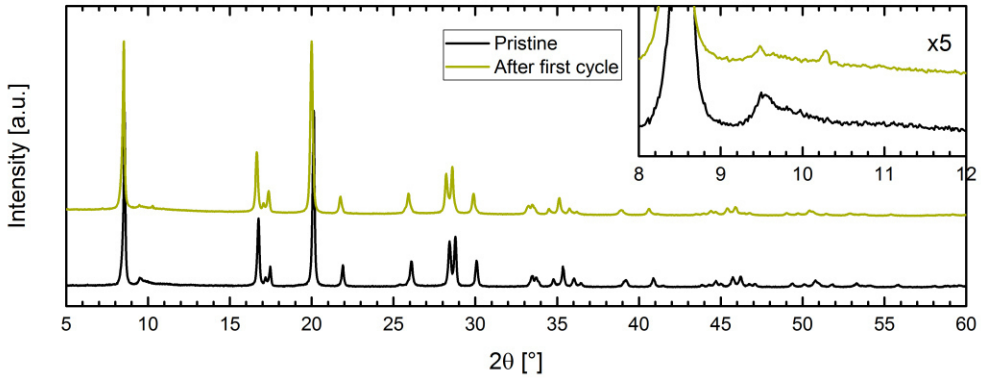

Figure S1. XRD patterns of the pristine material and from an electrode harvested in the discharged state after the first cycle. The intensity is normalized to the maximum intensity of the (003) reflection at 8.5°. The inset shows a magnification of the weak reflections between 9 and 12°. The XRD patterns were obtained in a 0.3 mm borosilicate capillary as sample holder (Debye-Scherrer geometry) with a STOE STADI P diffractometer (STOE, Germany) using Mo-$K_{\alpha 1}$ radiation (λ = 0.70932 Å, 50 kV, 40 mV) and a Mythen 1K detector.

2) Oxygen release due to Li_2MnO_3 activation

In the following section, the theoretical amount of oxygen evolved according to Eq. 1 in the main part is calculated. For this calculation, the following notation of our HE-NCM material is used: 0.42 Li_2MnO_3 • 0.58 $Li[Ni_{0.38}Co_{0.21}Mn_{0.41}]O_2$, corresponding to a molar mass of 104.8 g mol^{-1}. Assuming that the complete Li_2MnO_3 phase is converted into MnO_2, the expected amount of evolved O_2 would be

$$n^{\text{theor}}_{O_2,Li_2MnO_3} = \frac{1}{2} \cdot \frac{0.42}{104.8 \text{ g mol}^{-1}} \approx 2000 \text{ µmol}_{O_2} \text{ g}^{-1}_{AM} \quad [S1]$$

Using Faraday's law and $4e^-/O_2$, the gas evolution would lead to a charge capacity of ≈215 mAh g^{-1}_{AM}. Analogous to Eq. S1, the overall oxygen (as O_2) in the HE-NCM structure amounts to

$$n^{\text{theor}}_{O_2,\text{HE-NCM}} = \frac{1}{2} \cdot \frac{3 \cdot 0.42 + 2 \cdot 0.58}{104.8 \text{ g mol}^{-1}} \approx 11.5 \text{ mmol}_{O_2} \text{ g}^{-1}_{AM} \quad [S2]$$

This means that ca. 17% of the total oxygen in the HE-NCM lattice have to be extracted in case of a quantitative conversion of the Li_2MnO_3 phase according to Eq. 1.

3) O_2 and CO_2 solubility in the electrolyte

The O_2 concentration in the electrolyte can be derived from the so-called Bunsen coefficient, α. It is defined as the volume of gas, reduced to 273.15 K and 1 atm, which is adsorbed by unit volume of solvent (at the temperature of measurement) under a partial pressure of 1 atm (in units of $cm^3_{gas}\ cm^{-3}_{liquid}$).[S1] In the case of organic carbonates such as EC, PC, DMC, and DEC, measured as 1:1 binary mixtures with 1 M $LiPF_6$ at 25°C, the Bunsen coefficient of O_2 ranges from $\alpha \approx 0.05$ to 0.1.[S1] By applying the ideal gas law, this values translate to a concentration of ca. 2-4 mM O_2 in the electrolyte (which is consistent with 4.8 mM measured for 0.2 M TBATFSI in PC in a rotating ring-disk electrode study[S2]). For our electrolyte LP57 (1 M $LiPF_6$ in EC:EMC 3:7 by weight) we can suppose a similar solubility.

As the actual concentration in the electrolyte scales linearly with the applied partial pressure of O_2 (according to Henry's law), one has to find a general expression for the amount in the liquid phase, $n_{O_2,l}$, relative to the amount in the gas phase, $n_{O_2,g}$. The O_2 amount in the liquid phase is given by the Bunsen coefficient, the volume of liquid, V_l, and the molar fraction of O_2 in the gas phase, $x_{O_2,g}$,

$$n_{O_2,l} = \frac{V_{O_2,l}}{V_{m,l}} = \frac{\alpha \cdot V_l}{V_{m,l}} \cdot x_{o_2,g} \qquad [S3]$$

where $V_{m,l} = 22.414\ l\ mol^{-1}$ is the molar volume following the definition of the Bunsen coefficient (0°C and 1 atm). The molar fraction includes the partial pressure of O_2, $x_{O_2,g} = p_{O_2}/p^o$ (p^o = 1 atm).

The O_2 amount in the gas phase is defined by the cell volume, V_{OEMS}, and also $x_{O_2,g}$,

$$n_{O_2,g} = \frac{V_{O_2,g}}{V_{m,g}} = \frac{V_{OEMS}}{V_{m,g}} \cdot x_{o_2,g} \qquad [S4]$$

where $V_{m,g} = 24.465\ l\ mol^{-1}$ is the molar volume at the measurement conditions (25°C and 1 atm).

Consequently, the ratio $n_{O_2,l}/n_{O_2,g}$ can be calculated independently of the partial pressure as follows:

$$\frac{n_{O_2,l}}{n_{O_2,g}} = \frac{\alpha \cdot V_l}{V_{OEMS}} \cdot \frac{V_{m,g}}{V_{m,l}} = \frac{0.1 \cdot 100 \cdot 10^{-6}\ l}{10 \cdot 10^{-3}\ l} \cdot \frac{24.465\ l\ mol^{-1}}{22.414\ l\ mol^{-1}} = 1.1 \cdot 10^{-3} \qquad [S5]$$

Using the higher limit of the Bunsen coefficient ($\alpha = 0.1$), V_l = 100 µl, and V_{OEMS} = 10 ml, the fraction of O_2 dissolved in the electrolyte corresponds to ca. 0.1% relative to the gaseous O_2 and is thus negligible for the further analysis.

As the CO_2 solubility in the electrolyte is roughly one order of magnitude higher than O_2,[S3] the error amounts here to ca. 1%.

4) Literature overview about the formation of a spinel layer

There are several (S)TEM studies in the literature where a spinel-like surface layer was identified on Li- and Mn-rich layered oxides. A brief overview is provided in the following Table S1. Depending on the investigated conditions, a few nm thick spinel layer was either found on the pristine material,[S4] after the first cycle,[S7-S9] or during continuous cycling.[S10] Similar to the O_2 evolution at the end of the first charge, Qiu et al. have formed a ≈2 nm thick spinel/rock-salt-like phase by chemically creating oxygen vacancies on their material.[S5] Furthermore, Koga et al. have shown that the layered phase is converted into a spinel-type phase above 940°C during thermal treatment.[S6] This thermally induced phase transformation supports the analogy to the formation of a spinel surface layer through charging at high potentials.

Table S1. Overview of the literature which identified a spinel surface layer on Li- and Mn-rich layered oxides. For better comparison, the composition is given in the same way for all the materials, $Li_{1+x}Me_{1-x}O_2$. The abbreviations of the applied techniques stand for (scanning) transmission electron microscopy ((S)TEM), electron energy loss spectroscopy (EELS), X-ray energy dispersive spectroscopy (XEDS), thermal gravimetric analysis (TGA), and X-ray diffraction (XRD).

Reference	Material	Technique	Condition	Result
This work	$Li_{1.17}[Ni_{0.22}Co_{0.12}Mn_{0.66}]_{0.83}O_2$ = $Li_{1.17}Ni_{0.18}Co_{0.10}Mn_{0.55}O_2$	OEMS	After 1st charge	≈2-3 nm thick spinel-like surface layer calculated from evolved O_2 (and CO_2)
S4	$Li_{1.20}Ni_{0.13}Co_{0.13}Mn_{0.54}O_2$	STEM, EELS, XEDS	Pristine	≈2 nm thick Co- and/or Ni-rich spinel with antisite defects (on selected surface facets)
S5	$Li_{1.144-2x}Ni_{0.136}Co_{0.136}Mn_{0.544}O_{2-x}$ (with chemically created O vacancies on the surface)	(S)TEM, EELS	Pristine	≈2 nm thick spinel/rock-salt-like phase on the surface
S6	$Li_{1.20}Ni_{0.13}Co_{0.13}Mn_{0.54}O_2$	TGA, XRD	Variation of synthesis temperature	Spinel-type phase above 940°C (bulk transformation due to heat treatment)
S7, S8	$Li_{1.20}Ni_{0.18}Mg_{0.01}Mn_{0.61}O_2$ (Co replaced by Mg)	(S)TEM, EELS	After 1st charge (and discharge)	≈2-3 nm thick defect spinel phase at the edge of the particles
S9	$Li_{1.20}Ni_{0.13}Co_{0.13}Mn_{0.54}O_2$	(S)TEM	After 1st cycle	"Splayered" domains (i.e., between layered and spinel) at the external part of the particles
S10	$Li_{1.20}Ni_{0.20}Mn_{0.60}O_2$ (Co-free material)	(S)TEM, EELS, XEDS	Continuous cycling (100 cycles)	Ni-enriched surface reconstruction layer, sequential phase transition of $C2/m \rightarrow I41 \rightarrow$ Spinel

5) Oxygen release due to spinel transformation

According to the general Eq. 2, the gas evolution accompanied by the spinel transformation depends on the exact stoichiometry $Li_xMe_yO_2$, including the fraction of transition metal ions (y) and the degree of delithiation during charge (x). Regarding the first point, we consider the $Li_{1+x}Me_{1-x}O_2$ notation of the pristine material, $Li_{1.17}[Ni_{0.22}Co_{0.12}Mn_{0.66}]_{0.83}O_2$ (molar mass 86.8 g mol^{-1}), for which the theoretical delithiation capacity is ca. 360 mAh g^{-1}_{AM}. The degree of delithiation depends on the state of charge which was selected here at 4.6 V, where the O_2 (and CO_2) evolution due to spinel transformation starts. For the HE-NCM/Li measurement in Figure 3 (black lines), the charge capacity at 4.6 V accounts to ≈275 mAh g^{-1}_{AM}. Consequently, 76% of the theoretically available charge have been extracted, and if we assume that this capacity comes only from delithiation, 0.89 of the 1.17 lithium in the structure have been removed. Thus, the corresponding composition of the material at 4.6 V is $Li_{0.28}[Ni_{0.22}Co_{0.12}Mn_{0.66}]_{0.83}O_2$ ($Li_{0.28}Me_{0.83}O_2$, Me = Ni, Co, Mn), which undergoes the spinel transformation as written in Eq. 4. The theoretical amount of evolved O_2 for the complete conversion of the layered oxide of that composition into the spinel phase would be

$$n^{\text{theor}}_{O_2,\text{spinel}} = \frac{0.26}{86.8\ \text{g mol}^{-1}} \approx 3000\ \mu\text{mol}_{O_2}\ \text{g}^{-1}_{AM} \qquad [S6]$$

The molar fraction of the spinel phase, x_{spinel}, can be calculated by comparing this value to the measured gas evolution of O_2 and CO_2 derived from lattice oxygen:

$$x_{\text{spinel}} = \frac{n^{\text{meas}}_{O_2,\text{spinel}}}{n^{\text{theor}}_{O_2,\text{spinel}}} \leq 1 \qquad [S7]$$

6) Thickness of the spinel layer

Since we believe that the spinel transformation proceeds from the outer to the inner part of the HE-NCM particles, the spinel phase is formed as a spherical shell as depicted in Figure S2. In order to keep our model simple, we assume spherical primary particles. Their average radius is calculated from the BET surface area, A_{BET}, and the crystallographic density, ϱ, of the pristine material as follows:

$$r = \frac{3}{A_{\text{BET}} \cdot \varrho} \approx 110\ \text{nm} \qquad [S8]$$

We calculated the thickness of the spinel surface layer using the following geometrical relation of a spherical shell:

$$\frac{V_{\text{shell}}}{V} = \frac{r^3 - r'^3}{r^3} = 1 - \left(\frac{r'}{r}\right)^3 = x_{\text{spinel}} \ \leftrightarrow\ r' = r \cdot \left(1 - x_{\text{spinel}}\right)^{\frac{1}{3}} \qquad [S9]$$

$$t_{\text{spinel}} = r - r' \qquad [S10]$$

Taking the simplifying approximation that the density and molar mass of the layered oxide and the spinel phase are roughly the same, the volume ratio V_{shell}/V equals the molar fraction of the spinel phase, x_{spinel}.

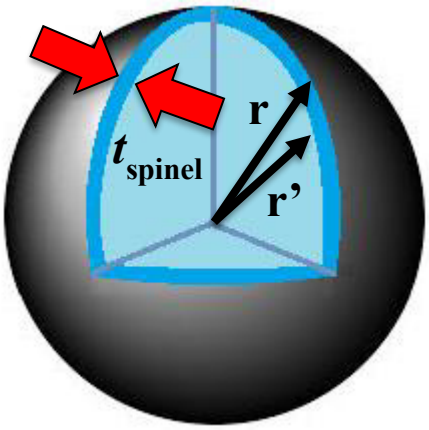

Figure S2. Schematic of the HE-NCM particles. The spinel phase is formed as a spherical shell with the thickness t_{spinel}.

References

S1. J. Read, K. Mutolo, M. Ervin, W. Behl, J. Wolfenstine, A. Driedger, and D. Foster, *J. Electrochem. Soc.*, **150**, A1351 (2003).

S2. J. Herranz, A. Garsuch, and H. A. Gasteiger, *J. Phys. Chem. C*, **116**, 19084 (2012).

S3. P. Kolář, H. Nakata, J.-W. Shen, A. Tsuboi, H. Suzuki, and M. Ue, *Fluid Phase Equilib.*, **228-229**, 59 (2005).

S4. A. K. Shukla, Q. M. Ramasse, C. Ophus, H. Duncan, F. Hage, and G. Chen, *Nat. Commun.*, **6**, 8711 (2015).

S5. B. Qiu, M. Zhang, L. Wu, J. Wang, Y. Xia, D. Qian, H. Liu, S. Hy, Y. Chen, K. An, Y. Zhu, Z. Liu, and Y. S. Meng, *Nat. Commun.*, **7**, 12108 (2016).

S6. H. Koga, L. Croguennec, P. Mannessiez, M. Ménétrier, F. Weill, L. Bourgeois, M. Duttine, E. Suard, and C. Delmas, *J. Phys. Chem. C*, **116**, 13497 (2012).

S7. A. Boulineau, L. Simonin, J.-F. Colin, E. Canévet, L. Daniel, and S. Patoux, *Chem. Mater.*, **24**, 3558 (2012).

S8. A. Boulineau, L. Simonin, J.-F. Colin, C. Bourbon, and S. Patoux, *Nano Lett.*, **13**, 3857 (2013).

S9. C. Genevois, H. Koga, L. Croguennec, M. Ménétrier, C. Delmas, and F. Weill, *J. Phys. Chem. C*, **119**, 75 (2015).

S10. P. Yan, A. Nie, J. Zheng, Y. Zhou, D. Lu, X. Zhang, R. Xu, I. Belharouak, X. Zu, J. Xiao, K. Amine, J. Liu, F. Gao, R. Shahbazian-Yassar, J.-G. Zhang, and C.-M. Wang, *Nano Lett.*, **15**, 514 (2015).

3.1.2 Oxygen Release and Its Effect on the Cycling Stability of $LiNi_xMn_yCo_zO_2$ (NMC) Cathode Materials for Li-Ion Batteries

In this section the article "Oxygen Release and Its Effect on the Cycling Stability of $LiNi_xMn_yCo_zO_2$ (NMC) Cathode Materials for Li-Ion Batteries" will be presented. It was published in the *Journal of the Electrochemical Society* on May 2, 2017 as open access article distributed under the terms of the Creative Commons Attribution Non-Commercial No Derivatives 4.0 License.[101] The results of the publication were presented on international conferences, e.g., by Roland Jung at the 231st Meeting of The Electrochemical Society (May 28- June 1, 2017) in New Orleans, USA (Abstract Number: #39). The permanent web-link to the publication is http://jes.ecsdl.org/content/164/7/A1361 and the DOI is 10.1149/2.0021707jes.

In the paper we compare the cycling stability of $LiNi_{1/3}Mn_{1/3}Co_{1/3}O_2$ (NMC111), $LiNi_{0.6}Mn_{0.2}Co_{0.2}O_2$ (NMC622), and $LiNi_{0.8}Mn_{0.1}Co_{0.1}O_2$ (NMC811) cathodes versus graphite anodes in LP57 electrolyte (1 M $LiPF_6$ in EC/EMC 3:7) and show that NMC111 and NMC622 can be cycled with a capacity retention of ≥90% after 300 cycles at a 1 C-rate, if the upper cut-off voltage of the NMC-graphite cell is limited to ≤4.4 V.[101] In contrast, for the NMC811 material a similar capacity retention of ≥90% can only be obtained if the cut-off potential is limited to ≤4.0 V. To find the origin of these different stability limits, we investigate the gas evolution occurring from NMC111, NMC622, and NMC811 using On-Line Electrochemical Mass Spectrometry (OEMS). We demonstrate that all three materials release reactive oxygen from the particle surface once ~80% of the lithium is removed from the layered structure, which simultaneously marks the potential limit for stable cycling performance.[101] In other words, stable charge/discharge cycling is possible as long as the upper cut-off voltage is below the onset potential of the oxygen release, yielding the above mentioned stability limits. Upon oxygen release, the surface of the layered NMC transforms into spinel and/or rock-salt type phases (MO_2 (layered) → M_3O_4 (spinel) → MO (rock-salt), corresponding to an increase of the metal/oxygen ratio from 1:2 → 3:4 → 1:1). In parallel to the oxygen release, i.e., at the O_2 evolution onset potential, we also observe the onset of CO_2 and CO evolution, suggesting that the released oxygen is reacting with the electrolyte forming CO_2 and CO. This reaction of released oxygen with electrolyte we refer to as *chemical* electrolyte oxidation. To investigate whether the CO_2 and CO really stem from *chemical* instead of *electrochemical* electrolyte oxidation, we investigate the gas evolution from the high-voltage spinel cathode $LiNi_{0.43}Mn_{1.57}O_4$ (LNMO). We neither observe any oxygen

release from the LNMO surface nor do we detect any CO_2 and CO until a potential of 5.0 V, proving that the vast majority of the observed CO_2 and CO when NMC electrodes are used are due to the release of reactive oxygen which reacts with the electrolyte. A more detailed study on the *chemical* in comparison to the *electrochemical* electrolyte oxidation will be presented in section 3.1.3. In the work presented in this section, all experiments were conducted at 25 °C. The temperature dependence of the onset potential for oxygen release, of the quantity of released gas, and of the NMC cycling stability will be presented in section 3.1.4.

The phase transformation of NMC from the layered to spinel and/or rock-salt was shown previously to occur when charged NMC is exposed to elevated temperatures. In particular, at temperatures ≥170°C, the bulk of the layered NMC structure transforms under lattice oxygen release into a spinel and eventually a rock-salt structure.[92-94, 98-100, 199, 200] Under battery operating conditions (<60 °C), several other studies on NMC[166], $LiNi_{0.8}Co_{0.2}O_2$[148, 149], $LiNiO_2$[150], and NCA ($LiNi_{0.80}Co_{0.15}Al_{0.05}O_2$)[151] demonstrated that the transformation into spinel and rock-salt phases is limited to the particle surface while keeping the bulk structure intact. This is most likely due to the limited diffusivity of lattice oxygen to the particle surface at battery operating conditions (<60 °C) where it can be released from the oxide structure as molecular oxygen. However, in none of the above mentioned studies oxygen release was shown, even though the occurrence of phase transitions at the outer surface of NMC particles suggested a release of oxygen from the particle surface. Explicit oxygen release was described in many publications to occur for Li- and Mn- rich NMC materials ($Li_{1+x}(Ni,Mn,Co)_{1-x}O_2$, overlithiated NMC, see section 3.1.1).[168, 190, 191, 201, 202] However, for stoichiometric NMCs there was only one publication showing oxygen release for NMC111 upon charging, yet no implications for the cycling stability were shown.[203]

Author Contributions

Roland Jung designed and performed the experiments and analyzed the data. Roland Jung, Michael Metzger, and Hubert Gasteiger wrote the manuscript. All authors discussed the results and commented on the manuscript.

Oxygen Release and Its Effect on the Cycling Stability of $LiNi_xMn_yCo_zO_2$ (NMC) Cathode Materials for Li-Ion Batteries

Roland Jung,[a,b,*,z] Michael Metzger,[a,*] Filippo Maglia,[b] Christoph Stinner,[b] and Hubert A. Gasteiger[a,]**

[a]*Chair of Technical Electrochemistry, Department of Chemistry and Catalysis Research Center, Technische Universität München, Garching, Germany*
[b]*BMW AG, Munich, Germany*

Layered $LiNi_xMn_yCo_zO_2$ (NMC) is a widely used class of cathode materials with $LiNi_{1/3}Mn_{1/3}Co_{1/3}O_2$ (NMC111) being the most common representative. However, Ni-rich NMCs are more and more in the focus of current research due to their higher specific capacity and energy. In this work we will compare $LiNi_{1/3}Mn_{1/3}Co_{1/3}O_2$ (NMC111), $LiNi_{0.6}Mn_{0.2}Co_{0.2}O_2$ (NMC622), and $LiNi_{0.8}Mn_{0.1}Co_{0.1}O_2$ (NMC811) with respect to their cycling stability in NMC-graphite full-cells at different end-of-charge potentials. It will be shown that stable cycling is possible up to 4.4 V for NMC111 and NMC622 and only up to 4.0 V for NMC811. At higher potentials, significant capacity fading was observed, which was traced back to an increase in the polarization of the NMC electrode, contrary to the nearly constant polarization of the graphite electrode. Furthermore, we show that the increase in the polarization occurs when the NMC materials are cycled up to a high-voltage feature in the dq/dV plot, which occurs at ∼4.7 V vs. Li/Li^+ for NMC111 and NMC622 and at ∼4.3 V vs. Li/Li^+ for NMC811. For the latter material, this feature corresponds to the H2 → H3 phase transition. Contrary to the common understanding that the electrochemical oxidation of carbonate electrolytes causes the CO_2 and CO evolution at potentials above 4.7 V vs. Li/Li^+, we believe that the observed CO_2 and CO are mainly due to the chemical reaction of reactive lattice oxygen with the electrolyte. This hypothesis is based on gas analysis using On-line Electrochemical Mass Spectrometry (OEMS), by which we prove that all three materials release oxygen from the particle surface and that the oxygen evolution coincides with the onset of CO_2 and CO evolution. Interestingly, the onsets of oxygen evolution for the different NMCs correlate well with the high-voltage redox feature at ∼4.7 V vs. Li/Li^+ for NMC111 and NMC622 as well as at ∼4.3 V vs. Li/Li^+ for NMC811. To support this hypothesis, we show that no CO_2 or CO is evolved for the $LiNi_{0.43}Mn_{1.57}O_4$ (LNMO) spinel up to 5 V vs. Li/Li^+, consistent with the absence of oxygen release. Lastly, we demonstrate by the use of ^{13}C labeled conductive carbon that it is the electrolyte rather than the conductive carbon which is oxidized by the released lattice oxygen. Taking these findings into consideration, a mechanism is proposed for the reaction of released lattice oxygen with ethylene carbonate yielding CO_2, CO, and H_2O.

Manuscript submitted January 16, 2017; revised manuscript received April 13, 2017. Published May 2, 2017. This article is a version of Paper 39 from the New Orleans, Louisiana, Meeting of the Society, May 28-June 1, 2017.

Li-Ion batteries have recently been used as power supply for electric vehicles (EVs). In order to penetrate the mass market, a significant reduction in costs and further performance improvements have to be achieved to realize a longer driving range of EVs.[1] The latter highly depends on the choice of the cathode active material, for which several potential materials exist,[2] of which layered lithium nickel manganese cobalt oxide ($LiNi_xMn_yCo_zO_2$, NMC) is one of the most promising class of cathode materials.[3] This is due to the high specific capacity and good stability of the layered structure which changes its volume by less than 2% during Li insertion/extraction.[4–6] Due to the sloped voltage profile of NMC, a higher capacity and energy density can be achieved when the upper cutoff voltage is increased.[7–9] Even though the theoretical capacity of NMC is as high as ∼275 mAh/g_{NMC}, not all of the lithium can be extracted due to structural instabilities occurring when an exceedingly large fraction of lithium is removed.[9,10] Additionally, the sloped voltage profile requires very high voltages to achieve complete removal of lithium, which in turn can lead to electrolyte oxidation, surface film formation, and transition metal dissolution, ultimately diminishing the cycling stability.[11–17] For these reasons, the operating potential of NMC based cathode materials is nowadays limited to ∼4.3 V, restricting their capacities to much below their theoretical values.[5] In order to improve the accessible capacity at reasonable upper cutoff voltages, Ni-rich NMCs (Ni-content >> Mn- and Co-content) recently became the focus of interest, as more lithium can be extracted from their structure within the same voltage window. Therefore, they provide larger specific capacities and energy densities, which are crucial for a longer driving range of electric vehicles.[2,18,19]

So far, however, Ni-rich NMCs suffer from a shorter lifetime due to a faster capacity fading compared to $LiNi_{1/3}Mn_{1/3}Co_{1/3}O_2$ (NMC111), the most common NMC material with a nickel:manganese:cobalt ratio of 1:1:1.[18–20] For example, Noh et al. reported initial capacities at a 0.1 C-rate and an end-of-charge potential of 4.3 V vs. Li/Li^+ of 203 mAh/g and 163 mAh/g for $LiNi_{0.8}Mn_{0.1}Co_{0.1}O_2$ (NMC811) and NMC111, respectively.[18] Unfortunately, the capacity retention for NMC811 in NMC-Li cells after 100 cycles at a 0.5 C-rate was only 70% compared to 92% for NMC111.[18] Furthermore, it was shown that layered oxides with rising Ni-contents are thermally less stable.[18,21] At temperatures ≥170°C, the bulk materials undergo a two-phase transition from their layered structure to a spinel structure and eventually to a rock-salt structure, both of which are accompanied by release of lattice oxygen.[18,21–27] For materials aged under battery operating conditions (<60°C), the formation of disordered spinel and rock-salt type phases was reported to happen on the particle surface with the bulk structure remaining intact, i.e., remaining in the rhombohedral structure as reported for NMC,[9] $LiNi_{0.8}Co_{0.2}O_2$,[28,29], $LiNiO_2$,[30], and NCA ($LiNi_{0.80}Co_{0.15}Al_{0.05}O_2$).[31] Even though it was not explicitly shown in these latter reports, the observed phase transitions suggest a release of oxygen from the particle surface, which was also pointed out in the reports by Abraham et al., Muto et al., and Hwang et al.[28–31] So far, a release of oxygen from the oxide lattice under battery operating conditions was shown only for overlithiated NMC materials ($Li_{1+x}(Ni,Mn,Co)_{1-x}O_2$), in which lithium additionally occupies the transition metal layers.[32–36] The exception is a recent publication by Guéguen et al., who showed oxygen evolution during battery cycling for NMC111.[37]

In this study, we will compare two Ni-rich NMCs, namely $LiNi_{0.6}Mn_{0.2}Co_{0.2}O_2$ (NMC622) and $LiNi_{0.8}Mn_{0.1}Co_{0.1}O_2$ (NMC811) to $LiNi_{1/3}Mn_{1/3}Co_{1/3}O_2$ (NMC111) with respect to their cycling

*Electrochemical Society Student Member.
**Electrochemical Society Fellow.
[z]E-mail: roland.jung@tum.de

stability in full-cells with graphite anodes. Through an evaluation of the anode and cathode polarization in a three-electrode set-up, we conclude that the capacity fading at high voltages is due to the NMC electrode rather than the graphite electrode. By means of On-line Electrochemical Mass Spectrometry (OEMS) we prove that at high degrees of delithiation all three NMC materials release oxygen already at room temperature. The onset of the oxygen evolution corresponds well with the onset of the formation of CO_2 and CO, which is typically assigned to electrochemical electrolyte oxidation, raising the question whether the evolution of O_2 actually causes the observed CO_2 and CO evolution. This question as well as the consequences of the oxygen release on the polarization and the cycling stability will be discussed with the experimental findings presented in this work.

Experimental

Electrode Preparation.—Layered NMC and spinel LNMO electrodes were prepared by dispersing the active material particles ($LiNi_{1/3}Mn_{1/3}Co_{1/3}O_2$ (NMC111), $LiNi_{0.6}Mn_{0.2}Co_{0.2}O_2$ (NMC622), $LiNi_{0.8}Mn_{0.1}Co_{0.1}O_2$ (NMC811) or $LiNi_{0.43}Mn_{1.57}O_4$ (LNMO), all from Umicore, Belgium) (91.5 $\%_{wt}$), conductive carbon (Super C65, Timcal, Switzerland) (4.4 $\%_{wt}$) and polyvinylidene fluoride binder (PVDF, Kynar HSV 900, Arkema, France) (4.1 $\%_{wt}$) in N-methylpyrrolidone (NMP, anhydrous, 99.5%, Sigma-Aldrich). The slurry was mixed in a planetary mixer (Thinky, USA) at 2000 rpm for 2×5 minutes. In between the two runs the slurry was ultrasonicated for 10 minutes in an ultrasonic bath. The resulting ink was spread onto aluminum foil (thickness 18 μm, MTI Corporation, USA) using a gap bar coater (RK PrintCoat Instruments, UK). For OEMS measurements, the ink was coated onto a H2013 polyolefin separator (Celgard, USA) or a stainless steel mesh (316 grade, 26 μm aperture, 25 μm wire diameter, The Mesh Company, UK) to allow for a short diffusion time of the evolved gases to the head-space of the OEMS cell and to the capillary leading to the mass spectrometer.[38,39] NMC622 electrodes containing ^{13}C-labeled carbon (99 $\%_{atom}$ ^{13}C, Sigma-Aldrich, Germany) were prepared with the same composition as the ones containing Super C65, however, due to strong agglomeration of the carbon, the ink was prepared in a ball mill (Pulverisette 7, Fritsch, Germany) using zirconia balls with a diameter of 10 mm at 180 rpm for 60 minutes. After drying at 50°C, electrodes were punched and dried overnight at 120°C (if coated on aluminum or stainless steel mesh) and at 95°C (if coated on H2013 separator) under dynamic vacuum in a glass oven (drying oven 585, Büchi, Switzerland) and transferred to a glove box (O_2 and $H_2O < 0.1$ ppm, MBraun, Germany) without exposure to ambient air.

The graphite electrodes were composed of graphite (MAG-D20, Hitachi), Super C65 (Timcal, Switzerland), sodium carboxymethylcellulose (Na-CMC, Dow Wolff Cellulosics) and styrene-butadiene rubber (SBR, JSR Micro) at a weight ratio of 95.8:1:1:2.2. The slurry was prepared by dispersing graphite, Super C65 and Na-CMC in highly pure water (18 MΩ cm, Merck Millipore, Germany) using a planetary mixer (Thinky, USA; at 2000 rpm for 30 minutes). The slurry was ultrasonicated for 10 minutes in an ultrasonic bath. SBR was added to the slurry and mixed at 500 rpm for 2 minutes. The ink was coated onto copper foil (thickness 12 μm, MTI Corporation, USA) using a gap bar coater (RK PrintCoat Instruments, UK). The coating was dried at 50°C in air, punched out, dried overnight at 120°C under vacuum in a glass oven (Büchi oven, s. above) and transferred to a glove box without exposure to ambient air.

The specific surface areas of the NMC and LNMO were determined by BET, using an Autosorb iQ nitrogen gas sorption analyzer (Quantachrome Instruments, USA). The determined BET areas of these materials are 0.26 m^2/g, 0.35 m^2/g, 0.18 m^2/g, and 0.23 m^2/g for NMC111, NMC622, NMC811, and LNMO, respectively.

Electrochemical characterization.—The electrochemical characterization of NMC was performed in Swagelok T-cells which were assembled in an argon filled glove box (O_2 and $H_2O < 0.1$ ppm, MBraun, Germany), with NMC as working electrode (10 mm diameter) and graphite as counter electrode (11 mm diameter). The areal mass loading of the NMC electrodes was 15.5 ± 1 mg/cm^2 and the one of the graphite electrodes was adapted according to the mass loading of the NMC electrodes and their specific capacities at the various cutoff voltages, aiming to achieve a constant balancing factor. The areal capacity of the anode (in mAh/cm^2) was 1.2-fold oversized compared to the cathode (referenced to the reversible capacities of NMC and graphite at a 1 C-rate; if referenced to 0.1 C, the anode is roughly 1.1-fold oversized). To monitor the potential of both the NMC cathode and the graphite anode, a lithium reference electrode (thickness 0.45 mm, battery grade foil, 99.9 %, Rockwood Lithium, USA) was used. Two glass fiber separators (glass microfiber filter, 691, VWR, Germany) punched to a diameter of 11 mm were used between working and counter electrode, and one at the reference electrode (diameter of 10 mm). 80 μL of LP57 electrolyte (1 M $LiPF_6$ in EC:EMC 3:7 wt/wt, < 20 ppm H_2O, BASF, Germany) were used between working and counter electrode and 40 μL were added to the reference electrode side. The cells were cycled in a climate chamber (Binder, Germany) at 25°C with a battery cycler (Series 4000, Maccor, USA). All cells were cycled 300 times at 1 C with a lower cutoff of 3 V and an upper cutoff of 4.2, 4.4, or 4.6 V for NMC111 and NMC622, and 4.0, 4.1, 4.2 V for NMC811. Prior to cycling, the formation of the cells was done with 2 cycles at 0.1 C in the voltage range between 3 V and 4.2 V. If the upper cutoff was >4.2 V, the first cycle after formation, i.e., the third cycle of the cell was also done at 0.1 C to the specified upper cutoff. For upper cutoff voltages <4.2 V, i.e., for the NMC811 cells also the upper cutoff during formation was adapted to this voltage. The C-rate was referenced to the approximate reversible capacity of the NMC at 1 C: i) 140, 160, and 180 mAh/g for NMC111 at upper cutoff voltages of 4.2, 4.4, and 4.6 V, respectively; ii) 160, 180, and 200 mAh/g for NMC622 at upper cutoff voltages of 4.2, 4.4, and 4.6 V, respectively; and, iii) 130, 150, and 170 mAh/g for NMC811 at cutoff voltages of 4.0, 4.1, and 4.2 V, respectively. The charge was done in constant current-constant voltage (CCCV) mode with a current limitation corresponding to C/20, while the discharge was done in constant current (CC) mode. Two cells were built for each combination of NMC material and cutoff voltage and the error bars in the figures represent the standard deviation from two cells for each combination.

For recording dq/dV plots, NMC-graphite full-cells were assembled as described above and were cycled in a climate chamber (Binder, Germany) at 25°C with a battery cycler (Series 4000, Maccor, USA). The formation of the cells was done at 0.1 C (two cycles) in the voltage range between 3 V and 4.2 V. In the third cycle, the cutoff voltage was increased to 4.8 V. The lower cutoff was kept constant at 3 V. The dq/dV plot of the third cycle will be shown in the Results section.

On-line electrochemical mass spectrometry (OEMS).—Two different types of OEMS experiments were designed and performed with either NMC or spinel LNMO (diameter 15 mm) as working electrode, and either metallic lithium or graphite as counter electrode. With metallic lithium as counter electrode (lithium metal foil, diameter 16 mm, thickness 0.45 mm, battery grade foil, 99.9 %, Rockwood Lithium, USA), two H2013 polyolefin separators (diameter 28 mm, Celgard, USA) and 120 μL of LP57 electrolyte (1 M $LiPF_6$ in EC:EMC 3:7 wt/wt, < 20 ppm H_2O, BASF, Germany) were employed. The cells were charged up to 5 V at a 0.05 C-rate (referenced to the theoretical capacities of NMC111, NMC622, NMC811, and LNMO of 277.8 mAh/g, 276.5 mAh/g, 275.5 mAh/g, and 147 mAh/g, respectively). The loadings of the cathodes were 15.8 mg/cm^2 (NMC111), 15.5 mg/cm^2 (NMC622), 15.0 mg/cm^2 (NMC811), and 17.5 mg/cm^2 (LNMO). All electrodes were coated on H2013 separator (Celgard, USA).

With graphite as the counter electrode (diameter 16 mm, see upper section for details on the type of graphite), two glass fiber separators (diameter 28 mm, glass microfiber filter, 691, VWR, Germany) and 400 μL of 1.5 M $LiPF_6$ in ethylene carbonate (EC, BASF, Germany) were employed. The mixture of EC with $LiPF_6$ is a liquid at room temperature due to the melting point depression caused by the addition

of $LiPF_6$. The cells were cycled 4 times at a 0.2 C-rate (referenced to the above given theoretical capacities of the NMC materials) in the voltage range 2.6–4.8 V for NMC111 and NMC622 and from 2.6–4.4 V for NMC811. The loadings of the cathode active material were 9.4 mg/cm^2 (NMC111), 11.4 mg/cm^2 (NMC622), and 9.3 mg/cm^2 (NMC811) and the electrodes were coated on stainless steel mesh (see above for details). The graphite counter electrode was capacitively 1.4-fold oversized (referenced to the theoretical capacities of NMC and graphite).

All cells were assembled in a glove box with argon atmosphere (O_2 and H_2O < 0.1 ppm, MBraun, Germany). The cells were placed in a climate chamber at 25°C (Binder, Germany) and connected to the potentiostat (Series G300 potentiostat, Gamry, USA) and the mass spectrometer system, which has been described in detail elsewhere.[39] The cells were held at OCV for 4 h before starting the above described protocols. The gas evolution during the OCV and the charging/cycling period was recorded by OEMS. All mass signals were normalized to the ion current of the ^{36}Ar isotope to correct for fluctuations of pressure and temperature. Conversion of the ion currents to concentrations was done for O_2, CO_2, H_2, C_2H_4, and CO using calibration gases (Ar with 2000 ppm each of H_2, O_2, C_2H_4, and CO_2 as well as Ar with 2000 ppm each of H_2, O_2, CO, and CO_2; Westfalen, Germany) and based on a cell volume of 9.5 cm^3. Unlike all other gases quantified in this work, CO does not have a unique m/z channel. Therefore the amount of CO was determined on channel m/z = 28, which was corrected for the fractions of C_2H_4 and CO_2 both of which give additional intensity to channel m/z = 28. The fraction of the signal on channel m/z = 28 stemming exclusively from CO was therefore calculated as the total signal on channel m/z = 28 subtracted by 1.51 times the signal on channel m/z = 26 and 0.14 times the signal on channel m/z = 44, with the factors 1.51 and 0.14 being the fractions of C_2H_4 and CO_2 on channel m/z = 28 compared to their unique signals on m/z = 26 (C_2H_4) and m/z = 44 (CO_2), respectively. These factors were determined by flowing pure C_2H_4 and CO_2 through the OEMS cell and recording the resulting signals originating from the pure gases.[40]

Results

Electrochemical cycling of NMC-graphite cells.—Figure 1a shows the cycling stability of NMC111-graphite full-cells with different upper cutoff voltages of 4.2, 4.4, and 4.6 V. The cells have a very stable cycling performance for upper cutoff voltages of 4.2 V and 4.4 V (black and gray lines), however, cycling to 4.6 V leads to a fast capacity fading (light gray line), which is in agreement with previous reports in the literature.[9,11,13] While the error bars are hardly visibly for cutoff voltages ≤4.4 V and at low cycle numbers at a cutoff of 4.6 V, the error bars at higher cycle numbers significantly increase, which is due to the delayed onset of the so-called rollover-failure for the two cells. This failure mechanism was described previously by Dubarry et al. and Burns et al. and was shown to be due to growing kinetic resistances or more generally an impedance buildup.[41,42] In our data the increasing polarization stems almost exclusively from the NMC cathodes, which will be discussed below. The coulombic efficiencies (right axis in Figure 1a) for cells cycled to 4.2 V and 4.4 V are in average >99.9%, indicating the absence of major side reactions. When the end-of-charge voltage is increased to 4.6 V, the coulombic efficiency decreases to ~99.6% (before the onset of the rollover-failure), reflecting an increasing loss of cyclable lithium. A further decrease of the coulombic efficiency is observed at the onset of the rollover-failure. On the other hand, any increase in the polarization during cell discharge can be monitored by plotting the charge-averaged mean discharge voltage, defined as:

$$\bar{V}_{discharge} = \int V_{discharge} \cdot dq_{discharge} \,/\, \int dq_{discharge} \qquad [1]$$

As the cells were cycled with a lithium reference electrode, $\bar{V}_{discharge}$ can be determined independently for the NMC111 cathode ($\equiv \bar{V}^{cathode}_{discharge}$) and the graphite anode ($\equiv \bar{V}^{anode}_{discharge}$) for each end-of-charge voltage as a function of the cycle number, which is depicted in Figure 1b by the solid and dashed lines, respectively. While the energy

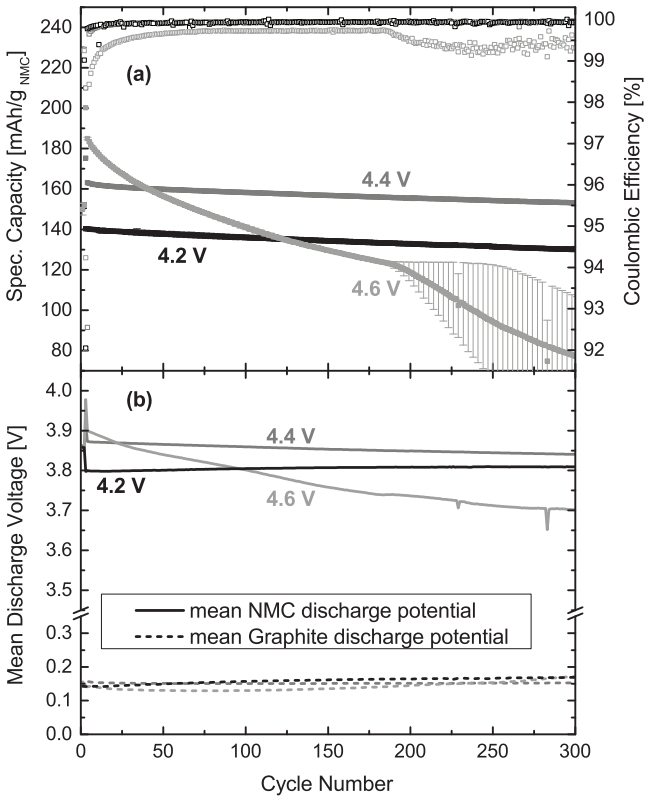

Figure 1. (a) Specific discharge capacity and coulombic efficiency of NMC111-graphite cells and (b) charge-averaged mean discharge voltage (s. Eq. 1) of the NMC111 cathode ($\equiv \bar{V}^{cathode}_{discharge}$; solid lines) and the graphite anode ($\equiv \bar{V}^{anode}_{discharge}$; dashed lines) vs. cycle number in LP57 electrolyte (1 M $LiPF_6$ in EC:EMC 3:7) operated with different upper cutoff voltages (4.2 V, 4.4 V, 4.6 V) and a constant lower cutoff voltage of 3.0 V. Formation was done at a rate of 0.1 C. Cycling was performed at 1 C and 25°C. For each condition, two independent cells were run and the data in the figure always represent the average of two cells (the error bars in (a) represent the standard deviation between the two cells).

fading of the cells is further detailed in the Discussion section, it may be noted here that the discharge energy for each cycle corresponds to the product of capacity and $\bar{V}_{discharge} = \bar{V}^{cathode}_{discharge} - \bar{V}^{anode}_{discharge}$. Under conditions where the loss of cyclable lithium is the only aging mechanism, i.e., in the absence of an impedance buildup, $\bar{V}^{cathode}_{discharge}$ for cathode active materials with a strongly sloping charge/voltage curve like NMC would be expected to gradually increase with the number of cycles. This can indeed be seen when cycling with an upper cutoff potential of 4.2 V (solid black line in Figure 1b). On the other hand, when impedance buildup becomes dominant, $\bar{V}^{cathode}_{discharge}$ decreases with the number of cycles, as can be seen when the upper cutoff potential reaches 4.6 V (solid light gray line in Figure 1b). Interestingly, the charge-averaged mean discharge voltages of the graphite anodes ($\bar{V}^{anode}_{discharge}$) remain fairly constant over the complete number of cycles, even at high end-of-charge voltages. This suggests that a crucial contributing factor for the fast capacity fading of the NMC111-graphite cells at an upper cutoff of 4.6 V is a strong impedance buildup on the NMC111 cathode rather than on the graphite anode. In fact, previous reports in the literature showed a drastic rise of the low frequency semicircle in the impedance spectra of NMC111-graphite[11] and NMC442-graphite cells,[43,44] which was attributed to the positive electrode. Later, Petibon et al. showed that the increase of impedance in NMC442-graphite cells operated at high cutoff potentials, indeed stems from the positive electrode, proven by using symmetric cells.[45] Even though these results are consistent with our observations on the charge-averaged mean discharge voltage (Figure 1b) one has to be careful since an additive-containing electrolyte was used in

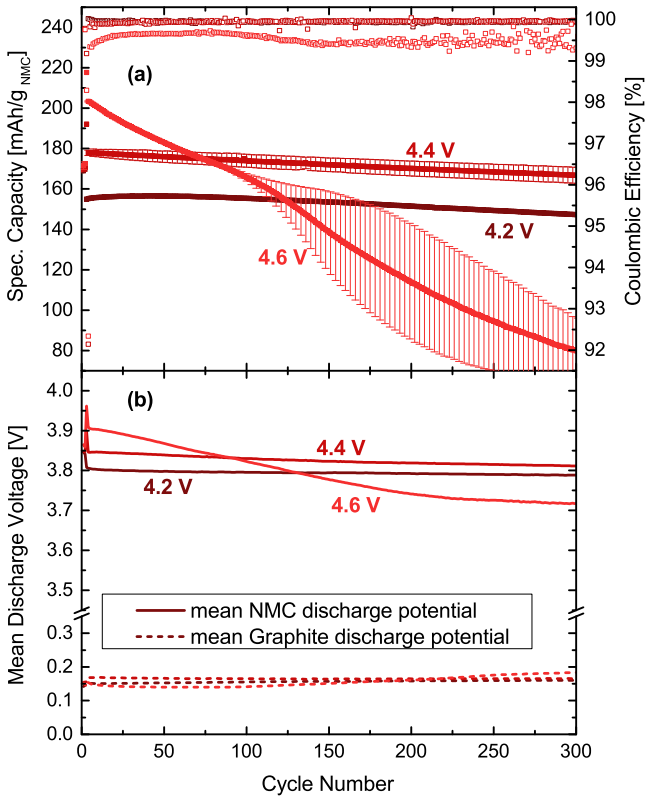

Figure 2. (a) Specific discharge capacity and coulombic efficiency of NMC622-graphite cells and (b) charge-averaged mean discharge voltage (s. Eq. 1) of the NMC622 cathode ($\equiv \bar{V}^{cathode}_{discharge}$; solid lines) and the graphite anode ($\equiv \bar{V}^{anode}_{discharge}$; dashed lines) vs. cycle number in LP57 electrolyte (1 M $LiPF_6$ in EC:EMC 3:7) operated with different upper cutoff voltages (4.2 V, 4.4 V, 4.6 V) and a constant lower cutoff voltage of 3.0 V. Formation was done at a rate of 0.1 C. Cycling was performed at 1 C and 25°C. For each condition, two independent cells were run and the data in the figure always represent the average of two cells (the error bars in (a) represent the standard deviation between the two cells).

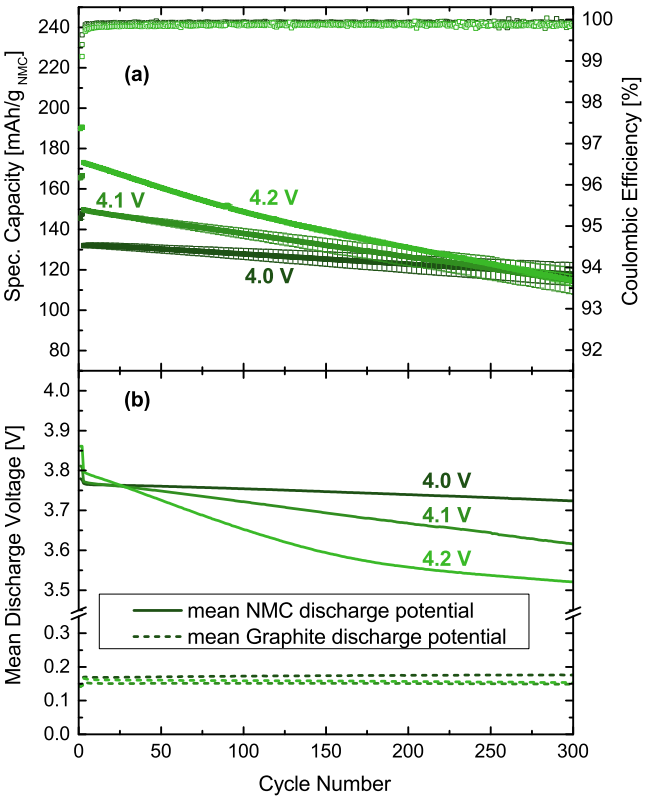

Figure 3. (a) Specific discharge capacity and coulombic efficiency of NMC811-graphite cells and (b) charge-averaged mean discharge voltage (s. Eq. 1) of the NMC811 cathode ($\equiv \bar{V}^{cathode}_{discharge}$; solid lines) and the graphite anode ($\equiv \bar{V}^{anode}_{discharge}$; dashed lines) vs. cycle number in LP57 electrolyte (1 M $LiPF_6$ in EC:EMC 3:7) operated with different upper cutoff voltages (4.0 V, 4.1 V, 4.2 V) and a constant lower cutoff voltage of 3.0 V. Formation was done at a rate of 0.1 C. Cycling was performed at 1 C and 25°C. For each condition, two independent cells were run and the data in the figure always represent the average of two cells (the error bars in (a) represent the standard deviation between the two cells).

References 43–45, which likely causes a different surface film formation and impedance. A detailed discussion about the reason for the rise in the polarization of NMC111 with upper cutoff potential is given in the Discussion section.

Figure 2a shows the cycling stability of NMC622-graphite cells. Similar to the case of the NMC111-graphite cells also NMC622-graphite cells can be cycled stably to upper cutoff voltages of 4.2 V and 4.4 V with excellent coulombic efficiencies of >99.9%, whereas at an upper cutoff potential of 4.6 V, the capacity fades rapidly and the coulombic efficiency decreases to ~99.6% (before the rollover-failure), as was observed for NMC111. In analogy to the cells with NMC111, the occurrence of a rollover-failure[41,42] at 4.6 V cutoff indicates growing polarization and causes the large error bars at high cycle numbers as described above. Also with respect to the mean discharge voltages, NMC622 (s. Figure 2b) is very similar to NMC111: $\bar{V}^{cathode}_{discharge}$ slightly increases with cycle number for 4.2 V cutoff voltage, remains essentially constant for 4.4 V cutoff voltage, and decreases rapidly at 4.6 V cutoff voltage, proving a continuous impedance growth of the cathode active material which causes the rollover-failure; on the other hand, $\bar{V}^{anode}_{discharge}$ remains essentially constant, independent of the cutoff voltage.

Figure 3a displays the cycling performance of $LiNi_{0.8}Mn_{0.1}Co_{0.1}O_2$ (NMC811)-graphite cells. Due to the less stable cycling behavior of NMC811, the upper cutoff voltages were limited to 4.0 V, 4.1 V, and 4.2 V. It can be observed that the NMC811 only performs fairly stable with a coulombic efficiency >99.9%, when the upper cutoff voltage is set to 4.0 V. For cutoff potentials of 4.1 V and 4.2 V, poor cycling stability is observed. In order to aid the comparison between the different NMCs, the capacity retentions measured between the 5th and the 300th cycles at a 1C-rate for all cells presented in Figures 1–3 are summarized in Table I. Stable cycling with capacity retentions ≥90 % is possible for NMC111 and NMC622 up to 4.4 V and for NMC811 only up to 4.0 V, whereby its capacity retention is still clearly lower than that for the cells with NMC111 and NMC622 cycled to 4.4 V. It is interesting to note that the measured specific capacity of NMC811 at a 4.2 V cutoff is similar to the one of NMC622 at 4.4 V (see values in parentheses in Table I), however, with the latter one still having a stable cycling performance. The impact of the different cutoff voltages on the specific energy of the cells will be picked-up again in the Discussion section. The coulombic efficiencies for the NMC811-graphite cells are >99.9% at 4.0 V cutoff potential, and even at 4.1 V and 4.2 V, where pronounced capacity fading is observed, their coulombic efficiency remains at ~99.9%, i.e., similar to that of the NMC111 and NMC622 cells at 4.4 V. The fact that the latter display substantially lower capacity fading suggests that its origin must be an enhanced cathode and/or anode impedance growth.

The mean discharge voltages versus cycle number of the NMC811 cathodes and the graphite anodes are shown in Figure 3b. Different from the constant or even slightly increasing $\bar{V}^{cathode}_{discharge}$ values with cycle number observed for NMC111 and NMC622 at 4.2 V cutoff potential, the NMC811 cells display a continuously decreasing $\bar{V}^{cathode}_{discharge}$ value, even at the lowest cutoff potential of 4.0 V. At 4.2 V cutoff, $\bar{V}^{cathode}_{discharge}$ drops as rapidly with cycle number for NMC811 as in the case of

Table I. Measured capacity retentions between the 5th and 300th cycle of the NMC-graphite cells shown in Figures 1–3. The values in brackets are the specific capacities in units of mAh/g_{NMC} of the 5th and the 300th cycles.

	4.0 V	4.1 V	4.2 V	4.4 V	4.6 V
NMC111	-	-	93% (140.2 → 130.0)	94% (162.8 → 153.2)	42% (183.4 → 77.1)
NMC622	-	-	95% (155.4 → 147.3)	94% (177.8 → 166.8)	39% (203.1 → 79.9)
NMC811	90% (131.9 → 118.1)	77% (149.3 → 114.4)	66% (172.5 → 114.7)	-	-

4.6 V for NMC111 and NMC622, indicating that the observed strong cathode impedance growth sets in at ∼0.4 V lower cutoff potentials for NMC811. On the other hand, the mean discharge potentials for the graphite anode in the NMC811-graphite cells ($\bar{V}^{anode}_{discharge}$) behave similarly as for the NMC111 and the NMC622 cells, showing negligible increase with cycle number for all cutoff potentials. In summary, the observed capacity decay at >4.0 V cutoff potential for NMC811 full-cells and at >4.4 V for NMC111 and NMC622 full-cells seems to be largely related to the onset of a strong cathode impedance growth (i.e., a strong fading of $\bar{V}^{cathode}_{discharge}$) above these cutoff potentials.

The above results clearly demonstrate a similarity between NMC111 and NMC622, but a big difference to NMC811 with respect to the onset of the cathode impedance growth. To investigate the origin of this difference and to find the reason for the instability occurring for NMC111 and NMC622 at 4.6 V and for NMC811 at 4.1–4.2 V, a dq/dV plot of the delithiation and lithiation of the three NMC materials in NMC-graphite cells of the 3rd cycle is depicted in Figure 4. The voltage region up to 3.8 V is very similar for all three NMC compositions, with two anodic peaks between 3.4 V and 3.8 V. While the first one originates from the lithium intercalation into the graphite anode, the second one stems from the phase transition from a hexagonal to a monoclinic (H1 → M) lattice of the NMC.[18,46–49] In the region >3.8 V, it becomes very obvious that the dq/dV curve for the NMC811 cell deviates substantially from that of the NMC111 and NMC622 cells. In particular, NMC811 has a small anodic feature at ∼3.95 V and a large anodic peak at ∼4.15 V, both of which are absent for the other NMCs. The first one belongs to the M → H2 phase transition and the latter one corresponds to the H2 → H3 phase transition as was reported before for $LiNiO_2$[46–48] and Ni-rich NMC[18,49] materials. In contrast, for NMCs with Ni-contents <80% the M → H2 and H2 → H3 phase transitions have not been reported. Accordingly, for NMC111 and NMC622 such distinct features are not observed. However, for NMC622 a broad peak around 4.1 V is visible, which might indicate an M → H2 phase transition. For both NMC111 as well as NMC622, a clear redox peak is observed at 4.6 V, which could correspond, in analogy to NMC811, to a H2 → H3 phase transition or could also indicate an oxygen redox feature, a process which has been suggested for $Li_2Ru_{1-y}Sn_yO_3$[50] and Li_2IrO_3[51] by Tarascon's group and was investigated theoretically using DFT.[52,53] The vertical dotted lines mark the upper cutoff voltages which were chosen for the cells presented in the Figures 1–3. Note that up to the onset of the H2 → H3 phase transition of NMC811 at >4.0 V and up to the onset of the redox feature at >4.4 V of NMC111 and NMC622, the capacity retention of the materials is very stable. In other words, stable cycling was only possible if the cutoff voltage was below the onset of the last peak in the dq/dV plot. The early onset of the H2 → H3 transition at >4.0 V (NMC811) explains why NMC811 cannot be cycled stably at >4.0 V cutoff voltages, whereas NMC111 and NMC622 cells show an excellent performance at potentials as high as 4.4 V. The detrimental effect of the H2 → H3 phase transition was already described before for $LiNiO_2$ and NMC811 and was explained by a significant reduction of the unit-cell volume upon this phase transition, which we will critically review in the Discussion section.[18,47]

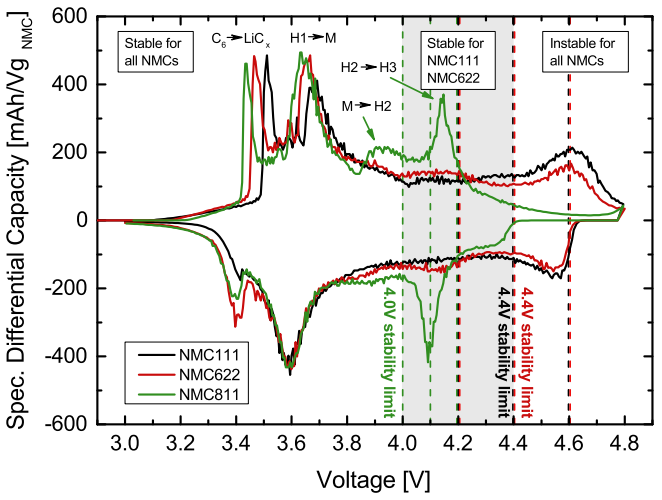

Figure 4. Differential capacity vs. cell voltage of NMC-graphite cells recorded at a 0.1 C-rate (3rd cycle). The vertical dotted lines mark the upper cutoff voltages, which were chosen for the cells in Figures 1–3. The peaks are assigned to their corresponding phase transitions with H1, H2 and H3 representing the three hexagonal phases and M the monoclinic one. C_6 → LiC_x indicates the lithiation of graphite.

Gas analysis of NMC-Li and LNMO-Li half-cells by OEMS.— Figure 5 shows the results of On-line Electrochemical Mass Spectrometry (OEMS) measurements with NMC-Li and LNMO-Li half-cells. For these experiments, metallic lithium was chosen as a counter-electrode in order to achieve a stable reference potential. Figure 5a displays the voltage profiles of NMC111 (black), NMC622 (red), NMC811 (green) as well as LNMO (blue) upon the first charging from OCV to 5 V at a 0.05 C-rate and 25°C as a function of the state-of-charge (SOC) (note that 100% SOC is defined as the removal of all lithium from the cathode materials; s. Experimental section). The three lower panels show the total moles of evolved gas, normalized to the BET surface area of the cathode active material (CAM) in units of $\mu mol/m^2_{CAM}$ for O_2 (Figure 5b), CO_2 (Figure 5c), and CO (Figure 5d). Note that normalization of the gassing data to the BET surface area is meant to account for the differences in the available surface area for electrochemical oxidation reactions. Figure 5b demonstrates that for all three NMC compositions a release of oxygen can be detected near a state-of-charge of ∼80–90%, corresponding to onset potentials for O_2 evolution of ∼4.3 V vs. Li/Li^+ (or ∼4.2 V cell voltage in a full-cell vs. graphite) for NMC811 and of ∼4.7 V vs. Li/Li^+ (or ∼4.6 V cell voltage in a full-cell vs. graphite) for NMC111 and NMC622 (this will be seen more clearly later, when discussing Figure 6). The observed onset for O_2 evolution on NMC111 at ∼80% SOC during electrochemical delithiation (s. Figure 5) is in surprisingly good agreement with the observed onset for oxygen loss upon the chemical delithiation of NMC111 (with NO_2BF_4), which was found to initiate at a lithium content corresponding to ∼75% SOC.[6] The scatter in the reported O_2 concentration of ca. ±0.5 $\mu mol_{O_2}/m^2_{CAM}$ for NMC111 and NMC622 and of ca. ±1 $\mu mol_{O_2}/m^2_{CAM}$ for NMC811 corresponds to our experimental error in quantifying the O_2 concentration of ca. ±10 ppm. As was already reported previously,[54] no O_2 evolution is observed for the LNMO half-cell up to 5.0 V.

At roughly the same potentials at which the evolution of O_2 initiates, a strong increase of the CO_2 (Figure 5c) and the CO (Figure 5d) evolution rates (i.e., an increase in the slope of the lines) is observed for all NMC materials. Here it should be noted that the more gradual increase of the CO_2 concentration (Figure 5c) starting at low SOC

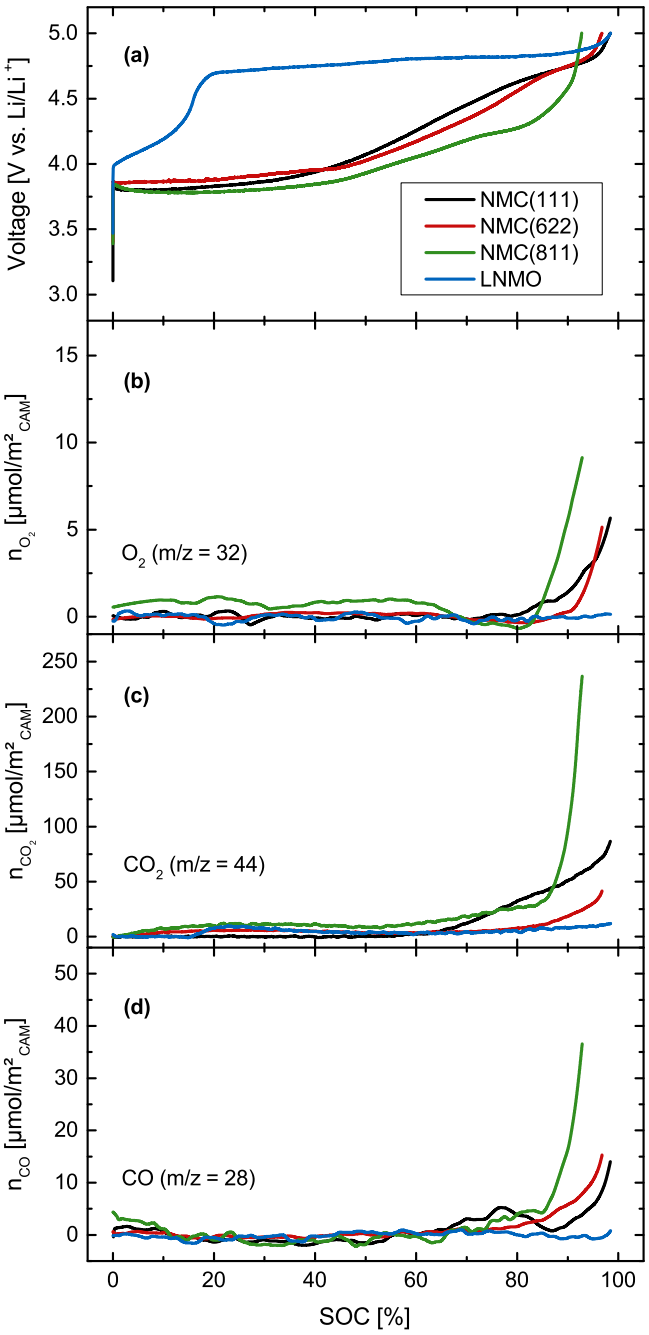

Figure 5. (a) Cell voltage vs. specific capacity of NMC-Li cells using NMC111 (black), NMC622 (red), NMC811 (green), and LNMO (blue). The cells contain 120 µL LP57 electrolyte (1 M $LiPF_6$ in EC:EMC 3:7) and Celgard H2013 separators. The total moles of evolved gases in the OEMS cell, normalized by the cathode active material (CAM) BET area versus the theoretical state-of-charge (SOC) is shown for (b) O_2, (c) CO_2, and (d) CO.

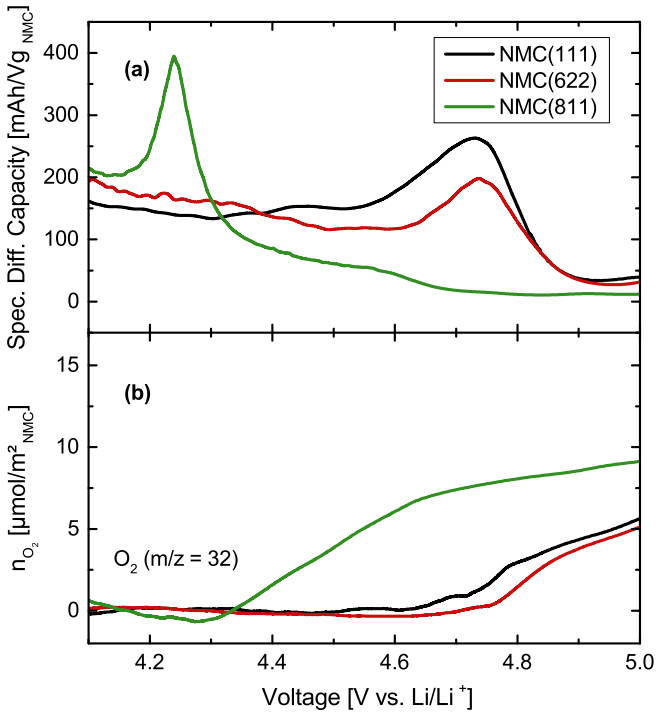

Figure 6. (a) Specific differential capacity vs. cell voltage of the NMC-Li cells shown in Figure 5. (b) Evolution of O_2 as a function of the cell voltage. The OEMS data are smoothed, baseline corrected, and converted into units of [µmol/m^2_{NMC}].

values is believed to be due to the electrooxidation of Li_2CO_3 impurities (reported to occur in the potential range above ~3.7 V[55] to ~4.0 V[12]) and possibly of transition metal carbonates in the first charge depicted in Figure 5. In this case, one would expect that the CO_2 evolution at low voltages (i.e., below ~4.2 V) would be absent in the second charge, which indeed is the case (see discussion of Figures 7–9). In addition, the fact that the evolution of CO does not occur until the onset of O_2 evolution (s. Figure 5d) is consistent with the assumption that the CO_2 evolution at lower potentials is due to the oxidation of carbonate impurities. The very similar onsets of O_2, CO_2, and CO evolution raise the question whether the formation of CO_2 and CO at higher potentials is only due to the electrooxidation of the electrolyte and/or the conductive carbon on the cathode surface, or if it is linked to the release of highly reactive oxygen (e.g., atomic oxygen or singlet oxygen) from the NMC lattice and its subsequent chemical reaction with electrolyte and/or conductive carbon to CO and CO_2. We will present a detailed answer to this fundamental question in the Discussion section, and first present the other experimental results.

Again, in contrast to the data shown for the NMC materials, no CO evolution is observed for the LNMO half-cell up to 5.0 V, and only minor amounts of CO_2 (~10 µmol/m^2_{CAM}) are formed at ~15% SOC (corresponding to ~4.5 V), which are likely due to the oxidation of low amounts of carbonate impurities on the surface of LNMO. This is at variance with Luo et al.,[35] who observed the formation of CO_2 on LNMO surfaces above 4.75 V (at room temperature), which they suggested to be due to the electrooxidation of electrolyte. While we cannot explain this discrepancy, we do not observe any significant CO/CO_2 formation on LNMO at >4.7 V and up to 5.0 V (i.e., after the initial formation from presumably surface impurities), so that we believe that the electrochemical oxidation of the electrolyte and/or the carbon support is negligible on LNMO surfaces up to 5.0 V at 25°C (this is consistent with our previous OEMS study[54]). The fact that hardly any gas evolution is observed at operating voltages as high as 5 V for LNMO but that significant CO/CO_2 formation is observed for the NMC materials at >4.2 V, supports the hypothesis that the CO and CO_2 evolution is at least partially a consequence of the release of reactive oxygen from the NMC lattice. A catalytic effect of Ni or Co on the electrolyte oxidation also appears unlikely, as the gas evolution for NMC111 and NMC622 shows great similarity, although the materials differ in both the Ni and the Co content. More clearly, a catalytic effect of Ni species can be ruled out due to their presence in LNMO, which evidently shows insignificant gas evolution up to 5.0 V.

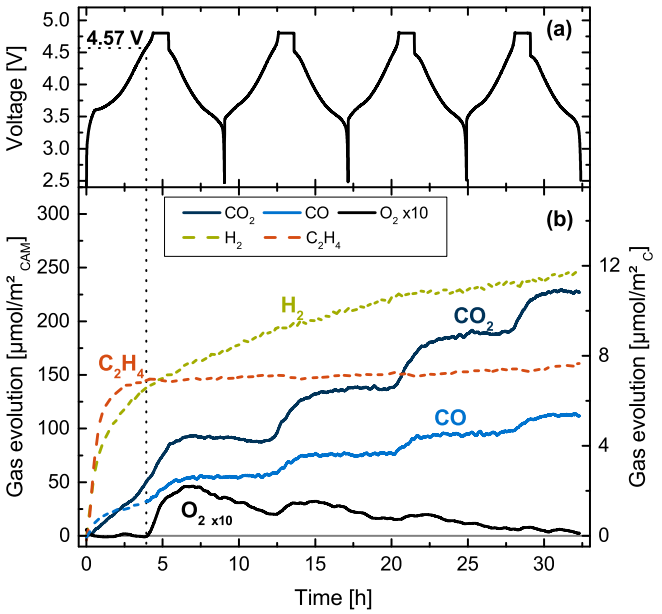

Figure 7. (a) Cell voltage vs. time of a NMC111-graphite cell over four charge/discharge cycles at 0.2 C and 25°C between 2.6 and 4.8 V, in a cell containing 400 µL of 1.5 M $LiPF_6$ in ethylene carbonate (EC), glass-fiber separators and 16.69 mg NMC111. (b) Evolution of CO_2 (dark blue), H_2 (green), C_2H_4 (orange), CO (blue), and O_2 (black, 10-fold magnified) as a function of time. Solid lines indicate the gases stemming from the NMC electrode and dashed lines from the graphite electrode; gas concentrations are referenced to the NMC BET area (left y-axis) and to the sum of graphite and conductive carbon BET area (right x-axis). The OEMS data are smoothed, baseline corrected, and converted into units of [$\mu mol/m^2_{NMC}$] and [$\mu mol/m^2_C$].

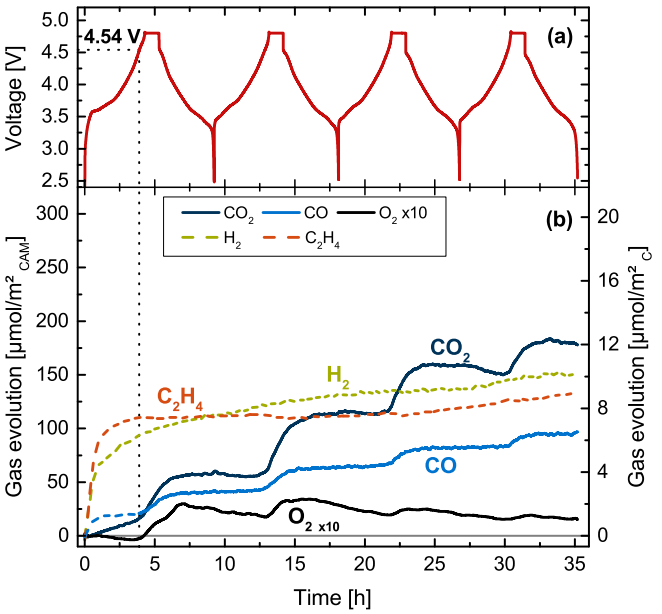

Figure 8. (a) Cell voltage vs. time of a NMC622-graphite cell over four charge/discharge cycles at 0.2 C and 25°C between 2.6 and 4.8 V, in a cell containing 400 µL of 1.5 M $LiPF_6$ in ethylene carbonate (EC), glassfiber separators and 20.23 mg NMC622. (b) Evolution of CO_2 (dark blue), H_2 (green), C_2H_4 (orange), CO (blue), and O_2 (black, 10-fold magnified) as a function of time. Solid lines indicate the gases stemming from the NMC electrode and dashed lines from the graphite electrode; gas concentrations are referenced to the NMC BET area (left y-axis) and to the sum of graphite and conductive carbon BET area (right x-axis). The OEMS data are smoothed, baseline corrected, and converted into units of [$\mu mol/m^2_{NMC}$] and [$\mu mol/m^2_C$].

In order to better visualize the gas evolution at the H2 → H3 phase transition for NMC811 and at the redox feature at ~4.6 V for NMC111 and NMC622, which were shown to be detrimental for the cycling stability, the charging curves of the NMC materials in Figure 5 are now plotted in their dq/dV representation and the corresponding O_2 evolution data are shown as a function of the potential (see Figure 6). The observed peaks in the specific differential capacity vs. voltage plot (Figure 6a) are in good agreement with the features observed in Figure 4 (note that the positive shift of ~0.1 V in the peak positions in Figure 6a is due to the fact that in Figure 4 the full-cell potential is plotted, whereas in Figure 6a the potential is plotted vs. Li). Figure 6b depicts the O_2 evolution and demonstrates clearly that the onset potential of O_2 evolution fits very well to the H2 → H3 phase transition (NMC811) and to the redox feature at ~4.6 V (NMC111 and NMC622), indicating that the release of oxygen is not related to a specific potential, but is rather depending on the occurrence of this very last peak in the dq/dV plot.

Gas analysis of NMC-graphite full-cells by OEMS.—In order to investigate if oxygen release occurs only in the first cycle or also in the subsequent ones, the gas evolution was measured for all three NMC materials cycled four times in a full-cell setup at 0.2 C vs. a graphite anode. In order to avoid signal fluctuations (i.e., on the oxygen channel m/z = 32) coming from the transesterification of the linear carbonate EMC,[40,56–58] the LP57 electrolyte is replaced by 1.5 M $LiPF_6$ in EC for these full-cell experiments. Additionally, due to the low vapor pressure of EC, the background signals from the electrolyte decrease by two orders of magnitude, leading to an improved signal to noise ratio in the mass spectrometer.[59] Since we are particularly interested in the oxygen release occurring at the last peak in the dq/dV plot (see Figure 4 and Figure 6), the upper cutoff potentials were 4.8 V for NMC111 and NMC622, and 4.4 V for NMC811 (compare to features in Figure 4 and Figure 6a). The first four cycles of the NMC111-graphite cell are depicted in Figure 7a together with the corresponding evolution/consumption of CO_2, H_2, O_2, CO, and C_2H_4 in Figure 7b. From the beginning of the first charge, a steep increase of the ethylene signal (dashed orange line) is observed, which is caused by the reduction of EC in the course of the SEI formation on the graphite electrode.[12,60–62] Once the SEI is formed, the reduction of EC stops, so that the ethylene concentration stays constant at around 8 $\mu mol/m^2_C$ (s. right-hand y-axis), an amount equal to ~1.2 monolayers of the main EC reduction product lithium ethylene dicarbonate (LEDC) on the graphite anode.[12] Simultaneously with the ethylene evolution, roughly 1.2 $\mu mol/m^2_C$ carbon monoxide (dashed light-blue line) are evolved (after ca. 2.5 hours), which are typically ascribed to a minor EC reduction pathway with the ring opening at the carbonyl carbon atom.[12,63] Subsequently, the CO signal shows a stepwise increase, which will be discussed in the next paragraph. Furthermore, hydrogen (dashed green line) starts to evolve from the beginning of the measurement, due to the reduction of trace water in the electrolyte.[12,64] The H_2 signal initially evolves at a fast rate and then gradually approaches a concentration of ~12 $\mu mol/m^2_C$ by the end of the measurement. The reason why the H_2 evolution does not stop after the first charge like the C_2H_4 evolution is, we believe, caused by the formation of protic species from electrolyte decomposition and their subsequent reduction at the graphite anode yielding continuous hydrogen evolution.[12]

Besides C_2H_4, CO, and H_2 one can also observe a linear increase of the CO_2 concentration in the first four hours of the measurement (up to ~4.6 V cell potential) to 50 $\mu mol/m^2_{NMC}$. This increase can be assigned to the oxidation of carbonate impurities on the NMC particles, which are typically around 0.1 $\%_{wt}$.[12,18] The total CO_2 signal of 50 $\mu mol/m^2_{NMC}$ corresponds to ~50 $\mu mol/m^2_{NMC}$ · 0.26 m^2/g · 16.69 mg_{NMC} = 217 nmol CO_2 or to 217 nmol of carbonate (in the case of Li_2CO_3, it was shown, that one mole of Li_2CO_3 releases one mole of CO_2 upon electrochemical oxidation[65]). If referenced to Li_2CO_3 (73.89 g/mol), which is customarily done, this would amount to 16 µg Li_2CO_3 equal to 0.10 $\%_{wt}$.

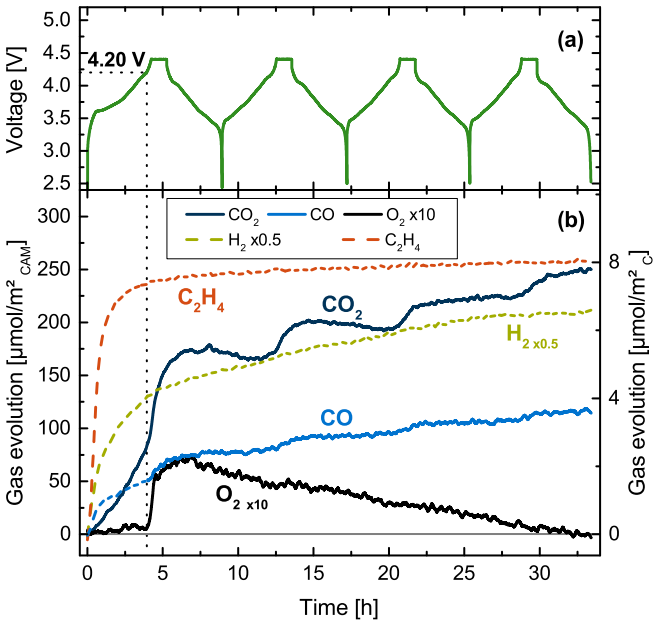

Figure 9. (a) Cell voltage vs. time of a NMC811-Graphite cell over four charge/discharge cycles at 0.2 C and 25°C between 2.6 and 4.4 V, in a cell containing 400 µL of 1.5 M $LiPF_6$ in ethylene carbonate (EC), glassfiber separators and 16.40 mg NMC811. (b) Evolution of CO_2 (dark blue), H_2 (green), C_2H_4 (orange), CO (blue), and O_2 (black, 10-fold magnified) as a function of time. Solid lines indicate the gases stemming from the NMC electrode and dashed lines from the graphite electrode; gas concentrations are referenced to the NMC BET area (left y-axis) and to the sum of graphite and conductive carbon BET area (right x-axis). The OEMS data are smoothed, baseline corrected, and converted into units of [µmol/m^2_{NMC}] and [µmol/m^2_C].

After four hours, the cell voltage reaches ~4.6 V and oxygen starts to evolve. The onset potential fits very well to the one found in Figure 6 (note that in the Figures 7–9 the NMC–graphite full-cell potential is reported, whereas in Figure 6 the potential is measured vs. a metallic lithium counter electrode, the potential of which is ~0.1 V below the potential of lithiated graphite). Simultaneously to O_2, the CO and CO_2 signals increase until the cell switches from the CV-phase at 4.8 V to the discharge, from which point on the CO and CO_2 concentrations stay constant until the cell voltage again increases above ~4.6 V in the following cycles, where O_2, CO, and CO_2 evolve again, leading to a stepwise increase of these signals. The fact that after the first cycle no CO_2 is evolved below ~4.6 V in any of the subsequent cycles confirms our prior hypothesis that the CO_2 evolution below 4.6 V is due to the oxidation of carbonate impurities in the first cycle (s. discussion of Figure 5). By subtracting the amount of CO evolved during the SEI formation (~1.2 µmol/m^2_C or ~25 µmol/m^2_{NMC}) and the amount of CO_2 related to carbonate impurity oxidation in the first cycle (~50 µmol/m^2_{NMC}), the total amount of CO and CO_2 evolved exclusively due to processes at high voltage after the four cycles are ~80 µmol/m^2_{NMC} and ~180 µmol/m^2_{NMC}, respectively.

While the step-like profile of the oxygen signal is similar to that of the CO and CO_2 signal, showing a rapid rise every time the potential goes above ~4.6 V, it does exhibit a superimposed potential-independent continuous decrease. This consumption of oxygen in the cell is most likely caused by a slow but steady reduction of the evolved oxygen at the graphite anode, which would be consistent with the observed decreasing consumption rate over time, as a more protective SEI is being formed (note that an analogous consumption of CO_2 is observed in the second and, to a much lesser degree in the third cycle, which appears smaller in magnitude than the O_2 consumption only due to the fact that the oxygen signal is magnified by a factor of ten). Thus, in order to estimate the total amount of evolved oxygen over the four cycles, one can sum up the steep increases of the oxygen signal in each cycle, which gives a total oxygen evolution of ~9 µmol/m^2_{NMC}. Note that all values which are summed up over the four cycles are corrected for the decreasing concentrations due to gas consumption (for CO_2 and O_2) on the graphite anode by summing up the increases rather than considering the total concentrations measured at the end of the experiment. Additionally, it is quite apparent that the amount of evolved oxygen decreases from cycle to cycle, which would be consistent with our assumption that the oxygen is released mainly from the near-surface regions of the NMC particles and that its release becomes slower as the oxygen depleted surface layer increases in thickness.[36] This hypothesis is also supported by the total amount of released oxygen, which will be discussed in further detail in the Discussion section.

The results of the analogous experiment with an NMC622-graphite cell cycling at 0.2 C between 2.6 V and 4.8 V are shown in Figure 8. For all gases, a very similar trend as for the NMC111-graphite cell is observed. The total amounts of evolved gases during SEI-formation are ~8 µmol/m^2_C of ethylene and ~1.2 µmol/m^2_C of CO. Additionally, ~10 µmol/m^2_C of hydrogen is evolved over the course of the experiment. Prior to the onset of oxygen evolution at ~4.54 V (vertical dotted line), the oxidation of carbonate impurities results in ~19 µmol/m^2_{NMC} CO_2. This corresponds to ~19 µmol/m^2_{NMC} · 0.35 m^2/g · 20.23 mg_{NMC} = 135 nmol CO_2 or to 135 nmol of carbonate. Again, if referenced to Li_2CO_3, this would amount to 10 µg Li_2CO_3 equal to 0.05 $\%_{wt}$. As was observed for NMC111, no CO_2 is evolved below ~4.5 V in any of the subsequent cycles, confirming our prior hypothesis that the CO_2 evolution below 4.5 V is due to the oxidation of carbonate impurities in the first cycle (s. discussion of Figure 5).

By subtracting the amount of CO evolved during the SEI formation (~1.2 µmol/m^2_C or ~20 µmol/m^2_{NMC}) and the amount of CO_2 related to carbonate impurity oxidation in the first cycle (~19 µmol/m^2_{NMC}), the total amount of CO and CO_2 evolved exclusively due to processes at high voltage after the four cycles are ~79 µmol/m^2_{NMC} and ~171 µmol/m^2_{NMC}, respectively. The estimated amount of evolved oxygen over the four charge/discharge cycles using the above described approach is ~6 µmol/m^2_{NMC}. The total amounts of gaseous species are very similar for both the NMC111-graphite and NMC622-graphite cells, illustrating once again a similarity also in the gassing behavior of NMC111 and NMC622 as it was shown in Figure 5 and Figure 6.

Lastly, a similar experiment was performed with an NMC811-graphite cell (see Figure 9), except that the upper cutoff voltage was reduced to 4.4 V, as this voltage is sufficient to include the complete peak stemming from the H2 → H3 transition (see Figure 4). During the SEI formation a total of ~8 µmol/m^2_C of ethylene and ~1.5 µmol/m^2_C of CO are evolved. These amounts fit very well to the gas amounts detected in the experiments with NMC111 and NMC622 (see Figure 7 and Figure 8), which is expected since the gases at this initial stage of the first cycle were shown to originate solely from the graphite electrode,[12] i.e., they are independent of the cathode material. Over the four cycles of the measurement, ~13 µmol/m^2_C of hydrogen are formed, which also fits to the amounts measured in the NMC111 and NMC622 cells. The upper cutoff potential can have an influence mainly on the hydrogen evolution as a result of the cross-talk between cathode and anode.[12,42,66] The underlying assumption of the following analysis is that the cross-talk effect be either similar for all the measurements or has only a minor effect on the overall gas evolution.

Prior to the onset of oxygen evolution at already ~4.2 V (vertical dotted line), the oxidation of carbonate impurities results in ~80 µmol/m^2_{NMC} CO_2. This corresponds to ~80 µmol/m^2_{NMC} · 0.18 m^2/g · 16.40 mg_{NMC} = 236 nmol CO_2 (or carbonate). Again, if referenced to Li_2CO_3, this would amount to 17 µg Li_2CO_3 equal to 0.11 $\%_{wt}$. By subtracting the amount of CO evolved during the SEI formation (~50 µmol/m^2_{NMC}) and the amount of CO_2 related to carbonate impurity oxidation in the first cycle (~80 µmol/m^2_{NMC}), the total amount of CO and CO_2 evolved exclusively at >4.2 V (i.e., after the onset of oxygen release) after the four cycles are ~70 µmol/m^2_{NMC} and ~170 µmol/m^2_{NMC}, respectively. The estimated oxygen release over the four cycles is ~8 µmol/m^2_{NMC}. Thus, even though the upper cutoff

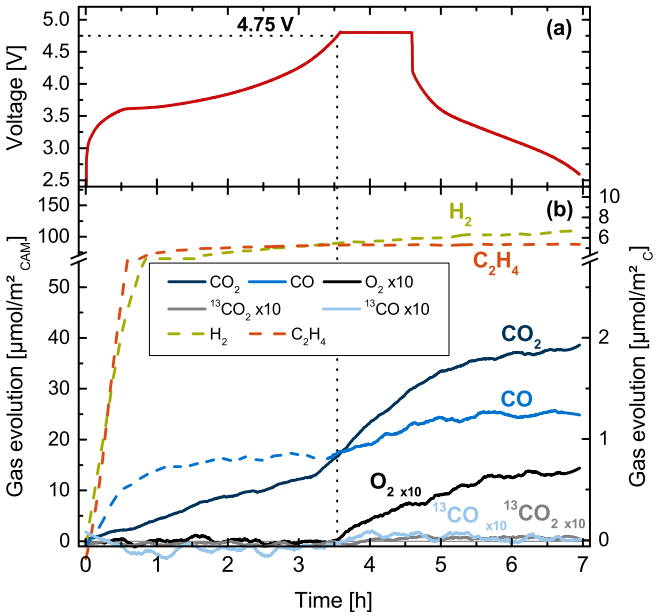

Figure 10. (a) Cell voltage vs. time of a NMC622-graphite cell over the first charge/discharge cycles at 0.2 C and 25°C between 2.6 and 4.8 V, in a cell containing 400 µL of 1.5 M $LiPF_6$ in ethylene carbonate (EC), glassfiber separators and 18.40 mg NMC622. The NMC622 electrode was prepared with ^{13}C-labeled carbon instead of Super C65. (b) Evolution of CO_2 (dark blue), H_2 (green), C_2H_4 (orange), CO (blue), and O_2 (black, 10-fold magnified), $^{13}CO_2$ (gray, 10-fold magnified) and ^{13}CO (bright blue, 10-fold magnified) as a function of time. Solid lines indicate the gases stemming from the NMC electrode and dashed lines from the graphite electrode; gas concentrations are referenced to the NMC BET area (left y-axis) and to the sum of graphite and conductive carbon BET area (right x-axis). The OEMS data are smoothed, baseline corrected, and converted into units of [µmol/m^2_{NMC}] and [µmol/m^2_C].

potential in the NMC811-graphite cell is reduced by 0.4 V compared to the NMC111 and NMC622 cells, the amounts of evolved CO, CO_2, and O_2 are very similar. This finding is remarkable, because if the CO and CO_2 were a result of electrochemical electrolyte oxidation a difference between the amounts measured at 4.4 V and 4.8 V would be expected, especially since the electrolyte is commonly believed to be stable against oxidation to CO and CO_2 at potentials as low as 4.4 V.[59,67,68] One could explain the similar amounts of gas with 4.4 V (NMC811) and 4.8 V (NMC111 and NMC 622) cutoff potentials, if one were to assume that CO_2 and CO are actually the result of the oxygen release from the NMC lattice. In consequence, this could mean that the electrochemical oxidation of carbonate electrolytes would actually be negligible or at least very low on NMC surfaces at both 4.4 V and even 4.8 V, if there were no release of lattice oxygen, which in turn would explain the complete absence of CO/CO_2 up to 4.8 V in EC-only electrolyte on a carbon black electrode at 25°C.[59] This is also supported by the fact that LNMO can be operated at a potential of 4.8 V with insignificant CO/CO_2 evolution due to the absence of oxygen release (see Figure 5).

Having presented substantial evidence that the CO/CO_2 evolution at high potentials is mostly caused by a chemical reaction of the released lattice oxygen, the question remains whether the evolved CO/CO_2 derive from its reaction with the electrolyte or with the conductive carbon in the NMC electrode. Therefore, an NMC622 electrode with 4.4 $\%_{wt}$ ^{13}C-labeled carbon as conductive additive was prepared, replacing the Super C65 conductive carbon, such that a reaction of released lattice oxygen with carbon would result in $^{13}CO/^{13}CO_2$, while its reaction with electrolyte would result in $^{12}CO/^{12}CO_2$. The NMC622-graphite cell with ^{13}C conductive carbon was charged to 4.8 V and subsequently discharged to 2.6 V (see Figure 10a). The capacity reached during the CC-phase was only 198 mAh/g_{NMC}, i.e., ~17% lower than for the NMC622 electrode with Super C65 (see Figure 8); this inferior electrode performance is likely caused by the strongly agglomerated structure of the ^{13}C-carbon, resulting in a poor electronic accessibility of the active material particles in the cathode. Nevertheless, also for this electrode, the release of oxygen can be clearly seen. It is shifted to a higher potential of 4.75 V, compared to the 4.54 V for NMC622 with Super C65 (s. Figure 8), which can be rationalized by the fact that the material contains more lithium at ~4.6 V due to the worse cathode performance, which in turn renders it more stable at this voltage. Additionally, the cutoff potential is only 50 mV above the O_2 onset, which is the reason for the overall lower oxygen evolution.

In total, by the end of the first cycle, ~1.5 µmol/m^2_{NMC}, ~23 µmol/m^2_{NMC} and ~9.3 µmol/m^2_{NMC} of O_2, CO_2, and CO were formed, respectively, whereby these values were again corrected by the ~13 µmol/m^2_{NMC} CO_2 stemming from carbonate oxidation prior to the onset of oxygen evolution and by the ~1.1 µmol/m^2_C CO originating from EC reduction on the graphite anode. In comparison, in the first cycle of the NMC622-graphite cell with Super C65 (Figure 8) ~2.9 µmol/m^2_{NMC}, ~40 µmol/m^2_{NMC} and ~19 µmol/m^2_{NMC} of O_2, CO_2 and CO were evolved, respectively (again, corrected for contributions from carbonate oxidation and EC reduction). It is interesting to note, that not only the amount of oxygen is cut in half, but also the amounts of CO_2 and CO are cut in half, which shows once more that these gases are linked to the oxygen evolution. Finally, Figure 10 clearly shows that neither the evolution of ^{13}CO nor $^{13}CO_2$ was observed, proving that the carbon additive in the cathode is stable at potentials of 4.8 V and also stable against the released oxygen from the NMC lattice. Therefore, the observed CO/CO_2 formation at high potentials can be ascribed to the oxidation of EC (possibly also the binder) rather than of the conductive carbon by released lattice oxygen.

Discussion

Correlation between oxygen release and surface structure of NMC.—We first want to focus on the correlation between the H2 → H3 phase transition at ~4.2 V for NMC811 and the high-voltage feature at ~4.6 V of NMC111 and NMC622 observed in the dq/dV analysis (Figure 4) and the oxygen release detected for the different NMCs by OEMS (Figures 7–9). For NMC111 it is known that upon lithium extraction the c-parameter increases until roughly 2/3 of the lithium is removed and it is ascribed to repulsive interactions of the negatively charged oxygen layers upon the removal of the positive lithium ions.[7,11] Upon further removal of lithium, i.e., at higher states of charge, a decreasing c-parameter is reported, which has been linked to increasing covalency between the metal and the oxygen.[7,69] Increasing covalency in principle corresponds to a decrease of the oxygen anion charge density, i.e., an oxidation of the lattice oxygen anions (from 2- in the idealized ionic structure to a lower charge density of the oxygen atom). This hypothesized oxidation of the oxygen anions (recently shown by Tarascon's group for the model compounds $Li_2Ru_{1-y}Sn_yO_3$ and Li_2IrO_3)[50,51] would also be consistent with the release of oxygen from the NMC material. The H2 → H3 phase transition was described in the literature for $LiNiO_2$ (LNO), where it occurs at ~4.2 V vs. Li/Li^+ [46–48] and Li et al. showed by in-situ XRD that the c-parameter of the LNO unit cell at low states of charges gradually increases and drastically shrinks at the H2 → H3 phase transition.[47] At roughly the same voltage, this phase transition also occurs for NMC811, as described by Noh et al. and Woo et al.,[18,49] and the associated volume contraction was hypothesized to lead to capacity fading.[18,49] We believe that in analogy to the interpretation in the case of NMC111 the shrinkage of the c-parameter for NMC811 at the H2 → H3 phase transition can be also a result of a decreasing repulsion between the oxygen layers, caused by the oxidation of the oxygen anions, which finally may result in O_2 release. As was reported by Strehle et al. on Li-rich NMC ($Li_{1+x}(Ni,Mn,Co)_{1-x}O_2$), we believe that due to the limited diffusion length of oxygen anions in the bulk NMC particles at 25°C, the oxygen release is limited to the surface-near region yielding a disordered spinel or rock-salt type layer while the bulk structure stays intact.[36]

By a detailed investigation of the dq/dV plot shown in Figure 4, one can observe that the peak assigned to the H2 → H3 phase transition (NMC811) as well as the high-voltage feature (NMC111 and NMC622) are reversible. If these features are at least partially related to oxygen redox, the reversibility of the peak also indicates a reversibility of the oxygen redox upon relithiation. This reversibility is not contradicting the experimentally observed irreversible oxygen loss, since the dq/dV analysis reflects mostly processes in the bulk, where no oxygen loss can occur due to the limited bulk diffusivity of oxygen anions in the layered oxide particle. We believe that the oxygen release would likely occur throughout the entire particle, if the oxygen anion diffusion were fast enough and/or if the NMC particles were small enough. In other words, the NMC structure is thermodynamically unstable at high degrees of delithiation, and only retains its oxygen and its layered bulk structure due to the kinetically hindered oxygen diffusion. This hypothesis is supported by the literature, where it is reported that layered NMC[21,25,27,70,71] and NCA[22,25,26,70] structures in the charged state (low lithium content) are not stable at high temperatures (> 170°C) and decompose under release of oxygen, forming a disordered spinel or rock-salt structure, which are thermodynamically more stable than the layered structure at low lithium contents. In these reports, the oxygen release is a bulk phenomenon due to the significantly faster oxygen anion diffusion at elevated temperatures. Consequently, a complete transformation of the layered structure into the spinel or rock-salt structure is observed.

The limitation of spinel or rock-salt structures to the surface-near regions was already reported before for various layered oxides.[9,28–31] In particular, Muto et al. found for NCA that the rock-salt formation on the surface can be up to 100 nm thick after 500 cycles at 80°C.[30] Jung et al. investigated NMC532 in the voltage range between 3–4.8 V and found a spinel layer thickness of 12–15 nm and a thickness of the rock-salt phase of 2–3 nm after 50 cycles at room temperature.[9] Abraham et al. observed a 35–45 nm thick rock-salt structure on $LiNi_{0.8}Co_{0.2}O_2$ after calendaric aging of a charged electrode at 60°C for 8 weeks.[28] They also stated that the oxygen release was expected to occur from the surface-near region of the material, as their XAS and EELS data showed both that the Ni:O and Co:O ratios were twice as high on the surface compared to the bulk and that the Ni oxidation states on the surface matched NiO whereas in the bulk it matched that of Ni in a layered structure.[28,29] Even though a release of oxygen could not be shown in these reports, it is implicitly required because of the lower oxygen to metal ratios in the spinel and rock-salt phases compared to the layered structure: MO_2 (layered) → M_3O_4 (spinel) → MO (rock-salt) (i.e., metal/oxygen = 1:2 → 3:4 → 1:1).

In Figures 7–9, the amount of released oxygen is largest in the first cycle and decreases in the subsequent cycles. This fits to the hypothesis that the oxygen is released only from surface-near regions and is therefore fastest in the first cycle, and lower in subsequent cycles, since then it has to diffuse through the already formed disordered spinel or rock-salt layer. In summary, a clear correlation can be made between the structural rearrangement of the NMC particle surface and the release of oxygen. Additionally, the spinel or rock-salt surface layer is very likely the cause of the increase in the polarization (represented by a decrease in the charge-averaged mean discharge voltage of the cathode, $\bar{V}^{cathode}_{discharge}$) observed during cycling in the Figures 1–3.

Connection between released O_2 and evolution of CO and CO_2.— The total amount of oxygen released during the four cycles (Figures 7–9) is similar for all three NMCs, ranging from 6–9 $\mu mol/m^2_{NMC}$ (see Table II) and for the chosen upper cutoff potentials there is no apparent correlation with the Ni or Co contents in the NMCs. Furthermore, Table II summarizes the measured amounts of CO_2 and CO within the four cycles shown in Figures 7–9. They are corrected for the CO_2 derived from carbonate oxidation and for the CO originating from EC reduction, such that only gassing processes at high-voltage are regarded. As was already discussed, a closer examination of the 2nd, 3rd, and 4th cycle in Figures 7–9 reveals that CO/CO_2 only evolve once the evolution of O_2 is observed, confirming that CO/CO_2 produced at low potentials in the 1st cycle is indeed due to SEI formation (CO) and carbonate impurity oxidation (CO_2). This raises the question, whether CO and CO_2 derive from the chemical reaction of the released lattice oxygen with the electrolyte. A significant reaction of the evolved oxygen with conductive carbon can be excluded, since it was shown in Figure 10 that no ^{13}CO and $^{13}CO_2$ was evolved when ^{13}C labeled carbon was used as conductive additive in the NMC electrode instead of conventional carbon (Super C65). Another interesting observation is that in the case of NMC811-graphite cells, O_2, CO, and CO_2 evolve already at ∼4.2 V. At this potential, no gas evolution is observed for the analogous cells with NMC111 (onset of O_2 evolution at ∼4.57 V) or NMC622 (onset of O_2 evolution at ∼4.54 V), so that it is too low to ascribe the evolved gases to the electrochemical oxidation of the electrolyte, which strongly supports our hypothesis that the evolution of O_2, CO, and CO_2 are of the same origin.

Table II. Total amounts of oxygen, carbon monoxide, and carbon dioxide evolved at high potentials over the first four cycles in the cells shown in the Figures 7–9 (the amounts of CO_2 stemming from oxidation of carbonate impurities as well as the CO originating from EC reduction, both in the first cycle, were subtracted).

		NMC111	NMC622	NMC811
O_2	[$\mu mol/m^2_{NMC}$]	9	6	8
CO	[$\mu mol/m^2_{NMC}$]	80	79	70
CO_2	[$\mu mol/m^2_{NMC}$]	180	171	170

The purely electrochemical oxidation of EC-only electrolyte on a carbon electrode, i.e., in the absence of any possible catalytic effect by transition metal surfaces, was studied in a recent report by Metzger et al. by applying a linear sweep voltammetry procedure from OCV up to 5.5 V with a scan rate of 0.2 mV/s.[59] There, the onset of CO_2 and CO evolution was at ∼4.8 V vs. Li/Li^+, where the sum of the CO and CO_2-evolution rate was determined to be 0.3 $\mu mol/(m^2_C \cdot h)$.[59] For comparison, in the NMC111-graphite cell (Figure 7), the total amount of CO and CO_2 produced between 4.6 V and the end of the first cycle is 59 $\mu mol/m^2_{NMC}$ and was detected within 1.5 h, corresponding to an average evolution rate of ∼39 $\mu mol/(m^2_{NMC} \cdot h)$; if referenced to the total surface area of conductive carbon and NMC in the cell (0.052 m^2_C and 0.0043 m^2_{NMC}), this equates to ∼3.0 $\mu mol/(m^2_{NMC+C} \cdot h)$. Comparing both values and excluding any catalytic effect of the active material for the above-described reasons, it becomes clear that the purely electrochemical oxidation of EC can only account for at best ∼10 % of the evolved CO and CO_2.

This estimate shows that the electrochemical electrolyte oxidation occurs to a certain extent at high potentials, consistent with previous reports in the literature, which show that the voltage of the NMC slowly drops during storage via a self-discharge caused by electrochemical electrolyte oxidation.[72–75] However, once the potential is above the threshold voltage for the release of lattice oxygen, the majority of CO and CO_2 generated in cells containing NMC stems from chemical electrolyte oxidation. A detailed discussion of the chemical and electrochemical pathways and their ratios on the total electrolyte oxidation will be presented below.

While the absence of oxygen evolution for the high voltage spinel makes sense, considering that the spinel phase is the stable phase which forms upon oxygen release of the layered material, it is interesting that no CO and CO_2 are evolved with LNMO up to a potential of 5 V (see Figure 5), on a surface for which one would not expect a substantially different catalytic effect (if there is any) for the electrochemical oxidation of electrolyte than for NMC surfaces. This implies that the electrolyte should be very stable (i.e. negligible or very minor electrochemical electrolyte oxidation) at the potentials used for the NMC-graphite cells, further supporting our hypothesis that most of the CO_2 and CO are produced by the chemical reaction of released lattice oxygen with the electrolyte. Here it should be noted that a chemical reaction of oxygen with EC is expected to be only possible at room temperature, if the oxygen is in a reactive form, e.g., as atomic oxygen or singlet oxygen, because EC does not decompose in dry air

at the operating temperatures of a lithium ion battery (i.e. it does not react with triplet oxygen). Furthermore, a catalytic effect of Ni or Co appears unlikely as NMC111 and NMC622 have almost identical gassing behavior despite their different Ni and Co composition, and as Ni is also present in the LNMO, which evidently does not exhibit significant electrolyte oxidation at room temperature up to 5.0 V.

In Figures 7–9, the oxygen evolution stops after some cycles, whereas the formation of CO and CO_2 from cycle to cycle decreases at a much slower rate. We believe that the more quickly decreasing oxygen signal over cycling is due to the very fast chemical reaction of released reactive oxygen with EC, so that oxygen can only be detected as O_2 gas if a larger amount is formed within a short period of time, preventing that all of the released oxygen reacts with the electrolyte to CO_2 and CO (i.e., allowing for the escape of some fraction of the oxygen into the head-space of the OEMS cell). This can be rationalized by considering that once reactive oxygen is released (in the following we assume that the reactive species is $^1O_2$) two different follow-up reactions are possible i) the chemical reaction with EC, and/or ii) the physical quenching of two singlet oxygen molecules forming triplet oxygen ($2\ ^1O_2 \rightarrow 2\ ^3O_2 + h\nu$). The rate of the first reaction can be written as

$$r_1 = k_1 \cdot \left[^1O_2\right] \cdot [EC] \quad [2]$$

and depends on the product of the concentrations of singlet oxygen $[^1O_2]$ and EC [EC] (first order reaction with respect to singlet oxygen) and determines how much CO_2 and CO are observed. In contrast, the rate of singlet oxygen quenching can be written as:

$$r_2 = k_2 \cdot \left[^1O_2\right]^2 \quad [3]$$

It depends on the squared concentration of singlet oxygen (second order reaction with respect to singlet oxygen) and determines how much triplet oxygen is detected in the mass spectrometer. The decay constant for $^1O_2$ in propylene carbonate was shown to be $3.3 \cdot 10^4\ s^{-1}$,[76] which we assume to be reasonably similar for ethylene carbonate. Additionally, Kazakov et al.[77] proved that both chemical as well as physical quenching occur in acetone, for which decay constants ranging from $2 \cdot 10^4 - 4 \cdot 10^4\ s^{-1}$ [76] were reported. The similarity of the decay constants led us to expect that also in our system both reactions can occur with the rate constants k_1 and k_2 having similar orders of magnitude, so that the extents of r_1 and r_2 should be mostly dependent on the reactant concentrations $[^1O_2]$ and [EC]. Due to the linear and squared dependency of r_1 and r_2, respectively, on the singlet oxygen concentration, which is fairly low compared to the concentration of EC, it is expected that $r_1 >> r_2$ explaining the much larger quantities of CO_2 and CO, which are roughly 20 times higher than the amount of O_2 (s. Table II). Furthermore, the ratio of r_2/r_1 derived from Reactions 2 and 3 is proportional to the detected ratio of O_2 to CO_2 (assuming that CO_2 is produced by Reaction 2, as discussed later) and can be written as

$$\frac{r_2}{r_1} = \frac{k_2}{k_1 \cdot [EC]} \cdot \left[^1O_2\right] \propto \frac{n(O_2)}{n(CO_2)} \quad [4]$$

With Eq. 4 it becomes clear that once the release of oxygen becomes slower (due to the growing thickness of the oxygen depleted surface layer), the local concentration of $^1O_2$ decreases, so that the ratio of O_2/CO_2 released to the gas phase (and detected by the mass spectrometer) is predicted to decrease over cycling, as indeed is observed. The gradually decreasing release of lattice oxygen over cycling, which we ascribe to a growing thickness of an oxygen depleted surface layer is also consistent with the observed decrease of the mean discharge potential of the cathode shown in the Figures 1–3. For Li-rich NMC materials ($Li_{1+x}(Ni,Mn,Co)_{1-x}O_2$) the total amount of released lattice oxygen is comparably large in the first cycle.[32–36] For this material class Strehle et al.[36] found a ratio of O_2/CO_2 close to 1/1 in contrast to ~1/20 for the NMC materials (s. Table II), which based on Eq. 4 would suggest a ~20-fold higher $^1O_2$ concentration near the active material surface, surprisingly consistent with the ~20-fold higher BET surface area of the ($Li_{1+x}(Ni, Mn, Co)_{1-x}O_2$) material examined by Strehle et al.[36]

In a recent publication by Li et al. on NMC811 it was suggested that the c-axis contraction of the unit cell at potentials of ~4.2 V may not be the reason for the poor cycling stability.[78] Instead, a rapid increase of the parasitic heat flow above 4.2 V vs. Li/Li^+ was detected and it was hypothesized that the highly delithiated cathode surface be very reactive toward the electrolyte causing an increased cathode impedance.[78] Our observation of a growing polarization is consistent with the study by Li et al., however, we believe that it might be the chemical reaction of the released oxygen with the electrolyte that drives the parasitic heat flow, rather than the direct electrochemical oxidation of the electrolyte on the surface. Additionally, Imhof et al. reported CO_2 evolution for LNO already at 4.2 V and ascribed it to the reactivity of the surface toward electrolyte.[79] However, since this onset potential coincides with the H2 → H3 phase transition,[47] we believe that it is more likely related to a release of oxygen from the layered LNO structure, followed by its chemical reaction with the electrolyte to CO_2 rather than to an electrochemical oxidation of the electrolyte at potentials as low as 4.2 V.

In summary, the above discussion strongly supports our hypothesis that the majority of the CO/CO_2 evolution (>90%) during cycling is due to the chemical reaction of released lattice oxygen with the electrolyte, with the exception of the CO/CO_2 evolved at low potentials in the first cycle, which we believe derive from SEI formation (EC reduction on graphite) and carbonate impurity oxidation.

Anode related C_2H_4 and H_2 signals.—The amounts of ethylene evolved in Figures 7–9 are between 7–9 $\mu mol/m_C^2$, very similar to what was observed in a previous report by Metzger et al.[12] In the same report, the hydrogen evolution which was detected from the beginning of the measurement and was ascribed to the reduction of trace water in the electrolyte.[12] The amount of hydrogen accumulated over the four cycles shown in Figures 7–9 ranges from 10–13 $\mu mol/m_C^2$. If we only consider the amount of hydrogen formed in the first cycle before the onset of O_2 evolution (which will lead to further formation of H_2O, as will be discussed later), we find ~6.6 $\mu mol/m_C^2$ H_2 for the NMC111 (Figure 7) and for the NMC622 (Figure 8) cell as well as ~8.0 $\mu mol/m_C^2$ H_2 for the NMC811 cell (Figure 9). The fact that all three values are reasonably similar supports the assumption that the evolution of H_2 up to this point is not related to the cathode active material. With the total surface area of the graphite-electrodes, this corresponds to an absolute amount of ~0.6–0.7 μmol H_2 being evolved. This amount would require 1.2–1.4 μmol H_2O in the electrolyte, if all H_2 were formed via $H_2O + e^- \rightarrow 0.5\ H_2 + OH^-$. Using the density of the electrolyte (1.5 g/mL)[80] and the electrolyte volume (400 μL), the above amount would correspond to a water content of 36–42 ppm for all three cells, which fits very well with the report by Metzger et al., who observed a hydrogen evolution corresponding to 33 ppm of trace water using an LP57 electrolyte.[12] In summary, the gases from the anode side are consistent with our previous findings.

Proposed mechanism of EC oxidation by reactive oxygen.—As discussed above, our data indicate that the majority of the evolved CO and CO_2 are actually a consequence of the reaction of the released oxygen from the NMC, which is likely very reactive in the moment it is released from the material (see Figures 7–9). In Figure 10, we demonstrated that the carbon source for the CO and CO_2 formation is not the conductive carbon in the electrode. The only remaining carbon source in the cell is therefore ethylene carbonate (EC) and possibly the binder. In Scheme 1, we propose a mechanism for how oxygen might react with EC, whereby it is clear that oxygen in its triplet ground state does not react with EC. As the reaction requires the oxygen to be reduced, there are only the two carbon atoms bound to the hydrogen which can be potentially oxidized (the carbonyl-carbon is already in its maximum oxidation state). Our proposed mechanism starts with an electrophilic attack on the carbon by the O_2 molecule, yielding a peroxo group carrying the proton which was initially bound to the carbon. The rather unstable peroxo group would immediately decompose, forming a carbonyl group and releasing a water molecule. This molecule could potentially decompose forming

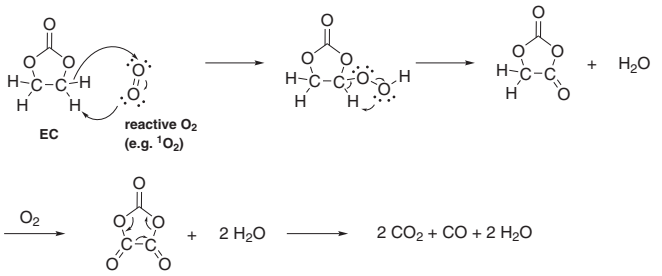

Scheme 1. Proposed mechanism for the oxidation of ethylene carbonate (EC) with reactive oxygen (e.g., singlet oxygen) released from the NMC structure and yielding CO_2, CO, and H_2O. The overall reaction equation is EC + 2 O_2 → 2 CO_2 + CO + 2 H_2O.

CO, CO_2 and formaldehyde, in which case, however, the predicted CO_2/CO ratio would be 1/1, which does not match the observed ratios in Figures 7—9 nor did we observe any formaldehyde in the mass spectrometer. Instead, a second $^1O_2$ molecule could attack the other carbon atom if the EC molecule attacked in the first step is assumed to be adsorbed at the NMC surface forming another carbonyl group and releasing another molecule of water. The formed molecule would readily decompose, yielding two molecules of CO_2, one molecule CO, aside with the previously formed two H_2O molecules. The formation of water upon the reaction of electrolyte with oxygen was already hypothesized before.[81,82]

The overall proposed reaction would thus be EC + 2 O_2 → 2 CO_2 + CO + 2 H_2O, predicting a CO_2 to CO ratio of 2:1. Examining the evolved amounts summarized in Table II, a somewhat higher CO_2:CO ratio ranging from 2.2:1 to 2.4:1 was measured. Considering that water is a reaction product, several follow-up reactions are likely to occur: i) H_2O can be reduced at the graphite anode, yielding H_2 and OH^-, as was reported previously by our group[64] and which would be consistent with the observed continuous evolution of H_2 in Figures 7–9; ii) OH^- produced by the reduction of H_2O at the anode was shown to lead to rather high rates of EC hydrolysis, producing CO_2 gas;[80] iii) chemical reaction of $LiPF_6$ with H_2O can yield $Li_xPO_yF_z$ species, which are frequently reported as surface species at the interface between electrolyte and the NMC cathode.[15,16] A combination of i) and ii) would lead to additional CO_2 evolution (as well as to the observed ongoing H_2 evolution) and therefore to a higher CO_2:CO ratio than the ratio of 2:1 predicted by Scheme 1, consistent with our observations (s. Table II). In order to check if the reduction of water forming H_2 and OH^- can be a reasonable, we will calculate the total amount of water which can be formed according to Scheme 1 and compare it to the H_2 formed at potentials ≥ 4.6 V in Figures 7–9. For the following calculation, we will use the values obtained for the NMC111-graphite cell as an example. As stated in Table II, ∼80 µmol/m^2_{NMC} CO are formed. Assuming the stoichiometry in Scheme 1, this would imply that ∼160 µmol/m^2_{NMC} H_2O be formed at the same time. Multiplying this value with the active material mass of the NMC electrode (16.69 mg) and the BET-surface area of the NMC111 (0.26 m^2/g), one obtains a total of 0.7 µmol H_2O (≡ 12.5 μg_{H_2O}). Analogous to the calculation in the previous section, this would correspond to an increase of the H_2O content in the electrolyte by 21 ppm. The reduction of this in-situ formed water at the negative graphite electrode via $H_2O + e^- \rightarrow 0.5\ H_2 + OH^-$ could yield 0.35 μmol_{H_2} which, when normalized to the NMC or carbon surface area would amount to 80 µmol/m^2_{NMC} and 3.8 µmol/m^2_C, respectively. Since water can be formed as soon as oxygen is released for the first time, we examine the hydrogen signal in Figure 7 from this point until the end of the measurement: the amount of H_2 increases from 6.6 µmol/m^2_C to 11.7 µmol/m^2_C, i.e., by 5.1 µmol/m^2_C, which may be compared to the above predicted value of 3.8 µmol/m^2_C. Analogous estimates can be made for the NMC622 and the NMC811 cells, for which the agreement is also within a factor of ∼2. Considering that besides the reduction of the formed water several additional reactions occur simultaneously like hydrogen formation from initially present trace water reduction (see Results section), hydrolysis of EC, as well as decomposition of $LiPF_6$, the calculated maximum of hydrogen from the reduction of in-situ generated water actually fits astonishingly well to the experimentally observed amount.

Table III. Electrode loading, moles of NMC, theoretically possible amounts of released oxygen and detected amounts of O_2, CO, and CO_2 of the cells shown in Figure 7–9 (the amounts of CO and CO_2 are corrected for the amounts originating from EC reduction and carbonate impurity oxidation). Based on these values, the equations in the text and assuming a layered to spinel or layered to rock-salt transformation the volume fractions (f_{spinel}, $f_{rock\text{-}salt}$) from which oxygen is released as well as the oxygen depleted surface layer thicknesses (t_{spinel}, $t_{rock\text{-}salt}$) are calculated considering either the sum of O_2 and twice the amount of CO (model I) or the sum of O_2 and CO_2 (model II) according to Scheme 1.

		NMC111	NMC622	NMC811
electrode loading	[mg_{NMC}/cm^2]	9.44	11.45	9.28
amount of NMC	[µmol]	173	209	169
max. $O_{2,spinel}$	[µmol]	51	59	42
max. $O_{2,rock\text{-}salt}$	[µmol]	81	96	74
detected O_2	[nmol]	39	42	24
detected CO	[nmol]	347	559	207
detected CO_2	[nmol]	781	1211	502
$f_{spinel,O_2,CO}$ (model I)	[%]	1.4	2.0	1.0
f_{spinel,O_2,CO_2} (model II)	[%]	1.6	2.1	1.3
$f_{rock\text{-}salt,O_2,CO}$ (model I)	[%]	0.9	1.2	0.6
$f_{rock\text{-}salt,O_2,CO_2}$ (model II)	[%]	1.0	1.3	0.7
$t_{spinel,O_2,CO}$ (model I)	[nm]	11.6	11.8	12.1
t_{spinel,O_2,CO_2} (model II)	[nm]	13.0	12.7	14.6
$t_{rock\text{-}salt,O_2,CO}$ (model I)	[nm]	7.3	7.2	6.9
$t_{rock\text{-}salt,O_2,CO_2}$ (model II)	[nm]	8.1	7.8	8.2

Estimation of oxygen depleted surface layer thickness.—Based on the OEMS data presented in Figures 7–9 and summarized in Table III, the oxygen depleted surface layer thickness was estimated as a compact, homogeneous layer around the NMC particles in a similar way as reported by Strehle et al.[36] We considered both scenarios, a layered to disordered spinel (Eq. 5) and a layered to rock-salt (Eq. 6) transformation using, in analogy to the literature,[21,22,36,83] the following general equations with M = (Ni, Mn, Co):

$$Li_xMO_2 \rightarrow \frac{x+1}{3} Li_{3-\frac{3}{x+1}} M_{\frac{3}{x+1}} O_4 + \frac{1-2x}{3} O_2 \quad [5]$$

spinel transformation

$$Li_xMO_2 \rightarrow (x+1)\, Li_{1-\frac{1}{x+1}} M_{\frac{1}{x+1}} O + \frac{1-x}{2} O_2 \quad [6]$$

rock-salt transformation

For the x-values in Eqs. 5 and 6 we determined the lithium content in the material at the end of the first charge from Figures 7–9 resulting in x = 0.06, 0.08 and 0.13 for NMC111, NMC622, and NMC811, respectively. Using these x-values the theoretical oxygen loss per mol of NMC can be calculated for the different NMCs:

NMC111:

$$Li_{0.06}MO_2 \rightarrow \frac{53}{150} Li_{9/53} M_{150/53} O_4 + \frac{22}{75} O_2 \quad [7]$$

spinel transformation

$$Li_{0.06}MO_2 \rightarrow \frac{53}{50} Li_{3/53} M_{50/53} O + \frac{47}{100} O_2 \quad [8]$$

rock-salt transformation

NMC622:

$$Li_{0.08}MO_2 \rightarrow \frac{9}{25}Li_{2/9}M_{25/9}O_4 + \frac{7}{25}O_2 \quad [9]$$

spinel transformation

$$Li_{0.08}MO_2 \rightarrow \frac{27}{25}Li_{2/27}M_{25/27}O + \frac{23}{50}O_2 \quad [10]$$

rock-salt transformation

NMC811:

$$Li_{0.13}MO_2 \rightarrow \frac{113}{300}Li_{39/113}M_{300/113}O_4 + \frac{37}{150}O_2 \quad [11]$$

spinel transformation

$$Li_{0.13}MO_2 \rightarrow \frac{113}{100}Li_{13/113}M_{100/113}O + \frac{87}{200}O_2 \quad [12]$$

rock-salt transformation

The active material loadings of the electrodes used in the OEMS measurements in Figures 7–9 are listed in Table III. Multiplying by the area (1.767 cm^2) and dividing by the molar mass of the NMC materials yields the amount of NMC in mol (see second row in Table III). Using the stoichiometric relation between the layered oxide on the left-hand-side and the evolved oxygen on the right-hand-side in Eqs. 7–12, the maximum amounts of oxygen which can be evolved if a spinel or rock-salt phase is formed (max. $O_{2,\,spinel}$ and max. $O_{2,\,rock\text{-}salt}$) can be calculated (see 3rd and 4th row in Table III). For the calculation of the layer thickness from our experimental data we use two different models based on the mechanism presented in Scheme 1. In model I we calculate the layer thickness for the spinel and rock-salt phase taking into account the sum of the detected oxygen plus twice the amount of CO (remember that one mol of CO is formed per two moles of released oxygen in Scheme 1). In contrast, model II is based on the measured amounts of O_2 and CO_2 (one mol of CO_2 is formed per mol of released oxygen). In an ideal case, i.e., if the ratio of CO_2/CO were exactly 2:1, both models would yield exactly the same results. As the measured CO_2/CO ratio is between 2.2:1 and 2.4:1 due to possible side reactions of the in-situ formed H_2O with EC yielding CO_2, the calculation with model II will slightly overestimate the layer thickness and can therefore be considered as an upper limit, whereas we believe that model I should yield the more precise values. The detected amounts of O_2, CO, and CO_2 are given in the 5th-7th row of Table III.

The molar fraction of cathode active material converted to a spinel (f_{spinel}) or rock-salt structure ($f_{rock\text{-}salt}$) was calculated by dividing either the detected O_2 plus twice the amount of detected CO (model I) or the measured amounts of O_2 and CO_2 (model II) by max. $O_{2,spinel}$ or max. $O_{2,rock\text{-}salt}$ (Table III, 8th to 11th row).

The thus estimated molar fractions should be equal to the ratio of the particle shell volume from which oxygen is released (V_{shell}) to the total particle volume ($V_{particle}$). Using Eq. 13 and the radius r_1 of the complete particle, one can calculate the radius r_2 of the intact fraction of the particle. The difference of r_1 and r_2 is the averaged surface-near layer thickness (t_{spinel}, $t_{rock\text{-}salt}$) of the oxygen depleted surface layer.

$$\frac{V_{shell}}{V_{particle}} = \frac{4/3\pi\left(r_1^3 - r_2^3\right)}{4/3\pi r_1^3} = 1 - \frac{r_2^3}{r_1^3} \quad [13]$$

The particle radius r_1 was obtained from the respective BET-surface area assuming spherical particles (Eq. 14) and a crystallographic density of NMC of $\rho_{NMC} = 4.8$ g/cm^3.

$$r_1 = \frac{3}{A_{BET} * \rho_{NMC}} \quad [14]$$

The resulting layer thicknesses for the spinel and rock-salt transformations ($t_{spinel,O_2,CO}$, t_{spinel,O_2,CO_2}, $t_{rock\text{-}salt,O_2,CO}$, $t_{rock\text{-}salt,O_2,CO_2}$) are shown in the 12th-15th row of Table III.

The calculated oxygen depleted volume fractions considering a spinel or rock-salt transformation are in the range 1.0% – 2.1% and 0.6% – 1.3%, respectively. It is interesting to note that the oxygen depleted volume fractions calculated for NMC622 are roughly doubled compared to the ones for NMC811, while the values for NMC111 are in between the two values. Interestingly, this parallels their BET surface area, with the one of NMC111 (0.26 m^2/g) being in between the ones of NMC622 (0.35 m^2/g) and NMC811 (0.18 m^2/g), the latter two being different by a factor of 2. This already suggests that the conversion of the layered to the spinel/rock-salt structure may be limited by the formed oxygen-depleted surface-near film.

Due to the differences in the BET surface area of the three NMCs, the obtained layer thicknesses turn out to be very similar. For model I, the calculated layer thicknesses for the spinel and rock-salt transformations are 11.6 nm–12.1 nm and 6.9 nm–7.3 nm, respectively. Also for the calculation based on model II, the obtained values are very close to the ones obtained using model I (12.7 nm–14.6 nm and 7.8 nm–8.2 nm, respectively). These calculated layer thicknesses are in good agreement with previous reports in the literature on NMC,[9] $LiNi_{0.8}Co_{0.2}O_2$[28], NCA[30] and Li-rich NMC.[36] As expected, a transformation to the spinel phase leads to a thicker surface layer than the transformation to the rock-salt phase, since the former contains more oxygen in its structure than the latter. Moreover, it is very likely that for the different NMC materials different ratios of spinel and rock-salt phases occur with higher rock-salt ratios for Ni-richer NMC as they tend to form rock-salt rather than spinel phases.[9,70] However, this would not significantly affect the estimated surface layer thickness, as shown in Table III. Additionally, as it was shown in Figures 7–9, an increase in the oxygen signal cannot be observed anymore after a few cycles; however, we believe that the oxygen release is ongoing also in subsequent cycles, but is only detected as CO and CO_2. This would also explain the steady decrease of the charge-averaged mean cathode discharge potential shown in Figures 1–3 (solid lines in panels b). All in all, we demonstrated in this section that the film thicknesses deduced from the gas evolution data from OEMS yield values which are consistent with microscopy data from the literature.

Potential dependence of electrochemical and chemical electrolyte oxidation.—In the sections above we showed that the release of reactive oxygen from the surface of the NMC is accompanied by the majority of the observed CO_2 and CO evolution (see Figures 7–9). In this section we want to schematically illustrate the relation between electrochemical and chemical electrolyte oxidation, taking into account the results of this work and previous reports in the literature. Scheme 2a depicts the here proposed electrochemical and chemical pathways, exemplified for the oxidation of the commonly used electrolyte constituent EC (analogous mechanisms can be envisioned for other solvents).

The purely electrochemical pathway (see upper left panel in Scheme 2a) sets in when the voltage of the cathode is raised above the stability limit of the electrolyte $V_{solvent\ oxidation}$ which can occur on the surface in contact with the electrolyte (e.g., on conductive carbon additive[59]), at a rate which increases with increasing cathode potential (Scheme 2b). In this process, EC is electro-oxidized to CO or CO_2 and protic species ($R\text{-}H^+$)[12] which increase the acidity of the electrolyte[84] whereby the in parallel occurring reduction of the protic species on the graphite anode leads to the observed strongly enhanced hydrogen evolution (see Figures 7–9). To compensate the negative charge transferred to the NMC electrode upon electrochemical solvent oxidation, Li^+-ions from the electrolyte have to be intercalated into the NMC active material. As a consequence, when storing a battery cell charged to a high cutoff voltage, the electrochemical solvent oxidation and the concomitant Li^+ intercalation induce an apparent self-discharge, which can be observed by a voltage drop due to the sloped voltage profile of NMC (s. upper right panel of Scheme 2a).[72–75] Note that during cycling instead of the intercalation of Li^+ into the NMC the

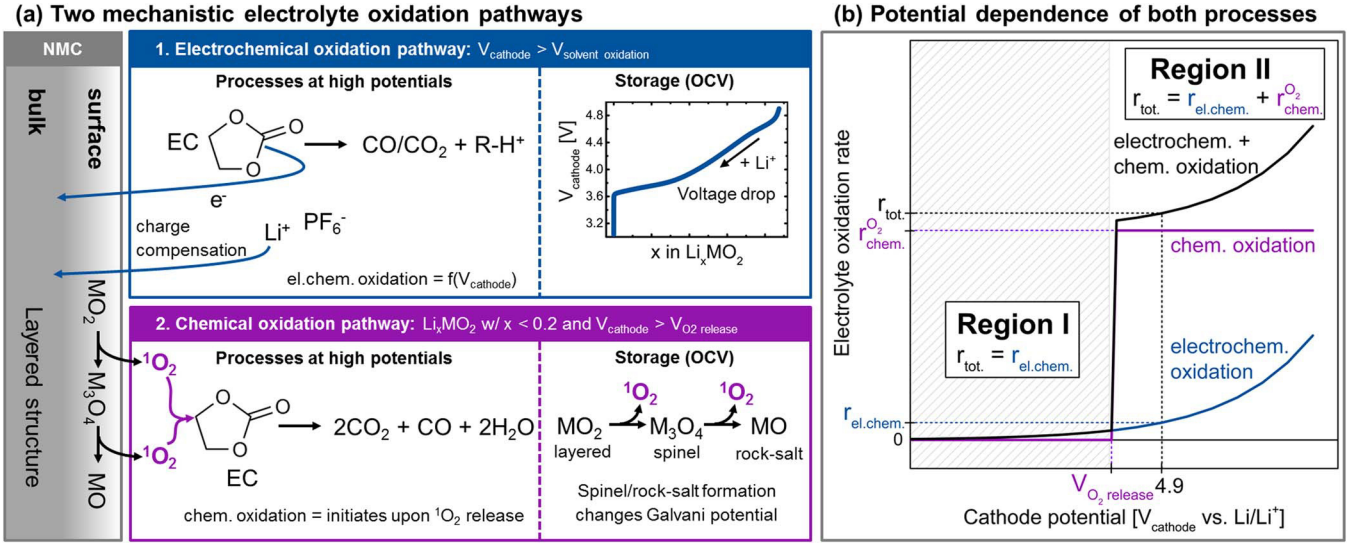

Scheme 2. (a) Schematic description of the proposed electrochemical and chemical electrolyte oxidation pathways (exemplarily shown for EC) which occur at high potentials, and their effect upon battery storage at high potentials. The shown electrochemical EC oxidation yields CO/CO_2 and protic $R\text{-}H^+$ species, and its rate increases with the cathode potential (upper left panel). The intercalation of Li^+ upon electrochemical EC oxidation causes a voltage drop during storage (upper right panel). The chemical EC oxidation initiates upon reactive oxygen release (e.g., singlet oxygen, $^1O_2$) from the NMC surface, which reacts with EC to CO_2, CO, and H_2O (lower left panel). During storage at OCV the surface reconstruction continues as long as the cathode potential is high enough to allow for oxygen release, which is expected to alter the Galvani potential (lower right panel). (b) Schematic potential dependence of both processes: for $V_{cathode} < V_{O_2\ release}$ (Region I), electrolyte oxidation only proceeds via the electrochemical pathway at the rate $r_{el.chem}$ (dark blue line; shown for electrolyte oxidation on conductive carbon[59]); for $V_{cathode} > V_{O_2\ release}$ (Region II), electrolyte oxidation proceeds simultaneously via both the chemical pathway at the rate $r^{O2}_{chem.}$ (purple line) and the electrochemical pathways. The sum of both reactions, $r_{tot.}$, is represented by the black line.

electrons can be transferred via the external circuit to the negative electrode and Li^+ would be intercalated into the graphite anode.

In contrast, the here proposed chemical electrolyte oxidation (lower left panel of Scheme 2a) initiates once the cathode potential exceeds the threshold voltage $V_{O_2\ release}$ for the release of reactive oxygen from the layered NMC structure (here depicted exemplarily as singlet oxygen, $^1O_2$). We showed that this surface transformation into a spinel or rock-salt phase occurs at very low lithium contents ($x < 0.2$ in Li_xMO_2) and that the threshold potential $V_{O_2\ release}$ varies for different NMC compositions, being ~4.7 V vs. Li/Li^+ for NMC111 and NMC622, and ~4.3 V vs. Li/Li^+ for NMC811. The rate of the chemical electrolyte oxidation associated with the release of reactive oxygen (accompanied by the evolution of CO_2 and CO, see Figures 7–9) is hardly potential dependent, i.e., it jumps from quasi zero to a rather high and fairly constant value (see Scheme 2b). Upon OCV storage, the surface reconstruction is ongoing as long as the cathode potential is high enough to allow for it, which is likely to affect the Galvani potential (and thus the OCV) due to the formation of the thermodynamically more stable spinel/rock-salt structure at the near surface layer (lower right panel of Scheme 2a). However, due to the above-described voltage drop during the simultaneously occurring electrochemical electrolyte oxidation (i.e., a gradual re-lithiation of the NMC), the oxygen release will stop as soon as $V_{cathode}$ falls below $V_{O_2\ release}$. Therefore, one would expect that the open circuit potential decay during extended OCV storage is mostly controlled by the rate of the electrochemical pathway.

Scheme 2b schematically summarizes the potential dependence of the electrochemical (dark blue line) and chemical electrolyte oxidation (purple line), with the sum of both processes represented by the black line. As described before, the electrochemical pathway is a function of the cathode voltage, which is shown to proceed at a rate increasing exponentially with potential (dark blue line). In contrast, the chemical pathway is likely to have a very weak potential dependence as long as the released lattice oxygen is provided, which would predict a sudden onset once the potential exceeds $V_{O_2\ release}$ with a weak potential dependence after that point (purple line). At $V_{cathode} < V_{O_2\ release}$ (Region I), no chemical electrolyte oxidation is expected, so that the total electrolyte oxidation rate (black line) is identical to the electrochemical oxidation (dark blue line). On the other hand, at $V_{cathode} > V_{O_2\ release}$ (Region II), the total electrolyte oxidation rate is the sum of the rates of the electrochemical and chemical pathways, with the latter being the dominant pathway. This implies that the intrinsic electrochemical stability of electrolyte solvents can only be measured with "inert" electrodes which do not release lattice oxygen, e.g., carbon black.[59] Note that the rate of the electrochemical pathway investigated in the report by Metzger et al.[59] at 5.0 V vs. Li/Li^+ would only be roughly 10% of the total electrolyte oxidation observed in this work on NMC111 (Figure 7) at 4.9 V vs. Li/Li^+ (see second paragraph of the Discussion section for a detailed calculation), which led us to the conclusion that the chemical pathway would be the dominant one at this potential.

In a recent report by Xia et al.,[72] a voltage drop from 4.7 V to roughly 4.5 V was observed for NMC442-graphite cells during storage at OCV for 500 h at 40°C with LP57 electrolyte. A voltage drop by 200 mV in a NMC material corresponds to roughly 20 mAh/g_{NMC}, corresponding to an exchanged amount of electrons of 746 $\mu mol_e/g_{NMC}$. As the BET-surface area of the used NMC442 material as well as the electrode composition were not stated, we will assume for the following calculation that its BET surface area was similar to that of our NMC111 (0.26 m^2/g) and that the electrode composition was also similar to that in our study (91.5% NMC and 4.4% C65). Dividing the specific amount of electrons by the estimated surface areas and accounting for the electrode composition, a total of 220 $\mu mol_e/m^2_{NMC+C}$ is obtained. Assuming that the electrochemical oxidation of one solvent molecule leads to the intercalation of one Li^+-ion into NMC, also 220 $\mu mol_{solvent}/m^2_{NMC+C}$ would be decomposed by this process. When dividing this value by the storage time of 500 h, an average decomposition rate of 0.44 $\mu mol_{solvent}/(m^2_{NMC+C}\cdot h)$ would be obtained at a potential ranging between 4.8 and 4.6 V vs. Li/Li^+. This may be compared with the electrochemical oxidation rate of EC on a carbon surface at 5 V vs. Li/Li^+ and 40°C, which was reported to be ~1.1 $\mu mol_{solvent}/(m^2_C\cdot h)$.[59] Thus, the average electrolyte oxidation rate between 4.8 and 4.6 V (vs. Li/Li^+) of 0.44 $\mu mol_{solvent}/(m^2_{NMC+C}\cdot h)$, which would be required to rationalize the observed potential decay

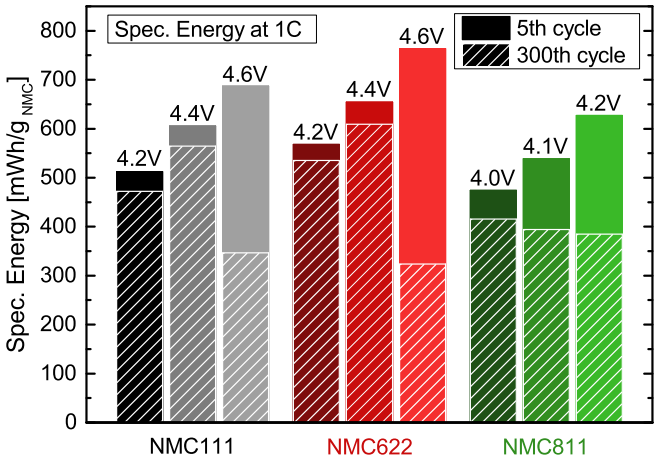

Figure 11. Specific energy of NMC111-graphite, NMC622-graphite and NMC811-graphite cells in LP57 electrolyte (1 M $LiPF_6$ in EC:EMC 3:7). The full columns represent the specific energy of the 5th cycle (1 C-rate), the dashed part of the columns of the 300th cycle (1 C-rate). The data are extracted from the cells shown in the Figures 1–3.

during the OCV hold by Xia et al.[72] is reasonably consistent with the electrochemical EC oxidation rate of ~1.1 $\mu mol_{solvent}/(m_C^2 \cdot h)$ at the higher potential of 5.0 V, particularly considering that the EMC oxidation rate in the LP57 electrolyte was found to be even higher (unpublished results). Consequently, we believe that during OCV storage the electrochemical oxidation is the dominating process that leads to the observed voltage drop, as was already stated in the reports by the Dahn group.[72–75] The apparent rate determined in this work, which includes the effect of the chemical electrolyte oxidation due to oxygen release at 25°C and ~4.9 V vs. Li/Li^+ is ~3.0 $\mu mol_{solvent}/(m_{NMC+C}^2 \cdot h)$ (see the detailed calculation in the second paragraph of the Discussion section), and is therefore ~3-fold higher than the rate of pure electrochemical solvent oxidation at higher temperature (40°C) and higher potential (5 V vs. Li/Li^+). Compared to the rate of pure electrochemical oxidation at 25°C and 5 V vs. Li/Li^+ of ~0.3 $\mu mol/(m_C^2 \cdot h)$ it is even ~10-fold higher.[59] This unambiguously demonstrates the dominating effect of the chemical electrolyte oxidation at potentials at which oxygen is released from the NMC lattice (Scheme 2b).

Specific energy densities of NMC111, NMC622 and NMC811.— In the previous sections it was demonstrated that the release of oxygen from the NMC surface has a very detrimental impact on the material stability, as it causes significant gas evolution (Figures 7–9) as well as a significant increase of the polarization of the cathode material most probably due to the oxygen depleted surface layer (Figures 1–3). For NMC811, the oxygen release occurs already at potentials as low as 4.3 V vs. Li/Li^+, whereas for NMC111 and NMC622 it occurs roughly at 4.7 V vs. Li/Li^+. These values limit the end-of-charge voltage that can be applied to achieve a stable cycling and they have therefore a severe impact on the achievable specific energy of these materials. We want to highlight that additional aging mechanisms will be occurring in parallel, like lithium loss due to SEI growth on the anode, electrochemical electrolyte oxidation at high potentials on the cathode, metal dissolution from the cathode, etc.; however, when cycling up to potentials where oxygen release occurs, the formation of a resistive surface layer is the most severe aging mechanism under these conditions, causing significant capacity and discharge voltage fading during extended charge/discharge cycling (Figures 1–3). The specific energies of the cells shown in the Figures 1–3 are depicted in Figure 11 with the full bars representing the specific energy of the 5th cycle at a 1C-rate. The dashed bars indicate the remaining specific energy after 300 cycles. As discussed before, stable cycling was possible for NMC111 and NMC622 up to 4.4 V and up to 4.0 V for NMC811. This is also clearly visible in Figure 11, as the differences between the specific energies in the 5th and 300th cycle are fairly low for these voltage limits, but increase significantly for the others. The highest specific energy with stable cycling was achieved with NMC622 cycled up to 4.4 V. Comparing only the cells with stable cycling performance, it becomes clear that NMC811 reaches the lowest specific energy, which is due to the very low applicable end-of-charge voltage of only 4.0 V.

This rather sobering outlook for NMC811 emphasizes the need to prohibit the oxygen release from the surface. Our results suggest that one way of making use of the high capacities of NMC811 and achieving stable cycling at the same time might be possible by either a core-shell structure in which the core consists of NMC811 with i) a shell that has a Ni-content of up to 60 % (surface like NMC622) and does not release oxygen until >4.4 V or ii) a shell consisting of an ordered spinel like high-voltage spinel (LNMO) that does hardly evolve any gases (Figure 5) due to the absence of oxygen release. In both cases the shell would need to be thick enough to prevent oxygen loss from the core structure via the limited diffusion of the oxygen anions. Indeed, these approaches have been used by several research groups and we believe that the prevention of oxygen release explains the successful use of core-shell[85–88] materials possessing Ni-contents in the core and shell of 80% and ≤55%, respectively, and full concentration gradient[89–91] materials with Ni-contents of ≥75% and ≤56% in the particle center and the surface, respectively. Additionally, also a superior performance of $LiMn_2O_4$ coated NMC over uncoated samples was reported by Cho et al.[92]

Conclusions

This work focused on a fundamental understanding of the aging phenomena at high voltage of $LiNi_{1/3}Mn_{1/3}Co_{1/3}O_2$ (NMC111), $LiNi_{0.6}Mn_{0.2}Co_{0.2}O_2$ (NMC622), and $LiNi_{0.8}Mn_{0.1}Co_{0.1}O_2$ (NMC811). NMC-graphite cells were cycled to different end-of-charge potentials and it was demonstrated that stable cycling is possible up to 4.4 V for NMC111 and NMC622 and only up to 4.0 V for NMC811. The capacity fading rates observed at 4.6 V for NMC111 and NMC622 and 4.1 V and 4.2 V for NMC811 are due to a significant increase in the polarization of the NMC electrode as evidenced by charge/discharge cycling in a 3-electrode setup with a lithium reference electrode. In contrast, the polarization of the graphite electrode remained rather constant. By a dq/dV analysis we demonstrated that the significant rise in the impedance occurs when the NMC materials are cycled up to a high-voltage feature at ~4.7 V vs. Li/Li^+ for NMC111 and NMC622 and up to the H2 → H3 phase transition at ~4.3 V vs. Li/Li^+ for NMC811; we hypothesize that this is caused by oxygen release from the NMC lattice.

Oxygen release is evidenced by On-line Electrochemical Mass Spectrometry (OEMS). Simultaneously with the oxygen evolution, also CO_2 and CO are evolved, which we suggest to be mostly due to a chemical reaction of electrolyte with released lattice oxygen rather than the electrochemical oxidation of electrolyte on the cathode surface. We proposed a mechanism for the reaction of released oxygen with ethylene carbonate yielding CO_2, CO and H_2O. By quantifying the evolved gases, we estimated the thickness of the oxygen depleted surface layer to be up to ~15 nm, which is in agreement with previous microscopy studies in the literature. Furthermore we showed that no oxygen is released from high voltage spinel (LNMO) and in consequence also no CO_2 or CO evolution was observed. These results support the hypothesis that the CO_2 and CO evolution at potentials up to 4.8 V is to a large extent linked to the release of oxygen, rather than to the electrochemical oxidation of the carbonate electrolyte.

The highest specific energy of ~650 mWh/g_{NMC} with a stable cycling performance at a 1 C-rate was obtained in NMC622-graphite cells cycled up to 4.4 V. Due to the low end-of-charge voltage limit of 4.0 V for a stable cycling of NMC811-graphite cells, the achieved specific energy is significantly lower than for the NMC622 cells. Therefore a stabilization of the NMC surface is necessary to prevent the release of oxygen from the particle surface.

Acknowledgment

The authors thank BMW AG for their financial support. Umicore is greatly acknowledged for supplying the cathode materials. We thank Benjamin Strehle and Sophie Solchenbach for very fruitful discussions and great contributions to this work. R. J. also thanks TUM-IAS for their support in the frame of the Rudolf-Diesel Fellowship of Dr. Peter Lamp. M. M. gratefully acknowledges funding by BASF SE through its electrochemistry and battery research network.

References

1. O. Groeger, H. A. Gasteiger, and J. -P. Suchsland, *Journal of The Electrochemical Society*, **162**, A2605 (2015).
2. D. Andre, S. -J. Kim, P. Lamp, S. F. Lux, F. Maglia, O. Paschos, and B. Stiaszny, *J. Mater. Chem. A*, **3**, 6709 (2015).
3. K. G. Gallagher, S. Goebel, T. Greszler, M. Mathias, W. Oelerich, D. Eroglu, and V. Srinivasan, *Energy Environ. Sci.*, **7**, 1555 (2014).
4. I. Belharouak, Y. K. Sun, J. Liu, and K. Amine, *J. Power Sources*, 2003, **123**, 247.
5. M. S. Whittingham, *Chem. Rev. (Washington, DC, U. S.)*, **104**, 4271 (2004).
6. J. Choi and A. Manthiram, *J. Electrochem. Soc.*, **152**, A1714 (2005).
7. N. Yabuuchi, Y. Makimura, and T. Ohzuku, *Journal of The Electrochemical Society*, **154**, A314 (2007).
8. M. G. Kim, H. J. Shin, J. -H. Kim, S. -H. Park, and Y. -K. Sun, *Journal of The Electrochemical Society*, **152**, A1320 (2005).
9. S. -K. Jung, H. Gwon, J. Hong, K. -Y. Park, D. -H. Seo, H. Kim, J. Hyun, W. Yang, and K. Kang, *Adv. Energy Mater.*, **4**, 1300787 (2014).
10. H. Gabrisch, T. Yi, and R. Yazami, *Electrochem. Solid-State Lett.*, **11**, A119 (2008).
11. I. Buchberger, S. Seidlmayer, A. Pokharel, M. Piana, J. Hattendorff, P. Kudejova, R. Gilles, and H. A. Gasteiger, *Journal of The Electrochemical Society*, **162**, A2737 (2015).
12. M. Metzger, B. Strehle, S. Solchenbach, and H. A. Gasteiger, *Journal of The Electrochemical Society*, **163**, A798 (2016).
13. D. R. Gallus, R. Schmitz, R. Wagner, B. Hoffmann, S. Nowak, I. Cekic-Laskovic, R. W. Schmitz, and M. Winter, *Electrochim. Acta*, **134**, 393 (2014).
14. H. Zheng, Q. Sun, G. Liu, X. Song, and V. S. Battaglia, *J. Power Sources*, **207**, 134 (2012).
15. Y. -C. Lu, A. N. Mansour, N. Yabuuchi, and Y. Shao-Horn, *Chemistry of Materials*, **21**, 4408 (2009).
16. A. M. Andersson, D. P. Abraham, R. Haasch, S. MacLaren, J. Liu, and K. Amine, *Journal of The Electrochemical Society*, **149**, A1358 (2002).
17. J. Wandt, A. Freiberg, R. Thomas, Y. Gorlin, A. Siebel, R. Jung, H. A. Gasteiger, and M. Tromp, *Journal of Materials Chemistry A*, **4**, 18300 (2016).
18. H. -J. Noh, S. Youn, C. S. Yoon, and Y. -K. Sun, *J. Power Sources*, **233**, 121 (2013).
19. W. Liu, P. Oh, X. Liu, M. -J. Lee, W. Cho, S. Chae, Y. Kim, and J. Cho, *Angew. Chem., Int. Ed.*, **54**, 4440 (2015).
20. J. Zheng, W. H. Kan, and A. Manthiram, *ACS Appl. Mater. Interfaces*, **7**, 6926 (2015).
21. S. -M. Bak, E. Hu, Y. Zhou, X. Yu, S. D. Senanayake, S. -J. Cho, K. -B. Kim, K. Y. Chung, X. -Q. Yang, and K. -W. Nam, *ACS Appl. Mater. Interfaces*, **6**, 22594 (2014).
22. S. -M. Bak, K. -W. Nam, W. Chang, X. Yu, E. Hu, S. Hwang, E. A. Stach, K. -B. Kim, K. Y. Chung, and X. -Q. Yang, *Chem. Mater.*, **25**, 337 (2013).
23. H. Konishi, T. Yuasa, and M. Yoshikawa, *J. Power Sources*, **196**, 6884 (2011).
24. H. Arai, S. Okada, Y. Sakurai, and J. -i. Yamaki, *Solid State Ionics*, **109**, 295 (1998).
25. I. Belharouak, W. Lu, D. Vissers, and K. Amine, *Electrochemistry Communications*, **8**, 329 (2006).
26. I. Belharouak, D. Vissers, and K. Amine, *Journal of The Electrochemical Society*, **153**, A2030 (2006).
27. S. -T. Myung, K. -S. Lee, C. S. Yoon, Y. -K. Sun, K. Amine, and H. Yashiro, *J. Phys. Chem. C*, **114**, 4710 (2010).
28. D. P. Abraham, R. D. Twesten, M. Balasubramanian, I. Petrov, J. McBreen, and K. Amine, *Electrochem. Commun.*, **4**, 620 (2002).
29. D. P. Abraham, R. D. Twesten, M. Balasubramanian, J. Kropf, D. Fischer, J. McBreen, I. Petrov, and K. Amine, *Journal of The Electrochemical Society*, **150**, A1450 (2003).
30. S. Muto, Y. Sasano, K. Tatsumi, T. Sasaki, K. Horibuchi, Y. Takeuchi, and Y. Ukyo, *Journal of The Electrochemical Society*, **156**, A371 (2009).
31. S. Hwang, W. Chang, S. M. Kim, D. Su, D. H. Kim, J. Y. Lee, K. Y. Chung, and E. A. Stach, *Chem. Mater.*, **26**, 1084 (2014).
32. F. La Mantia, F. Rosciano, N. Tran, and P. Novak, *J. Appl. Electrochem.*, **38**, 893 (2008).
33. P. Lanz, H. Sommer, M. Schulz-Dobrick, and P. Novak, *Electrochim. Acta*, **93**, 114 (2013).
34. A. R. Armstrong, M. Holzapfel, P. Novak, C. S. Johnson, S. -H. Kang, M. M. Thackeray, and P. G. Bruce, *J. Am. Chem. Soc.*, **128**, 8694 (2006).
35. K. Luo, M. R. Roberts, R. Hao, N. Guerrini, D. M. Pickup, Y. -S. Liu, K. Edström, J. Guo, A. V. Chadwick, L. C. Duda, and P. G. Bruce, *Nat Chem*, **8**, 684 (2016).
36. B. Strehle, K. Kleiner, R. Jung, F. Chesneau, M. Mendez, H. A. Gasteiger, and M. Piana, *Journal of The Electrochemical Society*, **164**, A400 (2017).
37. A. Guéguen, D. Streich, M. He, M. Mendez, F. F. Chesneau, P. Novák, and E. J. Berg, *Journal of The Electrochemical Society*, **163**, A1095 (2016).
38. M. Metzger, J. Sicklinger, D. Haering, C. Kavakli, C. Stinner, C. Marino, and H. A. Gasteiger, *Journal of The Electrochemical Society*, **162**, A1227 (2015).
39. N. Tsiouvaras, S. Meini, I. Buchberger, and H. A. Gasteiger, *Journal of The Electrochemical Society*, **160**, A471 (2013).
40. B. Strehle, S. Solchenbach, M. Metzger, K. U. Schwenke, and H. A. Gasteiger, to be submitted.
41. M. Dubarry, C. Truchot, B. Y. Liaw, K. Gering, S. Sazhin, D. Jamison, and C. Michelbacher, *J. Power Sources*, **196**, 10336 (2011).
42. J. C. Burns, A. Kassam, N. N. Sinha, L. E. Downie, L. Solnickova, B. M. Way, and J. R. Dahn, *Journal of The Electrochemical Society*, **160**, A1451 (2013).
43. L. Ma, J. Xia, and J. R. Dahn, *Journal of The Electrochemical Society*, **161**, A2250 (2014).
44. K. J. Nelson, G. L. d'Eon, A. T. B. Wright, L. Ma, J. Xia, and J. R. Dahn, *Journal of The Electrochemical Society*, **162**, A1046 (2015).
45. R. Petibon, L. Madec, D. W. Abarbanel, and J. R. Dahn, *Journal of Power Sources*, **300**, 419 (2015).
46. H. Arai, S. Okada, H. Ohtsuka, M. Ichimura, and J. Yamaki, *Solid State Ionics*, **80**, 261 (1995).
47. W. Li, J. N. Reimers, and J. R. Dahn, *Solid State Ionics*, 1993, **67**, 123.
48. J. P. Peres, F. Weill, and C. Delmas, *Solid State Ionics*, **116**, 19 (1999).
49. S. U. Woo, C. S. Yoon, K. Amine, I. Belharouak, and Y. K. Sun, *J. Electrochem. Soc.*, **154**, A1005 (2007).
50. M. Sathiya, G. Rousse, K. Ramesha, C. P. Laisa, H. Vezin, M. T. Sougrati, M. L. Doublet, D. Foix, D. Gonbeau, W. Walker, A. S. Prakash, M. Ben Hassine, L. DuPont, and J. M. Tarascon, *Nat Mater*, **12**, 827 (2013).
51. E. McCalla, A. M. Abakumov, M. Saubanere, D. Foix, E. J. Berg, G. Rousse, M. -L. Doublet, D. Gonbeau, P. Novak, G. Van Tendeloo, R. Dominko, and J. -M. Tarascon, *Science (Washington, DC, U. S.)*, **350**, 1516 (2015).
52. D. -H. Seo, J. Lee, A. Urban, R. Malik, S. Kang, and G. Ceder, *Nat Chem*, **8**, 692 (2016).
53. M. Saubanere, E. McCalla, J. M. Tarascon, and M. L. Doublet, *Energy & Environmental Science*, **9**, 984 (2016).
54. M. Xu, N. Tsiouvaras, A. Garsuch, H. A. Gasteiger, and B. L. Lucht, *J. Phys. Chem. C*, **118**, 7363 (2014).
55. S. A. Freunberger, Y. Chen, Z. Peng, J. M. Griffin, L. J. Hardwick, F. Bardé, P. Novák, and P. G. Bruce, *Journal of the American Chemical Society*, **133**, 8040 (2011).
56. E. S. Takeuchi, H. Gan, M. Palazzo, R. A. Leising, and S. M. Davis, *Journal of The Electrochemical Society*, **144**, 1944 (1997).
57. H. Yoshida, T. Fukunaga, T. Hazama, M. Terasaki, M. Mizutani, and M. Yamachi, *J. Power Sources*, **68**, 311 (1997).
58. R. Petibon, L. Rotermund, K. J. Nelson, A. S. Gozdz, J. Xia, and J. R. Dahn, *Journal of The Electrochemical Society*, **161**, A1167 (2014).
59. M. Metzger, C. Marino, J. Sicklinger, D. Haering, and H. A. Gasteiger, *Journal of The Electrochemical Society*, **162**, A1123 (2015).
60. B. Zhang, M. Metzger, S. Solchenbach, M. Payne, S. Meini, H. A. Gasteiger, A. Garsuch, and B. L. Lucht, *The Journal of Physical Chemistry C*, **119**, 11337 (2015).
61. M. Nie, D. Chalasani, D. P. Abraham, Y. Chen, A. Bose, and B. L. Lucht, *J. Phys. Chem. C*, **117**, 1257 (2013).
62. D. Aurbach, Y. Gofer, M. Ben-Zion, and P. Aped, *J. Electroanal. Chem.*, **339**, 451 (1992).
63. M. Onuki, S. Kinoshita, Y. Sakata, M. Yanagidate, Y. Otake, M. Ue, and M. Deguchi, *Journal of The Electrochemical Society*, **155**, A794 (2008).
64. R. Bernhard, M. Metzger, and H. A. Gasteiger, *Journal of The Electrochemical Society*, **162**, A1984 (2015).
65. S. Meini, N. Tsiouvaras, K. U. Schwenke, M. Piana, H. Beyer, L. Lange, and H. A. Gasteiger, *Phys. Chem. Chem. Phys.*, **15**, 11478 (2013).
66. R. Dedryvere, D. Foix, S. Franger, S. Patoux, L. Daniel, and D. Gonbeau, *J. Phys. Chem. C*, **114**, 10999 (2010).
67. L. Xing and O. Borodin, *Phys. Chem. Chem. Phys.*, **14**, 12838 (2012).
68. K. Abe, T. Hattori, K. Kawabe, Y. Ushigoe, and H. Yoshitake, *Journal of The Electrochemical Society*, **154**, A810 (2007).
69. Y. Koyama, N. Yabuuchi, I. Tanaka, H. Adachi, and T. Ohzuku, *Journal of The Electrochemical Society*, **151**, A1545 (2004).
70. L. Wu, K. -W. Nam, X. Wang, Y. Zhou, J. -C. Zheng, X. -Q. Yang, and Y. Zhu, *Chem. Mater.*, **23**, 3953 (2011).
71. K. -W. Nam, W. -S. Yoon, and X. -Q. Yang, *J. Power Sources*, **189**, 515 (2009).
72. J. Xia, K. J. Nelson, Z. Lu, and J. R. Dahn, *Journal of Power Sources*, **329**, 387 (2016).
73. J. Xia and J. R. Dahn, *Journal of Power Sources*, **324**, 704 (2016).
74. M. Nie, J. Xia, and J. R. Dahn, *Journal of The Electrochemical Society*, **162**, A1186 (2015).
75. J. Xia, M. Nie, J. C. Burns, A. Xiao, W. M. Lamanna, and J. R. Dahn, *Journal of Power Sources*, **307**, 340 (2016).
76. F. Wilkinson, W. P. Helman, and A. B. Ross, *Journal of Physical and Chemical Reference Data*, **24**, 663 (1995).
77. D. V. Kazakov, V. P. Kazakov, G. Y. Maistrenko, D. V. Mal'zev, and R. Schmidt, *The Journal of Physical Chemistry A*, **111**, 4267 (2007).
78. J. Li, L. E. Downie, L. Ma, W. Qiu, and J. R. Dahn, *Journal of The Electrochemical Society*, **162**, A1401 (2015).
79. R. Imhof and P. Novak, *J. Electrochem. Soc.*, **146**, 1702 (1999).
80. M. Metzger, B. Strehle, S. Solchenbach, and H. A. Gasteiger, *Journal of The Electrochemical Society*, **163**, A1219 (2016).
81. M. Jiang, B. Key, Y. S. Meng, and C. P. Grey, *Chem. Mater.*, **21**, 2733 (2009).
82. S. Meini, S. Solchenbach, M. Piana, and H. A. Gasteiger, *Journal of The Electrochemical Society*, **161**, A1306 (2014).
83. N. Yabuuchi, Y. -T. Kim, H. H. Li, and Y. Shao-Horn, *Chemistry of Materials*, **20**, 4936 (2008).

84. T. Ma, G. -L. Xu, Y. Li, L. Wang, X. He, J. Zheng, J. Liu, M. H. Engelhard, P. Zapol, L. A. Curtiss, J. Jorne, K. Amine, and Z. Chen, *The Journal of Physical Chemistry Letters*, 1072 (2017).
85. J. -Y. Liao and A. Manthiram, *J. Power Sources*, **282**, 429 (2015).
86. Y. -K. Sun, S. -T. Myung, B. -C. Park, J. Prakash, I. Belharouak, and K. Amine, *Nat. Mater.*, **8**, 320 (2009).
87. Y. -K. Sun, S. -T. Myung, M. -H. Kim, J. Prakash, and K. Amine, *J. Am. Chem. Soc.*, **127**, 13411 (2005).
88. Y. -K. Sun, D. -H. Kim, C. S. Yoon, S. -T. Myung, J. Prakash, and K. Amine, *Adv. Funct. Mater.*, **20**, 485 (2010).
89. Y. -K. Sun, Z. Chen, H. -J. Noh, D. -J. Lee, H. -G. Jung, Y. Ren, S. Wang, C. S. Yoon, S. -T. Myung, and K. Amine, *Nat. Mater.*, **11**, 942 (2012).
90. E. -J. Lee, H. -J. Noh, C. S. Yoon, and Y. -K. Sun, *J. Power Sources*, **273**, 663 (2015).
91. C. Hua, K. Du, C. Tan, Z. Peng, Y. Cao, and G. Hu, *J. Alloys Compd.*, **614**, 264 (2014).
92. Y. Cho, S. Lee, Y. Lee, T. Hong, and J. Cho, *Adv. Energy Mater.*, **1**, 821 (2011).

3.1.3 Chemical vs. Electrochemical Electrolyte Oxidation on NMC111, NMC622, NMC811, LNMO, and Conductive Carbon

In this section, the article "Chemical vs. Electrochemical Electrolyte Oxidation on NMC111, NMC622, NMC811, LNMO, and Conductive Carbon" will be presented, which was published in the *Journal of Physical Chemistry Letters* on September 14, 2017. It is reprinted with permission from *J. Phys. Chem. Lett.* 2017, 4820-4825.[147] Copyright 2017 American Chemical Society. The results of the publication were presented, together with the findings of the publication described in section 3.1.2, on international conferences, e.g., by Roland Jung at the 231st Meeting of The Electrochemical Society (May 28- June 1, 2017) in New Orleans, USA (Abstract Number: #39). The permanent web-link to the publication is http://pubs.acs.org/doi/10.1021/acs.jpclett.7b01927 and the DOI is 10.1021/acs.jpclett.7b01927.

The publication is a follow-up study of the work presented in section 3.1.2, in which we described the *chemical* electrolyte oxidation pathway,[101] and of a previous report by Metzger et al.,[157] in which the *electrochemical* electrolyte oxidation pathway was investigated. The target of the paper is i) to measure the intrinsic *electrochemical* stability of LP57 electrolyte, ii) to analyze changes to the electrolyte stability caused by *chemical* electrolyte oxidation induced by released lattice oxygen from NMC, and iii) to reexamine the wide-spread assumption that transition metals catalyze the *electrochemical* electrolyte oxidation.[177, 191, 204]

To determine the intrinsic *electrochemical* stability of LP57, we measure a linear sweep voltammogram of a conductive carbon (Super C65) electrode versus a lithium counter electrode while recording the gas evolution by OEMS. Thereby, we show that the gas evolution, in particular the evolution of CO_2 and CO, is a better indicator to measure *electrochemical* electrolyte oxidation than commonly used linear sweep voltammetry, because the latter does not allow to distinguish between *electrochemical* electrolyte oxidation and other electrochemical processes like PF_6^- anion intercalation into graphitic regions of the conductive carbon, which both occur at similar potentials.[51, 147] Therefore, by measuring the CO_2 and CO evolution we demonstrate that at 25 °C and within the time frame of the measurement no significant *electrochemical* electrolyte oxidation is occurring up to ~5 V vs. Li/Li^+. Only at potentials >5 V, an exponential increase of CO_2 and CO with rising voltage is observed, as expected based on Tafel kinetics. When the conductive carbon electrode is replaced by an LNMO cathode which does not release lattice oxygen upon complete

delithiation (see section 3.1.2), an almost identical potential dependence as in the case of conductive carbon is observed, indicating that LNMO neither catalyzes the *electrochemical* electrolyte oxidation nor initiates any *chemical* decomposition processes. When a NMC111, NMC622, or NMC811 cathode is used, CO_2 and CO already evolve once oxygen release from the NMC lattice sets in, i.e., at ~4.3 V for NMC811 and at ~4.6 V in the case of NMC111 and NMC622. This process, which is characterized by a parallel evolution of CO_2, CO, and O_2 (*chemical* electrolyte oxidation) is fundamentally different from *electrochemical* electrolyte oxidation, which is indicated by CO_2 and CO evolution in the absence of O_2 evolution. As *electrochemical* electrolyte oxidation at 25°C yields significant CO_2+CO amounts only at potentials >5 V, the vast majority of CO_2+CO in a Li-ion battery containing NMCs will stem from *chemical* rather than *electrochemical* electrolyte oxidation. This of course does not include the CO_2 and CO evolved from the graphite anode during the first formation cycle.[205] The presented findings are important for the future improvement of Li-ion cells containing NMC cathodes, because i) not only the *electrochemical* electrolyte stability has to be assured, which may become problematic especially at higher temperatures (in contrast to this study which was performed at 25°C) and/or during very long cycling, but also ii) oxygen release has to be avoided (by limiting delithiation to <80%) as it causes active material decomposition and the breakdown of the electrolyte. The latter effect may be reduced by the development of electrolytes which are *chemically* stable against the released oxygen which was shown to be at least in part $^1O_2$.[167]

The very similar voltage dependence of CO_2+CO evolution from NMC111 and NMC622 as well as the difference of roughly 0.3 V to NMC811 excludes a catalytic effect of the transition metals on electrolyte oxidation because all three NMCs differ in composition of all three metals. The basically equal CO_2+CO evolution of conductive carbon and LNMO further supports this finding. Therefore, our results indicate that the observation of lower electrolyte stability on Ni-rich layered oxide surfaces was falsely interpreted as a catalytic effect of the transition metal,[177, 191, 204] whereas the actual reason for the lower electrolyte stability is the *chemical* electrolyte oxidation pathway setting in upon oxygen release.

Author Contributions

Roland Jung and Michael Metzger designed and performed the experiments. Roland Jung analyzed the data. Roland Jung, Michael Metzger, and Hubert Gasteiger wrote the manuscript. All authors discussed the results and commented on the manuscript.

THE JOURNAL OF PHYSICAL CHEMISTRY Letters

Letter

pubs.acs.org/JPCL

Chemical versus Electrochemical Electrolyte Oxidation on NMC111, NMC622, NMC811, LNMO, and Conductive Carbon

Roland Jung,*[,†,‡,§] Michael Metzger,[†,§] Filippo Maglia,[‡] Christoph Stinner,[‡] and Hubert A. Gasteiger*[,†]

[†]Chair of Technical Electrochemistry, Department of Chemistry and Catalysis Research Center, Technische Universität München, Lichtenbergstrasse 4, 85748 Garching, Germany

[‡]BMW AG, Petuelring 130, 80788 Munich, Germany

ABSTRACT: We compare the stability of alkyl carbonate electrolyte on NMC111, -622, and -811, LNMO, and conductive carbon electrodes. We prove that CO_2 and CO evolution onset potentials depend on the electrode material and increase in the order NMC811 < NMC111 ≈ NMC622 < conductive carbon ≈ LNMO, which we rationalize by two fundamentally different oxidation mechanisms, the chemical and the electrochemical electrolyte oxidation. Additionally, in contrast to the widespread understanding that transition metals in cathode active materials catalyze the electrolyte oxidation, we will prove that such a catalytic effect on the electrochemical electrolyte oxidation does not exist.

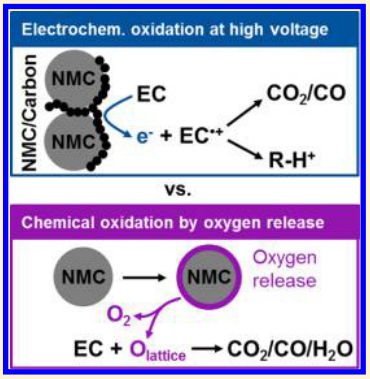

The market penetration of battery electric vehicles strongly depends on the accessible driving range.[1] For a range of 300 miles, a specific energy of 300−400 Wh/kg on battery cell level is required, which is ∼2.5 times more energy than today's Li-ion batteries can store.[2] To meet this target, improved cathode materials like spinel lithium nickel manganese oxide ($LiNi_{0.5}Mn_{1.5}O_4$, LNMO),[2] lithium- and manganese-rich layered oxides (e.g., $Li_{1+x}(Ni,Mn,Co)_{1-x}O_2$),[3] or nickel-rich layered lithium nickel manganese cobalt oxides ($LiNi_xMn_yCo_zO_2$ with $x + y + z = 1$, NMC)[2,3] are being developed. Stoichiometric NMC materials have a theoretical capacity of ∼275 mAh/g_{NMC}; however, the reversibly accessible capacity highly depends on the transition-metal ratio and increases with nickel content from ∼160 mAh/g_{NMC} for NMC111 ($LiNi_{1/3}Mn_{1/3}Co_{1/3}O_2$)[4−7] to ∼200 mAh/$g_{NMC}$ for NMC811 ($LiNi_{0.8}Mn_{0.1}Co_{0.1}O_2$)[4,7,8] at an upper cutoff voltage of 4.3 V versus Li/Li^+. Higher capacities are only accessible if higher cutoff voltages are applied, yet, for all of the above materials, the surface reactivity and electrolyte stability at high voltages are crucial because they can cause materials degradation and gas evolution detrimental to the cell performance/life.

Parasitic reactions like electrolyte oxidation result in low Coulombic efficiency that can be measured by high precision coulometry.[9] Isothermal microcalorimetry can be used to analyze the heat flow associated with such parasitic reactions.[10,11] Parasitic reactions can also be characterized by the total amount of gas evolved in a cell. For pouch-type lithium-ion cells this is done by measuring the buoyant force when submerging the cells in a liquid using Archimedes' principle.[12,13] Here we will use On-Line Electrochemical Mass Spectrometry (OEMS) to identify parasitic reactions at high voltage. OEMS not only allows quantifying the total amount of gas but also gives mechanistic insights into the governing processes by the ability to discern and quantify the various evolved gases.[7,14−18]

In the literature, different onset potentials (referenced to Li/Li^+ throughout this work) and gas concentrations are reported for the gas evolution (mostly CO_2 and CO) from electrolyte oxidation on various layered oxide compounds.[7,13,16,19−21] For instance, Imhof et al.[16] reported CO_2 evolution starting at ∼4.2 V with a $LiNiO_2$ electrode and a PC electrolyte with 1 M LiTFSI. On carbon black, $LiCoO_2$, and $LiMn_2O_4$, however, the same authors observed CO_2 only at potentials above 4.8 V.[16] Aiken et al.[19] detected significantly less gas evolution in $LiCoO_2$-graphite cells than in NMC442-graphite cells when charging the NMC to 4.8 V using Archimedes' principle. Li et al.[13] applied the same technique and reported hardly any gas evolution in NMC811 cells charged to 4.2 V and large amounts when charged to 4.4 V in LP57 electrolyte (1 M $LiPF_6$ in EC/EMC 3:7 wt/wt). In a more recent study by Guéguen et al.,[21] CO_2 evolution on NMC111 was observed to start at ∼4.2 V, followed by O_2 evolution at ∼4.55 V. It was concluded that the contribution of conductive carbon to electrolyte oxidation is substantial due to its large surface area fraction in the cathode. In our recent study on NMC materials,[7] we observed a similarly low onset potential for CO_2 evolution but ascribed it to the oxidation of carbonate surface impurities on the NMC active

Received: July 25, 2017
Accepted: September 14, 2017
Published: September 14, 2017

DOI: 10.1021/acs.jpclett.7b01927
J. Phys. Chem. Lett. 2017, 8, 4820−4825

material, while a second wave of CO_2 evolution simultaneous with the onset of O_2 evolution (at ~4.6 V) was interpreted as electrolyte oxidation caused by the release of lattice oxygen from the NMC surface.

To rationalize the above discussion, we propose two diverging mechanisms that can explain the discrepancy in electrolyte stability observed by different groups (see Scheme 1): (i) electrochemical oxidation of electrolyte, which is either

Scheme 1. Proposed Gassing Mechanisms in High-Voltage Lithium-Ion Cells Involving (i) Electrochemical Electrolyte Oxidation Proportional to the Exposed Surface Area (as shown below) and (ii) Chemical Electrolyte Oxidation Due to Release of Lattice Oxygen from Layered Oxide Cathodes and Its Reaction with Electrolyte[a]

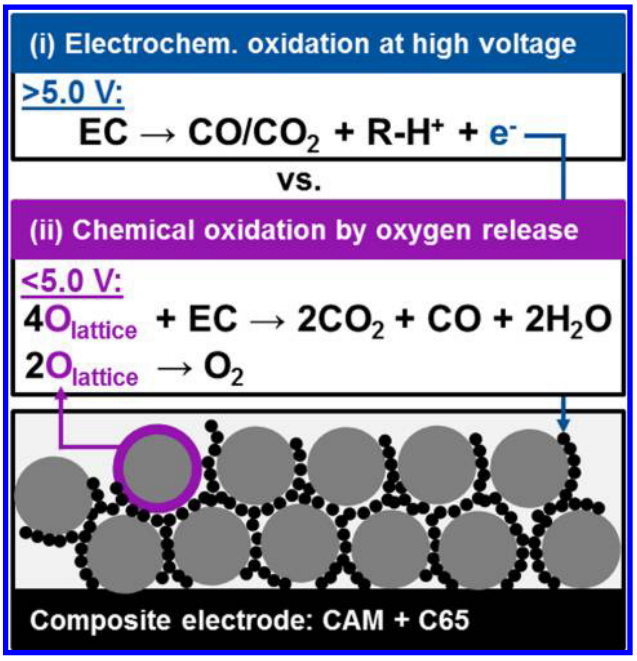

[a]Cathode active material (CAM) shown as gray spheres; conductive carbon shown as black spheres.

proportional to the sum of the total surface areas of the cathode active material (CAM) and the conductive carbon if it is a noncatalytic process or to only the CAM surface area if catalyzed by transition metals at the layered oxide surface, and (ii) chemical oxidation of electrolyte caused by the release of reactive oxygen (labeled as $O_{lattice}$ in Scheme 1) from the NMC surface or from other layered oxides like lithium- and manganese-rich NMC,[21−23] setting in at different voltages for different NMCs,[7] in which case the oxidation rate would again only depend on the CAM surface area.

To deconvolute the mechanisms illustrated in Scheme 1, we will use OEMS to determine the intrinsic electrochemical stability of LP57 electrolyte on a PVDF-bonded Super C65 (in the following abbreviated as C65) conductive carbon electrode. Afterward, we will compare this result to the electrolyte oxidation occurring on the layered oxide cathode materials $LiNi_{1/3}Mn_{1/3}Co_{1/3}O_2$ (NMC111), $LiNi_{0.6}Mn_{0.2}Co_{0.2}O_2$ (NMC622), $LiNi_{0.8}Mn_{0.1}Co_{0.1}O_2$ (NMC811), and the spinel $LiNi_{0.43}Mn_{1.57}O_4$ (LNMO). Additionally, we will show that OEMS is more feasible to determine electrolyte oxidation than commonly used linear sweep voltammetry. To account for the effect of different specific surface area on the observed gassing, all gas evolution data will be normalized to the BET-surface area either of both CAM and C65 or of only the CAM.

Table 1 summarizes the compositions, loadings, and surface areas of the electrodes investigated in this study. Because of the low specific surface area of the CAMs compared to C65, it is important to note that the surface area fraction of conductive carbon in typical cathodes is ~90% (last row in Table 1). Hence, without any catalytic effect of the CAM surface most electrochemical electrolyte oxidation should occur on the carbon surface.

In Figure 1 the linear sweep voltammogram of the C65 electrode measured between 3.1 and 5.7 V is depicted. Until the

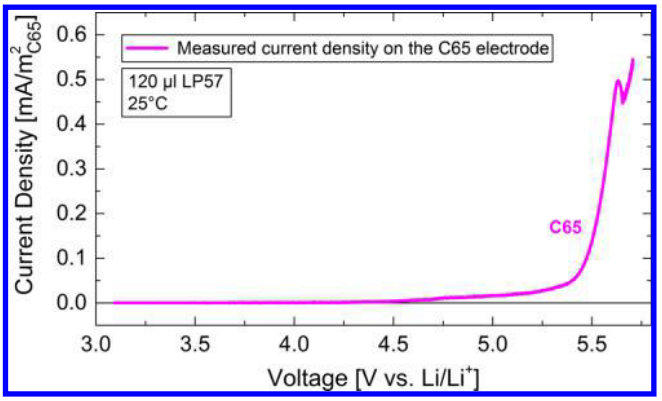

Figure 1. Current density versus voltage measured on a C65 electrode at 0.03 mV/s in LP57 electrolyte. The current is normalized to the surface area of C65 to obtain the current density.

voltage reaches 4.5 V, the current density is basically zero. Between 4.5 and 5.2 V, a fairly linear increase in the current density is observed, which turns into an exponential increase at potentials >5.2 V. This may be compared to the study by Moshkovich et al., who measured the current density in EC/DEC 1:1 mixtures on platinum, gold, and aluminum electrodes, noting significant currents already at potentials as low as 3.6 to 3.7 V, which they interpreted as the onset of electrochemical electrolyte oxidation.[24] Besides the difference in the onset of

Table 1. Properties of the Electrodes Investigated in This Study

	NMC111	NMC622	NMC811	LNMO	C65
composition ($\%_{wt}$)		91.5/4.4/4.1 (CAM/C65/PVDF)			50/50 (C65/PVDF)
BET-surface area (m^2/g)	0.26	0.35	0.18	0.23	65
loading (mg/cm^2)	NMC: 15.8	NMC: 15.5	NMC: 15.0	LNMO: 17.5	
	C65: 0.76	C65: 0.75	C65: 0.72	C65: 0.84	C65: 1.34
surface area of CAM (m^2)	7.26×10^{-3}	9.59×10^{-3}	4.78×10^{-3}	7.11×10^{-3}	
surface area of C65 (m^2)	87.4×10^{-3}	85.6×10^{-3}	83.1×10^{-3}	96.7×10^{-3}	154.3×10^{-3}
surface area fraction of C65 (%)	92	89	94	93	100

DOI: 10.1021/acs.jpclett.7b01927
J. Phys. Chem. Lett. 2017, 8, 4820−4825

appreciable oxidation currents of almost 1 V between their report and our work, the even more striking discrepancy is the difference in absolute value: At 4.4 to 4.5 V, Moshkovich et al. reported a current density of ~0.6 mA/cm^2 (≡ 6 × 10^3 mA/m$^2_{metal}$) for their smooth metal foil electrodes,[24] which is six orders of magnitude higher than what we measured at these potentials ((2 to 3) × 10^{-3} mA/m$^2_{C65}$) and still four orders of magnitude higher than what we found at even 5.7 V (5.5 × 10^{-1} mA/m$^2_{C65}$). Assuming a cell with an areal cathode capacity of 2 mAh/cm$^2_{geometric}$ containing NMC111 (corresponding to an NMC loading of 11.8 mg$_{NMC}$/cm$^2_{geometric}$ at 170 mAh/g at 4.5 V), the loading of C65 in the electrode (91.5%$_{wt}$ NMC, 4.4%$_{wt}$ C65, and 4.1%$_{wt}$ PVDF) would be 0.57 mg$_{C65}$/cm$^2_{geometric}$. With the BET-surface areas of 0.26 m^2/g$_{NMC}$ and 65 m^2/g$_{C65}$, the total surface area of the cathode electrode amounts to 0.04 m^2/cm$^2_{geometric}$. If the reported current density by Moshkovich et al.[24] was true, then this would yield a parasitic current at 4.4 to 4.5 V of 0.04 m^2/cm$^2_{geometric}$×6000 mA/m^2 = 240 mA/cm$^2_{geometric}$, which obviously cannot be true. (The current density at a 1 C-rate is only 2 mA/cm$^2_{geometric}$.) While one might argue that gold and platinum may act as catalysts for the electrochemical oxidation of the electrolyte, this would be unlikely in the case of the aluminum electrode in their experiments. While we can only speculate on the cause of this discrepancy, it may be possible that the extraordinarily high oxidation currents reported by Moshkovich et al. might have been related to the oxidation/corrosion of the metal surface in analogy to the aluminum current collector corrosion described by Ma et al. starting around 3.7 V[25] or the purity of the used electrolytes. The deviation from zero at >4.5 V in Figure 1 may be interpreted as electrochemical electrolyte oxidation, but because we observe an initially rather linear current increase followed only later on by the expected exponential increase (at >5.2 V), this initial current is likely related to a different process. As reported in the literature, at these potentials also intercalation of the PF_6^- anion into graphitic regions of C65 might occur.[26,27] Integrating the measured areal current between 4.5 and 5.0 V yields an areal charge of 0.0622 mAh/m$^2_{C65}$. If we were to assume that all the charge is due to PF_6^- intercalation into C65, then this would correspond to 0.0622 mAh/m$^2_{C65}$×65 m^2/g$_{C65}$ = 4 mAh/g$_{C65}$, a value that is very well possible according to previous reports.[26,27] Therefore, because of the two possible processes that could explain the observed current at >4.5 V, we will use the onset of gas evolution as the more reliable indicator for electrochemical electrolyte oxidation because it allows us to distinguish these two processes.

Figure 2a shows the total amount of CO_2 and CO gas (referred to as CO_2+CO; solid lines) as well as the O_2 gas (dashed lines) normalized to the total surface area of the electrode (sum of CAM and C65, see Table 1) versus electrode potential. We use the sum of CO_2 and CO because both gases are produced by the oxidation of electrolyte, irrespective of the oxidation mechanism (chemical[7] or electrochemical[17,28,29] oxidation; see Scheme 1).

For the C65 electrode (i.e., without CAM, pink lines) no CO_2+CO is observed as long as the potential of the electrode is <5.0 V. Only if the potential is increased above this potential of ~5.0 V does the CO_2+CO evolution (pink solid line) increase exponentially, as would be expected based on Tafel kinetics. Dividing the areal charge of 0.0622 mAh/m$^2_{C65}$ (measured between 4.5 and 5.0 V in Figure 1) by the Faraday constant, the total amount of exchanged electrons amounts to

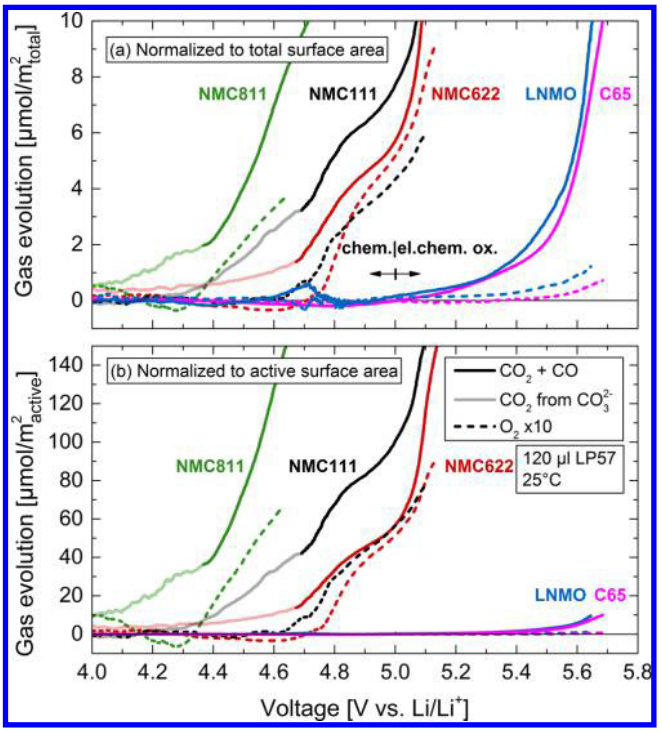

Figure 2. Oxidative stability limit of alkyl carbonate electrolyte LP57 on NMC811, -622, and -111, LNMO, and C65 measured by CO_2+CO (solid lines) and O_2 (dashed lines) evolution as a function of electrode potential. The gas evolution is normalized to (a) the total surface area (sum of CAM and C65 surface area) or (b) the active surface area (NMC surface area for layered oxide electrodes showing oxygen release or the total surface area for LNMO and C65 electrodes showing no oxygen release). Data for NMCs and LNMO are from our previous work[7] but now analyzed for their potential dependence for the purpose of this paper. Note that the O_2 signal is multiplied by a factor of 10 for better visibility. Transparent lines indicate CO_2 generated by electro-oxidation of residual carbonate surface impurities of the layered oxide materials.

2.32 μmol$_e$/m$^2_{C65}$. If we now were to assume that all current is due to electrochemical electrolyte oxidation and if we assume that the electrolyte is oxidized in a one electron mechanism releasing one CO_2 or CO,[18] then a gas evolution corresponding to 2.32 μmol$_{CO_2+CO}$/m$^2_{C65}$ would be expected. This value is well above the detection limit of the OEMS technique, as can be seen from Figure 2a; that is, if the current observed between 4.5 and 5 V in Figure 1 would be mostly due to electrochemical electrolyte oxidation, then we would definitely detect it in the CO_2+CO signal. Therefore, we conclude that at 25 °C and within the time frame of our measurement, we do not observe any significant electrochemical electrolyte oxidation until 5 V.

At potentials >5.5 V, very little O_2 evolution is detected in Figure 2 (note that the O_2 signal is multiplied by a factor of 10 for better visibility), which could be due to either the oxidation of trace water[17] or the corrosion of stainless steel parts[30] in the cell.

In contrast to C65, the onset of gas evolution with NMC111, -622, and -811 clearly shifts toward lower potentials, indicating that electrolyte oxidation on layered oxide surfaces cannot be rationalized by mere electrochemical oxidation. (The individual amounts of CO_2 and CO are shown in ref 7.)

First of all, the onsets of CO_2+CO (transparent lines) at 4.0 to 4.2 V are too low to be explained by electrolyte oxidation if one assumes that there is no catalytic effect of the transition

DOI: 10.1021/acs.jpclett.7b01927
J. Phys. Chem. Lett. 2017, 8, 4820−4825

metals, as it was proposed previously in the literature.[16,31,32] Later on we will show that there is indeed no evidence of transition-metal-catalyzed reactions. Instead, the total amount of ~15−45 $\mu mol_{CO_2+CO}/m^2_{CAM}$ that is evolved until O_2 evolution sets in (see transparent lines in Figure 2b) corresponds well to typical surface contamination of layered oxides with residual carbonates from synthesis on the order of ~0.04 to 0.08%$_{wt}$.[4,18] In this region, only CO_2 and no CO evolution is observed, as shown in our previous reports,[7,18,22] which is typical for the electro-oxidation of carbonates.[33,34]

Second, the CO_2+CO evolution rate (slope of solid lines in Figure 2a,b) changes strongly with the onset of O_2 evolution. At potentials >4.3 V, O_2 evolution is observed for NMC811 (dashed green line). At the same potential, also a steep increase in the CO_2+CO traces occurs. A similar coupling between O_2 and CO_2+CO is observed for NMC111 and 622 (black and red lines, respectively), setting in at ~4.6 V. This correlation suggests that the release of reactive oxygen from the NMC surface causes CO_2 and CO by a chemical reaction with the alkyl carbonate electrolyte.[7] Because the intrinsic stability limit of LP57 electrolyte determined on the C65 electrode is ~500 mV higher, most of the CO_2 and CO evolved from NMC electrodes in typical potential windows of charge/discharge cycling is not due to electrochemical electrolyte oxidation but is rather due to chemical electrolyte oxidation. Here it is important to note that the chemical electrolyte oxidation mechanism is characterized by a clear onset potential, which is defined by the potential at which the SOC of the NMC active material reaches ~80%, whereby, however, the amount of reactive oxygen released from the NMC surface decreases from cycle to cycle.[7] Therefore, the chemical electrolyte oxidation rate diminishes over time. Even though there are several reports showing a surface phase transformation from the layered oxide structure to spinel or rock-salt phases indicating oxygen release (MO_2 (layered) → M_3O_4 (spinel) → MO (rock-salt), corresponding to a decrease in the metal/oxygen ratio from 1:2 → 3:4 → 1:1),[7,35−39] to the best of our knowledge there are no reports in the literature available showing how fast the surface spinel/rock-salt layer is growing during extensive cycling, which could be used as an indication for the chemical electrolyte oxidation rate. In contrast, electrochemical electrolyte oxidation follows Tafel-like kinetics and therefore has no clear onset potential, but the oxidation rate increases exponentially with increasing potential. Low electrochemical electrolyte oxidation rates that may occur below 5 V, especially at temperatures >25 °C, may add up to a significant extent of oxidative charge and oxidation products during long-term cycling and thus may contribute to long-term impedance growth,[40−42] yet, as the CO_2+CO evolution at 25 °C on the C65 electrode surface is basically zero below 5 V, we believe that the chemical pathway is still dominating, all the more because of the roughly 100 times lower surface area of the CAM compared to C65, yielding only low absolute gas amounts from electrochemical electrolyte oxidation within typical potential windows. Recently, Nelson et al. reported for $Li[Ni_{0.42}Mn_{0.42}Co_{0.16}]O_2$/graphite cells cycled at 40 °C a rather low increase in impedance when the NMC was cycled up to at most ~4.55 V (4.45 V cell potential) and observed a huge jump in impedance when the potential was only slightly increased by 25 mV to ~4.575 V (4.475 V cell potential).[41] Because one would expect aging phenomena based on electrochemical electrolyte oxidation to develop more gradually (assuming Tafel-like kinetics), we believe that their observed sudden impedance increase is caused by the onset of chemical electrolyte oxidation (oxygen release from the NMC) rather than by a substantially higher electrochemical electrolyte oxidation rate for an only 25 mV increase in cell voltage. This explanation is in line with our previous study where we demonstrated that rapid capacity fading sets in once the upper cutoff potential is increased above the threshold voltage for oxygen release.[7]

The similarity in gas evolution between NMC111 and -622 as well as the clear difference to NMC811 in Figure 2 excludes any catalytic effect of electrolyte oxidation stemming from the transition metals because all three NMCs differ in composition. The reason why a catalytic effect of transition metals was proposed in the literature is, we believe, that the ppm-level amounts of oxygen for the NMCs that leave as O_2 instead of reacting chemically with electrolyte to CO_2+CO could not be detected in previous studies except for the work by Guéguen et al.[21] In the latter paper, however, still a significant effect of C65 on the electrolyte decomposition at typical NMC operating potentials was claimed.[21]

If there was no catalytic effect of the transition metals on the electrochemical electrolyte oxidation and also no chemical electrolyte oxidation pathway, the gas evolution for all cathode materials normalized to the total surface area (see Figure 2a) should be equal to the one of the C65 electrode. As shown in Figure 2a, this is only true for the LNMO electrode (blue lines), suggesting that the spinel LNMO surface neither catalyzes the electrochemical electrolyte oxidation nor initiates any chemical decomposition processes. The latter is evidenced by the fact that there is no oxygen release from the LNMO electrode at potentials <5.0 V (dashed blue line in Figure 2a). Hence, in a similar way as carbon, LNMO only acts as a conductive surface on which the electrochemical oxidation of electrolyte can take place. Because LNMO does contain nickel and manganese, yet the gas evolution is almost identical to the one on pure carbon electrodes, this further demonstrates that transition metals have no catalytic activity toward electrolyte oxidation. In Figure 2b the gas evolution is normalized to the surface, which primarily causes the electrolyte oxidation, that is, to the NMC surface area in the case of NMC111, -622, and -811 (chemical electrolyte oxidation) and to the total surface area in the case of LNMO and C65 (electrochemical electrolyte oxidation). This normalization clearly demonstrates that in a Li-ion cathode the very low surface area fraction of the NMC causes much more electrolyte decomposition via the chemical pathway than the large surface area fraction of C65 via the electrochemical pathway. This may have caused the erroneous interpretation that the transition metals in NMC might have a catalytic effect on the electrochemical electrolyte oxidation.[16,31,32]

In this work, we showed that CO_2 and CO evolution happens at much lower potentials for NMC electrodes than for LNMO electrodes or for electrodes containing only conductive carbon (Super C65). LNMO and Super C65 have an essentially identical potential dependence of the CO_2+CO evolution, as it is only attributed to electrochemical electrolyte oxidation. The reason for the CO_2+CO evolution at lower potentials for the NMCs was traced back to the release of reactive oxygen from the NMC surface, causing chemical oxidation of the electrolyte. This is fundamentally different and at variance with the widespread understanding that the transition metals catalyze the electrochemical electrolyte oxidation. This work also shows

DOI: 10.1021/acs.jpclett.7b01927
J. Phys. Chem. Lett. 2017, 8, 4820−4825

that the intrinsic oxidative stability of the electrolyte toward electro-oxidation is rather high at room temperature (>5.0 V), but the lattice oxygen release from layered oxide-based cathode active materials causes substantial chemical electrolyte oxidation at lower potentials (<5.0 V).

EXPERIMENTAL METHODS

Electrode Preparation. The NMC and LNMO electrodes contain 91.5%$_{wt}$ cathode active material (CAM) particles ($LiNi_{1/3}Mn_{1/3}Co_{1/3}O_2$ (NMC111), $LiNi_{0.6}Mn_{0.2}Co_{0.2}O_2$ (NMC622), $LiNi_{0.8}Mn_{0.1}Co_{0.1}O_2$ (NMC811), or $LiNi_{0.43}Mn_{1.57}O_4$ (LNMO)), 4.4%$_{wt}$ conductive carbon (Super C65, Timcal, Switzerland), and 4.1%$_{wt}$ polyvinylidene fluoride binder (PVDF, Kynar HSV 900, Arkema, France). Carbon electrodes were prepared with a composition of 50%$_{wt}$ conductive carbon (Super C65, Timcal, Switzerland) and 50%$_{wt}$ PVDF. All solids were dispersed in *N*-methylpyrrolidone (NMP, anhydrous, 99.5%, Sigma-Aldrich) and mixed in a planetary mixer (Thinky, USA) at 2000 rpm for 2 × 5 min. In between the two runs the slurry was ultrasonicated for 10 min in an ultrasonic bath. The resulting ink was spread onto a H2013 polyolefin separator (Celgard, USA) in the case of the NMCs and LNMO and on a stainless-steel mesh (316 grade, 26 μm aperture, 25 μm wire diameter, The Mesh Company, U.K.) in the case of the C65 electrode. The electrodes were dried at 120 °C under dynamic vacuum in a glass oven (drying oven 585, Büchi, Switzerland) and transferred to a glovebox (O_2 and H_2O < 0.1 ppm, MBraun, Germany) without exposure to ambient air.

The specific surface areas of the NMCs, LNMO, and Super C65 were determined by BET (see Table 1) using an Autosorb iQ nitrogen gas sorption analyzer (Quantachrome Instruments, USA).

Online Electrochemical Mass Spectrometry. OEMS experiments were performed using OEMS cells with NMC, LNMO, or C65 electrodes (diameter 15 mm) as working-electrode and metallic lithium (diameter 16 mm, thickness 0.45 mm, battery grade foil, 99.9%, Rockwood Lithium, USA) as counter-electrode.[7] The electrodes were separated by two H2013 polyolefin separators (diameter 28 mm, Celgard, USA) containing 120 μL of LP57 electrolyte (1 M $LiPF_6$ in EC:EMC 3:7 wt/wt, <20 ppm of H_2O, BASF, Germany).

The cells containing CAMs (NMC or LNMO) were charged at a 0.05 C-rate (referenced to the theoretical capacities of NMC111, NMC622, NMC811, and LNMO of 277.8, 276.5, 275.5, and 147 mAh/g, respectively). For the C65 cell a linear potential sweep from OCV (~3.1 V vs Li/Li^+) to 5.7 V vs Li/Li^+ at a scan rate of 0.03 mV/s was applied. This scan rate was chosen to mimic the average slope of the NMC622 potential curve from 4.0 to 5.0 V versus Li/Li^+, thereby achieving a comparable exposure time at high potentials. The loadings of the electrodes are summarized in Table 1.

All cells were assembled in an argon-filled glovebox (O_2 and H_2O < 0.1 ppm, MBraun, Germany). The cells were put into a climate chamber at 25 °C (Binder, Germany) and connected to the potentiostat (Series G300 potentiostat, Gamry or VMP3 potentiostat/galvanostat, Biologic) and the mass spectrometer system, which has been described in detail elsewhere.[14] Prior to starting the above-described protocols, the cells were held at OCV for 4 h. The gas evolution during the OCV and the charging period was recorded by OEMS. All mass signals were normalized to the ion current of the ^{36}Ar isotope to correct for fluctuations of pressure and temperature. Conversion of the ion currents to concentrations was done for O_2, CO_2, and CO using calibration gases (Ar with 2000 ppm each of H_2, O_2, CO, and CO_2; Westfalen, Germany); for details see ref 18.

AUTHOR INFORMATION

Corresponding Authors

*E-mail: roland.jung@tum.de (R.J.).
*E-mail: hubert.gasteiger@tum.de (H.G.).

ORCID

Roland Jung: 0000-0003-1135-7438
Hubert A. Gasteiger: 0000-0001-8199-8703

Author Contributions

[§]R.J. and M.M. contributed equally to this work.

Notes

The authors declare no competing financial interest.

ACKNOWLEDGMENTS

We acknowledge financial support from BMW AG and BASF SE. R.J. acknowledges TUM-IAS for support in the frame of the Rudolf-Diesel Fellowship of Dr. Peter Lamp.

REFERENCES

(1) Groeger, O.; Gasteiger, H. A.; Suchsland, J.-P. Review-Electromobility: Batteries or Fuel Cells? *J. Electrochem. Soc.* **2015**, *162*, A2605−A2622.

(2) Andre, D.; Kim, S.-J.; Lamp, P.; Lux, S. F.; Maglia, F.; Paschos, O.; Stiaszny, B. Future generations of cathode materials: an automotive industry perspective. *J. Mater. Chem. A* **2015**, *3*, 6709−6732.

(3) Gallagher, K. G.; Goebel, S.; Greszler, T.; Mathias, M.; Oelerich, W.; Eroglu, D.; Srinivasan, V. Quantifying the promise of lithium-air batteries for electric vehicles. *Energy Environ. Sci.* **2014**, *7*, 1555−1563.

(4) Noh, H.-J.; Youn, S.; Yoon, C. S.; Sun, Y.-K. Comparison of the structural and electrochemical properties of layered Li[NixCoyMnz]-O2 (x = 1/3, 0.5, 0.6, 0.7, 0.8 and 0.85) cathode material for lithium-ion batteries. *J. Power Sources* **2013**, *233*, 121−130.

(5) Buchberger, I.; Seidlmayer, S.; Pokharel, A.; Piana, M.; Hattendorff, J.; Kudejova, P.; Gilles, R.; Gasteiger, H. A. Aging Analysis of Graphite/LiNi1/3Mn1/3Co1/3O2 Cells Using XRD, PGAA, and AC Impedance. *J. Electrochem. Soc.* **2015**, *162*, A2737−A2746.

(6) Belharouak, I.; Sun, Y. K.; Liu, J.; Amine, K. Li(Ni1/3Co1/3Mn1/3)O2 as a suitable cathode for high power applications. *J. Power Sources* **2003**, *123*, 247−252.

(7) Jung, R.; Metzger, M.; Maglia, F.; Stinner, C.; Gasteiger, H. A. Oxygen Release and Its Effect on the Cycling Stability of LiNixMnyCozO2 (NMC) Cathode Materials for Li-Ion Batteries. *J. Electrochem. Soc.* **2017**, *164*, A1361−A1377.

(8) Li, J.; Downie, L. E.; Ma, L.; Qiu, W.; Dahn, J. R. Study of the Failure Mechanisms of LiNi0.8Mn0.1Co0.1O2 Cathode Material for Lithium Ion Batteries. *J. Electrochem. Soc.* **2015**, *162*, A1401−A1408.

(9) Burns, J. C.; Kassam, A.; Sinha, N. N.; Downie, L. E.; Solnickova, L.; Way, B. M.; Dahn, J. R. Predicting and Extending the Lifetime of Li-Ion Batteries. *J. Electrochem. Soc.* **2013**, *160*, A1451−A1456.

(10) Downie, L. E.; Dahn, J. R. Determination of the Voltage Dependence of Parasitic Heat Flow in Lithium Ion Cells Using Isothermal Microcalorimetry. *J. Electrochem. Soc.* **2014**, *161*, A1782−A1787.

(11) Downie, L. E.; Hyatt, S. R.; Dahn, J. R. The Impact of Electrolyte Composition on Parasitic Reactions in Lithium Ion Cells Charged to 4.7 V Determined Using Isothermal Microcalorimetry. *J. Electrochem. Soc.* **2016**, *163*, A35−A42.

(12) Aiken, C. P.; Xia, J.; Wang, D. Y.; Stevens, D. A.; Trussler, S.; Dahn, J. R. An Apparatus for the Study of In Situ Gas Evolution in Li-Ion Pouch Cells. *J. Electrochem. Soc.* **2014**, *161*, A1548−A1554.

DOI: 10.1021/acs.jpclett.7b01927
J. Phys. Chem. Lett. 2017, 8, 4820−4825

(13) Li, J.; Liu, H.; Xia, J.; Cameron, A. R.; Nie, M.; Botton, G. A.; Dahn, J. R. The Impact of Electrolyte Additives and Upper Cut-off Voltage on the Formation of a Rocksalt Surface Layer in LiNi0.8Mn0.1Co0.1O2 Electrodes. *J. Electrochem. Soc.* **2017**, *164*, A655−A665.
(14) Tsiouvaras, N.; Meini, S.; Buchberger, I.; Gasteiger, H. A. A novel on-line mass spectrometer design for the study of multiple charging cycles of a Li-O2 battery. *J. Electrochem. Soc.* **2013**, *160*, A471−A477.
(15) Vetter, J.; Holzapfel, M.; Wuersig, A.; Scheifele, W.; Ufheil, J.; Novák, P. In situ study on CO2 evolution at lithium-ion battery cathodes. *J. Power Sources* **2006**, *159*, 277−281.
(16) Imhof, R.; Novak, P. Oxidative electrolyte solvent degradation in lithium-ion batteries. An in situ differential electrochemical mass spectrometry investigation. *J. Electrochem. Soc.* **1999**, *146*, 1702−1706.
(17) Metzger, M.; Marino, C.; Sicklinger, J.; Haering, D.; Gasteiger, H. A. Anodic Oxidation of Conductive Carbon and Ethylene Carbonate in High-Voltage Li-Ion Batteries Quantified by On-Line Electrochemical Mass Spectrometry. *J. Electrochem. Soc.* **2015**, *162*, A1123−A1134.
(18) Metzger, M.; Strehle, B.; Solchenbach, S.; Gasteiger, H. A. Origin of H2 Evolution in LIBs: H2O Reduction vs. Electrolyte Oxidation. *J. Electrochem. Soc.* **2016**, *163*, A798−A809.
(19) Aiken, C. P.; Self, J.; Petibon, R.; Xia, X.; Paulsen, J. M.; Dahn, J. R. A Survey of In Situ Gas Evolution during High Voltage Formation in Li-Ion Pouch Cells. *J. Electrochem. Soc.* **2015**, *162*, A760−A767.
(20) Holzapfel, M.; Wuersig, A.; Scheifele, W.; Vetter, J.; Novak, P. Oxygen, hydrogen, ethylene and CO2 evolution in lithium-ion batteries. *J. Power Sources* **2007**, *174*, 1156−1160.
(21) Guéguen, A.; Streich, D.; He, M.; Mendez, M.; Chesneau, F. F.; Novák, P.; Berg, E. J. Decomposition of LiPF6 in High Energy Lithium-Ion Batteries Studied with Online Electrochemical Mass Spectrometry. *J. Electrochem. Soc.* **2016**, *163*, A1095−A1100.
(22) Strehle, B.; Kleiner, K.; Jung, R.; Chesneau, F.; Mendez, M.; Gasteiger, H. A.; Piana, M. The Role of Oxygen Release from Li- and Mn-Rich Layered Oxides during the First Cycles Investigated by On-Line Electrochemical Mass Spectrometry. *J. Electrochem. Soc.* **2017**, *164*, A400−A406.
(23) Lanz, P.; Sommer, H.; Schulz-Dobrick, M.; Novak, P. Oxygen release from high-energy xLi2MnO3·(1 - x)LiMO2 (M = Mn, Ni, Co): Electrochemical, differential electrochemical mass spectrometric, in situ pressure, and in situ temperature characterization. *Electrochim. Acta* **2013**, *93*, 114−119.
(24) Moshkovich, M.; Cojocaru, M.; Gottlieb, H. E.; Aurbach, D. The study of the anodic stability of alkyl carbonate solutions by in situ FTIR spectroscopy, EQCM, NMR and MS. *J. Electroanal. Chem.* **2001**, *497*, 84−96.
(25) Ma, T.; Xu, G.-L.; Li, Y.; Wang, L.; He, X.; Zheng, J.; Liu, J.; Engelhard, M. H.; Zapol, P.; Curtiss, L. A.; Jorne, J.; Amine, K.; Chen, Z. Revisiting the Corrosion of the Aluminum Current Collector in Lithium-Ion Batteries. *J. Phys. Chem. Lett.* **2017**, *8*, 1072−1077.
(26) Seel, J. A.; Dahn, J. R. Electrochemical Intercalation of PF 6 into Graphite. *J. Electrochem. Soc.* **2000**, *147*, 892−898.
(27) Fromm, O.; Meister, P.; Qi, X.; Rothermel, S.; Huesker, J.; Meyer, H. W.; Winter, M.; Placke, T. Study of the Electrochemical Intercalation of Different Anions from Non-Aqueous Electrolytes into a Graphite-Based Cathode. *ECS Trans.* **2014**, *58*, 55−65.
(28) Metzger, M.; Sicklinger, J.; Haering, D.; Kavakli, C.; Stinner, C.; Marino, C.; Gasteiger, H. A. Carbon Coating Stability on High-Voltage Cathode Materials in H2O-Free and H2O-Containing Electrolyte. *J. Electrochem. Soc.* **2015**, *162*, A1227−A1235.
(29) Zhang, X.; Pugh, J. K.; Ross, P. N. Computation of Thermodynamic Oxidation Potentials of Organic Solvents Using Density Functional Theory. *J. Electrochem. Soc.* **2001**, *148*, E183−E188.
(30) Sinha, N. N.; Burns, J. C.; Sanderson, R. J.; Dahn, J. Comparative Studies of Hardware Corrosion at High Potentials in Coin-Type Cells with Non Aqueous Electrolytes. *J. Electrochem. Soc.* **2011**, *158*, A1400−A1403.
(31) La Mantia, F.; Rosciano, F.; Tran, N.; Novak, P. Direct evidence of oxygen evolution from Li1+x(Ni1/3Mn1/3Co1/3)1-xO2 at high potentials. *J. Appl. Electrochem.* **2008**, *38*, 893−896.
(32) Jiang, M.; Key, B.; Meng, Y. S.; Grey, C. P. Electrochemical and Structural Study of the Layered, "Li-Excess" Lithium-Ion Battery Electrode Material Li[Li1/9Ni1/3Mn5/9]O2. *Chem. Mater.* **2009**, *21*, 2733−2745.
(33) Freunberger, S. A.; Chen, Y.; Peng, Z.; Griffin, J. M.; Hardwick, L. J.; Bardé, F.; Novák, P.; Bruce, P. G. Reactions in the Rechargeable Lithium−O2 Battery with Alkyl Carbonate Electrolytes. *J. Am. Chem. Soc.* **2011**, *133*, 8040−8047.
(34) Meini, S.; Tsiouvaras, N.; Schwenke, K. U.; Piana, M.; Beyer, H.; Lange, L.; Gasteiger, H. A. Rechargeability of Li-air cathodes pre-filled with discharge products using an ether-based electrolyte solution: implications for cycle-life of Li-air cells. *Phys. Chem. Chem. Phys.* **2013**, *15*, 11478−11493.
(35) Muto, S.; Sasano, Y.; Tatsumi, K.; Sasaki, T.; Horibuchi, K.; Takeuchi, Y.; Ukyo, Y. Capacity-Fading Mechanisms of LiNiO2-Based Lithium-Ion Batteries: II. Diagnostic Analysis by Electron Microscopy and Spectroscopy. *J. Electrochem. Soc.* **2009**, *156*, A371−A377.
(36) Abraham, D. P.; Twesten, R. D.; Balasubramanian, M.; Petrov, I.; McBreen, J.; Amine, K. Surface changes on LiNi0.8Co0.2O2 particles during testing of high-power lithium-ion cells. *Electrochem. Commun.* **2002**, *4*, 620−625.
(37) Abraham, D. P.; Twesten, R. D.; Balasubramanian, M.; Kropf, J.; Fischer, D.; McBreen, J.; Petrov, I.; Amine, K. Microscopy and Spectroscopy of Lithium Nickel Oxide-Based Particles Used in High Power Lithium-Ion Cells. *J. Electrochem. Soc.* **2003**, *150*, A1450−A1456.
(38) Jung, S.-K.; Gwon, H.; Hong, J.; Park, K.-Y.; Seo, D.-H.; Kim, H.; Hyun, J.; Yang, W.; Kang, K. Understanding the Degradation Mechanisms of LiNi0.5Co0.2Mn0.3O2 Cathode Material in Lithium Ion Batteries. *Adv. Energy Mater.* **2014**, *4*, 1300787.
(39) Hwang, S.; Chang, W.; Kim, S. M.; Su, D.; Kim, D. H.; Lee, J. Y.; Chung, K. Y.; Stach, E. A. Investigation of Changes in the Surface Structure of LixNi0.8Co0.15Al0.05O2 Cathode Materials Induced by the Initial Charge. *Chem. Mater.* **2014**, *26*, 1084−1092.
(40) Nelson, K. J.; d'Eon, G. L.; Wright, A. T. B.; Ma, L.; Xia, J.; Dahn, J. R. Studies of the Effect of High Voltage on the Impedance and Cycling Performance of Li[Ni0.4Mn0.4Co0.2]O2/Graphite Lithium-Ion Pouch Cells. *J. Electrochem. Soc.* **2015**, *162*, A1046−A1054.
(41) Nelson, K. J.; Abarbanel, D. W.; Xia, J.; Lu, Z.; Dahn, J. R. Effects of Upper Cutoff Potential on LaPO4-Coated and Uncoated Li[Ni0.42Mn0.42Co0.16]O2/Graphite Pouch Cells. *J. Electrochem. Soc.* **2016**, *163*, A272−A280.
(42) Abarbanel, D. W.; Nelson, K. J.; Dahn, J. R. Exploring Impedance Growth in High Voltage NMC/Graphite Li-Ion Cells Using a Transmission Line Model. *J. Electrochem. Soc.* **2016**, *163*, A522−A529.

DOI: 10.1021/acs.jpclett.7b01927
J. Phys. Chem. Lett. 2017, 8, 4820−4825

3.1.4 Temperature Dependence of Oxygen Release from $LiNi_{0.6}Mn_{0.2}Co_{0.2}O_2$ (NMC622) Cathode Materials for Li-Ion Batteries

In this section the article "Temperature Dependence of Oxygen Release from High Energy $LiNi_{0.6}Mn_{0.2}Co_{0.2}O_2$ (NMC622) Cathode Material for Li-Ion Batteries" will be presented. It was published in the *Journal of the Electrochemical Society* on September 7, 2018 as open access article distributed under the terms of the Creative Commons Attribution Non-Commercial No Derivatives 4.0 License.[165] The permanent web-link to the publication is http://jes.ecsdl.org/content/165/11/A2869 and the DOI is 10.1149/2.1261811jes.

In the article we investigate the oxygen release from NMC622 at 25, 40, and 50 °C and compare the changes in the onset potential as well as amounts of evolved gases. The onset of oxygen release at 25 °C occurs upon removal of ~81% of the lithium (81% SOC) from the NMC structure, corresponding to a full-cell potential of ~4.42 V (~4.52 V vs. Li/Li^+), which is around 0.1 V lower than the onset potential observed for NMC622 in the studies presented in the sections 3.1.2 and 3.1.3. In this present study a pristine NMC622 material from a different supplier without any surface treatments was used. Interestingly, a comparison of the SOC at the onset of oxygen release of the NMC622 used in this work with the surface treated NMC622 discussed in section 3.1.2[101] shows that they are constant at ~80%. This reveals that the SOC is the intrinsic parameter governing oxygen release, which can be rationalized by the fact that the layered structure is thermodynamically instable at high SOCs and its decomposition to spinel and/or rock-salt type surface phases is a chemical decomposition which does not depend on cathode potential but on the lithium content in the layered structure. In fact, the comparison of the SOCs measured in similar experiments using NMC111 and NMC811,[101] shows that also for other NMC compositions the onset of oxygen release occurs at ~80% SOC. Additionally, with increasing temperature, the onset for oxygen release of the NMC622 material used in this work again stays constant at ~81% SOC. Simultaneously, the onset potentials shift slightly to 4.38 V at 40 °C and to 4.36 V at 50 °C. These rather small shifts are caused by lower overpotentials due to faster kinetics when the temperature is increased. The onset at ~80% SOC matches very well the reports from the group of Manthiram, in which layered compounds were chemically delithiated and oxygen loss from the surface was observed at ~75% SOC for NMC111[159], at ~70% for $LiNi_{0.5}Co_{0.5}O_2$ [60], and at ~90% for $LiNi_{0.85}Co_{0.15}O_2$ [58]. Additionally, in a recent study by Streich et al.,[206] the onset of oxygen release was also found at ~80% SOC for NMC532,

NMC622, and NMC811. Only for NMC111, for unknown reasons, they observed oxygen release already at ~70% SOC.[206]

Besides the temperature dependent gas evolution, we also show the cycling stability of NMC622-graphite cells at 25, 40, and 50 °C and at upper cut-off voltages of 4.2 to 4.6 V in steps of 0.1 V. In analogy to the work presented in section 3.1.2, LP57 is used as electrolyte and a very similar cycling procedure is applied. For all temperatures, at upper cut-off voltages of 4.2 and 4.3 V, stable cycling is observed. At 4.4 V, a more significant capacity fading sets in, which turns into a very rapid capacity decay at 4.5 and 4.6 V upper cut-off potentials. The stable cycling up to 4.3 V and the onset of accelerated capacity fading at ≥4.4 V matches very well the measured onset potentials for oxygen release. Therefore, in agreement with the conclusions presented in section 3.1.2, also in this study we demonstrate once more that the onset of oxygen release limits the applicable upper cut-off voltage to allow for a stable cycling performance.

In this study, we furthermore investigate the observed CO_2 evolution prior to the onset of oxygen release. It is shown that there are two additional CO_2 sources both of which are only observed within the first charge cycle. In experiments using ^{13}C-labelled ethylene carbonate (^{13}C-EC) based electrolyte, and examining the temperature dependence of the amount of evolved CO_2 prior to O_2 release, we demonstrate that these sources are i) OH^- driven hydrolysis of EC forming CO_2, whereby OH^- is produced by the reduction of trace H_2O at the graphite anode to H_2 and OH^-, and ii) electrochemical oxidation of electrolyte impurities like ethylene glycol starting around 4 V vs. Li/Li^+. Additionally, in the experiment with ^{13}C-EC we show that the decomposition of (lithium) carbonate surface contaminants on NMC proceeds via a reaction with HF, which is formed as a consequence of lattice oxygen release from NMC and subsequent *chemical* electrolyte oxidation. This is in contrast to our previous understanding that the decomposition of the carbonate contaminants proceeds via an electrochemical oxidation reaction.[101, 147, 175]

Author Contributions

Roland Jung designed the experiments. Roland Jung and Philipp Strobl prepared the electrode coatings. Roland Jung performed the OEMS experiments. Philipp Strobl built the NMC-graphite cells. Roland Jung evaluated the data. Roland Jung and Hubert Gasteiger wrote the manuscript. All authors discussed the results and commented on the manuscript.

Temperature Dependence of Oxygen Release from $LiNi_{0.6}Mn_{0.2}Co_{0.2}O_2$ (NMC622) Cathode Materials for Li-Ion Batteries

Roland Jung,[1,2,z] Philipp Strobl,[1] Filippo Maglia,[2] Christoph Stinner,[2] and Hubert A. Gasteiger[1,*]

[1] *Chair of Technical Electrochemistry, Department of Chemistry and Catalysis Research Center, Technische Universität München, Garching, Germany*
[2] *BMW Group, Munich, Germany*

Promising cathode materials for Li-ion batteries are layered transition metal oxides ($LiNi_xMn_yCo_zO_2$, NMC). Here, we will investigate the temperature dependence of oxygen release from NMC622, caused by the transformation of the near-surface structure from the layered to spinel and/or rock-salt structure. We will demonstrate that oxygen release is not a potential driven process but occurs once ∼81% of the lithium ions are removed from the NMC structure. Consequently, the onset potential for oxygen release in NMC-graphite cells decreases only by ∼60 mV from 4.42 V at 25°C to 4.36 V at 50°C, which is simply due to lower overpotentials at higher temperature. The amount of evolved oxygen increases significantly with increasing temperature, indicating the formation of thicker spinel/rock-salt surface layers. As the released oxygen causes chemical oxidation of the electrolyte, the amounts of CO_2 and CO occurring simultaneously with O_2 release also increase with temperature. Further experiments in NMC-Li cells as well as with ^{13}C-labelled ethylene carbonate (EC) electrolyte show that CO_2 evolved prior to O_2 release results from i) EC hydrolysis and ii) electrolyte impurity oxidation. In agreement with the onset potentials for oxygen release, we will show that stable cycling of NMC622-graphite full-cells is possible at the different temperatures up to ∼81% state-of-charge.
 [DOI: 10.1149/2.1261811jes]

Manuscript submitted June 20, 2018; revised manuscript received August 10, 2018. Published September 7, 2018.

Li-Ion batteries are used in essentially all portable electronic devices like laptops and cell phones and more recently with the powertrains of battery electric vehicles (BEVs). Yet, BEVs are still a niche in the worldwide automotive market and an increase in their market share requires significantly reduced costs and longer driving ranges.[1] The latter necessitates materials with higher specific energies, with target values of ∼750 mWh/g on a positive electrode (cathode) material level.[2,3] The bottleneck in today's Li-ion batteries is the cathode active material, with layered lithium nickel manganese cobalt oxide ($LiNi_xMn_yCo_zO_2$, with x+y+z = 1; also referred to as NMC) and in particular nickel-rich (Ni-rich) NMCs being the most promising candidates.[2,4] Even though the theoretical capacity of any NMC is as high as ∼275 mAh/g_{NMC}, not all of the lithium can be extracted due to structural instabilities, e.g., phase transformations, occurring when an exceedingly large fraction of lithium is removed.[5–7] A larger fraction of the Li-ions can be reversibly de-/intercalated within a constant voltage window as the nickel content of the NMC is increased.[2] NMC622 with a Ni-content of 60% (x = 0.6, y = z = 0.2) is a promising cathode material, as it delivers ∼12–16% higher capacities than state-of-the-art NMC111 (x = y = z = 1/3)[7,8] and at the same time possesses better safety characteristics than the NMCs with higher nickel content (i.e. x > 0.6).[8,9]

In a recent study, we showed that oxygen release occurs at room temperature for NMC111, NMC622, and NMC811 (x = 0.8, y = z = 0.1) by a phase transformation at the surface of the layered NMC to spinel and rock-salt type phases.[7] By quantifying the evolved gas amounts we estimated the surface layer thickness to 7–15 nm.[7] The release of reactive oxygen leads to electrolyte decomposition by a chemical reaction of the released oxygen with the electrolyte,[7,10] which at least in part was shown to be released as highly reactive singlet oxygen.[11] This chemical electrolyte oxidation occurs once the onset potential for oxygen release is reached, which differs for different NMC compositions[7,11] and generally occurs before significant electrochemical electrolyte oxidation occurs.[10] Additionally, the phase transformation on the NMC particle surface leads to an impedance increase and therefore poor cycling stability. In other words, to achieve a stable cycling performance, the upper cutoff voltage has to stay below the onset potential for oxygen release. Such surface phase transformations were previously observed for NMC532,[6] $LiNi_{0.8}Co_{0.2}O_2$,[12,13] $LiNiO_2$,[14] and NCA ($LiNi_{0.80}Co_{0.15}Al_{0.05}O_2$),[15] albeit without the direct detection of released oxygen. At temperatures ≥170°C, this phase transformation was shown to occur throughout the bulk of the material, accompanied by the release of lattice oxygen.[8,9,16–21] While these temperatures are well above the operating temperature of Li-ion batteries, they are important to evaluate the safety of a material in case of a thermal runaway.

In this study, we will investigate the extent of oxygen release of NMC622 within the temperature range relevant for the regular usage of a Li-ion battery, making use of on-line electrochemical mass spectrometry (OEMS). In contrast to our previous study in which we analyzed the oxygen release for different NMC compositions at a constant temperature of 25°C,[7] here we will focus on NMC622 and temperatures of 25, 40, and 50°C. In addition, we will further examine the origin of the observed CO_2 evolution from NMCs during the first charge, occurring at potentials below the onset of O_2 release. Previously, we had ascribed this to the electrochemical oxidation of Li_2CO_3 surface contaminants.[7] Alternative views in the literature are either (i) that all CO_2 released during the first charge of NMCs is entirely due to Li_2CO_3 oxidation (i.e., that it does not derive from electrolyte oxidation)[22] or (ii) that all of the CO_2 released during the first charge derives from electrolyte oxidation.[23] Making use of ^{13}C-labelled ethylene carbonate based electrolyte, and examining the temperature dependence of the amount of evolved CO_2 prior to O_2 release, we will show that none of these three hypotheses are correct; instead we will show that other effects are responsible for the evolution of CO_2 at low potentials in the first cycle and that Li_2CO_3 will decompose chemically rather than electrochemically at higher potentials.

Experimental

Electrode preparation.—Throughout this study, $LiNi_{0.6}Mn_{0.2}Co_{0.2}O_2$ (NMC622, Ecopro, South Korea) is used as active material. The material is pristine without any surface treatment; its specific surface area of 0.31 m^2/g was determined

*Electrochemical Society Fellow.
[z]E-mail: roland.jung@tum.de

by BET using an Autosorb iQ nitrogen gas sorption analyzer (Quantachrome Instruments, USA). Electrodes were prepared by dispersing 91.5%$_{wt}$ NMC622, 4.4%$_{wt}$ conductive carbon (Super C65, Timcal, Switzerland) and 4.1%$_{wt}$ polyvinylidene fluoride binder (PVDF, Kynar HSV 900, Arkema, France) in N-methylpyrrolidone (NMP, anhydrous, 99.5%, Sigma-Aldrich). The slurry was mixed in a planetary mixer (Thinky, USA) at 2000 rpm for 2 × 5 minutes. In between the two mixing steps, the slurry was ultrasonicated for 10 minutes in an ultrasonic bath. The resulting ink was spread onto an aluminum foil (thickness 18 μm, MTI Corporation, USA) using a gap bar coater (RK PrintCoat Instruments, UK). For OEMS measurements, the ink was coated onto a stainless steel mesh (316 grade, 26 μm aperture, 25 μm wire diameter, The Mesh Company, UK) to allow for a short diffusion time of the evolved gases to the head-space of the OEMS cell where the capillary leading to the mass spectrometer is attached.[24,25] After drying at 50°C in air for about 1–2 hours, electrodes were punched and dried overnight at 120°C under dynamic vacuum in a glass oven (drying oven 585, Büchi, Switzerland) and transferred to a glove box (O_2 and H_2O < 0.1 ppm, MBraun, Germany) without exposure to ambient air.

The graphite electrodes were prepared by mixing 95.8%$_{wt}$ graphite (MAG-D20, Hitachi; BET area of 4.1 m^2/g), 1.0%$_{wt}$ Super C65 (Timcal, Switzerland; BET area of 65 m^2/g), 1.0%$_{wt}$ sodium carboxymethylcellulose (Na-CMC, Dow Wolff Cellulosics), and 2.2%$_{wt}$ styrene-butadiene rubber (SBR, JSR Micro). The slurry was prepared by dispersing graphite, Super C65 and Na-CMC in highly pure water (18 MΩcm, Merck Millipore, Germany) using a planetary mixer (Thinky, USA; at 2000 rpm for 30 minutes). Subsequently, the slurry was ultrasonicated for 10 minutes in an ultrasonic bath. Finally, SBR was added to the slurry and mixed at 500 rpm for 2 minutes. The ink was coated onto copper foil (thickness 12 μm, MTI Corporation, USA) using a gap bar coater (RK PrintCoat Instruments, UK). The coating was dried at 50°C in air, punched out, dried overnight at 120°C under vacuum in the above mentioned Büchi oven and transferred to a glove box without exposure to ambient air.

Electrochemical characterization.—The electrochemical characterization of NMC was performed in Swagelok T-cells which were assembled in an argon filled glove box (O_2 and H_2O < 0.1 ppm, MBraun, Germany), with NMC as working electrode (10.95 mm diameter) and graphite as counter electrode (10.95 mm diameter). The areal mass loading of the NMC electrodes was 13.3 ± 0.7 mg/cm^2 while the loading of the graphite electrodes was adjusted so as to achieve a constant balancing factor according to the mass loading of the NMC electrodes and its specific capacity at the various cutoff voltages. The areal capacity of the anode (in mAh/cm^2) was oversized 1.2-fold compared to the cathode (referenced to the reversible capacities of NMC and graphite at a 1 C-rate; if referenced to 0.1 C, the graphite anode is roughly 1.1-fold oversized). To monitor the potential of both the NMC cathode and the graphite anode, a lithium reference electrode (thickness 0.45 mm, battery grade foil, 99.9%, Rockwood Lithium, USA) was used. Two glass fiber separators (glass microfiber filter, 691, VWR, Germany) punched to a diameter of 11 mm were used between working and counter electrode, and one at the reference electrode (diameter of 10 mm). 80 μL of LP57 electrolyte (1 M $LiPF_6$ in EC:EMC 3:7 wt/wt, < 20 ppm H_2O, BASF, Germany) were used between working and counter electrode and 40 μL were added to the reference electrode side.

The cells were cycled in a climate chamber (Binder, Germany) at 25, 40, or 50°C with a battery cycler (Series 4000, Maccor, USA). All cells were cycled 300 times at 1 C at the respective temperature, with two initial formation cycles at 0.1 C and two diagnostic cycles at 0.1 C every 50 cycles. Charging was done in constant-current, constant-voltage (CCCV) mode with a current limitation corresponding to 0.05 C, while the discharge was done in constant-current (CC) mode. The lower cutoff voltage was kept constant at 3 V. The upper cutoff voltage was 4.3, 4.4, 4.5, or 4.6 V and additionally 4.2 V at 25 and 50°C.

The C-rate was referenced to the approximate reversible capacity of the NMC622 at 1 C: i) 155, 165, 175, 185 and 195 mAh/g at 25°C and upper cutoff voltages of 4.2, 4.3, 4.4, 4.5, and 4.6 V, respectively; ii) 175, 185, 195, and 205 mAh/g at 40°C and upper cutoff voltages of 4.3, 4.4, 4.5, and 4.6 V, respectively; and, iii) 170, 180, 190, 200, and 210 mAh/g at 50°C and upper cutoff voltages of 4.2, 4.3, 4.4, 4.5, and 4.6 V, respectively. Two cells were built for each combination of temperature and cutoff voltage and the error bars in the figure represent the standard deviation from two cells for each combination.

On-Line electrochemical mass spectrometry (OEMS).—OEMS experiments were performed with an NMC622 cathode (diameter 15 mm) and either a lithium (diameter 16 mm) or graphite anode (diameter 16 mm,), two glass fiber separators (diameter 28 mm, glass microfiber filter, 691, VWR, Germany), and 400 μL of 1.5 M $LiPF_6$ in ethylene carbonate (EC, BASF, Germany) or ^{13}C-isotope labelled ethylene carbonate (^{13}C-EC, isotopic purity 97 atom%, Sigma Aldrich). The mixture of EC with $LiPF_6$ is a liquid at room temperature due to the melting point depression caused by the addition of $LiPF_6$. The removal of the high vapor pressure component of the electrolyte (i.e. linear alkyl carbonate) greatly increases the signal to noise ratio of the mass spectrometer by lowering the background signal of the electrolyte measured.[26] In analogy to our previous study,[7] the cells were cycled one or four times at a C/5-rate (referenced to the theoretical capacity of 276.5 mAh/g$_{NMC}$ of NMC622) and with a one hour CV hold at the upper cutoff voltage. With a graphite or lithium anode, the voltage ranges were 2.6–4.8 V and 2.8–4.9 V, respectively. The rather high upper cutoff potential allows one to almost completely delithiate the NMC622 (~96% at 25°C) and therefore the data presented below give insights into the gas evolution arising over essentially the entire state of charge (SOC) of the NMC material. The loadings of the cathode active material were 9.3–10.0 mg$_{NMC}$/cm^2. The capacity of the graphite counter electrode was oversized 1.4-fold (referenced to the theoretical capacities of NMC and graphite).

The as received ^{13}C-EC contained ethylene glycol (EG) as a major impurity amounting to ~9–10% as was detected and quantified using ^{1}H- and ^{13}C-NMR spectroscopy. Most likely EG was formed by hydrolysis of EC with H_2O impurities, because the detected EG was also ^{13}C-labelled. To remove this and potentially other impurities the EC was thoroughly distilled and its purity was determined by ^{1}H- and ^{13}C-NMR spectra, in which no peaks corresponding to any impurities were detected after distillation.

All cells were assembled in a glove box with argon atmosphere (O_2 and H_2O < 0.1 ppm, MBraun, Germany). The cells were placed in a climate chamber at 25, 40, or 50°C (Binder, Germany) and connected to the potentiostat (Series G300 potentiostat, Gamry, USA) and the mass spectrometer system, which has been described in detail elsewhere.[25] The cells were held at OCV for 4 h before starting the above described protocols. The gas evolution during the OCV and the charging/cycling period was recorded by OEMS. All mass signals were normalized to the ion current of the ^{36}Ar isotope to correct for fluctuations of pressure and temperature. Conversion of the ion currents to concentrations was done for O_2, CO_2, H_2, C_2H_4, and CO using calibration gases (Ar with 2000 ppm each of H_2, O_2, C_2H_4, and CO_2 as well as Ar with 2000 ppm each of H_2, O_2, CO, and CO_2; Westfalen, Germany) and the internal OEMS cell volume of 9.5 cm^3.

Results

Gas analysis of NMC622-graphite full-cells at 25, 40, and 50°C by OEMS.—In the following we will present the results of the OEMS analysis of NMC622-graphite cells cycled at 25, 40, and 50°C. Figure 1 depicts the first four charge/discharge cycles of a NMC622-graphite cell at 25°C and the total moles of the evolved/consumed gases ethylene (C_2H_4), hydrogen (H_2), carbon monoxide (CO), carbon dioxide (CO_2), and oxygen (O_2), all normalized by the BET surface areas of NMC622 (left y-axis) and by the sum of anode graphite and conductive carbon (right y-axis) in units of μmol/m$^2_{NMC}$ and μmol/m^2_C, respectively. Right at the beginning of the first charge, a steep increase

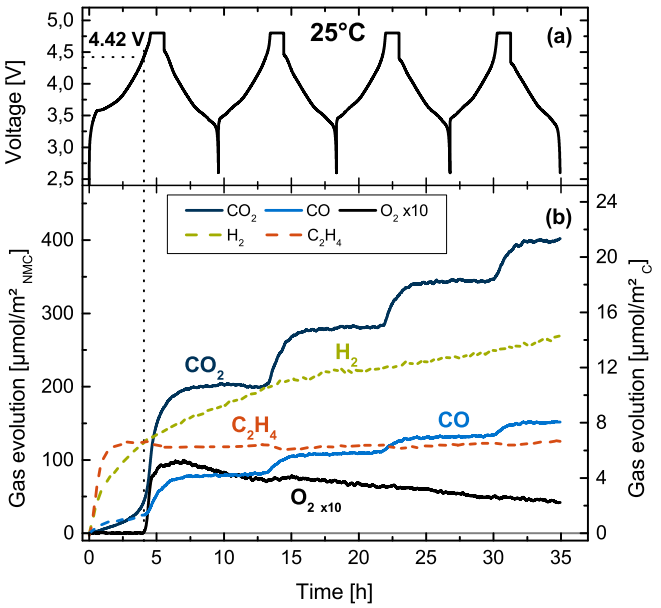

Figure 1. (a) Cell voltage vs. time of a NMC622-graphite cell over four charge/discharge cycles at C/5 rate and 25°C between 2.6 and 4.8 V, in a cell containing 400 µL of 1.5 M $LiPF_6$ in ethylene carbonate (EC), two glassfiber separators, and 17.28 mg NMC622. (b) Evolution of CO_2 (dark blue), H_2 (green), C_2H_4 (orange), CO (blue), and O_2 (black, 10-fold magnified) as a function of time. Solid lines indicate the gases stemming from the NMC electrode and dashed lines those from the graphite electrode; gas concentrations are referenced to the NMC BET area (left y-axis) and to the sum of the graphite and conductive carbon BET areas (right x-axis). The OEMS data are smoothed, baseline corrected, and converted into units of [µmol/m^2_{NMC}] and [µmol/m^2_C].

of the C_2H_4 trace is observed, stemming from the reduction of EC on the graphite anode during the SEI formation.[27–30] Once the SEI is completely formed, the C_2H_4 signal remains rather constant, indicating that the formed SEI prevents further solvent reduction. Simultaneous with the evolution of C_2H_4, the evolution of CO is observed which originates from an alternative EC reduction pathway.[27,31] The maximum amounts of ~7 µmol/m^2_C of C_2H_4 and ~1.4 µmol/m^2_C of CO (both measured after 2–3 hours) due to SEI formation on graphite are in good agreement with the measured amounts in earlier reports.[7,27] Starting after ~4 hours, the CO signal shows a stepwise increase, which will be discussed below.

Together with the gas evolution due to SEI formation, H_2 evolves, which is due to the reduction of trace water or trace HF in the electrolyte.[27,32,33] After an initially fast evolution of the H_2 signal (~8 µmol/m^2_C after four hours), the evolution rate decreases (i.e., the slope of the line in Figure 1 decreases) and gradually approaches a concentration of ~14 µmol/m^2_C at the end of the fourth cycle. We believe that the reason why the H_2 evolution continues after the first charge (contrary to the behavior of C_2H_4) are the following: i) due to the SEI formation, the rate of trace H_2O/HF reduction becomes slower and in principle depends on the 'quality' of the SEI,[32] and ii) due to oxidative electrolyte decomposition, H_2O and/or protic species are formed,[7,27,34,35] which may diffuse to and become reduced at the graphite anode to molecular hydrogen.

The CO_2 signal of the first cycle can be grouped into three distinct regions: i) within the first three hours of the measurement (up to ~4.0 V cell potential), a linear increase of the CO_2 signal is observed. In our previous studies, we had ascribed this to the oxidation of surface carbonate species,[7,27] but as we will show later, this assumption had been erroneous. ii) From 4.0–4.4 V a second process is observed with an increased CO_2 evolution rate. The origin of this process will be discussed later together with the findings of the other experiments. Finally, iii) very steep increase of the CO_2 signal caused by oxygen release from NMC and subsequent chemical electrolyte oxidation at cell potentials >4.4 V.[7,10] The latter is caused by the release of reactive oxygen from the NMC surface and is therefore observed in parallel with O_2 evolution after ~4 hours into the charging process. At this point the cell potential reaches 4.42 V and O_2 starts to evolve, amounting to ~10 µmol/m^2_{NMC} in the first charge; its subsequent slow but gradual decrease is likely due to its slow reduction at the graphite anode. Simultaneously to O_2, not only the sharp increase of the CO_2 signal but also of the CO signal are observed, which are due to a chemical reaction between the released oxygen with the electrolyte to form CO and CO_2,[7,10] most likely due to the fact that at least part of the oxygen is released as highly reactive singlet oxygen.[11] Once the cell is switched from the CV-phase at 4.8 V into discharge, the CO and CO_2 concentrations stay constant until the cell voltage again increases above ~4.42 V in the following charge cycles, leading to step-like increases of CO and CO_2. Note that the first two processes prior to oxygen release leading to CO_2 evolution are absent in the 2nd to 4th cycles, so that the CO_2 evolution in those cycles is caused mostly by chemical electrolyte oxidation as a consequence of oxygen release. We will discuss this observation in further detail later on and first present the other results.

In the second charge cycle, only a rather small amount of O_2 evolution is detected (~1.5 µmol/m^2_{NMC}), which we believe is due to the fact that the oxygen is released in a highly reactive form and can be observed as O_2 in the gas phase only if larger amounts of oxygen are released within a short period of time, as it otherwise quantitatively reacts with electrolyte to CO_2 and CO, indicated by their step-like increase every time a potential of ~4.42 V is reached.[7] As described previously, the growing oxygen-depleted surface layer requires oxygen to be released from deeper regions of the particle, slowing down the diffusion-limited rate of oxygen release.[7] This is also manifested by the observation that the total amounts of CO_2 and CO released at potentials ≥4.42 V are largest in the first cycle, i.e., ~130 µmol/m^2_{NMC} and ~50 µmol/m^2_{NMC} of CO_2 and CO, respectively, versus ~75 µmol/m^2_{NMC} and ~25 µmol/m^2_{NMC} in the second cycle. The evolved amount of CO_2 due to chemical electrolyte oxidation (i.e., released at potentials ≥4.42 V) in the first cycle was determined as the CO_2 signal at the end of the CV-step minus the one measured right at the onset of oxygen release. The amounts of CO_2 in the subsequent cycles were determined by measuring the step height between the different cycles.

As we used exactly the same experimental setup in our previous report with an NMC622 from another vendor, we can compare it to the gas evolution in Figure 1.[7] It can be seen that the onset potential for oxygen release of the NMC622 material in this work is ~120 mV lower than that observed for the different NMC622 material in our previous study. Yet, the state of charge (throughout this work, 100% SOC is defined as the removal of all lithium from the NMC) at which O_2 release is observed is identical (~81%),[7] which suggests that it is the SOC which is governing the onset of oxygen release rather than potential. This may be rationalized by considering that the layered oxide structure is only kinetically stable at high SOCs and that a transformation to spinel- or rock-salt phases would be thermodynamically favored but is kinetically limited at moderate temperatures by the slow solid state diffusion of the multivalent ions within the NMC lattice. Therefore, we believe that the different onset potentials are due to impedance effects, caused by a different surface structure and thus a different interfacial resistance between the NMCs from the different vendors. Incidentially, in a recent study by Streich et al.,[36] the onset of oxygen release for different NMCs was correlated with the estimated state of charge of the nickel in the NMCs, as in their case for unknown reasons, oxygen release from NMC111 already occurred at ~70% SOC, while all other compositions (NMC532, NMC622, and NMC811) showed O_2 release at ~80% SOC, consistent with the data in this and in our previous studies.[7,11]

Before moving to the experiments conducted at elevated temperatures, we would like to point out that even at these high potentials of 4.8 V at 25°C, gas evolution from electrochemical electrolyte oxidation was demonstrated to still be negligible compared to the gas amounts stemming from chemical electrolyte oxidation as a

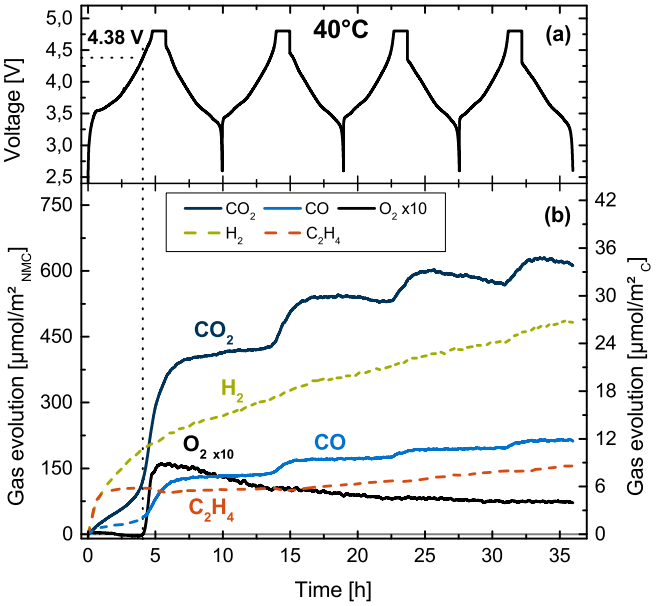

Figure 2. (a) Cell voltage vs. time of a NMC622-graphite cell over four charge/discharge cycles at C/5 rate and 40°C between 2.6 and 4.8 V, in a cell containing 400 µL of 1.5 M $LiPF_6$ in ethylene carbonate (EC), two glassfiber separators and 17.19 mg NMC622. (b) Evolution of CO_2 (dark blue), H_2 (green), C_2H_4 (orange), CO (blue), and O_2 (black, 10-fold magnified) as a function of time. Solid lines indicate the gases stemming from the NMC electrode and dashed lines those from the graphite electrode; gas concentrations are referenced to the NMC BET area (left y-axis) and to the sum of the graphite and conductive carbon BET areas (right x-axis). The OEMS data are smoothed, baseline corrected, and converted into units of [µmol/m^2_{NMC}] and [µmol/m^2_C].

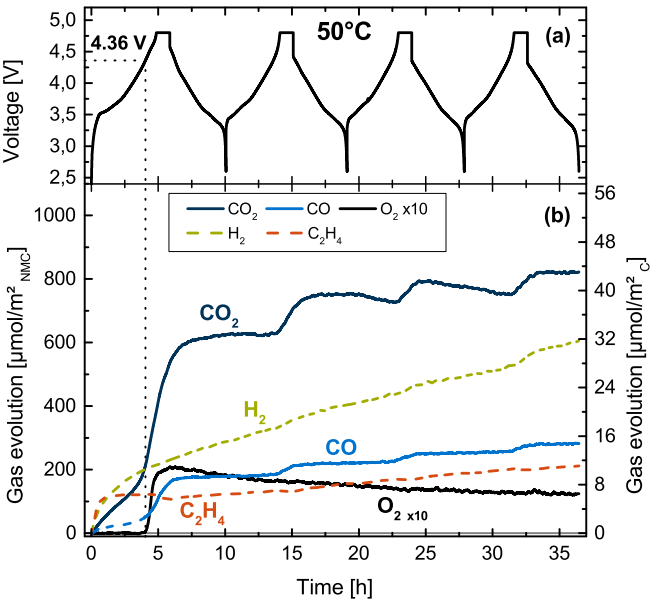

Figure 3. (a) Cell voltage vs. time of a NMC622-graphite cell over four charge/discharge cycles at C/5 rate and 50°C between 2.6 and 4.8 V, in a cell containing 400 µL of 1.5 M $LiPF_6$ in ethylene carbonate (EC), two glassfiber separators and 17.60 mg NMC622. (b) Evolution of CO_2 (dark blue), H_2 (green), C_2H_4 (orange), CO (blue), and O_2 (black, 10-fold magnified) as a function of time. Solid lines indicate the gases stemming from the NMC electrode and dashed lines those from the graphite electrode; gas concentrations are referenced to the NMC BET area (left y-axis) and to the sum of the graphite and conductive carbon BET areas (right x-axis). The OEMS data are smoothed, baseline corrected, and converted into units of [µmol/m^2_{NMC}] and [µmol/m^2_C].

consequence of the release of reactive oxygen.[10] As will be shown below, the qualitative trends of the evolved gases do not change significantly at elevated temperatures, indicating that also at the higher temperatures of 40 and 50°C, the majority of the evolved CO and CO_2 at high potentials stem from chemical electrolyte oxidation.

Figure 2 shows the results of an OEMS-experiment with an NMC622-graphite cell, now at a temperature of 40°C. Note, that the scale of the y-axis is different between Figure 1b and Figure 2b to account for the larger amounts of gas evolved at the higher temperature. In analogy to Figure 1, very similar amounts of C_2H_4 (~6.5 µmol/m^2_C) and CO (~2 µmol/m^2_C) evolve in the first cycle due to SEI formation. It is interesting to note that the C_2H_4 signal is not as stable after the first cycle as was the case for the measurement at 25°C (Figure 1), now increasing to ~9 µmol/m^2_C after four cycles. This observation indicates that, as expected, the EC-derived SEI becomes less stable at elevated temperatures. The evolution of H_2 is qualitatively also very similar to the experiment at 25°C, yet its total amount is significantly larger and reaches ~11 µmol/m^2_C after 4 hours and ~27 µmol/m^2_C after four cycles. While the reduction of initially present trace amounts of H_2O/HF should not depend on temperature, the electrolyte decomposition and formation of H_2O/protic species increases with temperature, as indicated by the increasing CO_2 and CO signals (see below). As in Figure 1, the CO_2 signal again can be split into the three regions as discussed above, yet the total amount of CO_2 significantly increases.

Oxygen evolution initiates once the cell potential reaches 4.38 V, which is 40 mV lower than at 25°C (see Figure 1), even though the SOC at the onset of oxygen release remains at 81%. The total amount of evolved O_2 is roughly 1.5-fold larger compared to the 25°C experiment, with ~16 µmol/m^2_{NMC} in the first cycle, but still only minor quantities in the subsequent cycles. Again, simultaneous with the O_2 evolution, also CO and CO_2 evolve. The latter again show the step-like increases from cycle to cycle once the cell voltage increases above ~4.38 V, the potential at which oxygen release is observed in the first cycle. In analogy to Figure 1, the amounts of CO_2 due to chemical electrolyte oxidation (i.e., released at potentials ≥4.38 V) decrease from ~230 µmol/m^2_{NMC} in the first to ~120 µmol/m^2_{NMC} in the second and to ~70 µmol/m^2_{NMC} in the third and fourth cycle. Similarly, the CO amounts decrease from ~90 µmol/m^2_{NMC} in the first, to ~35 µmol/m^2_{NMC} in the second, to ~20 µmol/m^2_{NMC} in the third, and to ~15 µmol/m^2_{NMC} in the fourth cycle. These decreasing amounts of CO and CO_2 over cycling are consistent with the expected decrease in the oxygen release rates as a consequence of the growing thickness of the oxygen-depleted layer.

Finally, Figure 3 depicts the OEMS measurement of a NMC622-graphite cell cycled at 50°C. The evolution of C_2H_4 and CO due to SEI formation on the graphite in the first cycle reaches ~6.5 µmol/m^2_C and ~2 µmol/m^2_C, respectively, and is therefore very similar to the amounts observed in Figure 1 and Figure 2. As already observed in the measurement at 40°C, the C_2H_4 signal is not perfectly stable after the first cycle and increases to ~11 µmol/m^2_C at the end of the experiment, indicating that, as expected, the EC-derived SEI is even less stable at 50°C compared to 40°C. The H_2 signal is again qualitatively similar to the experiments at 25°C and 40°C (Figure 1 and Figure 2), but its total amount increased slightly to ~12 µmol/m^2_C after 4 hours and to ~32 µmol/m^2_C at the end of the measurement. Also the CO_2 signal is qualitatively similar to the ones observed at 25°C and 40°C, however, the amount is even further increased (note the different scales of the y-axes in Figures 1–3).

At a cell potential of 4.36 V, O_2 evolution sets in, which is 60 mV lower than at 25°C (Figure 1) and 20 mV lower than at 40°C (Figure 2). However, the SOC at the onset of oxygen release again is at around 81% and thus is constant for all temperatures. The total O_2 evolution in the first cycle increases further compared to the 40°C experiment to ~21 µmol/m^2_{NMC} and only minor quantities are observed in the subsequent cycles. In analogy to Figure 1 and Figure 2, with the onset of O_2 evolution also CO and CO_2 evolve due to chemical electrolyte oxidation. The amounts of CO_2 due to chemical electrolyte oxidation (i.e., released at potentials ≥4.36 V) decrease

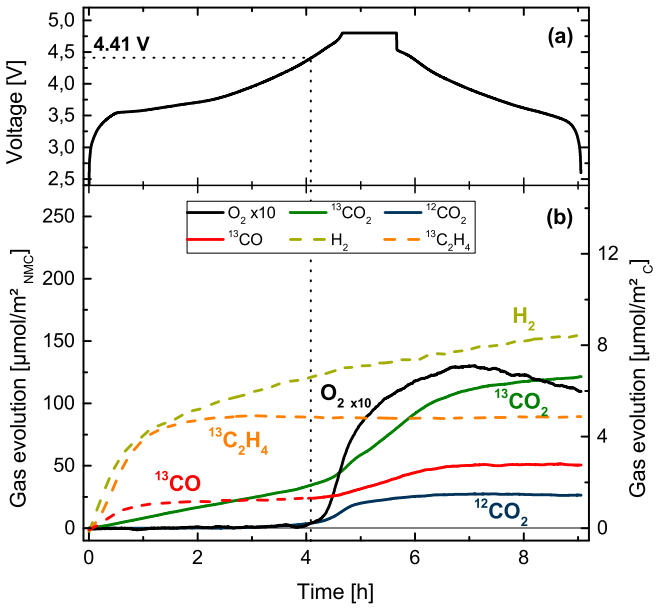

Figure 4. (a) Cell voltage vs. time of the first cycle of a NMC622-graphite cell at C/5 rate and 25°C between 2.6 and 4.8 V, in a cell containing 400 µL of 1.5 M $LiPF_6$ in **^{13}C-labelled** ethylene carbonate (^{13}C-EC), two glassfiber separators and 16.87 mg NMC622. (b) Evolution of $^{13}CO_2$ (dark green), $^{12}CO_2$ (dark blue), H_2 (green), $^{13}C_2H_4$ (bright orange), ^{13}CO (red), and O_2 (black, 10-fold magnified) as a function of time. Solid lines indicate the gases stemming from the NMC electrode and dashed lines those from the graphite electrode; gas concentrations are referenced to the NMC BET area (left y-axis) and to the sum of the graphite and conductive carbon BET areas (right x-axis). The OEMS data are smoothed, baseline corrected, and converted into units of [µmol/m^2_{NMC}] and [µmol/m^2_C].

from ~320 µmol/m^2_{NMC} in the first to ~130 µmol/m^2_{NMC} in the second and to ~70 µmol/m^2_{NMC} the third and fourth cycle. The CO amounts decrease from ~130 µmol/m^2_{NMC} in the first, to ~35 µmol/m^2_{NMC} in the second and to ~30 µmol/m^2_{NMC} in the third and fourth cycle.

Evaluation of the H_2 and CO_2 signals prior to oxygen release.— As it was presented above, the CO_2 signal of the first charge can be divided into three distinct regions. In the following we will have a closer look at the first two regions observed prior to oxygen release and will also discuss the H_2 signal in more detail. As it was demonstrated in Figures 1–3, the linear increase of the CO_2 signal within the first three hours into the charging process increases with temperature from 21 µmol/m^2_{NMC} (25°C) to 70 µmol/m^2_{NMC} (40°C) all the way to 129 µmol/m^2_{NMC} (50°C). In our previous work with NMC111, NMC622, and NMC811 from a different supplier, we ascribed the CO_2 increase observed only in the first cycle at 25°C (ranging from ~19–80 µmol/m^2_{NMC}) prior to the onset of oxygen release to the oxidation of residual carbonate impurities on the surface of the NMC (amounting to ~0.05–0.11%$_{wt}$ Li_2CO_3 equivalents for the three different NMCs).[7] While this explanation was consistent with the carbonate impurities specified by the supplier in this previous study, it is inconsistent with the observed dramatic increase in the initial CO_2 formation with temperature, as the residual carbonate content of course should not depend on the temperature at which the experiment is being conducted.

To test if the linear CO_2 signal may stem from electrolyte decomposition rather than from carbonate impurity oxidation, we conducted the following OEMS experiment using 1.5 M $LiPF_6$ in ^{13}C-labelled EC (^{13}C-EC). The first cycle of an analogous experiment as the one shown in Figure 1 is depicted in Figure 4. As already discussed above, due to SEI formation, ethylene and carbon monoxide evolve from the beginning of the measurement. Owing to the use of ^{13}C-EC, the ^{13}C-labelled gases $^{13}C_2H_4$ and ^{13}CO are observed in Figure 4. The H_2 signal is qualitatively very similar to the analogous experiment at 25°C (Figure 1). Interestingly, the clearly observed linear increase of carbon dioxide at the beginning of the measurement is $^{13}CO_2$ and therefore unequivocally stems from the electrolyte rather than from carbonate surface impurities.

It is important to note that in this experiment the linear CO_2 evolution is observed all the way until the onset of oxygen release. Therefore, the transition to a higher CO_2 evolution as it was observed in Figures 1–3 setting in after roughly three hours is absent in Figure 4. We will come back to this important observation in more detail later on when discussing the origin of this transition to higher CO_2 evolution rates.

At a cell potential of 4.41 V, O_2 evolution sets in (SOC = 81%) together with the formation of $^{13}CO_2$, ^{13}CO resulting from chemical electrolyte oxidation induced by the released oxygen, and the first appearance of $^{12}CO_2$ (^{12}CO was not observed throughout the entire measurement), which plateaus at ~25 µmol/m^2_{NMC} by the end of the first charge/discharge cycle. Surprisingly, no $^{12}CO_2$ is observed prior to the onset of oxygen release, disproving our original hypothesis that the electrochemical oxidation of (lithium) carbonate surface impurities would be responsible for the initial CO_2 formation. In principle, the $^{12}CO_2$ may derive from three sources: (i) the oxidation of the PVDF binder; (ii) the oxidation of the conductive carbon; and/or, (iii) the oxidation/decomposition of Li_2CO_3 and/or transition metal carbonates. As was shown by Metzger et al.,[26] the formation of CO_2 from PVDF binder does not occur below 5.0 V vs. Li^+/Li even at 60°C. Also, in our previous report with isotopically labelled conductive carbon (^{13}C), we did not observe any $^{13}CO_2$ or ^{13}CO up to potentials of 4.8 V vs. Li^+/Li at 25°C.[7] Therefore, the only possible source for the $^{12}CO_2$ evolved upon the onset of oxygen release in Figure 4 are carbonate surface impurities; if converted to Li_2CO_3 equivalents, the observed ~25 µmol/m^2_{NMC} would equate to ~0.06%$_{wt}$ Li_2CO_3. In previous work,[7,27] we had proposed that surface carbonate impurities would get oxidized to CO_2 at potentials above ~4.2 V vs. Li^+/Li, according to the following reaction:

$$Li_2CO_3 \rightarrow 2\,Li^+ + 2\,e^- + 0.5O_2 + CO_2 \uparrow \quad [1]$$

This was based on our earlier OEMS experiments with Li_2CO_3/carbon composite electrodes, where the evolution of CO_2 at a stoichiometry of $2e^-/CO_2$ was observed; since no evolution of O_2 could be detected by OEMS, this was rationalized by assuming that the released oxygen would be highly reactive, so that it would react immediately with the electrolyte solvent.[37] This mechanism was adopted later on also by others.[22,38] Based on the OEMS experiments with ^{13}C-labeled EC electrolyte, the more likely carbonate impurity decomposition mechanism (written in the following for Li_2CO_3) is a simple acid-base reaction:

$$Li_2CO_3 + 2\,HF \rightarrow 2\,LiF + H_2O + CO_2 \uparrow \quad [2]$$

Reaction 2 would be consistent with the experimental observations: (i) the lack of O_2 evolution for a Li_2CO_3/carbon composite electrode; and, (ii) the fact that carbonate decomposition does not occur until the onset of oxygen release on NMC cathodes, which we believe results in the formation of HF. This is based on the observation that at least some fraction of the released oxygen is singlet oxygen[11] which, as found recently,[39] reacts with ethylene carbonate to form H_2O_2, which is electrochemically oxidized above ~3.8 V vs. Li^+/Li, yielding protons, which in turn react with PF_6^- ions to PF_5 and HF.[40]

In a recent report by Renfrew et al.,[22] it was suggested that the CO_2 and CO evolved throughout the entire first charge of NMC622 would actually stem from the oxidation of Li_2CO_3 surface impurities. This, however, is clearly inconsistent with the experiment in Figure 4, which shows that (i) all the CO_2 evolved prior to O_2 evolution and the majority of the CO_2 evolved in parallel with oxygen release is $^{13}CO_2$, and (ii) that all CO is evolved as ^{13}CO. Therefore, the majority of the evolved CO_2 and all of the evolved CO in the first cycle must definitely stem from electrolyte decomposition.

In order to get further insights into the origin of the CO_2 evolution prior to the onset of O_2 evolution, we will next explore the effect

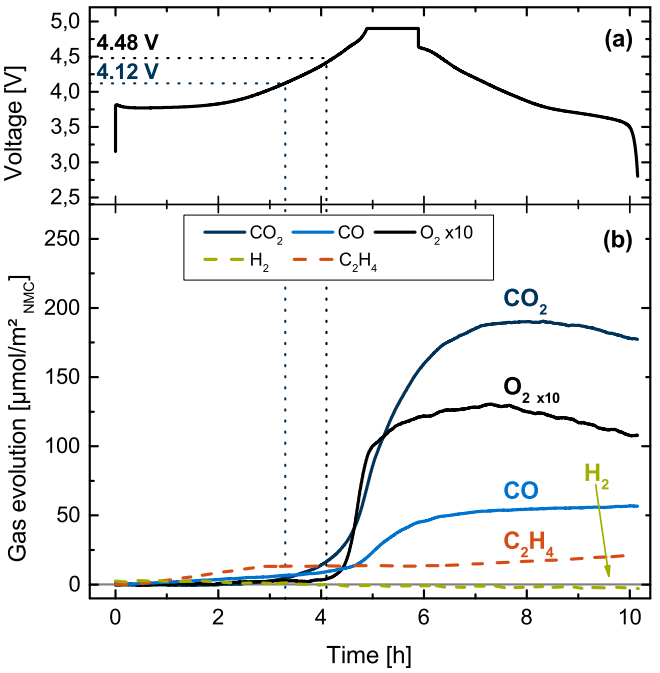

Figure 5. (a) Cell voltage vs. time of the first cycle of a NMC622-Li cell at C/5 rate and 25°C between 2.8 and 4.9 V, in a cell containing 400 µL of 1.5 M $LiPF_6$ in ethylene carbonate (EC), two glassfiber separators and 16.41 mg NMC622. (b) Evolution of CO_2 (dark blue), H_2 (green), C_2H_4 (orange), CO (blue), and O_2 (black, 10-fold magnified) as a function of time. Solid lines indicate the gases stemming from the NMC electrode and dashed lines those from the lithium electrode; gas concentrations are referenced to the NMC BET area. The OEMS data are smoothed, baseline corrected, and converted into units of [$\mu mol/m^2_{NMC}$].

of the counter-electrode by conducting an analogous experiment to that shown in Figure 1 and Figure 4, using lithium metal instead of a graphite counter-electrode. Examining the first cycle of an NMC622-Li cell with 1.5 M $LiPF_6$ in EC (Figure 5), the onset of O_2 release occurs at a ∼0.06–0.07 V higher cell voltage of ∼4.48 V, simply due to the lower potential of the lithium vs. the graphite counter-electrode. As can be seen clearly from Figure 5, the gas evolution traces in the high voltage region, i.e., in the potential region above the oxygen release, are essentially identical to those observed with a graphite counter-electrode (see Figure 1 and Figure 4) and will therefore not be discussed in greater detail. A marked difference is the substantially lower amount of C_2H_4 evolved in the first charge cycle and its gradual increase in the first discharge cycle: the former is due to the much smaller active surface area of metallic lithium vs. graphite, reducing the absolute amount of electrolyte reduction for SEI formation; the latter is due to the formation of fresh lithium surfaces during lithium plating and the concomitant formation of new SEI. Another clear difference is the absence of H_2 evolution during the first charge with a lithium metal counter-electrode (Figure 5), quite different from what we observed for a graphite counter-electrode (see Figure 1 and Figure 4). Finally, a quite striking feature of this experiment with a lithium counter-electrode is that the initial linear CO_2 evolution is absent and CO_2 evolution starts after ∼3 h at a potential of ∼4.12 V before it turns into a very steep slope once oxygen is released at ∼4.48 V. The potential of ∼4.12 V fits very well to the onset of the higher slope in the CO_2 signal observed in Figures 1–3 after ∼3 h at ∼4 V. The difference of ∼0.1 V in the potential again is simply caused by the potential difference between the graphite and the lithium counter-electrode.

The presence of the CO_2 evolution starting at ∼4 V in Figures 1–3 and at ∼4.12 V in Figure 5 but its absence in the experiment with the ^{13}C-labelled electrolyte (Figure 4) clearly rules out both the NMC cathode as well as the graphite and lithium counter-electrode as the origin of the CO_2. In fact, the only remaining difference is the electrolyte used (conventional EC in Figures 1–3 and Figure 5 compared to ^{13}C-EC in Figure 4). The as received ^{13}C-labelled EC contained a very significant amount of EG of ∼9–10%, which forms by a ring-opening reaction when the EC contains some H_2O under release of CO_2.[41] Therefore, it was thoroughly distilled to remove all EG and potential other impurities (see Experimental section) right before preparing the electrolyte for the experiment shown in Figure 4. In contrast, the EC used in the experiments presented in Figures 1–3 and Figure 5 was delivered as battery grade and therefore not further purified. We believe, that even though the latter was delivered as battery grade it still contained a small amount of EG (which will always form during storage when even minor quantities of water are present) or other impurities, which are electrochemically less stable than EC and become oxidized at ∼4 V and therefore give rise to the observed CO_2 evolution starting at ∼4 V before the onset of oxygen release. This hypothesis is supported by a study by Wang et al. who investigated the electrochemical oxidation of EG using DEMS and found CO_2 evolution starting at ∼3.7 V vs. Li^+/Li.[42] Even though they performed the experiment in aqueous media on a platinum surface the observation of CO_2 at reasonably similar potentials underlines that the oxidation of EG or other alcohols may be the reason for the CO_2 evolution in Figures 1–3 and Figure 5 starting at ∼4.1 V vs. Li^+/Li. The absence of this process in the second to fourth cycle can simply be explained by the quantitative oxidation of these species in the first cycle.

The remaining questions from Figure 5 are to understand why the initial linear CO_2 evolution is absent and why no H_2 evolution is observed in the first charge cycle with a lithium counter-electrode. To resolve this question, Figure 6 shows the mass traces on channels 44 (CO_2) and 2 (H_2) both normalized to the argon isotope on channel 36 for the preceding OCV period following cell assembly as well as for the first 5.5 hours of cycling recorded for the NMC622-graphite cell (Figure 1) and the NMC622-Li cell (Figure 5), both cycled at 25°C. In both panels, the data to the left of the dashed vertical line are from the OCV period. In general, upon attachment of the cell to the mass spectrometer system, a decaying background signal on all mass channels is observed, which is then used to fit a baseline that is subtracted from the mass signals recorded during the subsequent cell cycling to determine the gas evolution during charge/discharge cycling of a cell. For the cell with a graphite counter-electrode (Figure 6a), the signals recorded on m/z = 44 and m/z = 2 during OCV (∼0.2 V cell voltage) exponentially decay and approach a reasonably constant value by the time the cell is switched from OCV to galvanostatic charging for the first cycle. Right with the beginning of the charging process the evolution of H_2 and CO_2 can be clearly seen from the raw data, indicating that either the lithiation of the graphite electrode or the delithiation of the NMC cathode are responsible for the formation of these gases.

In contrast to the rather clear baseline in the NMC622-graphite experiment, the behavior of the baseline mass signals for CO_2 and H_2 for the NMC622-Li cell (Figure 6b) is very different. In fact, gradually increasing signals are observed for both channels even during the initial OCV period. The increasing mass signals during OCV indicate that there are chemical processes occurring during OCV which lead to the formation of both CO_2 and H_2 in the NMC622-Li cell. Electrochemical processes can be excluded due to the absence of any current during OCV. Since the potential of the NMC622 electrode is at ∼3.2 V vs. Li^+/Li for both cell configurations (inferred from the OCV potential ∼3.2 V in the NMC622-Li cell (Figure 6b) and considering that the lithium anode potential is 0 V vs. Li^+/Li), no reactions are expected to occur at the NMC cathode during OCV. In contrast, the anode is at a potential of ∼3.0 V vs. Li^+/Li in case of the NMC622-graphite cell (∼0.2 V OCV) and at 0 V vs. Li^+/Li in case of the NMC622-lithium cell. Consequently, the reduction of trace HF/H_2O to H_2 in a NMC622-Li cell already occurs during OCV when metallic lithium is present (Figure 6b), while it only occurs on a graphite electrode once the electrode potential drops below ∼1.7 V vs. Li^+/Li in the case of HF[33] or below ∼0.8 V vs. Li^+/Li in the case

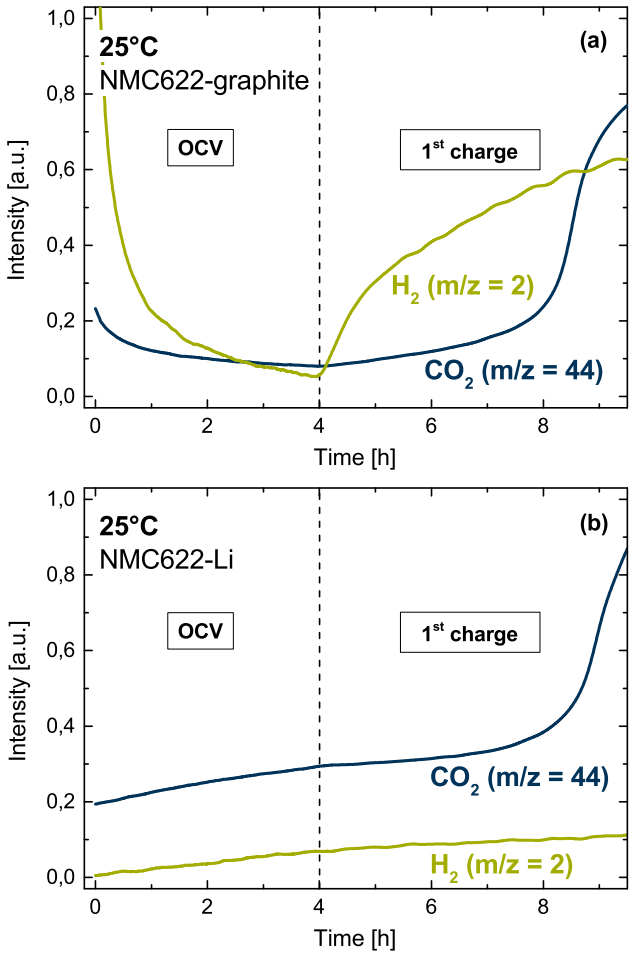

Figure 6. Mass traces of hydrogen (H_2, green) and carbon dioxide (CO_2, dark blue) recorded during the preceding OCV and the first 4.5 h of the 1st charge at 25°C of (a) the NMC622-graphite cell shown in Figure 1, and, (b) the NMC622-Li cell shown in Figure 5. The OCV region to the left of the dashed line was used for the baseline fits of the OEMS signals plotted in Figure 1 and Figure 5.

of H_2O.[27] For the balancing factor of 1.4 used in this cell, the graphite potential is expected to decrease below ~1.7 V vs. Li^+/Li once ~0.6% of the overall charge has been passed[43] (i.e., within ~1.5 min. after OCV in Figure 6a) and to below ~0.8 V vs. Li^+/Li once ~2.5% of the overall charge has been passed[43] (i.e., within ~8 min). This clearly explains the observed onset of H_2 evolution immediately following the switch from OCV to charging in Figure 6a. On the other hand, the increasing H_2 mass signal "baseline" during OCV is the reason why no H_2 evolution is visible in Figure 5 even though H_2 is evolved already during OCV.

This leaves the question as to the origin of the CO_2 evolution during OCV for the NMC622-lithium cell (Figure 6b) and during the initial ~3 hours of charging for the NMC622-graphite cell (Figure 6a). The explanation can be found by considering that the reduction of trace H_2O to H_2 is accompanied by the formation of hydroxide ions (OH^-), as shown by Bernhard et al.:[32]

$$2\,H_2O + 2\,e^- \rightarrow H_2 + 2\,OH^- \quad [3]$$

The thus produced OH^- ions cause the hydrolysis of EC into ethylene glycolate anion (EG^-), which may further polymerize with EC, and CO_2 at appreciable rates even at room temperature, as was shown in model experiments with TBAOH by Metzger et al.:[41]

$$OH^- + EC \rightarrow CO_2 + EG^- \quad [4]$$

In summary, the reduction of trace H_2O forming H_2 and OH^- that subsequently hydrolyzes EC causes the observed increasing CO_2 mass signal already during the OCV period in the NMC622-Li cell (Figure 6b) and, owing to the associated erroneous CO_2 baseline correction, is the cause for the apparent absence of an initial CO_2 evolution signal right at the beginning of the charging process (Figure 5). In fact, a similar increasing baseline of the CO_2 signal was shown before in graphite charging experiments with deliberate water additions to the electrolyte, becoming more pronounced with increasing water content.[26] On the other hand, no OH^- are produced during OCV in the NMC622-graphite cells (Figure 6b) and can only be formed at the beginning of the charging process, leading to the observed onset of CO_2 evolution due to EC hydrolysis (see Eq. 4) immediately upon cell charging, as seen in Figures 1–3 and Figure 4. The steeper slopes of the initial CO_2 evolution for high temperatures within the first ~3 hours observed in Figures 1–3 are due to the temperature activated EC hydrolysis by OH^-, with an apparent activation energy of ~40–50 kJ/mol.[41] We will compare this reported activation energy with our observations in the Discussion section. The absence of EC hydrolysis after the first cycle is most likely due to the fact that OH^- triggered EC hydrolysis is not a catalytic process but ends once the OH^- ions are depleted, which is likely the case within the first cycle due to only trace amounts of H_2O being present in the fresh cell.

Electrochemical cycling of NMC622-graphite cells.—In our previous work, we showed that a stable cycling of NMC-graphite cells is possible as long as the upper cut-off voltage is kept below the onset potential of oxygen release.[7] To investigate whether this is also true for charge/discharge cycling at different temperatures, we conducted long-term cycling experiments, now with a conventional LP57 electrolyte (1 M $LiPF_6$ in EC/EMC 3:7) instead of the model electrolyte (1.5 M $LiPF_6$ in EC) used for the above OEMS experiments. Figure 7 shows the specific discharge capacities at a rate of 1 C vs. cycle number, whereby every 50 cycles 2 cycles at 0.1 C were conducted; the specific capacities of the 5th and the 312th cycle (both at 1 C) and the capacity retention between these cycles are summarized in Table I.

At 25°C, as one would expect, the specific capacity increases with increasing upper cutoff voltage: at a 1 C-rate, the initial capacity increases from 154 mAh/g_{NMC} for 4.2 V to 189 mAh/g_{NMC} for 4.6 V; at 0.1 C-rate, it increases from 170 mAh/g_{NMC} to 209 mAh/g_{NMC}. Stable cycling at 25°C and 1 C-rate (Figure 7a) with capacity retentions of >90% over ~300 cycles is only possible with 4.2 and 4.3 V upper cutoff voltage (see Table I), which is very similar to our previous report using NMC622 from another vendor.[7] The fairly linear capacity loss over cycle numbers in these cells is most likely due to the loss of cyclable lithium into the graphite SEI.[44–47] With a 4.4 V cutoff, a significantly lower capacity retention of 84% is observed (see Table I), indicating that between 4.3 and 4.4 V an additional aging mechanism sets in. For 4.5 and 4.6 V, the cycling stability is rather poor, with capacity retentions of 66% and 53%, respectively (see Table I). The onset of this additional aging mechanism fits very well to the observed onset potential of oxygen release, which was shown previously to lead to increased impedance due to the formation of spinel- and rock-salt layers detrimental to the Li-ion conductivity.[6,7] The significantly worse cycling performance for 4.5 and 4.6 V may be rationalized by the fact that due to the higher SOC at the higher cutoff potentials, the driving force for the surface transformation becomes larger, yielding thicker and more resistive surface layers (also indicated by the clearly larger capacity loss at 1 C compared to 0.1 C; see Figure 7a). Additionally, the products of electrolyte degradation like protic species or water,[7,10,27,34] which would form HF upon reaction with the $LiPF_6$ salt[33,40] may further be detrimental to the anode SEI and the cathode active material.

When the temperature is increased to 40°C (Figure 7b), the specific capacities increase compared to cycling at 25°C due to faster kinetics, reaching 173 mAh/g_{NMC} (1 C) and 184 mAh/g_{NMC} (0.1 C) for 4.3 V, all the way up to 201 mAh/g_{NMC} (1 C) and 218 mAh/g_{NMC} (0.1 C) for 4.6 V. The capacity retention over ~300 cycles at 1 C for a 4.3 V cutoff decreases to 85% compared to 91% at 25°C. This is most likely due to faster lithium loss at higher temperatures due to a less stable SEI, as can be also observed in the increased C_2H_4 evolution in

Table I. Measured capacity retentions vs. upper cutoff potential between the 5th and the 312th cycle (at 1 C-rate) of the NMC-graphite cells shown in Figure 7 for 25, 40, and 50°C. The values in brackets are the specific capacities in units of mAh/g_{NMC} of the 5th and the 312th cycles.

	4.2 V	4.3 V	4.4 V	4.5 V	4.6 V
25°C	92% (154 → 142)	91% (165 → 150)	84% (174 → 147)	66% (180 → 119)	53% (189 → 101)
40°C	-	85% (173 → 147)	85% (184 → 157)	48% (192 → 92)	19% (201 → 39)
50°C	74% (169 → 125)	77% (181 → 140)	73% (190 → 139)	48% (197 → 94)	2% (204 → 4)

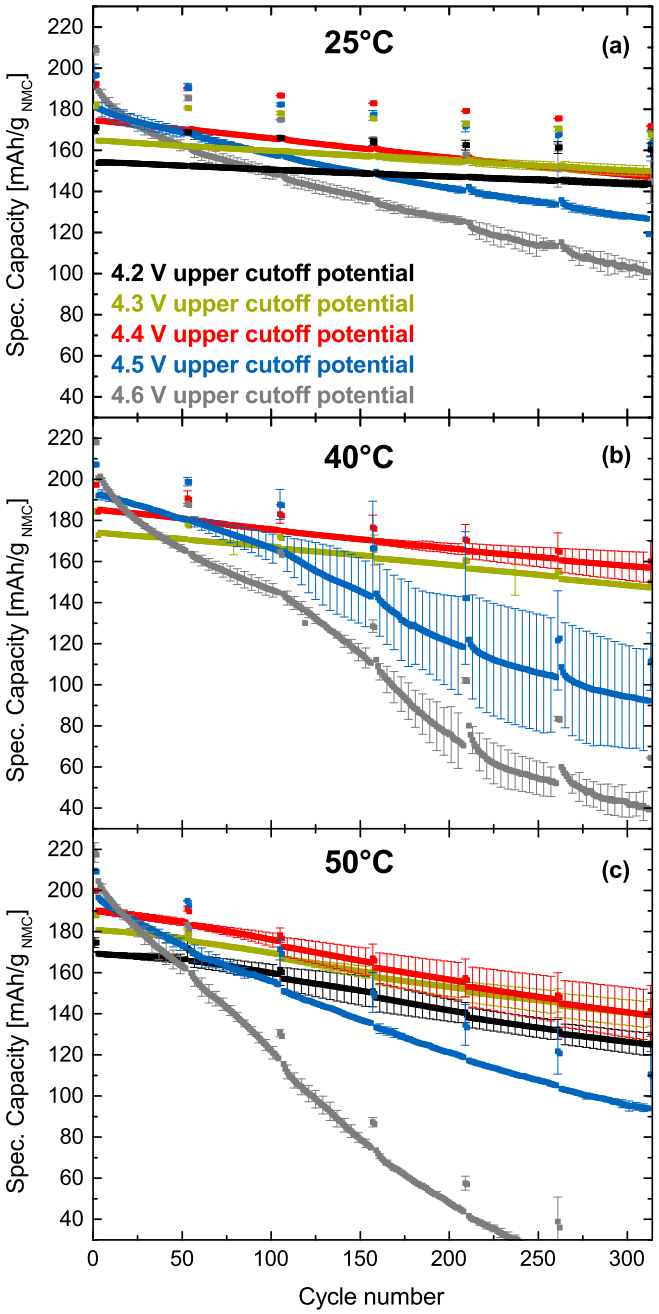

Figure 7. Specific discharge capacities of NMC622-graphite cells vs. cycle number in LP57 electrolyte (1 M $LiPF_6$ in EC:EMC 3:7 wt/wt), operated at (a) 25°C, (b) 40°C, or (c) 50°C with different upper cutoff voltages of 4.2 V (black), 4.3 V (green), 4.4 V (red), 4.5 V (blue), or 4.6 V (gray) and a constant lower cutoff voltage of 3.0 V. Formation was done at a rate of 0.1 C (2 cycles), and cycling was performed at 1 C with two cycles at 0.1 C after every 50 cycles. The error bars represent the standard deviations of two repeat measurements.

Figure 2.[44,47] Interestingly, with a 4.4 V cutoff, the capacity retention is the same as for 4.3 V even though 4.4 V is slightly above the onset of oxygen release (Figure 2). As 4.4 V is right at the onset of O_2 release at that temperature (~4.38 V, see Figure 2), it might be possible that the impedance increase due to a rather thin surface layer is compensated by faster kinetics at the higher temperature. For 4.5 and 4.6 V, thicker surface layers appear to overwhelm the faster kinetics at the higher temperature, yielding poor capacity retentions of 48% and 19%, respectively; in addition, even at the lower C-rate of 0.1 C, capacity fading is very high, suggesting accelerated electrolyte degradation associated with an accelerated loss of cyclable lithium.

Lastly, at 50°C (Figure 7c), the initial specific capacities further increase slightly to 169 mAh/g_{NMC} (1 C) and 175 mAh/g_{NMC} (0.1 C) for 4.2 V as well as to 204 mAh/g_{NMC} and 218 mAh/g_{NMC} (0.1 C) for 4.6 V. The capacity retentions at cutoff voltages below the detected onset of oxygen release (Figure 3), i.e., 4.2 and 4.3 V, are essentially identical with 74–77%, which is again lower than at 25 and 40°C and is most likely due to a less stable SEI at 50°C.[44] The capacity retention with a 4.4 V cutoff is 73%, similar compared to the cycling with 4.2 and 4.3 V cutoffs, which is probably the same reason as observed for 4.4 V at 40°C. The increase of the particle resistance is compensated by faster kinetics at the higher temperature. For voltage cutoffs of 4.5 and 4.6 V, a drastic increase in the rate of capacity fade is observed even at the slower rate of 0.1 C, which must be due to accelerated electrolyte decomposition and an associated accelerated loss of cyclable lithium.

We want to highlight that at 40 and 50°C, other aging mechanisms may also play a role in the cell aging; however, we believe that at potentials above the threshold voltage for oxygen release, accompanied by the formation of surface spinel and rock-salt layers, the degradation of the electrolyte by reactive oxygen species is a dominant factor governing cell aging as it causes the formation of protic species and HF. The latter may cause transition metal dissolution from NMC and its precipitation on the anode eventually leads to a loss of active lithium.[44,48–50] The impedance growth due to the formation of a surface film has a significant effect on the capacity fade at 25°C, where the capacity losses at 0.1 C and 1 C differ significantly at upper cutoff potentials >4.4 V (see Figure 7a), i.e., the capacity loss between the first and last cycle at the respective C-rates and 4.6 V upper cutoff potential is 64 mAh/g in the case of 0.1 C, while it is 88 mAh/g at 1 C indicating that a significant portion of the additional capacity loss at the latter C-rate is caused by an increasing resistance during cycling. In contrast, at 40°C the capacity losses for 4.6 V upper cutoff potential are rather similar with 154 mAh/g and 162 mAh/g at 0.1 C and 1 C, respectively (Figure 7b). At 50°C the capacity losses for 4.6 V upper cutoff potential are 195 mAh/g and 200 mAh/g at 0.1 C and 1 C, respectively, (Figure 7c) proving that the capacity loss is affected to a minor extent by a growing impedance. At higher cycle numbers (>100), we observed that the graphite anode potential dropped below 0 V vs. Li^+/Li during charge for cells with upper cutoff voltages of 4.6 V and even some with cutoffs of 4.5 V. The drop of anode potential below 0 V suggests the possibility of a Li-plating side reaction, which is likely a consequence of a drop of anode porosity associated with the growth of SEI as reported previously.[46] This additional growth of the SEI at ≥4.5 V may be a consequence of the electrolyte decomposition products formed on the cathode, being released into the

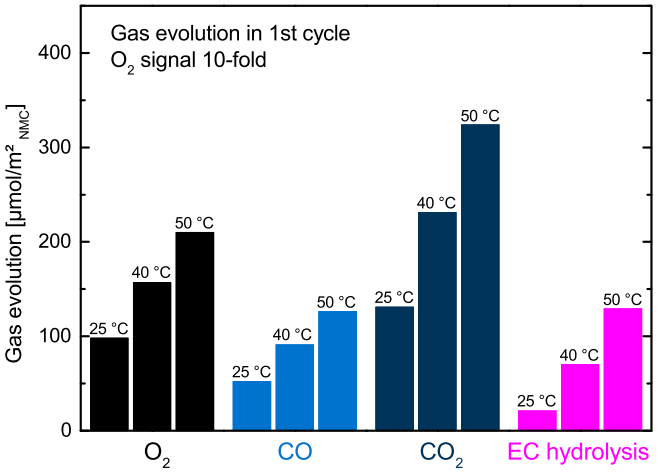

Figure 8. Temperature dependence of amounts of evolved O_2 (black bars), CO (light blue bars), and CO_2 (dark blue bars) due to oxygen release and subsequent chemical electrolyte oxidation as well as CO_2 evolved due to EC hydrolysis (pink bars) extracted from Figures 1–3. The values for CO and CO_2 are extracted from Figures 1–3 according to the following procedures: i) the here plotted amounts of CO are the total amount of evolved CO minus the amounts of CO evolved due to SEI formation on the graphite (dashed lines in Figures 1–3); ii) the CO_2 due to EC hydrolysis (pink bars) are the measured CO_2 amounts measured within the first three hours since during that period it is the only source of CO_2; and, iii) the values for CO_2 due to oxygen release (dark blue bars) are the amounts measured with the beginning of oxygen release until the end of the CV step in the first cycle.

electrolyte and damaging the anode SEI (via the so-called cross-talk phenomenon).[27,51,52]

Discussion

Temperature dependent gas evolution of NMC622-graphite cells.—Oxygen release was observed at 25, 40, and 50°C (Figures 1–3) starting at cell potentials of 4.42, 4.38, and 4.36 V, respectively. The onset of oxygen release occurs in all three cases at an SOC of ∼81%, indicating that at this SOC the layered structure becomes so instable that it decomposes under release of lattice oxygen. The slight shift in the onset potentials is therefore only due to lower overpotentials at higher temperatures, i.e., the same SOC is reached at lower cell potentials as the temperature increases. Interestingly, the same SOC was observed for the oxygen release in our previous publication for NMC111, −622, and −811 from another vendor, even though the onset potentials were different.[7] In a recent study, we also observed that at least part of the oxygen was released as singlet oxygen ($^1O_2$) at ∼80% SOC in case of NMC111, NMC811, and lithium-rich HE-NCM.[11] Additionally, in several reports by the group of Manthiram, oxygen loss from the surface of layered oxides delithiated chemically was observed at ∼70–90% SOC for NMC111[53] as well as for $LiNi_{0.5}Co_{0.5}O_2$, and $LiNi_{0.85}Co_{0.15}O_2$ (LNCO).[54,55]

In the following we will have a closer look on the amount of evolved gases in the NMC622-graphite cells as a function of temperature (Figures 1–3) to derive the activation energy of the processes. Figure 8 summarizes the amounts of evolved O_2, CO, and CO_2 due to oxygen release and subsequent chemical electrolyte oxidation as well as the CO_2 evolution due to EC hydrolysis. The O_2 amounts were simply determined by the maximum of the O_2 signal (black bars), whereas the CO amounts (blue bars) had to be corrected for the amounts due to SEI formation, so that only the amounts of CO formed as a consequence of oxygen release are accounted for. While the latter correction can be done quite easily as CO evolution from SEI formation is well separated from the one occurring during oxygen release, a precise quantification of the CO_2 amounts is more difficult since the processes causing CO_2 evolution (EC hydrolysis, electrolyte impurity oxidation, chemical electrolyte oxidation, decomposition of carbonate impurities) overlap. To extract the amounts and determine the activation energy of EC hydrolysis (pink bars), the CO_2 amounts evolved within the first three hours of the charging step were extracted from Figures 1–3. Within that period of time the CO_2 evolution from EC hydrolysis does not overlap with any of the other processes. It is important to mention that after three hours, EC hydrolysis is still ongoing so that the given amounts do not account for the complete CO_2 evolution related to EC hydrolysis. Nevertheless, due to the linear increase of the CO_2 signal during this period the absolute amounts do not influence the calculated activation energy. The CO_2 caused by chemical electrolyte oxidation due to oxygen release from NMC (dark blue bars) was determined as the CO_2 evolved right after the onset of oxygen release (vertical dashed line in Figures 1–3) until the end of the CV-step of the first charge. Clearly, the hereby determined CO_2 amounts will be somewhat inaccurate and are only a very rough estimate as the CO_2 evolution overlaps with EC hydrolysis, electrolyte impurity oxidation, and chemical decomposition of carbonate surface impurities on the NMC (acc. to Eq. 2). Yet, because of the rather high CO_2 evolution rate during oxygen release, it can be attributed to the largest extent to CO_2 evolved due to chemical electrolyte oxidation. Unfortunately, a reliable quantification of the electrolyte impurities causing CO_2 evolution is with the presented data not possible and will therefore not be considered for the evaluation of activation energies. Figure 8 clearly demonstrates the temperature dependence of the oxygen release as well as the dependence of EC hydrolysis on the temperature. Assuming that chemical EC oxidation due to oxygen release proceeds according to an overall net reaction EC + 2 O_2 → 2 CO_2 + CO + 2 H_2O and using the calculations described in detail in our previous work,[7] we can estimate the oxygen depleted surface layer thickness using the gas amounts summarized in Figure 8. At 25°C the estimated layer thickness corresponds to 4 or 7 nm, depending on whether a spinel or rock-salt layer is assumed, respectively. After the four cycles it grows to 10–16 nm, which is similar to the values of 7–12 nm, calculated in similar experiments for NMC111, −622, and −811.[7] After the first cycle, layer thicknesses of 8–12 nm and 11–16 nm are predicted on this basis for 40 and 50°C, respectively, growing to 14–22 nm and 20–30 nm after the fourth cycle. The calculated layer thicknesses based on the amount of evolved gases give only a rough estimate. Nevertheless, they do match very well the observed thicknesses from previous reports.[6,12,14] For instance, Muto et al. reported a rock-salt type layer formation on the surface of NCA of up to 100 nm after 500 cycles at 80°C.[14] Jung et al. studied NMC532 in the voltage range between 3–4.8 V after 50 cycles at room temperature and found spinel and rock-salt layer thicknesses of 12–15 nm and of 2–3 nm, respectively.[6] Abraham et al. reported 35–45 nm thick rock-salt layers on the surface of $LiNi_{0.8}Co_{0.2}O_2$ after calendaric aging of a charged electrode at 60°C for 8 weeks.[12] Despite the fact that the applied procedures are not the same we used in our work, the range of reported surface layer thicknesses from 2 nm up to 100 nm clearly show that the surface layers can grow significantly. This also should be expected considering that at high degrees of delithiation the layered NMC structure is thermodynamically less stable than the spinel and rock-salt phases. Therefore, the phase transformation on the surface is kinetically controlled, so that growing thicknesses at higher temperatures and longer cycling should be expected. Additionally, the rather good agreement between the approximate layer thicknesses projected from OEMS data and observed by high-resolution transmission electron microscopy (HR-TEM) was demonstrated in recent measurements with over-lithiated HE-NMC.[56] In the ultimate case of high temperatures >170°C the phase transformation becomes even a bulk effect and the complete particle may eventually transform into the spinel/rock-salt structure.[9,16,17]

In Figure 9, the evolved amounts of gas during the first charge determined in Figure 8 are plotted in an Arrhenius-type plot. For each gas and temperature, a linear curve is fitted through the data points. Interestingly, the slopes of the linear fits of O_2 (black line) as well as of CO (light blue line), and CO_2 (dark blue line) estimated to be derived from the chemical reaction with released oxygen are very similar. This correlation once again supports the previous findings that the

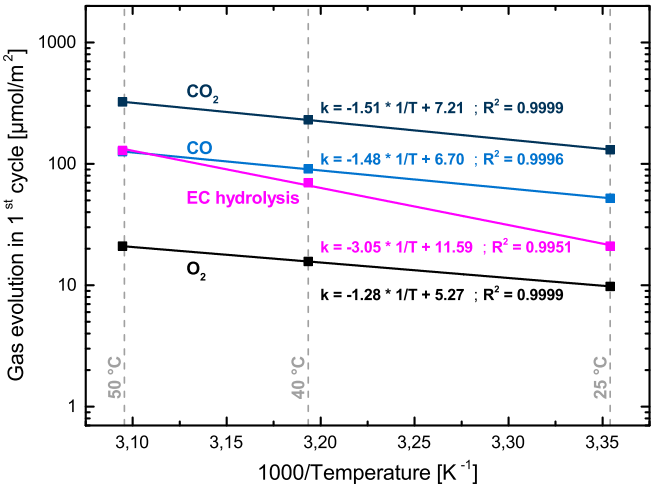

Figure 9. Arrhenius-type plot of the evolved O_2, CO, and CO_2 due to oxygen release and subsequent chemical electrolyte oxidation as well as CO_2 evolved due to EC hydrolysis, using the estimated values given in Figure 8.

oxygen release from layered oxides is responsible for most of the CO_2 and CO evolution (chemical electrolyte oxidation).[7,10] Multiplying the slope of the linear fit curves by $-R \times \ln(10)$, with R being the universal gas constant, yields an activation energy in the range of ~25–29 kJ/mol. In contrast, the resulting slope for the CO_2 evolved due to EC hydrolysis (pink line) is significantly steeper. The corresponding activation energy is ~58 kJ/mol, reasonably close to the reported value of ~40–50 kJ/mol by Metzger et al.,[41] thereby supporting our hypothesis that the initial linear increase of the CO_2 evolution in NMC-graphite cells is due to the OH^- catalyzed hydrolysis of EC (acc. to Eq. 4).

Temperature dependence of the specific energies of NMC622-graphite cells.—Figure 10 depicts the measured specific energies based on the cycling data shown in Figure 7. The total height of each bar represents the initial specific energy obtained at a rate of 0.1 C (2nd cycle), while the upper end of the uppermost hatched bars represent the initial specific energy at 1 C-rates (5th cycle). The specific energy after aging is shown by the upper end of the lower hatched bars, shown only for 1 C-rate (312th cycle), because less than 5% of the cycles are actually done at 0.1 C-rate so that the energy loss of

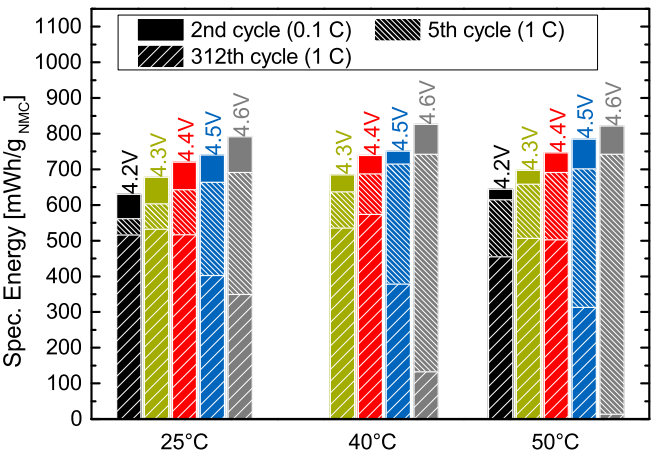

Figure 10. Measured specific energies of the 2nd (at 0.1 C-rate) as well as of the 5th and 312th cycle (both at 1 C-rate) cycle of the NMC622-graphite cells shown in Figure 7.

these few cycles will not represent the true energy loss of the material at 0.1 C cycling. With increasing temperature and constant upper cutoff voltage, the initial specific energies at both rates are increased because of the increased capacity (Figure 7), yet at the expense of a shorter lifetime as indicated by the growing specific energy difference between the 5th and the 312th cycles (indicated by the height of the upper hatched bars). Furthermore, with increasing upper cutoff potential, the measured specific energies also increase, yet as the cutoff potential exceeds 4.4 V, the potential at which the onset of oxygen evolution is observed, significant fade of the specific energy is observed.

Andre et al. defined specific energies of 750 ± 100 mWh/$g_{cathode}$ as a necessary target to reach a driving range of 300 miles under the assumption of the BMW i3 battery pack.[2] If we compare this value with the measured initial specific energies shown in Figure 10, we can see that NMC622 cannot achieve the target using a cutoff potential of 4.2 V (black bars), not even at 0.1 C rate and at 50°C (~640 mWh/g_{NMC}). Therefore, even with NMC622 as cathode material, cutoff potentials >4.2 V are required to reach the necessary specific energy targets. At cutoff potentials of 4.3 V (green bars) and 0.1 C rate, the measured initial specific energies are all within the target region and increase from ~675 mWh/g_{NMC} at 25°C, ~685 mWh/g_{NMC} at 40°C to ~700 mWh/g_{NMC} at 50°C. To reach the target region at a 1 C-rate, the cutoff potential needs to be further increased to 4.4 V (red bars), where initial specific energies of ~650 mWh/g_{NMC}, ~685 mWh/g_{NMC}, and 695 mWh/g_{NMC} can be reached at 25, 40, and 50°C, respectively. However, 4.4 V for this specific NMC622 material is right at the potential where oxygen release occurs, so that slight overcharging may cause a fast capacity decay, as is observed when the upper cutoff potential is 4.5 V (blue bars).

Conclusions

Studying the temperature dependence of oxygen release from layered $LiNi_{0.6}Mn_{0.2}Co_{0.2}O_2$ (NMC622) in NMC622-graphite cells, we found that the potential of oxygen release decrease with temperature from 4.42 V at 25°C, to 4.38 V at 40°C, to 4.36 V at 50°C. As at all temperatures the state-of-charge (SOC) at which oxygen release initiated was always ~81%, the decreasing onset potential for oxygen release with increasing temperature is simply due to reduced polarization. The oxygen release is ascribed to the formation of surface spinel and/or rock-salt phases once the SOC exceeds ~81%. Additionally, we showed that the total amount of released oxygen increases with increasing temperature, indicating the formation of thicker surface layers.

Simultaneous with the release of oxygen from the NMC surface, CO_2 and CO evolve as a consequence of the reaction of released oxygen with the alkyl carbonate electrolyte. Consequently, with growing temperature also the amounts of CO_2 and CO increase. Performing an Arrhenius-type analysis, we demonstrated that the extent of O_2 release and the concomitant evolution of CO_2 and CO exhibit very similar temperature dependences, underlining that they have the same origin. Further experiments showed that there are two additional sources of CO_2 prior to the onset of oxygen release, both of which are only observed within the first charge cycle. In particular, OH^- driven hydrolysis of EC forming CO_2, whereby OH- is produced by the reduction of trace H_2O at the graphite anode to H_2 and OH^-, and electrochemical oxidation of electrolyte impurities like ethylene glycol starting around 4 V. Experiments with ^{13}C-labelled ethylene carbonate (^{13}EC) showed that the decomposition of (lithium) carbonate surface contaminants on NMC proceeds via a reaction with HF, which is formed as a consequence of oxygen release and chemical electrolyte oxidation. It is therefore not linked to a direct electrooxidation of the carbonate contaminants.

Lastly, we also showed that charging NMC622-graphite cells to potentials >4.4 V, i.e., above the onset potential for O_2 release, leads to very poor cycling performance. Cycling only to 4.2 and 4.3 V, i.e., remaining below the onset potential for oxygen release, resulted in a rather stable cycling performance.

Acknowledgment

The authors thank BMW AG for their financial support. Ecopro is greatly acknowledged for supplying the NMC622 material. We thank Michael Metzger for very fruitful discussions and great contributions to this work. R.J. also thanks TUM-IAS for their support in the frame of the Rudolf-Diesel Fellowship of Dr. Peter Lamp.

ORCID

Roland Jung https://orcid.org/0000-0003-1135-7438

References

1. O. Groeger, H. A. Gasteiger, and J.-P. Suchsland, *J. Electrochem. Soc.*, **162**, A2605 (2015).
2. D. Andre, S.-J. Kim, P. Lamp, S. F. Lux, F. Maglia, O. Paschos, and B. Stiaszny, *J. Mater. Chem. A*, **3**, 6709 (2015).
3. D. Andre, H. Hain, P. Lamp, F. Maglia, and B. Stiaszny, *J. Mater. Chem. A*, **5**, 17174 (2017).
4. K. G. Gallagher, S. Goebel, T. Greszler, M. Mathias, W. Oelerich, D. Eroglu, and V. Srinivasan, *Energy Environ. Sci.*, **7**, 1555 (2014).
5. H. Gabrisch, T. Yi, and R. Yazami, *Electrochem. Solid-State Lett.*, **11**, A119 (2008).
6. S.-K. Jung, H. Gwon, J. Hong, K.-Y. Park, D.-H. Seo, H. Kim, J. Hyun, W. Yang, and K. Kang, *Adv. Energy Mater.*, **4**, 1300787 (2014).
7. R. Jung, M. Metzger, F. Maglia, C. Stinner, and H. A. Gasteiger, *J. Electrochem. Soc.*, **164**, A1361 (2017).
8. H.-J. Noh, S. Youn, C. S. Yoon, and Y.-K. Sun, *J. Power Sources*, **233**, 121 (2013).
9. S.-M. Bak, E. Hu, Y. Zhou, X. Yu, S. D. Senanayake, S.-J. Cho, K.-B. Kim, K. Y. Chung, X.-Q. Yang, and K.-W. Nam, *ACS Appl. Mater. Interfaces*, **6**, 22594 (2014).
10. R. Jung, M. Metzger, F. Maglia, C. Stinner, and H. A. Gasteiger, *J. Phys. Chem. Lett.*, 4820 (2017).
11. J. Wandt, A. T. S. Freiberg, A. Ogrodnik, and H. A. Gasteiger, *Materials Today*, In press.
12. D. P. Abraham, R. D. Twesten, M. Balasubramanian, I. Petrov, J. McBreen, and K. Amine, *Electrochem. Commun.*, **4**, 620 (2002).
13. D. P. Abraham, R. D. Twesten, M. Balasubramanian, J. Kropf, D. Fischer, J. McBreen, I. Petrov, and K. Amine, *J. Electrochem. Soc.*, **150**, A1450 (2003).
14. S. Muto, Y. Sasano, K. Tatsumi, T. Sasaki, K. Horibuchi, Y. Takeuchi, and Y. Ukyo, *J. Electrochem. Soc.*, **156**, A371 (2009).
15. S. Hwang, W. Chang, S. M. Kim, D. Su, D. H. Kim, J. Y. Lee, K. Y. Chung, and E. A. Stach, *Chem. Mater.*, **26**, 1084 (2014).
16. S.-M. Bak, K.-W. Nam, W. Chang, X. Yu, E. Hu, S. Hwang, E. A. Stach, K.-B. Kim, K. Y. Chung, and X.-Q. Yang, *Chem. Mater.*, **25**, 337 (2013).
17. H. Konishi, T. Yuasa, and M. Yoshikawa, *J. Power Sources*, **196**, 6884 (2011).
18. H. Arai, S. Okada, Y. Sakurai, and J.-I. Yamaki, *Solid State Ionics*, **109**, 295 (1998).
19. I. Belharouak, W. Lu, D. Vissers, and K. Amine, *Electrochem. Comm.*, **8**, 329 (2006).
20. I. Belharouak, D. Vissers, and K. Amine, *J. Electrochem. Soc.*, **153**, A2030 (2006).
21. S.-T. Myung, K.-S. Lee, C. S. Yoon, Y.-K. Sun, K. Amine, and H. Yashiro, *J. Phys. Chem. C*, **114**, 4710 (2010).
22. S. F. Renfrew and B. D. McCloskey, *J. Am. Chem. Soc.*, **139**, 17853 (2017).
23. K. Luo, M. R. Roberts, R. Hao, N. Guerrini, D. M. Pickup, Y.-S. Liu, K. Edström, J. Guo, A. V. Chadwick, L. C. Duda, and P. G. Bruce, *Nat. Chem.*, **8**, 684 (2016).
24. M. Metzger, J. Sicklinger, D. Haering, C. Kavakli, C. Stinner, C. Marino, and H. A. Gasteiger, *J. Electrochem. Soc.*, **162**, A1227 (2015).
25. N. Tsiouvaras, S. Meini, I. Buchberger, and H. A. Gasteiger, *J. Electrochem. Soc.*, **160**, A471 (2013).
26. M. Metzger, C. Marino, J. Sicklinger, D. Haering, and H. A. Gasteiger, *J. Electrochem. Soc.*, **162**, A1123 (2015).
27. M. Metzger, B. Strehle, S. Solchenbach, and H. A. Gasteiger, *J. Electrochem. Soc.*, **163**, A798 (2016).
28. B. Zhang, M. Metzger, S. Solchenbach, M. Payne, S. Meini, H. A. Gasteiger, A. Garsuch, and B. L. Lucht, *J. Phys. Chem. C*, **119**, 11337 (2015).
29. M. Nie, D. Chalasani, D. P. Abraham, Y. Chen, A. Bose, and B. L. Lucht, *J. Phys. Chem. C*, **117**, 1257 (2013).
30. D. Aurbach, Y. Gofer, M. Ben-Zion, and P. Aped, *J. Electroanal. Chem.*, **339**, 451 (1992).
31. M. Onuki, S. Kinoshita, Y. Sakata, M. Yanagidate, Y. Otake, M. Ue, and M. Deguchi, *J. Electrochem. Soc.*, **155**, A794 (2008).
32. R. Bernhard, M. Metzger, and H. A. Gasteiger, *J. Electrochem. Soc.*, **162**, A1984 (2015).
33. D. Strmcnik, I. E. Castelli, J. G. Connell, D. Haering, M. Zorko, P. Martins, P. P. Lopes, B. Genorio, T. Østergaard, H. A. Gasteiger, F. Maglia, B. K. Antonopoulos, V. R. Stamenkovic, J. Rossmeisl, and N. M. Markovic, *Nature Catalysis*, **1**, 255 (2018).
34. M. Jiang, B. Key, Y. S. Meng, and C. P. Grey, *Chem. Mater.*, **21**, 2733 (2009).
35. S. Meini, S. Solchenbach, M. Piana, and H. A. Gasteiger, *J. Electrochem. Soc.*, **161**, A1306 (2014).
36. D. Streich, C. Erk, A. Guéguen, P. Müller, F.-F. Chesneau, and E. J. Berg, *J. Phys. Chem. C*, **121**, 13481 (2017).
37. S. Meini, N. Tsiouvaras, K. U. Schwenke, M. Piana, H. Beyer, L. Lange, and H. A. Gasteiger, *Phys. Chem. Chem. Phys.*, **15**, 11478 (2013).
38. N. Mahne, S. E. Renfrew, B. D. McCloskey, and S. A. Freunberger, *Angew. Chem. Int. Ed.*, **57**, 5529 (2018).
39. A. T. S. Freiberg, M. K. Roos, J. Wandt, R. de Vivie-Riedle, and H. A. Gasteiger, *Manuscript in preparation*.
40. S. Solchenbach, M. Metzger, M. Egawa, H. Beyer, and H. A. Gasteiger, *Manuscript in preparation*.
41. M. Metzger, B. Strehle, S. Solchenbach, and H. A. Gasteiger, *J. Electrochem. Soc.*, **163**, A1219 (2016).
42. H. Wang, Z. Jusys, and R. J. Behm, *J. Electroanal. Chem.*, **595**, 23 (2006).
43. D. Pritzl, S. Solchenbach, M. Wetjen, and H. A. Gasteiger, *J. Electrochem. Soc.*, **164**, A2625 (2017).
44. I. Buchberger, S. Seidlmayer, A. Pokharel, M. Piana, J. Hattendorff, P. Kudejova, R. Gilles, and H. A. Gasteiger, *J. Electrochem. Soc.*, **162**, A2737 (2015).
45. J. A. Gilbert, J. Bareño, T. Spila, S. E. Trask, D. J. Miller, B. J. Polzin, A. N. Jansen, and D. P. Abraham, *J. Electrochem. Soc.*, **164**, A6054 (2017).
46. X.-G. Yang, Y. Leng, G. Zhang, S. Ge, and C.-Y. Wang, *J. Power Sources*, **360**, 28 (2017).
47. T. Waldmann, M. Wilka, M. Kasper, M. Fleischhammer, and M. Wohlfahrt-Mehrens, *J. Power Sources*, **262**, 129 (2014).
48. D. R. Gallus, R. Schmitz, R. Wagner, B. Hoffmann, S. Nowak, I. Cekic-Laskovic, R. W. Schmitz, and M. Winter, *Electrochim. Acta*, **134**, 393 (2014).
49. J. Wandt, A. Freiberg, R. Thomas, Y. Gorlin, A. Siebel, R. Jung, H. A. Gasteiger, and M. Tromp, *J. Mater. Chem. A*, **4**, 18300 (2016).
50. H. Zheng, Q. Sun, G. Liu, X. Song, and V. S. Battaglia, *J. Power Sources*, **207**, 134 (2012).
51. J. C. Burns, A. Kassam, N. N. Sinha, L. E. Downie, L. Solnickova, B. M. Way, and J. R. Dahn, *J. Electrochem. Soc.*, **160**, A1451 (2013).
52. R. Dedryvere, D. Foix, S. Franger, S. Patoux, L. Daniel, and D. Gonbeau, *J. Phys. Chem. C*, **114**, 10999 (2010).
53. J. Choi and A. Manthiram, *J. Electrochem. Soc.*, **152**, A1714 (2005).
54. S. Venkatraman, Y. Shin, and A. Manthiram, *Electrochem. Solid-State Lett.*, **6**, A9 (2003).
55. R. V. Chebiam, F. Prado, and A. Manthiram, *Chem. Mater.*, **13**, 2951 (2001).
56. T. Teufl, B. Strehle, P. Müller, H. A. Gasteiger, and M. Mendez, *J. Electrochem. Soc.*, **165**, A2718 (2018).

3.1.5 Effect of Ambient Storage on the Degradation of Ni-rich Positive Electrode Materials (NMC811) for Li-Ion Batteries

In this section, the article "Effect of Ambient Storage on the Degradation of Ni-rich Positive Electrode Materials (NMC811) for Li-Ion Batteries" will be presented. The study was done in collaboration with the group of Prof. Yang Shao-Horn at Massachusetts Institute of Technology (MIT). It was published in the *Journal of the Electrochemical Society* on January 6, 2017 as open access article distributed under the terms of the Creative Commons Attribution Non-Commercial No Derivatives 4.0 License.[187] The results of the publication were presented on international conferences, e.g., by Roland Jung at the 232nd Meeting of The Electrochemical Society (October 1-5, 2017) in National Harbor, USA (Abstract Number: #216).

The publication analyzes the formation of surface impurities on NMC811 in comparison to NMC111 upon exposure to ambient air. For this, electrode coatings are either prepared in an argon-filled glovebox (labelled as "fresh") or at ambient air, whereas the latter are stored for additional 3 months or 1 year at ambient air (labelled as "3 months" and "1 year"). For NMC811 we show that upon storage a significant peak in the voltage profile of the very first charge cycle is evolving, whereas for NMC111 no significant changes are observed even after one year of ambient air storage. Using Raman Spectroscopy we observe furthermore that upon storage no changes are observed for NMC111, whereas for NMC811 two intense bands are evolving. These observations indicate that NMC811, in contrast to NMC111, is very sensitive to ambient air storage. Measuring Raman spectra for several reference compounds, we are able to show that the formed surface impurities consist of a mixed phase composed of mostly nickel carbonate mixed with minor quantities of hydroxide and crystal water. This conclusion is supported by a comparison of the X-ray photoelectron spectra (XPS) of the NMC811 coatings prepared in the glovebox and the one stored for 1 year at ambient air. In particular, for the fresh sample the O 1s spectrum shows the presence of the oxygen lattice peak from the NMC lattice and the presence of a carbonate peak, proving that some residual carbonate is already present on the fresh sample as would be expected based on the previous literature.[99, 207] In contrast, for the 1 year old sample the carbonate peak intensity significantly increases and the oxygen lattice peak is completely absent, proving that a layer mostly consisting of carbonate is burying the oxygen lattice, so that it cannot be probed by XPS anymore. Investigating the Ni 2p spectra, we detect significant changes in the peak shape between the two samples, which clearly demonstrate changes in the chemical environment

around the nickel. Furthermore, the visibility of nickel on the 1 year old sample proves that nickel must be part of the surface impurity, as signals from the NMC lattice cannot be detected in the O 1s spectrum, as discussed above. Our finding that nickel is part of the surface impurity compound is contradicting the literature, in which the observed carbonate species are often arbitrarily assigned to Li_2CO_3.[102, 207-212] To quantify the total carbonate content, we inject hydrochloric acid to the sample and quantify the evolving amount of CO_2 using gas chromatography (GC). Thereby, we show that the carbonate content of the 1 year old sample increases to the 5-fold value of the fresh sample. Finally, NMC811-graphite cells are prepared and cycled 300 times. An increasingly more severe capacity fading is observed with increasing exposure of the sample to ambient air, which demonstrates that the surface film formation has a long-term effect on the stability of NMC811-graphite cells. Therefore, storage and handling of Ni-rich cathodes is an important parameter which affects the cycle life of Li-ion batteries.

Author Contributions

Roland Jung designed the experiments, prepared the electrode coatings, built the NMC-graphite cells and measured the Raman spectra. Robert Morasch built the NMC-Li cells. Roland Jung and Katherine Phillips performed the GC experiments. Pinar Karayaylali measured the XPS spectra. Roland Jung evaluated the data. Roland Jung, Yang Shao-Horn and Hubert Gasteiger wrote the manuscript. All authors discussed the results and commented on the manuscript.

Effect of Ambient Storage on the Degradation of Ni-Rich Positive Electrode Materials (NMC811) for Li-Ion Batteries

Roland Jung,[1,2,3,4,*,z] Robert Morasch,[1,4] Pinar Karayaylali,[4,5] Katherine Phillips,[3,4] Filippo Maglia,[2] Christoph Stinner,[2] Yang Shao-Horn,[3,4,5,6,] and Hubert A. Gasteiger[1,**]**

[1] *Chair of Technical Electrochemistry, Department of Chemistry and Catalysis Research Center, Technische Universität München, Garching, Germany*
[2] *BMW AG, Munich, Germany*
[3] *Research Laboratory of Electronics, Massachusetts Institute of Technology, Cambridge, Massachusetts 02139, USA*
[4] *Electrochemical Energy Laboratory, Massachusetts Institute of Technology, Cambridge, Massachusetts 02139, USA*
[5] *Department of Mechanical Engineering, Massachusetts Institute of Technology, Cambridge, Massachusetts 02139, USA*
[6] *Department of Materials Science & Engineering, Massachusetts Institute of Technology, Cambridge, Massachusetts 02139, USA*

Layered $LiNi_{0.8}Mn_{0.1}Co_{0.1}O_2$ (NMC811) is one of the high-energy positive electrode (cathode) materials for next generation Li-ion batteries. However, compared to the structurally similar $LiNi_{1/3}Mn_{1/3}Co_{1/3}O_2$ (NMC111), it can suffer from a shorter lifetime due to its higher surface reactivity. This work studied and compared the formation of surface contaminations on NMC811 and NMC111 when stored under ambient conditions using electrochemical cycling, Raman spectroscopy, and X-ray photoelectron spectroscopy. NMC811 was found to develop a surface layer of up to ~10 nm thickness that was mostly composed of nickel carbonate species mixed with minor quantities of hydroxide and water after ambient storage for 1 year, while no significant changes were observed on the NMC111 surface. The amount of carbonate species was quantified by gas chromatographic (GC) detection of carbon dioxide generated when the NMC particles were dispersed in hydrochloric acid. Surface impurity species formed on NMC811 upon ambient storage not only lead to a significant delithiation voltage peak in the first charge, but also markedly reduce the cycling stability of NMC811-graphite cells due to significantly growing polarization of the NMC811 electrode.
 [DOI: 10.1149/2.0401802jes]

Manuscript submitted November 7, 2017; revised manuscript received December 18, 2017. Published January 6, 2018. This was Paper 216 presented at the National Harbor, Maryland Meeting of the Society, October 1–5, 2017.

Secondary Li-ion batteries are alternatives to the combustion engine in vehicles, paving the way to electromobility. Andre et al. have reported that in order to reach a driving range of 300 miles, the specific energy of today's Li-ion batteries needs to be increased to ~750 Wh/kg on a cathode active material (CAM) level, corresponding, e.g., to ~200 mAh/g at an average voltage of ~3.8 V.[1] This demands the development and application of advanced positive electrode (cathode) materials and at the same time requires further improvements with respect to durability and costs for mass market penetration.[1,2] Layered lithium nickel manganese cobalt oxide ($LiNi_xMn_yCo_zO_2$, generally referred to as NMC) is one of the most promising classes of positive electrode materials with $LiNi_{1/3}Mn_{1/3}Co_{1/3}O_2$ (NMC111) being already commercialized for automotive applications.[1,3] However, its reversible capacity only reaches up to ~160 mAh/g_{NMC}[4–7] when cycled at 25°C up to 4.2 V cell voltage in NMC111-graphite full cells (i.e., ~4.3 V vs. Li/Li^+ at discharge rates of 0.1 C) or 4.4 V cell voltage (i.e., ~4.5 V vs. Li/Li^+ at 1 C). The latter results with the observed charge-averaged discharge voltage of ~3.85 V in a specific energy of ~620 Wh/kg,[7] which does not reach the above specific energy target.

Ni-rich NMCs (Ni-content >> Mn- and Co-content) have significantly higher specific capacities. In particular, reversible capacities of ~175–190 mAh/g_{NMC} have been reported for $LiNi_{0.8}Mn_{0.1}Co_{0.1}O_2$ (NMC811) at the lower cutoff voltage of 4.3 V vs. Li/Li^+ and at discharge rates of 0.2-1 C.[5,7,8] However, Ni-rich NMCs frequently exhibit faster capacity fading and shorter lifetime compared to NMC111,[5,9,10] which has in part been attributed to increasing amounts of Ni having more reactive surface oxygen.[11–14] In particular, Gauthier et al. have proposed that the reactivity of the surface oxygen in layered $LiMO_2$ (M = transition metals) can be increased from early to late transition metals, because the oxygen p-band is shifted closer to the Fermi level, rendering greater surface reactivity for NMC811 than NMC111.[11] Whether the proposed higher reactivity of nickel-rich surfaces only reduces their stability when exposed to the ambient or whether for the same state-of-charge (i.e., the same degree of delithiation during charge, controlled by the upper cutoff voltage) nickel-rich surfaces are intrinsically less stable is still unclear.

The high surface reactivity of Ni-rich positive electrodes can lead to the formation of surface impurity species upon reactions with carbon dioxide and water during ambient storage, which can cause problems during electrode slurry preparation, battery storage, and cycling.[15–18] In general, we can distinguish three processes that can be responsible for the presence of surface carbonates and hydroxides, which include i) residual impurities stemming from unreacted precursors during synthesis, ii) a higher equilibrium coverage of surface carbonates/hydroxides required to stabilize the surface of Ni-rich materials after the synthesis process, and/or iii) impurities formed during ambient storage. Paulsen et al. have shown that NMC materials can have different amounts of surface carbonates and hydroxides (referred to as the soluble base content (SBC)), which are dependent on the synthesis conditions such as Li:M ratio, temperature and reaction time.[15] If Li_2CO_3 or LiOH is used as Li-source during the synthesis, stoichiometric conversion is desired (e.g. MOOH + 0.5 Li_2CO_3 → $LiMO_2$ + 0.5 CO_2 + 0.5 H_2O having M = Ni, Co, Mn) as otherwise residual Li_2CO_3 or LiOH precursor would remain on the NMC particle surfaces.[15] When Li_2CO_3 is quantitatively converted, only a low soluble base content is present on the NMC surface.

Even though it appears intuitive to expect that an NMC without any carbonates or hydroxides on the surface should be ideal, Paulsen et al. have reported that the optimal SBC is different from zero, which is referred to as equilibrium SBC. This equilibrium SBC is given as ~20 μmol/g_{NMC} (for NMC622 with a BET surface area of ~0.2 m^2/g) and is proposed to be a surface termination which is required to stabilize the surface of the material and to allow for good cyclability rather than being a detrimental surface impurity.[15] NMCs with an SBC below the desired SBC equilibrium value have poor electrochemical performance.[15] On the other hand, too high carbonate and

*Electrochemical Society Student Member.
**Electrochemical Society Fellow.
[z]E-mail: roland.jung@tum.de

hydroxide contents (>150 μmol/g_{NMC}) cause gelation or flocculation during slurry preparation and extensive gassing during high temperature storage of charged battery cells.[15,19]

Upon storage at elevated temperature and/or high humidity, increasing carbonate contents have been reported for the Ni-rich compounds $LiNi_{0.81}Co_{0.16}Al_{0.03}O_2$,[17] $LiNi_{0.8}Co_{0.15}Al_{0.05}O_2$,[18–20] $LiNi_{0.6}Mn_{0.2}Co_{0.2}O_2$,[16] $LiNi_{0.5}Mn_{0.3}Co_{0.2}O_2$,[21] and $LiNiO_2$.[22] At the same time, Shizuka et al. have shown that NMC111 is not sensitive upon storage at 30°C, 80% relative humidity and one month of storage.[18] In most of the previously mentioned studies, the formed carbonate species are assumed to be Li_2CO_3,[12,13,15,17–20,22] although clear evidence for Li_2CO_3 is not presented. Yet, the chemical composition of the surface species is very important to understand the consequences for NMC-graphite cells.

Herein, we compare surface changes on NMC811 with those on NMC111 upon ambient storage, i.e., air storage at room temperature in the absence of excessively high humidity, and report their influence on battery cycling stability. Using X-ray photoelectron spectroscopy (XPS), Raman spectroscopy, and analysis of the carbonate content by gas chromatography (GC) we show that NMC811 is, in contrast to NMC111, sensitive when stored under ambient conditions, forming surface species mainly composed of nickel carbonate mixed with minor amounts of hydroxide and water. The presence of such impurities on NMC811 does not only induce a high initial voltage peak upon delithiation in the first charge, but also causes considerable impedance growth and capacity loss during cycling in NMC811-graphite cells. It is therefore critical to understand the formation and control the amounts of surface impurities on positive electrode materials to allow for low impedance and high cycling stability.

Experimental

Electrode preparation.—NMC electrodes were prepared by dispersing 91.5 $\%_{wt}$ of the active material particles $LiNi_{1/3}Mn_{1/3}Co_{1/3}O_2$ (NMC111, Umicore, Belgium) or $LiNi_{0.8}Mn_{0.1}Co_{0.1}O_2$ (NMC811, Umicore, Belgium), 4.4 $\%_{wt}$ conductive carbon (Super C65, Timcal, Switzerland) and 4.1 $\%_{wt}$ polyvinylidene fluoride binder (PVDF, Kynar HSV 900, Arkema, France) in N-methylpyrrolidone (NMP, anhydrous, 99.5%, Sigma-Aldrich). The powders were weighed in an Ar-filled glovebox (O_2 and H_2O < 0.1 ppm, MBraun, Germany), in which the pristine NMC materials were also stored. The slurry was mixed in a planetary mixer (Thinky, USA) at 2000 rpm for 2 × 5 minutes. In between the two mixing steps, the slurry was ultrasonicated for 10 minutes in an ultrasonic bath to break the agglomerates of the conductive carbon and achieve a more homogeneous mix of active material and Super C65. The resulting ink was spread onto aluminum foil (thickness 18 μm, MTI Corporation, USA) using a gap bar coater (RK PrintCoat Instruments, UK) with a gap size of 250 μm. After drying at 50°C, the electrodes were stored for 3 months (NMC811 3-months) or one year (NMC811 1-year and NMC111 1-year) in the laboratory at ambient air, punched and dried overnight at 120°C under dynamic vacuum in a glass oven (drying oven 585, Büchi, Switzerland) and transferred into a glovebox (O_2 and H_2O < 0.1 ppm, MBraun, Germany) without exposure to ambient air. The storage conditions, i.e., the temperature and humidity in the laboratory were 20–25°C and ~30–50%, respectively. The electrodes labeled as 'fresh' (NMC811 fresh and NMC111 fresh) had no contact to ambient air in any of the process steps, i.e., the slurry was spread onto aluminum, dried, punched and transferred into the glass oven inside the glovebox.

Graphite electrodes were prepared with graphite (MAG-D20, Hitachi), Super C65 (Timcal, Switzerland), sodium carboxymethylcellulose (Na-CMC, Dow Wolff Cellulosics) and styrene-butadiene rubber (SBR, JSR Micro) at a weight ratio of 95.8:1:1:2.2. For the slurry preparation, graphite, Super C65 and Na-CMC were dispersed in highly pure water (18 MΩcm, Merck Millipore, Germany) and mixed in a planetary mixer (Thinky, USA; at 2000 rpm for 30 minutes). Afterwards, the slurry was ultrasonicated for 10 minutes in an ultrasonic bath and SBR was added to the slurry and mixed at 500 rpm for 2 minutes. The ink was coated onto copper foil (thickness 12 μm, MTI Corporation, USA) using a gap bar coater (RK PrintCoat Instruments, UK). After the coating was dried at 50°C in air, electrodes were punched out, dried overnight at 120°C under vacuum in a glass oven (Büchi oven, see above) and transferred into a glovebox without exposure to ambient air.

The specific surface areas of the NMC materials determined by BET are 0.26 m^2/g and 0.18 m^2/g for NMC111 and NMC811, respectively.[7]

Electrochemical characterization.—Voltage profiles of the NMC electrodes were measured in coin cells (Hohsen Corp., Japan) in a half-cell NMC-lithium configuration. Cells were assembled in an argon filled glovebox (O_2 and H_2O < 0.1 ppm, MBraun, Germany) with NMC (14 mm diameter) as working and lithium foil (15 mm diameter, 0.45 mm thickness; battery grade foil, 99.9% purity, Rockwood Lithium, USA) as counter electrode, using two glass fiber separators (glass microfiber filter #691, VWR, Germany), and adding 160 μL LP57 electrolyte (1M $LiPF_6$ in EC:EMC (3:7 wt:wt), <20 ppm H_2O, BASF, Germany). The areal mass loading of the NMC electrodes was 15.3 ± 1 mg_{NMC}/cm^2. The cells were cycled in a climate chamber (Binder, Germany) at 25°C with a battery cycler (Series 4000, Maccor, USA). All cells were cycled 3 times at 0.05 C-rate between 3.0 V and 4.4 V vs. Li/Li^+, with the C-rate being referenced to the approximate reversible capacity of the NMC at 0.05 C, i.e., 170 mAh/g for NMC111 and 210 mAh/g for NMC811. Charging was done in constant current (CC) mode without a constant voltage step.

Electrochemical cycling of NMC811-graphite full-cells was performed in Swagelok T-cells, which were assembled in an argon filled glovebox (O_2 and H_2O < 0.1 ppm, MBraun, Germany), with NMC811 as working electrode (10 mm diameter) and graphite as counter electrode (11 mm diameter). The areal loading of the NMC811 electrodes was 16.4 ± 0.5 mg_{NMC}/cm^2 (2.13 ± 0.07 mAh/cm^2) and the loading of the graphite electrodes was adjusted to yield a constant balancing factor of ~1.2, referenced to the reversible capacities of NMC at a 1 C-rate and a cutoff voltage of 4.1 V vs Li/Li^+ corresponding to 130 mAh/g_{NMC} and of graphite corresponding to 355 mAh/g_C (if referenced to the reversible capacities at 0.1 C, the anode is roughly 1.1-fold oversized in areal capacity). Two glass fiber separators (glass microfiber filter, 691, VWR, Germany) punched to a diameter of 11 mm were used as separators with 80 μL of LP57 (1 M $LiPF_6$ in EC:EMC 3:7 wt/wt, < 20 ppm H_2O, BASF, Germany) electrolyte. The cells were cycled in a climate chamber (Binder, Germany) at 25°C with a battery cycler (Series 4000, Maccor, USA) between cell voltages of 3.0 and 4.0 V. All cells were cycled 300 times at 1 C with two cycles at 0.1 C at the beginning for formation as well as after every 50 cycles. Charging was done in constant current-constant voltage (CCCV) mode with a current limitation corresponding to 0.05 C, while the discharge was done in constant current (CC) mode.

Raman spectroscopy.—All Raman spectra were recorded on a HORIBA Scientific LabRAM HR Raman microscope system (Horiba, Japan) with a He-Ne laser (λ = 632.8 nm) and an objective with a 100-fold magnification to allow the focus on a single NMC particle in the NMC electrodes. Several spots were measured for each sample to assure that the measured spectra are representative for the whole sample. The Raman spectra were measured at air within ~1 h and the samples were not treated prior to the measurement. The following reference compounds (as powders) were used: $NiCO_3$, $MnCO_3$, $CoCO_3$ (Alfa Aesar, USA), $Ni(OH)_2$, Li_2CO_3, $LiOH{\cdot}H_2O$, $(NiCO_3)_2{\cdot}(Ni(OH)_2)_3{\cdot}4H_2O$ (Sigma-Aldrich, USA), and H_2O (18 MΩcm, Merck Millipore, USA). The reference compounds were measured as received without any further purification.

Gas chromatography (GC).—The determination of the carbonate content on the NMC electrodes was accomplished by using the reaction $CO_3^{2-} + 2\,HCl \rightarrow 2\,Cl^- + H_2O + CO_2$ and quantifying the amount of formed CO_2 by means of gas chromatography (GC, SRI 8610C, SRI Instruments, USA). All samples were dried at 120°C under vacuum in a glass oven, weighed in an Ar-filled glovebox (O_2

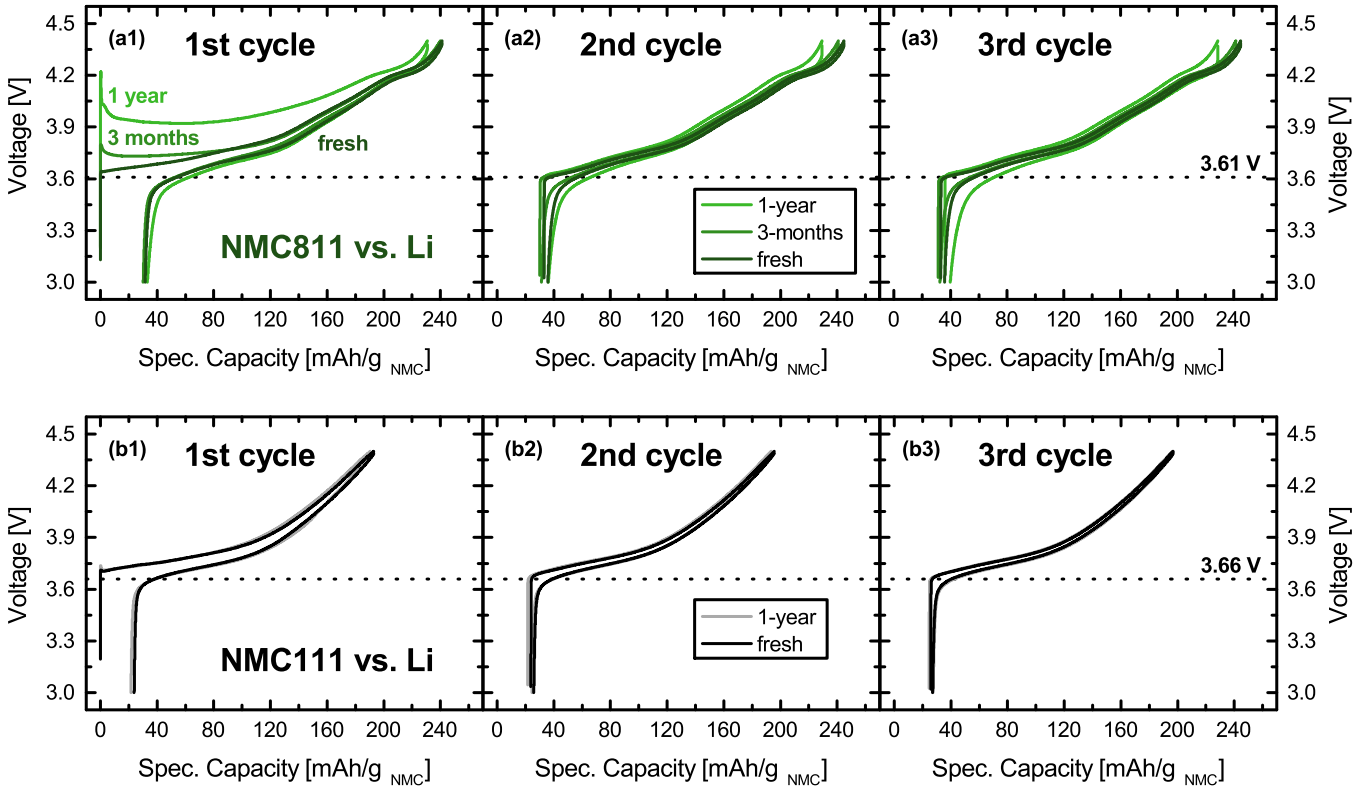

Figure 1. Voltage vs. specific capacity of the 1st, 2nd and 3rd cycle of NMC811-Li (a1, a2 and a3) and NMC111-Li half-cells (b1, b2 and b3) in LP57 electrolyte (1M $LiPF_6$ in EC:EMC 3:7) cycled between cell cutoff voltages of 3.0 V and 4.4 V at a rate of 0.05 C at 25°C (for electrode compositions see Experimental section).

and $H_2O < 0.5$ ppm, MBraun, USA) and put into 2 mL GC headspace vials (VWR, USA), which were sealed with a cap containing a silicone septum. Outside the glovebox, six droplets of 1.2 M hydrochloric acid were injected with a syringe into the vial. Afterwards, 0.5 mL of the headspace gas volume were drawn into a syringe and injected into the gas chromatograph. In order to quantify the formed amount of CO_2, the gas chromatograph was calibrated using a mixture of Li_2CO_3:NaCl 1:999 (wt:wt) prepared and measured in the same way as the samples.

X-ray photoelectron spectroscopy (XPS).—XPS spectra were measured using a PHI 5000 VersaProbe II (ULVAC-PHI, Japan) X-ray photoelectron spectrometer. The NMC electrodes were mounted in an Ar-filled glovebox (O_2 and $H_2O < 0.5$ ppm, MBraun, USA) onto the sample holder, put into a transfer vessel and dried for three hours in the small glovebox antechamber under dynamic vacuum. The transfer vessel was sealed to avoid contact to ambient air and transferred into the introduction chamber of the XPS spectrometer. The introduction chamber was evacuated and the samples were transferred to the XPS analysis chamber and measured at room temperature using a monochromatic Al-K_α (1486.6 eV) X-ray source and a spot diameter of 200 µm. All spectra were calibrated with the carbon 1s photoemission peak for adventitious hydrocarbons at 285.0 eV and background corrected using a Shirley background.

Results

Voltage profiles of fresh and aged NMC811 and NMC111.—Figure 1 shows the voltage profiles of the first three cycles of NMC811-Li (panels a1, a2 and a3) and NMC111-Li half-cells (panels b1, b2 and b3). The electrodes were stored at ambient air for one year (NMC811 1-year and NMC111 1-year), three months (NMC811 3-months), or had no contact to ambient air (NMC811 fresh and NMC111 fresh). Note, that after storage the electrodes were dried at 120°C under dynamic vacuum to remove moisture prior to cell assembly (see Experimental section). In the first cycle of the NMC811 samples (Figure 1a), an initial voltage peak appears at the very beginning of the charging process, similar to the observations in the literature for $LiNiO_2$,[22] NMC532,[21] and NMC622.[16] Its magnitude, i.e., the maximum initial peak voltage increases the longer the electrode was exposed to ambient air and reaches 3.80 V and 4.22 V for the 3-months old and for the 1-year old samples, respectively. In comparison, for the fresh sample no initial voltage peak is observed and delithiation of the NMC811 not exposed to the ambient starts at ~3.64 V. After the fresh and 3-months old samples are charged to ~80 mAh/g_{NMC}, their voltage profiles merge and no significant differences between the two coatings can be detected anymore. In contrast, the profile of the 1-year old sample does not merge with that of the fresh sample and reaches the cutoff voltage of 4.4 V at a specific capacity of 231 mAh/g_{NMC}, which is significantly lower than the specific capacity of 241 mAh/g_{NMC} reached by both the fresh and 3-months old samples. Furthermore, the charging curve of the 1-year old sample lies at higher voltages, indicating a larger resistance.

In the second and third cycle, the voltage profiles of the fresh and 3-months old samples are essentially identical, while the capacity of the 1-year old sample is lower and its charging potential remains at higher voltages, again indicating a larger resistance, albeit less severe as during the first charge (Figure 1a2 and a3). Additionally, the initial voltage peak feature of the aged samples is not anymore observed in the second and third cycles, and delithiation starts for all samples at ~3.61 V. This value is significantly lower than the 3.68 V, 3.73 V and 3.93 V, which were measured in the first cycle for the same degrees of delithiation of the fresh, 3-months and 1-year old samples, respectively (note that due to the irreversible capacity in the first cycle the here compared voltages are the values measured at ~31 mAh/g_{NMC}). This difference between the first and subsequent cycles indicates that

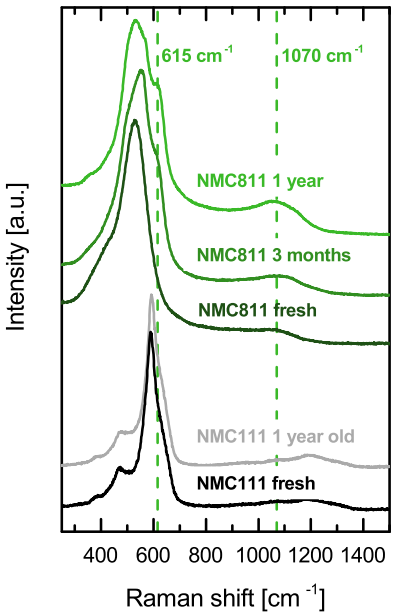

Figure 2. Raman spectra of the NMC111 and NMC811 electrodes shown in Figure 1 before cycling. The Raman spectra were measured at air within ~1 h and the samples were not treated prior to the measurement. The vertical dashed lines mark the bands of the impurities formed on NMC811 during storage at ambient air.

the reason causing the initial voltage peak for the stored samples might also be occurring on the fresh sample, albeit to a much lesser degree.

As the initial voltage peaks occurred when the electrodes were stored under ambient conditions, the formation of surface impurities is the most likely explanation. The most common impurities which can be formed by storage at ambient air are hydroxides via the reaction of the NMC surface with humidity as well as carbonates via the reaction of CO_2 with the initially formed surface hydroxides. It is known that the formation of surface impurities is more significant on Ni-rich NMC materials,[16–19,21,22] which would be consistent with the observed unchanged voltage profile and capacity after one year of ambient storage for NMC111 (see text below) in contrast to NMC811. The formation of hydroxide/carbonate surface impurities on Ni-rich surfaces could also explain the observed initial voltage peak feature, as these would likely form an insulating and therefore resistive layer covering the active material particles. Consequently, the absence of the initial voltage peak in subsequent cycles indicates that the impurity might be (at least partially) decomposed during the first charge.

In Figure 1b, similar experiments are shown for NMC111 both without ambient air exposure (NMC111 fresh) or stored for one year at ambient air (NMC111 1-year). In the first cycle (Figure 1b1) after one year of storage, only a very small initial voltage peak at the beginning of charge is observed, which has its maximum at 3.74 V. In comparison, for the fresh sample no peak is visible and delithiation starts around 3.71 V. Besides this rather small feature, the voltage profiles of the two NMC111 samples are essentially indistinguishable and their specific capacity at 4.4 V in the first cycle is 193 mAh/g_{NMC}. As in the case of the NMC811 samples, in the subsequent cycles no peak feature is observed for any of the samples and delithiation starts at ~3.66 V. At a comparable delithiation state in the first cycle, the measured voltage is 3.73 V (values measured at ~22 mAh/g_{NMC}). In analogy to the experiments with NMC811 (Figure 1a), this difference indicates the presence of a surface film also on the fresh sample, however, no significant changes occur during storage at ambient air. The presence of carbonates on fresh NMC111 would be consistent with the literature[5,15] and might be the reason for the slight difference between the first and the second cycle. A more detailed discussion on the difference of the initially present carbonate coverage to the one formed during storage for NMC811 will follow in the Discussion section.

Identification of the surface impurities upon ambient storage.— In order to examine the hypothesis that increasing amounts of carbonate and/or hydroxide species on the NMC surface lead to the initial voltage peak feature in the first charge (see Figure 1), we analyzed the electrodes using Raman spectroscopy. The measured Raman spectra of the electrodes examined in Figure 1 before cycling are displayed in Figure 2. For NMC111, two bands can be distinguished at 474 cm^{-1} and 591 cm^{-1}. As reported by Kerlau et al., these two bands are actually composed of bands at 474 cm^{-1} and 554 cm^{-1} corresponding to the Ni-O vibrations, at 594 cm^{-1} (Mn-O vibrations), and at 486 cm^{-1} and 596 cm^{-1} (Co-O vibrations), which are partially merged into one broad band.[23] For fresh NMC811, only one clear band is observed with a maximum intensity at 528 cm^{-1}; its shift to lower wave numbers compared to NMC111 can be explained by considering that for NMC811 the fraction of the Ni-O vibrations, which are observed at the lowest wave numbers, increase at the expense of the Mn-O and Co-O vibrations. As one might expect based on the cycling data presented in Figure 1, no significant differences of the Raman spectra are observed for fresh and 1-year old NMC111 (black and gray spectra in Figure 2). In contrast, the spectra of the NMC811 samples change considerably over the storage time. In particular, a shoulder in the NMC peak evolves with its maximum at ~615 cm^{-1}, and the initially rather small peak at ~1070 cm^{-1} in the fresh sample grows significantly after three months and even more after a year. We also measured Raman spectra of NMC811 electrodes dried at 120°C under dynamic vacuum, yet we observed no difference for any of the electrodes, i.e., the additional bands at ~615 cm^{-1} and ~1070 cm^{-1} are not removed during drying, which is in agreement with a very recent report by Faenza et al.[20]

To investigate the origins of the evolving Raman signals at ~615 cm^{-1} and ~1070 cm^{-1}, we compared the spectra of the battery materials with those of several carbonate and hydroxide compounds. Figure 3 depicts the Raman spectra of Li_2CO_3, $NiCO_3$, $CoCO_3$, $MnCO_3$, $LiOH*H_2O$, $Ni(OH)_2$, H_2O, $NiCO_3*x\,H_2O$, $Ni(OH)_2*x\,H_2O$, and $(NiCO_3)_2*(Ni(OH)_2)_3*4\,H_2O$ in comparison to the 1-year old NMC811 sample. Around 1070 cm^{-1}, NMC811 has a broad band (see uppermost spectrum), and it can be seen that the carbonates Li_2CO_3, $NiCO_3$, $CoCO_3$, and $MnCO_3$ (lowermost spectra) have a band that fits very well to the one observed for the NMC811 sample. In contrast to Li_2CO_3, $NiCO_3$, and $CoCO_3$, additional bands were measured for $MnCO_3$ which originate from H_2O (see the Raman spectra of H_2O in Figure 3 for comparison) due to residual moisture in the sample. A band around 1070 cm^{-1} is also observed for $LiOH * H_2O$, however, we believe that it is due to some Li_2CO_3 impurity in the $LiOH * H_2O$ (formed by a reaction of LiOH with CO_2 in air), which unfortunately is a common impurity.[24] Therefore, the band around 1070 cm^{-1} indicates that carbonates are formed on the surface; however, it is inconclusive which carbonate(s) might be present (i.e., Li_2CO_3 and/or transition metal carbonates). The fact that these surface impurities are only observed in the Raman spectra of aged NMC811 and not for aged NMC111 strongly suggests that the formation of the surface contamination is related to the nickel-content. More precisely, it may be related to the Ni^{3+} content, which is larger in the Ni-rich NMCs compared to layered oxides with low Ni-content.

In the region around the band at 615 cm^{-1} (Figure 3), it is clearly visible that this peak does not match with any of the carbonates nor with $LiOH * H_2O$. Also, $Ni(OH)_2$ does not have a band in this region; instead, water has a band close to 600 cm^{-1} (Figure 3), which might be the origin of the band at 615 cm^{-1} if it shifts when it is bound as crystal water rather than free water. To test this hypothesis, water was added to both $NiCO_3$ and $Ni(OH)_2$ and dried at 60°C under dynamic vacuum to remove most of the free water. For $NiCO_3$ mixed with water (labelled $NiCO_3*xH_2O$ in Figure 3), only the sum of the water and $NiCO_3$ spectra is measured, with no shifts of any band. In contrast, for $Ni(OH)_2$ the Raman spectrum slightly changes, indicating the formation of a hydrate. In particular, $Ni(OH)_2*xH_2O$ has the maximum intensity of

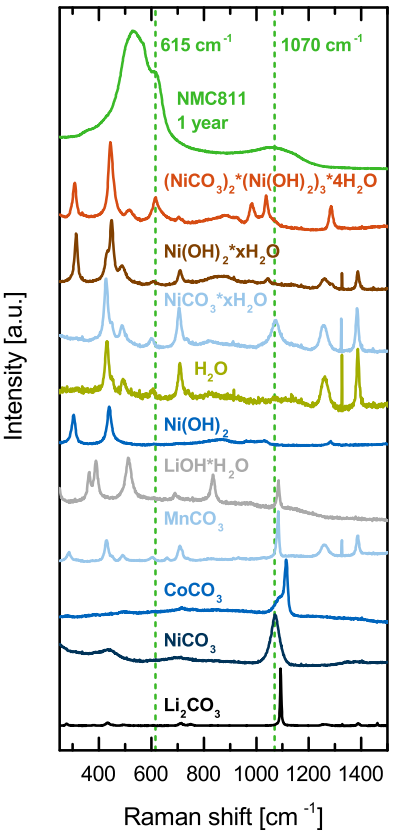

Figure 3. Raman spectra of the 1 year old NMC811 electrodes (same as in Figure 2) and of several carbonate and hydroxide reference compounds (as powders).The reference compounds were measured as received without any further purification.

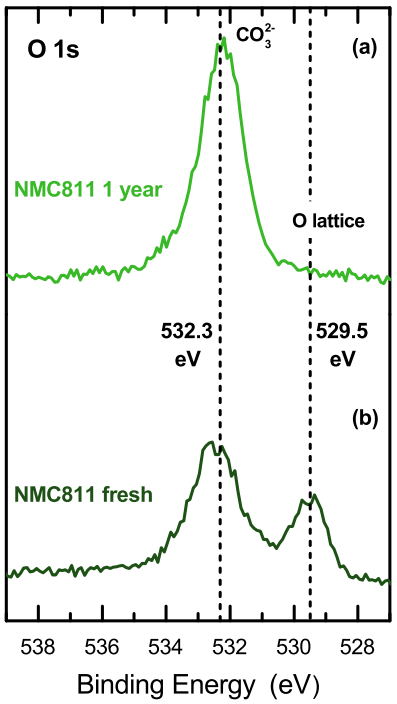

Figure 4. XPS spectra of the Oxygen 1s photoemission lines for the 1 year old (a) and fresh (b) NMC811 electrodes.

the largest band at 448 cm^{-1} and a shoulder at 433 cm^{-1}. Water-free $Ni(OH)_2$ has a band at 439 cm^{-1} and water has its largest band at 430 cm^{-1} with a shoulder at 449 cm^{-1}. The band at 488 cm^{-1} of water slightly shifts to 493 cm^{-1} in $Ni(OH)_2{*}xH_2O$. However, no significant shift was observed for the band around 600 cm^{-1} and its relative intensity even decreased. Lastly, the hydrate of the mixed crystal of nickel carbonate and hydroxide (labelled $(NiCO_3)_2{*}(Ni(OH)_2)_3{*}4H_2O$) was measured. For this compound, the band at 615 cm^{-1} is clearly visible, which shows that mixed crystals of hydroxides and carbonates display significantly altered Raman spectra compared to the pure compounds. This observation makes it very likely that a mixed hydrous carbonate hydroxide is formed, rather than two separate compounds. By comparing the Raman spectrum of this compound with the 1-year old NMC811 sample, it can be seen that the peaks at 307 cm^{-1}, 444 cm^{-1}, and 1286 cm^{-1} are not visible in the NMC811 sample. As these peaks clearly originate from the pure hydroxide or water, the mixed carbonate hydroxide compound formed on the NMC811 surface should have a much larger fraction of carbonate compared to hydroxide and water ($(NiCO_3)_x \cdot (Ni(OH)_2)_y \cdot zH_2O$ with $x \gg y, z$). This can be rationalized by considering that the hydroxide and crystal water can react with CO_2 to form the carbonate, thereby shifting the overall composition in favor of the carbonate. Also, as we did not store the material under excessively high humidity, we believe that this favors the formation of carbonates. Additionally, the bands around 1000 cm^{-1} for $(NiCO_3)_2{*}(Ni(OH)_2)_3{*}4H_2O$, which are significantly shifted compared to the pure carbonate, might cause the broadness of the band observed for the NMC811 around 1070 cm^{-1}, which is fairly narrow for the pure carbonates. While the involvement of Li and the other transition metals (Mn and Co) in the carbonate hydroxide hydrates cannot be excluded, the fact that the surface impurity is only formed on NMC811 and not on NMC111 indicates that Ni is essential for the formation of the surface film. Additionally, to the best of our knowledge, mixed crystals of Li_2CO_3 and LiOH do not exist and the shoulder at 615 cm^{-1} cannot be explained by the pure lithium compounds. Therefore, an involvement of nickel in the surface impurity appears very likely and the commonly stated assumption that all the impurities are due to LiOH and Li_2CO_3[12,13,15,17–19,22] would be inconsistent with our data and thus seems incorrect.

To gain further insight into the chemical nature of the surface impurity, XPS spectra were measured. Figure 4 depicts the oxygen 1s spectra of the 1-year old (a) and fresh (b) NMC811 samples. For the fresh sample, two well-separated peaks are observed at 532.3 eV, which corresponds to carbonate,[25,26] and at 529.5 eV[26] corresponding to the NMC lattice oxygen. The presence of carbonate even on the fresh sample is in agreement with the literature,[5,15] the Raman spectra (Figure 3), and the voltage profiles (Figure 1). In the 1-year old sample, the peak corresponding to the lattice oxygen is not visible anymore and only the intense carbonate peak can be observed, consistent with the observations by Shkrob et al.[21] and Liu et al.[22] This clearly indicates the growth of a surface layer of carbonate species covering the lattice oxygen on the surface of the 1-year old sample. As described by Seah et al., the inelastic mean free path of an electron can be estimated by $\lambda = B \cdot E^{0.5}$ with E being the energy of the photoelectron (in units of eV) and B being a material constant, which they showed to be around 0.096 nm for inorganic compounds.[27] For the ~1000 eV of the O 1s photoelectron (~1500 eV of the incident beam minus ~500 eV binding energy), the calculated inelastic mean free path is ~3 nm. Using Lambert-Beer's law, the O 1s lattice oxygen signal would decay to ~3% (and thus become undetectable in our measurements), if the surface were covered with an impurity layer of ~10 nm. Hence, the absent lattice oxygen signal for the 1-year old sample indicates that the surface contamination after one year of storage at ambient air should have a thickness in the range of ~10 nm, as discussed in more detail in the Discussion section. Additionally, the absence of a clearly pronounced hydroxide peak at 530.8 – 531.1 eV for LiOH[26,28,29] or at 530.8 – 531.0 eV for $Ni(OH)_2$[30,31] indicates only minor fractions of hydroxides on both the fresh and 1 year old sample, consistent with the expectations based on the Raman spectra (Figure 3) and previous reports in the literature.[17–19,22]

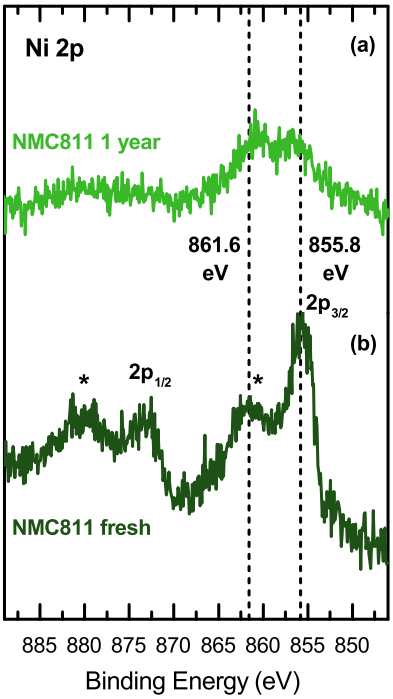

Figure 5. XPS spectra of the Nickel 2p photoemission lines for the 1 year old (a) and fresh (b) NMC811 electrodes. The peaks marked by a * are the satellites of the respective $2p_{3/2}$ and $2p_{1/2}$ peaks.

Figure 5 shows the corresponding nickel 2p spectra of the above discussed samples. The fresh NMC811 sample has two peaks, which are due to the spin-orbit splitting of the Ni 2p states ($2p_{3/2}$ and $2p_{1/2}$), and one satellite (marked by *) for each of the two 2p-states in analogy to $LiNi_{0.5}Co_{0.5}O_2$[32] and $LiNiO_2$.[22] For the NMC811 sample after storage in air for one year, the $2p_{3/2}$ peak slightly shifts to higher binding energies, while its satellite shifts to lower binding energies. Interestingly, this is in contrast to the report by Liu et al.[22] who observed a significant shift by 1.5 eV toward lower binding energies for the Ni $2p_{3/2}$ peak of $LiNiO_2$ after one year of ambient storage. However, they also detected a fraction of ∼13% of Li_2CO_3 of the total electrode material weight which is roughly 30-times more than what we detected (see below). Additionally, in Figure 5 the satellite peaks become larger with respect to the non-satellite peaks. While this feature is hard to interpret, the even more interesting observation is that nickel species are still visible after one year even though the lattice oxygen signals measured at the same time on the same sample is not visible anymore (see Figure 4). This is important, because the sensitivity for nickel is even lower than for oxygen (based on the above equation, the inelastic mean free path for Ni 2p is only ∼2.5 nm compared to ∼3 nm for O 1s), and if nickel would only be present in the NMC lattice and not in the surface impurity layer, it should not be detectable on the 1-year stored NMC811 as is the case for lattice oxygen. This observation demonstrates that nickel is still on the surface, but now bound in the surface impurity layer.

We also measured carbon 1s spectra, however, since the electrodes contain both Super C65 carbon as well as PVDF no conclusions can be drawn from these spectra.

Quantification of the surface impurities upon ambient storage.— Raman spectroscopy and XPS indicate that the vast majority of the formed contamination is carbonate, so that a quantification of the carbonate content is expected to be close to the total impurity content. For quantification, we applied gas chromatography as it has very low detection limits, good sensitivity, and allows the use of very low sample amounts of the electrode coatings. For the determination of the carbonate content we made use of the reaction $CO_3^{2-} + 2\,HCl \rightarrow 2\,Cl^- + H_2O + CO_2$ and quantified the amount of formed CO_2 (see Experimental section). The results are summarized in Table I and show that the fresh NMC111 and NMC811 electrode samples have very similar initial carbonate contents of 0.07 – 0.08$\%_{wt}$ The presence of carbonate on the fresh sample is consistent with the results obtained by XPS (Figure 4).

Table I. Mass fractions of CO_3^{2-} in $\%_{wt}$ on the NMC surface measured by gas chromatographic analysis of fresh and aged electrodes (error bars represent the standard deviation from at least four repeat measurements) as well as the calculated carbonate layer thickness assuming a compact layer with the crystallographic density ρ = 4.358 g/cm³ [33] of $NiCO_3$.

	CO_3^{2-} mass fraction [$\%_{wt}$]	Layer thickness [nm]
NMC811 fresh	0.08 ± 0.01	2.0 ± 0.3
NMC811 3-months	0.27 ± 0.05	6.8 ± 1.2
NMC811 1-year	0.39 ± 0.06	9.8 ± 1.5
NMC111 fresh	0.07 ± 0.02	1.2 ± 0.4
NMC111 1-year	0.08 ± 0.01	1.4 ± 0.2

If the mass ratios of carbonate were to be converted to lithium carbonate to compare it to the literature, the given values in Table I have to be multiplied by the ratio of the molar masses M of lithium carbonate and carbonate, i.e., $M(Li_2CO_3)/M(CO_3^{2-}) = 1.23$. For the fresh NMC111 and NMC811 electrodes, this would yield 0.09 and 0.1 $\%_{wt}$ Li_2CO_3, respectively, which is very close to the commonly reported values for NMC111.[5] During storage at ambient air, the carbonate content on NMC111 remains essentially constant, consistent with the voltage profiles (Figure 1b) and Raman spectra (Figure 2) which are identical for fresh and aged NMC111 electrodes. In contrast, the carbonate contents of NMC811 electrodes increase significantly from 0.08$\%_{wt}$ (fresh) to 0.27$\%_{wt}$ after three months and to 0.39$\%_{wt}$ after one year of ambient storage, which matches the expectations based on the voltage profiles (Figure 1a) and Raman spectra (Figure 2 and Figure 3). The theoretical layer thickness of the formed surface film during storage is shown in the last column of Table I. Thus the estimated layer thickness of ∼10 nm for the 1-year aged NMC811 electrode is consistent with the fact that no lattice oxygen O 1s signal can be observed anymore for this sample (see Figure 4); this will be discussed further in the Discussion section.

Cycling of NMC811-graphite full-cells.— To investigate the impact of the surface contamination on full-cells, NMC811-graphite T-cells equipped with a lithium reference electrode were cycled over 300 times and their discharge curves were compared. Figure 6a shows the specific discharge capacity (left y-axis) and coulombic efficiency (right y-axis) of these cells vs. cycle number. Note that in contrast to the voltage profiles depicted in Figure 1, the upper cutoff voltage was limited to 4.0 V cell potential (∼4.1 V vs. Li/Li^+ for the NMC cathode), which we showed in a recent publication to be the limit for the here used NMC811 material in order to avoid significantly growing cathode impedances due to the release of lattice oxygen from the surface of the NMC811 particles[7] (note that the upper cutoff potential limit for stable cycling performance might be different for NMC811 from different suppliers). As expected based on the voltage profiles and capacities shown in Figure 1, the initial capacities both at 1 C (solid lines) and 0.1 C (single data points) of the fresh and 3-months old electrodes are similar, but very different to the 1-year old sample. This underlines the significant damage to the material after one year of storage at ambient air. Interestingly, the specific capacity of the 1-year old NMC increases significantly over the first ∼25 cycles, analogous to what was reported for NMC532[21] over the course of a short 4-cycle test. We believe this is due to a more incomplete decomposition of the carbonate species within the first cycles, as the upper cutoff voltage was reduced compared to the data in Figure 1 (note that the initial voltage peak on the 1-year aged NMC811 electrode was at 4.22 V vs. Li/Li^+, which is slightly above the upper cutoff voltage used for Figure 6). Table II summarizes the specific capacity and energy retentions

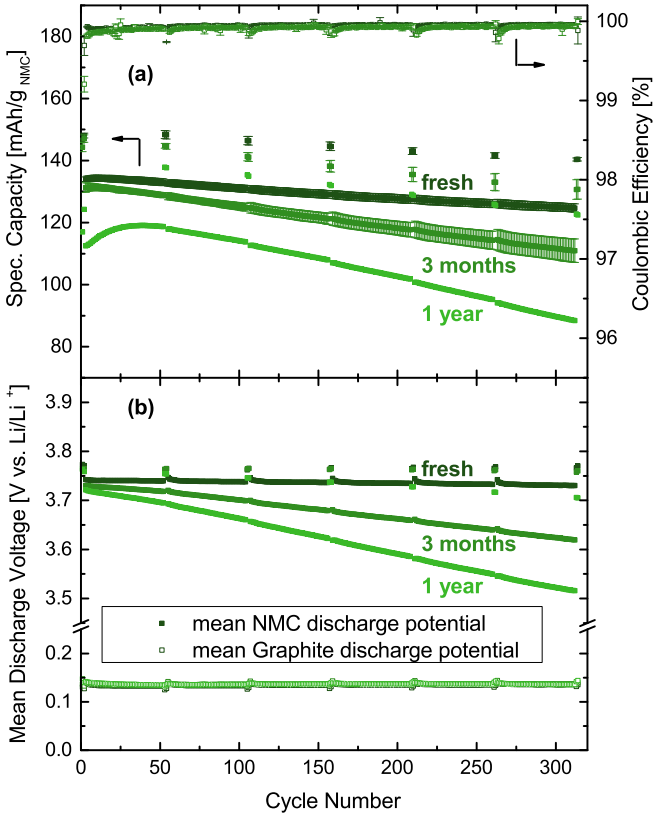

Figure 6. (a) Specific discharge capacity and coulombic efficiency of NMC811-graphite full-cells equipped with a lithium reference electrode for NMC811 cathodes which had no contact to ambient air (fresh) or which were stored for either 3 months or 1 year at ambient air prior to cell assembly. (b) Charge-averaged mean discharge voltage (s. Eq. 1) of the NMC811 cathodes ($\equiv \bar{V}^{cathode}_{discharge}$; full squares) and the graphite anodes ($\equiv \bar{V}^{anode}_{discharge}$; blank squares) vs. cycle number in LP57 electrolyte (1 M $LiPF_6$ in EC:EMC 3:7). The cells were operated between 3.0 V and 4.0 V cell potential at 25°C. Formation was done at a rate of 0.1 C (2 cycles) and cycling was performed at 1 C with two cycles at 0.1 C after every 50 cycles. The error bars for the fresh and 3-months electrodes represent the standard deviations of two repeat measurements.

of the cells depicted in Figure 6. The cells with fresh NMC811 have a very stable cycling performance (dark green squares), with a specific discharge capacity of 134 mAh/g_{NMC} in cycle 4 and 125 mAh/g_{NMC} in cycle 312 (both at a 1 C-rate) corresponding to a capacity retention of 93%. In contrast, the cells containing the 3-months old NMC811 (green squares) fade from 131 mAh/g_{NMC} (cycle 4) to 111 mAh/g_{NMC} (cycle 312), yielding a lower capacity retention of 84%. Lastly, the 1-year old NMC811 exhibits the poorest performance with a capacity of only 88 mAh/g_{NMC} in cycle 312 (light green line). Due to the increasing capacity for the first ~50 cycles we chose the capacity of 118 mAh/g_{NMC} measured in cycle 55 as 'initial' capacity yielding a capacity retention of 75%. The capacity retentions at a 0.1 C-rate are 94% and 89% for the fresh and the 3-months aged NMC811 (cycle 2 to 314) and 88% for the 1-year old NMC811 (cycle 54 to 314). The almost equal capacity retentions for the fresh samples at both C-rates indicate the absence of a significant impedance growth. This is in contrast to the 3-months and 1-year old samples which have higher capacity fading rates at 1 C compared to 0.1 C, as is summarized in Table II. The averaged coulombic efficiencies for the fresh and 3-months old samples at 1 C are >99.9%. For the 1-year old sample the coulombic efficiency in the first 50 cycles is in average ~99.8% and increases to >99.9% in the subsequent cycles.

In order to better understand how the formation of surface impurities causes poorer cycling performance, the charge-averaged mean discharge voltage of the NMC and the graphite electrodes are plotted in Figure 6b. The charge-averaged mean discharge voltage is defined according to Eq. 1 and can be used to monitor changes in the polarization during cell discharge.

$$\bar{V}_{discharge} = \int V_{discharge} \cdot dq_{discharge} \,/\, \int dq_{discharge} \qquad [1]$$

As the cells were cycled with a lithium reference electrode, $\bar{V}_{discharge}$ can be determined independently for the NMC811 cathode ($\equiv \bar{V}^{cathode}_{discharge}$) and the graphite anode ($\equiv \bar{V}^{anode}_{discharge}$) as a function of the cycle number, which is depicted by the full and blank squares in Figure 6b, respectively. It can be seen that $\bar{V}^{anode}_{discharge}$ is perfectly constant for all NMC811 electrodes over the 314 cycles (the small deviations every 50th cycle are caused by the change between C-rates of 1 C and 0.1 C). This independence of $\bar{V}^{anode}_{discharge}$ for fresh and aged NMC811 cathodes indicates that there is no significant cross-talk between anode and cathode,[34–36] i.e., while the impurity level of the various NMC811 electrodes obviously affects capacity retention (Figure 6a), it does not seem to affect the graphite anode (e.g., by releasing any soluble species into the electrolyte, which could be deposited on the graphite and thus would be expected to affect its impedance). In contrast, $\bar{V}^{cathode}_{discharge}$ strongly depends on the extent of aging of the NMC electrodes. In particular, in cycle 3 (i.e., the 1st cycle at 1 C), $\bar{V}^{cathode}_{discharge}$ is highest for the fresh and lowest for the 1-year old NMC811 electrodes, indicating a larger initial impedance on the stored NMC samples. During cycling, the mean discharge voltage of the fresh NMC811 cathodes remains essentially constant; however, a significant decrease in the mean discharge voltage is detected for the 3-months and even more so for the 1-year old NMC811 cathodes. Therefore, it is clear that the buildup of surface impurities during exposure to the ambient causes a higher initial impedance, which gradually increases during cycling concomitant with a deterioration of the NMC811-graphite cell performance. The impedance buildup is further supported by the fact that the difference between the mean discharge voltages of the 1-year old and the fresh NMC811 electrodes at 0.1 C only grows from ~10 mV (2nd cycle) to ~65 mV (314th cycle), in contrast to the much larger difference developing at 1C, starting at ~20 mV (3rd cycle) and ending at ~210 mV (312th cycle). Quite clearly, surface impurities produced during exposure of NMC811 to the ambient do not only deterioriate

Table II. Measured specific capacity and specific energy retentions in NMC-graphite full-cells between the 4th and 312th cycle at 1C and between the 2nd and 314th cycle at 0.1 C of the fresh and 3-months old NMC811 electrodes and between the 55th and 312th (1C) and the 54th and 314th cycle (0.1 C) of the 1-year old NMC811 electrodes extracted from the data depicted in Figure 6. The values in brackets are the specific capacities (left columns) in units of mAh/g_{NMC} and the specific energies (right columns) in units of mWh/g_{NMC} of the respective cycles.

	specific capacity		specific energy	
	1 C	0.1 C	1 C	0.1 C
NMC811 fresh	93 % (134 → 125)	94 % (149 → 140)	93 % (483 → 448)	94 % (541 → 510)
NMC811 3 months	84 % (131 → 111)	89 % (147 → 131)	82 % (472 → 386)	87 % (534 → 474)
NMC811 1 year	75 % (118 → 88)	88 % (138 → 122)	71 % (419 → 299)	87 % (501 → 435)

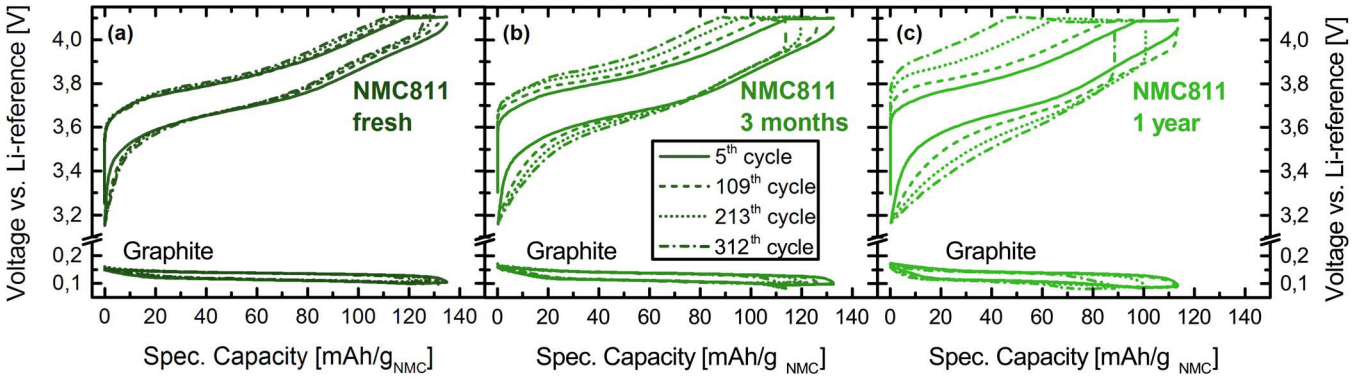

Figure 7. Voltage profiles of the 5th, 109th, 213th, and 312th cycles (all at 1 C-rate) of the cells depicted in Figure 6. The voltage profiles of the NMC811 cathode and graphite anode are shown versus the Li-reference electrode. The NMC811 cathodes had (a) no contact to ambient air or were stored for (b) 3 months or (c) 1 year at ambient air.

its initial capacity and mean discharge voltage, but also lead to an increasing impedance growth over extended charge/discharge cycles.

From Figures 6a and 6b the discharge energy for each cycle can be calculated as the product of capacity and $\bar{V}_{discharge} = \bar{V}^{cathode}_{discharge} - \bar{V}^{anode}_{discharge}$. Due to the substantially decreasing mean discharge voltage of the 3-months and 1-year old samples at 1 C-rate, their specific energy retentions (right-hand columns in Table II) are lower than the capacity retentions, contrary to the nearly identical capacity and energy retention of the fresh sample. At the lower rate of 0.1 C, the difference between capacity and energy retentions are minor for all samples.

Figure 7 shows the voltage profiles of the (a) fresh, (b) 3 months, and (c) 1 year old NMC811 and the respective graphite electrodes, both versus the Li-reference electrode, of the cells depicted in Figure 6. As already discussed above, the voltage profiles of the graphite anodes show no significant changes in their polarization in dependence of the cycle number and only become 'shorter' due to the loss of specific capacity. The voltage profile of the fresh NMC811 (Figure 6a) slightly shifts to lower specific capacities, yet the potential difference between the charge and the discharge curve, i.e., the polarization stays fairly constant. The share of the specific capacity delivered during the CV-phase is 11.8% in the 5th cycle and 11.4% in the 312th cycle, underlining once more the constant polarization during cycling of the NMC811 without air contact. In contrast, the voltage profiles of the NMC811 stored at ambient air significantly widen with increasing cycle number (Figures 6b and 6c). This effect is even more pronounced for the one stored for 1 year at air compared to the one which was stored for 3 months. For the 3-months old NMC811 the specific capacity share of the CV-phase is significantly increased from 13.9% (5th cycle) to 23.0% (312th cycle), while it is increased even more from 14.2% (5th cycle) to 47.2% (312th cycle) for the 1 year old NMC811.

Discussion

Estimation of the surface layer thickness.—Our Raman and XPS data indicate that the formed carbonates are $NiCO_3$ species mixed with minor fractions of hydroxide and water. We believe that the rather low fractions of hydroxide and water are a consequence of the storage conditions as we stored the material at ambient air rather than at high temperature and/or high humidity. The latter conditions seem to favor hydroxide formation, as storage experiments with NMC622 at 55°C and 80% relative humidity conducted by Chen et al.[16] showed LiOH Raman bands, contrary to our observations (Figure 3). Additionally, these authors reported a weight increase of NMC622 at their conditions after six weeks of about 5%, roughly an order of magnitude higher than what we observed. The formation of $NiCO_3$ species is in contrast to the literature, in which the carbonate species are typically assigned to Li_2CO_3,[12,13,15–19,22] yet no clear evidence was provided for this assumption. Interestingly, Shizuka et al.[18] and Liu et al.[22] reported for both NCA and $LiNiO_2$ a partial reduction of Ni^{3+} to Ni^{2+} upon storage, yet they still assumed the carbonate species to be Li_2CO_3. However, if Li^+ is removed from the layered oxide structure, an oxidation of the Ni-ions would be expected. Therefore, we believe that the reported partial reduction of Ni^{3+} to Ni^{2+} is actually due to Ni-reduction upon formation of the $NiCO_3$ species.

The observed initial potential peak during the first charge (Figure 1) indicates that the surface impurity forms a resistive film around the NMC811 particles, which, at least partially, has to be decomposed before delithiation can occur, because the initial delithiation potential of the NMC actually lies at lower potentials than the initial voltage peak and should therefore happen before if there were no kinetic barriers. A similar initial potential peak was reported in the literature upon storage of NMC532[21] and $LiNiO_2$.[22] The (partial) decomposition of the surface impurity film is supported by the absence of the initial potential peak feature in the second and third charge cycle (Figure 1). In the following, we will estimate the surface layer thickness based on the determined carbonate contents summarized in Table I. In the patent by Paulsen et al., the equilibrium soluble base content (SBC), which is required to allow for a stable cycling performance, was measured using pH-titration and was determined to be ~20 $\mu mol/g_{NMC}$ for NMC622 with a BET surface area of 0.2 m^2/g.[15] If we assume that all the impurity is CO_3^{2-}, it corresponds to a weight fraction of 0.12 $\%_{wt}$, which is very close to the values shown in Table I for the fresh NMC811 and NMC111 electrodes. Therefore, the low carbonate contents of the fresh materials are most probably the carbonate from the equilibrium coverage, and the presence of any residual Li_2CO_3 from the synthesis can likely be excluded. In the following, we will estimate the total surface layer thickness, including the contribution from the equilibrium coverage layer.

The total surface layer thickness is estimated as a homogeneous, compact layer of $NiCO_3$ around the NMC particles. The particle radius r_{NMC} of the NMC particle was calculated using the BET-surface area and assuming spherical particles (Eq. 2) with a crystallographic density of NMC of $\rho_{NMC} = 4.8\ g/cm^3$.

$$r_{NMC} = \frac{3}{A_{BET} * \rho_{NMC}} \quad [2]$$

The volume V_{NMC} and mass m_{NMC} of a NMC particle can be calculated with the radius r_{NMC} and ρ_{NMC} (Eqs. 3 and 4).

$$V_{NMC} = \frac{4}{3 * \pi * r_{NMC}^3} \quad [3]$$

$$m_{NMC} = V_{NMC} * \rho_{NMC} \quad [4]$$

With the mass ratio of carbonate (Table I) multiplied by $M(NiCO_3)/M(CO_3^{2-}) = 1.98$ ($M(NiCO_3)$ is the molar mass of nickel

carbonate) and m_{NMC}, the mass of the surface layer m_L is calculated. Dividing m_L by the density $\rho_L = 4.358$ g/cm^3 [33] of $NiCO_3$ the volume of the surface layer V_L is obtained. Since the NMC particle including the surface impurity has the volume of $V_{NMC+L} = V_{NMC} + V_L$, the radius r_{NMC+L} can be calculated. By subtracting r_{NMC} from r_{NMC+L}, the layer thickness is obtained, as summarized in Table I. For NMC811, the total surface (carbonate) layer thickness after storage at ambient air increases from ∼2 nm (fresh NMC811) to ∼7 nm and ∼10 nm after three months and one year, respectively. This calculated layer thickness is in good agreement with the surface layer reported by Shkrob et al. using STEM.[21] For the obtained total surface layer thickness of ∼10 nm after one year of ambient air storage of the NMC811 sample, the O 1s oxygen lattice signal would be expected to be attenuated by 97% based on the estimated mean free path of ∼3 nm (as derived above), while the total surface layer thickness of the fresh sample (∼2 nm) would result in an attenuation by only ∼48%. This is consistent with the pronounced O 1s lattice signal for the fresh NMC811 sample and its complete absence for the 1-year old sample (Figure 4).

Consequences of the surface layer formation on NMC811 cells.—Our results clearly show that NMC811 is very sensitive to air contact, contrary to NMC111 for which no changes after one year of storage were observed. This illustrates a growing sensitivity to air with increasing nickel contents (possibly related to the growing Ni^{3+} content in Ni-rich NMCs) and makes it very crucial to store the material under inert atmosphere and to potentially use a controlled atmosphere during electrode processing like slurry preparation to maximize capacity and cycle-life. In Figure 6 we showed that the formation of surface impurities upon ambient storage has a very detrimental long-term effect on NMC811-graphite cells, as it causes the impedance on the NMC811 cathode to increase gradually (Figure 6b), leading to the observed decrease in cycling stability. This gradual impedance increase during cycling is larger as the exposure time to ambient air is increased and is not observed for the fresh NMC811 (Figure 6b). The presence of the initial potential peak only in the very first cycle (Figure 1) strongly suggests a decomposition of the carbonate surface layer during the first charge (to 4.4 V vs. Li/Li^+, Figure 1), which subsequently may cause the continuous impedance buildup. It may be possible that the products of the decomposed carbonate layer either decrease the electrochemical stability of the electrolyte or chemically react with the electrolyte forming a growing layer on the NMC particles, both of which may be observed as an increasing impedance on the NMC811 cathode. Additionally to the carbonate decomposition, a further cause of the steadily growing impedance may be due to a Li^+/H^+ exchange mechanism as proposed by Shkrob et al.[21] This mechanism may explain the increase of the specific capacity over the first ∼25 cycles of the 1-year old NMC811 cells in Figure 6 by removing the H^+ ions over several cycles and intercalating Li^+ ions from the electrolyte instead.[21] The presence of protons in the electrolyte may subsequently form HF with the $LiPF_6$ salt causing an etching of the NMC active material, which in consequence may cause the observed steady impedance increase. Nevertheless, to fully understand the exact underlying mechanism further studies are required. While it is beyond the scope of this work to explain the detailed mechanism underlying this observation, we believe that the involvement of nickel in the surface impurity is likely to be the reason for the irreversible damage to the NMC811 material, namely by inducing a surface reconstruction causing loss of active material and yielding a surface layer, which is most probably detrimental for the Li-diffusion. The latter is most likely the major reason for the very negative impact of the surface impurity, since the carbonate mass fractions in Table I are rather small, so that the overall active material loss by itself cannot explain the observed continuous long-term degradation of the NMC811-graphite cells (Figure 6). With this work we want to stress that the surface contamination has a detrimental long-term effect on NMC-graphite cells and therefore contact of Ni-rich materials to ambient air has to be avoided or at least reduced to a minimum in order to allow for stable cycling performance. Our results demonstrate that storage and handling of Ni-rich materials is a parameter of growing importance, when NMC111 is replaced by Ni-rich cathodes in Li-ion batteries.

Conclusions

In this work we reported on the severe surface reactivity of NMC811 compared to NMC111. We showed that even after one year of storage at ambient air, the NMC111 surface remained unchanged. In contrast, the amount of surface impurities increased significantly for the NMC811 samples stored for three months and one year under ambient conditions. In particular, we show that both NMC111 and NMC811 have initial carbonate contents of 0.07 – 0.08%$_{wt}$, which stay constant for NMC111 and increase by a factor of 5 to 0.39%$_{wt}$ for NMC811 after one year of ambient storage. Using Raman spectroscopy and XPS we found that the majority of the impurities formed on the NMC811 surface are carbonates with minor fractions of hydroxides and water. We clearly show that Ni is part of the surface impurity, which necessarily leads to extraction of Ni from the layered NMC structure, decomposing the surface of the NMC.

By cycling these NMC811 electrodes in NMC-graphite cells with a lithium reference electrode, we showed that ambient air storage of NMC811 not only leads to faster capacity fading rates, but also increases the impedance of the NMC811 cathode. On the other hand, the impedance of the graphite anode is not affected by the deterioration of the cathode, indicating the absence of obvious cross-talk effects as, for example, transition metal deposition on the anode. Therefore, our results clearly demonstrate that NMC811 should be stored under inert conditions and that its handling is due to the higher surface reactivity more challenging than NMC111, which has to be accounted for when NMC111 is replaced by NMC811 in Li-ion batteries.

Acknowledgment

The authors thank BMW AG for the financial support of this work. Umicore is greatly acknowledged for supplying the NMC materials. R.J. thanks TUM-IAS for their support in the frame of the Rudolf-Diesel Fellowship of Dr. Peter Lamp. This work made use of the MRSEC Shared Experimental Facilities at MIT, supported by the National Science Foundation under award number DMR-1419807.

References

1. D. Andre, S.-J. Kim, P. Lamp, S. F. Lux, F. Maglia, O. Paschos, and B. Stiaszny, *J. Mater. Chem. A*, **3**, 6709 (2015).
2. O. Groeger, H. A. Gasteiger, and J.-P. Suchsland, *J. Electrochem. Soc.*, **162**, A2605 (2015).
3. K. G. Gallagher, S. Goebel, T. Greszler, M. Mathias, W. Oelerich, D. Eroglu, and V. Srinivasan, *Energy Environ. Sci.*, **7**, 1555 (2014).
4. I. Belharouak, Y. K. Sun, J. Liu, and K. Amine, *J. Power Sources*, **123**, 247 (2003).
5. H.-J. Noh, S. Youn, C. S. Yoon, and Y.-K. Sun, *J. Power Sources*, **233**, 121 (2013).
6. I. Buchberger, S. Seidlmayer, A. Pokharel, M. Piana, J. Hattendorff, P. Kudejova, R. Gilles, and H. A. Gasteiger, *J. Electrochem. Soc.*, **162**, A2737 (2015).
7. R. Jung, M. Metzger, F. Maglia, C. Stinner, and H. A. Gasteiger, *J. Electrochem. Soc.*, **164**, A1361 (2017).
8. J. Li, L. E. Downie, L. Ma, W. Qiu, and J. R. Dahn, *J. Electrochem. Soc.*, **162**, A1401 (2015).
9. W. Liu, P. Oh, X. Liu, M.-J. Lee, W. Cho, S. Chae, Y. Kim, and J. Cho, *Angew. Chem., Int. Ed.*, **54**, 4440 (2015).
10. J. Zheng, W. H. Kan, and A. Manthiram, *ACS Appl. Mater. Interfaces*, **7**, 6926 (2015).
11. M. Gauthier, T. J. Carney, A. Grimaud, L. Giordano, N. Pour, H.-H. Chang, D. P. Fenning, S. F. Lux, O. Paschos, C. Bauer, F. Maglia, S. Lupart, P. Lamp, and Y. Shao-Horn, *J. Phys. Chem. Lett.*, **6**, 4653 (2015).
12. D. Aurbach, *J. Power Sources*, **89**, 206 (2000).
13. D. Aurbach, K. Gamolsky, B. Markovsky, G. Salitra, Y. Gofer, U. Heider, R. Oesten, and M. Schmidt, *J. Electrochem. Soc.*, **147**, 1322 (2000).
14. L. Giordano, P. Karayaylali, Y. Yu, Y. Katayama, F. Maglia, S. Lux, and Y. Shao-Horn, *J. Phys. Chem. Lett.*, **8**, 3881 (2017).
15. J. Paulsen and J. H. Kim, ed. US2014/0054495A1, USA, 2012.
16. Z. Chen, J. Wang, J. Huang, T. Fu, G. Sun, S. Lai, R. Zhou, K. Li, and J. Zhao, *Journal of Power Sources*, **363**, 168 (2017).
17. K. Matsumoto, R. Kuzuo, K. Takeya, and A. Yamanaka, *J. Power Sources*, **81–82**, 558 (1999).
18. K. Shizuka, C. Kiyohara, K. Shima, and Y. Takeda, *J. Power Sources*, **166**, 233 (2007).
19. J. M. Paulsen, H.-K. Park, and Y. H. Kwon, ed. US8574541, USA, 2013.

20. N. V. Faenza, L. Bruce, Z. W. Lebens-Higgins, I. Plitz, N. Pereira, L. F. J. Piper, and G. G. Amatucci, *J. Electrochem. Soc.*, **164**, A3727 (2017).
21. I. A. Shkrob, J. A. Gilbert, P. J. Phillips, R. Klie, R. T. Haasch, J. Bareño, and D. P. Abraham, *Journal of The Electrochemical Society*, **164**, A1489 (2017).
22. H. S. Liu, Z. R. Zhang, Z. L. Gong, and Y. Yang, *Electrochem. Solid-State Lett.*, **7**, A190 (2004).
23. M. Kerlau, M. Marcinek, V. Srinivasan, and R. M. Kostecki, *Electrochimica Acta*, **52**, 5422 (2007).
24. K. U. Schwenke, M. Metzger, T. Restle, M. Piana, and H. A. Gasteiger, *Journal of The Electrochemical Society*, **162**, A573 (2015).
25. A. T. Appapillai, A. N. Mansour, J. Cho, and Y. Shao-Horn, *Chemistry of Materials*, **19**, 5748 (2007).
26. Y.-C. Lu, A. N. Mansour, N. Yabuuchi, and Y. Shao-Horn, *Chemistry of Materials*, **21**, 4408 (2009).
27. M. P. Seah and W. A. Dench, *Surface and Interface Analysis*, **1**, 2 (1979).
28. J.-C. Dupin, D. Gonbeau, P. Vinatier, and A. Levasseur, *Physical Chemistry Chemical Physics*, **2**, 1319 (2000).
29. C. D. Wagner, D. A. Zatko, and R. H. Raymond, *Anal. Chem.*, **52**, 1445 (1980).
30. L. Salvati Jr., L. E. Makovsky, J. M. Stencel, F. R. Brown, and D. M. Hercules, *J. Phys. Chem.*, **85**, 3700 (1981).
31. R. B. Shalvoy, P. J. Reucroft, and B. H. Davis, *Journal of Catalysis*, **56**, 336 (1979).
32. G. Cherkashinin, D. Ensling, and W. Jaegermann, *J. Mater. Chem. A*, **2**, 3571 (2014).
33. F. Pertlik, *Acta Crystallogr., Sect. C: Cryst. Struct. Commun.*, **C42**, 4 (1986).
34. R. Dedryvere, D. Foix, S. Franger, S. Patoux, L. Daniel, and D. Gonbeau, *J. Phys. Chem. C*, **114**, 10999 (2010).
35. M. Metzger, B. Strehle, S. Solchenbach, and H. A. Gasteiger, *J. Electrochem. Soc.*, **163**, A798 (2016).
36. J. C. Burns, A. Kassam, N. N. Sinha, L. E. Downie, L. Solnickova, B. M. Way, and J. R. Dahn, *J. Electrochem. Soc.*, **160**, A1451 (2013).

3.2 Degradation through Interaction between Cathode and Anode

Section 3.2 collects all the studies performed on aging mechanisms occurring due to the interaction between cathode and anode. The work presented in section 3.2.1 is embedded in its final published versions to this PhD thesis. The study presented in section 3.2.2 is unpublished at the time of submission of this PhD thesis and is therefore added as manuscript.

In section 3.2.1, we investigate the transition metal dissolution from NMC111 and its subsequent deposition on the graphite anode using operando XAS. Furthermore, we analyze the oxidation states of the transition metal deposits and discuss possible mechanisms leading to the experimental observations. Section 3.2.2 deals with the transition metal dissolution from NMC622 and its deposition on the graphite anode. The amounts of dissolved metals are compared to that observed from NMC111. Additionally, we investigate differences in the effects of Ni, Mn, and Co on NMC-graphite cells, which is important as the research focus is shifting more and more into the direction of Ni-rich layered oxides, causing Ni to be the metal which is dissolved in largest absolute quantities. We will discuss reasons causing accelerated cell aging due to transition metal deposits on the graphite anode and analyze their underlying mechanism.

3.2.1 Transition Metal Dissolution and Deposition in Li-ion batteries Investigated by Operando X-ray Absorption Spectroscopy

In this section the article "Transition Metal Dissolution and Deposition in Li-ion batteries Investigated by Operando X-ray Absorption Spectroscopy" will be presented. The paper is reproduced from *Journal of Materials Chemistry A*, 2016, 4, 18300-18305 with permission from The Royal Society of Chemistry.[152] Primarily the research work was conducted by Johannes Wandt, who is also the first author of the publication. The study was conducted in collaboration with the group of Prof. Moniek Tromp at University of Amsterdam and was published in the *Journal of Materials Chemistry A* on November 8, 2016. The results of the publication were presented at the Electrochemistry 2016 in Goslar, Germany (September 26-28, 2016). The permanent web-link to the publication is http://pubs.rsc.org/-/content/articlelanding/2016/ta/c6ta08865a/unauth#!divAbstract and the DOI is 10.1039/C6TA08865A.

In this article, we investigate the dissolution of manganese (Mn) from NMC111 and its subsequent deposition on the graphite anode using operando XAS.[152] The Ni and Co dissolution is measured at the beginning and at the end of the measurement to be able to compare the dissolved amounts of all three metals. The focus on Mn can be explained by the fact that it is considered the most harmful metal when deposited on the graphite anode.[176, 213] This will be also proven in the study which will be presented in the following section 3.2.2. Furthermore, we analyze the oxidation states of Mn, Co and Ni deposits on the graphite electrode. The experiments were performed at the synchrotron SOLEIL.

For the first two cycles of an NMC111-graphite cell between 3.0 – 4.6 V, we show a slightly increasing Mn concentration on the graphite electrode. After these two cycles, the cell voltage is ramped up to 5.0 V followed by a potential hold at 5.0 V for 200 minutes. Upon increasing the voltage above 4.6 V, the initially slowly increasing Mn concentration turns into a ~50-fold larger dissolution/deposition rate. The dissolved amounts of Mn, Ni, and Co show that the dissolution is nearly stoichiometric, which is confirmed by an ICP-OES measurement. After the end of the above described procedure, the edge positions in the X-ray absorption spectra were compared to various reference compounds with known oxidation states. It is shown that the oxidation states for all three metals deposited on the graphite anode are +2. Afterwards, the graphite electrode is dried, i.e., the electrolyte is removed, and the Mn, Ni, and Co spectra are measured again. While no changes are observed for Ni and Co, a clear shift of the edge

position of Mn towards lower energies is detected, proving the presence of metallic Mn on the dried graphite electrode. The latter observation is explained by a possible catalytic cycle in which deposited Mn is reduced on the graphite and subsequently reoxidized upon electrolyte reduction. If the rate of reoxidation of Mn is much faster than its reduction, one would expect to observe Mn^{2+} as long as electrolyte is present and metallic Mn on the dried electrode. Further mechanisms how transition metal deposits might influence the aging of Li-ion cells will be discussed in the next section. The changing oxidation states in dependence of the measurement conditions may explain the large variety of reported Mn oxidation states on graphite in the literature, ranging from metallic Mn up to Mn^{4+},[214-219] and emphasize the importance of operando techniques to understand the mechanisms leading to accelerated cell aging.

Author Contributions

Johannes Wandt, Hubert Gasteiger, and Moniek Tromp developed the concept for this study. Johannes Wandt and Anna Freiberg performed the electrochemical experiments and prepared the beamtime. Roland Jung prepared reference cells to compare the electrochemical behavior of the operando XAS cell and prepared the cells for ICP-OES analysis. Rowena Thomas evaluated the XAS spectra. Participants of the beamtime: Roland Jung, Rowena Thomas, Johannes Wandt, and Anna Freiberg. Johannes Wandt, Hubert Gasteiger, and Moniek Tromp wrote the manuscript. All authors discussed the results and commented on the manuscript.

Journal of Materials Chemistry A

COMMUNICATION

View Article Online
View Journal | View Issue

Cite this: J. Mater. Chem. A, 2016, 4, 18300

Received 12th October 2016
Accepted 8th November 2016

DOI: 10.1039/c6ta08865a

www.rsc.org/MaterialsA

Transition metal dissolution and deposition in Li-ion batteries investigated by *operando* X-ray absorption spectroscopy†

Johannes Wandt,[a] Anna Freiberg,[a] Rowena Thomas,*[b] Yelena Gorlin,[a] Armin Siebel,[a] Roland Jung,[a] Hubert A. Gasteiger[a] and Moniek Tromp[c]

In Li-ion batteries the dissolution of transition metals from the cathode and their subsequent deposition on the anode are known to contribute to capacity fading. In this study, we investigate these processes using an NMC cathode and a graphite anode under operating conditions using X-ray absorption spectroscopy. The experiments are carried out in an *operando* cell, which allows both the time/voltage and spatially resolved determination of metal concentration and oxidation state of transition metal deposits on the graphite electrode. NMC shows a strong increase of the metal dissolution rate, if the upper cut off potential exceeds 4.6 V. Under operating conditions, the oxidation state of manganese, cobalt and nickel are found to be always +2 both on lithiated and delithiated graphite. In contrast, manganese is found to be present in the metallic state on lithiated graphite in the *ex situ* analysis, thus highlighting the importance of the *operando* characterization.

Electrification of the transport sector will be of vital importance for the containment of global warming and lithium ion batteries (LIB) are a key technology for the development of plug-in hybrid and electric vehicles. To achieve mass market penetration of battery electric vehicles, the driving range of BEVs will need to significantly increase. The necessary increase in the driving range has been recently estimated to require an increase in the energy density of Li-ion batteries by a factor of 2.5 over the next 15 years.[1] In a typical Li-ion cell, the single heaviest cell component is the cathode active material.[2] During recent years, intensive research has led to the development of a series of manganese-oxide based high energy density cathode materials such as layered $LiNi_{0.33}Mn_{0.33}Co_{0.33}O_2$ (NMC-111) or spinel structures like $LiMn_2O_4$ (LMO) or $LiNi_{0.5}Mn_{1.5}O_2$ (LNMO). While these materials offer good energy densities, a major problem for many manganese-oxide based cathode materials is the dissolution of manganese ions from the cathode which causes severe capacity fading in full cells.[3,4] Manganese ions dissolve in the electrolyte and accumulate on the anode, where they trigger irreversible side reactions leading to ongoing electrolyte reduction, SEI and impedance growth and the loss of cycleable lithium.[4–7] The fact that manganese induced side reactions on the anode side rather than structural damage of the cathode or loss of cathode material are the main cause for capacity fading is highlighted by the better capacity retention of LNMO half cells over LNMO full cells[8] and by the capacity recovery of NMC electrodes harvested from full cells at end of life.[4]

The mechanism of the detrimental effect of manganese accumulation on the graphite electrode is not yet fully understood. For a detailed understanding of these processes it is crucial to know the oxidation state of manganese species on the graphite electrode, which is still controversially discussed despite intensive research during recent years, with suggested manganese oxidation states ranging from Mn(0)[9,10] to Mn(III)[11] or even Mn(IV).[3] There are two different experimental approaches which are typically used for the investigation of manganese deposition on graphite which can be categorized by the manganese source: either manganese salts are intentionally added to the electrolyte[9,11–13] or manganese is dissolved directly from the cathode during normal cell operation.[3,6,14]

The presence of manganese species with oxidation states of +2 or even higher on graphite electrodes has been reported by several groups using either X-ray photoelectron (XPS)[3,11] or X-ray absorption spectroscopy (XAS).[6] Based on this observation, Zhan *et al.* proposed that the accumulation of manganese on graphite is caused by a metathesis reaction between Mn^{2+} and

[a]Technische Universität München, Chair of Technical Electrochemistry, Department of Chemistry and Catalysis Research Center, Germany

[b]Technische Universität München, Institute for Catalyst Characterization, Germany. E-mail: rowena.thomas@tum.de

[c]Van't Hoff Institute for Molecular Sciences, University of Amsterdam, Amsterdam, Netherlands

† Electronic supplementary information (ESI) available: Details regarding electrode preparation and cell assembly, electrochemical testing, experimental details regarding X-ray absorption spectroscopy and ICP-OES analysis, estimation of redox potentials in carbonate based electrolytes; additional manganese K-edge XAS spectra measured in the separator and graphite electrode and optical images of cycled graphite electrode. See DOI: 10.1039/c6ta08865a

Li^+ containing SEI species rather than by an electrochemical reduction of Mn^{2+}.[6] Unfortunately, in these three publications[3,6,11] it is not clearly stated, whether the graphite electrodes were harvested in a lithiated or delithiated state before the *ex situ* analysis. To the best of our knowledge, the first experimental observation of metallic manganese on graphite electrodes was presented by Ochida *et al.* in 2012 using XPS.[15] Delacourt *et al.* also proposed that manganese is initially reduced to the metallic state at low potential on a copper model electrode, although their surface sensitive soft energy Mn L-edge XAS spectra only show Mn(II).[13] Gowda *et al.* identified Mn(0) in XAS spectra of lithiated graphite electrodes,[9] whereas Xiao *et al.* found both Mn(0) and MnF_2 nano-particles on the same graphite electrode (unknown state of charge).[10] Shkrob *et al.* were the first to point out that the seemingly contradictory information regarding manganese oxidations states might mainly be caused by differences in the state of charge at which the graphite electrodes are harvested before analysis. This was confirmed by their XAS results which showed reduced manganese on lithiated graphite electrodes and Mn(II) on delithiated graphite electrodes.[14]

In all of the above mentioned publications, the analytical investigation of the manganese oxidation state was carried out solely *ex situ* after preparation of the electrode. The details of sample preparation differ, but in general the electrodes are first harvested from the cycled cell, then washed in order to remove the conducting salt and ethylene carbonate and then dried. Without a doubt, *ex situ* data are very valuable and offer important insights into the mechanisms of manganese deposition and its oxidation state. Still, one cannot entirely rule out the possibility that the oxidation state changes during sample preparation. For example, Gowda *et al.* observed that washing the electrodes with dimethyl carbonate significantly decreased the amount of reduced manganese species.[9] Furthermore, the presence of electrolyte or electrolyte degradation products like hydrofluoric acid might also affect the oxidation states of the transition metals.

In order to address these issues and investigate the oxidation state of manganese on graphite under operating conditions, we performed time and spatially resolved *operando* XAS experiments with a special cell which is described in detail in our previous publication.[16] The cell has been slightly modified to allow the use of a reference electrode (see ESI and Fig. S1† for details). The cell consists of an NMC-111 positive electrode (120 μm thickness), a natural graphite negative electrode (170 μm thickness), two glassfiber separators (at a total compressed thickness of ≈400 μm) and 1 M $LiPF_6$ in EC/EMC (3 : 7) as electrolyte (for details see ESI†). The electrode arrangement and geometry of our *operando* cell design in combination with an X-ray beam focused onto a 140 × 1000 μm area allows the selective measurement of XANES or EXAFS spectra on either one of the two electrodes or in the separator region.[17]

Fig. 1a shows manganese K-edge XANES spectra measured in the *operando* XAS cell in these three different positions before the start of cell cycling. The raw spectra (not normalized) display the difference in signal intensity, reflected by the XAS edge height which is directly proportional to the amount of Mn in the beam. It is possible to continuously follow the manganese dissolution from the positive electrode during cell cycling by selectively monitoring manganese species deposited on the graphite counter electrode, as the diffusion time from cathode to anode (in the order of 500 s) is in the same order of magnitude as the time resolution of the XAS experiments (≈24 minutes per spectrum) and as transition metals are known to accumulate on the negative electrode rather than in the electrolyte.[14] The raw manganese K-edge XANES spectra (Fig. 1b) measured on the graphite electrode during battery cycling display a continuous increase of the manganese concentration upon cell cycling. The initial non-zero manganese concentration (lower panel of Fig. 1c) arises from impurities in the graphite electrode, the electrolyte, and the X-ray window. During cell charge/discharge cycling (Fig. 1c), manganese K-edge XANES spectra were mainly recorded in the graphite position in order to maximize the time/voltage resolution, justified by the fact that manganese is considered to be the most detrimental metal for graphite performance.[12] A single manganese K-edge spectrum (spectrum shown in Fig. S2†) was measured in the electrolyte (separator position) during the electrochemical procedure (pink star at ≈13 h in the lower panel of Fig. 1c) to confirm the above mentioned accumulation of manganese on the graphite electrode (see ESI† for details). Additionally, cobalt and nickel K-edge XAS spectra were also recorded before the start and after the end of the electrochemical procedure to determine their initial and final oxidation states as well as their concentration increase.

In the following section, we will first discuss the influence of the cell potential on the metal dissolution from the NMC electrode. In the second part we will discuss the oxidation states of manganese, nickel and cobalt species as observed on the graphite electrode. Furthermore, we consider the influence of the graphite potential on the transition metal oxidation states and the differences observed when comparing *operando* and *ex situ* spectra. Finally, we examine the implications of our findings for the capacity fading of full-cells.

Fig. 1c (lower panel) shows the increase of the manganese concentration on the graphite electrode upon cell cycling (upper panel) due to its dissolution from the NMC cathode, its diffusion through the separator, and its subsequent deposition on the anode. The manganese content in the graphite electrode was estimated by determining the Mn K edge XAS edge height of manganese solutions of known concentrations filled into our *operando* XAS cell (see ESI† for details). In the initial two cycles with an upper cut-off voltage of 4.6 V, the manganese concentration increases by 20 μmol h^{-1} $L_{electrode}{}^{-1}$ (≈0.34×10^{-9} mol h^{-1} or ≈1.0×10^{-9} mol per cycle) which equals a dissolution rate of ≈$0.0017\%_{Mn}$ per cycle when referring to the total manganese content in the NMC electrode (for details s. Section 6 of the ESI†). This manganese dissolution rate is essentially identical to our previous results for the same NMC material, where the manganese deposit on the graphite electrode was quantified after 230 cycles in the same potential range by post-mortem PGAA (prompt-gamma-activation analysis; s. Section 6 of the ESI† for details).[18]

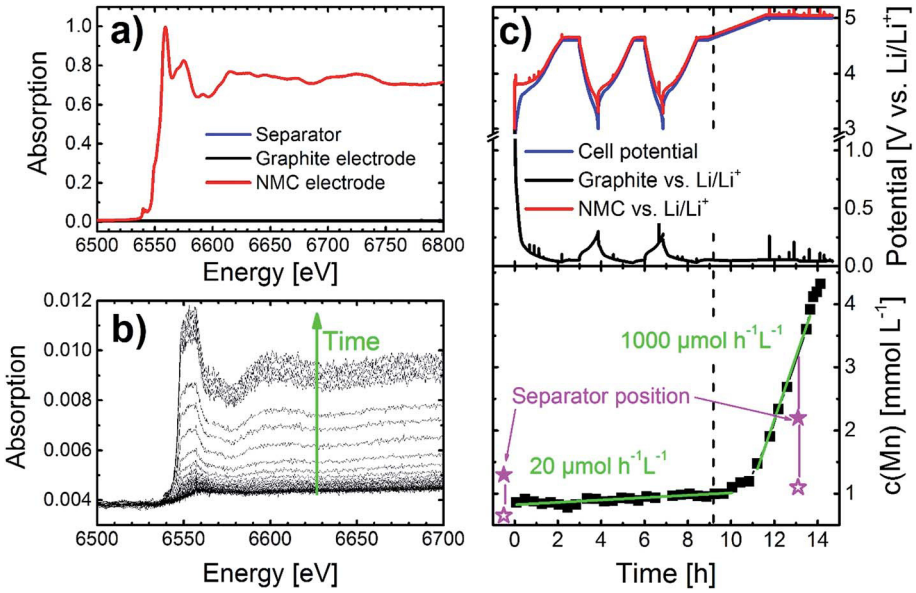

Fig. 1 Graphite/NMC full-cell data obtained in the operando XAS cell with 1 M $LiPF_6$ in EC/EMC (3 : 7) as electrolyte. (a) Initial Mn K-edge spectra (non-normalized) measured in the separator, the graphite electrode, and the NMC electrode position before electrochemical cycling, demonstrating the spatial resolution of the operando XAS cell. (b) Non-normalized operando Mn K-edge spectra measured on the graphite electrode during cell cycling (the first spectrum in (b) is a zoom into the graphite spectrum shown in (a)). (c) Upper panel: cell potential as well as individual electrode potentials *vs.* a metallic lithium reference electrode (*i.e., vs.* Li/Li^+) during cell cycling (see ESI† for detailed cycling procedure); lower panel: respective manganese concentrations on the graphite electrode as derived from the edge height of the operando Mn K-edge spectra (shown in (b)). The filled pink stars show the manganese concentration in the electrolyte (measured in the separator position); the empty pink stars show the theoretical manganese concentration which would be expected in the graphite position if there would be no accumulation on the graphite surface (considering the porosity of 50% of the graphite electrode, see ESI† for details).

When the NMC potential exceeds 4.6 V, the rate of manganese dissolution rapidly increases by a factor of ≈50 to 1000 mol h^{-1} L^{-1} ($\equiv 17 \times 10^{-9}$ mol h^{-1}, s. Section 6 of the ESI†). The total metal dissolution over the course of the experiment (s. upper panel of Fig. 1c) determined by XAS (s. Section 6 of the ESI†) is 0.09 mol% for Mn, 0.26 mol% for Co, and 0.17 mol% for Ni. These amounts are within a factor of 2 of what we obtained by *ex situ* ICP-OES analysis (0.165 ± 0.015% for Mn, 0.125 ± 0.002% for Co and 0.116 ± 0.002% for Ni), which indicates that the XAS calibration procedure is reasonably accurate. In storage experiments with NMC-111 charged to 4.6 V, Gallus *et al.*[19] showed that the concentrations of Mn, Co, and Ni dissolved in the electrolyte are identical within roughly ±20%; on the other hand, after extended charge/discharge cycling of NMC-111/graphite cells between 3.0 and 4.6 V (including a CV step at 4.6 V to C/20), the amount of Mn deposited on the graphite electrode was twice as high as that of Co and Ni.[18] Unfortunately, no data are available for an extended potential hold at 5.0 V as was done in our XAS experiments. In general, the fact that the deposited/dissolved amounts of transition metals are within a factor of three points towards acidic corrosion as the governing metal dissolution mechanism at ≥4.6 V. In a recent study, it was shown by On-line Electrochemical Mass Spectrometry (OEMS) that at around 4.7 V significant amounts of protic species are formed upon electrolyte oxidation,[20] which could lead to a quasi homogeneous "etching" of the NMC material, resulting in a near stoichiometric dissolution/deposition of the three transition metals. Others have proposed that water might be produced by electrolyte oxidation at high potentials, which would lead to the formation of hydrofluoric acid from the $LiPF_6$ salt,[21] which in turn would trigger metal dissolution from transition metal oxide materials.[22,23] Manganese(III) disproportionation, which has also been suggested to contribute to the metal dissolution,[24,25] would cause a significantly increased manganese concentration in comparison to cobalt and nickel and is therefore likely negligible at potentials of ≥4.6 V.

In the following part we will discuss the oxidation state of manganese species deposited on the graphite electrode during the cycling procedure shown in Fig. 1c (upper panel). Fig. 2a and b compare the normalized reference Mn K-edge XANES spectra to the normalized Mn K-edge spectra measured *operando* on the graphite electrode (s. green line in Fig. 2b) at the end of the procedure shown in Fig. 1c (upper panel). Analyzing the edge position (see Section 5 of the ESI† for details), the oxidation state of the manganese species is predominantly +2 throughout the entire experiment (only final spectrum shown), independent of the graphite potential which varied between 80 mV and 250 mV *vs.* Li/Li^+. Although the edge position of the final *operando* Mn species is consistent with Mn^{2+} (s. red symbol in Fig. S3†), the structure of the XANES post-edge region differs from our Mn^{2+} references, which is not unexpected as this region depends strongly on the local geometry and ligand type around the Mn atom (s. Sections 4 and 5 of the ESI†). In the Mn^{2+} references, the Mn^{2+} is in an (close to) octahedral coordination sphere, whereas Mn^{2+} deposited on the graphite surface is not likely to be in such a geometry. The XANES spectra

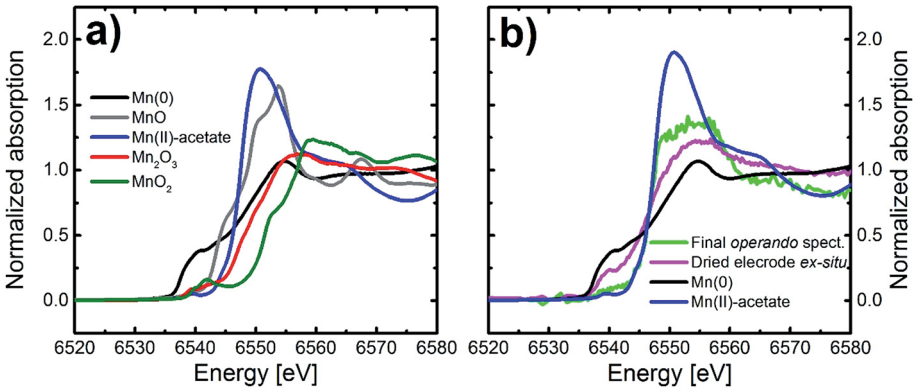

Fig. 2 (a) Mn K-edge spectra of reference compounds with different manganese oxidation states (s. also Sections 4 and 5 in the ESI†). (b) Final operando Mn K–edge spectrum (green line) measured in the operando cell on the lithiated graphite electrode at the end of the procedure shown in Fig. 1c (upper panel) and *ex situ* spectrum (pink line) of the same electrode after drying of the same electrode for 15 minutes under dynamic vacuum in the glovebox antechamber.

in fact indicate a lower symmetry based on the reduced main peak intensity and overall broadening. The spectrum also seems to differ from the *ex situ* spectra obtained by Gowda *et al.*[9] and Shkrob *et al.*,[14] with our data exhibiting a broader main peak. This is not surprising since our XANES spectra are recorded *operando* in the presence of electrolyte and those by the other authors *ex situ*, which will likely change the coordination geometry of the metal due to sample preparation. Unfortunately, we were not able to obtain full EXAFS spectra in a reasonable time scale at a sufficiently high signal/noise ratio, so we cannot deduce the local structure. The presence of Mn(II) on the lithiated graphite electrode is surprising, considering the low potential of lithiated graphite (80 mV and 250 mV *vs.* Li/Li^+), which is well below the Mn(0)/Mn(II) redox potential (s. Section 7 of the ESI†). Our observation of Mn(II) under operating conditions is also noteworthy because Gowda *et al.*[9] and Shkrob *et al.*[14] both found reduced manganese in their *ex situ* analysis on lithiated graphite (note, that in ref. 9 it is not entirely clear whether the *ex situ* XAS spectra were recorded in the absence or presence of electrolyte due to inconclusive experimental details). In order to rule out the possibility that the rather unusual cycling procedure of the cell shown in Fig. 1 is somehow responsible for the presence of Mn(II), a second cell was investigated after 22 "conventional" charge/discharge cycles between 3.0 and 4.6 V (s. Section 2 of the ESI†). *Operando* XANES spectra of the Mn K-edge were recorded while the graphite electrode was polarized to 0.095 V (cell charged, *i.e.*, graphite lithiated; s. pink line in Fig. S6†) or 1.5 V *vs.* Li/Li^+ (cell discharged, *i.e.*, graphite delithiated; s. green line in Fig. S6†), but independent of the graphite potential, the manganese oxidation state was again predominantly +2 under operating conditions, thus confirming the results shown in Fig. 2b (green line) for the *operando* XAS measurements on the graphite after polarization to 5 V.

After finishing the cycling procedure in the *operando* cell (s. Fig. 1c), the cell was brought back into the glove box and the graphite electrode was harvested in the lithiated state (*i.e.*, after the 200 minute cell potential hold at 5.0 V). The unwashed graphite electrode was dried in the antechamber for 15 minutes and then sealed again in an *operando* cell without a NMC counter electrode and without electrolyte. The subsequent *ex situ* Mn K-edge XANES spectrum measured on the dried graphite electrode (s. pink line in Fig. 2b) clearly shows a reduced manganese oxidation state which indicates the presence of Mn(0), in addition to Mn(II). The amounts of Mn(0) and Mn(II) present on the dried graphite electrode appear to be of a similar order of magnitude but further analysis to identify the species present was not possible from this data set. Again, for clarification, both the last *operando* spectrum consistent with the presence of Mn(II) (green line in Fig. 2b) and the *ex situ* spectrum showing a mixture of Mn(0) and Mn(II) (pink line in Fig. 2b) were measured on the same graphite electrode in the very same state of charge and using the same aluminized Kapton window, the only difference being the presence/absence of electrolyte. The fact that our *ex situ* data is consistent with the literature, *viz.*, showing reduced manganese, confirms that the observation of Mn(II) under operating conditions is not an artefact caused by our experimental set up. To the best of our knowledge, the XAS data presented here is the first experimental proof that manganese is predominantly present in oxidation state +2 on lithiated graphite under operating conditions and that it is being (partially) reduced during subsequent drying of the electrode which is actually unavoidable during *ex situ* sample preparation. This interpretation is supported by a simple optical observation: (i) directly after disassembling the cell in an argon filled glove box, the lithiated graphite electrode has a golden appearance, as one would expect for fully lithiated (*i.e.*, fully charged) graphite (s. Fig. S7a†); (ii) upon drying the top layer of the electrode for different periods of time, the surface quickly turns black (s. Fig. S7b–d†); (iii) scratching of the blackened surface of the graphite electrode shows that its inner parts still have the golden appearance characteristic of lithiated graphite (s. Fig. S7e†). Delacourt *et al.* have linked the appearance of a black conducting film on their model copper electrodes to the presence of metallic manganese,[13] which we believe is also the cause

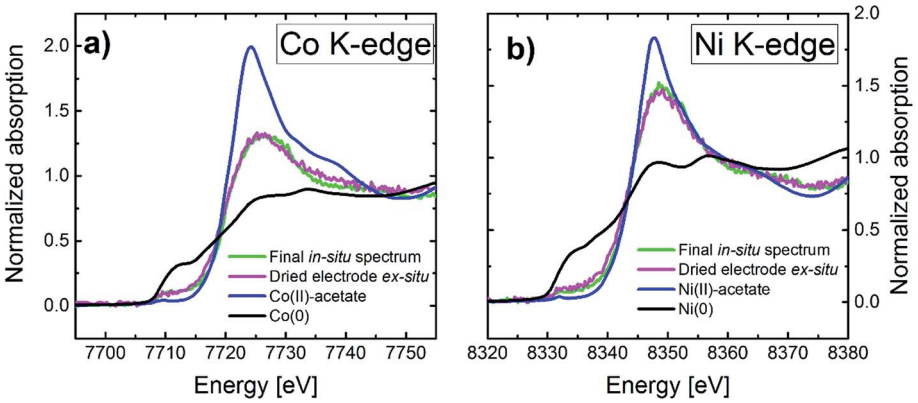

Fig. 3 K-edge spectra of (a) cobalt and (b) nickel measured at the lithiated graphite electrode at the end of the procedure shown in Fig. 1c (upper panel); for both metals the final operando spectrum measured in the operando XAS cell is compared with the *ex situ* spectrum of the same electrode after drying of the electrode for 15 minutes under dynamic vacuum in the glovebox antechamber.

for the black film observed on our graphite electrode. The observation that the black film is only present on the surface of the dried graphite electrode while the bulk of the graphite electrode is still golden, indicates the preferential manganese deposition on the graphite electrode surface which was facing the NMC electrode, an assumption which is consistent with XPS depth profiling data presented by Yang *et al.*[3]

When considering the question of why reduced manganese is only present in the *ex situ* analysis, a likely hypothesis is that under operating conditions Mn(II) is constantly reduced at the graphite electrode (the reduction rate limited by electron transfer through the SEI), but then rapidly reoxidized by electrolyte as suggested by Delacourt *et al.*[13] This would be consistent with XPS data published by Ochida *et al.*,[15] showing the oxidation of metallic manganese to MnO on delithiated graphite after a 24 hour hold at OCV and with DFT calculations by Han *et al.*,[26] showing that the oxidation of isolated Mn(0) by ethylene carbonate through a ring-opening reaction is exothermic. Thus, the different manganese oxidation state in *operando vs. ex situ* experiments could be explained by assuming that the reduction of Mn(II) on the graphite electrode is rate limiting (*i.e.*, sufficiently slowed down by the SEI), in which case the predominant manganese oxidation state would be +2 as long as electrolyte is available (*i.e.*, in the *operando* experiments), while it would gradually be reduced to an oxidation state of 0 in the absence of electrolyte (*i.e.*, in *ex situ* experiments). The suggested reduction of Mn(II) on the graphite electrode and subsequent re-oxidation by electrolyte corresponds to a Mn(II)/Mn(0) catalyzed redox cycle with a net reaction being continuous electrolyte reduction at the graphite electrode. In an actual battery cell the consequence would be ongoing active lithium loss and increased SEI formation. Accordingly, this Mn(II)/Mn(0) redox cycle might be the underlying mechanism causing the enhanced capacity fading and impedance rise typically observed for graphite/NMC full cells operating under conditions favoring transition metal dissolution (*e.g.* high cut-off potentials).[18]

Interestingly, both the *operando* (in the presence of electrolyte) and the *ex situ* (dried electrode) K-edge XANES spectra show that nickel and cobalt, which also accumulate on the graphite electrode, are always present in oxidation state +2 as shown in Fig. 3. This is surprising considering the more noble character of cobalt and nickel in comparison to manganese (see ESI† for details). The redox potentials for Co/Co^{2+} and Ni/Ni^{2+} are in the range of 2.2 to 2.5 V which is clearly above the potential for electrolyte reduction.[27] Accordingly, one would expect metallic cobalt and nickel both in the absence and presence of electrolyte; it is therefore not surprising that cobalt and nickel show the same oxidation state in the *operando* and *ex situ* spectra, but it is surprising that this oxidation state is +2 rather than zero. A possible reason for the trapping of cobalt and nickel in the +2 oxidation state might be the immobilization of cobalt and nickel in the outer SEI at a greater distance to the actual graphite surface, thus preventing their reduction to the metallic state. The influence of the exact site of the metal deposition within the graphite SEI on the oxidation state has been shown by an XPS depth profiling study carried out by Peled *et al.*,[28] where arsenic deposits from $LiAsF_6$ salt reduction were found to be mainly in oxidation state +III and +V in the outer SEI while they were dominated by As^0 near the graphite/SEI interface. For manganese, Shkrob *et al.* combined the results of electron paramagnetic resonance (EPR) spectroscopy and XAS to show that it is predominantly deposited on the inner SEI in a Li_2CO_3 matrix, thus enabling reduction of Mn^{2+} due to the close vicinity to the actual graphite surface.[14] To the best of our knowledge, there is no such information available for cobalt and nickel deposits. In the future, experiments which characterize the transition metal species in the SEI using high-quality K-edge EXAFS spectra at a micro-focus beamline, which would offer much higher flux and therefore a better signal-to-noise ratio, could clarify the chemical environment of manganese, cobalt and nickel compounds deposited on graphite under operating conditions.

In summary, we used time and spatially resolved XAS to study transition metal dissolution and deposition in Li-ions cells under operating conditions. This is, to the best of our knowledge, the first study of these processes under real cell conditions. The manganese dissolution rate was found to

drastically increase at potentials >4.6 V. Under operating conditions manganese deposits on the graphite electrode were always in oxidation state +2, independent of the state of charge. In contrast, *ex situ* analysis of the same lithiated graphite electrode showed reduced manganese species, indicating the presence of Mn(0), which is consistent with *ex situ* data in the literature. Cobalt and nickel deposits were always found in oxidation state +2 both in *operando* and *ex situ* spectra. We believe, that the change in the manganese oxidation state upon sample preparation clearly highlights the importance of using a dedicated *operando* technique in order to obtain a comprehensive picture of transition metal deposition on graphite anodes and its role in cell capacity fading.

Acknowledgements

We gratefully acknowledge Soleil for provision of beamtime (proposal number 20141256) and Dr Andrea Zitolo for his assistance using SAMBA. We thank Dominik Haering for experimental support during the beamtime. J. W. and R. T. gratefully acknowledge the financial support by the Bavarian Ministry of Economic Affairs and Media, Energy and Technology under the auspices of the EEBatt project. R. J. was supported by BMW AG, and Y. G. gratefully acknowledges the support of the Alexander von Humboldt Postdoctoral Fellowship and Carl Friedrich von Siemens Fellowship Supplement.

References

1 D. Andre, S.-J. Kim, P. Lamp, S. F. Lux, F. Maglia, O. Paschos and B. Stiaszny, *J. Mater. Chem. A*, 2015, **3**, 6709–6732.
2 F. T. Wagner, B. Lakshmanan and M. F. Mathias, *J. Phys. Chem. Lett.*, 2010, **1**, 2204–2219.
3 L. Yang, M. Takahashi and B. Wang, *Electrochim. Acta*, 2006, **51**, 3228–3234.
4 H. Zheng, Q. Sun, G. Liu, X. Song and V. S. Battaglia, *J. Power Sources*, 2012, **207**, 134–140.
5 K. Amine, Z. Chen, Z. Zhang, J. Liu, W. Lu, Y. Qin, J. Lu, L. Curtis and Y.-K. Sun, *J. Mater. Chem.*, 2011, **21**, 17754.
6 C. Zhan, J. Lu, A. J. Kropf, T. Wu, A. N. Jansen, Y.-K. Sun, X. Qiu and K. Amine, *Nat. Commun.*, 2013, **4**, 2437.
7 T. Joshi, K. Eom, G. Yushin and T. F. Fuller, *J. Electrochem. Soc.*, 2014, **161**, 1–33.
8 N. P. W. Pieczonka, Z. Liu, P. Lu, K. L. Olson, J. Moote, B. R. Powell and J.-H. Kim, *J. Phys. Chem. C*, 2013, **117**, 15947–15957.
9 S. R. Gowda, K. G. Gallagher, J. R. Croy, M. Bettge, M. M. Thackeray and M. Balasubramanian, *Phys. Chem. Chem. Phys.*, 2014, **16**, 6898–6902.
10 X. Xiao, Z. Liu, L. Baggetto, G. M. Veith, K. L. More and R. R. Unocic, *Phys. Chem. Chem. Phys.*, 2014, **16**, 10398–10402.
11 S. Komaba, T. Itabashi, T. Ohtsuka, H. Groult, N. Kumagai, B. Kaplan and H. Yashiro, *J. Electrochem. Soc.*, 2005, **152**, A937.
12 S. Komaba, N. Kumagai and Y. Kataoka, *Electrochim. Acta*, 2002, **47**, 1229–1239.
13 C. Delacourt, a. Kwong, X. Liu, R. Qiao, W. L. Yang, P. Lu, S. J. Harris and V. Srinivasan, *J. Electrochem. Soc.*, 2013, **160**, A1099–A1107.
14 I. A. Shkrob, A. J. Kropf, T. W. Marin, Y. Li, O. G. Poluektov, J. Niklas and D. P. Abraham, *J. Phys. Chem. C*, 2014, **118**, 24335–24348.
15 M. Ochida, Y. Domi, T. Doi, S. Tsubouchi, H. Nakagawa, T. Yamanaka, T. Abe and Z. Ogumi, *J. Electrochem. Soc.*, 2012, **159**, A961–A966.
16 Y. Gorlin, A. Siebel, M. Piana, T. Huthwelker, H. Jha, G. Monsch, F. Kraus, H. A. Gasteiger and M. Tromp, *J. Electrochem. Soc.*, 2015, **162**, A1146–A1155.
17 Y. Gorlin, M. U. M. Patel, A. Freiberg, Q. He, M. Piana, M. Tromp and H. A. Gasteiger, *J. Electrochem. Soc.*, 2016, **163**, A930–A939.
18 I. Buchberger, S. Seidlmayer, A. Pokharel, M. Piana, J. Hattendorff, P. Kudejova, R. Gilles and H. A. Gasteiger, *J. Electrochem. Soc.*, 2015, **162**, A2737–A2746.
19 D. R. Gallus, R. Schmitz, R. Wagner, B. Hoffmann, S. Nowak, I. Cekic-Laskovic, R. W. Schmitz and M. Winter, *Electrochim. Acta*, 2014, **134**, 393–398.
20 M. Metzger, J. Sicklinger, D. Haering, C. Kavakli, C. Stinner, C. Marino and H. A. Gasteiger, *J. Electrochem. Soc.*, 2015, **162**, A1227–A1235.
21 H. Yang, G. V. Zhuang and P. N. Ross, *J. Power Sources*, 2006, **161**, 573–579.
22 J. C. Hunter, *J. Solid State Chem.*, 1981, **39**, 142–147.
23 D. Aurbach, M. Levi, K. Gamulski, B. Markovsky, G. Salitra, E. Levi, U. Heider, L. Heider and R. Oesten, *J. Power Sources*, 1999, **81–82**, 472–479.
24 Y. Xia and M. Yoshio, *J. Electrochem. Soc.*, 1996, **143**, 825–833.
25 D. H. Jang, Y. J. Shin and S. M. Oh, *J. Electrochem. Soc.*, 1996, **143**, 2204–2211.
26 Y.-K. Han, K. Lee, S. Kang, Y. S. Huh and H. Lee, *Comput. Mater. Sci.*, 2014, **81**, 548–550.
27 R. Jung and H. A. Gasteiger, 2016, manuscript in preparation.
28 D. Bar-Tow, E. Peled and L. Burstein, *J. Electrochem. Soc.*, 1999, **146**, 824.

Supporting Information

Transition metal dissolution and deposition in Li-ion batteries investigated by operando x-ray absorption spectroscopy

Johannes Wandt[1], Anna Freiberg[1], Rowena Thomas[#], Yelena Gorlin[1], Armin Siebel[1], Roland Jung[1], Hubert A. Gasteiger[1], Moniek Tromp[2]

[1]Technische Universität München, Chair of Technical Electrochemistry, Department of Chemistry and Catalysis Research Center, Germany

[2] Van't Hoff Institute for Molecular Sciences, University of Amsterdam, Amsterdam, Netherlands

Table of content

1) Electrode preparation and cell assembly

Cathodes based on commercial $LiNi_{0.33}Mn_{0.33}Co_{0.33}O_2$ (NMC) active material were prepared by dispersing NMC (96wt%), polyvinylidene difluoride (PVdF, KynarHSV 900, Arkema, France) (2 wt%), and carbon black (Super C65, TIMCAL, Switzerland) (2 wt%) in N-methyl-2-pyrrolidone (NMP, Sigma Aldrich, Germany) and mixing them altogether in a planetary centrifugal vacuum mixer (Thinky, USA) at 2000 rpm for 15 min. The resulting viscous slurry with a solid content of 1.9 g/mL was cast onto a thin aluminum foil (thickness 18 µm, MTI corporation, USA) using the doctor blade method (RK Print Coat Instruments, UK) with a wet-film thickness of 240 µm. Graphite electrodes were produced analogously, using a mixture of 90 wt% graphite (Timcal, Germany) and 10 wt% PVdF binder in NMP (solids content of 0.88 g/ml) and a copper foil as current collector (10µm, MTI corporation, USA). After drying at room temperature, electrodes with a size of 10×10 mm (squares) were punched out and dried under dynamic vacuum for 12 hours at 120 °C (Büchi, Switzerland) and transferred into an Argon filled glove box (MBRAUN). Active material loadings were about 14.8 mg cm^{-2} for graphite and 18.0 mg cm^{-2} for NMC electrodes. NMC electrodes were compressed at a pressure of 130 MPa to a thickness of 125 µm and a porosity of 30%; graphite electrodes were used without compression (170 µm thickness, 50% porosity).

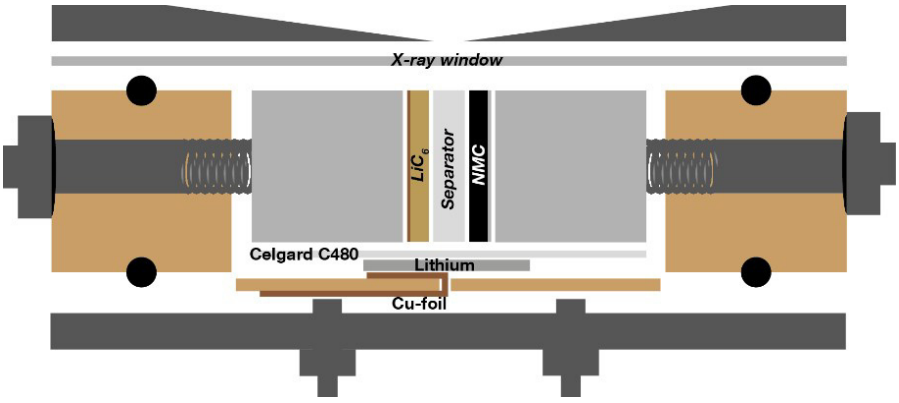

Figure S1 Schematic drawing of the spectro-electrochemical *operando* XAS cell showing the incorporation of the reference electrode. A detail exploded view and description of the cell design is provided in reference [1].

The XAS cell design is described in detail elsewhere.[1] It has been slightly modified in comparison to the work by Gorlin *et al.*[1] in order to accommodate a metallic lithium reference electrode as shown in Figure S1. The lithium reference electrode was placed in a central position underneath the electrode stack and contacted through a screw in the back

plate of the cell. The x-ray window consisted of an aluminized 12 µm Kapton® foil (aluminized side placed towards the cell exterior) and an additional 25 µm Kapton® foil (placed on top of the aluminum layer) to prevent mechanical damage of the thin aluminum layer. The cell was assembled with two glassfiber separators (250 µm uncompressed thickness, glass microfiber filter 691, VWR) and 300 µL electrolyte (1 M $LiPF_6$ in EC/EMC 3:7, BASF).

2) Electrochemical testing

Electrochemical testing was carried out using a Biologic SP200 battery cycler. Two different cycling procedures were used within this project. For the *operando* procedure (s. Fig. 1), the cell was mounted in the XAS sample stage directly after assembly and then cycled for two cycles between 3.0 and 4.6 V with a C/2 CCCV charge (C/20 current cut off) and 1C CC discharge followed by a single CC charge to 4.6 V followed by another CV step. The discharge capacities in the first two cycles were 174 mAh g_{NMC}^{-1} and 169 mAh g_{NMC}^{-1}, respectively. The potential was then increased with a sweep rate of 2.5 mV min^{-1} to 5.0 V, where it was held for 200 minutes. A second cell ("conventional cycling procedure") was cycled inside the glovebox for 22 cycles between 3.0 and 4.6 V: after a C/10 formation cycle, the cell was cycled with a C/2 CCCV charge (C/20 current cut off) and 1C CC discharge. The last cycle showed a discharge capacity retention of 169 mAh g_{NMC}^{-1}, which is comparable to the performance in a standard Swagelok cell.[2] After cycling, the cell was sealed in a pouch bag inside the glove box and transported to the synchrotron in the charged state, thus eliminating the possibility of oxygen intrusion. After mounting the cell in the sample stage, XAS spectra were recorded in the charged state (graphite potential +0.095 V vs. Li/Li^+) and in the entirely discharged state (graphite potential +1.5 V vs. Li/Li^+).

3) XAS experiments

The X-ray absorption spectra were measured at the SAMBA beamline, a hard X-ray bending magnet beamline at Soleil synchrotron, France. The acquisition time for each spectrum presented in this work was approximately 24 minutes. The synchrotron was operating in multibunch top up mode. A sagittaly focusing double crystal monochromator consisting of two Si 220 crystals was used to select the incoming energy and the beam was focused using Pd coated mirrors before being cut with slits to achieve a beam size of 100 micrometer in the horizontal and approximately 1000 micrometer in the vertical dimension. The cells were

assembled as described above, and measured in fluorescence mode, with an energy selective Canberra 35-element monolithic planar Ge pixel array detector to collect the photons. Photon energies were calibrated using the first peak in the first derivative of the pure metal foils, which were measured in fluorescence before and after the operando studies, and background corrections of the spectra were carried out using the IFEFFIT software package.[3,4]

4) Manganese K-edge spectrum of electrolyte

Figure S2 shows a manganese K-edge spectrum measured in the electrolyte (separator position, pink line) during the 5 V constant potential step as indicated in Figure 1c (main paper). The oxidation state of the dissolved manganese is clearly +2 which is consistent with the literature.[5]

The XAS spectra, which are measured in the graphite position actually show a superposition of manganese deposited on the surface of the graphite particles and manganese species dissolved in the electrolyte which is contained within the pores of the graphite electrode (50% porosity). It is therefore only possible to reliably determine the oxidation state of manganese deposits on the graphite electrode, if the spectrum measured in the graphite position is dominated by manganese deposits rather than by dissolved manganese species. The edge jump measured in the separator (Figure S2) corresponds to a manganese concentration of about 2.2 mmolar (s. filled pink star at ≈13 h in the lower panel of Fig. 1c). If the concentration of the dissolved manganese species were constant across the entire cell, the dissolved manganese species would correspond to a ≈1.1 mmolar concentration in the graphite position considering the porosity of the graphite electrode of 50% (s. empty pink star at ≈13 h in the lower panel of Fig. 1c). If one interpolates the manganese concentration determined in the graphite position directly before and after the separator spectrum to the time at which the separator spectrum was measured, one contains a manganese concentration of 3.2 mmolar for the graphite position. Therefore, at this point in time (about 13 hours) the higher limit for the contribution of dissolved manganese to the spectrum measured in the graphite position can be estimated to be about 25% (=1.1/(1.1+3.2)). The real contribution of the dissolved manganese will be significantly smaller due to two reasons: Firstly, the above estimation is based on the assumption that the concentration of dissolved manganese is identical (1.1 mmolar) for electrolyte contained within the pores of

the graphite electrode and the separator. In reality, the manganese is being released into the electrolyte at the NMC electrode and then diffuses through the separator to the graphite electrode. As this diffusion is driven by a concentration gradient, the manganese concentration has to be lower in the electrolyte contained in the graphite electrode in comparison to the electrolyte contained in the separator, which is closer to the NCM electrode. Secondly, the fact that manganese is being accumulated in the graphite electrode means that it is being extracted from the electrolyte. As a direct consequence, the manganese concentration in the electrolyte contained within the porous graphite electrode is further reduced in comparison to the respective concentration in the separator. Therefore, the manganese K-edge spectra measured within the graphite electrode during the 5V hold step can reliably be assigned to manganese deposits.

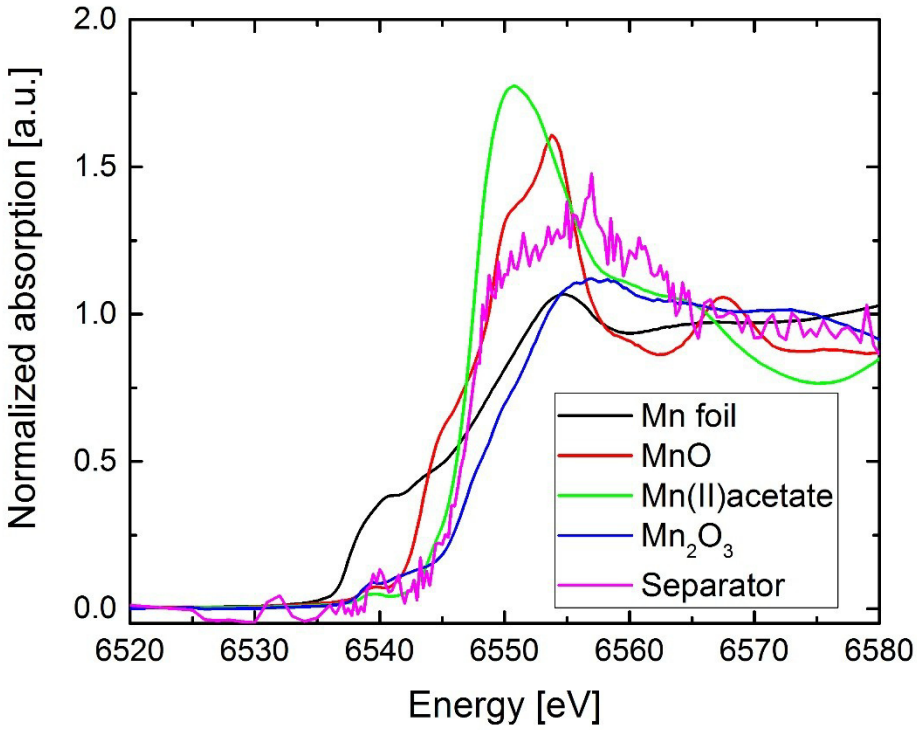

Figure S2 Mn K-edge spectra of reference compounds as well as *operando* spectrum measured in the electrolyte (= separator position) at the beginning of the 5 V potential hold after the initial charge/discharge cycles in the operando XAS cell. The exact time at which the *operando* spectrum was measured is indicated by the pink star at the right-hand-side of the lower panel of Figure 1c (main text).

The situation is a little less clear in the initial spectra due to the lower difference in the manganese concentration measured in the graphite position (0.9 mmolar) in comparison to the electrolyte (1.3 mmolar, or 0.65 mmolar considering 50 % porosity of the graphite

electrode; see full and empty pink star near 0 h in the lower panel of Fig. 1c). Accordingly, the contribution of dissolved manganese to the first manganese spectrum measured in the graphite position can be estimated to be about 42% (=0.65/(0.65+0.9)). Nevertheless, the main conclusion derived from the manganese spectra in the graphite position, that the manganese deposits are always present in oxidation state +2 irrespective of the graphite potential, is in no way hampered by the slight contribution of dissolved manganese in the initial spectra.

5) Analysis of manganese oxidation states

The edge positions of the Mn samples were determined by taking the position of the second peak in the 1st derivative of the K-edge XANES spectra. In Figure S3 the edge positions of all Mn references (black points) are plotted against formal oxidation state in order to more clearly see the trend in edge shifts. From this it is clear that the edge position of the final *operando* graphite spectrum (red point) is consistent with the values obtained for a formal oxidation state of +2. A linear fit is not possible due to the rather wide range of edge values for a single oxidation state, as demonstrated by the values obtained for Mn^{2+}, due to the fact that the edge values for transition metals also depend on geometry and ligand coordination.[6] The relatively poor signal-to-noise ratio for the 1st derivative spectrum of the ex situ sample makes assigning a precise edge position difficult, this is further discussed below. The references measured were as follows: Mn foil (Mn(0)), MnO (Mn(II)), $Mn(CH_3COO)_2 \cdot 4\,H_2O$ (Mn(II)), manganocene (Mn(II)), Mn_2O_3 (Mn(III)), MnO_2 (Mn(IV)), and pristine NMC material (Mn(IV)). All Mn references were purchased from Sigma-Aldrich (Germany), with the exception of the NMC material (see above). Pellets were prepared using boron nitride as a diluent and measured in transmission. The 1st derivative XANES spectrum of the ex situ graphite sample (Figure S4, blue line) shows a broad peak at the edge position (6542-6550 eV) which has intensity spanning the edge position for Mn(0) and Mn(II), as depicted here by spectra from a Mn foil (black line) and $Mn(II)(CH_3COO)_2 \cdot 4\,H_2O$ (red line). Therefore, we believe a combination of Mn(0) and Mn(II) is present, both in significant amounts. This is supported by an examination of the associated XANES spectra (Figure S4), which shows that the rising edge is located between those of Mn foil and $Mn(II)(CH_3COO)_2 \cdot 4\,H_2O$. Unfortunately, due to the data quality and lack of suitable reference spectra further analysis by principle components analysis is not possible.

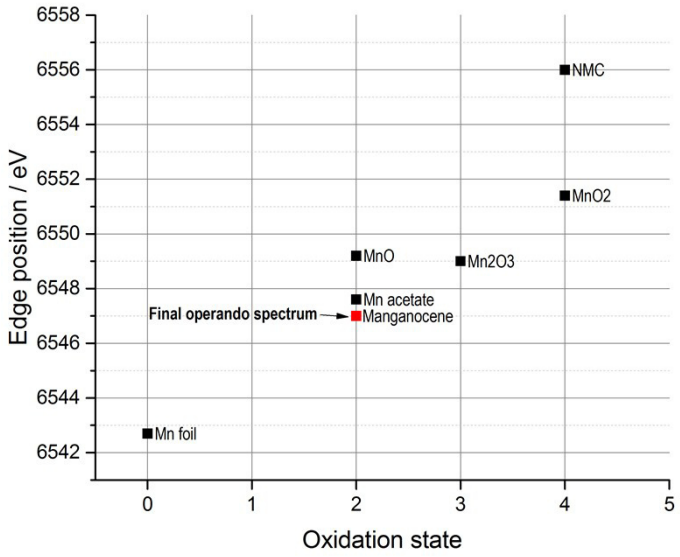

Figure S3 Edge position in Mn K-edge spectra for several reference compounds (black dots) as a function of their formal oxidation state and the final *operando* spectrum measured on the graphite electrode (red dot, see Figure 2b in main text). The final *operando* spectrum occurs at the same energy as manganocene, so the two data points are overlaid.

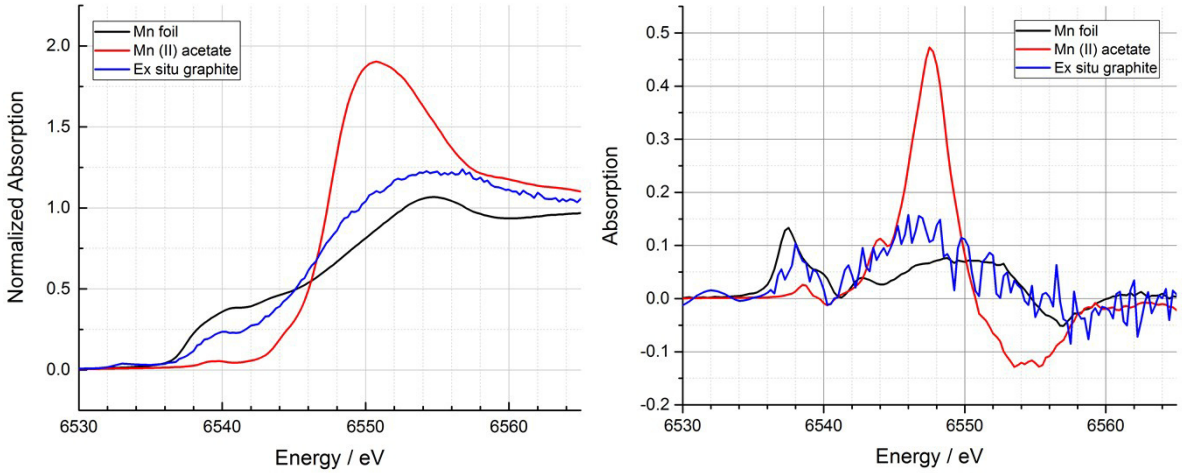

Figure S4 Mn K-edge XANES spectra (left) and the 1st derivative Mn K-edge XANES spectra (right) of the ex situ graphite sample overlaid with the spectra of Mn (II) acetate and Mn foil reference samples to demonstrate relative edge positions.

6) Quantification of transition metal deposition on graphite

In order to quantify the amount of transition metal deposited on the graphite electrode calibration curves (Figure S5) were measured containing manganocene, cobaltocene and nickelocene (all Sigma-Aldrich) in concentrations of zero (≡ background signal for pure electrolyte), 0.4, 4 and 20 mM dissolved in LP57 electrolyte. The calibration curves were measured directly in the *operando* XAS cell in the same geometry, thus eliminating the necessity of performing a correction for differences in x-ray penetration depths. For the calibration measurements, the cells contained only two glass fiber separators and no electrodes The calibration can be used to convert experimentally determined edge jumps into concentrations (in mol L^{-1}). The experimentally determined transition metal concentrations are all in the low mmolar range, which is close to the detection limit for the XAS experiment; furthermore, the manganese and cobalt calibration curves show no ideal linear behavior in this concentration range (Figure S5). Accordingly, the transition metal concentrations determined by XAS will contain an error which cannot be exactly determined due to the non-linear behavior of the calibration curve in the relevant concentration range. Nevertheless, they present a reasonable estimate for the transition metal concentration.

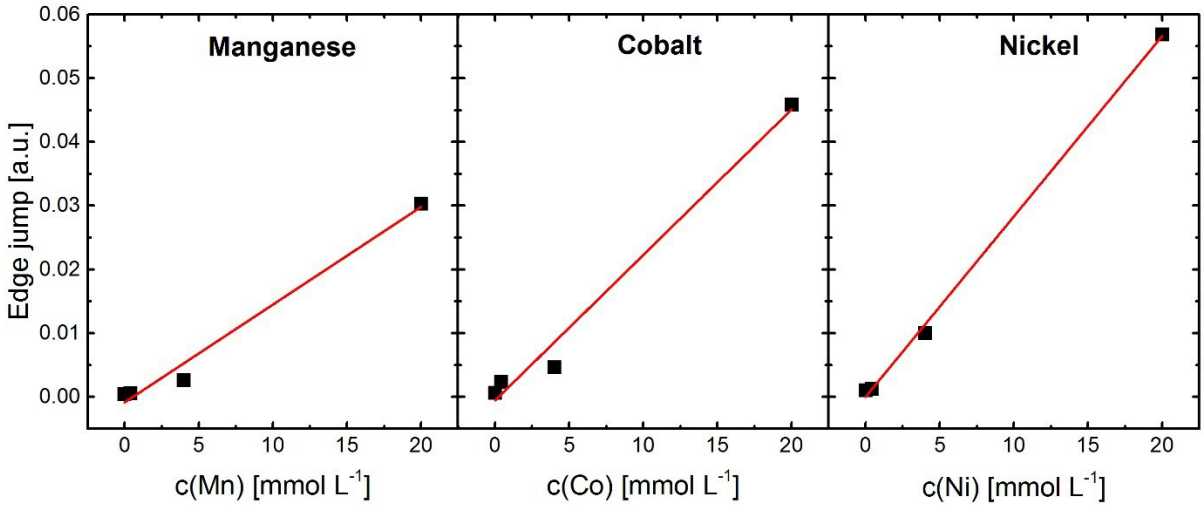

Figure S5 Calibration curves of manganocene, cobaltocene and nickelocene dissolved in LP57 electrolyte in concentrations of zero (= pure electrolyte), 0.4, 4 and 20 mM measured directly in the operando XAS cell.

By comparing the initial and the final XAS spectra measured in the operando cell, concentration increases during cycling of ≈ 3, 9, and 6 mmol L^{-1} were found for Mn, Co, and Ni, respectively (the Mn concentration increase is shown in the lower panel of Figure 1, main text). From this concentration increase, the total amount of each metal deposited on the

graphite electrode (in mol) can be calculated considering the volume of the graphite electrode, which equals 10 mm × 10 mm × 0.17 mm = 17 ·10^{-6} L. The relative amount of the dissolved transition metals can be calculated by dividing by the total amount of each transition metal in the NMC electrode (containing 17.08 mg $LiNi_{0.33}Mn_{0.33}Co_{0.33}O_2$ for this cell with a molecular weight of 96.46 g/mol), which is 59 · 10^{-6} mol for Mn, Co and Ni. Accordingly, the concentration increases over the entire course of the experiment (3, 9 and 6 mmol L^{-1} for Mn, Co and Ni) can be converted into dissolution fractions of 0.09, 0.26 and 0.17% of the total metal content in the NMC electrode. These values agree within a factor of two with *ex-situ* ICP-OES analysis (0.165 ± 0.015 % for Mn, 0.125 ± 0.002 % for Co and 0.116 ± 0.002 % for Ni) of harvested electrodes as explained in the next section.

For manganese, it is also possible to extract dissolution rates from the time resolved *operando* experiments shown in Figure 1 (main text). For the first two cycles between 3.0 and 4.6 V, an average dissolution rate of 0.34 · 10^{-9} mol h^{-1} can be estimated (based on the slope of 20 μmol h^{-1} L^{-1} shown in the lower panel of Fig. 1c multiplied by the graphite electrode volume of 17 ·10^{-6} L) which for an approximate cyle time of 3.5 h (s. upper panel of Fig. 1c) corresponds to a manganese loss of ≈1.0 · 10^{-9} mol/cycle or ≈0.0017%$_{Mn}$/cycle. This may be compared to a previous study, where the same NMC material was cycled in a NMC/graphite full-cell in the same potential range (3.0/4.6 V) at similar conditions (1C CCCV charge (C/20 cut-off) and 1C discharge vs. 0.5C CCCV charge (C/20 cut-off) and 1C CC discharge in the present study), resulting in a total amount of Mn deposited on the graphite electrode of 0.35%$_{Mn}$ of the total Mn content of the NMC electrode (measured by post-mortem prompt-gamma-activation analysis).[2] If normalized by the number of cycles, the latter value equates to ≈0.0015%$_{Mn}$/cycle, which is in excellent agreement with our XAS based measurements. At potentials above 4.6 V, the manganese dissolution rate equals 17 · 10^{-9} mol h^{-1} (based on the now higher slope of 1000 μmol h^{-1} L^{-1} shown in the lower panel of Fig. 1c multiplied by the graphite electrode volume of 17 ·10^{-6} L), which is ≈50-fold higher than the rate found between 3.0 and 4.6 V.

In order to verify the amount of transition metal deposition on the graphite counter electrode with a second analytical technique, two nominally identical cells were cycled with the same procedure as shown in Figure 1c (upper panel). Directly after the end of the procedure, the graphite electrodes were harvested in the charged state, at the end of the

200 minute hold at 5 V. The copper current collector and glass fiber residue were removed and the graphite coating was immersed in 1 mL 65 %HNO_3 (analytical grade, Sigma Aldrich) for one week. The determination of the manganese, cobalt and nickel concentration in HNO_3 was then carried out by ICP-OES (Mikroanalytisches Labor Pascher, Remagen, Germany). The thus quantified metal content of the graphite electrode –expressed as fraction of the total metal content in the NMC electrode – amounts to 0.165 ± 0.015 % for Mn, 0.125 ± 0.002 % for Co and 0.116 ± 0.002 % for Ni, respectively (the error corresponds to the standard deviation from analyzing the graphite electrode harvested from the two nominally identical cells). For all three metals, the contents determined via *operando* XAS and ICP-OES are consistent within a factor of two (s. above). Note, however, that the trend is inverted, with cobalt showing the highest concentration in the XAS determination and manganese showing the highest concentration in the ICP-OES determination. It is not entirely clear whether the XAS or ICP-OES analysis is more accurate as both techniques contain possible sources of error which are difficult to quantify. One can therefore only conclude that the dissolution rate is in the same order of magnitude for all three transition metals without knowing exactly which metal shows the highest dissolution rate. In comparison, Gallus *et al.*[7] found very similar manganese, cobalt and nickel contents in the electrolyte after storage experiments whereas the post-mortem PGAA analysis by Buchberger et al.[2] found the manganese content to be twice as high as that of cobalt and nickel.

7) Estimation of redox potentials in carbonate based electrolytes

It is not possible to state exact potentials for the expected Mn(II), Co(II) and Ni(II) reduction potential vs. Li/Li^+ because, to the best of our knowledge, there is no consistent data for the redox potentials of these transition metals in carbonate based electrolytes. According to the standard electrode potential series in aqueous electrolyte, the Mn(0)/Mn(II) potential is about 900 mV more negative than the respective values for cobalt and nickel. If the redox potentials are corrected for the different solvation energies in water and ethylene carbonate,[8] the resulting redox potential of Mn(0)/Mn(II) is 690 mV more negative than Ni(0)/Ni(II) and 1100 mV more negative than Co(0)/Co(II). Accordingly, in carbonate based solutions the same trend in redox potentials holds true as in aqueous solutions with manganese being the least noble metal.

8) Mn-K edge spectra on graphite electrode after "conventional" cycling

For a description of the cycling procedure see Section 2 in the supplementary information.

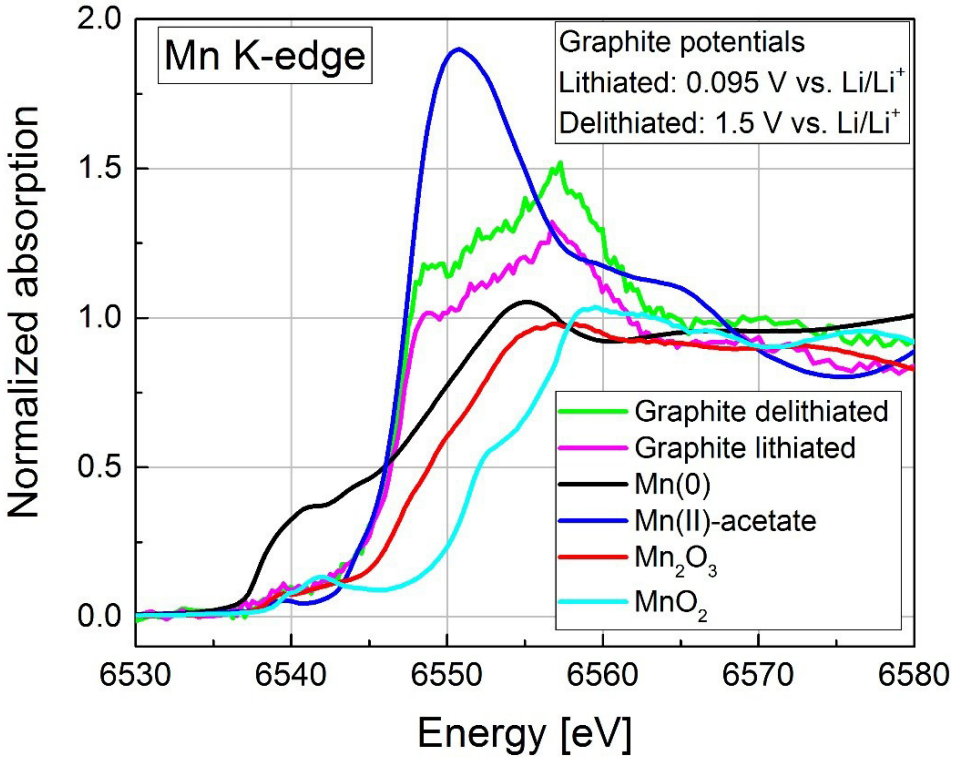

Figure S6 Mn K-edge spectra of reference compounds and *operando* spectra of the graphite electrode either in the lithiated (at 0.095 V vs. Li/Li^+) or delithiated (at 1.5 V vs. Li/Li^+) state. The *operando* spectra were obtained with a Graphite/NMC *operando* XAS cell after 22 "conventional cycles" between 3.0 V and 4.6 V with 1M $LiPF_6$ in EC/EMC as electrolyte.

9) Optical images of lithiated graphite electrodes

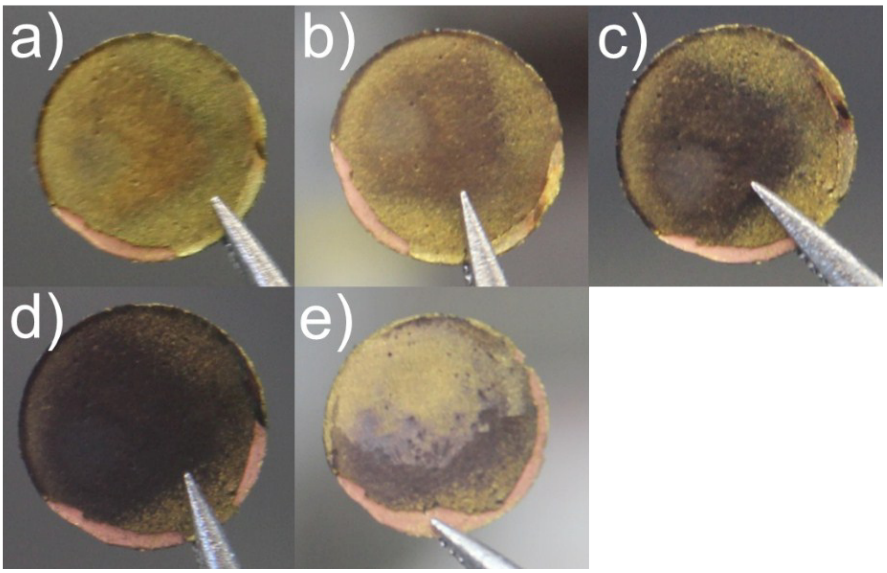

Figure S7 Graphite electrode harvested inside the glove box from Swagelok T-cells after finishing the same procedure which was conducted for the *operando* XAS measurements (s. upper panel of Fig. 1c in the main manuscript. The Images show the top side of the graphite electrode which had faced the NMC electrode during cycling: **a)** directly after harvesting the graphite electrode from the cell inside the glove box, **b)** after drying for 40 minutes in the glove box, **c)** after drying for 80 minutes in the glove box, **d)** after drying for 2 days in the glove box, and, **e)** after scratching off the top layer of the graphite electrode with a scalpel after two days of drying in the glove box.

References

[1] Y. Gorlin, A. Siebel, M. Piana, T. Huthwelker, H. Jha, G. Monsch, F. Kraus, H. A. Gasteiger, M. Tromp, *J. Electrochem. Soc.* **2015**, *162*, A1146–A1155.

[2] I. Buchberger, S. Seidlmayer, A. Pokharel, M. Piana, J. Hattendorff, P. Kudejova, R. Gilles, H. A. Gasteiger, *J. Electrochem. Soc.* **2015**, *162*, A2737–A2746.

[3] B. Ravel, M. Newville, *J. Synchrotron Radiat.* **2005**, *12*, 537–541.

[4] M. Newville, *J. Synchrotron Radiat.* **2001**, *8*, 322–324.

[5] A. Jarry, S. Gottis, Y.-S. Yu, J. Roqué-Rosell, C. Kim, J. Cabana, J. Kerr, R. Kostecki, *J. Am. Chem. Soc.* **2015**, *137*, 3533–3539.

[6] M. Tromp, J. Moulin, G. Reid, J. Evans, *AIP Conf. Proc.* **2007**, *882*, 699–701.

[7] D. R. Gallus, R. Schmitz, R. Wagner, B. Hoffmann, S. Nowak, I. Cekic-Laskovic, R. W. Schmitz, M. Winter, *Electrochim. Acta* **2014**, *134*, 393–398.

[8] Y.-K. Han, K. Lee, S. Kang, Y. S. Huh, H. Lee, *Comput. Mater. Sci.* **2014**, *81*, 548–550.

3.2.2 Nickel, Manganese, and Cobalt Dissolution from Ni-rich NMC and Their Effects on NMC622-graphite cells

In this section, the article "Nickel, Manganese, and Cobalt Dissolution from Ni-rich NMC and Their Effects on NMC622-graphite cells" will be presented. The study was conducted in collaboration with the group of Prof. Moniek Tromp at University of Amsterdam. At the date of submission of this PhD thesis, the work has not yet been submitted for publication and is therefore added as manuscript to this thesis.

The manuscript deals with the dissolution of Ni, Mn, and Co from Ni-rich NMC622 and their detrimental effects on the cell performance of NMC622-graphite cells. Using operando XAS at the European Synchrotron Radiation Facility (ESRF), we measure the transition metal dissolution and subsequent deposition on the graphite anode, applying a very similar procedure as described in section 3.2.1. We demonstrate that at high potentials >4.7 V, stoichiometric dissolution of Ni, Mn, and Co occurs. For NMC622 and Ni-rich NMCs in general, this means that the absolute amount of dissolved transition metals is highest for Ni. A comparison of the total amount of dissolved Ni, Mn, and Co from NMC622 in this study is very similar to that found for NMC111 in the work presented in section 3.2.1. The oxidation states of deposited Ni and Co in presence of electrolyte were found to be +2, whereas for Mn we cannot clearly distinguish between +2 or +3. Since in the previous literature, mostly the effect of dissolved Mn on the cell aging was investigated,[216, 220, 221] this study focusses on a comparison of the effect and mechanism of dissolved transition metals on cell aging. By polarizing a conductive carbon electrode in electrolyte containing Ni^{2+}, Mn^{2+}, or Co^{2+} (as TFSI salts), we show that these ions are reduced at ~2.2 V, ~1.3 V, and ~2.5 V vs. Li/Li^+, respectively. As a graphite electrode is operated at potentials <0.4 V vs. Li/Li^+, all three metals could thus be expected to be reduced to their metallic state on the graphite anode in a NMC622-graphite cell, contradicting at a first glance the oxidation states determined via XAS. As in a conventional Li-ion cell an SEI will be formed on the graphite anode prior to any deposition of transition metals on the anode, we investigate the influence of the SEI to get insights into the underlying mechanism. We show that as long as no SEI is present on a conductive carbon electrode, reversible reduction and oxidation of Ni is possible between 1.5 and 4.0 V vs. Li/Li^+. However, if we scan down to a potential of 50 mV vs. Li/Li^+, Ni reduction and SEI formation occurs. Upon reverse scanning to 4 V vs. Li/Li^+, no Ni oxidation is observed anymore. This observation shows that it must be a chemical reaction with the SEI rather than an electrochemical one that causes the Ni to be observed in its +2 state on the

graphite anode. This chemical reaction decomposing the SEI is likely also the origin of the detrimental effect of deposited transition metals on the graphite anode. Cycling NMC622-graphite cells with and without the addition of either $Ni(TFSI)_2$, $Mn(TFSI)_2$, or $Co(TFSI)_2$ to LP57 electrolyte, we show that the addition of any of the transition metals causes poorer cycling stability compared to the pure electrolyte. More specifically, the cycling stability decreases in the order LP57 > Ni ≈ Co > Mn. To obtain further insights into the mechanism leading to faster cell aging in presence of transition metals, we use in-situ XRD to determine the dependence of the lattice parameters on the degree of delithiation, which serves as a calibration to determine the remaining lithium content in the NMC in the discharged state after cycling. Thereby, we demonstrate that the main aging mechanism induced by all three metals is the loss of active lithium in the anode SEI, most likely caused by the chemical decomposition and subsequent formation of additional SEI, yet the magnitude is larger for Mn in comparison to Ni and Co.

Author Contributions

Roland Jung designed the experiments. Roland Jung and Fabian Linsenmann prepared the electrode coatings. Roland Jung coordinated the beamtime at ESRF. Rowena Thomas evaluated the XAS spectra. Participants of the beamtime: Roland Jung, Rowena Thomas, Johannes Wandt, and Karin Kleiner. Fabian Linsenmann performed the CV experiments and built the NMC-graphite cells. Roland Jung performed the in-situ XRD measurement. Roland Jung evaluated the data. Roland Jung, Moniek Tromp and Hubert Gasteiger wrote the manuscript. All authors discussed the results and commented on the manuscript.

Nickel, Manganese, and Cobalt Dissolution from Ni-rich NMC and Their Effects on NMC622-graphite cells

Roland Jung[a,b,z], Fabian Linsenmann[a], Rowena Thomas[c], Johannes Wandt[a], Sophie Solchenbach[a], Filippo Maglia[b], Christoph Stinner[b], Moniek Tromp[d], and Hubert A. Gasteiger[a]

[a]*Chair of Technical Electrochemistry, Department of Chemistry and Catalysis Research Center, Technische Universität München, Lichtenbergstrasse 4, Garching, Germany*

[b]*BMW AG, Petuelring 130, Munich, Germany*

[c]*Institute for Catalyst Characterization, Technische Universität München, Lichtenbergstrasse 4, Garching, Germany*

[d]*Van't Hoff Institute for Molecular Sciences, University of Amsterdam, Amsterdam, Netherlands*

[z]E-mail: roland.jung@tum.de

ABSTRACT

Transition metal dissolution from the cathode active material and its deposition on the anode is known to be a significant cause of cell aging, with manganese being the most investigated transition metal in the literature. However, the current research focus is shifting towards nickel rich layered $LiNi_xMn_yCo_zO_2$ (NMC) with $x > 0.5$, as they exhibit higher specific capacities and energies compared to commonly used NMC111 ($x = y = z = 1/3$). Due to the high Ni amounts in Ni-rich NMCs, especially the effect of Ni dissolution needs to be understood to evaluate its impact on cell degradation. In this study, the dissolution of transition metals from a NMC622 electrode and the subsequent deposition on a graphite anode using operando X-ray absorption spectroscopy (XAS) is investigated. We show that at high potentials >4.6 V in NMC622-graphite cells transition metals dissolve nearly stoichiometric, highlighting the significance of investigating Ni deposition on the anode. Using NMC622-graphite full cells with electrolyte containing the bis(trifluoromethane)sulfonimide (TFSI) salts of either Ni, Mn or Co, we compare the detrimental impact of these metals on the cell performance. By the use of in-situ and ex-situ XRD, it is shown that the aging mechanism induced by all three metals is the loss of active lithium in the solid electrolyte interface (SEI) on the graphite anode induced by a decomposition of the anode SEI. This loss of cycleable lithium is larger in magnitude when Mn is present in the electrolyte compared to Ni and Co indicating a higher activity of deposited Mn in comparison to Ni and Co.

Introduction

Li-ion batteries are a key technology on the way to electro mobility and have already proven to be capable as power supply for electric vehicles (EVs) or hybrid electric vehicles (HEVs). So far, the market of EVs and HEVs is rather small compared to the overall vehicle market. Yet, a longer driving range achieved by improved specific energies as well as significantly reduced costs might enable penetration of the mass market.[1, 2] Among several potential cathode active materials (CAMs), layered lithium nickel manganese cobalt oxide ($LiNi_xMn_yCo_zO_2$, NMC) is one of the most promising classes of materials.[3, 4] While NMC111 is already widely used in EVs, the research focus is shifting to the so-called nickel rich (Ni-rich) NMCs with $x > 0.5$ because with growing Ni-content more lithium can be extracted from the layered NMC structure within a constant voltage range, resulting in improved specific energies.[3, 5-7] The dissolution of transition metals, in particular of manganese (Mn), was first identified as a major aging mechanism in $LiMn_2O_4$ (LMO) spinel cathodes causing severe capacity fading in full cells.[8-13] Later on, transition metal dissolution was also investigated for the layered NMC materials showing that this phenomenon is not limited to LMO.[14-18] The detrimental effect of transition metal dissolution can have two origins: i) loss of CAM, and ii) dissolution into the electrolyte and subsequent deposition and accumulation on the graphite anode. The former is only of minor importance, as only rather small amounts of the overall transition metal amounts in the CAMs are dissolved. For example, Choi et al. soaked various CAMs in electrolyte and determined the overall metal dissolution which was 0.9% for NMC111.[18] Buchberger et al. found for NMC111-graphite cells an overall transition metal dissolution corresponding to 0.08% and 0.77% of the CAM when the cells were cycled at 25 °C to 4.2 (300 cycles) and 4.6 V (235 cycles), respectively.[14] In contrast, the deposition and accumulation of dissolved transition metals on the graphite anode was shown to induce irreversible side reactions leading to ongoing SEI formation and electrolyte reduction causing the loss of active lithium and impedance growth.[17, 19-23] For instance, Pieczonka et al. reported significant Ni and Mn dissolution from $LiNi_{0.5}Mn_{1.5}O_4$ (LNMO) and showed that LNMO-Li can be cycled with high capacity retention excluding a direct effect of CAM decomposition, yet, for LNMO-graphite cells, which possess only a limited lithium inventory defined by the lithium contained in the LNMO cathode, severe capacity fading was observed which was attributed to the loss of active lithium caused by the deposited Ni and Mn on the graphite anode.[23] Additionally, Buchberger et al. also showed transition metal dissolution and deposition on the graphite anode after cyclic aging of NMC111-graphite cells cycled to 4.2 V

leading to the loss of active lithium. After reassembling the NMC electrode in a NMC-Li cell, the full capacity of the NMC electrode was recovered, proving that the active material stayed intact.[14]

In the literature, the most investigated transition metal is Mn, yet Ni is the metal with the highest proportion in Ni-rich NMCs, and therefore its effect in comparison to Mn has to be understood in order to be able to estimate the impact of transition metal dissolution on the lifetime of a battery cell when Ni-rich NMCs are used. Additionally, the detrimental effect of Ni can also be expected to be significant for other Ni-rich materials like NCA ($LiNi_{0.8}Co_{0.15}Al_{0.05}O_2$). Herein, we report the transition metal dissolution and subsequent deposition on the graphite anode from a NMC622-graphite cell using operando X-ray absorption spectroscopy (XAS). Furthermore, we present a comparative study of the detrimental effect of Ni, Mn, and Co on the cycling stability of NMC622-graphite cells. We will investigate the aging mechanism caused by the different metals leading to accelerated cell aging. In the course of previous literature reports and our results, we will discuss possible mechanisms causing the faster cell degradation induced by transition metal deposits on the anode.

Experimental

Electrode Preparation

$LiNi_{0.6}Mn_{0.2}Co_{0.2}O_2$ (NMC622, Umicore, Belgium) electrodes were prepared by dispersing 91.5 $\%_{wt}$ of the active material particles, 4.4 $\%_{wt}$ conductive carbon (Super C65, Timcal, Switzerland) and 4.1 $\%_{wt}$ polyvinylidene fluoride binder (PVDF, Kynar HSV 900, Arkema, France) in N-methylpyrrolidone (NMP, anhydrous, 99.5%, Sigma-Aldrich). The slurry was mixed in a planetary mixer (Thinky, USA) at 2000 rpm for 2x5 minutes. In between the two runs, the slurry was ultrasonicated for 10 minutes in an ultrasonic bath. The resulting ink was spread onto aluminum foil (thickness 18 µm, MTI Corporation, USA) using a gap bar coater (RK PrintCoat Instruments, UK). For the in situ XRD measurement, the NMC cathode was prepared by coating the slurry through a mask (12 mm diameter circle) onto an aluminum foil with a diameter of 42 mm, whereby the aluminum foil serves both as current collector and X-ray window.

Graphite electrodes were composed of 95.8 $\%_{wt}$ graphite (MAG-D20, Hitachi), 1 $\%_{wt}$ Super C65 (Timcal, Switzerland), 1 $\%_{wt}$ sodium carboxymethylcellulose (Na-CMC, Dow Wolff Cellulosics) and 2.2 $\%_{wt}$ styrene-butadiene rubber (SBR, JSR Micro). For the slurry preparation, graphite, Super C65 and Na-CMC were dispersed in highly pure water (18 MΩcm, Merck Millipore, Germany) and mixed in a planetary mixer (Thinky, USA) at 2000 rpm for 30 minutes. The slurry was ultrasonicated for 10 minutes in an ultrasonic bath. SBR was added to the slurry and mixed at 500 rpm for 2 minutes. The ink was coated onto copper foil (thickness 12 µm, MTI Corporation, USA) using a gap bar coater (RK PrintCoat Instruments, UK).

Electrodes containing only conductive carbon (Super C65, Timcal, Switzerland) had a composition of 50 $\%_{wt}$ Super C65 and 50 $\%_{wt}$ polyvinylidene fluoride binder (PVDF, Kynar HSV 900, Arkema, France). The solids were dispersed in N-methylpyrrolidone (NMP, anhydrous, 99.5%, Sigma-Aldrich), mixed in a planetary mixer (Thinky, USA) at 2000 rpm for 30 minutes and coated onto copper foil (thickness 12 µm, MTI Corporation, USA) or stainless steel mesh (316 grade, 26 µm aperture, 25 µm wire diameter, The Mesh Company, UK) using a gap bar coater (RK PrintCoat Instruments, UK).

All coatings were dried at 50 °C in air, electrodes were punched out, dried overnight at 120 °C under dynamic vacuum in a glass oven (drying oven 585, Büchi, Switzerland) and

transferred into a glovebox (O_2 and H_2O < 0.1 ppm, MBraun, Germany) without exposure to ambient air.

Operando X-ray absorption spectroscopy

Operando X-ray absorption spectroscopy was used to measure the dissolution of transition metals from NMC622 and their subsequent deposition on a graphite electrode. The X-ray absorption spectra were measured at the ESRF synchrotron (BM23 beamline), France. The acquisition time for each spectrum presented in this work was approximately 9 minutes. The synchrotron was operating in 7/8+1 top up mode. A sagittaly focusing double crystal monochromator consisting of two Si 111 crystals was used to select the incoming energy and the beam was focused using Si coated mirrors before being cut with slits to achieve a beam size of 140 µm in the horizontal and approximately 1000 µm in the vertical dimension. With the incident angle of 45° this yields a probing area of 198 x 1000 µm. These dimensions allow focusing the beam exclusively on the graphite electrode, which had a dimension of 226 x 10000 µm. The cells were assembled as described below, and measured in fluorescence mode, with an energy selective 13-element Ge detector to collect the photons. Photon energies were calibrated using the first peak in the first derivative of the pure metal foils, which were measured in fluorescence before and after the operando studies, and background corrections of the spectra were carried out using the IFEFFIT software package.[24, 25]

NMC622-graphite cells were assembled using the XAS cell design described by Gorlin et al.[26] Both electrodes were square shaped with a side length of 10 mm and had an NMC-loading of 25.36 mg_{NMC}/cm^2 (5.07 mAh/cm², thickness: 92 µm) and a graphite loading of 20.05 $mg_{graphite}/cm^2$ (7.12 mAh/cm², thickness: 226 µm). In between the electrodes, two glassfiber separators (250 µm uncompressed thickness, glass microfiber filter 691, VWR) and 300 µL electrolyte (1 M $LiPF_6$ in EC:EMC 3:7, BASF, Germany) were used. In analogy to the work by Wandt et al.[15], the X-ray window consisted of an aluminized 12 µm Kapton foil (aluminized side placed towards the cell exterior) and an additional 25 µm Kapton foil on top of the aluminum layer in order to prevent mechanical damage to the thin aluminum layer. The X-ray beam was focused on the graphite electrode making it possible to selectively measure the XANES spectra transition metal deposits within the anode. The operando cell was connected to a SP200 potentiostat (SP200, Biologic, France) and two charge/discharge cycles

between 2.6 and 4.6 V were performed at a 0.5 C-rate (referenced to the reversible discharge capacity of 200 mAh/g at 4.6 V). Charging was done in CCCV mode with 0.05 C cut-off and discharge was performed in CC mode. Afterwards the cell was charged to 4.6 V (0.5 C-rate) and the potential ramped up to 5.0 V with 2.5 mV/min, followed by a CV step over 3 h. The reference samples Mn-foil, Mn(II) acetate, Mn_2O_3, MnO_2, Ni-foil, Ni(II) acetate, Co-foil, and Co(II) acetate were taken from Wandt et al.[15] Conversion of the measured edge jump to concentrations (in mol/L) was done by measuring a calibration curve.[15] Therefore, bis(isopropylcyclopentadienyl)manganese, bis(cyclopentadienyl)nickel, and bis(cyclopentadienyl)cobalt (all Sigma-Aldrich) were dissolved in concentrations of 0 mM (background signal of pure LP57 electrolyte), 2 mM, 4 mM, and 20 mM in LP57 electrolyte. The calibration curves were measured in the operando XAS cell in the same geometry, thereby eliminating any differences in X-ray penetration depths. The cells contained only two glass fiber separators and the graphite electrode on which the beam was focused.

Conversion of the determined concentrations to moles of transition metals was done by multiplying with the volume of the graphite electrode of 1 cm x 1 cm x 0.0226 cm = 0.0226 cm³. Dividing by the total amount of each transition metal in the NMC electrode (25.34 mg NMC622 → 262 μmol_{NMC} → 157 μmol_{Ni}, 52 μmol_{Mn}, 52 μmol_{Co}) yielded the amount of dissolved transition metals in % from the NMC622 electrode.

The transition metal deposits on a graphite anode were additionally quantified using ICP-OES. Therefore, two NMC622-graphite cells were cycled with the same procedure as described above. Right at the end of the procedure, the graphite electrodes were harvested in the charged state. The copper current collector and glass fiber residues were removed and the graphite was immersed in 0.5 mL 65 % HNO_3 (analytical grade, Sigma Aldrich) for one week. The Ni, Mn, and Co concentrations in HNO_3 were quantified by ICP-OES (Mikroanalytisches Labor Pascher, Remagen, Germany).

Electrochemical Characterization

Electrochemical cycling of NMC622-graphite cells was performed in Swagelok T-cells assembled in an argon filled glove box (O_2 and H_2O < 0.1 ppm, MBraun, Germany), with NMC as working electrode (10 mm diameter) and graphite as counter electrode (11 mm diameter). The areal mass loading of all NMC electrodes was 16.2 ± 0.6 mg_{NMC}/cm^2 and the

one of the graphite electrodes was adapted according to the loading of the NMC electrodes to achieve a constant balancing factor. The areal capacity of the anode (in mAh/cm^2) was 1.2-fold oversized compared to the cathode (referenced to the reversible capacities of NMC and graphite at a 1 C-rate; if referenced to 0.1 C, the anode is roughly 1.1-fold oversized). To monitor the potential of both the NMC cathode and the graphite anode, a lithium reference electrode (thickness 0.45 mm, battery grade foil, 99.9 %, Rockwood Lithium, USA) was used. Two glass fiber separators (glass microfiber filter, 691, VWR, Germany) punched to a diameter of 11 mm were used between working and counter electrode, and one at the reference electrode (diameter of 10 mm). Formation of the cells was done with 2 cycles at 0.1 C-rate in the voltage range between 3.0 and 4.2 V using 80 µL of LP57 electrolyte (1 M $LiPF_6$ in EC:EMC 3:7 wt/wt, < 20 ppm H_2O, BASF, Germany) between working and counter electrode and 40 µL were added to the reference electrode side. The C-rate was referenced to the approximate reversible specific capacity of the NMC of 160 mAh/g_{NMC} at 1 C. The cells were cycled in a climate chamber (Binder, Germany) at 25 °C with a battery cycler (Series 4000, Maccor, USA). The cells were opened inside the glovebox and the separators were replaced by two fresh ones to remove most of the electrolyte. Then LP57, LP57 + $Ni(TFSI)_2$, LP57 + $Mn(TFSI)_2$, or LP57 + $Co(TFSI)_2$ were added and the cells were cycled 300 times at 1 C-rate between 3.0 V and 4.2 V at 25 °C. The concentrations of the transition metals were 30 mM or 60 mM.

At the end of the cycling procedure, the cells were dissembled in a glovebox and a XRD pattern of the NMC622 cathode was measured. Any contact to air was prevented by putting the electrode into an airtight sample holder with aluminum windows as reported previously.[27] The XRD patterns were obtained in transmission mode using a STOE STADI P diffractometer (STOE, Germany) with Mo-$K_{\alpha 1}$ radiation (λ = 0.70932 Å) and a Mythen 1K detector. The diffraction patterns were measured at room temperature in a 2θ-range between 6.5–52° with a step size of 0.015° and 5 seconds per step.

Cyclic voltammograms (CVs) were recorded in 2032-type coin cells with two glass fiber separators (diameter of 16 mm) and 160 µL of electrolyte at a scan rate of 0.1 mV/s. CVs were measured in two different set-ups: i) Conductive carbon electrode coated on a Cu current collector versus a lithium counter electrode using LP57, LP57 + 60 mM $Ni(TFSI)_2$, LP57 + 60 mM $Mn(TFSI)_2$, or LP57 + 60 mM $Co(TFSI)_2$. The carbon electrode was polarized starting from 3 V to 0.01 V and back to 3 V. ii) Conductive carbon electrode coated on a stainless steel mesh versus an LFP electrode (3.5 mAh/cm², Custom Cells, Itzehoe,

Germany) precharged to 50% SOC using LP57 + 60 mM $Ni(TFSI)_2$ as electrolyte. The carbon electrode was polarized starting from 3 V to 4 V, down to 1.5 V, up to 4 V and subsequently down to 0.05 V, up to 4 V and back to 3 V, with all potential values calculated vs. Li/Li^+, which was determined by considering a stable LFP potential of 3.45 V vs. Li/Li^+.

In-situ X-ray diffraction (XRD)

The in-situ XRD cell used to analyze the changes of the NMC lattice parameters was described in detail elsewhere.[14] The NMC622 working electrode (20.8 mg_{NMC}/cm^2) was coated on aluminum, which acts both as a current collector and X-ray window. As counter electrode lithium metal foil (thickness 0.45 mm, battery grade foil, 99.9 %, Rockwood Lithium, USA) was used. Four glass fiber separators (14 mm diameter, glass microfiber filter 691, VWR) and 160 µL LP57 electrolyte were placed in between the two electrodes. The in-situ cell was connected to a SP200 potentiostat (SP200, Biologic, France) and charged/discharged at a 0.1 C-rate (referenced to the reversible capacity at 4.3 V of 180 mAh/g). After one hour of charge/discharge the cell was put to OCV and XRD patterns were collected at well-defined states of charge. The in-situ XRD patterns were collected in Bragg-Brentano geometry using non-monochromatized Mo-K_α radiation to obtain a higher flux yielding higher signal to noise ratios. The diffraction patterns were measured at room temperature in repetition mode with two repetitions per sample. The patterns were collected in a 2θ-range between 7–52° with a step size of 0.012° and 10 seconds dwell time. Data analysis was performed using WinXPow program package (WinXPow software version 3.0.2.1, 2011, by STOE & Cie GmbH, Darmstadt, Germany). The determination of the lattice parameters was done using FullProf software (version 3.0, June 2015).

Results

Operando determination of transition metal dissolution and deposition from NMC622-graphite cell

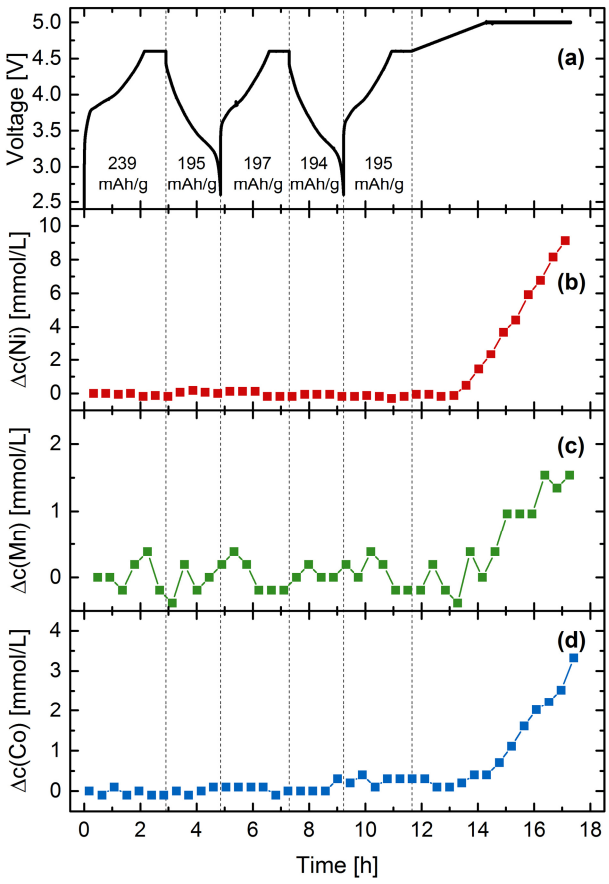

Figure 1. (a) Cell voltage of a NMC622-graphite full cell obtained in the operando XAS cell in LP57 (1 M $LiPF_6$ in EC:EMC 3:7) electrolyte and measured concentration changes of (b) nickel, (c) manganese, and (d) cobalt on the graphite anode.

Figure 1a depicts the voltage curve of a NMC622-graphite full cell cycled in the operando XAS cell. The first charge and discharge capacities are 239 mAh/g_{NMC} and 195 mAh/g_{NMC}, respectively. In the second cycle, capacities of 197 and 194 mAh/g_{NMC} were measured. These capacities match very well the measured capacity values in our previous publication with the same NMC622 material showing that the operando XAS cell performs similar to a standard cell set-up.[7] The concentration changes of Ni, Mn, and Co on the graphite anode are shown in **Figure 1b-d** and were determined by measuring the edge jumps in the X-ray absorption spectra. Conversion of the edge jump to concentrations was done via a calibration with standard solutions (see experimental section). Because of the constant measurement time for each spectrum at the Ni, Mn, and Co K-edges, the obtained data for the Mn concentrations

are noisiest. This is due to the lowest energy of the Mn K-edge (~6545 eV) yielding the poorest signal to noise ratio in comparison to the Ni (~8340 eV) and Co (~7715 eV) K-edges. During cycling to 4.6 V, no significant increases in the transition metal concentrations can be detected. It is important to note that there might be a slow dissolution of transition metals; however, we could not detect it within two cycles using XAS. Wandt et al. observed in a NMC111-graphite cell cycled with the same procedure a slight increase of the Mn concentration of ~20 $\mu mol/(L \cdot h)$,[15] yet this increase is close to the magnitude of the background noise of the experiment. When the cell voltage is ramped up to roughly 4.8 V (after ~13.5 h in **Figure 1**), a steep increase in the concentrations of all three transition metals is observed. The concentrations of Ni, Mn, and Co increase by ~9 mM, ~1.5 mM, and ~3.5 mM, respectively. This clearly demonstrates that in case of the Ni-rich NMC622 the dissolved amount of Ni is highest in agreement with its highest content in the NMC622 material. A conversion of the concentrations to the percentage of dissolved metals from NMC will be presented in the Discussion section.

In **Figure 2** the Ni, Mn, and Co K-edges are depicted. The black curves represent the last spectra measured within the graphite during the electrochemical procedure shown in **Figure 1**. The spectra measured earlier looked the same and are therefore not shown. Reference spectra of the transition metals in the metallic state and +II are shown in every panel, for Mn also reference compounds in the oxidation states +III and +IV are added. In the spectra measured at the Ni and Co K-edges (**Figure 2a** and **c**), it can be seen that the edge positions for both metals match the edge positions of the +II oxidation state very well. The Mn spectrum measured on the graphite electrode is very noisy due to the low concentration of Mn deposited on the graphite and due to the low energy of the Mn K-edge. The oxidation states 0 and +IV can be excluded, however, due to the very close edge positions and the rather noisy spectrum, we cannot distinguish between a Mn oxidation state of +II or +III, or even a mix of both. The observed oxidation states of the different metals will be discussed in greater detail and compared to the reports in the literature in the Discussion section.

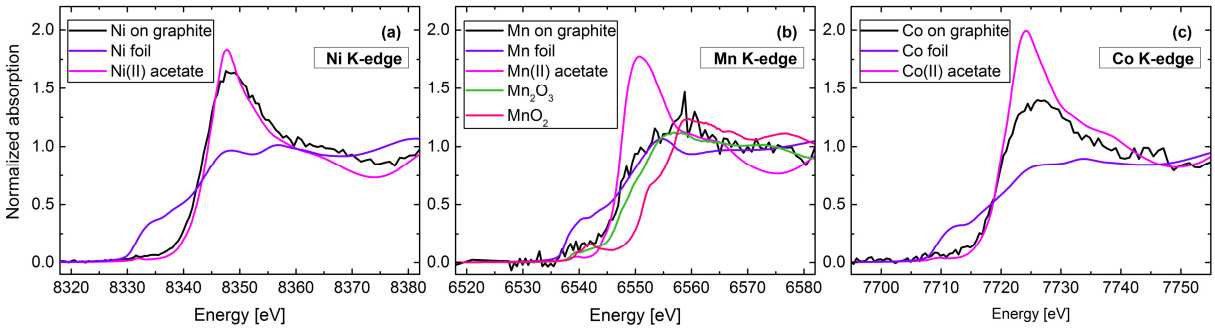

Figure 2. K-edge spectra (black lines) of (a) nickel, (b) manganese and (c) cobalt measured in the operando XAS cell on the lithiated graphite electrode at the end of the experiment shown in **Figure 1**. The spectra are compared to reference samples containing the transition metals in different oxidation states.

Reduction potentials of Ni^{2+}, Mn^{2+}, and Co^{2+}

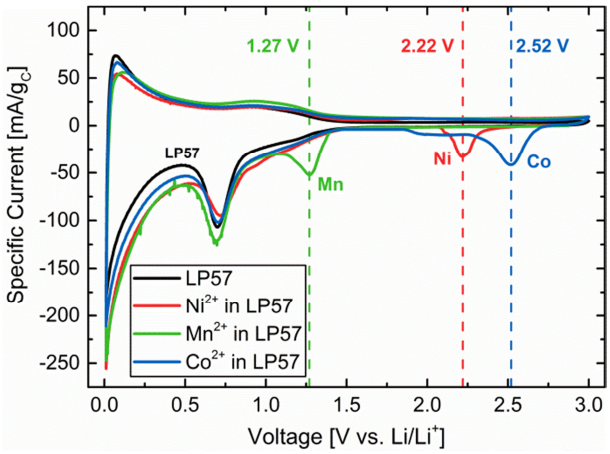

Figure 3. First cycle of a cyclic voltammogram of a Super C65 electrode in LP57 (black), LP57 + 60 mM $Ni(TFSI)_2$ (red), LP57 + 60 mM $Mn(TFSI)_2$ (green), and LP57 + 60 mM $Co(TFSI)_2$ (blue). The experiment was started close to OCV at 3 V vs. Li/Li^+. The carbon electrode was polarized to 0.01 V vs. Li/Li^+ and back to 3 V vs. Li/Li^+ at a scan rate of 0.1 mV/s.

The reduction potentials of Ni, Mn, and Co in LP57 electrolyte were measured by cyclic voltammetry on a conductive carbon (Super C65) electrode vs. a lithium metal counter electrode in a standard coin cell. **Figure 3** illustrates the measured specific current as a function of the voltage of the conductive carbon working electrode. For pure LP57 electrolyte (black line), without the addition of any transition metal, one reduction peak at ~0.7 V vs. Li/Li^+ can be observed, stemming from the reduction of electrolyte forming the SEI on the carbon surface.[28, 29] Below ~0.4 V the reductive specific current increases which presumably stems from lithium intercalation into the graphitic regions of the conductive carbon. The delithiation can be observed as the positive peak at ~0.08 mV. As expected, no reversible

oxidation peak corresponding to the SEI formation exists due to the irreversibility of the SEI forming reaction. When Ni, Mn, or Co (60 mM solution of $Ni(TFSI)_2$, $Mn(TFSI)_2$, $Co(TFSI)_2$) is added to LP57, the same reduction peak for SEI formation is observed as for pure LP57 without any significant changes, yet an additional reductive peak can be observed at higher potentials corresponding to the reduction of the transition metals. The maxima of the reduction peaks are at 2.22 V (Ni, red line), 1.27 V (Mn, green line) and 2.52 V (Co, blue line), all vs. Li/Li^+. Compared to the standard reduction potentials in aqueous media (2.80 V (Ni/Ni^{2+}), 1.87 V (Mn/Mn^{2+}) and 2.77 V (Co/Co^{2+}), all vs. Li/Li^+)[30], the measured values are slightly lower due to differences in the solvation energies caused by H_2O and EC,[15] yet the difference in reduction potentials of ~1 V of Mn compared to Ni and Co stays roughly constant. Note that during the oxidative scan in **Figure 3**, we do not observe any peak corresponding to the re-oxidation of the deposited metals on the carbon surface. This is somewhat surprising since one could expect that the reduction and oxidation of the transition metals should be a reversible process. To better understand this observation and the effect of the SEI on the reversibility of the metal reduction and oxidation, we modified the experimental set-up: i) The conductive carbon was coated on stainless steel in order to allow scanning to potentials > 3 V, which would not be possible with a copper current collector due to its limited oxidative stability, aiming to understand if the absence of a transition metal oxidation peak in **Figure 3** is caused by a high overpotential for the transition metal oxidation. ii) The Li counter electrode was replaced by a LFP counter electrode, which was precharged to 50% SOC and has therefore a stable potential at ~3.45 V vs. Li/Li^+, at which no transition metal reduction and also no electrolyte oxidation/reduction is possible. The results of the CV experiment with this modified set-up are shown in **Figure 4**. The voltage of the carbon electrode vs. Li/Li^+ in **Figure 4** is calculated by assuming a stable potential of the LFP electrode of 3.45 V vs. Li/Li^+. First, we polarized the conductive carbon in LP57 + 60 mM $Ni(TFSI)_2$ to 4 V vs. Li/Li^+ (black solid line in **Figure 4**) to test if an oxidation of the dissolved Ni^{2+} to Ni^{3+} or Ni^{4+} might be possible. As it can be seen in the inset of **Figure 4**, no current is observed up to 4 V vs. Li/Li^+, excluding the oxidation of Ni^{2+}. Subsequently, the carbon electrode was polarized to a potential of 1.5 V vs. Li/Li^+ (pink dashed line), so that Ni is reduced on the carbon surface, but the formation of the SEI is avoided. Afterwards, the carbon electrode is polarized back to 4 V vs. Li/Li^+. In this case, re-oxidation of deposited Ni is observed at 3.7 V vs. Li/Li^+ (pink dashed line). In the following cycle, the electrode was polarized down to 50 mV vs. Li/Li^+ (purple dotted line), in which case both Ni reduction and SEI formation is observed. Finally, polarizing the electrode back to 4 V vs. Li/Li^+ yields no

oxidation peak corresponding to Ni oxidation (purple dotted line). Therefore, a reversible oxidation of reduced Ni in presence of an SEI can be excluded. This clearly demonstrates that the SEI has a severe impact on the reversibility of the transition metal reduction/oxidation. We will discuss this in more detail in the Discussion section.

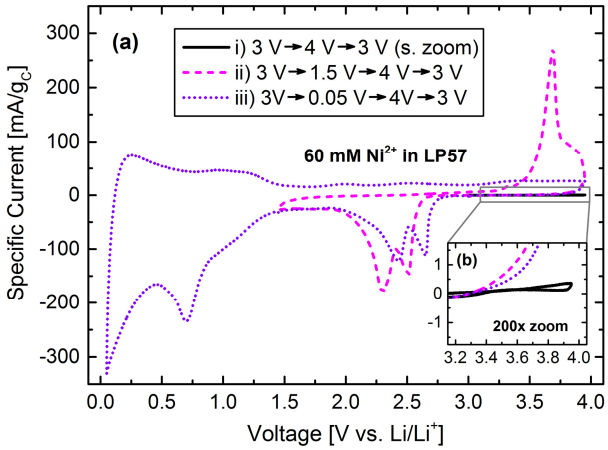

Figure 4. Cyclic voltammograms of a Super C65 electrode cycled vs. LFP (50% SOC) in LP57 + 60 mM $Ni(TFSI)_2$. The experiment was started close to OCV at 3 V vs. Li/Li^+. The carbon electrode was polarized at a scan rate of 0.1 mV/s in three steps: i) from 3 V to 4 V vs. Li/Li^+ and back (black solid line), ii) to 1.5 V, up to 4 V and back to 3 V (pink dashed line), and iii) to 0.05 V, up to 4 V and back to 3 V (purple dotted line).

Electrochemical cycling of NMC622-graphite cells

To investigate and compare the impact of Ni, Mn and Co on the electrochemical performance of NMC622-graphite cells, electrolytes containing a concentration of 30 mM and 60 mM of $Ni(TFSI)_2$, $Mn(TFSI)_2$, or $Co(TFSI)_2$ were used for cell cycling. The formation of the cells (initial two cycles) was always done in pure LP57 electrolyte to mimic the realistic scenario in which the SEI is already present on the graphite anode before significant amounts of transition metals dissolve from the NMC cathode during extended charge-discharge cycling. **Figure 5** shows the results of NMC622-graphite cells cycled between 3.0 V and 4.2 V in pure LP57 (black), and in LP57 containing $Ni(TFSI)_2$ (red), $Mn(TFSI)_2$ (green), or $Co(TFSI)_2$ (blue). Note that the cells cycled in LP57 were also reassembled after the two formation cycles to test if the SEI may be damaged when the electrolyte used during formation (LP57) is replaced by the one used during extended cycling (again LP57 or LP57 with the addition of the transition metal salts). Yet, we did not observe any impact on the electrochemical behavior of disassembling the cells after formation, proving that the SEI stayed intact. For all cells a specific discharge capacity of 171±1 mAh/g was obtained in the formation cycles at a

0.1 C-rate. In the third cycle, the cells containing LP57 reached 157.6 mAh/g and faded to 148.2 mAh/g within 298 cycles at a 1 C-rate. The measured specific capacities of the third and 300^{th} cycles of the cells cycled in transition metal containing electrolyte are summarized in Table I. It can be observed that in the third cycle the specific capacities are significantly lower for cells with transition metal ions than the ones obtained for the cells in pure LP57. This indicates that significant irreversible reactions occur right after the transition metals are added into the cell. Upon cycling, the capacity fading is much more significant within the first 50 cycles than from cycle 50 to 300, indicating that the detrimental effect of the transition metals is reduced during cycling (**Figure 5**). Furthermore, the specific capacity decay is fairly similar for all cells at cycle numbers > 100. These observations are in good agreement with the measured coulombic efficiencies. In particular, low efficiencies were observed at cycle numbers < 50 only for the cells containing transition metals and similar coulombic efficiencies to the LP57 cells at cycle numbers > 100.

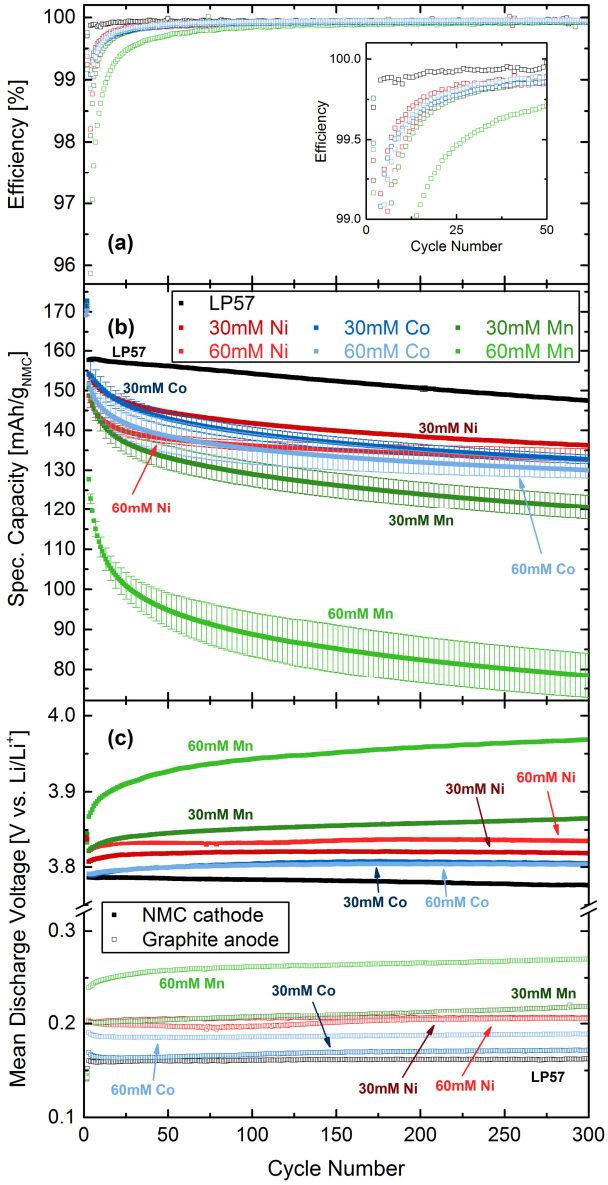

Figure 5. (a) Coulombic efficiency, (b) specific discharge capacity, and (c) mean discharge voltage of NMC cathode and graphite anode vs. cycle number of NMC622-graphite cells containing LP57 (1 M $LiPF_6$ in EC:EMC 3:7) (black), LP57 + $Ni(TFSI)_2$ (red), LP57 + $Mn(TFSI)_2$ (green), or LP57 + $Co(TFSI)_2$ (blue). The concentrations of Ni^{2+}, Mn^{2+}, and Co^{2+} were 30 mM or 60 mM. The cells were cycled between 3.0 V and 4.2 V. Formation was done at 0.1 C-rate. Cycling was performed at 1 C-rate and 25°C. For each condition, two independent cells were run and the data in the figure always represent the average of two cells (the error bars in (a) represent the standard deviation between the two cells).

Table I. Measured specific discharge capacities of the third and 300th cycle (both at 1 C-rate) of the cells depicted in **Figure 5**.

Cell characteristics	Cycle 3 [mAh/g]	Cycle 300 [mAh/g]
LP57	158	148
30mM Ni	153	136
30mM Mn	150	120
30mM Co	154	133
60mM Ni	149	134
60mM Mn	128	79
60mM Co	152	130

Comparing the effect of the different metals, it is very striking that Mn has the most detrimental impact on the NMC622-graphite cells. In particular, LP57 + 30 mM $Mn(TFSI)_2$ yields lower specific capacities of 120 mAh/g (cycle 300) than cells with 30 mM or even 60 mM of $Ni(TFSI)_2$ or $Co(TFSI)_2$, for which the specific capacities of cycle 300 are $\geq$ 130 mAh/g. In the case of LP57 + 60 mM $Mn(TFSI)_2$, the specific capacity of the third cycle is already as low as 128 mAh/g and fades to 79 mAh/g in the 300th cycle. Interestingly, Ni and Co addition to the electrolyte yields very similar specific capacities both in the third and 300th cycles. Additionally, for these two metals only slightly lower capacities are measured for 60 mM electrolyte solutions compared to 30 mM solutions.

In **Figure 5**c the charge averaged mean discharge voltages of the NMC (full squares) and the graphite (open squares) electrodes vs. the Li reference electrode are depicted. The charge averaged mean discharge voltage is defined as:

$$\overline{V}_{discharge} = \int V_{discharge} \cdot dq_{discharge} \,/\, \int dq_{discharge} \quad (1)$$

The major influences on $\overline{V}_{discharge}$ during electrochemical cycling are i) changes in the polarization and ii) changes due to the relative shift in state-of-charge window of the positive and negative electrode (e.g. caused by the loss of active lithium). In the literature, it was shown that transition metals deposited on the graphite anode cause the loss of active lithium by irreversible side reactions on the anode leading to additional SEI formation.[17, 19-23] The latter was hypothesized to lead to an impedance growth on the anode.[17, 20] On the NMC cathode Li-loss causes an increase in $\overline{V}_{discharge}^{cathode}$, whereas impedance growth causes a decrease in $\overline{V}_{discharge}^{cathode}$. In contrast, on the graphite anode both Li-loss as well as impedance growth cause increasing values of $\overline{V}_{discharge}$. For the LP57 cells $\overline{V}_{discharge}^{cathode}$ and $\overline{V}_{discharge}^{anode}$ are nearly constant, indicating only minor changes in the polarization and also rather small amounts of lithium loss, which cannot be resolved by $\overline{V}_{discharge}$. However, $\overline{V}_{discharge}^{cathode}$ of the NMC electrode in the transition metal containing cells is clearly higher, showing that origin of the specific capacity fading is the loss of active lithium. The increase in $\overline{V}_{discharge}^{cathode}$ is most significant within the first cycles after transition metal addition and for the cells containing Mn, which both is expected based on the data in **Figure 5a** and **b**. Qualitatively, the evolution of $\overline{V}_{discharge}^{anode}$ is very similar to $\overline{V}_{discharge}^{cathode}$, i.e., increasing values for $\overline{V}_{discharge}^{anode}$ in transition metal containing cells. Due to the same trend on $\overline{V}_{discharge}^{anode}$ caused by Li-loss and polarization growth, we cannot assess whether besides the loss of active lithium also a rising polarization on the graphite anode to some extent causes some loss in specific capacity. We will discuss this in greater detail in the Discussion section.

In order to quantify the loss of active lithium and thereby evaluate if this aging mechanism is responsible for all the capacity fading observed in **Figure 5**, we determined the Li-loss by measuring the lithium content in the NMC electrodes at the end of cycling (in discharged state) using a XRD analysis similar to a previous report of our group.[14] In brief, as the NMC electrode is capacity limiting in the cells depicted in **Figure 5**, in an ideal case all lithium which is extracted during charge will be re-intercalated during discharge. However, due to side reactions, e.g., SEI formation on the anode, active lithium is irreversibly lost.[31-35] As the lattice parameters of NMC deviate with changing lithium content, the amount of irreversibly lost lithium can be determined by measuring the lattice parameters of the NMC after cycling. This value can be compared to the capacity loss during cycling to determine whether or not the loss of active lithium is the dominating aging mechanism.

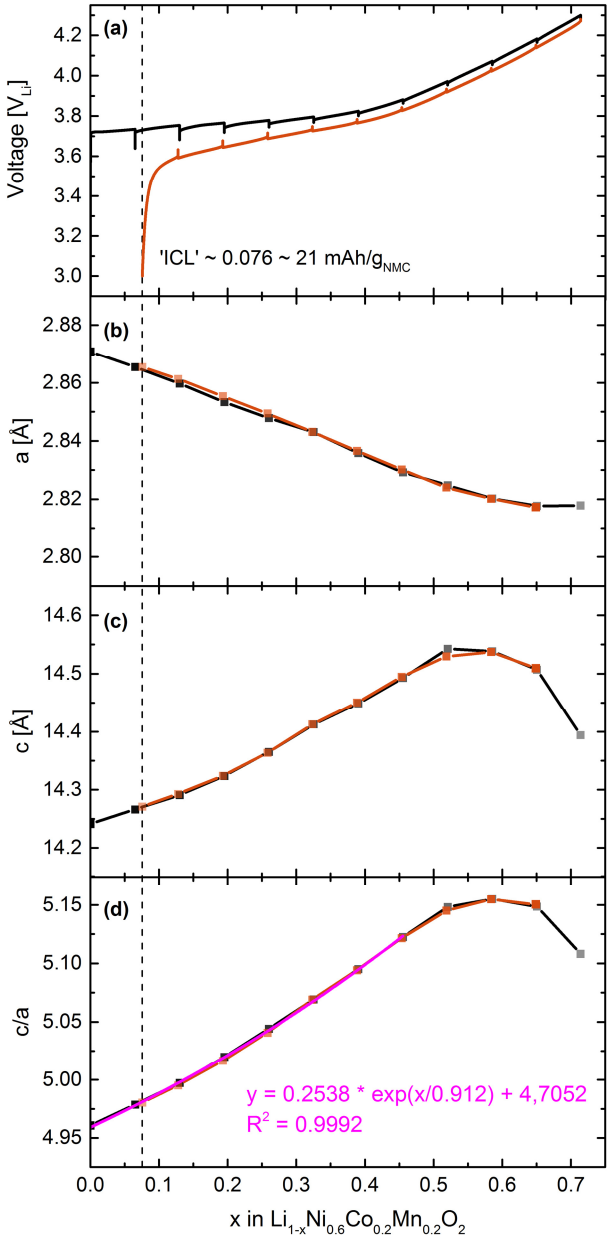

Figure 6. (a) Cell voltage of a NMC622-Li cell obtained in an in-situ XRD cell in LP57 electrolyte, (b) lattice parameter a, (c) lattice parameter c, and (d) c/a ratio as a function of the degree of delithiation. The voltage profile and lattice parameters during charge and discharge are marked in black and orange, respectively. The exponential fit between x = 0 and 0.46 yields c/a = 0.2538 · exp(x/0.912) + 4.7052 with R^2 = 0.9992.

To obtain the correlation of the lithium content (x in $Li_{1-x}Ni_{0.6}Mn_{0.2}Co_{0.2}O_2$) and the lattice parameters (**Figure 6**), XRD patterns of an NMC622 electrode charged vs. metallic lithium were measured in-situ in steps of x = 0.065 up to a cut-off voltage of 4.3 V vs. Li/Li^+. Subsequently, the cell was discharged in equal steps to a cut-off of 3 V vs. Li/Li^+. The voltage profile of the NMC622-Li cell is shown in **Figure 6a**, with the spikes indicating the

SOCs at which the cell was put into OCV to measure the XRD pattern (due to the absence of a current during OCV the cell potential relaxes yielding the spikes in the cell voltage). **Figure 6a** shows that the NMC cannot be fully relithiated during discharge. A remaining lithium amount (~0.076 = 21 mAh/g_{NMC} yielding $Li_{0.924}Ni_{0.6}Mn_{0.2}Co_{0.2}O_2$ at the end of discharge) cannot be reintercalated because of the kinetic hindrance to fully relithiate the NMC structure as described before.[14] In **Figure 6b-d** the evolutions of the lattice parameters 'a' and 'c' and their ratio are depicted (the corresponding X-ray diffractograms will be shown in **Figure 7**). Lattice parameter 'a' decreases fairly linear until $x = 0.5$ and stays rather constant between $x = 0.6$ and $x = 0.7$. In contrast, the 'c'-parameter increases exponentially until $x = 0.5$ and decreases for $x > 0.6$. Qualitatively, the evolution of the lattice parameters of NMC622 (**Figure 6**) is very similar to the ones reported for NMC111[14, 36] and NMC811[37]. In general, a change of the 'a'-parameter indicates changes in the metal-metal or oxygen-oxygen distances and changes of the 'c'-parameter represent a changing interlayer distance.[36] Therefore, the decreasing 'a'-parameter for $x < 0.5$ can be explained by the increasing oxidation state of the transition metals upon lithium extraction causing stronger metal-oxygen interaction. Concurrently, the increase of the 'c'-parameter can be explained by stronger repulsion of the oxygen layers when lithium is removed from the NMC structure and the subsequent decreasing 'c'-parameter at $x > 0.6$ has been linked to an increasing covalency between the metal and the oxygen,[36, 38] i.e., a reduced anion charge density in the vicinity of the oxygen. This is in agreement with the reports by Yoon et al. and Petersburg et al., who reported an oxidation of the lattice oxygen in NMC111 at SOCs > 45%.[39, 40] Additionally, lattice oxygen oxidation was also reported for the oxides $Li_2Ru_{1-y}Sn_yO_3$[41] and Li_2IrO_3[42]. Ultimately, the oxidation of the oxygen is likely to lead to the release of lattice oxygen for NMC622 at $x \geq 80\%$.[7, 43] In **Figure 6d** the c/a ratio is plotted. The region for $x < 0.5$ can be fitted by an exponential function which will serve as calibration curve to determine the lithium content of the NMC electrodes after cycling of the cells shown in **Figure 5** by ex-situ XRD. The correlation between the lithium loss and the capacity loss will be presented in Table III in the Discussion section.

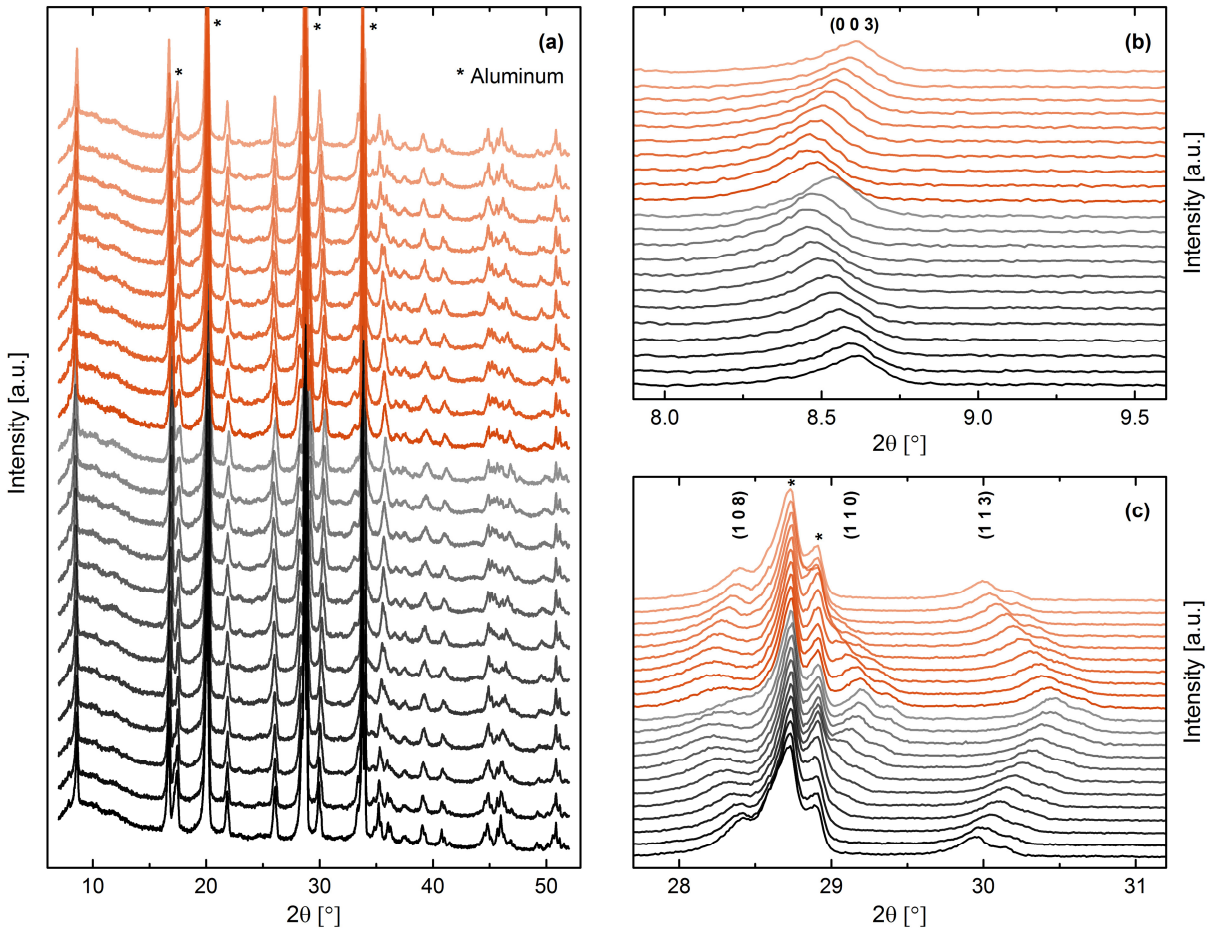

Figure 7. (a) X-ray diffractograms in the range between 7-52° 2θ of the NMC measured in the NMC622-Li cell (**Figure 6**), (b) zoom into the 7.9-9.6° 2θ range showing the (0 0 3) reflection, and (c)) zoom into the 27.7-31.2° 2θ range showing the (0 0 3) reflection. The diffractograms are arbitrarily shifted for better visibility. From bottom to top the black diffractograms are stacked with growing states-of-charge; the orange diffractograms are measured during discharge and are stacked in the order of decreasing states-of-charge. All visible reflections stemming from the aluminum window of the in-situ XRD cell are labeled with a star. The reflections are indexed with the R$\bar{3}$m space group of the NMC crystal structure.

The measured X-ray diffractograms of the cell shown in **Figure 6** are depicted in **Figure 7**. In **Figure 7a** it can be seen that besides the NMC phase additional reflections originate from the aluminum window of the in-situ XRD cell (marked with a star). The crystal structure of the NMC622 can be indexed with the space group R$\bar{3}$m. The black and orange diffractograms are measured during charge and discharge (**Figure 6**a), respectively and are stacked for better visibility in the order they were measured, i.e., with decreasing lithium content during charge and decreasing lithium content during discharge. **Figure 7b** and **c** show zooms into the regions of 7.9-9.6° 2θ and 27.7-31.2° 2θ. During delithiation the (003) reflection of the NMC622 (**Figure 7b**) is gradually shifting towards lower angles until 50-60% of the lithium is removed from the layered NMC structure representing an increasing unit cell along the c-axis as seen in **Figure 6c** (the (003) reflection has no contribution from the unit cell parameter 'a' and depends only on the 'c'-parameter). Very prominent is the large shift of the

(003) reflection to higher angles between 65-72% lithium extraction (second last and last diffractogram measured during charge (black)) representing the contraction of the unit cell along the c-axis at rather high states-of-charge (**Figure 6c**) similar to NMC111[14, 36] and NMC811[37]. Upon discharge the measured angle of the (003) reflection decreases very rapidly and then increases gradually until the end of discharge. A very similar shift during charge/discharge is observed for the (108) reflection in **Figure 7c.** In contrast to the (003) and (108) reflections, the (110) and (113) reflections shift continuously to higher angles during charge and to lower angles during discharge. Note, that the (110) reflection is independent of the 'c'-parameter, whereas the (113) reflection is only slightly influenced by the 'c'-parameter. Therefore, a shift to higher angles during charge corresponds to a decreasing 'a'-parameter as depicted in **Figure 6b** and vice versa during discharge.

Comparing the positions of the reflections in the first diffractogram (bottom, fully lithiated NMC) with the last one at the end of discharge (top) the maxima of the reflections move almost completely back to their initial positions representing a high reversibility of the lithium de-/intercalation. The remaining offsets are due to the kinetic hindrance to fully relithiate the NMC structure (after discharge the NMC composition is $Li_{0.924}Ni_{0.6}Mn_{0.2}Co_{0.2}O_2$, see **Figure 6a**).[14]

Discussion

Quantification of deposited transition metals on a graphite anode

Table II. Percentage of Ni, Mn and Co dissolved from the NMC622 electrode (in % of the total metal content of the corresponding transition metal in NMC622) and deposited on the graphite electrode determined either based on the measured concentrations in **Figure 1b-d** (XAS) or by ICP-OES analysis. The values of the ICP-OES measurements are the average of the results of two different cells with the errors representing the standard deviation between the two measurements.

Deposited metals on graphite	XAS [%]	ICP-OES [%]
Ni	0.13	0.25±0.01
Mn	0.08	0.23±0.03
Co	0.15	0.27±0.01

The concentrations of deposited Ni, Mn, and Co on the graphite anode (**Figure 1**) can be correlated with the total amount of the metals in NMC. With the graphite electrode thickness of 226 µm and an area of 1 x 1 cm², a volume of 22.6 µL is obtained. Multiplying the measured concentration changes with the volume of the graphite electrode yields the moles of deposited metals being 0.2 $\mu mol_{Ni,XAS}$, 0.04 $\mu mol_{Mn,XAS}$, and 0.08 $\mu mol_{Co,XAS}$. This can be compared to the total amount of transition metals in the NMC cathode (25.36 mg_{NMC} corresponds to 262 μmol_{NMC} and therefore 157.2 $\mu mol_{Ni,total}$ and each 52.4 $\mu mol_{Mn,total}$ and 52.4 $\mu mol_{Co,total}$) yielding 0.13%$_{Ni}$, 0.08%$_{Mn}$, and 0.15%$_{Co}$ (Table II). These values are within a factor of 2-3 of the values we obtained using ex-situ ICP-OES analysis, for which we measured 0.25%$_{Ni,ICP}$, 0.23%$_{Mn,ICP}$, and 0.27%$_{Co,ICP}$ (Table II) with deviations between two nominally identical measurements being ≤0.03%. These amounts may be compared with the ones reported by Wandt et al.[15] of 0.17%$_{Ni,XAS}$, 0.09%$_{Mn,XAS}$, and 0.26%$_{Co,XAS}$ and 0.12%$_{Ni,ICP}$, 0.17%$_{Mn,ICP}$, and 0.13%$_{Co,ICP}$ using the same procedure on a NMC111-graphite cell. The similar percentages for NMC111 and NMC622 show that the metal dissolution is very similar for these two materials, and the major difference is that in case of Ni-rich NMCs dissolved Ni-ions are based on the absolute moles the dominating species because of the larger Ni-content in Ni-rich NMC compared to Mn and Co. The fact that the percentages of dissolved metals are very similar for all three metals indicates that at potentials > 4.6 V the metals dissolve according to their stoichiometry in the NMC material. This is in agreement with the reported nearly stoichiometric dissolution of Ni, Mn, and Co by Gallus et al.,[16] and Choi et al.[18] for NMC111. The onset of transition metal dissolution in **Figure 1b-d** is observed at

~4.8 V, which is reasonably close to the observed release of reactive oxygen from the same NMC622 material starting around 4.7 V vs. Li/Li^+, as it was shown in recent publications by our group.[7, 43] In these reports we showed that the reactive oxygen reacts chemically with electrolyte and we proposed a mechanism yielding besides CO_2 and CO also H_2O.[7] The formation of water[44, 45] or protons[46] upon electrolyte oxidation was already suggested before both of which might react with the $LiPF_6$ salt in the electrolyte forming HF, which subsequently leads to an etching of the NMC cathode causing transition metal dissolution as reported in the literature.[16, 47, 48] Therefore, it might be possible that the release of oxygen from the NMC surface triggers the dissolution of transition metals.

Impact of transition metals on the electrochemical cycling of NMC622-graphite cells

To investigate the impact of dissolved transition metals on the cycling stability of NMC622-graphite cells, we chose rather high concentrations of transition metals in the electrolyte in order to accelerate cell aging. The 30 mM and 60 mM solutions correspond to a transition metal amount equal to 2-11 % (30 mmol/L x 80 µL = 2.4 µmol transition metals; with 16.2 mg_{NMC}/cm^2 and A = 0.785 cm^2 → 12.72 mg_{NMC} → 131.4 μmol_{Ni} and 43.8 μmol_{Mn} and 43.8 μmol_{Co}) of the transition metals in the active material. Due to the high concentrations of the intentionally added transition metals, further dissolution occurring from the NMC622 electrode during the 300 cycles in **Figure 5** can be neglected, all the more because the upper cut-off voltage is limited to 4.2 V. In particular, as demonstrated by Buchberger et al., under exactly the same cycling conditions only 0.08% (<< 2-11%) of the transition metals were dissolved from an NMC111 electrode.[14]

In the third cycle (first cycle after addition of transition metals, **Figure 5**) a significant drop in coulombic efficiency and specific capacity was observed for the cells containing transition metals compared to the LP57 cells. In particular, efficiencies and capacities in the third cycle increase in the order Mn < Ni ≈ Co < LP57. During further cycling, the efficiency for transition metal containing cells increases and approaches after 50-100 cycles very similar values as the ones measured for the LP57 cells (**Figure 5**). At that point, also the capacity decay per cycle number is very similar for all the cells in **Figure 5**, indicating that the transition metals are probably covered under newly formed SEI. The lower specific capacities upon addition of transition metals is in agreement with the report by Joshi et al., who also observed a significantly lower capacity when adding a mixture of Ni(II), Co(II) and Mn(II) in

an overall concentration of 30 mM to NMC111-graphite cells.[20] However, in their study the effect of the single metals cannot be distinguished since they used an electrolyte containing all three metals. As it is shown in **Figure 5**, we observed a clear difference between Ni and Co on the one hand side and Mn on the other hand side.

In the literature, it was suggested that the deposition of transition metals on graphite anodes causes additional SEI formation leading to loss of active lithium.[17, 19-23] To test if this holds for all three transition metals, we will compare the observed capacity loss of the cells shown in **Figure 5** to the lithium content of the NMC622 electrode after cycling determined via the unit cell dimensions (c/a ratio in **Figure 6**) in analogy to the report by Buchberger et al.[14] Table III summarizes the capacity loss $\Delta C_{cycling}$ (second column) of these cells over the course of the cycles at 1 C-rate. To this amount we need to add $\Delta C_{2\rightarrow 3}$, which is the difference in specific discharge capacity between cycle 2 and cycle 3, thereby accounting for kinetic barriers causing lower capacities when switching from a 0.1 C-rate during formation to a 1 C-rate during extensive cycling and the lower capacity in the third cycle caused by the addition of transition metals. This yields a total "missing" lithium amount in the NMC electrode after 300 cycles of $\sum_{EC}$ (fourth column in Table III). Note that the capacity loss due to a kinetic barrier occurring when switching from 0.1 C to 1 C cycling is not a real loss of lithium and could be recovered if the cells were cycled at 0.1 C-rate.

If all capacity loss during cycling in **Figure 5** was exclusively due to loss of active lithium, we would expect that the lithium amount corresponding to $\sum_{EC}$ would be missing in the NMC electrode after cycling. Therefore, $\sum_{EC}$ will be compared to the determined lithium content of the NMC electrodes via XRD analysis. The c/a ratios of the cycled NMC electrodes are summarized in the fifth column of Table III. Using the calibration curve shown in **Figure 6d** the missing lithium content (x in $Li_{1-x}NMC$, sixth column in Table III) is calculated. This value has to be corrected for the irreversible capacity loss observed for the NMC electrode in the first cycle ($x = 0.076$, **Figure 6a**), which is in our experiments slightly larger than the capacity loss due to SEI formation on the graphite anode in analogy to the report by Buchberger et al.[14] By converting $x_{ICL\text{-}corr.}$ to specific capacity values in mAh/g_{NMC}, $\sum_{XRD}$ is obtained. A comparison of $\sum_{EC}$ and $\sum_{XRD}$ shows that for the LP57 cells as well as for the transition metal containing cells the values are very similar within an error of ± 5 mAh/g_{NMC}, which we believe, is within the precision of the used techniques. Therefore, the vast majority

of the observed specific capacity losses are due to the loss of active lithium, which is in agreement with the report by Vissers et al.[49]

Table III. Capacity losses $\Delta C_{cycling}$ (second column) of NMC622-graphite cells depicted in **Figure 5** after 300 cycles at 1 C-rate. $\Delta C_{2\rightarrow 3}$ is the change in specific discharge capacity between the second and third cycle accounting for the higher kinetic barrier at higher C-rate and the drop in capacity upon addition of the transition metals. $\sum_{EC}$ (fourth column) is the sum of $\Delta C_{cycling}$ and $\Delta C_{1\rightarrow 3}$ indicating the "missing" lithium amount in the NMC electrode based on the electrochemical data. $\sum_{EC}$ is compared to the capacity losses obtained from XRD analysis $\sum_{XRD}$ of harvested NMC622 electrodes (discharged state) via quantification of the c/a-value (fifth column) by ex situ XRD. Conversion into x in $Li_{1-x}NMC$ was done using the in situ XRD calibration curve (**Figure 6**). By subtracting the lithium ion loss due to the irreversible capacity of the first cycle $x_{ICL\text{-}corr.}$ is yielded. Conversion of $x_{ICL\text{-}corr.}$ into mAh/g (using the theoretical capacity of 276.5 mAh/g_{NMC}) yields $\sum_{XRD}$.

Cell characteristics	Electrochemical cycling data			XRD data			
	$\Delta C_{cycling}$ [mAh/g]	$\Delta C_{2\rightarrow 3}$ [mAh/g]	$\sum_{EC}$ [mAh/g]	c/a	x in $Li_{1-x}NMC$	$x_{ICL\text{-}corr.}$ (-0.076)	$\sum_{XRD}$ [mAh/g]
LP57	9.4	13.0	22.4	5.0045	0.15	0.074	20.5
30mM Ni	17.0	16.8	33.8	5.0179	0.19	0.114	31.5
30mM Mn	31.2	21.3	52.5	5.0457	0.27	0.0194	53.1
30mM Co	23.3	15.0	38.3	5.0254	0.21	0.136	37.6
60mM Ni	15.5	21.7	37.2	5.0233	0.21	0.1295	35.8
60mM Mn	46.0	42.2	88.2	5.1016	0.41	0.3305	91.4
60mM Co	18.8	16.0	34.8	5.0264	0.22	0.1390	38.7

In the following we will briefly discuss the effect of polarization increase induced by the additional SEI formation which goes hand in hand with the active lithium loss. By comparing the absolute values of $\overline{V}^{anode}_{discharge}$ in **Figure 5c** of the 60 mM Mn cell and the LP57 cell, i.e., the cells with worst and best cycling stability, one can observe that the difference is only ~0.1 V at a 1 C-rate. Even if we assigned the total difference in $\overline{V}^{anode}_{discharge}$ to an increase in impedance, the polarization growth would only have a minor contribution; all the more because this assignment is definitely overestimating the polarization effect ($\overline{V}^{anode}_{discharge}$ is also increased by the evident lithium loss, which is especially large in the 60 mM Mn cells). Additionally, the concentration of 60 mM corresponds to an exceedingly high dissolution of 11% of the NMC active material. In other words, even though additional SEI is formed, the Li-ion resistivity through it has no or at best only minor influence on the cycling stability. This is in agreement with Gilbert et al. who observed only minor changes in the impedance of the graphite electrode in NMC532-graphite cells after 400 cycles, even though they showed

transition metal deposition on the graphite anode.[21] This phenomenon can be explained by the structure of the SEI in which Li-ion transport occurs via a hopping mechanism (ion-exchange mechanism), i.e., an incoming Li^+ releases another Li^+ close to the graphite surface.[21, 50]

It is important to note that based on the data in Table III, irrespective of which transition metal is added, lithium loss is the main aging mechanism under the used cycling conditions, yet the magnitude is very different for Mn compared to Ni and Co but for all higher than in pure LP57.

Proposed mechanism of the lithium loss caused by transition metal deposits

To understand the mechanism behind the lithium loss in NMC-graphite cells caused by the transition metal deposition, we first want to discuss the observed oxidation states of the transition metal deposits. Based on the reduction potentials of Ni, Mn, and Co presented in **Figure 3** and the very low voltage of a graphite anode (<0.4 V vs. Li/Li^+) metallic states could be expected for the deposits of all three transition metals. However, as shown in the operando XAS spectra in **Figure 2**, Ni and Co are deposited on the graphite anode in their +II state, which is in agreement with our previous report using the same XAS technique.[15] For Mn deposition on graphite very differing results were reported with oxidation states ranging from Mn(0)[51, 52], Mn(II)[19], Mn(III)[53, 54] up to Mn(IV)[8]. Due to the comparably low energy of the Mn K-edge and the low signal intensity causing a rather noisy spectrum, we cannot state whether the deposits are Mn(II) or Mn(III). However, Mn(0) or Mn(IV) in an operating cell in presence of electrolyte can be ruled out based on our results.

Wandt et al. and Delacourt et al. proposed that Mn deposited on graphite undergoes catalytic cycles in which Mn is electrochemically reduced on the graphite anode and subsequently re-oxidized by reducing electrolyte, thereby, causing a constant loss of active lithium.[15, 55] The presence of Mn^{2+} was observed as long as electrolyte was present and changed to Mn(0) when the electrolyte was removed.[15] This was rationalized by a much higher rate for the Mn re-oxidation than the reduction yielding the oxidized species as the one being observed in presence of electrolyte.[15] Upon removal of the electrolyte the catalytic cycle is stopped preventing the re-oxidation of Mn(0).[15] Yet, a similar occurrence of Ni(0) or Co(0) was not observed in absence of electrolyte.[15] This is somewhat surprising as the reduction potentials of Ni and Co are ~1 V higher than the one of Mn (**Figure 3**). It was hypothesized that Ni and

Co might be trapped in the outer SEI in their +2 oxidation state preventing their reduction to the metallic state.[15] Bar-Tow et al. reported for arsenic deposits on graphite using XPS depth profiling the presence of different oxidation states in dependency of their position in the SEI. In particular, As(0) was found in the inner SEI and As(III) and As(IV) in the outer SEI.[56] Unfortunately, for Ni and Co similar data do not exist, however, for Mn, Shkrob et al. showed that it is predominantly deposited in the inner SEI in a lithium carbonate matrix.[57] Using XPS Joshi et al. observed the formation of Li_2CO_3 in the SEI formed with EC-based electrolyte when Ni, Co and Mn was added, while it was absent in electrolyte without transition metal addition.[20] This is in line with previous reports showing that the addition of transition metals leads to a growing fraction of the inorganic components in the SEI.[22, 52, 55] Based on these reports and our observations we hypothesize that the metals are probably initially electrochemically deposited on the carbon in their metallic state, which explains their accumulation on the anode,[15, 55] but are subsequently chemically re-oxidized by a reaction with an SEI component, thereby damaging the SEI and forming more of the inorganic components.

The reason why we expect a reaction with the SEI instead of a direct reaction with electrolyte (which is assumed in the catalytic cycle mechanism mentioned above) is because a direct chemical reaction of transition metals with electrolyte in the absence of an SEI is unlikely. Firstly, because the reduction potentials of the transition metals are higher than the one of the LP57 electrolyte (**Figure 3**), i.e., the reduction of electrolyte with concurrent oxidation of the metal would be endergonic and, secondly, in **Figure 4** a re-oxidation of deposited Ni on the carbon surface was possible in the absence of an SEI, proving that as long as no SEI is formed reversible oxidation/reduction is possible. Therefore, the detrimental effect of the transition metals might originate from a chemical decomposition of the SEI components as recently suggested by Leung.[58] The more negative effect of Mn compared to Ni and Co could be due to a faster reaction with the SEI components or even a different reaction yielding different reaction products, which may cause more damage to the SEI. One possible reaction would be LEDC reduction to Li_2CO_3 in case of an EC-based SEI, which could also explain the Li_2CO_3 formation reported by Joshi et al.[20] and the Li_2CO_3 environment around the Mn deposits reported by Shkrob et al.[57] Additionally, a chemical reaction with the SEI is also in line with the proposed metathesis reaction of Mn^{2+} with Li^+-containing SEI compounds by Zhan et al.[19] Such a reaction scenario also explains why we did not observe a re-oxidation peak of deposited Ni in the presence of an SEI in **Figure 4** because it was already chemically

oxidized to Ni^{2+}, which agrees also with the observed Ni^{2+} in **Figure 2**, even though according to the reduction potentials presented in **Figure 3** metallic states could be expected. Finally, such a chemical reaction pathway would go along with locally destroying the SEI layer, which in consequence leads to additional SEI formation and the observed Li-loss (Table III) causing a faster cell aging (**Figure 5**).

Conclusion

In this work we investigated the transition metal dissolution from NMC622 and precipitation of Ni, Mn, and Co on graphite using operando X-ray absorption spectroscopy. We showed that at high potentials Ni, Mn, and Co dissolve nearly stoichiometrically, therefore, the absolute amounts of Ni deposited on the graphite anode are highest. By a comparison with the literature, we also proved that the total amount of dissolved metals for the used NMC622 electrode is very similar to the one of NMC111. As in Ni-rich NMCs Ni is the metal which is dissolved most, we compared the detrimental effect of Ni to Mn and Co on NMC622-graphite cells to estimate the significance of every single metal on battery cell aging. We demonstrated that the major aging mechanism for all three transition metals is the loss of active lithium, which likely stems from a decomposition of the SEI layer by a chemical reaction of the deposited metals with the SEI. Finally, we showed that the total lithium loss is significantly larger when Mn is deposited on graphite than in the case of Ni and Co. For the latter two very similar lithium losses were observed. This shows that replacing commonly used NMC111 cathodes by Ni-rich NMCs like NMC622 not only the specific energy of a Li-ion battery can be increased but also the detrimental effect of metal dissolution might become a smaller problem.

ACKNOWLEDGEMENT

The authors would like to thank BMW AG for the financial support of this work. Umicore is greatly acknowledged for supplying the NMC622 cathode material. We thank Dr. Karin Kleiner for experimental support during the beamtime. R.J. thanks TUM-IAS for their support in the frame of the Rudolf-Diesel Fellowship of Dr. Peter Lamp. F.L. acknowledges the BMBF (Federal Ministry of Education and Research, Germany) for funding within the project “ExZellTUM II”, grant number 03XP0081. R.T., J.W., and M.T. acknowledge financial support by the Bavarian Ministry of Economic Affairs and Media, Energy and Technology under the auspices of the EEBatt project. S.S. thanks BASF SE for funding

through its electrochemistry and battery research network. M.T. acknowledges financial support by NOW VIDI, 723.014.010 and the Research Priority Area Sustainable Chemistry of the UvA.

REFERENCES

1. O. Groeger, H. A. Gasteiger and J.-P. Suchsland, Review-Electromobility: Batteries or Fuel Cells? *J. Electrochem. Soc.*, **2015**, 162, A2605-A2622.
2. F. T. Wagner, B. Lakshmanan and M. F. Mathias, Electrochemistry and the Future of the Automobile. *J. Phys. Chem. Lett.*, **2010**, 1, 2204-2219.
3. D. Andre, S.-J. Kim, P. Lamp, S. F. Lux, F. Maglia, O. Paschos and B. Stiaszny, Future generations of cathode materials: an automotive industry perspective. *J. Mater. Chem. A*, **2015**, 3, 6709-6732.
4. K. G. Gallagher, S. Goebel, T. Greszler, M. Mathias, W. Oelerich, D. Eroglu and V. Srinivasan, Quantifying the promise of lithium-air batteries for electric vehicles. *Energy Environ. Sci.*, **2014**, 7, 1555-1563.
5. H.-J. Noh, S. Youn, C. S. Yoon and Y.-K. Sun, Comparison of the structural and electrochemical properties of layered $Li[Ni_xCo_yMn_z]O_2$ (x = 1/3, 0.5, 0.6, 0.7, 0.8 and 0.85) cathode material for lithium-ion batteries. *J. Power Sources*, **2013**, 233, 121-130.
6. W. Liu, P. Oh, X. Liu, M.-J. Lee, W. Cho, S. Chae, Y. Kim and J. Cho, Nickel-Rich Layered Lithium Transition Metal Oxide for High-Energy Lithium-Ion Batteries. *Angew. Chem., Int. Ed.*, **2015**, 54, 4440-4457.
7. R. Jung, M. Metzger, F. Maglia, C. Stinner and H. A. Gasteiger, Oxygen Release and Its Effect on the Cycling Stability of $LiNi_xMn_yCo_zO_2$ (NMC) Cathode Materials for Li-Ion Batteries. *J. Electrochem. Soc.*, **2017**, 164, A1361-A1377.
8. L. Yang, M. Takahashi and B. Wang, A study on capacity fading of lithium-ion battery with manganese spinel positive electrode during cycling. *Electrochim. Acta*, **2006**, 51, 3228-3234.
9. T. Inoue and M. Sano, An Investigation of Capacity Fading of Manganese Spinels Stored at Elevated Temperature. *J. Electrochem. Soc.*, **1998**, 145, 3704-3707.
10. A. Du Pasquier, A. Blyr, P. Courjal, D. Larcher, G. Amatucci, B. Gérand and J. M. Tarascon, Mechanism for Limited 55°C Storage Performance of $Li_{1.05}Mn_{1.95}O_4$ Electrodes. *J. Electrochem. Soc.*, **1999**, 146, 428-436.
11. J. Cho and M. M. Thackeray, Structural Changes of LiMn2 O 4 Spinel Electrodes during Electrochemical Cycling. *J. Electrochem. Soc.*, **1999**, 146, 3577-3581.
12. Y. Xia, Y. Zhou and M. Yoshio, Capacity Fading on Cycling of 4 V Li / $LiMn_2O_4$ Cells. *J. Electrochem. Soc.*, **1997**, 144, 2593-2600.
13. D. H. Jang, Y. J. Shin and S. M. Oh, Dissolution of Spinel Oxides and Capacity Losses in 4 V Li / $Li_xMn_2O_4$ Cells. *J. Electrochem. Soc.*, **1996**, 143, 2204-2211.
14. I. Buchberger, S. Seidlmayer, A. Pokharel, M. Piana, J. Hattendorff, P. Kudejova, R. Gilles and H. A. Gasteiger, Aging Analysis of Graphite/$LiNi_{1/3}Mn_{1/3}Co_{1/3}O_2$ Cells Using XRD, PGAA, and AC Impedance. *J. Electrochem. Soc.*, **2015**, 162, A2737-A2746.
15. J. Wandt, A. Freiberg, R. Thomas, Y. Gorlin, A. Siebel, R. Jung, H. A. Gasteiger and M. Tromp, Transition metal dissolution and deposition in Li-ion batteries investigated by operando X-ray absorption spectroscopy. *J. Mater. Chem. A*, **2016**, 4, 18300-18305.
16. D. R. Gallus, R. Schmitz, R. Wagner, B. Hoffmann, S. Nowak, I. Cekic-Laskovic, R. W. Schmitz and M. Winter, The influence of different conducting salts on the metal dissolution and capacity fading of NCM cathode material. *Electrochim. Acta*, **2014**, 134, 393-398.
17. H. Zheng, Q. Sun, G. Liu, X. Song and V. S. Battaglia, Correlation between dissolution behavior and electrochemical cycling performance for $LiNi_{1/3}Co_{1/3}Mn_{1/3}O_2$-based cells. *J. Power Sources*, **2012**, 207, 134-140.

18. W. Choi and A. Manthiram, Comparison of Metal Ion Dissolutions from Lithium Ion Battery Cathodes. *J. Electrochem. Soc.*, **2006**, 153, A1760-A1764.
19. C. Zhan, J. Lu, A. J. Kropf, T. Wu, A. N. Jansen, Y.-K. Sun, X. Qiu and K. Amine, Mn(II) deposition on anodes and its effects on capacity fade in spinel lithium manganate-carbon systems. *Nat. Commun.*, **2013**, 4, 3437, 8 pp.
20. T. Joshi, K. Eom, G. Yushin and T. F. Fuller, Effects of dissolved transition metals on the electrochemical performance and SEI growth in lithium-ion batteries. *J. Electrochem. Soc.*, **2014**, 161, A1915-A1921, 7 pp.
21. J. A. Gilbert, J. Bareño, T. Spila, S. E. Trask, D. J. Miller, B. J. Polzin, A. N. Jansen and D. P. Abraham, Cycling Behavior of NCM523/Graphite Lithium-Ion Cells in the 3–4.4 V Range: Diagnostic Studies of Full Cells and Harvested Electrodes. *J. Electrochem. Soc.*, **2017**, 164, A6054-A6065.
22. H. Tsunekawa, S. Tanimoto, R. Marubayashi, M. Fujita, K. Kifune and M. Sano, Capacity Fading of Graphite Electrodes Due to the Deposition of Manganese Ions on Them in Li-Ion Batteries. *J. Electrochem. Soc.*, **2002**, 149, A1326-A1331.
23. N. P. W. Pieczonka, Z. Liu, P. Lu, K. L. Olson, J. Moote, B. R. Powell and J.-H. Kim, Understanding Transition-Metal Dissolution Behavior in $LiNi_{0.5}Mn_{1.5}O_4$ High-Voltage Spinel for Lithium Ion Batteries. *The Journal of Physical Chemistry C*, **2013**, 117, 15947-15957.
24. M. Newville. *J. Synchrotron Radiat.*, **2001**, 8, 322-324.
25. B. Ravel and M. Newville. *J. Synchrotron Radiat.*, **2005**, 12, 537-541.
26. Y. Gorlin, A. Siebel, M. Piana, T. Huthwelker, H. Jha, G. Monsch, F. Kraus, H. A. Gasteiger and M. Tromp, Operando Characterization of Intermediates Produced in a Lithium-Sulfur Battery. *J. Electrochem. Soc.*, **2015**, 162, A1146-A1155.
27. S. Meini, N. Tsiouvaras, K. U. Schwenke, M. Piana, H. Beyer, L. Lange and H. A. Gasteiger, Rechargeability of Li-air cathodes pre-filled with discharge products using an ether-based electrolyte solution: implications for cycle-life of Li-air cells. *Phys. Chem. Chem. Phys.*, **2013**, 15, 11478-11493.
28. M. Metzger, B. Strehle, S. Solchenbach and H. A. Gasteiger, Origin of H_2 Evolution in LIBs: H2O Reduction vs. Electrolyte Oxidation. *J. Electrochem. Soc.*, **2016**, 163, A798-A809.
29. B. Zhang, M. Metzger, S. Solchenbach, M. Payne, S. Meini, H. A. Gasteiger, A. Garsuch and B. L. Lucht, Role of 1,3-Propane Sultone and Vinylene Carbonate in Solid Electrolyte Interface Formation and Gas Generation. *J. Phys. Chem. C*, **2015**, 119, 11337-11348.
30. M. Pourbaix, *Atlas of electrochemical equilibria in aqueous solutions*, National Association of Corrosion Engineers, **1974**.
31. E. Peled, The Electrochemical Behavior of Alkali and Alkaline Earth Metals in Nonaqueous Battery Systems—The Solid Electrolyte Interphase Model. *J. Electrochem. Soc.*, **1979**, 126, 2047-2051.
32. J. Christensen and J. Newman, Cyclable lithium and capacity loss in Li-ion cells. *J. Electrochem. Soc.*, **2005**, 152, A818-A829.
33. E. Peled, D. Bar Tow, A. Merson, A. Gladkich, L. Burstein and D. Golodnitsky, Composition, depth profiles and lateral distribution of materials in the SEI built on HOPG-TOF SIMS and XPS studies. *Journal of Power Sources*, **2001**, 97, 52-57.
34. E. Peled and S. Menkin, Review—SEI: Past, Present and Future. *J. Electrochem. Soc.*, **2017**, 164, A1703-A1719.
35. V. Eshkenazi, E. Peled, L. Burstein and D. Golodnitsky, XPS analysis of the SEI formed on carbonaceous materials. *Solid State Ionics*, **2004**, 170, 83-91.

36. N. Yabuuchi, Y. Makimura and T. Ohzuku, Solid-State Chemistry and Electrochemistry of $LiCo_{1/3}Ni_{1/3}Mn_{1/3}O_2$ for Advanced Lithium-Ion Batteries. *J. Electrochem. Soc.*, **2007**, 154, A314-A321.
37. J. Li, L. E. Downie, L. Ma, W. Qiu and J. R. Dahn, Study of the Failure Mechanisms of $LiNi_{0.8}Mn_{0.1}Co_{0.1}O_2$ Cathode Material for Lithium Ion Batteries. *J. Electrochem. Soc.*, **2015**, 162, A1401-A1408.
38. Y. Koyama, N. Yabuuchi, I. Tanaka, H. Adachi and T. Ohzuku, Solid-State Chemistry and Electrochemistry of $LiCo_{1/3}Ni_{1/3}Mn_{1/3}O_2$ for Advanced Lithium-Ion Batteries: I. First-Principles Calculation on the Crystal and Electronic Structures. *J. Electrochem. Soc.*, **2004**, 151, A1545-A1551.
39. W.-S. Yoon, C. P. Grey, M. Balasubramanian, X.-Q. Yang, D. A. Fischer and J. McBreen, Combined NMR and XAS Study on Local Environments and Electronic Structures of Electrochemically Li-Ion Deintercalated $Li_{1-x}Co_{1/3}Ni_{1/3}Mn_{1/3}O_2$ Electrode System. *Electrochem. Solid-State Lett.*, **2004**, 7, A53-A55.
40. C. F. Petersburg, Z. Li, N. A. Chernova, M. S. Whittingham and F. M. Alamgir, Oxygen and transition metal involvement in the charge compensation mechanism of $LiNi_{1/3}Mn_{1/3}Co_{1/3}O_2$ cathodes. *J. Mater. Chem.*, **2012**, 22, 19993-20000.
41. M. Sathiya, G. Rousse, K. Ramesha, C. P. Laisa, H. Vezin, M. T. Sougrati, M. L. Doublet, D. Foix, D. Gonbeau, W. Walker, A. S. Prakash, M. Ben Hassine, L. Dupont and J. M. Tarascon, Reversible anionic redox chemistry in high-capacity layered-oxide electrodes. *Nat Mater*, **2013**, 12, 827-835.
42. E. McCalla, A. M. Abakumov, M. Saubanere, D. Foix, E. J. Berg, G. Rousse, M.-L. Doublet, D. Gonbeau, P. Novak, G. Van Tendeloo, R. Dominko and J.-M. Tarascon, Visualization of O-O peroxo-like dimers in high-capacity layered oxides for Li-ion batteries. *Science (Washington, DC, U. S.)*, **2015**, 350, 1516-1521.
43. R. Jung, M. Metzger, F. Maglia, C. Stinner and H. A. Gasteiger, Chemical versus Electrochemical Electrolyte Oxidation on NMC111, NMC622, NMC811, LNMO, and Conductive Carbon. *J. Phys. Chem. Lett.*, **2017**, 4820-4825.
44. M. Jiang, B. Key, Y. S. Meng and C. P. Grey, Electrochemical and Structural Study of the Layered, "Li-Excess" Lithium-Ion Battery Electrode Material $Li[Li_{1/9}Ni_{1/3}Mn_{5/9}]O_2$. *Chem. Mater.*, **2009**, 21, 2733-2745.
45. S. Meini, S. Solchenbach, M. Piana and H. A. Gasteiger, The Role of Electrolyte Solvent Stability and Electrolyte Impurities in the Electrooxidation of Li_2O_2 in Li-O_2 Batteries. *J. Electrochem. Soc.*, **2014**, 161, A1306-A1314.
46. M. Metzger, J. Sicklinger, D. Haering, C. Kavakli, C. Stinner, C. Marino and H. A. Gasteiger, Carbon Coating Stability on High-Voltage Cathode Materials in H_2O-Free and H_2O-Containing Electrolyte. *J. Electrochem. Soc.*, **2015**, 162, A1227-A1235.
47. J. C. Hunter, Preparation of a new crystal form of manganese dioxide: λ-MnO_2. *Journal of Solid State Chemistry*, **1981**, 39, 142-147.
48. D. Aurbach, M. D. Levi, K. Gamulski, B. Markovsky, G. Salitra, E. Levi, U. Heider, L. Heider and R. Oesten, Capacity fading of $Li_xMn_2O_4$ spinel electrodes studied by XRD and electroanalytical techniques. *Journal of Power Sources*, **1999**, 81, 472-479.
49. D. R. Vissers, Z. Chen, Y. Shao, M. Engelhard, U. Das, P. Redfern, L. A. Curtiss, B. Pan, J. Liu and K. Amine, Role of Manganese Deposition on Graphite in the Capacity Fading of Lithium Ion Batteries. *ACS Applied Materials & Interfaces*, **2016**, 8, 14244-14251.
50. O. Borodin, G. V. Zhuang, P. N. Ross and K. Xu, Molecular Dynamics Simulations and Experimental Study of Lithium Ion Transport in Dilithium Ethylene Dicarbonate. *The Journal of Physical Chemistry C*, **2013**, 117, 7433-7444.

51. S. R. Gowda, K. G. Gallagher, J. R. Croy, M. Bettge, M. M. Thackeray and M. Balasubramanian, Oxidation state of cross-over manganese species on the graphite electrode of lithium-ion cells. *Phys. Chem. Chem. Phys.*, **2014**, 16, 6898-6902.
52. X. Xiao, Z. Liu, L. Baggetto, G. M. Veith, K. L. More and R. R. Unocic, Unraveling manganese dissolution/deposition mechanisms on the negative electrode in lithium ion batteries. *Phys. Chem. Chem. Phys.*, **2014**, 16, 10398-10402.
53. Z. Li, A. D. Pauric, G. R. Goward, T. J. Fuller, J. M. Ziegelbauer, M. P. Balogh and I. C. Halalay, Manganese sequestration and improved high-temperature cycling of Li-ion batteries by polymeric aza-15-crown-5. *J. Power Sources*, **2014**, 272, 1134-1141.
54. S. Komaba, T. Itabashi, T. Ohtsuka, H. Groult, N. Kumagai, B. Kaplan and H. Yashiro, Impact of 2-Vinylpyridine as Electrolyte Additive on Surface and Electrochemistry of Graphite for C / $LiMn_2O_4$ Li-Ion Cells. *J. Electrochem. Soc.*, **2005**, 152, A937-A946.
55. C. Delacourt, A. Kwong, X. Liu, R. Qiao, W. L. Yang, P. Lu, S. J. Harris and V. Srinivasan, Effect of manganese contamination on the solid-electrolyte-interphase properties in Li-ion batteries. *J. Electrochem. Soc.*, **2013**, 160, A1099-A1107.
56. D. Bar-Tow, E. Peled and L. Burstein, A Study of Highly Oriented Pyrolytic Graphite as a Model for the Graphite Anode in Li-Ion Batteries. *J. Electrochem. Soc.*, **1999**, 146, 824-832.
57. I. A. Shkrob, A. J. Kropf, T. W. Marin, Y. Li, O. G. Poluektov, J. Niklas and D. P. Abraham, Manganese in Graphite Anode and Capacity Fade in Li Ion Batteries. *J. Phys. Chem. C*, **2014**, 118, 24335-24348.
58. K. Leung, First-Principles Modeling of Mn(II) Migration above and Dissolution from $Li_xMn_2O_4$ (001) Surfaces. *Chemistry of Materials*, **2017**, 29, 2550-2562.

3.3 Degradation Phenomena of Anode Materials

In section 3.3, studies were performed with a focus on the anode active material. All of the works are integrated in their published versions into this PhD thesis.

In section 3.3.1, we investigate the electrolyte consumption, in particular of FEC, on silicon-carbon composite electrodes. The electrodes comprise silicon as the only active material and the cells are cycled versus metallic lithium. In contrast, in section 3.3.2, graphite is added as additional active material component and cycling is conducted versus a capacitively oversized LFP cathode in order to avoid any reactions of the electrolyte on the counter electrode. Expanding on the findings in section 3.3.1, the study in section 3.3.2 investigates the aging mechanisms occurring on electrodes with different silicon to graphite ratios. Lastly, in section 3.3.3, a study on the applicability of carbon and binder free germanium electrodes possessing an inverse opal structure is presented.

3.3.1 Consumption of Fluoroethylene Carbonate (FEC) on Si-C Composite Electrodes for Li-Ion Batteries

In this section the article "Consumption of Fluoroethylene Carbonate (FEC) on Si-C Composite Electrodes for Li-Ion Batteries" will be presented, which was published in the *Journal of the Electrochemical Society* on June 9, 2016 as open access article distributed under the terms of the Creative Commons Attribution Non-Commercial No Derivatives 4.0 License.[30] The results of the publication were presented on international conferences, e.g., by Roland Jung at the 230th Meeting of The Electrochemical Society (October 2 – 7, 2016) in Honolulu, USA (Abstract Number: #284). The permanent web-link to the publication is http://jes.ecsdl.org/content/163/8/A1705 and the DOI is 10.1149/2.0951608jes.

In this study we compare the cycling stability of Si-carbon composite electrodes comprised of 40%$_{wt}$ Si, 40%$_{wt}$ carbon fibers (VGCF-H), and 20%$_{wt}$ lithium polyacrylate (LiPAA) cycled versus metallic lithium in LP57 electrolyte with an addition of 0, 1%$_{wt}$, 5%$_{wt}$, 10%$_{wt}$, or 20%$_{wt}$ fluoroethylene carbonate (FEC). As expected based on previous reports in the literature,[33, 35, 37, 222] we demonstrate that FEC significantly improves the cycling stability of silicon anodes. Furthermore, when FEC is added to the electrolyte, the capacity fading rate is initially very similar, independent of the amount of FEC in the cell. However, during extended charge/discharge cycling, a rapid capacity drop is observed which occurs at lower cycle numbers as the amount of FEC is being reduced. With the use of ^{19}F-NMR we analyze the electrolyte after cell cycling and thereby prove that it is the total consumption of FEC which causes the rapid drop in capacity. Applying a three-electrode set-up with a lithium reference electrode we show that the impedance of the silicon electrode significantly increases once all FEC is consumed, which can be traced back to the formation of a more resistive EC based SEI instead of the one formed with FEC. In order to be able to correlate the cumulative irreversible capacity measured during cell cycling with the consumption of FEC, we determine the ratio of FEC reduction to EC reduction via OEMS. As FEC and EC form different gases upon reduction, namely CO_2 [223] and C_2H_4,[128, 224, 225] respectively, we can quantify the FEC to EC ratio in the SEI formation by determining the CO_2 to C_2H_4 ratio in the OEMS. Thereby, we show that the presence of FEC almost entirely suppresses EC reduction (CO_2 to C_2H_4 ratio ~95:5). Therefore, all cumulative irreversible capacity during cell cycling can be ascribed to a reasonably high accuracy to FEC reduction. Conversion of the cumulative irreversible capacity into a number of electrons divided by the amount of FEC in the fresh electrolyte yields a consumption of four electrons per decomposed FEC molecule. Based on

our findings and previous reports in the literature, we propose a mechanism for the reductive decomposition of FEC. Furthermore, we also quantitatively compare the FEC consumption on a metallic lithium electrode to the one on a silicon electrode and show that for the same transferred coulombs both electrodes consume nearly the same amount of FEC. This unfortunately shows that untreated silicon is not any better than a metallic lithium electrode with respect to electrolyte consumption. Finally, we show in this study that it is the absolute amount in moles of FEC rather than its concentration in the electrolyte which determines the lifetime of a silicon electrode.

Author Contributions

Roland Jung, Cyril Marino, Nikolaos Tsiouvaras, and Dominik Haering designed the cycling experiments. Roland Jung prepared the electrodes and performed the cycling and ^{19}F-NMR experiments. Roland Jung and Michael Metzger performed the OEMS experiments. Roland Jung, Michael Metzger, and Sophie Solchenbach developed the FEC reduction mechanism. Roland Jung and Hubert Gasteiger wrote the manuscript. All authors discussed the results and commented on the manuscript.

Consumption of Fluoroethylene Carbonate (FEC) on Si-C Composite Electrodes for Li-Ion Batteries

Roland Jung,[a,b,*,z] Michael Metzger,[a,*] Dominik Haering,[a,*] Sophie Solchenbach,[a,*] Cyril Marino,[a,c] Nikolaos Tsiouvaras,[b] Christoph Stinner,[b] and Hubert A. Gasteiger[a,]**

[a]*Chair of Technical Electrochemistry, Department of Chemistry and Catalysis Research Center, Technische Universität München, Garching, Germany*
[b]*BMW AG, Munich, Germany*

The electrolyte additive fluoroethylene carbonate (FEC) is known to significantly improve the lifetime of Li-ion batteries with silicon anodes. In this work, we show that FEC can indeed improve the lifetime of silicon-carbon composite anodes but is continuously consumed during electrochemical cycling. By the use of ^{19}F-NMR spectroscopy and charge/discharge cycling we demonstrate that FEC is only capable to stabilize the cell performance as long as FEC is still remaining in the cell. Its total consumption causes a significant increase of the cell polarization leading to a rapid capacity drop. We show with On-line Electrochemical Mass Spectrometry (OEMS) that the presence of FEC in the electrolyte prohibits the reduction of other electrolyte components almost entirely. Consequently, the cumulative irreversible capacity until the rapid capacity drop correlates linearly with the specific amount of FEC (in units of $\mu mol_{FEC}/mg_{electrode}$) in the cell. The latter quantity therefore determines the lifetime of silicon anodes rather than the concentration of FEC in the electrolyte. By correlating the cumulative irreversible capacity and the specific amount of FEC in the cell, we present an easy tool to predict how much cumulative irreversible capacity can be tolerated until all FEC will be consumed in either half-cells or full-cells. We further demonstrate that four electrons are consumed for the reduction of one FEC molecule and that one carbon dioxide molecule is released for every FEC molecule that is reduced. Using all information from this study and combining it with previous reports in literature, a new reductive decomposition mechanism for FEC is proposed yielding CO_2, LiF, Li_2O, Li_2CO_3, H_2 and a partially cross-linked polymer.
 [DOI: 10.1149/2.0951608jes]

Manuscript submitted March 11, 2016; revised manuscript received May 23, 2016. Published June 9, 2016.

In the emerging market of electric vehicles (EVs), the development of batteries with higher energy density and improved cycle-life is essential.[1] However, their penetration of the mass market significantly depends on cost and the available driving range.[2] The US Advanced Battery Consortium (USABC) defined the target value of 235 Wh/kg (at a C/3 rate) on a battery level until 2020.[3] As outlined in the recent review by Andre et al.,[4] reaching this goal requires an increase of the energy density of today's batteries by a factor of roughly 2 to 2.5 and can only be achieved by the development and integration of novel anode and cathode active materials. A critical element to reach this goal is the implementation of anode active materials with much higher specific capacity than currently used graphite anodes (372 mAh/g[1,5,6]), with silicon being considered as the most likely next generation anode material due to its high natural abundance and very high theoretical specific capacity of roughly 3600 mAh/g (corresponding to the $Li_{15}Si_4$ phase[7]).

The alloying of silicon with lithium is accompanied by large structural changes, resulting in a volume increase by 310% upon full lithiation.[5,7–11] These huge volumetric changes upon lithium insertion and extraction are responsible for the generally shorter cycle-life of silicon electrode materials compared to commonly used graphite anodes. On the one hand, the volume expansion leads to irreversible capacity loss due to SEI formation on newly created surfaces induced by volume expansion/contraction during charge/discharge, so that electrolyte is continuously consumed during cycling. On the other hand, the volumetric changes can cause particle cracking, resulting in the loss of electrical contact. By using nanostructured electrodes, the mechanical cracking of the particles causing loss of electrical contact can be avoided.[11–18] In particular, Liu et al. showed that silicon particles with a diameter of up to 150 nm can be lithiated without crack formation.[16] However, the surface area increases drastically when nanosized silicon is used and therefore the irreversible capacity loss caused by solid electrolyte interface (SEI) formation also rises. For example, Chan et al. used silicon nanowires which showed almost no capacity fading for the first ten cycles, but observed an irreversible capacity of around 27% in the first cycle.[12] Li et al. on the other hand used nanostructured silicon particles with a diameter of 78 nm and reported high capacities with comparably high areal loadings but at the same time high capacity fading from ≈2100 mAh/g_{Si} to ≈1730 mAh/g_{Si} within ten cycles.[19] Even though the particle cracking can be prevented, mathematical modeling suggests that the SEI formed on the silicon particles cracks during the volumetric changes, causing a continuous electrolyte consumption and loss of active lithium.[20,21] However, Etacheri et al. showed that substantial improvement can be achieved by using fluoroethylene carbonate (FEC) as electrolyte additive, which significantly reduces irreversible capacities and leads to improved cycling stability.[22] In particular, a reduction of the irreversible capacity by roughly 50% was observed when FEC was used in comparison to FEC-free electrolytes. Furthermore, comparing FEC-containing and FEC-free electrolytes, the capacity decay from cycle 2 to cycle 30 was drastically reduced from 80% to 30%.[22] This is consistent with the earlier report by Choi et al., who observed a capacity retention after 80 cycles of 89% with FEC additive in contrast to only 68% in FEC-free electrolyte.[23] Due to the significant improvement caused by FEC, it is nowadays established as a standard additive for silicon electrodes, even though the exact working principle and decomposition mechanism are not fully understood yet.[22–25]

In this study, we examine the effect and in particular the consumption of FEC on silicon-carbon composite electrodes. The continuous consumption of FEC is shown by ^{19}F-NMR spectroscopy and an observed sudden cell failure which is detected as a rapid drop in capacity is analyzed and related to the total consumption of FEC. It will be shown that FEC nearly suppresses the reduction of any other electrolyte component, which is consistent with the previous literature and suggests that the rate of FEC reduction is greater than the reduction of EC and linear carbonates.[26–31] Furthermore, due to the continuous consumption of FEC quantified by ^{19}F-NMR, the number of charge/discharge cycles over which silicon anodes can by stabilized by FEC is directly proportional to the total moles of FEC per

*Electrochemical Society Student Member.
**Electrochemical Society Fellow.
[c]Present address: Electrochemistry Laboratory, Paul Scherrer Institut, CH-5232 Villigen, Switzerland.
[z]E-mail: roland.jung@tum.de

gram of anode electrode, rather than the FEC concentration in the electrolyte. As a consequence, 10–20%$_{wt}$ FEC additive are highly effective when examined at the high electrolyte/active material weight ratios commonly used in small-scale test cells (e.g., coin cells), but are predicted to not provide long-term protection under the much lower electrolyte/active material weight ratios used in commercial cells. Combining our experimental observations with on-line electrochemical mass spectrometry (OEMS), it is possible to reveal that the reduction of FEC is an overall four-electron process, releasing one molecule of CO_2 per molecule of FEC; a new mechanism for the reductive decomposition of FEC is proposed.

Experimental

Electrode preparation.—The preparation of the binder lithium polyacrylate (LiPAA) was done in analogy to literature as a 10%$_{wt}$ solution in water,[32] diluting a 35%$_{wt}$ polyacrylic acid solution in water (PAA, $M_w \approx 250{,}000$ g/mol, from Sigma-Aldrich, Germany) with deionized water and neutralizing it with lithium hydroxide (LiOH, Sigma-Aldrich, Germany) to a pH-value of ≈8.

Electrodes were prepared with silicon particles (≈100 nm diameter, from Alfa Aesar, Germany), vapor grown carbon fibers (VGCF-H, from Showa Denko, Japan), and the above described LiPAA solution, setting a weight ratio of 40:40:20 Si/VGCF-H/LiPAA. The slurry was mixed with water in a planetary ball-mill (Pulverisette 7, from Fritsch, Germany) using zirconia balls with a diameter of 10 mm at 400 rpm for 3 × 15 minutes. For coin cell testing, the resulting ink was spread onto copper foil (thickness 12 μm, MTI Corporation, USA) using a gap bar coater (RK PrintCoat Instruments, UK). After drying at room temperature, electrodes with 10 mm diameter (0.79 cm^2 area) were punched, then dried overnight at 120°C under vacuum in a glass oven (drying oven 585, from Büchi, Switzerland), and subsequently transferred into a glove box without exposure to ambient air. The final loading of these electrodes used for half-cell testing in coin cells and Swagelok T-cells was 3.0 ± 0.6 mg$_{electrode}$/cm^2 (corresponding to a silicon loading of 1.2 ± 0.2 mg$_{Si}$/cm^2) and an electrode thickness of ≈50 μm. The theoretical areal capacity of these electrodes is thus 4.3 ± 0.9 mAh/cm^2 (≡1440 mAh/g$_{electrode}$) based on a theoretical capacity of 3600 mAh/g$_{Si}$[7] and neglecting the small capacity of the VGCF-H fibers (<80 mAh/g). For full-cell testing the loading of the Si electrode was 1.4 mg$_{electrode}$/cm^2 (0.6 mg$_{Si}$/cm^2, 2.1 mAh/cm^2). As counter electrode, a commercial LFP electrode with an areal capacity of 3.5 mAh/cm^2 (from Custom Cells, Itzehoe, Germany) was used.

The specific surface areas of electrode components were determined by BET, using an Autosorb iQ nitrogen gas sorption analyzer (Quantachrome Instruments, USA). The determined BET areas are 19 m^2/g for the silicon nanoparticles and 13 m^2/g for the VGCF-H fibers.

Electrochemical characterization.—Electrochemical cycling was performed in coin cells (Hohsen Corp., Japan) or Swagelok T-cells, assembled in an argon filled glove box (O_2 and H_2O < 0.1 ppm, from MBraun, Germany) using pure lithium (diameter of 15 mm in coin cells and 11 mm in Swagelok T-cells and thickness of 0.45 mm; battery grade foil, 99.9% purity, from Rockwood Lithium, USA) as anode, two glass fiber separators (glass microfiber filter #691, from VWR, Germany), and 75 or 150 μL LP57 electrolyte (1 M $LiPF_6$ in EC:EMC (3:7 wt/wt), <20 ppm H_2O, from BASF, Germany) to which different amounts of fluoroethylene carbonate (FEC, from Solvay, Belgium) were added. Additionally, for full-cell testing a cell was assembled using two H2013 separators (from Celgard, USA) and 30 μL LP57 electrolyte containing 2%$_{wt}$ FEC. As will be shown in the Results section, a critical variable is the molar amount of FEC normalized by the silicon electrode mass (in units of μmol$_{FEC}$/mg$_{electrode}$), thereafter referred to as specific amount of FEC, which is calculated from the added electrolyte volume, the electrolyte density (1.19 g/cm^3), the %$_{wt}$ of added FEC, and the molecular weight of FEC (106 g/mol).

In the case of Swagelok T-cells, a lithium reference electrode was used to monitor the potentials of working and counter electrode. The cells were cycled in a climate chamber (Binder, Germany) at 25°C with a battery cycler (Series 4000, from Maccor, USA) according to the following procedure: 3 cycles at a C-rate of C/10 and up to 450 cycles at C/3; the C-rate was referenced to the above described theoretical capacity of 4.3 ± 0.9 mAh/cm^2 (≡1440 mAh/g$_{electrode}$). The cells were cycled between 10 mV and 1.2 V vs. Li/Li$^+$ in constant current (CC) mode.

^{19}F-NMR.—After the cycling experiments, the coin cells were opened, the retrieved separators were soaked in 800 μL DMSO-d_6, and the resulting solution was filled into air-tight NMR tubes. The ^{19}F-NMR spectra were collected on a Bruker Ascend 400 (400 MHz) with and without proton decoupling. For the comparison of integral ratios only the non-decoupled spectra were used.

On-line electrochemical mass spectrometry (OEMS).—For OEMS experiments, it is necessary to use working electrodes coated on a porous substrate to allow for fast diffusion of evolved gases into the cell head space.[33] Coatings on aluminum or copper foil current collectors cannot be used, because the long diffusion time of gas produced at the working electrode to the head space of the cell would compromise the time and voltage resolution.[34] In this study, silicon electrodes were prepared by coating the above described ink onto carbon fiber paper (H2315, from Freudenberg, Germany). Since carbon fiber paper can also intercalate lithium, the overall electrode capacity is derived from the silicon capacity plus the capacity of the carbon fiber paper, which was determined to be roughly 190 mAh/g$_{C\text{-}paper}$. The working electrodes had a diameter of 15 mm (≡1.77 cm^2), with an areal weight of 1.04 mg/cm^2 for the Si/VGCF-H/LiPAA electrode and of 7.75 mg/cm^2 for the carbon fiber paper, corresponding to an overall areal capacity of 2.96 mAh/cm^2 (i.e., 1.50 mAh/cm^2 from the Si/VGCF-H/LiPAA electrode and 1.46 mAh/cm^2 from the carbon fiber paper). The surface area per cm^2 of electrode (Si + VGCF-H + C-paper) was determined by multiplying the areal masses of each component with its BET surface area. The measured BET surface area of the C-fiber paper was 0.5 m^2/g$_{C\text{-}paper}$ and with the surface areas of Si and VGCF-H (see above), the total surface area of the electrode was calculated to be 0.017 m^2/cm$^2_{electrode}$.

As counter electrode, a commercial LFP electrode with an areal capacity of 3.5 mAh/cm^2 (from Custom Cells, Itzehoe, Germany) and a diameter of 16 mm was used. Both electrodes were dried overnight at 120°C under vacuum in a glass oven (drying oven 585, from Büchi, Switzerland).

The OEMS cell was assembled in a glove box with argon atmosphere (O_2 and H_2O < 0.1 ppm, MBraun, Germany), using two glass fiber separators (glass microfiber filter #691, from VWR, Germany) and 320 μL LP57 electrolyte (1 M $LiPF_6$ in EC:EMC (3:7 wt/wt), <20 ppm H_2O, BASF, Germany) with added 5%$_{wt}$ FEC (Solvay, Belgium). The cell was placed in a climate chamber at 25°C (Binder, Germany) and connected to the potentiostat (Series G300 potentiostat, Gamry, USA) and the mass spectrometry system, which was described in detail elsewhere.[34] The cell was held at OCV for 3 h, followed by a galvanostatic charge from OCV (open circuit voltage) to 3.44 V with a current of 148 μA/cm^2, corresponding to a C-rate of C/20. The gas evolution during the OCV and the charging period was recorded by OEMS. All mass signals were normalized to the ion current of the ^{36}Ar isotope to correct for fluctuations of pressure and temperature. Conversion of the ion currents to concentrations was done for the CO_2, H_2 and C_2H_4 using a calibration gas (Ar with 2000 ppm H_2, O_2, C_2H_4 and CO_2, Westfalen, Germany). The total moles of each gas can then be determined from the OEMS cell volume (9.5 mL) and the ideal gas law.

Results

Electrochemical cycling of Si-based anodes.—Figs. 1 and 2 display the coulombic efficiency and specific lithiation capacity vs. cycle number for Si-Li coin cells with 75 μL (Fig. 1) or 150 μL (Fig. 2) of electrolyte. All cells contained an electrolyte based on 1 M $LiPF_6$

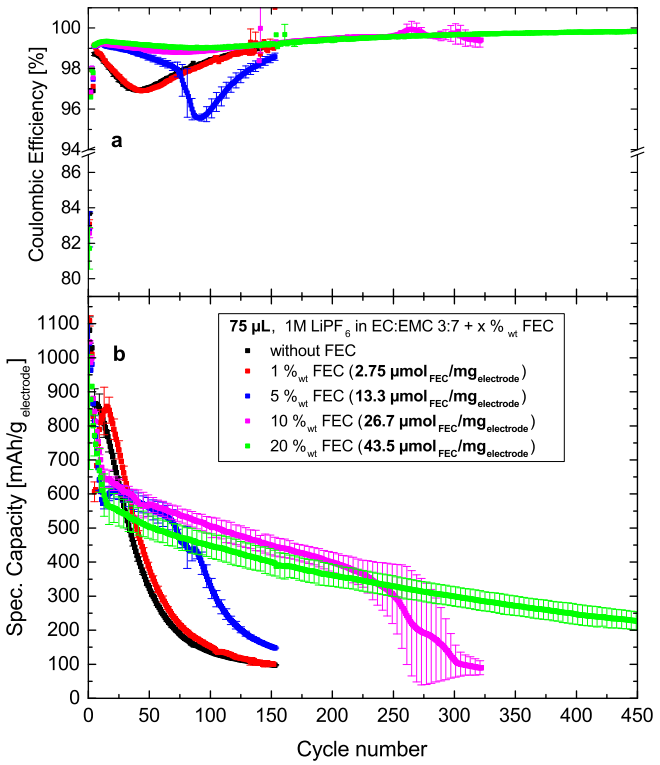

Figure 1. (a) Coulombic efficiency and (b) specific lithiation capacity vs. cycle number of Si-Li coin cells with 75 µL LP57 electrolyte containing different amounts of FEC. The first three cycles are conducted at C/10 followed by cycling at C/3. The theoretical capacity is 1440 mAh/$g_{electrode}$ and the specific amount of FEC (in $\mu mol_{FEC}/mg_{electrode}$) is specified in the figure.

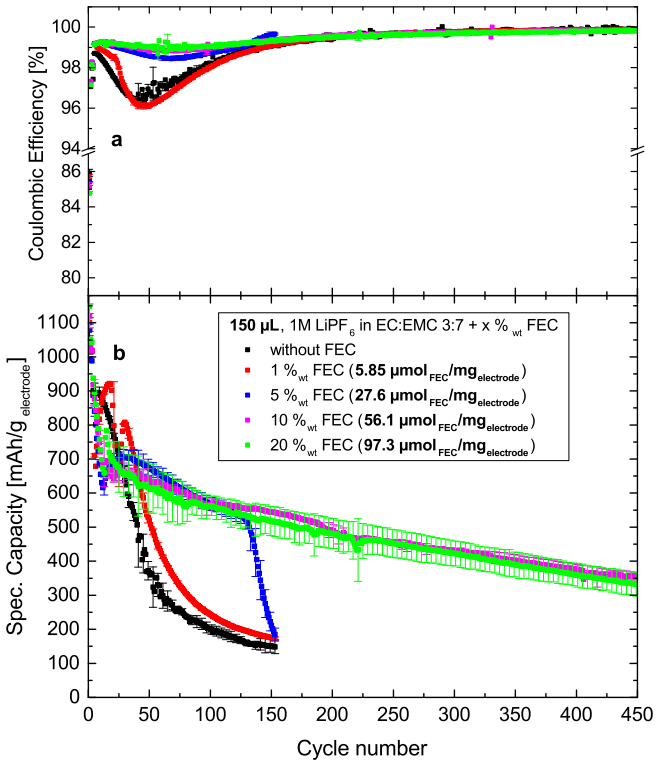

Figure 2. (a) Coulombic efficiency and (b) specific lithiation capacity vs. cycle number of Si-Li coin cells with 150 µL LP57 electrolyte containing different amounts of FEC. The first three cycles are conducted at C/10 followed by cycling at C/3. The theoretical capacity is 1440 mAh/$g_{electrode}$ and the specific amount of FEC (in $\mu mol_{FEC}/mg_{electrode}$) is specified in the figure.

in EC:EMC (3:7 wt/wt) with different levels of FEC (0, 1%$_{wt}$, 5%$_{wt}$, 10%$_{wt}$ and 20%$_{wt}$), and two cells were tested for each electrolyte composition. Two different volumes of electrolytes were selected in order to compare systems with equal concentrations but different amounts of FEC, thereby examining whether it is the concentration or the total moles of FEC which controls the lifetime of silicon based electrodes. Therefore, both the %$_{wt}$ of FEC as well as its molar amount referenced to the electrode mass (in units of $\mu mol_{FEC}/mg_{electrode}$) are specified in Figs. 1 and 2. The cells were cycled between 10 mV and 1.2 V vs. Li/Li^+ in constant current (CC) mode (first three cycles at C/10, followed by cycling at C/3). No constant voltage (CV) period was applied due to two reasons: i) it is reported in the literature that at voltages below 50 mV $Li_{15}Si_4$ starts to crystallize,[7] which is suspected to be very reactive and thus to diminish the lifetime of silicon electrodes;[35] ii) it significantly increases the sensitivity of electrochemical cells to changes in the polarization, since the CV phase would deliver additional capacity due to a shrinking polarization caused by a decreasing current.

The specific lithiation capacities in the third cycle at C/10 range from 915 to 1043 mAh/$g_{electrode}$ for all experiments shown in Figs. 1 and 2, equating to 63–73% of the theoretical capacity of 1440 mAh/$g_{electrode}$ (see Experimental section). For the cells containing 75 µL electrolyte (Fig. 1), two different trends can be observed. Firstly, the cells containing 0 and 1%$_{wt}$ FEC have a relatively poor coulombic efficiency and their specific capacities fade very rapidly from the very beginning, dropping to 150 mAh/$g_{electrode}$ after only 100 cycles (red and black symbols in Fig. 1). In contrast, cells containing $\geq$5%$_{wt}$ FEC show substantially improved coulombic efficiency and a fast decrease in specific capacity until cycle 15, which is likely due to the formation of an initially more resistive SEI with FEC, as was suggested before.[36] After this initially fast capacity loss, the capacity fading in the presence of FEC is much less than in electrolytes with <5%$_{wt}$ FEC. However, this trend is interrupted when a rapid capacity drop is observed at roughly cycle 70 for 5%$_{wt}$ FEC and at roughly cycle 225 for 10%$_{wt}$ FEC. The reason for the large error bars around the cycle numbers where the rapid capacity drop is observed is caused by the small offset between cycle numbers where the capacity drops occur in the two nominally identical cells. Interestingly, for the cells with 5%$_{wt}$ FEC, the rapid capacity drop is accompanied by a drop in the coulombic efficiency, indicating significant changes in the parasitic reactions related to SEI formation on silicon. This is not observed for the cells with 10%$_{wt}$ FEC, which might be due to the already very thick SEI after $\approx$200 cycles, in which case the disappearance of FEC (see below) has a less drastic effect. On the other hand, the cells containing 20%$_{wt}$ FEC do not display this rapid capacity drop until the end of the cycling test after 450 cycles. The cells with 150 µL electrolyte (Fig. 2) show the same overall behavior, except that the rapid capacity drop for the cells with 5%$_{wt}$ FEC now occurs at a higher cycle number (roughly cycle 130) and that it is not observed anymore for the cells with 10%$_{wt}$ FEC up to 450 cycles. However, for the cells containing 1%$_{wt}$ FEC the rapid capacity drop can be seen around cycle 25 (not observed with 75 µL FEC in Fig. 1) along with a simultaneous drop in coulombic efficiency. Remarkably, in analogy to the case for 10%$_{wt}$ FEC and 75 µL electrolyte (Fig. 1), for 150 µL the drop in coulombic efficiency after the rapid capacity drop is not observed for 5%$_{wt}$ FEC. A comparison of the data with 75 and 150 µL electrolyte (see Figs. 1 and 2) reveals that an increase of the specific amount of FEC ($\mu mol_{FEC}/mg_{electrode}$) is responsible for enhanced cycle life, rather than simply the concentration (%$_{wt}$) of FEC. This in turn suggests that the consumption of FEC might be the reason for the observed capacity drop. The correlation between FEC content and the onset of the rapid capacity drop is subject to the Discussion section.

Another interesting observation is that cells with FEC-free electrolyte have higher absolute capacities for the first 30–40 cycles. A very similar behavior was observed by Schroder et al., who reported higher capacities for FEC-free electrolytes until cycle 37, with similarly high fading rates.[36] This feature was explained by assuming that a sufficiently thick and stable SEI is formed in the presence of

FEC from the very beginning, whereas the SEI in FEC-free electrolyte might initially be thinner, causing less polarization and higher capacities, but at the same time is not stable enough for long term cycling.

NMR analysis of electrolyte before and after the capacity drop.— In order to understand the reason for the rapid capacity drop, we analyzed the electrolyte before and after the drop by ^{19}F-NMR spectroscopy to quantify the amount of remaining FEC in the cells. Fig. 3a shows three cells which were cycled in LP57 with 5%$_{wt}$ FEC. The cell shown in green (cell Si-Li #3) was stopped seven cycles after the clearly visible onset of the rapid capacity drop after roughly 120 cycles. This is somewhat larger than what was observed for the nominally identical experiment shown in Fig. 1 (blue line, with also 75 µL electrolyte and 5%$_{wt}$ FEC), which is due to the slightly higher specific amount of FEC used in Fig. 3a (15.7 µmol$_{FEC}$/mg$_{electrode}$ for the green line) compared to what was used in Fig. 1 (13.3 µmol$_{FEC}$/mg$_{electrode}$); the quantitative relationship between the specific amount of FEC and the cycle number at which the rapid capacity drop is observed will be shown in the Discussion section. The cells plotted in black (cell Si-Li #1) and red (cell Si-Li #2) were stopped when roughly one third

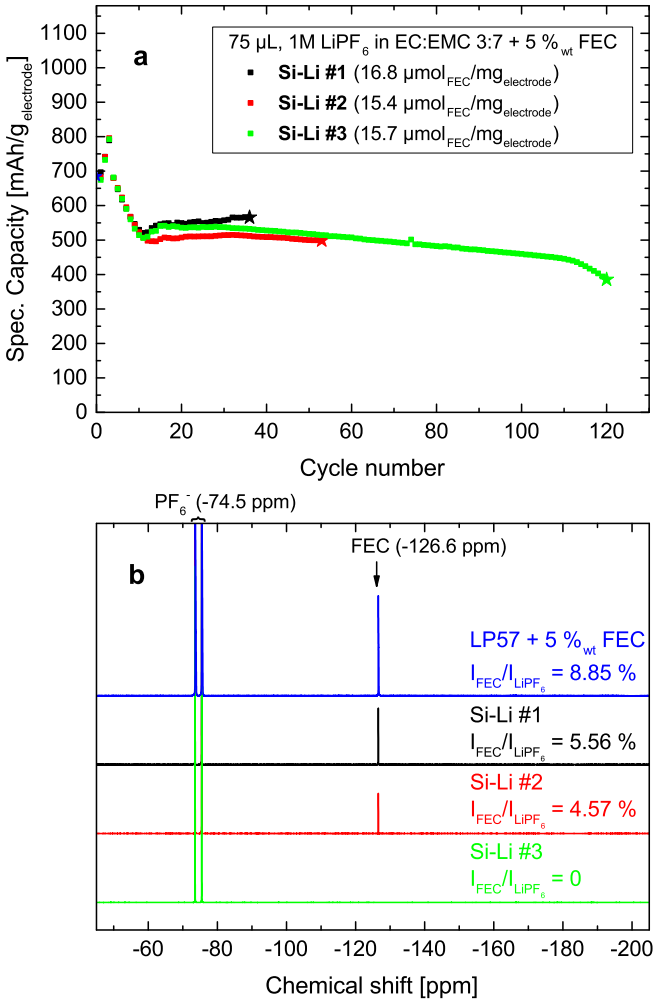

Figure 3. (a) Specific lithiation capacity vs. cycle number of Si-Li coin cells (Si-Li #1 = black line; Si-Li #2 = red line; Si-Li #3 = green line) with 75 µL LP57 electrolyte containing 5%$_{wt}$ FEC (the moles of FEC per mg$_{electrode}$ is specified in the figure); cycling rates are C/10 for the first 3 cycles and C/3 for all subsequent cycles. (b) ^{1}H-decoupled ^{19}F-NMR-spectra of the electrolyte before cycling (blue) and after cycling of the three cells shown in (a); the intensity ratios between the fluoride signal from FEC and from $LiPF_6$ (I_{FEC}/I_{LiPF6}) is given in the figure and were calculated from the non-decoupled spectra.

and one half of the FEC were expected to be consumed, respectively (i.e., after cycle 36 and 53). For all the cells, the electrolytes were extracted and liquid state ^{19}F-NMR spectra were measured (Fig. 3b). Since the decomposition of $LiPF_6$ in comparison to the solvent is expected to be negligible, $LiPF_6$ was used as an internal standard to quantify the amount of remaining FEC, namely by determining the integral ratio of the fluorine signal from FEC and that of $LiPF_6$; note that the integral ratio of the electrolyte before cycling (blue spectrum in Fig. 3b) fits exactly the expected ratio of FEC:$LiPF_6$ in pure LP57 + 5%$_{wt}$ FEC. The assumption that the $LiPF_6$ concentration does not change significantly over the course of the experiments is supported by a detailed inspection of the NMR-spectra, revealing no additional peaks from salt decomposition products like $PO_2F_2^-$. Additionally, no signals originating from SiF_6^{2-} (typically observed product in the event of glass fiber separator decomposition by HF)[37] were observed in the ^{19}F-NMR experiments, proving that the glass fiber separator is stable under our experimental conditions.

When comparing the integral ratios of FEC and $LiPF_6$ in Fig. 3b, a steady decrease of the FEC concentration with increasing cycle number can be observed. While 63% of FEC is still left in the cell after cycle 36 (from $(I_{FEC}/I_{LiPF6})_{36\ cycles}$ / $(I_{FEC}/I_{LiPF6})_{0\ cycles}$; see black lines/numbers in Fig. 3), the remaining amount of FEC has dropped to 52% after 53 cycles (see red lines/numbers in Fig. 3). For the Si-Li cell which was opened after the capacity drop at cycle 120, the remaining FEC concentration based on the ^{19}F NMR data is zero (see green lines/numbers in Fig. 3). This provides clear evidence for the continuous consumption of FEC during charge/discharge cycling of silicon based anodes, consistent with the proposed cracking of the SEI upon volume expansion.[20,21] Extension of this NMR analysis further suggests that the rapid capacity drops observed in Figs. 1 and 2 occur at the point once the FEC additive is consumed. This explains why the rapid capacity drop appears at higher cycle numbers when the specific amount of FEC (i.e., the µmol$_{FEC}$/mg$_{electrode}$) is increased, as can be observed by comparing Figs. 1 and 2. A more detailed quantitative correlation will be provided in the Discussion section.

Analysis of cell polarization by three electrode setup.— A three electrode set-up with lithium reference electrode (Swagelok T-cells) is used to separately analyze the voltage evolution of the silicon working electrode and the lithium counter electrode in order to determine the polarization of the silicon electrode over the course of the charge/discharge cycles. Figs. 4a and 4b show the cycle number dependence of the Si-Li cell capacity and the evolution of the mean charge/discharge voltage polarization ΔV_{mean} for each electrode, whereby ΔV_{mean} is the difference between $\int(V_{delith.} \cdot dq_{delith.})/\int dq_{delith.}$ and $\int(V_{lith.} \cdot dq_{lith.})/\int dq_{lith.}$ evaluated for each charge/discharge cycle with voltages referenced to the potential of the lithium reference electrode. The cycle number at which the rapid capacity drop occurs as well as its correlation to the specific amount of FEC is more difficult to predict in these measurements in Swagelok T-cells, since contrarily to coin cells, the exact amount of available electrolyte in a Swagelok T-cell cannot be determined reliably.

It can be seen that the polarization of the lithium counter electrode changes very little when the capacity starts to fade more rapidly (see red line in Fig. 4b), indicating that lithium is not much affected by the consumption of FEC. In contrast, the polarization of the silicon electrode increases significantly (see black line in Fig. 4b) from roughly 300 mV to over 400 mV once FEC is consumed. This significant rise of the silicon overpotential is probably the reason for the rapid capacity drop near cycle 40. This effect can be also seen in the cell-voltage profiles of the 30th (before the rapid capacity drop) and 50th cycle (after the rapid capacity drop) shown in Fig. 4c. An increase of the mean cell polarization from around 266 mV to 365 mV is observed. As the lithiation potential profile has a very flat slope, this higher polarization leads to a significantly lower lithiation capacity at the point at which the lower cutoff voltage is reached and consequently causes the rapid drop in capacity.

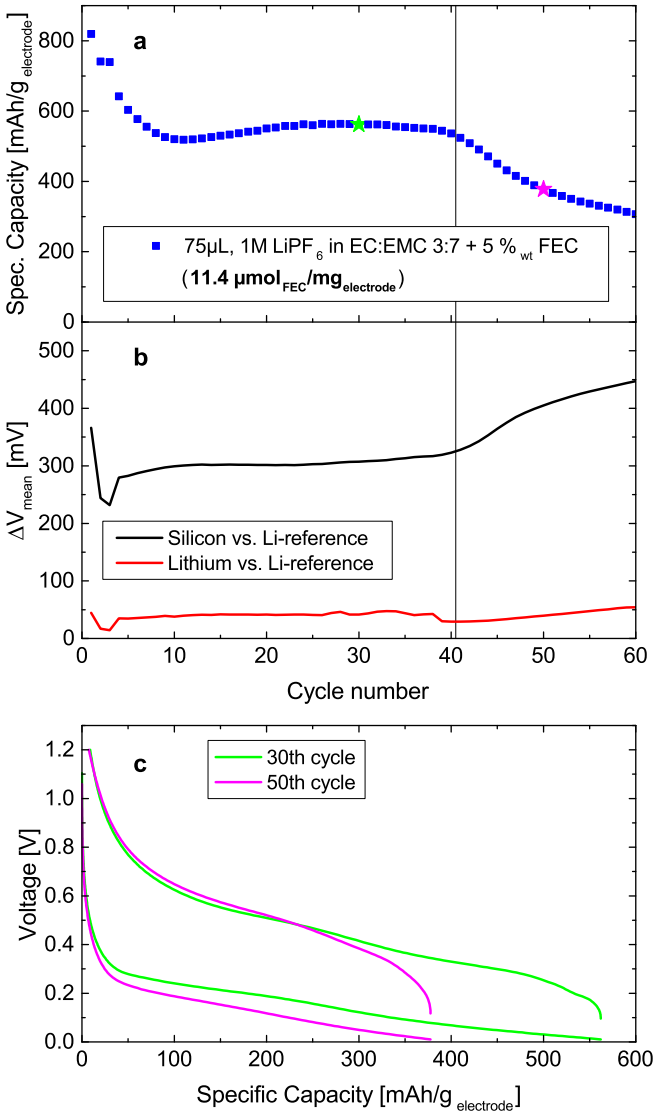

Figure 4. (a) Specific lithiation capacity vs. cycle number of a Si-Li Swagelok T-cell with a metallic lithium reference electrode using 75 µL LP57 electrolyte containing 5%$_{wt}$ FEC at a C-rate of C/10 for the first three cycles followed by cycles at C/3. (b) Mean charge/discharge voltage ΔV_{mean} (see definition in the text) vs. cycle number of both the silicon and lithium electrode with respect to the lithium reference electrode potential. (c) Cell voltage profile of the 30th cycle (i.e., before the rapid capacity drop) and the 50th cycle (i.e., after the rapid capacity drop) of the cell shown in (a).

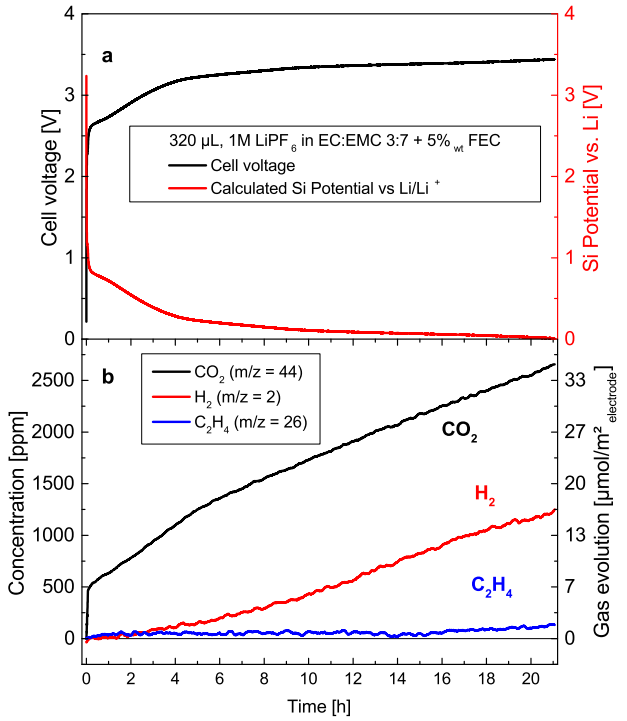

Figure 5. (a) Cell-voltage (black) and calculated silicon potential (red) vs. time of a cell using a silicon working electrode coated on carbon paper vs. a LFP counter electrode with 320 µl electrolyte (1 M $LiPF_6$ in EC:EMC (3:7 wt/wt) + 5%$_{wt}$ FEC), galvanostatically charged with a rate of C/20 from OCV to 3.44 V. (b) Evolution of CO_2 (black), H_2 (red) and C_2H_4 (blue) as a function of time. The OEMS data are smoothed, baseline corrected, and converted into units of [ppm] and [µmol/m^2$_{electrode}$]. The latter is calculated by converting the ppm into µmol and normalizing it to the surface area of Si + VGCF-H + C-fiber paper. The specific amount of FEC referenced to the Si/VGCF-H/LiPAA electrode is 91.8 µmol$_{FEC}$/mg$_{electrode}$.

Gas analysis of Si-LFP cell by OEMS.—The results of the online electrochemical mass spectrometry (OEMS) measurement of a Si-LFP cell during silicon lithiation are shown in Fig. 5. In the upper panel (Fig. 5a), the cell voltage profile during lithiation is shown by the black line, while the red line gives the potential of the silicon electrode vs. the Li/Li^+ potential calculated from the known LFP potential of ≈3.45 V. The use of LFP instead of Li metal will prevent the decomposition of the electrolyte on the counter electrode, since the electrolyte is stable at the potential of the LFP electrode so that all evolved gases can be traced back to reactions occurring on the silicon working electrode. In the lower panel (Fig. 5b), the mass traces of carbon dioxide (black), hydrogen (red) and ethylene (blue) are shown in terms of ppm in the cell head space and in terms of µmol/m^2$_{electrode}$; note that the surface area is the sum of the surface areas of silicon, VGCF-H, and the C-fiber paper (see Experimental section). It is known that EC reduction leads to ethylene evolution,[38–40] whereas FEC reduction causes carbon dioxide evolution,[41] analogous to the CO_2 evolution observed during the reduction of chloroethylene carbonate.[42] Therefore, a quantification of these two gases gives information on the ratio of decomposed FEC and EC. The observed gas evolution (Fig. 5b) shows 2700 ppm of carbon dioxide, whereas the ethylene concentration amounts to only ≈100 ppm at the end of the lithiation process. That the latter is strikingly low can be seen by comparing it with the ≈2000 ppm C_2H_4 which were observed during the first lithiation of a graphite electrode with comparable areal capacity (2.5 mAh/cm^2) in the same electrolyte without FEC additive.[43] This, together with the fact that the molar ratio of evolved CO_2 to C_2H_4 at the end of the measurement is very large (n_{CO2}/n_{C2H4} ≈ 95:5) clearly proves that FEC almost entirely suppresses the reduction of EC. Hence, one can assume that FEC is exclusively reduced as long as there is FEC present in the electrolyte. This fits well with the earlier observation that the interfacial resistance and thus the SEI changes significantly once the FEC is consumed (see Fig. 4).

In the evolution of CO_2, three regions with different rates (i.e., different slopes in Fig. 5b) can be observed. One with very high CO_2 evolution rate at the very beginning, where 460 ppm CO_2 are formed within the first 4.2 minutes of the measurement. A second region with a lower and constant rate until roughly five hours into the charging process, and a third region with a yet lower CO_2 evolution rate lasting until the end of the measurement. In contrast, the evolution of hydrogen does not start until about 2–3 hours after the start of the charging process and then proceeds with a more or less constant rate. During the entire measurement, no carbon monoxide was detected. Also, no SiF_4 (typical product upon HF attack on glass fiber separator)[44] was observed in the OEMS measurement, proving once again the stability of the separator under our experimental conditions. A more detailed analysis including the interpretation of these observations will be subject of the Discussion section.

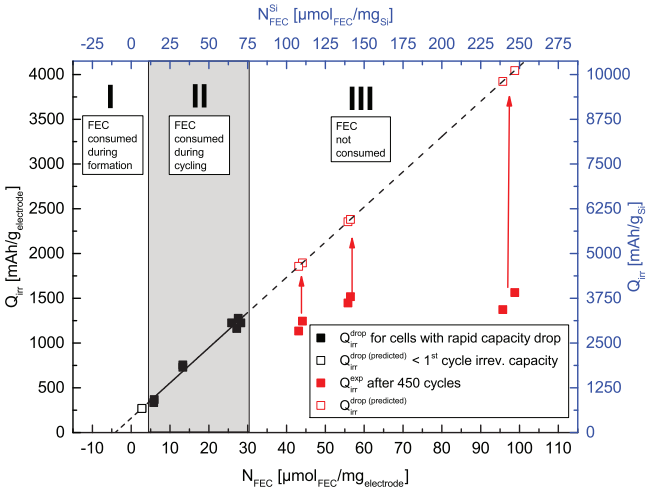

Figure 6. Cumulative irreversible capacity Q_{irr}, (see Equation 1) vs. specific amount of FEC in the cell (N_{FEC}) obtained from the cycling data shown in Figs. 1 and 2. Black squares: cells for which a rapid capacity drop was observed during cycling; full red squares: cells which did not show a rapid capacity drop until the end of the cycling experiment (450 cycles); open red squares: predicted Q_{irr} ($\equiv Q_{irr}^{drop\ (predicted)}$) by which one would expect to observe a rapid capacity drop; open black square: cells for which the specific amount of FEC was too low to obtain improved cycle life (i.e., all FEC gets consumed in the first formation cycle). The black line is a least-squares regression line through the data obtained for the 8 cells which showed a rapid capacity drop (black squares): $Q_{irr}^{drop\ (predicted)} = 39.3\ (mAh/g_{electrode})/(\mu mol_{FEC}/mg_{electrode}) \times N_{FEC} + 162\ mAh/g_{electrode}$ ($R^2 = 0.978$), with an x-axis intercept of 4.1 $\mu mol_{FEC}/mg_{electrode}$. Additionally, Q_{irr} and the specific amount of FEC normalized to the mass of silicon (N_{FEC}^{Si}) are shown in blue (right and top axes, respectively); normalized to silicon, the black regression line is: $Q_{irr}^{drop\ (predicted)} = 39.3\ (mAh/g_{Si})/(\mu mol_{FEC}/mg_{Si}) \times N_{FEC}^{Si} + 405\ mAh/g_{Si}$.

Discussion

Correlation between the cumulative irreversible capacity and FEC consumption.—The pronounced difference in cycling stability between the cells with and without FEC (Figs. 1 and 2) suggests that the SEI formed with FEC is significantly more stable. It is very interesting that independent of the amount of FEC, the cycling stability is nearly equal for all the cells as long as FEC is present in the electrolyte. This is due to the almost exclusive SEI formation by FEC, since its decomposition is preferred over that of EC and other electrolyte components, suppressing their decomposition to a very minimum. This is in accordance with the findings by Wang et al., who did not observe any EC reduction peak in a cyclic voltammetry experiment once FEC was present in the electrolyte.[31] Assuming therefore that all irreversible capacity is caused exclusively by FEC reduction, the lifetime of the cells should correlate with the irreversible capacity. In order to prove this for all cells with an observable rapid capacity drop (Fig. 1 and 2), the cumulative irreversible capacity, Q_{irr}, was calculated according to Equation 1, with $Q_i^{lithiation}$ and $Q_i^{delithiation}$ being the specific lithiation and delithiation capacity of the i^{th} cycle, summed up from the first cycle i = 1 until either the cycle where the rapid capacity drop occurs or to the end of the experiment (450 cycles):

$$Q_{irr} = \sum_i \left(Q_i^{lithiation} - Q_i^{delithiation}\right) \quad [1]$$

The calculated value of Q_{irr} for all the cells is plotted in Fig. 6 versus their respective specific amount of FEC, N_{FEC}. The full black squares represent the cells for which a rapid capacity drop was observed during the cycling experiment, yielding $Q_{irr} \equiv Q_{irr}^{drop}$. With increasing specific amounts of FEC in the cells, Q_{irr}^{drop} increases linearly (see black symbols in Fig. 6), representing the longer lifetime of cells with higher specific amount of FEC. If the reduction of FEC would be only one among several side reactions, one would not expect the clearly linear trend of Q_{irr}^{drop} vs. N_{FEC}, which in turn strongly supports the hypothesis that there is only one source of irreversible capacity, namely the reduction of FEC. The intercept of the linear correlation line with the y-axis (i.e., at $N_{FEC} = 0$) can be interpreted as the irreversible capacity of the first cycle (formation cycle) equating to 162 $mAh/g_{electrode}$. On the other hand, the x-axis intercept (i.e., at $Q_{irr} = 0$) represents the specific amount of FEC consumed during the first formation cycle, viz., 4.1 $\mu mol_{FEC}/mg_{electrode}$. Alternatively, the latter can also be interpreted as the minimum amount of FEC necessary in a cell to improve its cyclability.

Table I. Specific amount of FEC (N_{FEC}) and experimentally observed cumulative irreversible capacity (Q_{irr}^{exp}) for cells for which no rapid capacity drop was observed, either because all FEC was already consumed in the first cycle (rows 1 and 2) or because the total number of cycles in the experiment (450 cycles) was too low to lead to rapid capacity loss, i.e., too low to consume all the FEC (rows 3-8). For the latter, the predicted cumulative irreversible capacity at which one would expect the rapid capacity drop ($Q_{irr}^{drop\ (predicted)}$) obtained from the linear regression line in Fig. 6 is also given. The data are extracted from the experiments shown in Figs. 1 and 2.

Cell details	N_{FEC} [$\mu mol_{FEC}/mg$]	Q_{irr}^{exp} [mAh/g]	$Q_{irr}^{drop\ (predicted)}$ [mAh/g]
1% FEC, 75 µL	2.73	-	-
1% FEC, 75 µL	2.78	-	-
20% FEC, 75 µL	43.13	1135	1860
20% FEC, 75 µL	44.10	1245	1898
10% FEC, 150 µL	55.82	1448	2361
10% FEC, 150 µL	56.45	1518	2386
20% FEC, 150 µL	95.69	1374	3939
20% FEC, 150 µL	98.77	1565	4061

This model is well suited to predict at which cumulative irreversible capacity values cells with a defined specific amount of FEC, N_{FEC}, start to experience a rapid capacity drop due to the total consumption of FEC. The open question, however, is why for some cells the rapid capacity drop was not observed during the cycling experiments. To address this question, the cumulative irreversible capacity up to 450 cycles (Q_{irr}^{exp}) of the cells which did not exhibit a rapid capacity drop are plotted vs. N_{FEC} in Fig. 6 (full red squares). After 450 cycles (i.e., after the end of the experiment), the Q_{irr}^{exp}-values of these cells clearly lie below the Q_{irr}^{drop}-values predicted by the linear correlation line in Fig. 6, $Q_{irr}^{drop\ (predicted)}$ (see open red squares in Fig. 6), which suggests that the FEC additive had not been consumed at this point. For these cells, the values of N_{FEC}, Q_{irr}^{exp}, and $Q_{irr}^{drop\ (predicted)}$ obtained from the regression line equation (see caption of Fig. 6) are listed in Table I. The two cells with 1%$_{wt}$ FEC and 75 µL electrolyte (first two rows in Table I and open black squares in Fig. 6) contain only 2.73 and 2.78 $\mu mol_{FEC}/mg_{electrode}$, which is below the 4.1 $\mu mol_{FEC}/mg_{electrode}$ consumed during formation and is thus consistent with the fact that no improved lifetime was observed.

In order to make this model more generally applicable to other silicon based electrodes, the top x-axis and right y-axis in Fig. 6 (blue axes) were re-scaled to show the specific amount of FEC and the cumulative irreversible capacity normalized to the mass of silicon. This depiction is very useful under the assumption that all irreversible capacity stems from side reactions on silicon (expected to be the case after the first cycle for any silicon-carbon composite electrode), in which case the equation correlating Q_{irr} and N_{FEC}^{Si} (given in the caption of Fig. 6) can serve as an easy tool to calculate from a known specific amount of FEC how much irreversible capacity can be accumulated until all FEC is consumed. Only if one uses electrodes with low silicon and high graphite content, one would need to correct the y-axis intercept by the SEI formed on graphite. The slope, however, would stay constant since even for these electrodes, the irreversible

Table II. Comparison of the remaining amount of FEC after the cycling of various cells with either 2 or 5%$_{wt}$ FEC in LP57 electrolyte. The remaining FEC content was calculated from Q_{irr}^{exp} and $Q_{irr}^{drop\ (predicted)}$ using Equation 2 ($FEC_{rem.\ (EC)}$) or from the changes of the integral ratio of the FEC and the $LiPF_6$ peak in the NMR-spectrum ($FEC_{rem.\ (NMR)}$). Three different cell types were tested/evaluated: a) the data for the cells Si-Li #1-3 are taken from Fig. 3; b) the Li-Li cells were cycled at the same current over the same time as the Si-Li #1 cell, passing the same amount of total coulombs (the data in the table represent the average of three independent experiments); c) the Si-LFP cells consisted of a silicon-carbon composite anode with a lower loading and a commercial LFP electrode (see Experimental) which were cycled by the same procedure as that used for the Si-Li #1-3 cells (i.e., cycling at C/10 for the first 3 cycles and C/3 for all subsequent cycles). Si-LFP #1 was cycled with glass fiber and Si-LFP #2 with Celgard H2013 separators.

		Electrochemical data				NMR data	
Electrolyte		N_{FEC} [μmol/mg]	Q_{irr}^{exp} [mAh/g]	$Q_{irr}^{drop\ (predicted)}$ [mAh/g]	$FEC_{rem.\ (EC)}$ [%]	$\frac{I_{FEC}}{I_{LiPF_6}}$ [%]	$FEC_{rem.\ (NMR)}$ [%]
75 μL LP57 + 5%$_{wt}$ FEC	Electrolyte	-	-	-	**100**	8.85	**100**
	Si-Li #1	16.80	313	822	**62**	5.56	**63**
	Li-Li cell	-	-	-	**-**	5.62	**63**
	Si-Li #2	15.45	380	769	**51**	4.57	**52**
	Si-Li #3	15.73	880	780	**0**	0	**0**
75 μL LP57 + 2%$_{wt}$ FEC	Electrolyte	-	-	-	**100**	3.75	**100**
	Si-LFP #1	14.80	776	1488 (see text)	**48**	1.76	**47**
30 μL LP57 + 2%$_{wt}$ FEC	Electrolyte	-	-	-	**100**	3.29	**100**
	Si-LFP #2	5.45	482	752 (see text)	**36**	1.07	**33**

side reactions after the first cycle will be dominated by reactions occurring on silicon.

To validate our above interpretation of the linear regression model, viz., that it describes the point at which FEC will be consumed, we will do a more detailed analysis of the ^{19}F-NMR data shown in Fig. 3. As discussed before, no decomposition products of $LiPF_6$ are observed by NMR (Fig. 3b), so that the PF_6^- peak can be used as internal standard. The cells presented in Fig. 3 are listed in Table II as Si-Li #1-3, with Si-Li #1 and Si-Li #3 being the cells with the least and the most number of cycles, respectively. Knowing N_{FEC} of these cells and applying the model developed in Fig. 6, $Q_{irr}^{drop\ (predicted)}$ was calculated and compared to the experimentally observed Q_{irr}^{exp}. The remaining FEC in the cells ($FEC_{left\ (EC)}$) was then calculated from the electrochemical data as:

$$FEC_{rem.\ (EC)} = 1 - \frac{Q_{irr}^{exp}}{Q_{irr}^{drop\ (predicted)}} \quad [2]$$

The resulting values for the remaining FEC obtained by Equation 2 were then compared to the NMR data for which the remaining FEC ($FEC_{rem.\ (NMR)}$) was obtained from the integral ratio of the FEC and PF_6^- peaks. As shown in Table II, both ways of determining the remaining amount of FEC result in essentially identical values for the cells in Fig. 3 (Si-Li #1-3), thereby validating the assumptions underlying the respective analyses, particularly the assumption that FEC is reduced exclusively and that therefore essentially all of the observed cumulative irreversible capacity goes into FEC reduction.

In order to understand the reductive decomposition of FEC in more detail, the cumulative irreversible capacity at the cycle where the rapid capacity drop initiates was converted into a total molar amount of electrons, n_e (in units of μmol) "consumed" in parasitic reactions involved in the continuous renewal of the SEI. This was done by converting the measured irreversible capacity into units of As and dividing it by the Faraday constant. Similarly, the specific amount of FEC was converted into a total molar amount of FEC, n_{FEC}, in the cells. Both n_e and n_{FEC} obtained for all cells for which a rapid capacity drop was observed are summarized in Table III. By dividing n_e through n_{FEC}, the parameter β is obtained, which is a measure for the apparent number of electrons consumed per FEC molecule. The $\beta_{apparent}$-values for all the tested cells vary around two, with an average value and standard deviation of $\beta_{apparent} = 1.9 \pm 0.3$. This could be interpreted to indicate that the reduction of FEC might follow a 2-electron mechanism. However, one has to be aware that the parasitic reactions on the lithium electrode in a silicon-lithium cell, i.e., with a virtually infinite amount of lithium, are not discernible in the irreversible capacity. Therefore, since it is likely that lithium will also decompose FEC, one needs to quantify the amount of decomposed FEC on the lithium counter electrode in order to determine its contribution to the FEC consumption in the Si-Li cells.

In order to answer the question of how much FEC is consumed on the lithium electrode, three Li-Li cells were prepared and cycled with the same current and over the same time like the Si-Li #1 cell (i.e., passing the same amount of total coulombs as during the cycling of the Si-Li #1 cell), also using 75 μL LP57 electrolyte with 5%$_{wt}$ FEC (Table II). Right after the Li-Li cells were cycled, ^{19}F-NMR spectra of the electrolytes were recorded. Since in this case two lithium electrodes are used, the amount of FEC decomposition on the two lithium electrodes should be exactly twice that which would be decomposed on the lithium electrode in the Si-Li #1 cell. Interestingly, the remaining FEC in the Li-Li cells was identical to that found for the Si-Li #1 cell, suggesting that ≈50% of the overall FEC consumption in a Si-Li cell is due to its reaction at the lithium counter electrode. Since the FEC consumption on lithium does not add to the cumulative irreversible capacity, this means that in fact only 50% of the FEC decomposition is accounted for in the cumulative irreversible capacity. This in turn means that the apparent 2-electron reduction of FEC in Si-Li cells (i.e., $\beta_{apparent} = 1.9 \pm 0.3$ obtained from Table III) is 2-fold lower than the actual number of electrons involved in the overall FEC reduction process, viz., $\beta_{actual} = 3.8 \pm 0.6$.

Scheme 1 (left panel) visualizes these processes on the silicon and the lithium electrode in a Si-Li cell, using an exemplary amount of four FEC molecules in the electrolyte and for simplicity assuming

Table III. Total moles of electrons, n_e, consumed in parasitic reactions and total moles of FEC, n_{FEC}, in the Si-Li cells for which a rapid capacity drop was observed (data shown in Figs. 1 and 2). The value of n_e was calculated from of the cumulative irreversible capacity up to the cycle where the rapid capacity drop initiated. The apparent number of electrons per consumed FEC, $\beta_{apparent}$, is defined as n_e/n_{FEC}.

Cell details	n_e [μmol]	n_{FEC} [μmol]	$\beta_{apparent}$
5% FEC, 75 μL	80.8	39.4	**2.05**
5% FEC, 75 μL	83.7	39.4	**2.12**
10% FEC, 75 μL	133.9	75.7	**1.77**
10% FEC, 75 μL	130.9	75.7	**1.73**
1% FEC, 150 μL	34.6	16.1	**2.16**
1% FEC, 150 μL	37.4	16.1	**2.33**
5% FEC, 150 μL	125.9	78.9	**1.60**
5% FEC, 150 μL	127.8	78.9	**1.62**

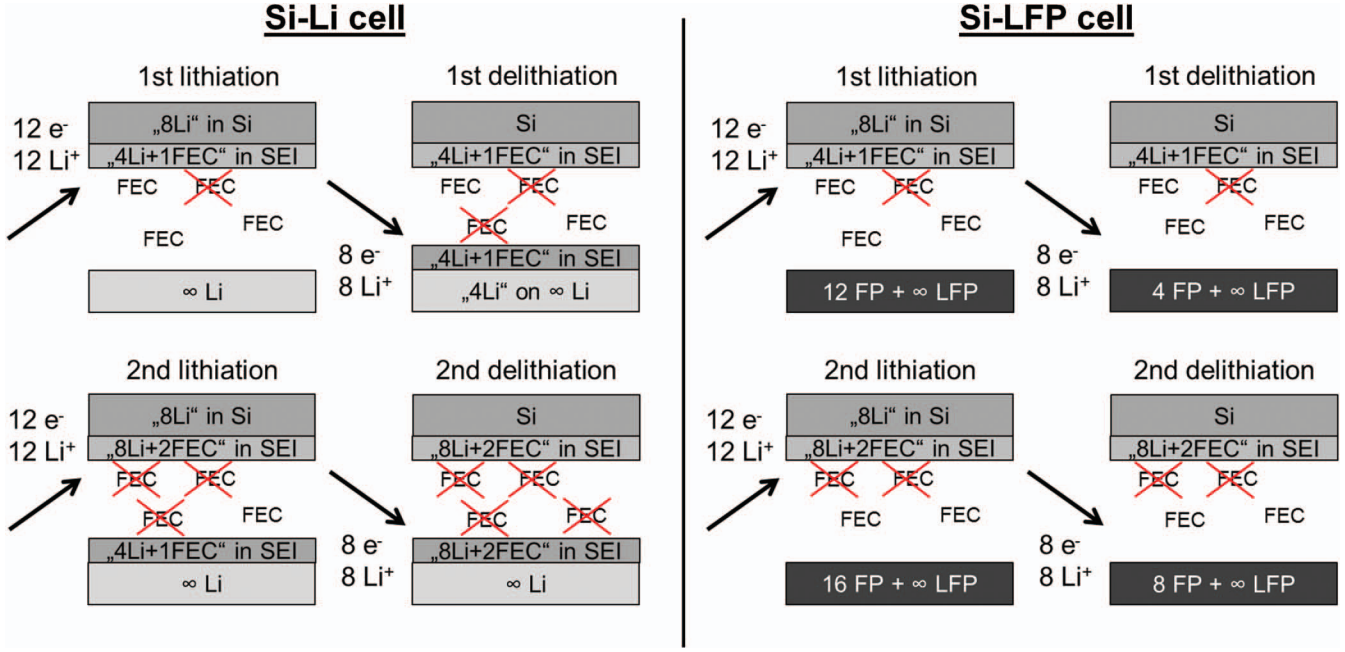

Scheme 1. Illustration of the FEC consumption in a Si-Li (left) and Si-LFP cell (right). The large excess of lithium in the lithium and the LFP counter electrodes compared to the capacity of the silicon electrodes is indicated by the ∞ sign.

that the reduction of FEC requires four electrons (i.e., $\beta_{actual} = 4$). If we then construct an example where 12 e^- and 12 Li^+ are transferred to the silicon electrode during the first lithiation cycle, then 8 ($e^- + Li^+$) could alloy with the silicon, while the remaining 4 ($e^- + Li^+$) could reduce one molecule of FEC ($\beta_{actual} = 4$) to build up the SEI. Since these four electrons are irreversibly consumed in the SEI formation, only 8 ($e^- + Li^+$) can be dealloyed from silicon during the first delithiation. From these 8 ($e^- + Li^+$) four go into the reduction of another FEC molecule on the lithium electrode and the other four are plated as lithium metal. As the lithium metal is an infinite reservoir of lithium, in the following cycle again 12 ($e^- + Li^+$) can be stripped from the lithium metal, starting the cycle over again. Summing up over each of the two cycles, the apparent irreversible capacity is four electrons and two molecules of FEC are reduced, giving a total of two electrons per consumed FEC or, in other words, $\beta_{apparent} = 2$.

In order to further prove that the total FEC decomposition in a Si-Li cell is split 50/50 between the silicon and the lithium electrode, the lithium counter electrode was replaced by an electrode on which no FEC decomposition would occur, namely with an LFP counter electrode. Under this premise, a Si-LFP cell was cycled with 75 µL LP57 electrolyte containing 2%$_{wt}$ FEC ($N_{FEC} = 14.80$ $\mu mol_{FEC}/mg_{electrode}$; see Si-LFP #1 in Table II); note that the FEC/$LiPF_6$ integral ratio determined by NMR for this 2%$_{wt}$ FEC electrolyte (=3.75) is 6% higher than predicted from the ratio obtained with the 5%$_{wt}$ FEC electrolyte (i.e., $2/5 \cdot 8.85 = 3.54$, Table II), which is due to pipetting errors when adding very small amounts of FEC. For Si-Li cells, the predicted cumulative irreversible capacity until the onset of the rapid capacity drop derived from the linear regression correlation of $Q_{irr}^{drop\ (projected)}$ vs. N_{FEC} (see caption of Fig. 6) would amount to 744 mAh/$g_{electrode}$, at which point all FEC should be consumed. Based on the above finding that 50% of the FEC is decomposed on the lithium counter electrode in Si-Li cells, the predicted cumulative irreversible capacity until the rapid capacity drop for Si-LFP cells would be 1488 mAh/$g_{electrode}$, since FEC is not decomposed on the LFP. Therefore, we stopped the cycling of the Si-LFP #1 cell once a cumulative irreversible capacity of 776 mAh/$g_{electrode}$ was reached (i.e., close to 744 mAh/$g_{electrode}$), at which point we would expect that ≈50% of the FEC would still remain in the cell. Indeed, as shown in Table II (last row), 47% FEC remain in the cell after a cumulative irreversible capacity of 776 mAh/$g_{electrode}$, providing further proof to the above finding that 50% of the FEC are consumed by the lithium electrode when cycling Si-Li cells. The number of electrons per FEC can now be determined from the cumulative irreversible capacity of the Si-LFP #1 cell (776 mAh/$g_{electrode}$ ≡ 29.0 $\mu mol_{electrons}/mg_{electrode}$) and the molar consumption of FEC (53% of 14.8 $\mu mol_{FEC}/mg_{electrode}$ amounting to 7.84 $\mu mol_{FEC}/mg_{electrode}$), yielding a value of $\beta_{actual} = 3.7$, essentially identical with the above derived value.

Additionally, a second Si-LFP cell (Si-LFP #2 in Table II) was tested replacing the two glass fiber separators by two conventionally used H2013 polyolefin separators (note that the FEC/$LiPF_6$ integral ratio of 3.29 of this freshly made 2%$_{wt}$ FEC containing electrolyte is 7% lower than what would be predicted based on the 5%$_{wt}$ electrolyte, which again (see above) is due to pipetting errors for very low FEC contents). Due to the lower pore volume of the polyolefin separators, the electrolyte volume was reduced to 30 µL. Assuming the above proposed four electron reduction of FEC the total FEC depletion is expected at a cumulative irreversible capacity of 752 mAh/$g_{electrode}$. As the cell was stopped at a cumulative irreversible capacity of 482 mAh/$g_{electrode}$, 36% of the added FEC is expected to remain in the cell. This is in excellent agreement with the subsequent quantification by ^{19}F-NMR, which reveals that 33% of the initial FEC is still present in the electrolyte. This clearly proves that the FEC consumption in the here presented experiments is not affected by the nature of the separator and indeed proceeds according to an overall four-electron reduction.

The processes in a Si-LFP cell with a capacity-wise largely oversized LFP counter electrode (Scheme 1, right panel) can again be illustrated using four molecules of FEC and $\beta_{actual} = 4$. During the first lithiation, as for the Si-Li case, 12 ($e^- + Li^+$) are transferred, with 8 ($e^- + Li^+$) alloying the silicon and 4 ($e^- + Li^+$) reducing one molecule of FEC (i.e., $\beta_{actual} = 4$). In the subsequent delithiation, 8 ($e^- + Li^+$) are removed from silicon. In contrast to the Si-Li case, all 8 ($e^- + Li^+$) are intercalated into FP and no further FEC molecule is decomposed. As the LFP is capacitively oversized, 12 ($e^- + Li^+$) can be deintercalated again in the following cycle. Summing up for each of the two cycles, the apparent irreversible capacity is again four electrons, but only one molecule of FEC is decomposed, giving a total of four electrons per consumed FEC. Thus, since the LFP electrode is an "inert" electrode, the irreversible capacity in a Si-LFP system shows

the real amount of four electrons necessary to reduce one molecule of FEC, i.e., $\beta_{apparent} = \beta_{actual}$.

Summarizing the above analysis, the continuous reduction of FEC on both lithium and silicon electrodes consumes close to four electrons per decomposed FEC molecule ($\beta_{actual} = 3.8 \pm 0.6$), which is substantially larger than in the most reduction mechanisms proposed in the literature.[22,26–28,30,31,36,46–49] A mechanism which would be consistent with this β-value will be presented below. Another important aspect of the FEC consumption analysis in Si-Li vs. Li-Li cells is that the FEC consumption per electrode during charge/discharge cycling only depends on the overall exchanged coulombs. Thus, the continuous parasitic electrolyte reduction with silicon anodes is not any different from that with metallic lithium anodes, at least when silicon is cycled between 10 mV and 1.2 V vs. Li/Li^+. This, unfortunately, suggests that silicon anodes may not have any hoped-for advantages in terms of continuous electrolyte consumption over metallic lithium anodes.

Gas analysis of Si-LFP cell by OEMS.—As presented before, three phases with different CO_2 evolution rates were observed in the OEMS measurement (Fig. 5b), which might be interpreted as: i) fast initial formation of an SEI monolayer on the electrode; ii) subsequent slower growth of a multi-layered SEI; and, iii) continuous formation of new SEI due to cracks caused by silicon volume expansion/contraction during lithiation/delithiation. In comparison, no hydrogen was evolved during the fast initial SEI formation phase and was only observed after a few hours into the charging process conducted at a rate of C/20. The hydrogen evolution rate, however, closely matches the CO_2 evolution rate in the third phase of the charging process (indicated by essentially parallel lines of concentration vs. time after ≈10 hours in Fig. 5b).

In the following, we will take a closer look at the first phase of the lithiation process, as it can provide information on the number of CO_2 molecules produced during the decomposition of an FEC molecule. After 4.2 minutes of the first-cycle lithiation at C/20 (≡ 148 μA/cm^2 or 262 μA), the CO_2 concentration in the OEMS accumulates to 460 ppm while the silicon electrode remains above ≈800 mV vs. Li/Li^+ (see Fig. 5a). At this potential, no intercalation into graphite nor into silicon is expected. Therefore, all current passed within these first 4.2 minutes will go into FEC reduction. The total amount of electrons during that period is n_e = 66 mAs = 684 nmol and the 460 ppm of CO_2 equate to a total of 178 nmol (based on an OEMS cell volume of 9.5 mL and 24.5 L/mol at 25°C/1 bar for an ideal gas). From this we can calculate the electrons per CO_2:

$$\frac{n_e}{n_{CO_2}} = \frac{684\ \text{nmol}}{178\ \text{nmol}} \approx 3.8\ \frac{e^-}{CO_2} \qquad [3]$$

Comparing the value of $e^-/CO_2 \approx 3.8$ with the above determined value of $e^-/FEC \approx 3.8 \pm 0.6$ (≡ β_{actual}), clearly indicates that the decomposition of one molecule of FEC produces one molecule of CO_2.

Next we will evaluate whether our above assumption of the formation of an SEI monolayer within the very initial phase of the lithiation process is reasonable. During this phase, CO_2 is evolved at a very high rate, producing 178 nmol within the first 4.2 minutes (see above). As determined in the Experimental section, the overall BET surface area of silicon, VGCF-H fibers, and the carbon fiber paper in the OEMS electrode equates to 0.017 m^2/cm$^2_{electrode}$ or to 0.030 m^2 per electrode. Since we have shown that each FEC molecule produces one CO_2 molecule during its decomposition and consumes ≈4 e^- (i.e., ≈4 Li^+), the grantedly most simple estimate would be that the decomposition product should be composed of 11 atoms (10 atoms/FEC - 3 atoms/CO_2 + 4 Li atoms). Assuming that every atom occupies a square with a side length equal to a carbon-carbon single bond length of 0.15 nm,[45] the area covered by one FEC decomposition product would be 11 × (0.15 nm)^2 = 0.25 nm^2. Consequently, the total area covered by 178 nmol of decomposition products can be estimated to be roughly 178 nmol × 0.25 nm^2 × N_A = 0.027 m^2 ($N_A = 6.023 \cdot 10^{23}$ atoms/mol). This estimated monolayer area very well matches the total surface area of the electrode (0.030 m^2), providing strong evidence that the high CO_2 evolution rate in the initial part of the first-cycle lithiation is due to an SEI monolayer formation on the electrode.

Reductive decomposition mechanism of fluoroethylene carbonate.—In the literature, a large variety of reduction mechanisms for FEC have been proposed.[22,26–28,30,31,36,46–49] However, there is neither a consensus on the reduction products nor on the number of electrons which are transferred to FEC and its decomposition products. For example, Wang et al. proposed a 1-electron reduction of the FEC molecule leading to a ring opening and followed by a dimerization to a dicarbonate.[31] Similar to this mechanism, Chen et al. proposed the ring opening in a 1-electron mechanism followed by a dimerization or, as an alternative pathway, a defluorination resulting in LiF and $(CH_2CHOCO_2Li)_n$.[47] Etacheri et al. proposed the transformation of FEC to vinylene carbonate (VC) by HF elimination with subsequent formation of LiF and reduction of the formed double bond, initiating the polymerization to poly(VC).[22] This was revised in a later publication by the same group, with Markevich et al. proposing a mechanism leading to the release of CO_2 aside with a variety of further decomposition products like H_2, LiF, Li_2CO_3 and a polymeric compound.[46] Nakai et al. proposed a 3-electron mechanism yielding LiF, Li_2CO_3, H_2 and a polymer.[30]

Even numerous, partially contradicting mechanisms have been proposed, there is a common finding. In particular, LiF was observed or proposed independently by several authors,[22,26–28,30,36,46–49] whereby the study by Schroder et al. indicates that the LiF content of the SEI is higher in the presence of FEC.[36] Formation of LiF also is consistent with our observations since we did not see any soluble fluorine containing decomposition products in the electrolyte by ^{19}F-NMR, even though we cannot exclude the formation of other fluoride containing solids. In recent publications by Balbuena and co-workers, applying ab initio modeling, the 1-electron reduction of FEC was suggested to yield an FEC-radical anion, decomposing into CO_2, F^-, and a vinoxyl-radical.[27,28] The formation of the vinoxyl-radical was also detected experimentally by Shkrob et al. by means of EPR experiments.[49] The release of CO_2 accompanied with the formation of LiF and the vinoxyl-radical is further supported by our observation that per FEC molecule also one molecule of CO_2 is released.

Based on the literature and our measurements, our proposed mechanism (Scheme 2) also starts with an initial electron transfer to the carbonyl carbon (1st electron transfer), which due to its bond to three oxygens is the most positively charged atom of the FEC molecule. Subsequently, the ring of the radical anion is opened, followed by the elimination of CO_2 and fluoride, which forms LiF with lithium ions in the electrolyte. It is quite reasonable to assume that the possibility to eliminate fluoride ions is the reason why the structurally similar molecules FEC and EC lead to very different decomposition products, resulting in significantly different structures of the respective SEIs. After fluoride and CO_2 elimination, the vinoxyl-radical remains, which is stabilized via the carbon-oxygen double bond. The formation of CO can be ruled out by our OEMS measurement, contradicting some theoretical calculations in literature where release of CO was proposed to lead to alternative pathways which do not produce the vinoxyl-radical.[27,28] Since we found the release of one CO_2 per FEC molecule, we believe that the pathway leading to the vinoxyl-radical, CO_2, and LiF is at least the most predominant one. Neither in the paper by Shkrob et al.[49] nor in the papers by the group of Balbuena[27,28] further electron transfer to the vinoxyl-radical was considered, as there was no information on the total number of electrons involved in the reduction of FEC, even though it was pointed out by Leung et al. that further electron transfer cannot be ruled out.[28] Our results, however, clearly show that a total of four electrons are consumed in the reductive decomposition of FEC. Therefore, the vinoxyl-radical has to be further reduced (2nd electron transfer), which should easily be possible considering its structure with a carbon-oxygen double bond, resulting in lithium-ethenolate (see second line in Scheme 2).

Lithium-ethenolate can be further reduced (3rd electron transfer) to lithium oxide and an ethenyl-radical (see second line in Scheme 2). We believe that the driving force for this reaction is the formation of the

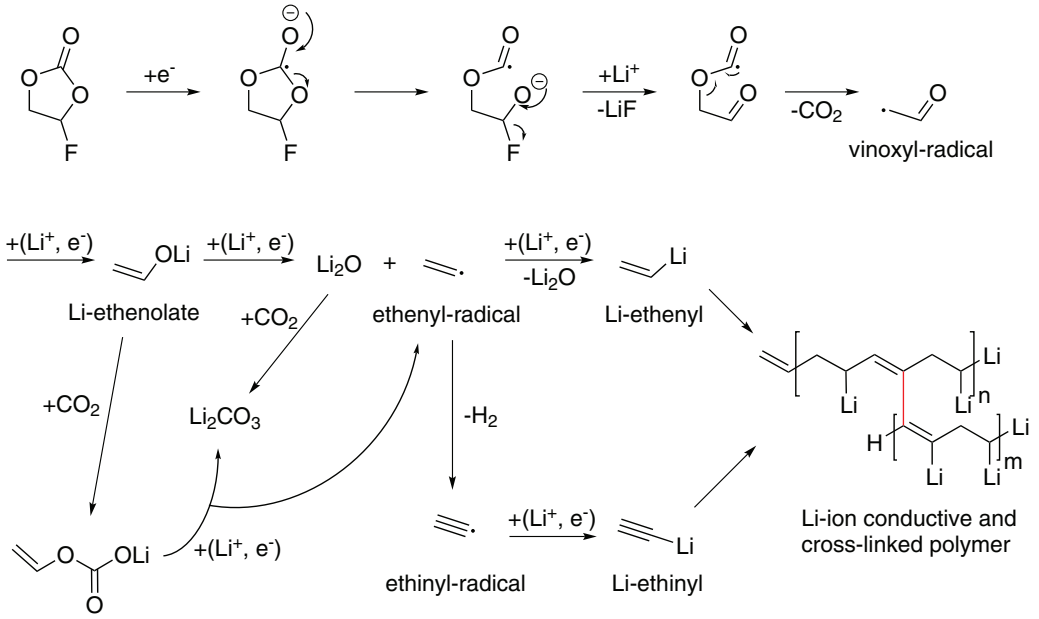

Scheme 2. Proposed mechanism for the reductive decomposition of fluoroethylene carbonate (FEC), with an overall consumption of four electrons per FEC molecule, leading to CO_2, LiF, Li_2O, H_2, Li_2CO_3, and a partially cross-linked polymer.

stable Li_2O, which was found as part of the SEI by XPS measurements of a cycled silicon anode if FEC was present in EC/DEC electrolyte.[36] An alternative 3rd electron transfer step leading to the same ethenyl-radical, is the chemical reaction of lithium-ethenolate with CO_2 to an alkylcarbonate, which can then be reduced to the ethenyl-radical and Li_2CO_3 (see third line in Scheme 2). The latter is reported as SEI component in the literature, but different formation mechanisms were proposed.[30,46] Li_2CO_3 could also be formed by the reaction of Li_2O with CO_2, which might also explain why it was not considered an energetically feasible FEC reduction product in the calculations by Leung et al.[28]

Even though we currently have no experimental evidence for it, we believe that in accordance with the reports by Shkrob et al.[49] and Markevich et al.[46] a cross-linked[49] and oxygen-poor[46] polymer is formed. Therefore we assume that further direct reduction of the reactive ethenyl-radical (4th electron transfer) yields lithium-ethenyl. Alternatively, the ethenyl-radical could first be stabilized by release of hydrogen, yielding an ethinyl-radical, which is then further reduced to lithium-ethinyl. The latter pathway would be consistent with the observation that the CO_2 and the H_2 evolution rate are very similar in the latter stages of the first lithiation cycle (see Fig. 5b).

Both lithium-ethenyl and lithium-ethinyl would likely polymerize, yielding a partially cross-linked polymer, which might be lithium ion conductive due to the weak carbon-lithium bond. This property might give the SEI the desired property of an electron insulating but lithium ion conductive layer, and might explain why the observed impedances in electrolytes with FEC are lower compared to the ones in FEC-free electrolytes after extended cycling;[22,26,36,49] the initially higher impedance with FEC containing electrolytes can be explained by the initially faster SEI formation with FEC.[36] In addition, the cross-linking renders the polymer elastomeric, which might enable it to better withstand the stresses caused by the volumetric expansion/contraction of silicon particles during lithiation/delithiation, reducing the extent of SEI rupture.

Implications for commercial silicon cells.—From the above analysis, it is clear that FEC is able to extend the cycle-life of silicon anodes until it is consumed, so that the cumulative irreversible capacity until the rapid capacity drop occurs is simply related to the specific amount of FEC, described by the added $\mu mol_{FEC}/mg_{electrode}$. In the following, we will replace the cumulative irreversible capacity by the number of cycles until the rapid capacity drop to give a rough estimate on how long FEC can stabilize the performance in commercial cells with realistic electrolyte/active material ratios. Note that the transformation from the universally applicable cumulative irreversible capacity to the number of cycles in this calculation is only valid for the silicon electrodes and cycling conditions used in this work, as other systems with different silicon morphology, particle size, or less volume expansion achieved by limiting the silicon capacity will definitely influence the irreversible capacity loss per cycle. Figs. 1 and 2 show that the rapid capacity drop is not observed within 450 charge/discharge cycles for $20\%_{wt}$ FEC and 75 µL of electrolyte ($\equiv 43.5\ \mu mol_{FEC}/mg_{electrode}$; see green line in Fig. 1) and for $\geq 10\%_{wt}$ FEC and 150 µL of electrolyte (i.e., for $\geq 56.1\ \mu mol_{FEC}/mg_{electrode}$; see magenta line in Fig. 2). This is consistent with the literature, which shows that the use of FEC as co-solvent (typically $\geq 10\%_{wt}$ FEC) strongly stabilizes the cycle-life of silicon anodes.[22,25,46] The cycle number of the Si-Li cells at which the rapid capacity drop occurs is depicted by the black symbols in Fig. 7 (data from Figs. 1 and 2). Since the cumulative irreversible capacity at the rapid capacity drop, Q_{irr}^{drop}, is the intrinsic physical-chemical parameter that correlates with N_{FEC} (see Fig. 6), the correlation between cycle number at the rapid capacity drop with N_{FEC} is less stringent due to the fact that the coulombic efficiencies of the different cells are not perfectly identical. Nevertheless, the x-axis intercept of the linear regression line in Fig. 7 (black line) which represents the consumption of FEC during the first cycle ($3.3\ \mu mol_{FEC}/mg_{electrode}$), is reasonably close to the more precise value obtained in Fig. 6 ($4.1\ \mu mol_{FEC}/mg_{electrode}$). Therefore, while not being exactly correct, the black regression line in Fig. 7 can provide a rough estimate for the numbers of cycles until the rapid capacity drop will occur for a given specific amount of FEC in Si-Li cells. To be more generally applicable to any type of silicon anode, the specific amount of FEC should be referenced to the mass of silicon (N_{FEC}^{Si} in $\mu mol_{FEC}/mg_{Si}$), as was explained in the discussion of Fig. 6.

Since we found that 50% of the FEC in Si-Li cells is consumed at the lithium electrode, the correlation between the number of cycles until the rapid capacity drop and N_{FEC}^{Si} must be corrected for this effect in the case of Si full-cells. This is given by the red line in Fig. 7, where it is assumed that the potential of the Si full-cell cathode is sufficiently low to not oxidize FEC (i.e., the x-axis intercept is half of its value for the black line and the slope is doubled). In analogy, also the model obtained in Fig. 6 can be modified analogously to

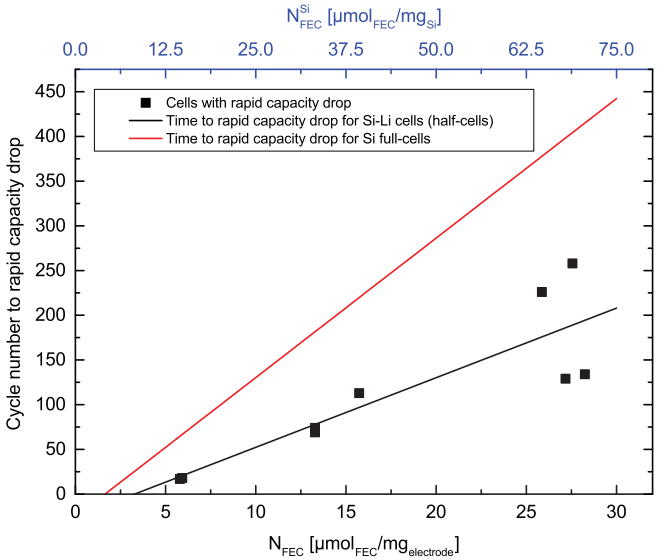

Figure 7. Cycle number at which the rapid capacity drop is observed or expected vs. specific amount of FEC in the cell (N_{FEC}) based on the data in Figs. 1 and 2 and on the Si-Li #3 cell in Fig. 3. The black line is a least-squares regression line through the data obtained for these 9 cells: cycle#$_{drop}$ = 7.8 ($\mu mol_{FEC}/mg_{electrode}$)$^{-1}$ × N_{FEC} – 25.5, with an x-axis intercept of 3.3 $\mu mol_{FEC}/mg_{electrode}$. The red line is the predicted cycle life for Si full-cells with cathodes at sufficiently low potential to not oxidize FEC: cycle#$_{drop}$ = 15.6 ($\mu mol_{FEC}/mg_{electrode}$)$^{-1}$ × N_{FEC} – 25.7, with an x-axis intercept of 1.65 $\mu mol_{FEC}/mg_{electrode}$. The top x-axis displays the amount of FEC normalized to the mass of silicon.

account for Si full-cells. In other words, by simply summing up the irreversible capacities, one can predict how much FEC is left in the cell and at which value of the cumulative irreversible capacity it will be entirely consumed.

With regards to the expected impact of FEC co-solvent in real batteries, one has to consider the fact that the amount of electrolyte used in coin cell testing typically ranges from ≈50–200 µL/cm^2, (e.g., 75 and 150 µL of added electrolyte in Fig. 1 corresponds to 95 and 190 µL/cm^2). On the other hand, the amount of added electrolyte in real batteries is only slightly above the value corresponding to the void volume in the electrodes (≈35%) and the separator (≈50%), which results in an electrolyte/anode/cathode mass fraction of ≈20/25/55 (not counting the current collectors).[50] For a battery with 2 mAh/cm^2 areal capacity using active materials with anode/cathode specific capacities of ≈360/≈150 mAh/g (e.g., graphite/NMC) at an active material content of 90%$_{wt}$, the electrode areal weights (anode and cathode without current collector) would amount to ≈21 mg/cm^2, which would require the addition ≈5 µL/cm^2 of electrolyte (using the above given weight fraction and assuming a density of ≈1 g/cm^3). Thus, the amount of electrolyte volume per area in a real typical battery is ≈10–40 times lower than what is used in typical coin cell testing. Based on these considerations, we can now estimate the $\mu mol_{FEC}/mg_{electrode}$ which would be available in a real battery using 20%$_{wt}$ FEC as co-solvent and assuming that also 5 µL/cm^2 electrolyte (corresponding to ≈9.4 $\mu mol_{FEC}/cm^2$) would be added to a battery with 2 mAh/cm^2 areal capacity. If one were to achieve the theoretical specific capacity of 1440 mAh/$g_{electrode}$ for our 40%$_{wt}$ Si electrodes, the required areal weight of the silicon electrode would be ≈1.4 $mg_{electrode}/cm^2$, resulting in a specific FEC amount of ≈6.8 $\mu mol_{FEC}/mg_{electrode}$. A comparison with Fig. 7 shows, that the specific amount of FEC estimated to be present in a real battery with 20%$_{wt}$ FEC co-solvent would only stabilize the silicon anode performance for roughly 75 cycles (red line in Fig. 7). We believe that this is the explanation for frequently reported long cycle life of cells with silicon anodes and FEC co-solvent if tested in coin cells (>hundreds of cycles),[25,46] while to our knowledge this has never been reported for actual batteries, in which the amount of electrolyte in terms of µL/cm^2 is much smaller.

Conclusions

This work focused on a fundamental understanding of the effect of fluoroethylene carbonate (FEC) on the SEI formation on silicon-carbon composite electrodes. Consistent with the literature, it was found that the cyclability of cells is significantly improved when FEC is used as electrolyte additive. However, these cells experienced a sudden failure with a rapid capacity drop, depending on the specific amount of FEC in the cells (in units of $\mu mol_{FEC}/mg_{electrode}$). It was shown by ^{19}F-NMR spectroscopy that this rapid capacity drop occurs once all of the added FEC has been consumed, at which point the polarization of the silicon-carbon composite electrode increases as evidenced by charge/discharge experiments with a lithium reference electrode. By the use of On-line Electrochemical Mass Spectrometry (OEMS) it was proven that in the presence of FEC the reduction of other electrolyte components is prevented, i.e. FEC gets reduced almost exclusively. Therefore, the cumulative irreversible capacity until the rapid capacity drop is linearly related to the specific amount of FEC (in units of $\mu mol_{FEC}/mg_{electrode}$) in the cell. The quantification of the FEC consumption by ^{19}F-NMR is further proposed as a new method to study the continuous electrolyte reduction during cycling of cells with silicon anodes.

A comparison of the FEC consumption of Si-Li half-cells with that in Li-Li as well as Si-LFP cells revealed that ≈50% of the FEC in Si-Li half-cells is consumed by the Li-electrode. This in turn means that the electrolyte consumption of Si-anodes if cycled between 10 mV and 1.2 V vs. Li/Li$^+$ is identical to that of metallic lithium anodes, and only dependent on the total amount of charge passed in the respective charge/discharge cycles. Finally, based on the correlation between the cumulative irreversible capacity and the specific amount of FEC in the cell it was shown that the reductive decomposition of one FEC molecule consumes four electrons. Additionally, by quantification of the evolved gases in the cell using OEMS it was found that one molecule of CO_2 is released for every molecule of FEC that is reduced. Combining our results with previous findings in literature, a new mechanism for the reductive decomposition of FEC was proposed yielding CO_2, LiF, Li_2O, Li_2CO_3, H_2 and a partially cross-linked polymer.

Acknowledgment

The authors thank BMW for financial support. S. S. and M. M. gratefully acknowledge funding by BASF SE through its electrochemistry and battery research network. We thank Jeff Dahn (University of Dalhousie) for very fruitful discussions. Many thanks also go to Uta Schwenke and Morten Wetjen from our group for helpful advices and great contributions to this work.

Note added in proof.—After submission of our manuscript for review, an article appeared by R. Petibon et al.,[51] who observed the same phenomenon of a rapid capacity drop after the consumption of FEC in 200 mAh pouch cells with $LiCoO_2$ cathodes and Si-alloy/graphite composite anodes. The similarity of their results and ours clearly point out that the continuous electrolyte consumption is a severe problem for silicon-based electrodes and that the electrolyte to active material ratio always has to be considered when Si-electrodes are used.

References

1. M. T. McDowell, S. W. Lee, W. D. Nix, and Y. Cui, *Adv. Mater. (Weinheim, Ger.)*, **25**, 4966 (2013).
2. O. Groeger, H. A. Gasteiger, and J.-P. Suchsland, *J. Electrochem. Soc.*, **162**, A2605 (2015).
3. USABC http://www.uscar.org/guest/article_view.php?articles_id=85, accessed on 02/19/2016.
4. D. Andre, S.-J. Kim, P. Lamp, S. F. Lux, F. Maglia, O. Paschos, and B. Stiaszny, *J. Mater. Chem. A*, **3**, 6709 (2015).

5. U. Kasavajjula, C. Wang, and A. J. Appleby, *J. Power Sources*, **163**, 1003 (2007).
6. L. Lu, X. Han, J. Li, J. Hua, and M. Ouyang, *J. Power Sources*, **226**, 272 (2013).
7. M. N. Obrovac and L. Christensen, *Electrochem. Solid-State Lett.*, **7**, A93 (2004).
8. D. Larcher, S. Beattie, M. Morcrette, K. Edstroem, J.-C. Jumas, and J.-M. Tarascon, *J. Mater. Chem.*, **17**, 3759 (2007).
9. P. Limthongkul, Y.-I. Jang, N. J. Dudney, and Y.-M. Chiang, *Acta Mater.*, **51**, 1103 (2003).
10. W.-J. Zhang, *J. Power Sources*, **196**, 13 (2011).
11. L. Y. Beaulieu, K. W. Eberman, R. L. Turner, L. J. Krause, and J. R. Dahn, *Electrochem. Solid-State Lett.*, **4**, A137 (2001).
12. C. K. Chan, H. Peng, G. Liu, K. McIlwrath, X. F. Zhang, R. A. Huggins, and Y. Cui, *Nat Nano*, **3**, 31 (2008).
13. H. Kim, B. Han, J. Choo, and J. Cho, *Angew. Chem., Int. Ed.*, **47**, 10151 (2008).
14. N. Liu, H. Wu, M. T. McDowell, Y. Yao, C. Wang, and Y. Cui, *Nano Lett.*, **12**, 3315 (2012).
15. R. A. Huggins and W. D. Nix, *Ionics*, **6**, 57 (2000).
16. X. H. Liu, L. Zhong, S. Huang, S. X. Mao, T. Zhu, and J. Y. Huang, *ACS Nano*, **6**, 1522 (2012).
17. A. Magasinski, P. Dixon, B. Hertzberg, A. Kvit, J. Ayala, and G. Yushin, *Nat Mater*, **9**, 353 (2010).
18. K. Evanoff, J. Khan, A. A. Balandin, A. Magasinski, W. J. Ready, T. F. Fuller, and G. Yushin, *Adv. Mater. (Weinheim, Ger.)*, **24**, 533 (2012).
19. H. Li, X. Huang, L. Chen, Z. Wu, and Y. Liang, *Electrochem. Solid-State Lett.*, **2**, 547 (1999).
20. J. Christensen and J. Newman, *J. Electrochem. Soc.*, **151**, A1977 (2004).
21. J. Christensen and J. Newman, *J. Electrochem. Soc.*, **152**, A818 (2005).
22. V. Etacheri, O. Haik, Y. Goffer, G. A. Roberts, I. C. Stefan, R. Fasching, and D. Aurbach, *Langmuir*, **28**, 965 (2012).
23. N.-S. Choi, K. H. Yew, K. Y. Lee, M. Sung, H. Kim, and S.-S. Kim, *J. Power Sources*, **161**, 1254 (2006).
24. E. Markevich, G. Salitra, K. Fridman, R. Sharabi, G. Gershinsky, A. Garsuch, G. Semrau, M. A. Schmidt, and D. Aurbach, *Langmuir*, **30**, 7414 (2014).
25. Y.-M. Lin, K. C. Klavetter, P. R. Abel, N. C. Davy, J. L. Snider, A. Heller, and C. B. Mullins, *Chem. Commun. (Cambridge, U. K.)*, **48**, 7268 (2012).
26. C. Xu, F. Lindgren, B. Philippe, M. Gorgoi, F. Bjoerefors, K. Edstroem, and T. Gustafsson, *Chem. Mater.*, **27**, 2591 (2015).
27. J. M. Martinez de la Hoz and P. B. Balbuena, *Phys. Chem. Chem. Phys.*, **16**, 17091 (2014).
28. K. Leung, S. B. Rempe, M. E. Foster, Y. Ma, J. M. Martinez del la Hoz, N. Sai, and P. B. Balbuena, *J. Electrochem. Soc.*, **161**, A213 (2014).
29. Y. Ma and P. B. Balbuena, *J. Electrochem. Soc.*, **161**, E3097 (2014).
30. H. Nakai, T. Kubota, A. Kita, and A. Kawashima, *J. Electrochem. Soc.*, **158**, A798 (2011).
31. Z. Wang, J. Xu, W.-H. Yao, Y.-W. Yao, and Y. Yang, *ECS Trans.*, **41**, 29 (2012).
32. V. L. Chevrier, L. Liu, D. B. Le, J. Lund, B. Molla, K. Reimer, L. J. Krause, L. D. Jensen, E. Figgemeier, and K. W. Eberman, *J. Electrochem. Soc.*, **161**, A783 (2014).
33. M. Metzger, J. Sicklinger, D. Haering, C. Kavakli, C. Stinner, C. Marino, and H. A. Gasteiger, *J. Electrochem. Soc.*, **162**, A1227 (2015).
34. N. Tsiouvaras, S. Meini, I. Buchberger, and H. A. Gasteiger, *J. Electrochem. Soc.*, **160**, A471 (2013).
35. B. Key, R. Bhattacharyya, M. Morcrette, V. Seznec, J.-M. Tarascon, and C. P. Grey, *J. Am. Chem. Soc.*, **131**, 9239 (2009).
36. K. Schroder, J. Alvarado, T. A. Yersak, J. Li, N. Dudney, L. J. Webb, Y. S. Meng, and K. J. Stevenson, *Chem. Mater.*, **27**, 5531 (2015).
37. S. P. Kuksenko and I. O. Konovalenko, *Russ. J. Appl. Chem.+*, **84**, 1179 (2011).
38. B. Zhang, M. Metzger, S. Solchenbach, M. Payne, S. Meini, H. Gasteiger, A. Garsuch, and B. L. Lucht *J. Phys. Chem. C*, **119**, 11337 (2015).
39. M. Nie, D. Chalasani, D. P. Abraham, Y. Chen, A. Bose, and B. L. J. Lucht *Phys. Chem. C*, **117**, 1257 (2013).
40. D. Aurbach, Y. Gofer, M. Ben-Zion, and P. J. Aped, *Electroanal. Chem.*, **339**, 451 (1992).
41. M. E. Spahr, T. Palladino, H. Wilhelm, A. Wuersig, D. Goers, H. Buqa, M. Holzapfel, and P. J. Novak, *Electrochem. Soc.*, **151**, A1383 (2004).
42. M. Winter and P. J. Novak, *Electrochem. Soc.*, **145**, L27 (1998).
43. M. Metzger, B. Strehle, S. Solchenbach, and H. A. Gasteiger, *J. Electrochem. Soc.*, **163**, A798 (2016).
44. S. F. Lux, I. T. Lucas, E. Pollak, S. Passerini, M. Winter, and R. Kostecki, *Electrochem. Commun.*, **14**, 47 (2012).
45. D. R. Lide, *Tetrahedron*, **17**, 125 (1962).
46. E. Markevich, K. Fridman, R. Sharabi, R. Elazari, G. Salitra, H. E. Gottlieb, G. Gershinsky, A. Garsuch, G. Semrau, M. A. Schmidt, and D. J. Aurbach, *Electrochem. Soc.*, **160**, A1824 (2013).
47. X. Chen, X. Li, D. Mei, J. Feng, M. Y. Hu, J. Hu, M. Engelhard, J. Zheng, W. Xu, J. Xiao, J. Liu, and J.-G. Zhang, *ChemSusChem*, **7**, 549 (2014).
48. M. Nie, D. P. Abraham, Y. Chen, A. Bose, and B. L. J. Lucht, *Phys. Chem. C*, **117**, 13403 (2013).
49. I. A. Shkrob, J. F. Wishart, and D. P. Abraham, *J. Phys. Chem. C*, **119**, 14954 (2015).
50. F. T. Wagner, B. Lakshmanan, and M. F. J. Mathias, *Phys. Chem. Lett.*, **1**, 2204 (2010).
51. R. Petibon, V. L. Chevrier, C. P. Aiken, D. S. Hall, S. R. Hyatt, R. Shunmugasundaram, and J. R. Dahn, *J. Electrochem. Soc.*, **163**, A1146 (2016).

3.3.2 Differentiating the Degradation Phenomena in Silicon-Graphite Electrodes for Lithium-Ion Batteries

In this section the article "Differentiating the Degradation Phenomena in Silicon-Graphite Electrodes for Lithium-Ion Batteries" will be presented, which was published in the *Journal of the Electrochemical Society* on September 19, 2017 as open access article distributed under the terms of the Creative Commons Attribution 4.0 License.[29] The research work was primarily conducted by Morten Wetjen, who is also the first author of the publication. The content of the paper was presented on international conferences, e.g., at the 230th Meeting of The Electrochemical Society (October 2 – 7, 2016) in Honolulu, USA (Abstract Number: #280). The permanent web-link to the publication is http://jes.ecsdl.org/content/164/12/A2840 and the DOI is 10.1149/2.1921712jes.

In this publication we investigate the aging phenomena of silicon-graphite composite electrodes with different silicon to graphite ratios cycled versus capacitively oversized LFP. In particular, silicon:graphite ratios of 60:10, 50:25, 35:45, and 20:65 are used. We show that for all electrode compositions we can distinguish between two distinct aging mechanisms, namely based on silicon particle degradation and on the structural degradation of the electrode. The former is characterized by an initially steep sigmoidal increase of the cumulative irreversible capacity over the cycle number as well as a dip in the coulombic efficiency. It is caused by a roughening of the silicon particles and the formation of a nanoporous, sponge-like structure of the silicon particles, yielding significant SEI growth. After ~45 cycles, the accumulated irreversible capacity gain levels off, indicating that the silicon particle morphology does not change significantly anymore. The thus obtained lower slope in the cumulative irreversible capacity versus cycle number plot is caused by a continuous electrolyte consumption due to SEI cracking and repair as a consequence of the steady volume changes of the silicon particles during lithiation and delithiation. When the cumulative irreversible capacity is normalized to the mass of the silicon in the electrode, the curves for all four compositions essentially overlay, showing that the silicon particle degradation is independent of the silicon to graphite ratio. Analogously, we show that the FEC consumption is only dependent on the transferred amount of charge and discharge capacity, and is therefore independent of the silicon to graphite ratio. This demonstrates that the FEC consumption is basically independent of the amount of graphite, supporting the conclusion from the work in section 3.3.1 according to which all irreversible capacity can be ascribed to the reduction of FEC. In contrast to the silicon particle degradation, the electrode

degradation mechanism is characterized by an initially distinct capacity fading which occurs at lower cycle numbers and becomes more severe with increasing silicon content. Simultaneously, the electrode degradation causes a higher resistance during delithiation, leading to a larger capacity share during the CV-step. This is rationalized by the different microstructure of the electrodes with different silicon to graphite ratio. While in the electrodes with low silicon content the graphite particles form a conductive backbone within the electrode structure, this does not exist in the high silicon content electrodes, resulting in a hindered electronic pathway due to a lower number of silicon/graphite contacts. Upon the surface roughening of the silicon particles, this causes the partial loss of electrode integrity, leading to higher electrode resistance.

Author Contributions

Morten Wetjen designed the experiments, prepared the electrodes, and performed the cycling experiments. Roland Jung and Morten Wetjen performed the ^{19}F-NMR experiments and worked on the FEC consumption analysis. Reza Ghadimi measured the SEM micrographs. Morten Wetjen and Hubert Gasteiger wrote the manuscript. All authors discussed the results and commented on the manuscript.

Differentiating the Degradation Phenomena in Silicon-Graphite Electrodes for Lithium-Ion Batteries

Morten Wetjen,[a,*,z] Daniel Pritzl,[a,*] Roland Jung,[a,*] Sophie Solchenbach,[a,*] Reza Ghadimi,[b] and Hubert A. Gasteiger[a,]**

[a] *Chair of Technical Electrochemistry, Department of Chemistry and Catalysis Research Center, Technical University of Munich, D-85748 Garching, Germany*
[b] *JEOL (Germany) GmbH, D-85356 Freising, Germany*

Silicon-graphite electrodes usually experience an increase in cycling performance by the addition of graphite, however, the relation of the silicon/graphite ratio and the aging mechanisms of the individual electrode and electrolyte compounds still requires a more fundamental understanding. In this study, we present a comprehensive approach to understand and quantify the degradation phenomena in silicon-graphite electrodes with silicon contents between 20-60 wt%. By evaluating the cycling performance and total irreversible capacity of silicon-graphite electrodes vs. capacitively oversized $LiFePO_4$ electrodes in presence of a fluoroethylene carbonate (FEC)-containing electrolyte, we demonstrate that the aging of silicon-based electrodes can be distinguished into two distinct phenomena, which we describe as silicon particle degradation and electrode degradation. Cross-sectional scanning electron microscopy (SEM) images and a detailed analysis of the electrode polarization upon cycling complement our discussion. Further, we deploy post-mortem ^{19}F-NMR spectroscopy to (i) quantify to loss of moles of FEC in the electrolyte and correlate this with the amount of charge that was exchanged by the silicon-graphite electrodes, (ii) estimate the pore volume of the silicon-graphite electrodes that is occupied by FEC decomposition products, and (iii) derive implications for the relation of the electrolyte volume and cycle life of commercial silicon-based Li-ion batteries.

Manuscript submitted June 26, 2017; revised manuscript received September 5, 2017. Published September 19, 2017. This was Paper 280 presented at the Honolulu, Hawaii, Meeting of the Society, October 2–7, 2016.

Silicon-based electrodes are very promising candidates to enable the next generation of Li-ion batteries with energy densities on the cell level beyond 350 Wh kg^{-1}.[1,2] In contrast to conventional intercalation anode materials, such as graphite (LiC_6, 372 mAh g^{-1}, 890 Ah L^{-1}), the specific capacity of silicon alloy electrodes is significantly higher ($Li_{15}Si_4$, 3579 mAh g^{-1}, 2194 Ah L^{-1}).[3] Nonetheless, commercialization of silicon-based electrodes is still hampered because of two major challenges:[4]

(i) Large volume expansions up to 280% upon repeated (de-)lithiation of silicon particles deteriorate the electrode integrity, thus causing isolation of active material.[5–7] The formerly reported pulverization of micron-sized silicon particles due to mechanical stress upon repeated volume expansion has been partially solved by using nanometer-sized particles. However, reduction of the silicon particle size also leads to inferior electronic conduction due to more numerous interparticle contacts, and higher solid-electrolyte-interphase (SEI) losses due to the larger relative surface area.[8–10]

(ii) Continuous side reactions at the silicon/electrolyte interface caused by repeated volume expansion and contraction result in ongoing electrolyte decomposition and in a gradual loss of active lithium.[8] In the course of this, SEI-forming additives in the electrolyte, e.g., FEC, are depleted, which was shown to result in a significant increase in cell polarization and a concomitant rapid capacity drop.[8,11]

Various strategies have been proposed to overcome the detrimental effects associated with the volume expansion during (de-)lithiation of silicon and to reduce concomitant irreversible capacity losses, including preparation of silicon thin-films with a significantly reduced silicon/electrolyte interface,[6,12–14] Si-Al-Fe active/inactive alloy electrodes that reduce the volume expansion of the active phase,[5,15,16] and design of nanostructured silicon materials with carbonaceous compounds, such as graphite, to improve the electrical conductivity within the electrode and to better accommodate the volume expansion of silicon.[17–20] Although the surface area per capacity usually increases for nanostructured silicon materials with decreasing diameter,[21] which leads to a higher first cycle irreversible capacity loss, silicon nanowires offer the advantage of a smaller relative surface area change upon (de-)lithiation and in addition usually reveal less morphological changes, due to a reduced mechanical stress within the materials.[22] Therefore, irreversible capacity losses upon cycling are expected to be lower compared to conventional nanoparticles.

Further studies on the degradation mechanisms of silicon-based electrodes were performed with respect to the actual conditions in commercial Li-ion batteries. While some research groups, including those from Obrovac,[15] Guyomard,[23,24] and Abraham,[25–27] already reported studies on full-cell configurations, the majority of the academic literature still refers to half-cell measurements, using lithium metal counter electrodes and an excess of electrolyte. However, side reactions at the lithium metal/electrolyte interface and the usually 10 times larger amount of electrolyte (i.e. >50 µL cm^{-2} instead of 5 µL cm^{-2} in commercial cells)[11] make it difficult to evaluate the degradation phenomena occurring at the silicon-based electrode, including the loss of active lithium and depletion of the electrolyte.[28–30]

In this study, we present a comprehensive approach to understand the degradation mechanisms in silicon-graphite electrodes. Hence, we prepare silicon-graphite electrodes with practical areal capacities between 1.8 and 2.3 mAh cm^{-2}, composed of physical mixtures of different silicon/graphite active material ratios, with silicon contents between 20–60 wt%.[31] By use of cyclic voltammetry, we investigate the electrochemical (de-)lithiation of silicon and graphite as a function of the active material ratio. To evaluate the electrode degradation upon cycling, we introduce pseudo-full cells, comprising silicon-graphite negative electrodes and capacitively oversized $LiFePO_4$ positive electrodes. This cell configuration offers several advantages over practical full-cells, namely: (i) a stable reference potential of 3.45 V vs. Li/Li$^+$ to monitor the silicon-graphite potential in a two-electrode coin-cell configuration, and (ii) to provide a defined lithium reservoir, which allows to investigate exclusively the degradation of the silicon-graphite electrode without an additional capacity loss due to the depletion of cyclable lithium. While these conditions would also be satisfied by a lithium metal electrode, the third reason is (iii) to minimize side reactions of the electrolyte at the positive electrode (here: $LiFePO_4$), which would alter the electrolyte (and FEC) decomposition and thus influence its quantification. As electrolyte we use 1 M $LiPF_6$ in EC:EMC (LP57) with 5 wt% of the widely used fluoroethylene carbonate (FEC) as additive, which is known to significantly improve the cycling stability of the silicon-graphite

*Electrochemical Society Student Member.
**Electrochemical Society Fellow.
[z]E-mail: morten.wetjen@tum.de

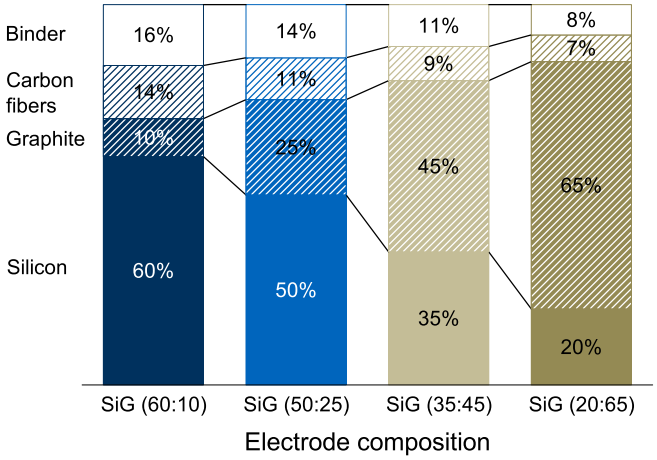

Scheme 1. Silicon-graphite electrode compositions (in wt%) that were investigated in this study.

electrode.[32] We also added a comparably large amount of electrolyte to the coin cells (130 µL or 84 µL cm^{-2}; ~15 times larger compared to large-scale cells), because it allows for a more precise quantification of the FEC consumption via ^{19}F-NMR.[11] From the analysis of the differential capacity curves and the electrode polarization upon cycling, we deconvolute the different degradation mechanisms arising from silicon-graphite electrodes. In addition, we evaluate the consumption of FEC as primary source for electrolyte decomposition through ^{19}F-NMR analysis of the electrolyte harvested from coin-cells after 120 cycles. Finally, we discuss the implications of these results on commercial Li-ion batteries with silicon-based electrodes by estimating the volume of the electrolyte decomposition products and forecasting cycle lifetimes, taking into account practical electrolyte amounts.

Experimental

Electrode preparation.—Silicon-graphite (SiG) electrodes, consisting of silicon nanoparticles (~200 nm, silicon, Wacker Chemie AG, Germany) and graphite (~20 µm, T311, SGL Carbon GmbH, Germany), were prepared through an aqueous ink procedure. Hence, silicon and graphite were thoroughly mixed with vapor grown carbon fibers (VCGF-H, Showa Denko, Japan) and lithium poly(acrylate) (LiPAA, MW = 250,000 g mol^{-1}, Sigma-Aldrich, Germany) in a planetary ball mill (Pulverisette 7, Fritsch, Germany) with ZrO_2 balls (10 mm diameter) under stepwise addition of 18 MΩ cm Milli-Pore water (final solid content ~30 wt%). The resulting ink was cast onto Cu-foil (thickness 25 µm, Goodfellow, USA), using a gap bar coater (RK PrintCoat Instruments, UK). Electrode discs of 14 mm in diameter were punched out and were subsequently dried in a Büchi oven for at least 12 h at 100°C, before being transferred into an Ar atmosphere MBraun glove box (H_2O and O_2 concentration <0.1 ppm) without exposure to air. The areal capacity of the resulting SiG electrodes ranged from 1.8 to 2.3 mAh cm^{-2}, which corresponds to a silicon-graphite active material loading of 0.71–1.84 mg_{SiG} cm^{-2}, depending on the active material ratio.

Scheme 1 summarizes the electrode compositions that were investigated in this study. As one can see, the weight contribution of the active materials (silicon and graphite) accounted for 70–85 wt% of the total electrode mass. Herein, the fraction of silicon was stepwise decreased from 60 to 20 wt%, while the fraction of graphite was simultaneously increased from 10 to 65 wt%. To accomplish adequate electrode integrity and to maintain sufficient electrical conductivity upon cycling, the amount of conductive additive and binder were adjusted to the amount of silicon in the electrode. In accordance with Marks et al.,[33] we adjusted the binder coverage to ~6.3 mg m_{BET}^{-2} in all compositions, considering a BET surface area of ~40 m^2 g^{-1} for silicon in the delithiated state, ~5 m^2 g^{-1} for graphite, and ~13 m^2 g^{-1} for the carbon fibers. During the optimization of the electrode compositions, we explored different binder and conductive carbon contents that affected the integrity and cycling stability of the electrodes to a certain extent; yet they did not impact the relation of the FEC consumption and the exchanged capacity, as will be explained in detail in the Discussion section. As the theoretical electrode capacities ranged from 960 to 2,200 mAh g^{-1}_{el} (taking theoretical active material capacities of 372 mAh g^{-1}_{C} and 3579 mAh g^{-1}_{Si}),[21] the electrode coating thicknesses were adjusted to 15-31 µm (measured by Mitutoyo *Litematic VL-50*, Japan), thus providing a consistent areal capacity of 1.8–2.3 mAh cm^{-2}.

Electrolyte and test cell assembly.—Electrochemical characterization was performed in coin-cells (CR2032, Hohsen, Japan) that were assembled in an Ar-filled glove box (MBraun, Germany) by sandwiching two porous glass fiber separators (Ø 16 mm, thickness 250 µm, VWR, USA) soaked with 130 µL electrolyte solution (i.e., 84 µL cm^{-2}) between a silicon-graphite electrode (Ø 14 mm, 1.8–2.3 mAh cm^{-2}) and either a lithium metal electrode (Ø 15 mm, 450 µm thickness, Rockwood Lithium, USA) for cyclic voltammetry or a capacitively oversized $LiFePO_4$ (LFP) electrode (Ø 15 mm, 3.5 mAh cm^{-2}, Custom cells, Germany) for cell cycling. As electrolyte solution, 1 M $LiPF_6$ dissolved in a mixture of ethylene carbonate (EC) and ethyl methyl carbonate (EMC) (3:7 w:w; LP57, BASF, Germany) and 5 wt% of fluoroethylene carbonate (FEC, BASF, Germany) was used.

Electrode morphology.—The morphology of the pristine silicon-graphite electrodes was investigated by scanning electron microscopy (SEM). First, electrode cross-sections were prepared by Argon ion beam polishing, using a JEOL Cross Section Polisher IB-09010CP (JEOL, Japan). Afterwards, SEM images were measured by use of a JEOL JSM-7800F PRIME (JEOL, Japan) with a field-emission electron source and a secondary electron detector.

Cyclic voltammetry.—The electrochemical (de-)lithiation of the SiG electrodes was characterized by cyclic voltammetry in a Li//SiG coin-cell setup. Alternating linear potentiodynamic sweeps with a scan rate of 25 µV s^{-1} were applied, forcing the cell potential from open circuit potential (typically ~2.6 V vs. Li/Li^+) to 0.01 V vs. Li/Li^+ (lower vertex potential) and then back to 1.5 V vs. Li/Li^+ (upper vertex potential). All measurements were performed in a climate chamber (Binder, Germany) at 25°C (±0.5°C), using a multi-channel potentiostat VMP3 (BioLogic, France).

Cell cycling.—Electrode polarization and cycling performance of SiG electrodes were investigated through galvanostatic cycling of SiG//$LiFePO_4$ coin-cells. Initially, a formation cycle between 0.01 and 1.25 V vs. Li/Li^+ (corresponding to 3.44 and 2.2 V cell voltage) was applied to all cells using a C-rate of 0.05 h^{-1} (~0.1 mA cm^{-2}). Two constant voltage (CV) steps were performed at the end of SiG lithiation/delithation (i.e., at 0.01/1.25 V vs. Li/Li^+) with a current limit of 0.02 h^{-1}. For the subsequent cycles, the C-rate was increased to 0.5 h^{-1} (~1.0 mA cm^{-2}). All measurements were performed in a climate chamber (Binder, Germany) at 25°C (±0.5°C), using a battery cycler (Series 4000, Maccor, USA).

Electrolyte consumption.—Consumption of fluoroethylene carbonate (FEC) during galvanostatic cycling was investigated by ^{19}F-NMR spectra which were obtained post-mortem from the electrolyte solutions. For this, SiG//$LiFePO_4$ coin-cells were disassembled after 120 cycles and the glass fiber separators were subsequently dipped into deuterated dimethyl sulfoxide (DMSO-d6, anhydrous, Sigma-Aldrich, USA). The resulting solutions were then filled into air-tight NMR tubes and ^{19}F-NMR spectra were measured using a Bruker Ascend 400 (400 MHz). As described by Jung et al., the resulting ^{19}F-NMR spectra show only peaks that can either be ascribed to PF_6^- or FEC, i.e., no additional peaks from $PO_2F_2^-$ or PO_3F^{2-} can be observed that originate from salt decomposition or separator

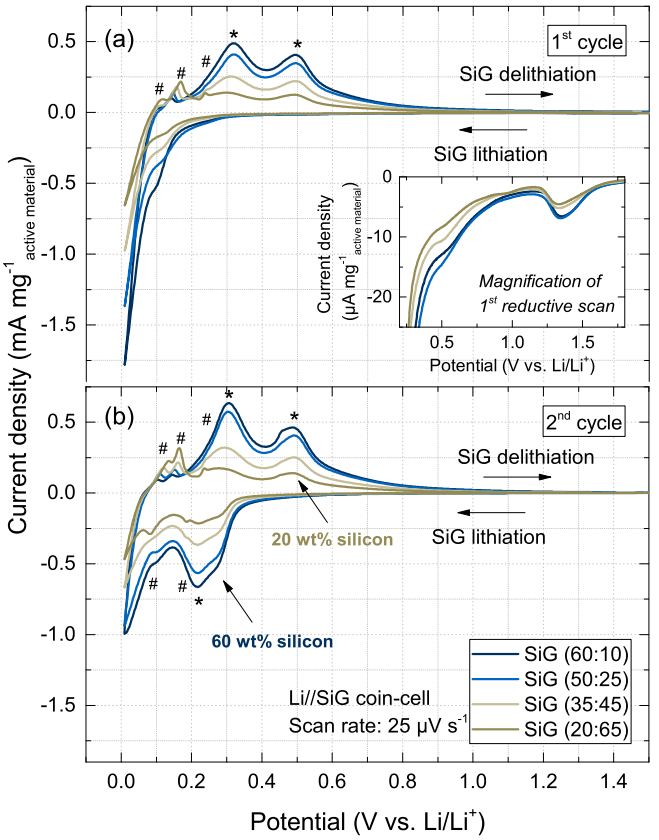

Figure 1. Cyclic voltammetry responses of the first (panel a) and the second cycle (panel b) of Li//SiG coin-cells, incorporating silicon-graphite electrodes with different active material ratios. Characteristic features are labelled either by star (silicon) or hash (graphite). Electrolyte: 130 μL LP57 with 5 wt% FEC, scan rate: 25 μV s^{-1}, vertex potentials: 0.01 and 1.5 V, electrode area: 1.54 cm^2, areal capacities ranged from 1.8 to 2.3 mAh cm^{-2}, temperature: 25°C.

decomposition by HF.[11,34] As a result, the concentration of PF_6^- in the electrolyte solution shows no quantitative changes upon cycling and can thus be defined as an internal standard. For that reason, changes in the ratio of PF_6^- peak integrals to FEC peak integrals allow to monitor the consumption of FEC after a selected number of cycles. A previous work from our group,[11] which deployed this method provided the same four-electron mechanism for the reduction of FEC as an independently conducted analysis via gas chromatography coupled with mass spectrometry (GC-MS) by Petibon et al.[35]

Results

Electrode characterization.—Table I summarizes the properties of the silicon-graphite electrodes that were investigated in this study. Based on measured areal loadings of the electrode coatings, the known electrode composition, and the measured electrode thicknesses, the calculated electrode densities of all electrodes range between ~0.6–0.7 g cm^{-3}_{el}, corresponding to electrode porosities ranging in between ~67–73%, were obtained for all compositions. We ascribe this characteristic to a combination of the similar bulk densities of silicon (~2.3 g cm^{-3}) and graphite (~2.2 g cm^{-3}) and of the large and well dispersed carbon fibers (diameter: 150 nm, length: 10–20 μm) that create a substantial amount of void spaces.

The electrochemical (de-)lithiation of the silicon-graphite electrodes was investigated by cyclic voltammetry. Figure 1 shows the current responses of (a) the first and (b) the second cycle obtained from the different SiG electrode compositions. While the lithiation features of silicon and graphite are largely superimposed during the first reductive scan at potentials below 0.18 V vs. Li/Li^+, the oxidative scan clearly reveals two characteristic delithiation peaks of silicon at 0.31 and 0.50 V vs. Li/Li^+,[36] as well as three delithiation peaks of graphite at 0.11, 0.16, and 0.24 V vs. Li/Li^+, which correspond to the voltage plateaus of lithium-graphite intercalation compounds LiC_x.[37] The silicon features appear more pronounced in the 60 wt% and 50 wt% silicon electrodes (blue curves), whereas the graphite peak currents decrease, according to the lower graphite content in these electrodes. As expected, the lithiation behavior of silicon changes between the first and second cycle (see Figure 1b). Once the silicon has become amorphous after the first reductive scan, lithiation in subsequent scans starts at more positive potentials of about 0.21 V and continues below 0.11 V vs. Li/Li^+. In agreement with Fuchsbichler et al.,[17] graphite is lithiated (<0.19 V vs. Li/Li^+) and delithiated (<0.24 V vs. Li/Li^+) step-wise at slightly more negative potentials compared to silicon.

The inset in Figure 1a shows a magnification of the first reductive scan. The feature at about 1.3 V vs. Li/Li^+ can be assigned to the reductive decomposition of FEC.[38] As it was reported earlier in the literature, FEC is reduced at more positive potentials than EC and EMC, thereby forming an SEI layer on the active material particles, which significantly reduces further electrolyte decomposition.[39–41]

Cycling performance in SiG//LFP cells.—The cycling performance of the silicon-graphite electrodes (1.8–2.3 mAh cm^{-2}) was investigated vs. capacitively oversized $LiFePO_4$ electrodes (~3.5 mAh cm^{-2}). To fully utilize the theoretical specific capacity of the different silicon-graphite electrodes, the cutoff potentials were set to 0.01 V vs. Li/Li^+ during lithiation (3.44 V cell voltage) and 1.25 V vs. Li/Li^+ during delithiation (2.2 V cell voltage). In addition, constant voltage steps were applied at the end of lithiation and delithiation. Figure 2 shows (a) the coulombic efficiency (in %) and (b) the gravimetric delithiation capacities normalized to the entire electrode mass (in mAh g^{-1}_{el}) as a function of the cycle number. Table I summarizes relevant data of the first cycle and the capacity retention upon

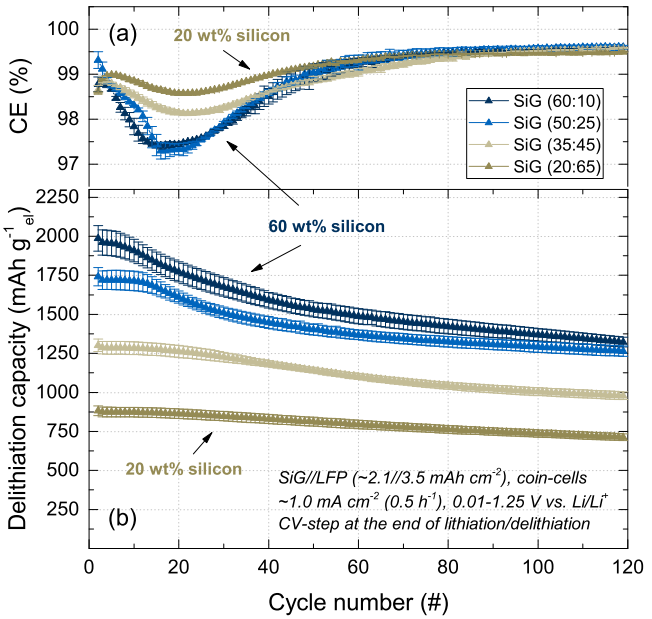

Figure 2. Galvanostatic cycling of SiG//LFP coin-cells, with different silicon-graphite electrode compositions. Areal capacities: SiG (1.8-2.3 mAh cm^{-2}), LFP (~3.5 mAh cm^{-2}), electrolyte: 130 μL LP57 with 5 wt% FEC, applied currents: ~0.1 mA cm^{-2} (0.05 h^{-1}) during formation cycle and ~1.0 mA cm^{-2} (0.5 h^{-1}) during consecutive cycles, SiG electrode cutoff potentials of 0.01 and 1.25 V vs. Li/Li^+, constant voltage steps at 0.01/1.25 V vs. Li/Li^+ at the end of (de-)lithiation with a current limit of 0.02 h^{-1}. Panel (a): Coulombic efficiency obtained from the ratio of delithiation/ lithiation capacity, and panel (b): Delithiation capacity in mAh g^{-1}_{el} per silicon-graphite electrode. The error bars represent the standard deviation of at least two independent repeat measurements.

Table I. Properties of the silicon-graphite electrodes that were investigated in this study. Selected data from the first galvanostatic cycle at 0.05 h^{-1} between 0.01 and 1.25 V vs. Li/Li^+ and from ^{19}F-NMR FEC consumption measurements after 120 cycles. The ± values represent the standard deviation of at least two independent repeat measurements.

		Electrode composition			
Electrode properties	Units	SiG (60:10)	SiG (50:25)	SiG (35:45)	SiG (20:65)
Theoretical electrode capacity	mAh g^{-1}_{el}	2,185	1,883	1,420	958
Capacity contribution from silicon	%	98.3	95.1	88.2	74.7
Areal capacity	mAh cm^{-2}	2.3 ± 0.2	1.8 ± 0.2	1.8 ± 0.2	2.1 ± 0.2
Electrode mass loading	mg cm^{-2}	1.06	0.94	1.30	2.17
Active material loading	mg_{SiG} cm^{-2}	0.74	0.71	1.04	1.84
Electrode thickness	µm	15 ± 2	16 ± 2	21 ± 2	31 ± 2
Electrode density	g cm^{-3}_{el}	0.71	0.59	0.62	0.70
Electrode porosity	%	67	73	72	68
Electrode BET area (delithiated)	m^2_{BET} g^{-1}	26	23	17	12
Binder coverage	mg m^{-2}_{BET}	6.1	6.2	6.3	6.6
1st cycle coulombic efficiency	%	87.6 ± 0.8	86.1 ± 0.7	86.3 ± 0.5	87.1 ± 0.5
1st cycle irreversible capacity	mAh_{irr} g^{-1}_{el}	272	272	201	128
1st cycle delithiation capacity	mAh g^{-1}_{el}	1,933	1,685	1,265	860
Capacity retention in cycle 120	mAh g^{-1}_{el}	1,323	1,264	979	713
Capacity retention cycle 3–120	%	67	74	76	82
cycle # at 80% capacity retention	#	44	58	87	>120
Total irreversible capacity after 120 cycles	Ah_{irr} g^{-1}_{el}	2.47	2.17	1.62	0.93
	mAh_{irr} cm^{-2}	2.62	2.04	2.11	2.02
Capacity per FEC after 120 cycles	mAh_{tot} µmol^{-1}	11.5	12.9	14.5	15.7
	$mAh_{tot, Si}$ µmol^{-1}	11.3	12.2	12.8	11.7
FEC per irreversible capacity after 120 cycles	µmol mAh^{-1}_{irr}	13.0	12.3	11.5	13.1

cycling. As can be seen from Figure 2b, the different electrode compositions demonstrate delithiation capacities between 860 mAh g^{-1}_{el} (20 wt% silicon, dark brown curve) and 1,930 mAh g^{-1}_{el} (60 wt% silicon, dark blue curve) during the first cycle (see also Table I). Interestingly, all electrodes indicate a very similar first cycle capacity utilization and coulombic efficiency, both in the range of ∼85–88%, independent of the electrode composition (i.e., all electrodes reveal a similar areal irreversible capacity loss of 0.28 ± 0.02 mAh cm^{-2} in the first cycle). These first cycle coulombic efficiencies of the SiG electrodes are very similar as for the silicon electrodes without graphite but using the same silicon particles (40 wt% silicon, 20 wt% VGCF, 20 wt% LiPAA) with 85–86% (data not shown), and are only slightly lower compared to the ∼92% for pure graphite electrodes (95 wt% graphite, 5 wt% PVdF). We explain this behavior by the similar BET surface area per capacity of both active materials (11–13 m^2_{BET} Ah^{-1}) in the delithiated state, suggesting that the initial SEI formation process is similar at silicon and graphite. As the irreversible capacity loss of the first cycle, which is commonly associated with SEI formation, is proportional to the BET surface area of the active material, the amount of SEI loss per delivered capacity, and thus the coulombic efficiency, must consequently be the similar for all compositions.[42] Thus, contrary to common perception, the first cycle coulombic efficiencies of silicon and graphite are actually quite similar in this case. As a corollary, for silicon particles with a lower BET area (i.e., with a lower m^2_{BET} Ah^{-1} value), one would expect them to exhibit equal or even superior coulombic efficiency compared to graphite, as the first-cycle coulombic efficiency seems to scale with m^2_{BET} Ah^{-1} value. Consistent with this assumption, Yoon et al. recently reported a coulombic efficiency of ∼91.5% for silicon particles with a diameter of 700 nm, which is higher than that of graphite.[30]

Within the first 60 cycles, all electrodes reveal a distinct capacity decay (see Figure 2b), which occurs earlier and increases in extent with increasing silicon content. Here we would like to note that this loss of reversible capacity is not related to the depletion of FEC as described by Jung et al.,[11] because our ^{19}F-NMR analysis after 120 cycles revealed a residual FEC concentration of at least ∼1.2 wt% in the electrolyte (originally 5 wt%). The cycling stability notably improves after the initial capacity decays, leading to similar capacity fading rates for all compositions. The resulting capacity retentions between the 3rd (i.e., after formation) and the 120th cycle at 0.5 h^{-1} lie between 67% for the 60 wt% silicon electrode and 82% for the 20 wt% silicon electrode (see Table I), meaning that the silicon/graphite ratio displays a trade-off between the initial delithation capacity and subsequent cycling stability. In addition, all electrode compositions show a minimum in the coulombic efficiency around the 20th cycle (see Figure 2a), followed by a gradual increase to values above 99.5%. Like the capacity decay, the minimum coulombic efficiency value at ∼20 cycles decreases with increasing silicon content. At this point we would like to note that the capacity fade in Figure 2b is not related to a depletion of active lithium, i.e. the capacity of the LFP positive electrode after 120 cycles is still large enough to avoid a limitation in cyclable lithium. The same cycling behavior was also obtained in preliminary experiments in half-cells vs. lithium metal.[31]

Irreversible capacity loss upon cycling.—To understand the irreversible processes taking place in the silicon-graphite electrodes at different stages of cycle life, the total irreversible capacity $\sum Q_{irr}$ as a function of the cycle number is shown in Figure 3. Here, $\sum Q_{irr}$ was calculated as described by Equation 1, with $Q_i^{lithiation}$ and $Q_i^{delithiation}$ being the specific lithiation and delithiation capacities in Ah_{irr} g^{-1}_{el}, while the index *i* stands for the respective cycle number.

$$\sum Q_{irr} = \sum_{i}^{120} \left(Q_i^{lithiation} - Q_i^{delithiation} \right) \quad [1]$$

As can be seen in Figure 3, the $\sum Q_{irr}$ evolution of all electrode compositions is characterized by a sigmoidal shape. The first part consists of an initial offset in $\sum Q_{irr}$ of about 0.13–0.27 Ah_{irr} g^{-1}_{el}, corresponding to the first cycle irreversible capacity described in Table I, and subsequent sigmoidal increase in $\sum Q_{irr}$, with a maximum in the slope after ∼20 cycles, whereby the slope increases with increasing silicon content. The second part after about ∼45 cycles, however, is characterized by a less steep and nearly linear growth of $\sum Q_{irr}$ with cycle number. Interestingly, the sigmoidal increase of $\sum Q_{irr}$ within the first ∼45 cycles implies that the irreversible processes go through a maximum after ∼20 cycles, which also corresponds to the minimum in coulombic efficiency in Figure 2a. We

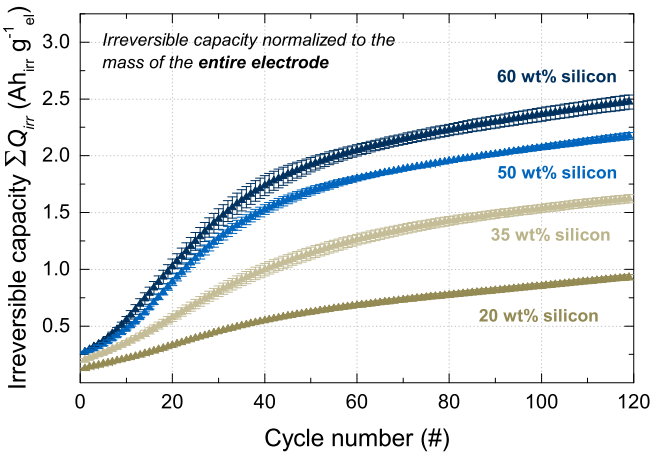

Figure 3. Total irreversible capacity $\sum Q_{irr}$ in units of $Ah_{irr}\ g^{-1}_{el}$ (defined by Equation 1) as a function of the cycle number, obtained from the galvanostatic cycling data of the SiG//LFP coin-cells shown in Figure 2. The error bars represent the standard deviation of at least two independent repeat measurements.

expect that this behavior is caused by the degradation of the silicon particles, which will be explained in more detail in the Discussion section. In contrast to the first phase, the $\sum Q_{irr}$ slopes in the second phase are almost constant and very similar for all electrode compositions (see Figure 3). In this stage, residual irreversible capacity losses are significantly reduced and mainly scale with the delivered capacity, but seem to be independent of the electrode composition.

Silicon-graphite electrode capacity decay.—Figure 4 shows cyclic voltage profiles of the 20 wt% silicon electrode as a function of the exchanged capacity for the 2nd, 20th, 60th, and 120th cycle. For this electrode with the highest graphite content of 65 wt%, the capacity contribution from the graphite active material can be most clearly distinguished from the contributions by silicon. In addition, we plotted the differential capacity curve of the same electrode in Figure 5a, which allows a direct identification of the (de-)lithiation potentials of silicon and graphite (highlighted by hash signs). Accordingly, the cyclic voltage profiles in Figure 4 are increasingly compressed in x-direction upon continued cycling, reflecting a decrease in the reversible capacity of the silicon-graphite electrode. To identify the origin of this capacity decay, we first consider that the delithiation capacity contribution in Figure 4 at potentials below 0.25 V vs. Li/Li^+ stays constant at about 250 mAh g^{-1}_{el}. Taking into account the graphite delithiation potentials obtained from cyclic voltammetry in Figure 1 and the theoretical capacity contribution of ~25% from graphite in the 20 wt% silicon electrode (~75% of the total theoretical capacity of 960 mAh g^{-1}_{el} are contributed by silicon; see Table I), we can conclude that the loss of reversible capacity is mainly associated with the silicon active material at delithiation potentials above 0.25 V vs. Li/Li^+. This conclusion is additionally confirmed by the differential capacity curve shown in Figure 5a, which clearly shows that the integral of the peaks associated with the delithiation from graphite (see hash signs) remain almost constant.

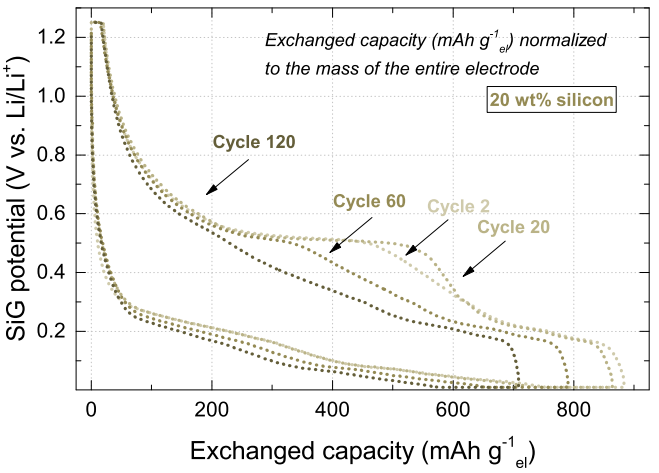

Figure 4. Cyclic voltage profiles of the 20 wt% silicon electrode plotted as a function of the exchanged capacity (mAh g^{-1}_{el}), obtained from galvanostatic cycling of SiG//LFP coin-cells. The SiG electrode potential was calculated from the SiG//LFP cell voltage, referring to a constant LFP electrode potential of 3.45 V vs. Li/Li^+.

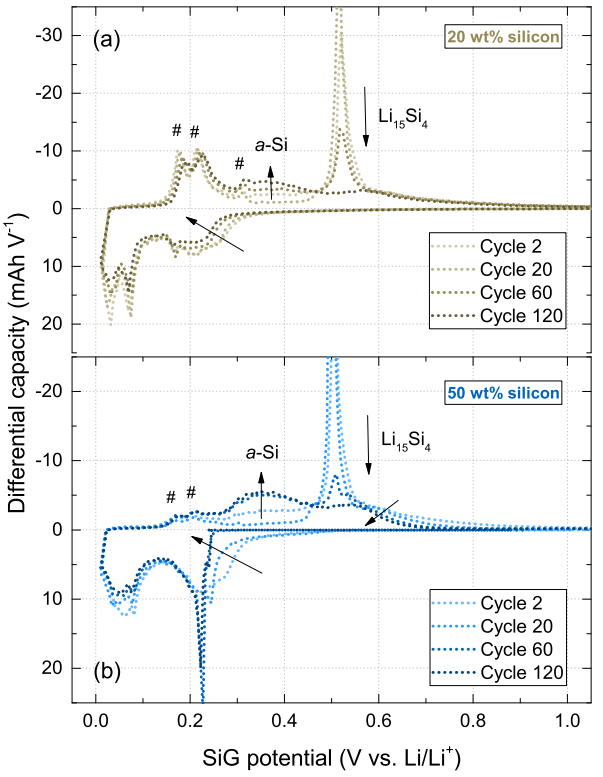

Figure 5. Differential capacity curves of the (a) 20 wt% silicon electrode and (b) 50 wt% silicon electrode plotted as a function of the silicon graphite potential (V vs. Li/Li^+). The data were obtained from galvanostatic cycling of SiG//LFP coin-cells. The SiG electrode potential was calculated from the SiG//LFP cell voltage, referring to a constant LFP electrode potential of 3.45 V vs. Li/Li^+.

In addition, Figure 5b shows the differential capacity profile of the 50 wt% silicon electrode for the 2nd, 20th, 60th, and 120th cycle as a function of the silicon-graphite potential. Both electrodes reveal almost no polarization during the lithiation at potentials below 0.2 V vs. Li/Li^+ upon cycling, however, a distinct potential drop after 60 cycles for the 50 wt% silicon electrode can be observed at low degrees of lithiation, i.e., at potentials above 0.2 V vs. Li/Li^+. As a result, the loss of reversible capacity must be largely caused by an incomplete lithiation of the silicon active material, which can be clearly seen by the disappearance of the lithiation shoulder in the 0.25-0.5 V vs. Li/Li^+ region. Analogously, during delithiation both electrodes reveal significant changes at potentials above 0.25 V vs. Li/Li^+ upon cycling. Between the 2nd and the 20th cycle, a distinct peak at about 0.45 V vs. Li/Li^+ can be seen, which is ascribed to the two-phase delithiation reaction from crystalline $Li_{15}Si_4$ to amorphous $Li_{\sim 2}Si$.[43] As expected, the extent of this peak is larger in the 50 wt% electrode. Several studies on different alloy electrodes indicated that these two-phase boundaries cause additional particle damage due to inhomogeneous volume changes compared

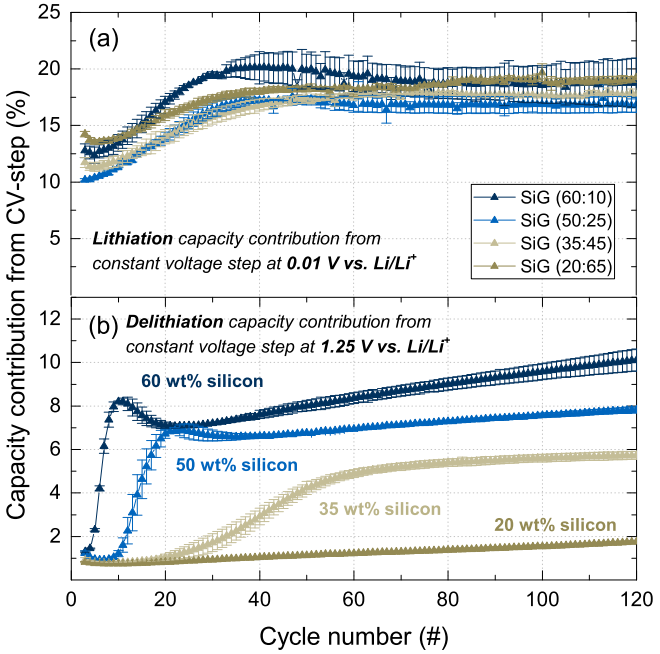

Figure 6. Capacity contribution (in %) from constant voltage steps at the end of (a) lithiation at 0.01 V vs. Li/Li$^+$ and (b) delithiation at 1.25 V vs. Li/Li$^+$, obtained from galvanostatic cycling at 0.5 h^{-1} of SiG//LFP coin-cells shown in Figure 2. The first two cycles were omitted to exclude any effects that may result from the lower C-rate of 0.05 h^{-1} during the first cycle. The error bars represent the standard deviation of at least two independent repeat measurements.

to single-phase reactions and that they often coincide with a capacity fade of the respective electrodes.[7,44] For silicon-based electrodes, Iaboni and Obrovac demonstrated recently that the formation of $Li_{15}Si_4$ during cycling can be used as a sensitive indicator for weakly bound silicon regions and coincides with the detachment of silicon particles, leading to a capacity decay.[6] In agreement with their report, the extent of the $Li_{15}Si_4$ peak shown in Figure 5 increases within the first 20 cycles, which corresponds to a simultaneous decrease of the delithiation from amorphous silicon-lithium alloy (*a*-Si). In other words, during lithiation within the first cycles more silicon is reduced to form the highly lithiated crystalline $Li_{15}Si_4$ phase. However, analogous to the cycling data shown in Figure 2b after 60 cycles a continuous decrease of the $Li_{15}Si_4$ peak can be observed, which, though it is partially compensated by a smaller increase of the delithiation capacity from amorphous silicon-lithium alloy (*a*-Si), indicates that the silicon particles no longer reach the highly crystalline $Li_{3.75}Si$ stoichiometry. Although this effect is more pronounced in electrodes with higher silicon content and can be explained by an incomplete lithiation, the decay of the delithiation capacity at potentials above 0.6 V vs. Li/Li$^+$, i.e. at low degrees of lithiation, is even more severe and the main source for the loss of reversible capacity, which agrees with the disappearance of the shoulder during lithiation at potentials between 0.25 and 0.5 V vs. Li/Li$^+$. This phenomenon is most likely caused by insufficiently connected silicon particles, which suffer either from incomplete lithiation or, more likely, incomplete delithiation because of a higher contact and interfacial resistance during particle shrinkage.[30]

Figure 6 shows the capacity contributions $Q_{CV,\%}$ from the constant voltage steps at the end of (a) the lithiation step at 0.01 V vs. Li/Li$^+$ and (b) the delithiation step at 1.25 V vs. Li/Li$^+$ for the different electrode compositions. The contributions for each cycle were calculated according to Equation 2,

$$Q_{CV,\%} = \frac{Q_{CV}}{Q_{CC} + Q_{CV}} \cdot 100 \qquad [2]$$

where Q_{CC} is the capacity from the constant current step and Q_{CV} is the capacity from the constant voltage step. As can be seen in Figure 6a, the lithiation of the silicon-graphite electrodes is characterized by a continuous increase of $Q_{CV,\%}$ by ~6%-points before stabilizing between 17–19% across all electrode compositions. In other words, after ~45 cycles approximately one fifth of the lithiation capacity is derived from the constant voltage step at 0.01 V vs. Li/Li$^+$. The slope of $Q_{CV\%}$ vs. cycle number reaches a maximum after ~20 cycles before it decreases to essentially zero after about ~45 cycles. The occurrence of this inflection point seems to be independent of the electrode composition and again coincides with the minimum in the coulombic efficiency in Figure 2a. We assume that the initial rise in $Q_{CV,\%}$ results from a minor increase in electrode polarization (as shown in Figure 5, the voltage polarization increase for the lithiation process is rather small), which we believe originates from enhanced electrolyte decomposition in the initial cycles due to silicon particle degradation (i.e., surface growth) and subsequent growth of the SEI layer. Upon continued cycling (i.e., after ~45 cycles), the increase in $Q_{CV,\%}$ is only minor across all electrode compositions. As it is known that the SEI layer mainly consists of electrically insulating electrolyte decompositions products, e.g., inorganic LiF and Li_2CO_3 compounds as well as organic alkyl carbonates and alkoxides, its growth is limited to a certain thickness.[45,46] Hence, we expect that the silicon surface does not change significantly after cycle 45.

As the electrode polarization during lithiation does not seem to depend on the electrode composition, there must exist a second degradation phenomenon during delithiation that leads to the observed composition-dependent capacity drop shown in Figure 2. To further investigate this, the capacity contribution from the CV-step at 1.25 V vs. Li/Li$^+$ during delithiation is shown Figure 6b. Initially, $Q_{CV,\%}$ is in the range of ~1% across all electrode compositions and thus much smaller compared to that of the lithiation CV step. This can be explained by considering exemplarily the differential capacity curves in Figure 5, according to which the delithiation cutoff potential of all silicon-graphite electrodes, independent of the silicon content, is significantly higher than the average delithiation potential of ~0.5 V vs. Li/Li$^+$. However, for the silicon-rich SiG electrode with 60 wt% silicon, $Q_{CV,\%}$ rises rapidly after the first cycle, reaching ~8% within less than 10 cycles, which indicates an increased difficulty to completely delithiate the silicon particles. The same is observed for the 50 wt% and the 35 wt% SiG electrodes, which display a sharp increase of the $Q_{CV,\%}$ value after ~10 and ~20 cycles, respectively. While also for the Si-poor SiG electrode with 20 wt% silicon a gradual increase of $Q_{CV,\%}$ is observed after ~30 cycles, the magnitude of this increase is substantially smaller than for the electrodes with higher silicon content. In summary, the higher the silicon content of the SiG electrodes, the earlier initiates the observed increase in $Q_{CV,\%}$ and the higher is the magnitude of the $Q_{CV,\%}$ increase. Remarkably, the onset and the extent of the increase of $Q_{CV,\%}$ during the delithiation cycles shown in Figure 6b coincides with the onset and the extent of the distinct capacity decay within the first 60 cycles as shown in Figure 2. The origin of this phenomenon will be further examined in the Discussion section.

Electrolyte consumption.—Besides the capacity decay, continuous consumption of the electrolyte constitutes a severe challenge to silicon-based electrodes. To quantify the loss of electrolyte caused by side reactions at the silicon/electrolyte interface, we harvested the electrolyte-soaked separators from the cycled SiG//LFP coin-cells after 120 cycles and measured ^{19}F-NMR of the extracted electrolytes. As FEC is reduced at more positive potentials than EC or EMC, Jung et al. demonstrated by on-line electrochemical mass spectrometry (OEMS) that FEC almost entirely suppresses the decomposition of EC as long there is FEC present in the electrolyte.[11] Hence, we consider in the following the change in the ratio of the FEC and PF_6^- peak integrals as a sensitive indicator for the electrolyte consumption upon cycling.

Figure 7a shows the total charge+discharge capacity per mole of FEC obtained from the SiG//LFP coin-cells depicted in Figure 2 after 120 cycles. This consumption rate was calculated by Equation 3,

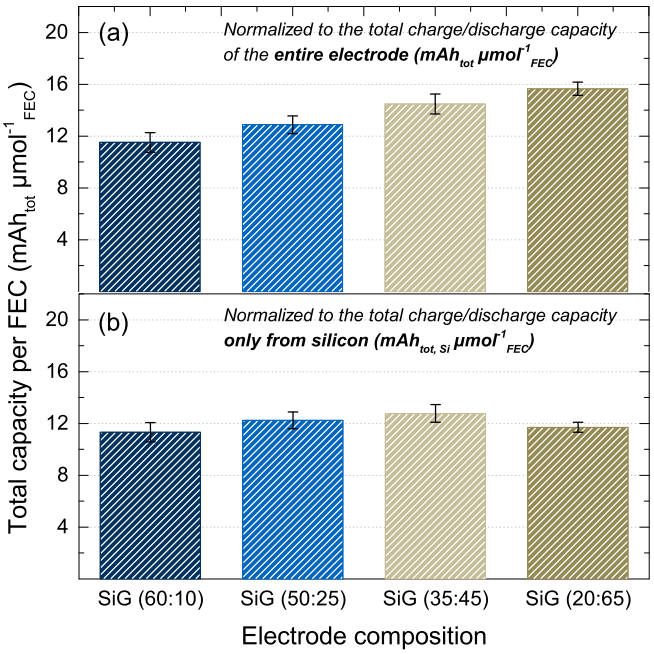

Figure 7. Total charge+discharge capacity (as defined by Equation 4) per mole of FEC after 120 cycles, using the cycling procedure described in Figure 2. The consumed amount of FEC was determined by ^{19}F-NMR spectroscopy from electrolytes that were harvested from SiG//LFP coin-cells after 120 cycles. (a) Total capacity of the entire electrode (mAh$_{tot}$ µmol$^{-1}_{FEC}$), (b) Total capacity contributed only from the silicon active material (mAh$_{tot, Si}$ µmol$^{-1}_{FEC}$). The error bars represent the standard deviation of at least two independent repeat measurements.

where $\sum Q_{tot}$ is the total charge exchanged during charging and discharging in mAh$_{tot}$ (see Equation 4) and n_{FEC} is the FEC consumption in µmol$_{FEC}$ as determined from integral analysis of the ^{19}F-NMR spectra. In other words, this thus determined capacity per FEC describes the amount of charge that can be exchanged by the silicon active material until 1 µmol of FEC is consumed by concomitant side reactions.

$$Capacity\ per\ FEC = \frac{\sum Q_{tot}}{n_{FEC}} \quad [3]$$

$$\sum Q_{tot} = \sum_{i}^{120} \left(Q_i^{lithiation} + Q_i^{delithiation}\right) \quad [4]$$

As can be seen, the total capacity per mole of FEC increases gradually with decreasing silicon content from 11.5 mAh$_{tot}$ µmol$^{-1}_{FEC}$ in the 60 wt% silicon electrode to 15.7 mAh$_{tot}$ µmol$^{-1}_{FEC}$ in the 20 wt% silicon electrode. Taking into account a density of 1.41 g cm^{-3} for FEC, this would correspond to a total capacity per µL FEC of 150–210 mAh$_{tot}$ µL$^{-1}_{FEC}$. Interestingly, this difference is comparatively small, especially when considering that the 60 wt% silicon electrode contains nominally three times more silicon compared to the 20 wt% silicon electrode. For that reason, we applied Equation 5 to correct the total exchanged capacity by the capacity contribution from graphite to obtain the capacity that results only from the (de-)lithiation of silicon (mAh$_{tot, Si}$ µmol$^{-1}_{FEC}$) as shown in Figure 7b,

$$\sum Q_{tot,\ Si} = \sum Q_{tot} \cdot \frac{x_{Si} \cdot Q_{Si}^{theo}}{x_{Si} \cdot Q_{Si}^{theo} + x_C \cdot Q_C^{theo}} \quad [5]$$

where $\sum Q_{tot,Si}$ is the total capacity from silicon, $\sum Q_{tot}$ is the total capacity from the entire electrode (see 1st and 2nd rows in Table I), Q_{Si}^{theo} is the theoretical capacity of silicon, Q_C^{theo} is the theoretical capacity of graphite, x_{Si} is the relative amount of silicon, and x_C is the relative amount of graphite. It is to note that for reasons of simplicity, we make the approximation that the ratio of the capacity contributions of silicon and graphite remains constant throughout cycling. As the silicon accounts for the majority of the capacity (>75%) in any case, the error arising from this assumption should be low, even if the capacity of graphite and silicon in the SiG electrodes would fade at different rates. Using Equation 5 to quantify the charge+discharge capacity contribution from silicon and dividing its value by the measured FEC consumption, it can be seen in Figure 7b that the thus calculated total capacity from silicon per mole of FEC falls within a very narrow range, with mean values for each SiG electrode composition which differ from each other by less than one standard deviation, so that the overall capacity per consumed FEC can be averaged for all four SiG electrode compositions to 12.0 ± 0.8 mAh$_{tot, Si}$ µmol$^{-1}_{FEC}$. From this, we conclude that the total capacity exchanged by silicon causes the same FEC consumption across all SiG electrode compositions, suggesting that the graphite content has no influence on the FEC consumption rate.

$$FEC\ per\ irreversible\ capacity = \frac{n_{FEC}}{\sum Q_{irr}} \quad [6]$$

$$Electrons\ per\ FEC = \frac{\sum Q_{irr}}{n_{FEC} \cdot F} \quad [7]$$

To further support our conclusion, we applied Equation 6 to normalize the FEC consumption n_{FEC} after 120 cycles to the total irreversible capacity $\sum Q_{irr}$ (see Equation 1). As a result of the repeated volume expansion of silicon (~280%) and the resulting cracking and continuous renewal of the SEI layer, we assume that the irreversible capacity losses after 120 cycles can be almost fully ascribed to the side reactions at the silicon/electrolyte interface. In accordance with that, the normalization reveals a similar ratio of 11.5-13.1 µmol$_{FEC}$ mAh$^{-1}_{irr}$ across all electrode compositions (shown in Table I), which is in good agreement with the results obtained by Jung et al. and additionally confirms their hypothesis according to which there is only one major source of irreversible capacity loss on silicon when using FEC containing electrolytes, namely the reduction of FEC.[11] However, by use of Equation 7, the conversion of the µmol$_{FEC}$ mAh$^{-1}_{irr}$ into the number of electrons that are consumed by the reduction of FEC reveals a slightly lower value of 3.0 ± 0.2 compared to the proposed four-electron mechanism of Jung et al.[11] We ascribe this discrepancy to the influence of the two constant voltage steps at 0.01 and 1.25 V vs. Li/Li$^+$ in the present study, as result of which our silicon-graphite electrodes experienced these limiting potentials for a much longer time compared to the constant current procedure of Jung et al.,[11] which in turn seem to affect the reduction processes at the silicon/electrolyte interface.

Building up on the relation of the FEC consumption and the irreversible capacity of 11.5–13.1 µmol$_{FEC}$ mAh$_{irr}$, we can now compare the silicon-graphite electrodes with a standard graphite:PVdF (95:5) electrode with the same graphite particles in a conventional graphite//LFP full-cell cycling procedure (~1.7 mAh cm^{-2}, CCCV cycling between 2.0–4.0 V at 1 C), which shows a total irreversible capacity of ~0.34 mAh per 550 mAh total charge-discharge capacity (after ~200 cycles). By multiplying the total irreversible capacity with the FEC consumption rate (here: 13.1 µmol$_{FEC}$ mAh$_{irr}$), we obtain an absolute FEC consumption of 4.45 µmol$_{FEC}$ (see Equation 6). Subsequent normalization of the total charge-discharge capacity of 550 mAh to the absolute FEC consumption in accordance with Equation 3 results in a total capacity per FEC of ~124 mAh µmol$_{FEC}$. Comparing this value to the capacities per FEC for the different silicon-graphite electrodes of 11.5–15.7 mAh µmol$_{FEC}$ (see Figure 7a) clearly shows that the FEC consumption caused by the (de-)lithiation of graphite is more than one order of magnitude smaller as for silicon and likely mainly results from the initial SEI formation during the first cycles.

Discussion

Differentiating the degradation phenomena in silicon-graphite electrodes.—A close inspection of the galvanostatic cycling data

(Figure 2) and the two different regions in the corresponding total irreversible capacity vs. cycle number plot (Figure 3) suggest that our silicon-graphite electrodes undergo two distinct degradation phenomena. There seems to be one degradation mechanism common to all SiG electrodes, which results in an initial dip in the coulombic efficiency over the first ~45 cycles, which goes through a minimum after ~20 cycles (see Figure 2a), and which results in a rapid initial increase in the CV-step lithiation capacity (see Figure 6a). Although the extent of the coulombic efficiency minimum increases with the silicon content in the electrodes, it occurs after the same number of charge/discharge cycles across all electrode compositions, independent of the silicon/graphite active material ratio. In contrast, there seems to be another degradation mechanism which depends on the silicon/graphite ratio, namely the initially rapid and distinct capacity decay (see Figure 2b) as well as the clearly different increase in the delithiation capacity during the CV-step (see Figure 6b). As will be outlined in the following, we propose that the first phenomenon is mostly related to the intrinsic properties of the silicon active material such as particle size and morphology (furtheron referred to as *silicon particle degradation*), whereas the second phenomenon depends not only on the silicon material but also on the electrode composition, viz., the silicon/graphite ratio (furtheron described as *electrode degradation*).

Our hypothesis that the first degradation mechanisms, i.e., the silicon particle degradation mechanism indeed mostly depends on the intrinsic properties of the silicon particles can be illustrated by normalizing the accumulated irreversible capacity $\sum Q_{irr}$ (in $Ah_{irr}\ g^{-1}_{el}$) shown in Figure 3 by the silicon content of the respective silicon-graphite electrodes and plotting the resulting $\sum Q_{irr,Si}$ (in $Ah_{irr}\ g^{-1}_{Si}$) as a function of the cycle number, as shown in Figure 8a, as well as a function of the total charge-discharge capacity (see Figure 8b). The most important finding of this analysis is that all four SiG electrode compositions now show an essentially identical behavior, thus revealing that the total irreversible capacity only depends on the amount of silicon in the electrodes, with apparently negligible contributions from the silicon/graphite ratio or from the graphite content. Furthermore, by plotting $\sum Q_{irr,Si}$ versus the total amount of exchanged charge (see Equation 4), Figure 8b shows that $\sum Q_{irr,Si}$ is identical for all SiG electrodes, consistent with the observation that the FEC consumption of all SiG electrodes only depends on the total charge+discharge capacity (see Figure 7b).

To explain the initial sigmoidal increase of the accumulated irreversible capacity losses ($\sum Q_{irr}$), we consider that alloy electrode materials suffer from an enhanced particle roughening and from the formation of nanoporous particle morphologies as a consequence of the repeated volume changes during lithiation/delithiation, as was reported for tin[7] and silicon[10] (analogous to the structures formed during dealloying reactions).[47] Assuming that nanoporous silicon particles are being created during the early phase of the charge/discharge cycling, the sigmoidal behavior of the accumulated irreversible capacity versus cycle number (see Figure 8a) can easily be rationalized: the associated rapid initial increase in silicon particle surface area would lead to an initial steep increase in the accumulated irreversible capacity due to enhanced SEI formation, which subsequently would slow down once a fully developed nanoporous particle morphology has been reached. As this phenomenon would only depend on the silicon particle size and morphology, its effect would have to be independent of the silicon/graphite ratio of the SiG electrodes, as long as the electrodes are cycled between identical potential limits (i.e., between identical degrees of silicon lithiation/delithation), as indeed is observed in Figure 8. Furthermore, this hypothesis is consistent with the fact that the characteristic dip in the coulombic efficiency with a minimum after the same number of cycles is the same for all SiG electrode compositions, independent of the silicon/graphite ratio (see Figure 2a).

As can be seen in Figure 8, the silicon particle degradation is significantly decreased after ~ 45 cycles, leading to a much reduced slope of the accumlated irreversible capacity versus cycle number or total exchanged charge. This would be consistent with the assumption

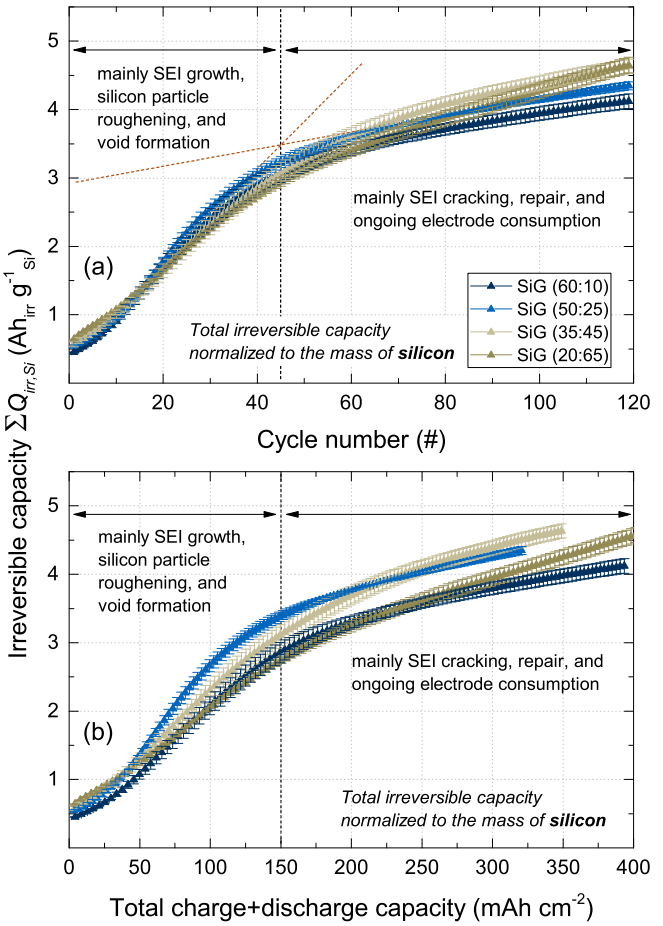

Figure 8. Total irreversible capacity $\sum Q_{irr,Si}$ ($mAh_{irr}\ g^{-1}_{Si}$) normalized to the mass of silicon in the SiG electrodes compositions (same color codes as in Figure 3) and plotted (a) as a function of the cycle number, and (b) as a function of the total charge+discharge capacity. The data were obtained from galvanostatic cycling of SiG//LFP coin-cells, as shown in Figure 2.

that a steady-state morphology of the silicon particles is reached after the initial ~45 cycles, i.e., that the silicon surface area has reached a final steady-state value. We explain this behavior by a reduction of the mechanical stress during insertion and extraction of lithium in the nano-sized silicon features, resulting from the initial morphological changes. In addition, this may also be related to the fact that the hypothesized increased surface area and porosity of the silicon particles would lead to a decrease of the effective surface-normalized current density, which in turn would reduce the mechanical stresses due to volume changes during cycling. In other words, the degradation of the silicon particles results in morphological changes that simultaneously diminish the root cause for their mechanical degradation, namely the mechanical stress upon insertion and extraction of lithium.[22] Once the surface growth of silicon has reached a minimum and the silicon particles are fully covered by an electronically insulating SEI layer, further irreversible capacity losses at a now much lower rate would mainly originate from ongoing electrolyte decomposition due to cracking and repair of the existing SEI layer, which is caused by the repeated volume changes upon cycling.

While the here given hypothesis is consistent with the literature, we are currently seeking to provide microscopic proof for the proposed relationship between nanoporous particle formation and the behavior of the accumulated irreversible capacity versus cycle number.[48]

In contrast to the silicon particle degradation mechanism, the electrode degradation mechanism is highly dependent on the electrode composition, with an observed earlier (in terms of cycle number) and more severe decay of the reversible capacity with increasing silicon

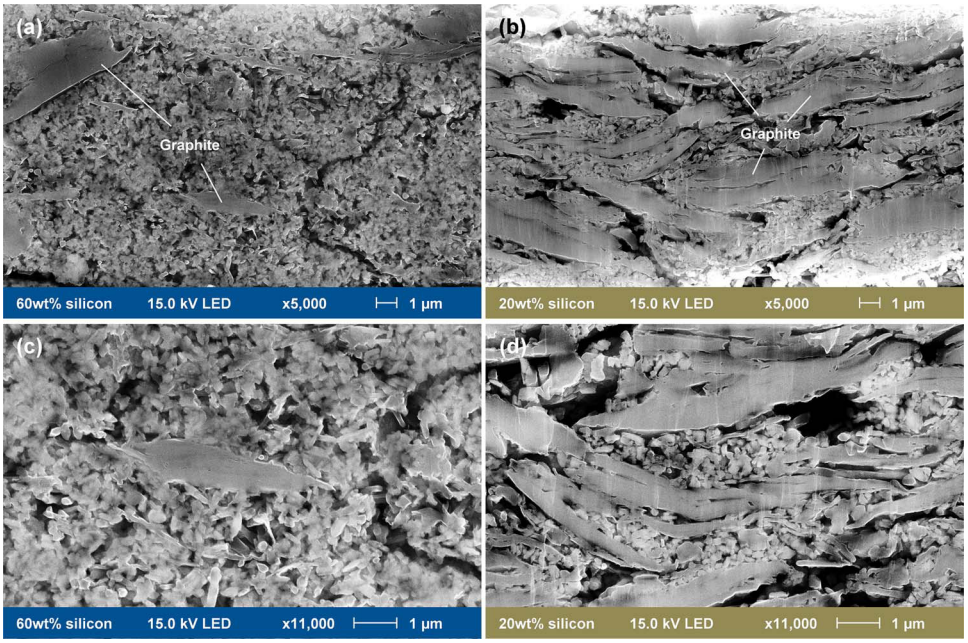

Figure 9. Scanning electron microscope cross-sectional images of (a, c) the 60 wt% silicon electrode, and (b, d) the 20 wt% silicon electrode. Secondary electron detector (SE), 15.0 kV electron acceleration voltage, magnification x5,000 (upper panels) and x11,000 (lower panels). Cross-sections were prepared with an Ar-ion beam cross-section polisher.

content as shown in Figure 2b. Similarly, the delithiation capacity contribution of the CV-step at 1.25 V vs. Li/Li$^+$ in Figure 6b strongly increases with increasing silicon content, indicating an increasingly significant polarization of the delithiation reaction of the silicon particles. To understand how the electrode composition might lead to these observations, Figure 9 shows representative cross-sectional scanning electron microscope (SEM) images of (a, c) the 60 wt% silicon electrode and (b, d) the 20 wt% silicon electrode. The lower SEM images (c, d) depict magnifications of the upper electrodes (a, b) at 11,000x. As can be seen in (a) and (c), the 60 wt% silicon electrode consists of a dense matrix of nanometer-sized silicon particles into which a few graphite flake-like particles are widely dispersed. Therefore, electronic conduction through this silicon-rich electrode involves the contribution of a large number of silicon/silicon and silicon/carbon fiber contact junctions, with the associated electronic contact resistances. In contrast, the 20 wt% silicon electrode in (b) and (d) consists of a nearly contiguous graphite backbone structure, whose interspaces are partially filled by silicon particles, leading to a much smaller average distance between the individual silicon particles and adjacent graphite particles. Therefore, the electronic conductivity of the SiG electrodes is expected to be significantly improved with increasing graphite content.

Although the SEI growth is largely driven by the above described silicon particle degradation mechanism, the mean electron conduction path length from the individual silicon particles to the graphite particles is crucial to maintain sufficient electronic conductivity throughout the electrode, which we tried to capture by Scheme 2. Based on this, one would expect that the progressive surface roughening of the silicon particles in the early stages of SEI growth would lead to a substantial loss of electrode integrity and subsequent increase of the electrode resistance. This, however, seems to be only partially consistent with the analysis of the potential profiles (see Figure 5) over extended charge/discharge cycling: while the gradual disappearance of the $Li_{15}Si_4$ phase is consistent with an electronic conduction resistance induced electrode polarization, the observed overpotential increase during charge and discharge is rather small and there are no obvious differences between the different SiG composites. On the other hand, our hypothesis of increased local electronic resistance contributions with increasing silicon content seems to hold when examining the capacity contribution during the delithiation CV step (at 1.25 V vs. Li/Li$^+$, see Figure 6b), which rapidly rises for silicon-rich electrodes in contrast to SiG electrodes with low silicon content. This can be easily explained by the silicon particle shrinkage during delithiation, resulting in a temporary particle isolation and incomplete delithiation, as was shown previously by Yoon et al.[30] Consistent with this hypothesis is the observation that the capacity contribution during the lithiation CV step (at 0.01 V vs. Li/Li$^+$, see Figure 6a) is similar for all SiG composites, as the expanded volume of the lithiated silicon particles will reduce the effect of inter-particle electronic contact resistances. The fact that the electrode polarization effects only set in toward the end of the delithiation process now also explains why it is not apparent in the overall differential capacity curves (Figure 5). In summary, we believe that the increasing capacity decay rate with increasing silicon content is due to silicon particle detachment and loss of electrical contact, particularly during the delithiation step, caused by the increasingly long mean electron conduction

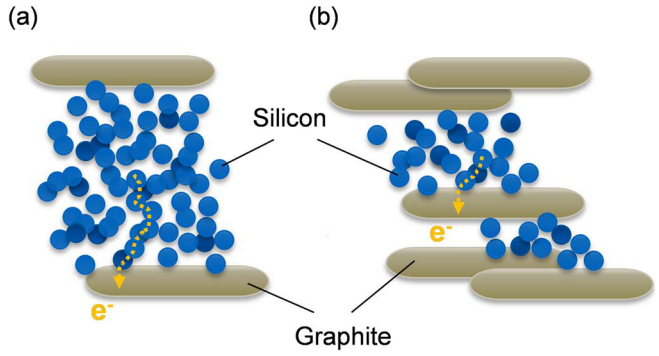

Scheme 2. Illustration of the difference in the mean electron conduction path length from the individual silicon particles to the electronically conductive graphite particles as a function of the silicon/graphite ratio sketched for (a) an Si-rich electrode (based on Figures 9a and 9c) and (b) an Si-poor electrode (based on Figures 9b and 9d). The different path lengths for electron conduction are illustrated by the yellow dotted line.

path length with increasing silicon content (see Scheme 2). Thus, in contrast to the silicon particle degradation mechanism, the electrode degradation mechanism and the concomitant capacity decay of the SiG electrodes is largely determined by the silicon/graphite active material ratio.

To estimate the contribution from the incomplete delithiation to the total irreversible capacity, we first considered that the loss of reversible capacity of the 60 wt% silicon electrode between the 3rd and the 120th cycle accounted for 634 mAh g^{-1}_{el} (see Figure 2b). Taking into account that the incomplete delithiation mainly affects silicon particles at low degrees of lithiation, i.e., below roughly 25% state-of-charge (compare Figure 5b), the maximum amount of immobilized lithium in these particles is 159 mAh g^{-1}_{el} (= 0.25 × 634 mAh g^{-1}_{el}). Comparing this number to the total irreversible capacity of 2.47 Ah g^{-1}_{el} after 120 cycles shown in Figure 3 yields a contribution of less than ∼6.4%. With decreasing silicon content and improved electrical conductivity within the electrodes (compare Figure 6b) this value is expected to decrease further. As a result, despite its harmful impact on the reversible capacity, the irreversible capacity caused by incomplete delithiation of the silicon particles displays only a minor contribution compared to irreversible capacity caused by the continuous electrolyte decomposition at the silicon/electrolyte interface.

Estimation of the electrode pore clogging upon cycling.—The sheer extent of the electrolyte consumption shown in Figure 7 suggests that the SEI on silicon is less a conformal surface layer formed in the initial cycles that evenly surrounds the silicon particles, but instead an increasingly thick and electrically insulating matrix (see above discussion and Figure 6b) that penetrates the entire porous electrode structure. For that reason, we decided to modify the approach of calculating the number of monolayers that are formed on the electrode's surface, which was recently reported by Jung et al.[11] and Pritzl et al.,[49] and characterize the electrolyte decomposition products by an average density rather than an average area defined by a C-C single bond length and thus also take into account the reduction of previously evolved CO_2 gas. To quantify how much SEI volume the SiG electrodes could accommodate before being entirely clogged by electrolyte decomposition products, we will present in the following an estimate of the relative SEI volume after 120 cycles and compare it to the pore volume of the pristine electrodes. Starting from the electrode properties shown in Table I, we first calculate the absolute pore volumes V_{pore} of the different electrode compositions, according to Equation 8,

$$V_{pore} = d \cdot A \cdot \varepsilon \quad [8]$$

where d is the pristine electrode thickness (see Table I), A is the electrode area (1.54 cm^2), and ε is the electrode porosity (see Table I). As can be seen from Table II, the resulting pore volumes increase with decreasing silicon content from 1.54 μL (∼1.00 μL cm^{-2}) for the 60 wt% electrode to 3.26 μL (2.21 μL cm^{-2}) for the 20 wt% silicon electrode, due to the increase of the electrode thickness from ∼15 to ∼30 μm at nearly similar electrode porosities (∼67–73%, see Table I).

In the next step, we approximate the mass of the SEI m_{SEI} from Equation 9 by taking into account the FEC consumption n_{FEC} determined by post-mortem ^{19}F-NMR analysis. Herein, we assume that the SEI has an equivalent mass as the preceding FEC decomposition product m_{FEC*}. In addition, we correct the molar mass of FEC (M_{FEC} = 106.05 g mol^{-1}) by the molar mass of four lithium atoms (M_{Li} = 6.84 g mol^{-1}) that are also incorporated into the SEI compounds (e.g., LiF or Li_2O),[11] leading to an effective molar mass M_{FEC*} of the FEC decomposition product of 133.41 g mol^{-1}.

$$m_{SEI} \equiv m_{FEC^*} = n_{FEC} \cdot M_{FEC^*} \quad [9]$$

Building up on this, we can further calculate the SEI volume V_{SEI}, as described by Equation 10, thereby assuming an average density ρ_{SEI} of 1.4–1.8 g cm^{-3} for the SEI. This value is a very rough zero order estimate based on the densities of the different SEI compounds, including ∼50% of inorganic compounds, inter alia LiF (2.64 g cm^{-3}), Li_2CO_3 (2.11 g cm^{-3}), Li_2O (2.01 g cm^{-3}), and ∼50% organic compounds, such as lithium alkoxides (∼1.0 g cm^{-3}), which are typically observed via for cycled silicon electrodes in FEC-containing electrolyte by XPS spectroscopy.[50–52]

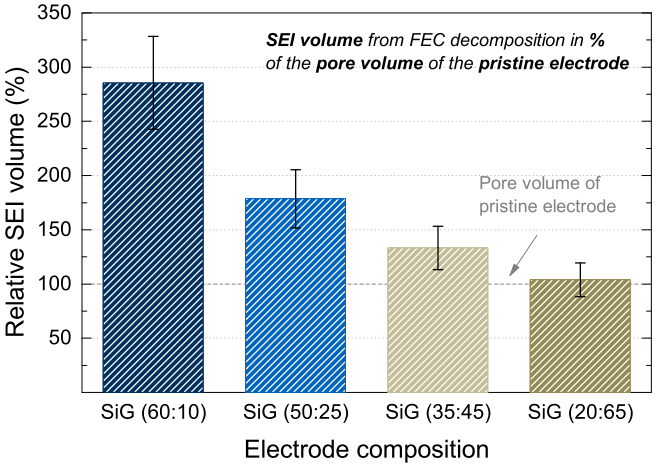

Figure 10. Estimated relative SEI volume defined by the fraction of pore volume of the pristine silicon-graphite electrodes which is occupied by FEC decompositions products. The values were calculated from a zero-order estimate based on the FEC consumption from ^{19}F-NMR. The SEI volume was calculated based on an average density of 1.6 g cm^{-3} for the FEC decomposition products. The error bars represent a variation in the density between 1.4–1.8 g cm^{-3}.

$$V_{SEI} = \frac{m_{SEI}}{\rho_{SEI}} \quad [10]$$

Finally, we divide the SEI volume V_{SEI} by the pore volume V_{pore} of the pristine electrodes by using Equation 11 to obtain the relative SEI volume v_{SEI}, which gives us an impression of the fraction of the original pore volume that would be occupied by electrolyte decomposition products after 120 cycles.

$$v_{SEI} = \frac{V_{SEI}}{V_{pore}} \quad [11]$$

Figure 10 shows the resulting zero order estimates of the relative SEI volumes normalized to the pore volume of the pristine electrodes. While this very simple approximation does not include the swelling of the electrodes over the course of cycling, it nonetheless provides a semi-quantitative measure of the volume of the electrolyte decomposition products and how it compares to the initially available void volume of the SiG electrodes. A comparison of the different electrode compositions in Figure 10 reveals a strong dependence of the relative SEI volume after 120 cycles on the silicon/graphite ratio, decreasing with decreasing silicon content from ∼280% to ∼100%. This grantedly simple estimate provides a reasonably convincing argument that the FEC decomposition products after 120 cycles would have to lead to an essentially complete pore blocking in the case of the 20 wt% silicon electrode and could not even be accommodated in the 60 wt% silicon electrode. Therefore, considering that about three quarters of the accumulated irreversible capacity occur within the first ∼45 cycles (see Figure 8a), and given that the SEI formation is proportional to irreversible capacity, we can assume that without any changes in electrode morphology and thickness, all ionic pathways would be filled by electrolyte decomposition products after less than 45 cycles. However, as our results from galvanostatic cycling clearly prove a residual reversible capacity of ∼70% after 120 cycles for the 60 wt% silicon electrode (see Figure 2), we conclude that the electrodes must significantly swell upon cycling in order to increase the available pore volume and thus facilitate the accommodation of the FEC decomposition products while simultaneously conserving the ionic conduction pathways. These conclusions agree well with the thickness

Table II. Pore volumes of the pristine electrodes and calculated SEI volumes after 120 cycles, based on the FEC consumption after 120 cycles n_{FEC} determined by post-mortem ^{19}F-NMR. The SEI volume was calculated based on an average density of 1.6 g cm^{-3} for the FEC decomposition products.

		Electrode composition			
Measures	Units	SiG (60:10)	SiG (50:25)	SiG (35:45)	SiG (20:65)
Electrode pore volume V_{pore}	µL	1.54	1.79	2.32	3.26
FEC consumption after 120 cycles n_{FEC}	µmol	53	38	37	41
Mass of FEC* precipitates m_{FEC*}	mg	7.1	5.1	4.9	5.4
Absolute SEI volume V_{SEI}	µL	4.4	3.2	3.1	3.4
Relative SEI volume	%	285	179	133	104

measurements and cross-sectional SEM images of cycled silicon electrodes reported by Mazouzi et al.[53]

Obrovac and co-workers measured the coating thickness of Si-alloy/graphite composite electrodes in their fully lithiated state and found that the entire coating expanded by about ∼96%, which was very similar to the expected expansion of the lithiated Si-alloy (∼115%).[15] Interestingly, the porosity of these electrodes remained nearly the same as in the delithiated state, leading them to the conclusion that the pore size expands by the same amount as the silicon particles. Transferring these observations to our electrodes, the silicon particle volume increase of about 280% upon full lithiation would result in an additional pore volume of 60–170% (e.g., 60 wt% silicon x 280% expansion = ∼170% additional pore volume), depending on the electrode composition. As the pores are increasingly filled by decomposition products upon cycling, they likely cannot shrink back to their initial volume when silicon is delithiated. Hence, the electrode thickness will increase continuously, in particular during the silicon particle degradation phase, where electrolyte decomposition and subsequent SEI growth are strongest. In contrast, a higher graphite content of the composite electrodes increases the total pore volume and simultaneously improves the electrode conductivity with graphite acting as an electrically conductive backbone.

Cycle life dependence on the electrolyte amount.—Besides the electrode morphology, the amount of SEI-forming additives in the electrolyte also plays a crucial role for the cycling performance of silicon-based electrodes. Thus it was shown that a rapid capacity drop can be observed for silicon based anodes at the point where the capacity-stabilizing FEC additive was found to be depleted quantitatively.[11,35] As in commercial-scale Li-ion batteries the electrolyte amount is in the order of ∼5 µL cm^{-2} and thus much smaller compared to typical lab-scale measurements (∼85 µL cm^{-2} for our coin cells), the available moles of FEC per mass of silicon are substantially lower in commercial-scale cells, so that the expected cycle life of silicon-based electrodes in commercial-scale cells should consequently be much shorter.[11] To quantify this difference, we approximate the number of cycles prior to FEC depletion of SiG electrodes in lab-scale versus commercial-scale cells by considering the constant ratio of the FEC consumption n_{FEC} and the irreversible capacity loss $\sum Q_{irr}$ (see Table I). Assuming a commercial-scale cell using 5 µL cm^{-2} electrolyte with 20 wt% FEC additive and our lab-scale cells using 85 µL cm^{-2} electrolyte with 5 wt% FEC additive, we use Equation 12 to first determine the absolute amount of FEC n_{FEC}^{tot} in the two electrolytes.

$$n_{FEC}^{tot} = \frac{V_{el} \cdot \rho_{el} \cdot x_{FEC}}{M_{FEC}} \quad [12]$$

where V_{el} is the electrolyte volume, ρ_{el} is the electrolyte density (∼1.19 g cm^{-3}), x_{FEC} is the mass fraction of FEC in the electrolyte, and M_{FEC} is the molar mass of FEC (106.05 g mol^{-1}). Accordingly, the commercial-scale cell would contain ∼11 µmol cm^{-2} of FEC, whereas the lab-scale cells tested in this work contain ∼48 µmol cm^{-2} of FEC, i.e, the ∼5-fold amount. In the next step, we use the inverse of the constant ratio of the FEC consumption n_{FEC} to irreversible capacity loss $\sum Q_{irr}$ (in units of µmol$_{FEC}$ Ah$^{-1}_{irr}$, calculated by Equation 6, shown in Table I) to calculate the maximal irreversible capacity $\sum Q_{irr}^{max}$ that corresponds to a total depletion of FEC from the respective electrolytes, according to Equation 13,

$$\sum Q_{irr}^{\max} = n_{FEC}^{tot} \cdot \frac{\sum Q_{irr}}{n_{FEC}} \cdot \frac{1}{m_{Si}} \quad [13]$$

where m_{Si} is the mass of silicon in the electrode (in mg$_{Si}$ cm^{-2}), and n_{FEC}^{tot} is the total amount of FEC per cm^2 electrode area (µmol$_{FEC}$ cm^{-2}). Table III summarizes the maximal irreversible capacities $\sum Q_{irr}^{max}$ of the various silicon-graphite electrodes in either lab-scale cells or in commercial-scale cells. To forecast the number of cycles until the depletion of FEC, we can compare the accumulated irreversible capacity versus cycle number in Figure 8a with the maximal irreversible capacity until FEC depletion (in units of Ah$_{irr}$ g$^{-1}_{Si}$) listed in Table III for both cell formats. For the commercial-scale cells, this analysis suggests that FEC would already be consumed within the first ∼20–30 charge/discharge cycles. In contrast, the number of cycles prior to FEC depletion predicted for our lab-scale cells substantially exceeds the here tested 120 cycles (at this point, $\Sigma Q_{irr,Si}$ in Figure 8a is still much below the projected estimated maximal irreversible capacity given in Table III). That FEC, as predicted, is not depleted after 120 cycles in our lab-scale experiments is confirmed by our post-mortem ^{19}F-NMR measurements, which show a residual FEC content of >1.2 wt% in the electrolyte (originally 5 wt%) after the 120 cycles.

Thus, we conclude that the lifetime of silicon-graphite electrodes in commercial-scale cells with a reasonably sized positive electrode would be limited by the amount of FEC in the electrolyte, rather than by the degradation of the electrode structure. These findings highlight again the importance of an effective SEI on silicon-based electrodes and the need for a proper quantification of the electrolyte consumption. Therefore, we recommend that future investigations of silicon-based electrodes in lab-scale cells should take into account the actual FEC consumption in µmol$_{FEC}$ and to compare this to the FEC inventory in commercial-scale cells. As our results from ^{19}F-NMR analysis reveal an almost constant ratio of the consumed FEC n_{FEC} to cumulative irreversible capacity $\sum Q_{irr}$ of 11.5-13.1 µmol$_{FEC}$ mAh$^{-1}_{irr}$, Equation 14 can be used as an approximation to assess the FEC consumption from battery cycling. We would like to note that this relation is only valid for cell chemistries that do not have further electrolyte decomposition reactions at the positive electrode, e.g., $LiFePO_4$, and involve two constant voltage steps. If the cycling protocol does not include any constant voltage steps, the ratio r_{FEC} of the consumed FEC n_{FEC} to total irreversible capacity $\sum Q_{irr}$ approaches the four electron reduction mechanism of FEC, which was reported by Jung et al.,[11] corresponding to a value of 9.4 ± 0.4 µmol$_{FEC}$ mAh$^{-1}_{irr}$.[54]

$$n_{FEC} = r_{FEC} \cdot \sum Q_{irr} \quad [14]$$

Conclusions

In this study, we presented a comprehensive approach to understand the degradation phenomena in silicon-graphite electrodes with different graphite/silicon ratios (20–60 wt% silicon) and areal

Table III. Maximal irreversible capacity and forecasted cycle life of silicon-graphite electrodes calculated for typical lab-scale and commercial-scale cells. The upper segments provide the specifications of the various SiG electrodes as well as the measured FEC consumption per accumulated irreversible capacity over 120 cycles (taken from Table I). The middle and the lower segments provide the estimated number of cycles for lab-scale and commercial-scale cells by which the available amount of FEC will be consumed.

		Electrode composition			
Measures	Units	SiG (60:10)	SiG (50:25)	SiG (35:45)	SiG (20:65)
Silicon-graphite electrode specifications					
Silicon content	%	60	50	35	20
Silicon loading	mg_{Si} cm^{-2}	0.64	0.47	0.46	0.43
FEC consumption per irr. capacity	$\mu mol\ mAh^{-1}{}_{irr}$	13.0	12.3	11.5	13.1
Lab-scale cell (85 $\mu L\ cm^{-2}$ electrolyte with 5 wt% FEC additive)					
Maximal irreversible capacity	$Ah_{irr}\ g^{-1}{}_{Si}$	5.8	8.3	9.1	8.4
Cycle lifetime acc. Figure 8a	#	>120	>120	>120	>120
Commercial-scale cell (5 $\mu L\ cm^{-2}$ electrolyte with 20 wt% FEC additive)					
Maximal irreversible capacity	$Ah_{irr}\ g^{-1}{}_{Si}$	1.4	1.9	2.2	2.0
Cycle lifetime acc. Figure 8a	#	20	25	30	25

capacities of 1.8–2.3 mAh cm^{-2}. By use of an FEC-containing electrolyte and capacitively oversized $LiFePO_4$ cathodes, we could clearly distinguish two degradation phenomena, which we described as silicon particle degradation and electrode degradation. While the former is mainly determined by the intrinsic properties of the silicon active material, such as particle size and morphology, as well as the amount of charge that is exchanged by the silicon particles, the electrode degradation mechanism depends not only on the silicon material but also on the electrode composition, i.e., the silicon/graphite ratio. Increasing the silicon content results in an increase of the number of interparticle contacts, e.g., silicon-silicon, which leads to a higher contact resistance. During discharge, i.e., in delithiated silicon electrodes, this phenomenon is even more pronounced because of a reduced contact pressure at these interfaces.

Based on our results from ^{19}F-NMR analysis we could demonstrate that the consumption of FEC after 120 cycles is independent of the graphite/silicon ratio and only depends on the total accumulated exchanged charge (i.e., sum of charge and discharge) experienced by the silicon. Based on this, we could show that: (i) the irreversible capacity loss correlates linearly with the decomposition of FEC on silicon, and can thus be used to estimate the extent of FEC consumption from the cycling data; (ii) the estimated volume of the FEC decomposition products increases with the silicon content and for all investigated SiG compositions largely exceeds the pore volume of the pristine electrodes, explaining the commonly observed swelling of silicon electrodes upon cycling; and (iii) the comparatively low molar quantity of FEC in commercial electrolytes is the most critical factor in determining the cycle life of silicon-based electrodes.

Acknowledgments

The German Federal Ministry for Economic Affairs and Energy is acknowledged for funding (Project “LiMo”, funding number 03ET6045D). Wacker Chemie AG is kindly acknowledged for providing the silicon nanoparticles. Susanne Cornfine and JEOL (Germany) GmbH are kindly acknowledged for supporting the SEM measurements. The authors also kindly thank Yelena Gorlin, Manu Patel, Qi He, and Anne Berger (all TUM) for fruitful discussions.

References

1. D. Andre, S.-J. Kim, P. Lamp, S. F. Lux, F. Maglia, O. Paschos, and B. Stiaszny, *J. Mater. Chem. A*, **3**(13), 6709 (2015).
2. O. Gröger, H. A. Gasteiger, and J.-P. Suchsland, *J. Electrochem. Soc.*, **162**(14), A2605 (2015).
3. V. L. Chevrier, L. Liu, D. B. Le, J. Lund, B. Molla, K. Reimer, L. J. Krause, L. D. Jensen, E. Figgemeier, and K. W. Eberman, *J. Electrochem. Soc.*, **161**(5), 783 (2014).
4. D. Ma, Z. Cao, and A. Hu, *Nano-Micro Lett*, **6**(4), 347 (2014).
5. M. N. Obrovac, L. Christensen, D. B. Le, and J. R. Dahn, *J. Electrochem. Soc.*, **154**(9), A849 (2007).
6. D. S. M. Iaboni and M. N. Obrovac, *J. Electrochem. Soc.*, **163**(2), 255 (2016).
7. M. N. Obrovac and V. L. Chevrier, *Chem. Rev.*, **114**, 11444 (2014).
8. R. Petibon, V. Chevrier, C. P. Aiken, D. S. Hall, S. Hyatt, R. Shunmugasundaram, and J. R. Dahn, *J. Electrochem. Soc.*, **163**(7), 1146 (2016).
9. J. O. Besenhard, J. Yang, and M. Winter, *J. Power Sources*, **68**, 87 (1997).
10. M. T. McDowell, S. W. Lee, J. T. Harris, B. A. Korgel, C. Wang, W. D. Nix, and Y. Cui, *Nano Lett*, **13**(2), 758 (2013).
11. R. Jung, M. Metzger, D. Haering, S. Solchenbach, C. Marino, N. Tsiouvaras, C. Stinner, and H. A. Gasteiger, *J. Electrochem. Soc.*, **163**(8), A1705 (2016).
12. V. Baranchugov, E. Markevich, E. Pollak, G. Salitra, and D. Aurbach, *Electrochem. commun.*, **9**(4), 796 (2007).
13. E. Markevich, K. Fridman, R. Sharabi, R. Elazari, G. Salitra, H. E. Gottlieb, G. Gershinsky, A. Garsuch, G. Semrau, M. A. Schmidt, and D. Aurbach, *J. Electrochem. Soc.*, **160**(10), A1824 (2013).
14. E. Markevich, G. Salitra, and D. Aurbach, *J. Electrochem. Soc.*, **163**(10), 2407 (2016).
15. Z. Du, R. A. Dunlap, and M. N. Obrovac, *J. Electrochem. Soc.*, **161**(10), 1698 (2014).
16. M. D. Fleischauer, M. N. Obrovac, J. D. Mcgraw, R. A. Dunlap, J. M. Topple, and J. R. Dahn, *J. Electrochem. Soc.*, **153**(3), 484 (2006).
17. B. Fuchsbichler, C. Stangl, H. Kren, F. Uhlig, and S. Koller, *J. Power Sources*, **196**(5), 2889 (2011).
18. C.-H. Yim, F. M. Courtel, and Y. Abu-Lebdeh, *J. Mater. Chem. A*, **1**(5), 8234 (2013).
19. T. Yim, S. J. Choi, J.-H. Park, W. Cho, Y. N. Jo, T.-H. Kim, and Y.-J. Kim, *Phys. Chem. Chem. Phys.*, **17**(4), 2388 (2014).
20. M. Ko, S. Chae, and J. Cho, *ChemElectroChem*, **2**(11), 1645 (2015).
21. F. Luo, B. Liu, J. Zheng, G. Chu, K. Zhong, H. Li, X. Huang, and L. Chen, *J. Electrochem. Soc.*, **162**(14), A2509 (2015).
22. M. T. McDowell, S. W. Lee, W. D. Nix, and Y. Cui, 4966 (2013).
23. N. Dupré, P. Moreau, E. De Vito, L. Quazuguel, M. Boniface, A. Bordes, C. Rudisch, P. Bayle-Guillemaud, and D. Guyomard, *Chem. Mater.*, **28**(8), 2557 (2016).
24. N. Delpuech, N. Dupre, P. Moreau, J. S. Bridel, J. Gaubicher, B. Lestriez, and D. Guyomard, *ChemSusChem*, **9**(8), 841 (2016).
25. M. Klett, J. A. Gilbert, S. E. Trask, B. J. Polzin, A. N. Jansen, D. W. Dees, and D. P. Abraham, *J. Electrochem. Soc.*, **163**(6), A875 (2016).
26. M. Klett, J. A. Gilbert, K. Z. Pupek, S. E. Trask, and D. P. Abraham, *J. Electrochem. Soc.*, **164**(1), 6095 (2017).
27. S. E. Trask, K. Z. Pupek, J. A. Gilbert, M. Klett, B. J. Polzin, A. N. Jansen, and D. P. Abraham, *J. Electrochem. Soc.*, **163**(3), A345 (2016).
28. C. Erk, T. Brezesinski, H. Sommer, R. Schneider, and J. Janek, *ACS Appl. Mater. Interfaces*, **5**(15), 7299 (2013).
29. J. H. Ryu, J. W. Kim, Y. Sung, and S. M. Oh, *Electrochem. Solid State Lett.*, **7**(10), 306 (2004).
30. T. Yoon, C. C. Nguyen, D. M. Seo, and B. L. Lucht, *J. Electrochem. Soc.*, **162**(12), A2325 (2015).
31. M. Wetjen, R. Jung, D. Pritzl, and H. A. Gasteiger, *ECS Meet*, **230** (2016), Abstr. #280.
32. E. Markevich, K. Fridman, R. Sharabi, R. Elazari, G. Salitra, H. E. Gottlieb, G. Gershinsky, A. Garsuch, G. Semrau, M. a Schmidt, and D. Aurbach, *J. Electrochem. Soc.*, **160**(10), A1824 (2013).
33. T. Marks, S. Trussler, A. J. Smith, D. Xiong, and J. R. Dahn, *J. Electrochem. Soc.*, **158**(1), A51 (2011).
34. A. V Plakhotnyk, L. Ernst, and R. Schmutzler, *J. Fluor. Chem.*, **126**(1), 27 (2005).
35. R. Petibon, V. L. Chevrier, C. P. Aiken, D. S. Hall, S. R. Hyatt, R. Shunmugasundaram, and J. R. Dahn, *J. Electrochem. Soc.*, **163**(7), A1146 (2016).
36. K. W. Schroder, H. Celio, L. J. Webb, and K. J. Stevenson, *J. Phys. Chem. C*, **116**, 19737 (2012).
37. T. Ohzuku, Y. Iwakoshi, and K. Sawai, *J. Electrochem. Soc.*, **140**(9), 2490 (1993).
38. T. Swamy and Y.-M. Chiang, *J. Electrochem. Soc.*, **162**(13), A7129 (2015).

39. C. Xu, F. Lindgren, B. Philippe, M. Gorgoi, F. Björefors, K. Edström, and T. Gustafsson, *Chem. Mater.*, **27**(7), 2591 (2015).
40. T. Jaumann, J. Balach, M. Klose, S. Oswald, U. Langklotz, A. Michaelis, J. Eckert, and L. Giebeler, *Phys. Chem. Chem. Phys.*, **17**(38), 24956 (2015).
41. D. Aurbach, *J. Power Sources*, **89**, 206 (2000).
42. T. Placke, S. Rothermel, O. Fromm, P. Meister, S. F. Lux, J. Huesker, H. Meyer, and M. Winter, *J. Electrochem. Soc.*, **160**, A1979 (2013).
43. M. N. Obrovac and L. Christensen, *Electrochem. Solid-State Lett.*, **7**(5), A93 (2004).
44. J. Li and J. R. Dahn, *J. Electrochem. Soc.*, **154**(3), A156 (2007).
45. D. Aurbach, E. Zinigrad, Y. Cohen, and H. Teller, *Solid State Ionics*, **148**, 405 (2002).
46. M. Gauthier, T. J. Carney, A. Grimaud, L. Giordano, N. Pour, H. Chang, D. P. Fenning, S. F. Lux, O. Paschos, C. Bauer, F. Maglia, S. Lupart, P. Lamp, and Y. Shao-horn, *J. Phys. Chem. Lett.*, **6**, 4653 (2015).
47. J. Erlebacher, M. J. Aziz, A. Karma, N. Dimitrov, and K. Sieradzki, *Nature*, **410**, 450 (2001).
48. M. Wetjen, S. Solchenbach, D. Pritzl, J. Hou, V. Tileli, and H. A. Gasteiger, Manuscript in preparation.
49. D. Pritzl, S. Solchenbach, M. Wetjen, and H. A. Gasteiger, *J. Electrochem. Soc.*, **164** (12), A2625 (2017).
50. X. Cheng, R. Zhang, C. Zhao, F. Wei, J. Zhang, and Q. Zhang, *Adv. Sci.*, **3**, 1 (2016).
51. E. Peled, D. Golodnitsky, and G. Ardel, *J. Electrochem. Soc.*, **144**(8), 208 (1997).
52. K. Schroder, J. Alvarado, T. A. Yersak, J. Li, N. Dudney, L. J. Webb, Y. S. Meng, and K. J. Stevenson, *Chem. Mater.*, **27**(16), 5531 (2015).
53. D. Mazouzi, N. Delpuech, Y. Oumellal, M. Gauthier, M. Cerbelaud, J. Gaubicher, N. Dupré, P. Moreau, D. Guyomard, L. Roué, and B. Lestriez, *J. Power Sources*, **220**, 180 (2012).
54. M. Wetjen, G. Hong, S. Solchenbach, D. Pritzl, and H. A. Gasteiger, Manuscript in preparation.

3.3.3 A Wet-Chemical Route for Macroporous Inverse Opal Ge Anodes for Lithium Ion Batteries with High Capacity Retention

In this section, the article "A wet-chemical route for macroporous inverse opal Ge anodes for lithium ion batteries with high capacity retention" will be presented. The paper is reproduced from *Sustainable Energy & Fuels*, 2017 with permission from The Royal Society of Chemistry.[226] The research work was primarily performed by the first author of the paper Sebastian Geier. The study was conducted in collaboration with the group of Prof. Thomas Fässler at Technical University Munich. It was published in the *Sustainable Energy & Fuels* on October 23, 2017. The permanent web-link to the article is http://pubs.rsc.org/en/Content/ArticleLanding/2017/SE/C7SE00422B#!divAbstract and the DOI is 10.1039/C7SE00422B.

In this paper we investigate germanium (Ge) thin layer electrodes without any carbon and binder as potential anode materials. The electrodes have an inverse opal structure, a macroporous structure with channel diameters of roughly 275 nm which allows for good electrolyte penetration throughout the complete electrode. The electrode is manufactured by coating a copper current collector with a polymethyl methacrylate (PMMA) substrate which forms an opal structure. Afterwards, a well-defined volume of a K_4Ge_9 solution in ethylene diamine is added to fill the voids of the opal PMMA structure. Annealing under a flow of $GeCl_4$ removes the PMMA host structure and yields the inverse opal Ge structure. Cycling the Ge electrodes versus metallic lithium in LP57 with the addition of $5\%_{wt}$ FEC yields capacity values close to the theoretically expected ones, proving that the Ge structure is in complete electrochemical contact. Furthermore, after 100 cycles a capacity retention of 73% is shown. Post-mortem SEM analysis furthermore shows that the macroporous structure is maintained even after 100 charge-discharge cycles. Therefore, this study successfully shows that structured Ge electrodes without carbon and binder can be used as anode material for Li-Ion batteries.

Author Contributions

Sebastian Geier prepared the electrodes. Roland Jung built the test cells and analyzed the electrochemistry data. Roland Jung and Sebastian Geier measured the electrode cross-sectional images. Sebastian Geier and Thomas Fässler wrote the manuscript. All authors discussed the results and commented on the manuscript.

Sustainable Energy & Fuels

COMMUNICATION

View Article Online
View Journal

Cite this: DOI: 10.1039/c7se00422b

Received 31st August 2017
Accepted 20th October 2017

DOI: 10.1039/c7se00422b

rsc.li/sustainable-energy

A wet-chemical route for macroporous inverse opal Ge anodes for lithium ion batteries with high capacity retention†

Sebastian Geier,[a] Roland Jung,[b] Kristina Peters,[c] Hubert A. Gasteiger,[b] Dina Fattakhova-Rohlfing[d] and Thomas F. Fässler *[a]

Germanium holds great potential as an anode material for lithium ion batteries due to its high specific capacity and its favorable properties such as good lithium ion diffusivity and electronic conductivity. However, the high cost of germanium and large volume changes during cycling, which lead to a rapid capacity fading for bulk Ge materials, demand for nanostructured thin film devices. Herein we report the preparation and electrochemical properties of thin films of porous, inverse opal structured Ge anodes obtained *via* a simple, up-scalable wet-chemical route utilizing $[Ge_9]^{4-}$ Zintl ions. In the absence of conductive additives, they show high initial capacities of >1300 mA h g^{-1} and promisingly high coulombic efficiencies of up to 99.3% and deliver over 73% of their initial capacity after 100 cycles when cycled *vs.* metallic lithium. In contrast to many other porous structured Ge electrodes, they show very little to almost no capacity fading after an initial drop, which makes them promising candidates for long life applications.

Introduction

In recent years, studies have focused attention on group 14 elements such as silicon and germanium as anode materials for Li ion batteries due to their favorable properties for electrochemical applications.[1,2] Si shows a very high theoretical gravimetric capacity (3579 mA h g^{-1} compared to 372 mA h g^{-1} for commercial graphite), while still being a relatively cheap material.[3,4] Si based anodes have also proven to be safe for use which makes them even more attractive for everyday applications. The main issue that hinders practical usage of Si based anodes for Li ion batteries is the enormous volume changes (about 310%) the material undergoes during the charge and discharge process leading to rapid capacity fading.[5] Most strategies to overcome this issue have focused on nano-sized porous Si morphologies such as hollow nanospheres,[6–8] nanowires,[9,10] 3D porous particles[11] and porous thin films.[12,13] However, all these highly porous materials suffer from a substantial lack of volumetric or areal capacity.

In comparison to silicon, germanium on the one hand has a lower but still sufficiently high gravimetric capacity (1385 mA h g^{-1}, $Li_{15}Ge_4$).[14] On the other hand, its volumetric capacity (7366 A h L^{-1}) is similar to that of Si (8334 A h L^{-1}) which makes Ge a reasonable alternative to Si for highly porous anodes.[15] Apart from that, Ge shows approximately 15 times higher lithium ion diffusivity at 360 °C (2.14×10^{-7} cm^2 s^{-1} *vs.* 1.48×10^{-8} cm^2 s^{-1} for Si) and roughly 400 times higher lithium ion diffusivity as well as four orders of magnitude higher electronic conductivity at room temperature than Si.[16,17] Grey *et al.* recently investigated structural changes in Ge anodes in Li ion batteries.[14] Since the volume change upon lithiation of Ge and Si to $Li_{15}Ge_4$ and $Li_{15}Si_4$ is within 15%, the volume changes during cycling still remain a main issue when using Ge anodes for Li ion batteries.[18]

Nano-structured and macro-porous materials allow for volume changes and several attempts have been made to design porous Ge materials. Besides electrochemical methods,[19] inverse opal structures have also been achieved by template supported methods, mostly utilizing SiO_2-opals as the template structure.[20,21] Paik *et al.* used inverse Ge opals made by chemical vapor deposition (CVD) of germane gas on a silica opal template as an anode in lithium ion batteries. Template removal was performed using hydrofluoric acid.[22] Recent studies also focused on embedding nanoparticles in sponge-like graphene or CNT matrices to provide sufficient porosity during battery cycling.[23–26]

Recently we succeeded in performing a wet-chemical synthesis on Ge inverse opal structures which should also

[a]Technical University Munich, Department of Chemistry, Chair of Inorganic Chemistry with Focus on Novel Materials, Lichtenbergstraße 4, 85747 Garching, Germany. E-mail: Thomas.faessler@lrz.tu-muenchen.de

[b]Technical University Munich, Department of Chemistry, Chair of Technical Electrochemistry, Lichtenbergstraße 4, 85747 Garching, Germany

[c]Ludwig-Maximilians-Universität München (LMU Munich), Department of Chemistry, Center for NanoScience (CeNS), Butenandtstraße 11, 81377 Munich, Germany

[d]Forschungszentrum Jülich GmbH, Institute of Energy and Climate Research (IEK-1), Materials Synthesis and Processing, Wilhelm-Johnen-Straße, 52425 Jülich, Germany

† Electronic supplementary information (ESI) available. See DOI: 10.1039/c7se00422b

offer free space as a buffer for structural widening and contraction during charge and discharge. The method provided the basis for a rational and general fabrication method for complex Ge nanomorphologies, which used preformed anionic Ge atom clusters.[27] The so-called Zintl clusters formed by polyanionic cages offer a wide variety of possibilities for material synthesis enabling compositional variety, shape control, and elemental mixing at a molecular level,[28,29] and thus suitable for electrochemical applications. $[Ge_9]^{4-}$ Zintl clusters were used for fabricating films with a controllable morphology *via* anodic deposition,[30] and for the formation of semiconducting nanostructures.[31–38] We found that the excellent solubility of $[Ge_9]^{4-}$ in selected organic solvents with up to 1 mol Ge per L enables them to easily handle Ge precursors allowing for potentially upscalable coating techniques such as spray-coating, where a germanium-containing solution can be homogenously sprayed over much larger areas utilizing a simple and automatable process. Their reactivity makes them promising precursors for making nanostructures with tunable composition and electronic properties.[39]

Herein we report a straightforward synthetic route to inverse opal structured Ge anodes for lithium ion batteries starting from the soluble binary alloy K_4Ge_9. The presented method involves controlled coupling of $[Ge_9]^{4-}$ clusters in a poly(methyl methacrylate) (PMMA) scaffold based on a synthetic protocol developed before for thin film solar cells on a wide variety of substrates (silicon, silica, sapphire, FTO, and ITO) (Scheme 1).

We showed by means of SEM, TEM, grazing incidence small angle X-ray scattering and Raman spectroscopy that the morphology of the films is retained as an ordered structure over a large area and that a control over amorphous and crystalline Ge walls is possible.[27] We now report on the first successful wet chemical synthesis of Ge films on copper substrates which can be used as electrodes and on electrochemical measurements using these films to investigate their cycling performance and rate capability.

Results and discussion

Fig. 1 shows the scanning electron microscope (SEM) images of an inverse opal structured Ge thin film on a copper electrode. The PMMA template was applied on the copper surface by dip-coating. The cavities in between the PMMA spheres were infiltrated by a 0.06 mol L^{-1} K_4Ge_9/en solution. After cross-linking the $[Ge_9]^{4-}$ clusters by impregnation with $GeCl_4$ and removing the solvent by flash annealing, amorphous Ge with an inverse opal structure was obtained (Scheme 1) after thermal and solvate assisted removal of PMMA and KCl, respectively. The pore size of the inverse opal network can easily be controlled by size variation of the applied PMMA spheres. The PMMA particle size was monitored using dynamic light scattering.

Here we obtained pores with an inner diameter of 275 nm, an outer diameter of 450 nm and a wall thickness of 90 nm. A close up SEM image reveals that the pores form a three-dimensional macroporous framework predetermined by the PMMA opal structure (Fig. 1b), providing essential electron and Li ion pathways for battery applications.

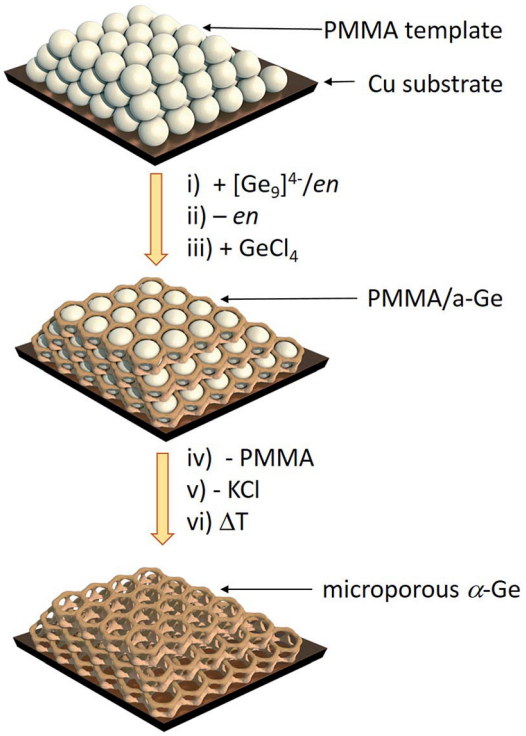

Scheme 1 Synthesis route to inverse Ge opals using a polymethyl methacrylate (PMMA) template.[27] (i) Infiltration of the PMMA beads (grey spheres) with a solution of K_4Ge_9 in en, (ii) solvent removal *via* evaporation, (iii) impregnation with $GeCl_4$, (iv) thermal removal of the PMMA template, (v) removal of KCl *via* washing with dimethyl sulfoxide (DMSO) and tetrahydrofuran (THF) leaving an inverse opal structure of a-Ge, and (vi) an optional crystallization step to obtain α-Ge.

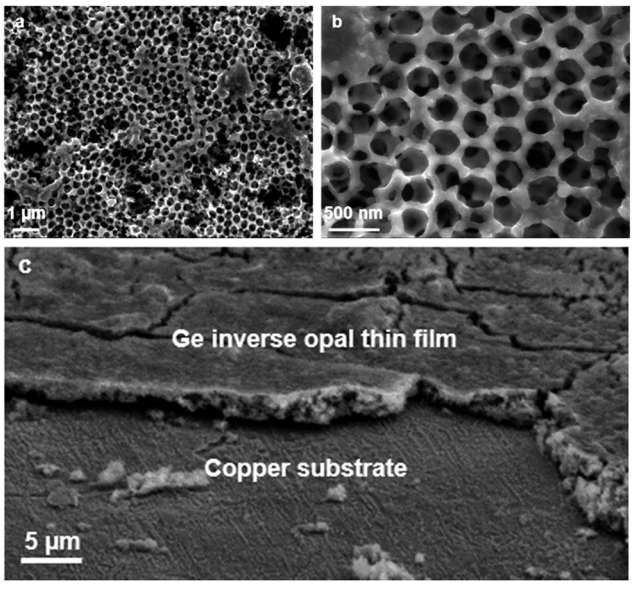

Fig. 1 SEM images of the Ge inverse opals on a copper substrate: (a) 10000× magnification, (b) 37000× magnification, and (c) SEM cross section of a thin film of the Ge inverse opals on a copper substrate, 1500× magnification. Measured film thickness: 2.5–3.0 µm.

Using this method, films with a thickness of around 2.5–3.0 μm can be obtained as was determined *via* SEM cross sections (Fig. 1c) and profilometry. Raman spectroscopy (Fig. S1 and S2†) shows that either amorphous a-Ge or crystalline α-Ge films can be obtained, depending on the preparation method. Energy-dispersive X-ray spectroscopy (EDS) also verifies that the obtained thin films consist of Ge (Fig. S3†).

Ge inverse opal films on a copper substrate can directly be used as electrodes for lithium batteries. Fig. 2a displays the voltage profiles for charge and discharge of the fourth cycle of a Ge inverse opal electrode with 5 wt% fluoroethylene carbonate (FEC) added to the electrolyte and a CV (constant voltage) step during discharge. Notice that no conductive materials such as carbon are added. All measurements displayed in Fig. 2 were performed based on a theoretical capacity of 1385 mA h g^{-1} for $Li_{15}Ge_4$, even though $Li_{17}Ge_4$ with a gravimetric capacity of 1564 mA h g^{-1} is the Li-richest phase.[40] This decision was made due to recent studies suggesting that $Li_{15}Ge_4$ is the Li-richest phase that is formed during lithiation of germanium electrodes in standard Li ion battery systems.[14,41,42]

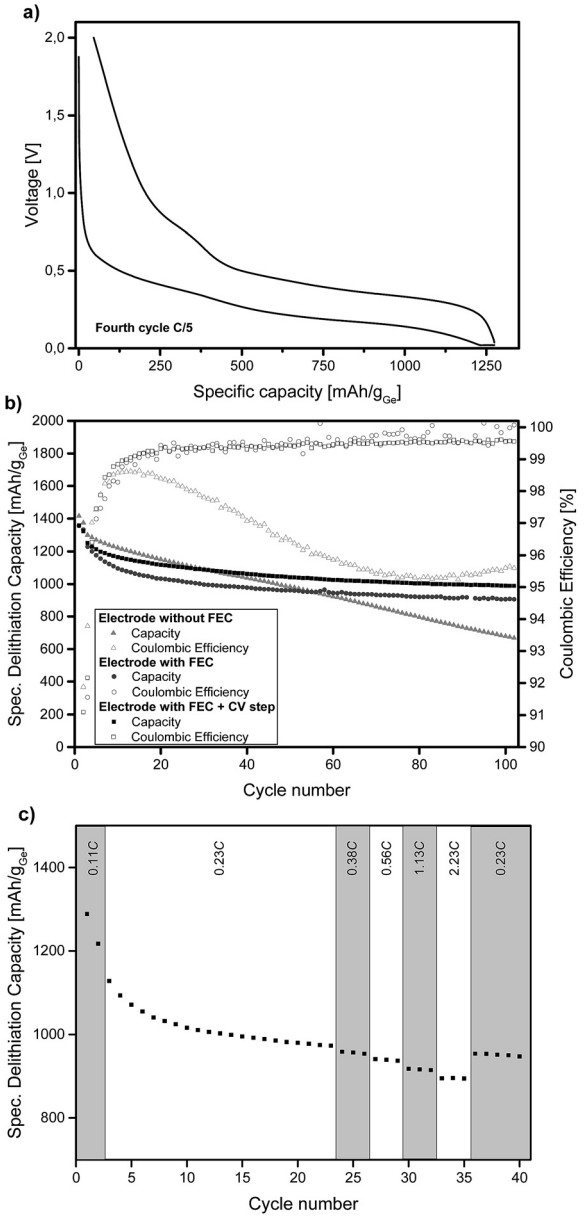

Fig. 2 Electrochemical measurements of the prepared Ge inverse opal electrodes cycled *vs.* metallic lithium. (a) Voltage profile of the fourth cycle of an electrode cycled in LP57 + 5 wt% FEC and with a CV step during lithiation at 20 mV. (b) Specific delithiation capacity over extended cycling at a rate of 0.2C (first two cycles at 0.1C). (c) Specific delithiation capacity at various C-rates of an electrode with FEC and an extra CV step.

During discharge and charge, the material shows long plateaus at ~0.25 V and 0.4–0.5 V, respectively. These can be assigned to lithiation and delithiation reactions. The small linear region at the end of discharge represents the CV step. The difference in lithiation and delithiation capacity is due to SEI formation. All electrodes shown in Fig. 2 consist of amorphous Ge. We also succeeded in obtaining α-Ge on our Cu substrates by applying an additional heating step. However, the α-Ge shows much lower capacity as compared to amorphous Ge (see Fig. S4†), mainly due to flaws in the inverse opal structure and connectivity issues caused by the more invasive temperature treatment. Therefore, amorphous Ge electrodes were used for further characterization.

Fig. 2b illustrates the cycling stability of a Ge inverse opal electrode with and without the addition of 5 wt% FEC to LP57 electrolyte (light grey triangles and dark grey circles, respectively). Additionally, a cell was assembled with the FEC-containing electrolyte and applying a constant voltage step during lithiation at 20 mV (see the Experimental section). All capacities mentioned in the following section are in very good agreement with the theoretical capacity of 1385 mA h g^{-1} for $Li_{15}Ge_4$.

The electrode cycled without FEC in the electrolyte shows a different cycling performance than the ones with FEC. Its starting delithiation capacity is ≈1420 mA h g^{-1} and the capacity retention after 100 cycles is only 47% with the capacity fading intensifying after about 60 cycles. The coulombic efficiency of this electrode is 91.9% after the second cycle. There is a strong decrease in efficiency after the first few cycles from ~98% to ~95%.

The electrodes cycled in LP57 + 5 wt% FEC show a much better capacity retention after 100 cycles and also much higher coulombic efficiencies. The electrode without an extra CV step during lithiation delivers an initial capacity of ≈1360 mA h g^{-1} and retains 67% of this capacity after 100 cycles. This value is mainly influenced by the relatively fast capacity fading during the initial cycles; the capacity retention for the last 80 cycles is 88%. During the very last cycles almost no capacity fading is observable and the capacity retention for the last 20 cycles is 98.3%. Therefore it can be assumed that even after more than 100 charge–discharge cycles, reasonably high capacities can be retained which we believe might be due to the high porosity of the electrode as shown in Fig. 3.

Compared to the cells cycled with FEC-free electrolyte, the capacity retention and coulombic efficiency are much higher and the electrodes with FEC are much more stable during cycling. The addition of FEC to the electrolyte clearly reduces

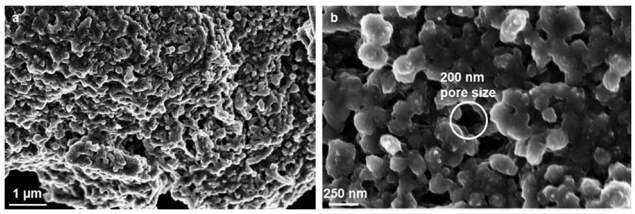

Fig. 3 SEM images of the Ge electrodes after 100 charge–discharge cycles: (a) 25000× magnification and (b) 80000× magnification.

the irreversible capacity. Similar effects of FEC on the cycling performance have been reported for Si based anodes for lithium-ion batteries.[43,44]

The coulombic efficiency after the second cycle for our Ge inverse opal electrode with FEC is 89.1% and when averaged from the 4th to the 100th cycle it is 99.5%. These coulombic efficiencies are significantly higher compared to those of previously reported Ge inverse opal electrodes[18] and much higher than those of different Ge thin film electrodes[14] and compare well with more difficult to prepare Ge nanowires with a coulombic efficiency of 99.9% after the 50th cycle,[31] macroporous Ge particles (99.5% after 200 cycles) and Ge nanoparticles (98.6% after 90 cycles).[32,33] Compared to these previously published results, our thin film Ge inverse opal electrodes show coulombic efficiencies that are higher than those of other Ge thin film electrodes and in the same range as those of porous Ge electrodes with different structures.

Ge inverse opal electrodes have been reported before. The method presented here however is very simple and can be performed with ordinary lab equipment avoiding more complex synthetic protocols utilizing GeH_4 as the Ge source for chemical vapor deposition (CVD). The electrodes fabricated *via* the wet-chemical route show a much slower capacity fading towards the last cycles, making them more attractive for potential long-lifetime applications,[22] and again compare well to Ge nanowires retaining up to 98% of their initial capacity after 100 cycles, 3D macroporous Ge particles with up to 96% capacity retention after 200 cycles and Ge nanoparticles with up to 86% capacity retention after 90 cycles.[45–47] Zitoun *et al.* designed Ge nanoparticles starting from the Zintl phase $Na_{12}Ge_{17}$ but obtained only 60% retention of their initial capacity after 10 cycles.[48] Recent studies have also focused on hybrid materials consisting of Ge@C core–shell particles and graphene oxide nanosheets; they have obtained up to 96.5% capacity retention after 600 cycles.[49]

Using a CV step during lithiation further improves the cycling performance of our electrodes, the curve in Fig. 2b is shifted towards higher capacities. The measured electrode shows an initial delithiation capacity of ≈1360 mA h g^{-1} and still delivers ~73% of this capacity after 100 cycles. The coulombic efficiency after the second cycle is 91.6% and when averaged from the 4th to the 100th cycle it is 99.3%. The capacity fading behaviour is similar to that of the cell without the CV step as discussed before. The capacity remains very stable after an initial drop; the capacity retention from the 20th cycle to the 100th cycle is ~89% and for the last 20 cycles it is ~99%. As expected, the capacities are higher than those in the case without the additional CV step; after 100 cycles this electrode exhibits a capacity of ≈990 mA h g^{-1} whilst the electrode without the CV step shows a capacity of ≈905 mA h g^{-1}. Fig. S5† displays the voltage profiles for charge and discharge of the 100th cycle of an electrode with FEC and the additional CV step. The good comparability of these voltage profiles to the ones shown in Fig. 2a further illustrates the cycling stability of the anode.

Fig. 2c shows the specific lithiation capacities of electrodes cycled in FEC-containing electrolyte and applying a CCCV procedure during lithiation at different C-rates ranging from 0.23C to 2.23C. The capacities show in good approximation a linear decrease of the specific capacity with increasing C-rates. At a rate of 0.56C, 96.3% of the capacity at 0.23C is obtained. Even at 2.23C, the electrode delivers 91.8% of the capacity compared to 0.23C. To sum up, a more than ten times higher C-rate means a capacity loss of only 8.2%. This shows that these Ge inverse opal electrodes exhibit outstanding intrinsic rate capabilities, which makes them promising for applications due to the fact that they can be charged and discharged relatively fast (their rate capability for applications where higher areal capacities are usually required still needs to be examined).

As shown in Fig. 3, the inverse opal structure of the Ge thin films has changed after 100 charge–discharge cycles, though the material still remains porous with randomly distributed vertical channels and pores with diameters between 200 and 300 nm, which are remnants of the initial pores. Retaining porosity is a key benefit for long-lifetime applications, since it offers Li ion pathways and therefore allows for high capacities, even after a large number of charge–discharge cycles at fast charging rates.

Conclusions

To conclude, Ge inverse opal structured electrodes were synthesized using a simple and effective wet-chemical procedure starting from $[Ge_9]^{4-}$ Zintl clusters. The preservation of the highly porous structure though changing its nature was demonstrated *via* SEM images before and after 100 charge–discharge cycles. The germanium electrodes show high capacities and capacity retentions as well as outstanding intrinsic rate capabilities. Their very high capacity retention after a small initial capacity fading makes them promising candidates for actual battery applications. The rather simple wet-chemical preparation method principally allows for an easy up-scaling process. Since related silicon–germanium mixed clusters $[Ge_{9-x}Si_x]^{4-}$ are also accessible,[28,29] a transfer to an alloyed $Si_{1-x}Ge_x$ system including the cheaper element silicon is imminent.

Experimental section

Synthesis of PMMA opals

The polymethyl methacrylate (PMMA) opals were prepared by emulsion polymerization according to Smarsly *et al.*[50] 35.5 g methyl methacrylate (MMA) and 5.0 mg sodium dodecyl sulfate (SDS) were added under stirring to water (98.0 mL), which had

been purged with nitrogen under reflux conditions for 0.5 h. After stirring at 90 °C for 1 h, 56.0 mg potassium persulfate dissolved in 2 mL water were added to the solution. The reaction mixture was stirred at 90 °C for an additional 2.5 h. The reaction was then stopped by ice cooling and further stirred at room temperature overnight. The white PMMA product was filtered and washed by several centrifugation and redispersion steps. A dispersion of 15 wt% PMMA in water was used for thin film preparation.

Synthesis of K_4Ge_9

Potassium (Merck, 99%) and germanium (ChemPur, 99.9999+) were added stoichiometrically with a 10 mol% excess of potassium into a stainless-steel tube.[51] The mixture was heated at 650 °C for 46 h. The purity of the product was checked *via* powder X-ray diffraction.

Preparation of the K_4Ge_9/en solution

50.0 mg (0.06 mmol) K_4Ge_9 were added into 1 mL ethylenediamine (en) and stirred at room temperature for 1 h.

Electrode preparation

Copper substrates ($\varnothing = 1.0$ cm) were punched out of copper foil (Advent, 0.20 mm thickness, 99.9%). The substrates were first cleaned by ultrasonication in an ammoniacal hydrogen peroxide solution and secondly by ultrasonication in diluted hydrochloric acid. The substrates were then dried under vacuum and stored under argon. The PMMA spheres were applied *via* dip-coating. After drying under vacuum at 100 °C for 4 h, the PMMA template was infiltrated with a K_4Ge_9/en solution by drop-casting 7 μL of the solution directly onto the substrate. After 1 h at 100 °C under vacuum, the substrates were treated with $GeCl_4$ vapour for 3 days. The PMMA template was then removed by heating at 500 °C for 5 min under vacuum. For optional crystallization, an additional heating step at 600 °C for 1 h under argon was applied. Finally, the substrates were washed with dimethyl sulfoxide (DMSO) and tetrahydrofuran (THF) and dried under vacuum. The germanium loading of the sample is estimated (see the ESI†) to be ≈0.31 mg (or ≈0.40 mg cm^{-2}). This is the maximum loading of Ge calculated from the amount of Ge in the K_4Ge_9/en solution.

For further analysis of the cycled electrodes, the cells were disassembled and the electrodes were extracted under argon. SEM and Raman spectroscopy were performed without any prior washing steps.

Analytical methods

Electrochemical measurements. The electrochemical measurements were performed in Swagelok T-cells which were assembled in an argon filled glovebox (O_2 and H_2O < 0.1 ppm, MBraun, Germany) with Ge as the working electrode ($\varnothing$ = 1.0 cm) and metallic lithium (thickness 0.45 mm, battery grade foil, 99.9%, Rockwood Lithium, USA) as the counter electrode ($\varnothing$ = 1.0 cm). Cell testing was done in a climate chamber (Binder, Germany) at 25 °C using a battery cycler (Series 4000, Maccor, USA). Two glass fiber separators (glass microfiber filter, 691, VWR, Germany, $\varnothing = 1.1$ cm) were used between the working and counter electrodes. 80 μL of LP57 electrolyte (1 M $LiPF_6$ in EC : EMC 3 : 7 wt/wt, <20 ppm H_2O, BASF, Germany) or LP57 with the addition of 5%$_{wt}$ FEC were used. For the cycling experiments, the first two cycles were performed at a 0.11 C-rate referenced to the theoretical capacity of 1385 mA h g^{-1} for $Li_{15}Ge_4$; for the other cycles, a rate of 0.23C was applied. The cells were cycled in the voltage range of 0.02–2 V *vs.* Li/Li$^+$. The measurements were stopped after 100 charge–discharge cycles. Rate tests were performed at rates of 0.23C, 0.38C, 0.56C, 1.13C and 2.23C after the first 20 cycles (two cycles at 0.11C and 18 cycles at 0.23C) in order to avoid a strong overlap of the capacity fading within the first 20 cycles in the rate test. Three cycles were performed at every rate. Lithiation of the germanium electrodes was either done in constant current (CC) mode or in constant current–constant voltage (CCCV) mode with a current limitation corresponding to 0.05C, while delithiation was done in CC mode.

Scanning electron microscopy. Scanning electron micrographs (SEM) were recorded with a JEOL JSM-6500F scanning electron microscope equipped with a field emission gun operated at 5–30 kV. Cross sections were recorded with a JEOL JCM 6000 equipped with a tungsten filament at 15 kV. SEM images of the electrodes after cycling were obtained with an FEI Helios NanoLab G3 UC scanning electron microscope equipped with a field emission gun operated at 3–5 kV.

Profilometry. The film thickness and roughness were characterized with a Veeco Dektak profilometer.

Dynamic light scattering. Dynamic light scattering (DLS) was carried out on a Malvern Zetasizer.

Raman spectroscopy. Raman spectroscopy was performed using a LabRAM HR UV-vis (HORIBA JOBIN YVON) Raman microscope (OLYMPUS BX41) with a SYMPHONY CCD detector and a He–Ne laser (λ = 633 nm).

Conflicts of interest

There are no conflicts to declare.

Acknowledgements

The authors acknowledge the funding of this work in the scope of the project “Solar Technologies go Hybrid”. R. J. gratefully acknowledges funding by BMW AG. The authors thank Dominique Marchand Fässler for the design of Scheme 1.

Notes and references

1 W.-J. Zhang, *J. Power Sources*, 2011, **196**, 13.
2 M. T. McDowell, S. W. Lee, W. D. Nix and Y. Cui, *Adv. Mater.*, 2013, **25**, 4966.
3 M. Obrovac and L. Christensen, *Electrochem. Solid-State Lett.*, 2004, **7**, A93.
4 M. Winter, J. O. Besenhard, M. E. Spahr and P. Novák, *Adv. Mater.*, 1998, **10**, 725.

5 L. Beaulieu, K. Eberman, R. Turner, L. Krause and J. Dahn, *Electrochem. Solid-State Lett.*, 2001, **4**, A137.
6 Y. Yao, M. T. McDowell, I. Ryu, H. Wu, N. Liu, L. Hu, W. D. Nix and Y. Cui, *Nano Lett.*, 2011, **11**, 2949.
7 D. Chen, X. Mei, G. Ji, M. Lu, J. Xie, J. Lu and J. Y. Lee, *Angew. Chem., Int. Ed. Engl.*, 2012, **51**, 2409.
8 H. Ma, F. Cheng, J. Y. Chen, J. Z. Zhao, C. S. Li, Z. L. Tao and J. Liang, *Adv. Mater.*, 2007, **19**, 4067.
9 C. K. Chan, H. Peng, G. Liu, K. McIlwrath, X. F. Zhang, R. A. Huggins and Y. Cui, *Nat. Nanotechnol.*, 2008, **3**, 31.
10 A. M. Morales and C. M. Lieber, *Science*, 1998, **279**, 208.
11 H. Kim, B. Han, J. Choo and J. Cho, *Angew. Chem., Int. Ed. Engl.*, 2008, **47**, 10151.
12 A. Esmanski and G. A. Ozin, *Adv. Funct. Mater.*, 2009, **19**, 1999.
13 J. Graetz, C. Ahn, R. Yazami and B. Fultz, *Electrochem. Solid-State Lett.*, 2003, **6**, A194.
14 H. Jung, P. K. Allan, Y.-Y. Hu, O. J. Borkiewicz, X.-L. Wang, W.-Q. Han, L.-S. Du, C. J. Pickard, P. J. Chupas, K. W. Chapman, A. J. Morris and C. P. Grey, *Chem. Mater.*, 2015, **27**, 1031.
15 X. H. Liu, S. Huang, S. T. Picraux, J. Li, T. Zhu and J. Y. Huang, *Nano Lett.*, 2011, **11**, 3991.
16 J. Graetz, C. C. Ahn, R. Yazami and B. Fultz, *J. Electrochem. Soc.*, 2004, **151**, A698.
17 C. Fuller and J. Severiens, *Phys. Rev.*, 1954, **96**, 21.
18 M. N. Obrovac and V. L. Chevrier, *Chem. Rev.*, 2014, **114**, 11444.
19 X. Meng, R. Al-Salman, J. Zhao, N. Borissenko, Y. Li and F. Endres, *Angew. Chem., Int. Ed. Engl.*, 2009, **48**, 2703.
20 H. Miguez, F. Meseguer, C. Lopez, M. Holgado, G. Andreasen, A. Mifsud and V. Fornés, *Langmuir*, 2000, **16**, 4405.
21 E. C. Hernan Miguez, F. Garcia-Santamaria, M. Ibisate, S. John, C. Lopez, F. Meseguer, J. P. Mondia, G. A. Ozin, O. Toader and H. M. van Driel, *Adv. Mater.*, 2001, **13**, 1634.
22 T. Song, Y. Jeon, M. Samal, H. Han, H. Park, J. Ha, D. K. Yi, J.-M. Choi, H. Chang, Y.-M. Choi and U. Paik, *Energy Environ. Sci.*, 2012, **5**, 9028.
23 J. Qin, X. Wang, M. Cao and C. Hu, *Chem.–Eur. J.*, 2014, **20**, 9675.
24 Y. Xu, X. Zhu, X. Zhou, X. Liu, Y. Liu, Z. Dai and J. Bao, *J. Phys. Chem. C*, 2014, **118**, 28502.
25 X. Zhou, L. Yu, X.-Y. Yu and X. W. D. Lou, *Adv. Energy Mater.*, 2016, **6**, 1601177.
26 X. Zhou, J. Bao, Z. Dai and Y.-G. Guo, *J. Phys. Chem. C*, 2013, **117**, 25367.
27 M. M. Bentlohner, M. Waibel, P. Zeller, K. Sarkar, P. Müller-Buschbaum, D. Fattakhova-Rohlfing and T. F. Fässler, *Angew. Chem., Int. Ed. Engl.*, 2016, **128**, 2487.
28 M. Waibel, C. B. Benda, B. Wahl and T. F. Fässler, *Chem.–Eur. J.*, 2011, **17**, 12928.
29 M. Waibel and T. F. Fässler, *Inorg. Chem.*, 2013, **52**, 5861.
30 N. Chandrasekharan and S. C. Sevov, *J. Electrochem. Soc.*, 2010, **157**, C140.
31 D. Sun, A. E. Riley, A. J. Cadby, E. K. Richman, S. D. Korlann and S. H. Tolbert, *Nature*, 2006, **441**, 1126.
32 G. S. Armatas and M. G. Kanatzidis, *Nature*, 2006, **441**, 1122.
33 S. D. Korlann, A. E. Riley, B. L. Kirsch, B. S. Mun and S. H. Tolbert, *J. Am. Chem. Soc.*, 2005, **127**, 12516.
34 G. S. Armatas and M. G. Kanatzidis, *Science*, 2006, **313**, 817.
35 G. S. Armatas and M. G. Kanatzidis, *J. Am. Chem. Soc.*, 2008, **130**, 11430.
36 G. S. Armatas and M. G. Kanatzidis, *Adv. Mater.*, 2008, **20**, 546.
37 A. E. R. Scott, D. Korlann, B. Simon Mun and S. H. Tolbert, *J. Phys. Chem. C*, 2009, **113**, 7697.
38 A. E. Riley, S. D. Korlann, E. K. Richman and S. H. Tolbert, *Angew. Chem., Int. Ed. Engl.*, 2005, **45**, 235.
39 S. Scharfe, F. Kraus, S. Stegmaier, A. Schier and T. F. Fässler, *Angew. Chem., Int. Ed. Engl.*, 2011, **50**, 3630.
40 M. Zeilinger and T. F. Fässler, *Dalton Trans.*, 2014, **43**, 14959.
41 L. Baggetto, E. J. Hensen and P. H. Notten, *Electrochim. Acta*, 2010, **55**, 7074.
42 K. C. Klavetter, S. M. Wood, Y.-M. Lin, J. L. Snider, N. C. Davy, A. M. Chockla, D. K. Romanovicz, B. A. Korgel, J.-W. Lee and A. Heller, *J. Power Sources*, 2013, **238**, 123.
43 V. Etacheri, O. Haik, Y. Goffer, G. A. Roberts, I. C. Stefan, R. Fasching and D. Aurbach, *Langmuir*, 2012, **28**, 965.
44 R. Jung, M. Metzger, D. Haering, S. Solchenbach, C. Marino, N. Tsiouvaras, C. Stinner and H. A. Gasteiger, *J. Electrochem. Soc.*, 2016, **163**, A1705.
45 B. Farbod, K. Cui, M. Kupsta, W. P. Kalisvaart, E. Memarzadeh, A. Kohandehghan, B. Zahiri and D. Mitlin, *J. Mater. Chem. A*, 2014, **2**, 16770.
46 H. Jia, R. Kloepsch, X. He, J. P. Badillo, P. Gao, O. Fromm, T. Placke and M. Winter, *Chem. Mater.*, 2014, **26**, 5683.
47 Y. Xiao and M. Cao, *ACS Appl. Mater. Interfaces*, 2014, **6**, 12922.
48 M. Pelosi, M. Tillard and D. Zitoun, *J. Nanopart. Res.*, 2013, **15**, 1872.
49 B. Wang, Z. Wen, J. Jin, X. Hong, S. Zhang and K. Rui, *J. Power Sources*, 2017, **342**, 521.
50 T. Wang, O. Sel, I. Djerdj and B. Smarsly, *Colloid Polym. Sci.*, 2006, **285**, 1.
51 T. F. Fässler, *Coord. Chem. Rev.*, 2001, **215**, 347.

Electronic Supplementary Material (ESI) for Sustainable Energy & Fuels.

Wet-chemical Route to Macroporous Inverse Opal Ge Anodes for Lithium Ion Batteries with High Capacity Retention

Sebastian Geier, [a] Roland Jung, [b] Kristina Peters, [c] Hubert A. Gasteiger,[b] Dina Fattakhova-Rohlfing,[d] and Thomas F. Fässler*[a]

[a, b] Department of Chemistry, Technische Universität München, Lichtenbergstraße 4, 85747 Garching, Germany

[c] Department of Chemistry and Center for NanoScience (CeNS), Ludwig-Maximilians-Universität München, Butenandtstr. 11, 81377 Munich, Germany

[d] Materials Synthesis and Processing, Institute of Energy and Climate Research (IEK-1), Wilhelm-Johnen-Straße, 52425 Jülich, Germany

Contents

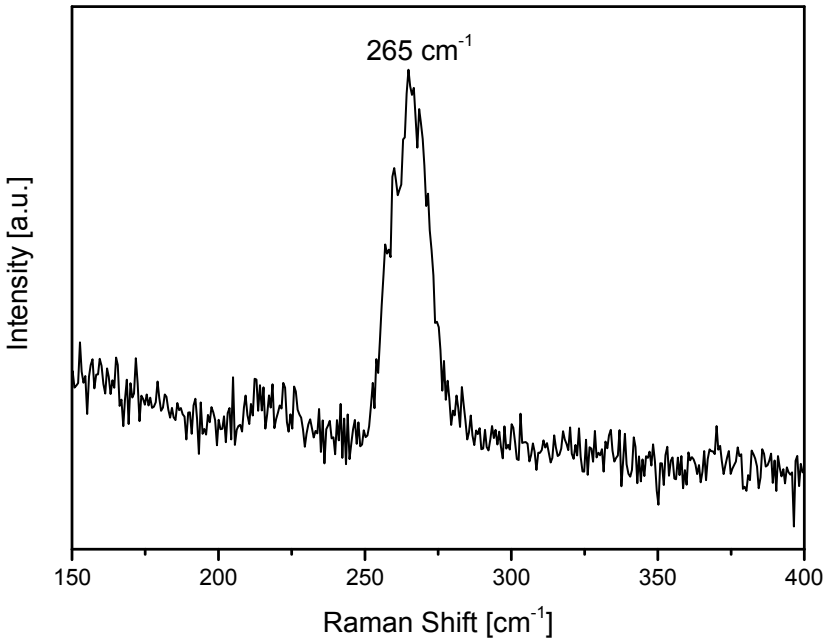

Figure S1: Raman spectrum of an amorphous Ge thin film on a Cu substrate.

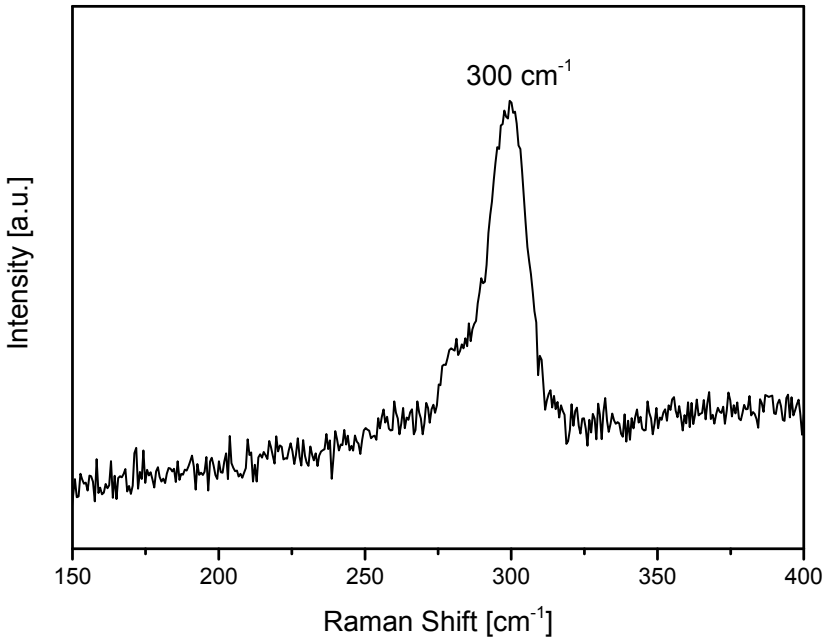

Figure S2: Raman spectrum of an α-Ge thin film on a Cu substrate.

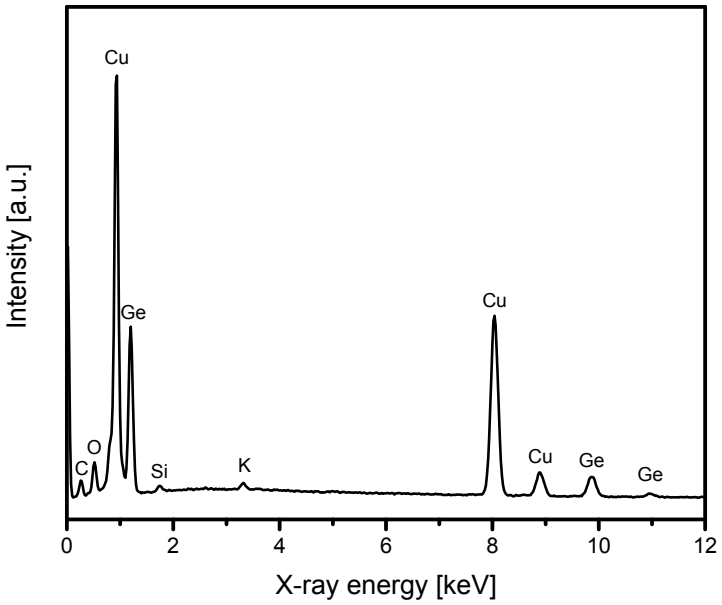

Figure S3: EDS spectrum of an amorphous Ge thin film on a Cu substrate.

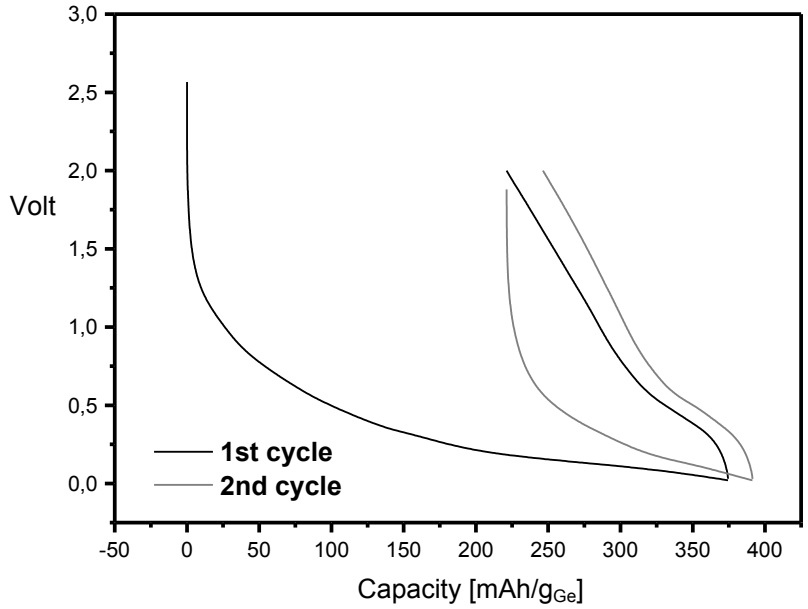

Figure S4: Voltage profile of the first and second cycle of an electrode made of an inverse opal-structured α-Ge thin film on a Cu substrate.

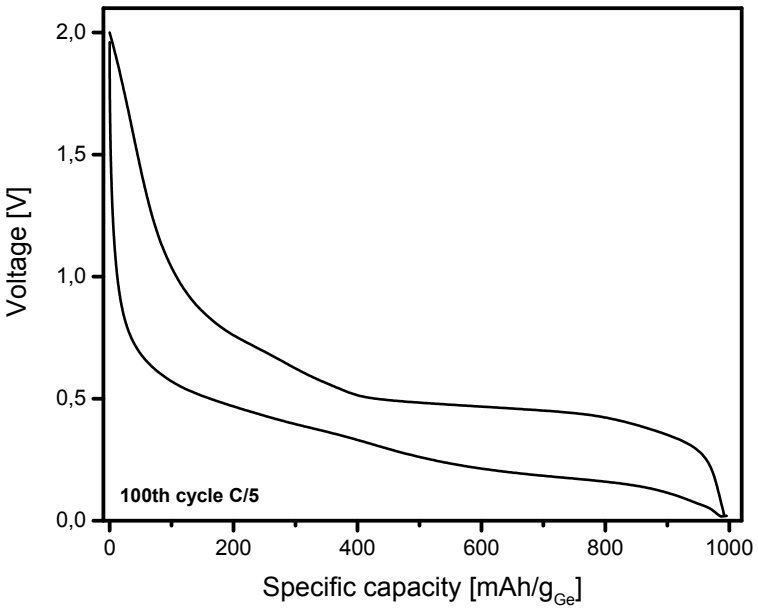

Figure S5: Voltage profile of the 100th cycle of an as-prepared inverse opal-structured amorphous Ge electrode.

Determination of the mass loading

The electrodes were prepared by infiltration of the PMMA spheres with 7 µL of a 0.1 mol/L K_4Ge_9/*en* solution which leads to a maximum loading of 282 µg of active material. Treatment with $GeCl_4$ vapor adds another 31 µg of Ge by cross-linking of the $[Ge_9]^{4-}$-clusters, and thus in total a maximum loading of 313 µg is achieved. The applied drop-casting process goes hand in hand with inevitable losses. Therefore we estimated the real mass loading of our electrodes by two different methods: using the before-mentioned concentration of the solution and the film thickness, we calculated the loading as follows:

$$V = \pi \times r^2 \times h \times (1 - 0.74) \quad (1)$$

where V is the volume, r the radius, h the height, and where the term between parentheses describes the spherical packing of the inverse opal structure, assuming a fcc packing of the PMMA opals.

This calculation under the assumption of an averaged film thickness of 2.75 µm gives a loading of 300 µg which is in good agreement with the maximum loading. For the determination of *C*-rates and capacities we went with a maximum loading of 313 µg to avoid an overestimation of our capacities.

4. Conclusion

Today's strive for higher energy densities is mostly driven by the desire to use Li-ion batteries as energy supply in electric vehicles, thereby reducing the worldwide emissions of CO_2. To reach this goal, novel and innovative cathode and anode materials are required to obtain specific energies ≥300 Wh/kg on a cell level. The safe and durable application of novel materials requires detailed knowledge on the mechanisms leading to battery cell aging and, eventually, to a total failure of the cell. In this PhD thesis, some of the root causes of battery cell degradation are investigated. The bottleneck in today's battery material development is the positive electrode (cathode) active material, yet also the other components like the negative electrode (anode) active material or the electrolytes need to be improved to reach the energy density targets. Ni-rich NMCs are probably the most promising class of future cathode materials and were primarily investigated within this PhD thesis. Additionally, degradation mechanisms related to the interaction between cathode and anode are also examined as well as aging phenomena related to silicon or germanium electrodes.

In section 3.1, aging mechanisms related to cathode material degradation were presented. In particular, first oxygen release from Li- and Mn-rich NMC (HE-NMC) is examined. By a quantification of the evolved gas amounts it is shown that oxygen is released from a thin layer (2-3 nm thickness) on the particle surface rather than from the bulk of the material via the alleged conversion of the Li_2MnO_3 phase. Upon oxygen release, the surface layer transforms into a spinel structure; its estimated thickness based on an analysis of the gases evolved during its formation is in good agreement with previous (S)TEM analyses. In section 3.1.2, the gas evolution from stoichiometric NMC111, NMC622, and NMC811 is investigated. We show that also for stoichiometric NMC materials oxygen release occurs from the surface, causing a transformation of the layered surface structure to spinel and rock-salt type phases. The formation of this surface layer is accompanied by a significant increase of the cathode impedance due to hindered Li-ion diffusion through the surface layer. In consequence, charging the NMC cathode above the threshold voltage for oxygen release will cause poor cycling performance. Oxygen release sets in when ~80% of the lithium ions are removed from the layered structure, which simultaneously marks the maximum amount of lithium ions that can be deintercalated to allow for stable charge/discharge cycling. Besides the surface reconstruction, another detrimental effect of oxygen release is the reaction of the released reactive oxygen with the electrolyte, causing *chemical* electrolyte oxidation. This type of

electrolyte oxidation is the dominant mechanism causing gas evolution in NMC-graphite cells charged to high voltages (section 3.1.3) and has to be distinguished from the *electrochemical* electrolyte oxidation. For conventionally used LP57 electrolyte (1 M $LiPF_6$ in EC/EMC 3:7), we show that at 25 °C significant *electrochemical* electrolyte oxidation sets in at potentials ≥5.0 V (section 3.1.3), which is well above the typical end-of-charge voltage of NMC-graphite cells. In section 3.1.4 we demonstrate for NMC622 that oxygen release occurs upon removal of ~80% of the lithium ions, independent of the temperature which was varied between 25 and 50 °C. Due to the constant state of charge for oxygen release, the onset potential for O_2 evolution decreases only by ~60 mV as the temperature is increased from 25 to 50 °C, which is a consequence of the lower overpotentials when the temperature is increased. This proves that it is an intrinsic chemical instability of the layered NMC structure at high degrees of delithiation that causes the release of oxygen, rather than a voltage dependent electrochemical process.

Due to the growing interest in applying highly Ni-rich NMCs like NMC811, we studied its storage stability at ambient air in comparison to NMC111, which is today's state-of-the-art cathode material. We found that NMC811 is very sensitive to air contact by forming a surface layer mostly composed of nickel carbonate mixed with minor quantities of hydroxide and crystal water. This surface layer is formed by a chemical reaction of the NMC surface with CO_2 and humidity and has a long-term effect on the cycling stability of NMC811-graphite cells, as it leads to a continuous increase of the NMC811 impedance and thereby causes a fast capacity fading. This sensitivity towards ambient air storage is not observed to today's most predominant NMC111 material, so that for the anticipated replacement of NMC111 by NMC811 for future battery cells, a strict requirement for inert atmospheres for storage and handling of the Ni-rich cathode material must be considered.

In section 3.2, transition metal dissolution from NMC111 and NMC622 and its subsequent deposition on the graphite anode was investigated using XAS. We found that Ni and Co deposit on the graphite electrode in the oxidation state +2. For Mn we could not clearly distinguish between +2 and +3 because of the very close edge position of the two oxidation states in the X-ray absorption spectrum. When the electrode was dried, a partial reduction of the Mn deposits to metallic Mn was detected. Furthermore, it was found that the total amounts of dissolved transition metals at high potentials ≥4.7 V are very similar for both cathode materials and that the dissolution of Ni, Co, and Mn is nearly stoichiometric. Consequently, for Ni-rich NMCs, Ni is the transition metal which is dissolved in largest absolute quantities.

Therefore, we investigated the detrimental effect of deposited Ni in comparison to Co and Mn. We demonstrated that deposits of all three metals lead to worse cycling performance of NMC-graphite cells and that the mechanism causing the capacity fading is a chemical decomposition reaction of the SEI with the metal deposits, leading to a loss of cycleable lithium due to the formation of additional SEI. Interestingly, the extent of SEI formation and the accompanied capacity fading caused by the deposition of Mn on the graphite anode is significantly larger than for Ni and Co which behave very similarly. This in turn implies that battery cell aging caused by transition metal dissolution may become less pronounced when state-of-the-art NMC111 is replaced by Ni-rich NMCs or even manganese-free materials like NCA in future Li-ion batteries.

Lastly, in section 3.3, aging mechanisms related to the anode active material were presented. In particular, we showed that FEC significantly improves the cycling stability of silicon anodes, but is continuously consumed during extended charge/discharge cycling. The total FEC consumption causes a significant increase of the silicon electrode impedance, leading to a rapid capacity drop. Therefore, the lifetime of the silicon anode is a linear function of the absolute amount of FEC expressed as $\mu mol_{FEC}/mg_{Si}$ rather than its concentration in the electrolyte (section 3.3.1). The rationale behind these observations is that FEC suppresses the reduction of other electrolyte components, e.g., EC, so that the SEI is almost exclusively formed by FEC decomposition products; yet, upon its total consumption, EC starts to be reduced, forming a much more resistive SEI on the silicon particles than the one derived only by FEC decomposition products. By quantifying the cumulative irreversible capacity during charge/discharge cycling and correlating it with the total amount of FEC in the cell, we showed that four electrons reduce one FEC molecule (section 3.3.1). This correlation in combination with the coulombic inefficiency per cycle allows a prediction of how much FEC is required in a Li-ion battery cell containing a Si anode in order to reach a defined lifetime of the battery cell.

Since for real applications, pure Si electrodes will likely be used in a mixture with graphite, Si-graphite composite electrodes with Si:graphite ratios of 60:10, 50:25, 35:45, and 20:65 were investigated in section 3.3.2. Two degradation phenomena were distinguished, viz., silicon particle degradation and electrode degradation, with the former being independent and the latter depending on the silicon:graphite ratio. Silicon particle degradation occurs because of the formation of a nanoporous, sponge-like structure of the silicon particles upon cycling yielding significant SEI growth concomitant with continuous FEC consumption as described

before. The electrode degradation mechanism instead depends on the silicon:graphite ratio because of the different microstructure caused by the different active material ratios. In particular, in electrodes with high graphite content, the graphite flakes form a conductive backbone within the electrode structure in which the silicon particles are dispersed. For low graphite contents, such a backbone structure does not exist, causing a hindered electronic pathway. The knowledge about the different aging phenomena is of particular importance when more and more silicon is added to conventional graphite electrodes in order to increase the energy density of a Li-ion battery.

In the last study presented in section 3.3.3, inverse opal structured germanium electrodes are investigated. The electrodes were free of carbon and binder and were successfully cycled versus metallic lithium yielding capacity values close to the theoretical ones, proving that the Ge structure is in complete electrochemical contact. Such artificially structured electrodes might become very interesting to enable improved Li-ion diffusion within the electrode, which is essential when high charge/discharge rates are required.

List of Figures

References

1. Y. Nishi, The Dawn of Lithium-Ion Batteries. *Electrochem. Soc. Interface*, **2016**, 25, 71-74.
2. M. Winter and J. O. Besenhard, Teil I: Wiederaufladbare Batterien. *Chemie in unserer Zeit*, **1999**, 33, 252-266.
3. M. Winter and J. O. Besenhard, Teil II: Wiederaufladbare Batterien. *Chemie in unserer Zeit*, **1999**, 33, 320-332.
4. D. Andre, H. Hain, P. Lamp, F. Maglia and B. Stiaszny, Future high-energy density anode materials from an automotive application perspective. *J. Mater. Chem. A*, **2017**, 5, 17174-17198.
5. D. Andre, S.-J. Kim, P. Lamp, S. F. Lux, F. Maglia, O. Paschos and B. Stiaszny, Future generations of cathode materials: an automotive industry perspective. *J. Mater. Chem. A*, **2015**, 3, 6709-6732.
6. Push EVs webpage, http://pushevs.com/2017/02/20/details-samsung-sdi-94-ah-battery-cell/, Accessed October 10, 2018.
7. O. Egbue and S. Long, Barriers to widespread adoption of electric vehicles: An analysis of consumer attitudes and perceptions. *Energy Policy*, **2012**, 48, 717-729.
8. E. J. Berg, C. Villevieille, D. Streich, S. Trabesinger and P. Novák, Rechargeable Batteries: Grasping for the Limits of Chemistry. *J. Electrochem. Soc.*, **2015**, 162, A2468-A2475.
9. O. Groeger, H. A. Gasteiger and J.-P. Suchsland, Review-Electromobility: Batteries or Fuel Cells? *J. Electrochem. Soc.*, **2015**, 162, A2605-A2622.
10. K. G. Gallagher, S. Goebel, T. Greszler, M. Mathias, W. Oelerich, D. Eroglu and V. Srinivasan, Quantifying the promise of lithium-air batteries for electric vehicles. *Energy Environ. Sci.*, **2014**, 7, 1555-1563.
11. G. E. Blomgren, The Development and Future of Lithium Ion Batteries. *J. Electrochem. Soc.*, **2017**, 164, A5019-A5025.
12. BMW i3 technical datasheet, http://www.bmw.de/de/neufahrzeuge/bmw-i/i3/2017/technische-daten.html, Accessed November 1, 2017.
13. F. T. Wagner, B. Lakshmanan and M. F. Mathias, Electrochemistry and the Future of the Automobile. *J. Phys. Chem. Lett.*, **2010**, 1, 2204-2219.
14. M. Wetjen, Studies on the Differentiation and Quantification of Degradation Phenomena in Silicon-Graphite Anodes for Lithium-Ion Batteries, *PhD Thesis*, Technical University Munich, **2018**.
15. M. Winter and R. J. Brodd, What are batteries, fuel cells, and supercapacitors? *Chem. Rev. (Washington, DC, U. S.)*, **2004**, 104, 4245-4269.
16. M. S. Whittingham, Electrical Energy Storage and Intercalation Chemistry. *Science*, **1976**, 192, 1126-1127.
17. M. S. Whittingham, Chalcogenide battery. US4009052, **1976**.
18. M. S. Whittingham, Lithium Batteries and Cathode Materials. *Chem. Rev. (Washington, DC, U. S.)*, **2004**, 104, 4271-4301.
19. A. Manthiram, *Lithium Batteries - Science and Technology*, Springer, New York, **2003**.
20. K. Mizushima, P. C. Jones, P. J. Wiseman and J. B. Goodenough, Li_xCoO_2 ($0<x<1$): A new cathode material for batteries of high energy density. *Materials Research Bulletin*, **1980**, 15, 783-789.
21. M. Armand, *Materials for Advanced Batteries*, Plenum Press, **1980**.
22. E. Peled and S. Menkin, Review—SEI: Past, Present and Future. *J. Electrochem. Soc.*, **2017**, 164, A1703-A1719.

23. E. Peled, D. Golodnitsky and J. Penciner, Handbook of Battery Materials, *The anode electrolyte interface*, Wiley-VCH, Weinheim, **2012**.
24. A. Yoshino, K. Sanechika and T. Nakajima, Secondary battery, US4668595. **1987**.
25. Y. Nishi, The development of lithium ion secondary batteries. *Chem. Rec.*, **2001**, 1, 406-413.
26. R. Fong, U. von Sacken and J. R. Dahn, Studies of Lithium Intercalation into Carbons Using Nonaqueous Electrochemical Cells. *J. Electrochem. Soc.*, **1990**, 137, 2009-2013.
27. E. Peled, The Electrochemical Behavior of Alkali and Alkaline Earth Metals in Nonaqueous Battery Systems—The Solid Electrolyte Interphase Model. *J. Electrochem. Soc.*, **1979**, 126, 2047-2051.
28. M. N. Obrovac and L. Christensen, Structural Changes in Silicon Anodes during Lithium Insertion/Extraction. *Electrochem. Solid-State Lett.*, **2004**, 7, A93-A96.
29. M. Wetjen, D. Pritzl, R. Jung, S. Solchenbach, R. Ghadimi and H. A. Gasteiger, Differentiating the Degradation Phenomena in Silicon-Graphite Electrodes for Lithium-Ion Batteries. *J. Electrochem. Soc.*, **2017**, 164, A2840-A2852.
30. R. Jung, M. Metzger, D. Haering, S. Solchenbach, C. Marino, N. Tsiouvaras, C. Stinner and H. A. Gasteiger, Consumption of Fluoroethylene Carbonate (FEC) on Si-C Composite Electrodes for Li-Ion Batteries. *J. Electrochem. Soc.*, **2016**, 163, A1705-A1716.
31. M. N. Obrovac and V. L. Chevrier, Alloy Negative Electrodes for Li-Ion Batteries. *Chem. Rev.*, **2014**, 114, 11444-11502.
32. M. T. McDowell, S. W. Lee, W. D. Nix and Y. Cui, 25th Anniversary Article: Understanding the Lithiation of Silicon and Other Alloying Anodes for Lithium-Ion Batteries. *Adv. Mater. (Weinheim, Ger.)*, **2013**, 25, 4966-4985.
33. V. Etacheri, O. Haik, Y. Goffer, G. A. Roberts, I. C. Stefan, R. Fasching and D. Aurbach, Effect of Fluoroethylene Carbonate (FEC) on the Performance and Surface Chemistry of Si-Nanowire Li-Ion Battery Anodes. *Langmuir*, **2012**, 28, 965-976.
34. H. Li, X. Huang, L. Chen, Z. Wu and Y. Liang, A high capacity nano-Si composite anode material for lithium rechargeable batteries. *Electrochem. Solid-State Lett.*, **1999**, 2, 547-549.
35. N.-S. Choi, K. H. Yew, K. Y. Lee, M. Sung, H. Kim and S.-S. Kim, Effect of fluoroethylene carbonate additive on interfacial properties of silicon thin-film electrode. *J. Power Sources*, **2006**, 161, 1254-1259.
36. E. Markevich, K. Fridman, R. Sharabi, R. Elazari, G. Salitra, H. E. Gottlieb, G. Gershinsky, A. Garsuch, G. Semrau, M. A. Schmidt and D. Aurbach, Amorphous columnar silicon anodes for advanced high voltage lithium ion full cells: dominant factors governing cycling performance. *J. Electrochem. Soc.*, **2013**, 160, A1824-A1833.
37. Y.-M. Lin, K. C. Klavetter, P. R. Abel, N. C. Davy, J. L. Snider, A. Heller and C. B. Mullins, High performance silicon nanoparticle anode in fluoroethylene carbonate-based electrolyte for Li-ion batteries. *Chem. Commun. (Cambridge, U. K.)*, **2012**, 48, 7268-7270.
38. R. Petibon, V. L. Chevrier, C. P. Aiken, D. S. Hall, S. R. Hyatt, R. Shunmugasundaram and J. R. Dahn, Studies of the Capacity Fade Mechanisms of $LiCoO_2$/Si-Alloy: Graphite Cells. *J. Electrochem. Soc.*, **2016**, 163, A1146-A1156.
39. H. Jung, P. K. Allan, Y.-Y. Hu, O. J. Borkiewicz, X.-L. Wang, W.-Q. Han, L.-S. Du, C. J. Pickard, P. J. Chupas, K. W. Chapman, A. J. Morris and C. P. Grey, Elucidation of the Local and Long-Range Structural Changes that Occur in Germanium Anodes in Lithium-Ion Batteries. *Chem. Mater.*, **2015**, 27, 1031-1041.

40. J. Graetz, C. C. Ahn, R. Yazami and B. Fultz, Nanocrystalline and Thin Film Germanium Electrodes with High Lithium Capacity and High Rate Capabilities. *J. Electrochem. Soc.*, **2004**, 151, A698-A702.
41. A. Laumann, M. Bremholm, P. Hald, M. Holzapfel, K. Thomas Fehr and B. B. Iversen, Rapid Green Continuous Flow Supercritical Synthesis of High Performance $Li_4Ti_5O_{12}$ Nanocrystals for Li Ion Battery Applications. *J. Electrochem. Soc.*, **2011**, 159, A166-A171.
42. M. Metzger, Studies on Fundamental Materials Degradation Mechanisms in Lithium-ion Batteries via On-line Electrochemical Mass Spectrometry, *PhD Thesis*, Technical University Munich, **2017**.
43. M. M. Thackeray, W. I. F. David, P. G. Bruce and J. B. Goodenough, Lithium insertion into manganese spinels. *Materials Research Bulletin*, **1983**, 18, 461-472.
44. Y. Xia, Y. Zhou and M. Yoshio, Capacity Fading on Cycling of 4 V Li / $LiMn_2O_4$ Cells. *J. Electrochem. Soc.*, **1997**, 144, 2593-2600.
45. T. Inoue and M. Sano, An Investigation of Capacity Fading of Manganese Spinels Stored at Elevated Temperature. *J. Electrochem. Soc.*, **1998**, 145, 3704-3707.
46. D. H. Jang, Y. J. Shin and S. M. Oh, Dissolution of Spinel Oxides and Capacity Losses in 4 V Li / $Li_xMn_2O_4$ Cells. *J. Electrochem. Soc.*, **1996**, 143, 2204-2211.
47. A. Du Pasquier, A. Blyr, P. Courjal, D. Larcher, G. Amatucci, B. Gérand and J. M. Tarascon, Mechanism for Limited 55°C Storage Performance of $Li_{1.05}Mn_{1.95}O_4$ Electrodes. *J. Electrochem. Soc.*, **1999**, 146, 428-436.
48. J. Cho and M. M. Thackeray, Structural Changes of $LiMn_2O_4$ Spinel Electrodes during Electrochemical Cycling. *J. Electrochem. Soc.*, **1999**, 146, 3577-3581.
49. K. Amine, H. Tukamoto, H. Yasuda and Y. Fujita, Preparation and electrochemical investigation of $LiMn_{2-x}Me_xO_4$ (Me: Ni, Fe, and x = 0.5, 1) cathode materials for secondary lithium batteries. *J. Power Sources*, **1997**, 68, 604-608.
50. Q. Zhong, A. Bonakdarpour, M. Zhang, Y. Gao and J. R. Dahn, Synthesis and Electrochemistry of $LiNi_xMn_{2-x}O_4$. *J. Electrochem. Soc.*, **1997**, 144, 205-213.
51. D. Pritzl, S. Solchenbach, M. Wetjen and H. A. Gasteiger, Analysis of Vinylene Carbonate (VC) as Additive in Graphite/$LiNi_{0.5}Mn_{1.5}O_4$ Cells. *J. Electrochem. Soc.*, **2017**, 164, A2625-A2635.
52. A. K. Padhi, K. S. Nanjundaswamy and J. B. Goodenough, Phospho-olivines as Positive-Electrode Materials for Rechargeable Lithium Batteries. *J. Electrochem. Soc.*, **1997**, 144, 1188-1194.
53. K. Amine, H. Yasuda and M. Yamachi, Olivine $LiCoPO_4$ as 4.8 V Electrode Material for Lithium Batteries. *Electrochem. and Solid-State Lett.*, **2000**, 3, 178-179.
54. N. N. Bramnik, K. G. Bramnik, T. Buhrmester, C. Baehtz, H. Ehrenberg and H. Fuess, Electrochemical and structural study of $LiCoPO_4$-based electrodes. *J. Solid State Electrochem.*, **2004**, 8, 558-564.
55. S. Okada, S. Sawa, M. Egashira, J.-i. Yamaki, M. Tabuchi, H. Kageyama, T. Konishi and A. Yoshino, Cathode properties of phospho-olivine $LiMPO_4$ for lithium secondary batteries. *J. Power Sources*, **2001**, 97-98, 430-432.
56. J. M. Lloris, C. Pérez Vicente and J. L. Tirado, Improvement of the Electrochemical Performance of $LiCoPO_4$ 5 V Material Using a Novel Synthesis Procedure. *Electrochem. Solid-State Lett.*, **2002**, 5, A234-A237.
57. J. N. Reimers and J. R. Dahn, Electrochemical and In Situ X-Ray Diffraction Studies of Lithium Intercalation in Li_xCoO_2. *J. Electrochem. Soc.*, **1992**, 139, 2091-2097.
58. S. Venkatraman, Y. Shin and A. Manthiram, Phase relationships and structural and chemical stabilities of charged $Li_{1-x}CoO_{2-\delta}$ and $Li_{1-x}Ni_{0.85}Co_{0.15}O_{2-\delta}$ Cathodes. *Electrochem. Solid-State Lett.*, **2003**, 6, A9-A12.

59. S. Venkatraman and A. Manthiram, Synthesis and Characterization of P3-Type $CoO_{2-\delta}$. *Chem. Mater.*, **2002**, 14, 3907-3912.
60. R. V. Chebiam, F. Prado and A. Manthiram, Soft Chemistry Synthesis and Characterization of Layered $Li_{1-x}Ni_{1-y}Co_yO_{2-\delta}$ ($0 \leq x \leq 1$ and $0 \leq y \leq 1$). *Chem. Mater.*, **2001**, 13, 2951-2957.
61. R. V. Chebiam, F. Prado and A. Manthiram, Comparison of the Chemical Stability of $Li_{1-x}CoO_2$ and $Li_{1-x}Ni_{0.85}Co_{0.15}O_2$ Cathodes. *J. Solid State Chem.*, **2002**, 163, 5-9.
62. J. R. Dahn, U. von Sacken and C. A. Michal, Structure and electrochemistry of $Li_{1\pm y}NiO_2$ and a new Li_2NiO_2 phase with the $Ni(OH)_2$ structure. *Solid State Ionics*, **1990**, 44, 87-97.
63. J. R. Dahn, U. von Sacken, M. W. Juzkow and H. Al-Janaby, Rechargeable $LiNiO_2$ / Carbon Cells. *J. Electrochem. Soc.*, **1991**, 138, 2207-2211.
64. G. Dutta, A. Manthiram, J. B. Goodenough and J. C. Grenier, Chemical synthesis and properties of $Li_{1-\delta-x}Ni_{1+\delta}O_2$ and $Li[Ni_2]O_4$. *J. Solid State Chem.*, **1992**, 96, 123-131.
65. A. Hirano, R. Kanno, Y. Kawamoto, Y. Takeda, K. Yamaura, M. Takano, K. Ohyama, M. Ohashi and Y. Yamaguchi, Relationship between non-stoichiometry and physical properties in $LiNiO_2$. *Solid State Ionics*, **1995**, 78, 123-131.
66. R. Kanno, H. Kubo, Y. Kawamoto, T. Kamiyama, F. Izumi, Y. Takeda and M. Takano, Phase Relationship and Lithium Deintercalation in Lithium Nickel Oxides. *J. Solid State Chem.*, **1994**, 110, 216-225.
67. T. Ohzuku, A. Ueda, M. Nagayama, Y. Iwakoshi and H. Komori, Comparative study of $LiCoO_2$, $LiNi_{1/2}Co_{1/2}O_2$ and $LiNiO_2$ for 4 volt secondary lithium cells. *Electrochim. Acta*, **1993**, 38, 1159-1167.
68. J. R. Dahn, E. W. Fuller, M. Obrovac and U. von Sacken, Thermal stability of Li_xCoO_2, Li_xNiO_2 and λ-MnO_2 and consequences for the safety of Li-ion cells. *Solid State Ionics*, **1994**, 69, 265-70.
69. Z. Zhang, D. Fouchard and J. R. Rea, Differential scanning calorimetry material studies: implications for the safety of lithium-ion cells. *J. Power Sources*, **1998**, 70, 16-20.
70. F. Schipper, E. M. Erickson, C. Erk, J.-Y. Shin, F. F. Chesneau and D. Aurbach, Review—Recent Advances and Remaining Challenges for Lithium Ion Battery Cathodes: I. Nickel-Rich, $LiNi_xCo_yMn_zO_2$. *J. Electrochem. Soc.*, **2017**, 164, A6220-A6228.
71. L. Croguennec, P. Deniard and R. Brec, Electrochemical Cyclability of Orthorhombic $LiMnO_2$: Characterization of Cycled Materials. *J. Electrochem. Soc.*, **1997**, 144, 3323-3330.
72. I. J. Davidson, R. S. McMillan, J. J. Murray and J. E. Greedan, Lithium-ion cell based on orthorhombic $LiMnO_2$. *J. Power Sources*, **1995**, 54, 232-235.
73. S. K. Mishra and G. Ceder, Structural stability of lithium manganese oxides. *Phys. Rev. B*, **1999**, 59, 6120-6130.
74. F. Capitaine, P. Gravereau and C. Delmas, A new variety of $LiMnO_2$ with a layered structure. *Solid State Ionics*, **1996**, 89, 197-202.
75. A. R. Armstrong and P. G. Bruce, Synthesis of layered $LiMnO_2$ as an electrode for rechargeable lithium batteries. *Nature*, **1996**, 381, 499-500.
76. R. Chen and M. S. Whittingham, Cathodic Behavior of Alkali Manganese Oxides from Permanganate. *J. Electrochem. Soc.*, **1997**, 144, L64-L67.
77. Y. Shao-Horn, S. A. Hackney, A. R. Armstrong, P. G. Bruce, R. Gitzendanner, C. S. Johnson and M. M. Thackeray, Structural Characterization of Layered $LiMnO_2$ Electrodes by Electron Diffraction and Lattice Imaging. *J. Electrochem. Soc.*, **1999**, 146, 2404-2412.

78. A. R. Armstrong, A. D. Robertson, R. Gitzendanner and P. G. Bruce, The Layered Intercalation Compounds $Li(Mn_{1-y}Co_y)O_2$: Positive Electrode Materials for Lithium–Ion Batteries. *J. Solid State Chem.*, **1999**, 145, 549-556.
79. C. Delmas and I. Saadoune, Electrochemical and physical properties of the $Li_xNi_{1-y}Co_yO_2$ phases. *Solid State Ionics*, **1992**, 53-56, 370-375.
80. W. Li and J. C. Currie, Morphology Effects on the Electrochemical Performance of $LiNi_{1-x}Co_xO_2$. *J. Electrochem. Soc.*, **1997**, 144, 2773-2779.
81. R. V. Chebiam, F. Prado and A. Manthiram, Structural Instability of Delithiated $Li_{1-x}Ni_{1-y}Co_yO_2$ Cathodes. *J. Electrochem. Soc.*, **2001**, 148, A49-A53.
82. A. M. Kannan and A. Manthiram, Structural Stability of $Li_{1-x}Ni_{0.85}Co_{0.15}O_2$ and $Li_{1-x}Ni_{0.85}Co_{0.12}Al_{0.03}O_2$ Cathodes at Elevated Temperatures. *J. Electrochem. Soc.*, **2003**, 150, A349-A353.
83. W. Liu, P. Oh, X. Liu, M.-J. Lee, W. Cho, S. Chae, Y. Kim and J. Cho, Nickel-Rich Layered Lithium Transition Metal Oxide for High-Energy Lithium-Ion Batteries. *Angew. Chem., Int. Ed.*, **2015**, 54, 4440-4457.
84. M. K. Aydinol, A. F. Kohan, G. Ceder, K. Cho and J. Joannopoulos, Ab initio study of lithium intercalation in metal oxides and metal dichalcogenides. *Phys. Rev. B*, **1997**, 56, 1354-1365.
85. Y.-I. Jang, B. Huang, H. Wang, G. R. Maskaly, G. Ceder, D. R. Sadoway, Y.-M. Chiang, H. Liu and H. Tamura, Synthesis and characterization of $LiAl_yCo_{1-y}O_2$ and $LiAl_yNi_{1-y}O_2$. *J. Power Sources*, **1999**, 81-82, 589-593.
86. S. Madhavi, G. V. Subba Rao, B. V. R. Chowdari and S. F. Y. Li, Effect of aluminium doping on cathodic behaviour of $LiNi_{0.7}Co_{0.3}O_2$. *J. Power Sources*, **2001**, 93, 156-162.
87. T. Ohzuku, A. Ueda and M. Kouguchi, Synthesis and Characterization of $LiAl_{1/4}Ni_{3/4}O_2$ ($R\bar{3}m$) for Lithium-Ion (Shuttlecock) Batteries. *J. Electrochem. Soc.*, **1995**, 142, 4033-4039.
88. Q. Zhong and U. von Sacken, Crystal structures and electrochemical properties of $LiAl_yNi_{1-y}O_2$ solid solution. *J. Power Sources*, **1995**, 54, 221-223.
89. C. Julien, G. A. Nazri and A. Rougier, Electrochemical performances of layered $LiM_{1-y}M_{y'}O_2$ (M=Ni, Co; M′=Mg, Al, B) oxides in lithium batteries. *Solid State Ionics*, **2000**, 135, 121-130.
90. Y. I. Jang, B. Huang, H. Wang, D. R. Sadoway, G. Ceder, Y. M. Chiang, H. Liu and H. Tamura, $LiAl_yCo_{1-y}O_2$ ($R\bar{3}m$) Intercalation Cathode for Rechargeable Lithium Batteries. *J. Electrochem. Soc.*, **1999**, 146, 862-868.
91. N. Nitta, F. Wu, J. T. Lee and G. Yushin, Li-ion battery materials: present and future. *Materials Today*, **2015**, 18, 252-264.
92. I. Belharouak, W. Lu, D. Vissers and K. Amine, Safety characteristics of $Li(Ni_{0.8}Co_{0.15}Al_{0.05})O_2$ and $Li(Ni_{1/3}Co_{1/3}Mn_{1/3})O_2$. *Electrochem. Comm.*, **2006**, 8, 329-335.
93. I. Belharouak, D. Vissers and K. Amine, Thermal Stability of the $Li(Ni_{0.8}Co_{0.15}Al_{0.05})O_2$ Cathode in the Presence of Cell Components. *J. Electrochem. Soc.*, **2006**, 153, A2030-A2035.
94. S.-M. Bak, K.-W. Nam, W. Chang, X. Yu, E. Hu, S. Hwang, E. A. Stach, K.-B. Kim, K. Y. Chung and X.-Q. Yang, Correlating Structural Changes and Gas Evolution during the Thermal Decomposition of Charged $Li_xNi_{0.8}Co_{0.15}Al_{0.05}O_2$ Cathode Materials. *Chem. Mater.*, **2013**, 25, 337-351.
95. Z. Liu, A. Yu and J. Y. Lee, Synthesis and characterization of $LiNi_{1-x-y}Co_xMn_yO_2$ as the cathode materials of secondary lithium batteries. *J. Power Sources*, **1999**, 81-82, 416-419.
96. Z. Lu, D. D. MacNeil and J. R. Dahn, Layered $Li[Ni_xCo_{1-2x}Mn_x]O_2$ Cathode Materials for Lithium-Ion Batteries. *Electrochem. Solid-State Lett.*, **2001**, 4, A200-A203.

97. T. Ohzuku and Y. Makimura, Layered Lithium Insertion Material of $LiCo_{1/3}Ni_{1/3}Mn_{1/3}O_2$ for Lithium-Ion Batteries. *Chemistry Letters*, **2001**, 30, 642-643.
98. S.-M. Bak, E. Hu, Y. Zhou, X. Yu, S. D. Senanayake, S.-J. Cho, K.-B. Kim, K. Y. Chung, X.-Q. Yang and K.-W. Nam, Structural Changes and Thermal Stability of Charged $LiNi_xMn_yCo_zO_2$ Cathode Materials Studied by Combined In Situ Time-Resolved XRD and Mass Spectroscopy. *ACS Appl. Mater. Interfaces*, **2014**, 6, 22594-22601.
99. H.-J. Noh, S. Youn, C. S. Yoon and Y.-K. Sun, Comparison of the structural and electrochemical properties of layered $Li[Ni_xCo_yMn_z]O_2$ (x = 1/3, 0.5, 0.6, 0.7, 0.8 and 0.85) cathode material for lithium-ion batteries. *J. Power Sources*, **2013**, 233, 121-130.
100. H. Konishi, T. Yuasa and M. Yoshikawa, Thermal stability of $Li_{1-y}Ni_xMn_{(1-x)/2}Co_{(1-x)/2}O_2$ layer-structured cathode materials used in Li-Ion batteries. *J. Power Sources*, **2011**, 196, 6884-6888.
101. R. Jung, M. Metzger, F. Maglia, C. Stinner and H. A. Gasteiger, Oxygen Release and Its Effect on the Cycling Stability of $LiNi_xMn_yCo_zO_2$ (NMC) Cathode Materials for Li-Ion Batteries. *J. Electrochem. Soc.*, **2017**, 164, A1361-A1377.
102. J. M. Paulsen, H.-K. Park and Y. H. Kwon, Process of Making Cathode Material Containing Ni-based Lithium Transition Metal Oxide. US 8574541, **2013**.
103. J. Cho, C. S. Kim and S. I. Yoo, Improvement of Structural Stability of $LiCoO_2$ Cathode during Electrochemical Cycling by Sol-Gel Coating of SnO_2. *Electrochem. Solid-State Lett.*, **2000**, 3, 362-365.
104. J. Cho, Y. J. Kim and B. Park, $LiCoO_2$ Cathode Material That Does Not Show a Phase Transition from Hexagonal to Monoclinic Phase. *J. Electrochem. Soc.*, **2001**, 148, A1110-A1115.
105. A. M. Kannan, L. Rabenberg and A. Manthiram, High Capacity Surface-Modified $LiCoO_2$ Cathodes for Lithium-Ion Batteries. *Electrochem. Solid-State Lett.*, **2003**, 6, A16-A18.
106. J. Cho, Y.-W. Kim, B. Kim, J.-G. Lee and B. Park, A Breakthrough in the Safety of Lithium Secondary Batteries by Coating the Cathode Material with $AlPO_4$ Nanoparticles. *Angew. Chem. Int. Ed.*, **2003**, 42, 1618-1621.
107. J. Cho, Y. J. Kim and B. Park, Novel $LiCoO_2$ Cathode Material with Al_2O_3 Coating for a Li Ion Cell. *Chem. Mater.*, **2000**, 12, 3788-3791.
108. S. U. Woo, C. S. Yoon, K. Amine, I. Belharouak and Y. K. Sun, Significant improvement of electrochemical performance of AlF_3-coated $Li[Ni_{0.8}Co_{0.1}Mn_{0.1}]O_2$ cathode materials. *J. Electrochem. Soc.*, **2007**, 154, A1005-A1009.
109. D. Wang, X. Li, Z. Wang, H. Guo, Z. Huang, L. Kong and J. Ru, Improved high voltage electrochemical performance of Li_2ZrO_3-coated $LiNi_{0.5}Co_{0.2}Mn_{0.3}O_2$ cathode material. *Journal of Alloys and Compounds*, **2015**, 647, 612-619.
110. Y. Chen, Y. Zhang, B. Chen, Z. Wang and C. Lu, An approach to application for $LiNi_{0.6}Co_{0.2}Mn_{0.2}O_2$ cathode material at high cutoff voltage by TiO_2 coating. *J. Power Sources*, **2014**, 256, 20-27.
111. W. Cho, S.-M. Kim, J. H. Song, T. Yim, S.-G. Woo, K.-W. Lee, J.-S. Kim and Y.-J. Kim, Improved electrochemical and thermal properties of nickel rich $LiNi_{0.6}Co_{0.2}Mn_{0.2}O_2$ cathode materials by SiO_2 coating. *J. Power Sources*, **2015**, 282, 45-50.
112. Y. Shi, M. Zhang, D. Qian and Y. S. Meng, Ultrathin Al_2O_3 Coatings for Improved Cycling Performance and Thermal Stability of $LiNi_{0.5}Co_{0.2}Mn_{0.3}O_2$ Cathode Material. *Electrochim. Acta*, **2016**, 203, 154-161.
113. D. Mohanty, K. Dahlberg, D. M. King, L. A. David, A. S. Sefat, D. L. Wood, C. Daniel, S. Dhar, V. Mahajan, M. Lee and F. Albano, Modification of Ni-Rich FCG

NMC and NCA Cathodes by Atomic Layer Deposition: Preventing Surface Phase Transitions for High-Voltage Lithium-Ion Batteries. *Sci. Rep.*, **2016**, 6, 26532.

114. Y.-K. Sun, S.-T. Myung, M.-H. Kim, J. Prakash and K. Amine, Synthesis and characterization of $Li[(Ni_{0.8}Co_{0.1}Mn_{0.1})_{0.8}(Ni_{0.5}Mn_{0.5})_{0.2}]O_2$ with a microscale core-shell structure as the positive electrode material for lithium batteries. *J. Am. Chem. Soc.*, **2005**, 127, 13411-13418.
115. Y.-K. Sun, S.-T. Myung, B.-C. Park, J. Prakash, I. Belharouak and K. Amine, High-energy cathode material for long-life and safe lithium batteries. *Nat. Mater.*, **2009**, 8, 320-324.
116. Y.-K. Sun, B.-R. Lee, H.-J. Noh, H. Wu, S.-T. Myung and K. Amine, A novel concentration-gradient $Li[Ni_{0.83}Co_{0.07}Mn_{0.10}]O_2$ cathode material for high-energy lithium-ion batteries. *J. Mater. Chem.*, **2011**, 21, 10108-10112.
117. Y.-K. Sun, D.-H. Kim, C. S. Yoon, S.-T. Myung, J. Prakash and K. Amine, A novel cathode material with a concentration-gradient for high-energy and safe lithium-ion batteries. *Adv. Funct. Mater.*, **2010**, 20, 485-491.
118. Y.-K. Sun, Z. Chen, H.-J. Noh, D.-J. Lee, H.-G. Jung, Y. Ren, S. Wang, C. S. Yoon, S.-T. Myung and K. Amine, Nanostructured high-energy cathode materials for advanced lithium batteries. *Nat. Mater.*, **2012**, 11, 942-947.
119. J.-Y. Liao and A. Manthiram, Surface-modified concentration-gradient Ni-rich layered oxide cathodes for high-energy lithium-ion batteries. *J. Power Sources*, **2015**, 282, 429-436.
120. J. H. Lee, C. S. Yoon, J.-Y. Hwang, S.-J. Kim, F. Maglia, P. Lamp, S.-T. Myung and Y.-K. Sun, High-energy-density lithium-ion battery using a carbon-nanotube-Si composite anode and a compositionally graded $Li[Ni_{0.85}Co_{0.05}Mn_{0.10}]O_2$ cathode. *Energ. Environ. Sci.*, **2016**, 9, 2152-2158.
121. U.-H. Kim, S.-T. Myung, C. S. Yoon and Y.-K. Sun, Extending the Battery Life Using an Al-Doped $Li[Ni_{0.76}Co_{0.09}Mn_{0.15}]O_2$ Cathode with Concentration Gradients for Lithium Ion Batteries. *ACS Energy Lett.*, **2017**, 2, 1848-1854.
122. M. M. Thackeray, C. S. Johnson, K. Amine and J. Kim, Lithium metal oxide electrodes for lithium cells and batteries. US6677082, **2001**.
123. Z. Lu, D. D. MacNeil and J. R. Dahn, Layered Cathode Materials $Li[Ni_xLi_{(1/3-2x/3)}Mn_{(2/3-x/3)}]O_2$ for Lithium-Ion Batteries. *Electrochem. Solid-State Lett.*, **2001**, 4, A191-A194.
124. J. Hong, H. Gwon, S.-K. Jung, K. Ku and K. Kang, Review—Lithium-Excess Layered Cathodes for Lithium Rechargeable Batteries. *J. Electrochem. Soc.*, **2015**, 162, A2447-A2467.
125. J. Zheng, W. H. Kan and A. Manthiram, Role of Mn Content on the Electrochemical Properties of Nickel-Rich Layered $LiNi_{0.8-x}Co_{0.1}Mn_{0.1+x}O_2$ ($0.0 \leq x \leq 0.08$) Cathodes for Lithium-Ion Batteries. *ACS Appl. Mater. Interfaces*, **2015**, 7, 6926-6934.
126. J. C. Burns, A. Kassam, N. N. Sinha, L. E. Downie, L. Solnickova, B. M. Way and J. R. Dahn, Predicting and Extending the Lifetime of Li-Ion Batteries. *J. Electrochem. Soc.*, **2013**, 160, A1451-A1456.
127. R. Dedryvere, D. Foix, S. Franger, S. Patoux, L. Daniel and D. Gonbeau, Electrode/electrolyte interface reactivity in high-voltage spinel $LiMn_{1.6}Ni_{0.4}O_4/Li_4Ti_5O_{12}$ lithium-ion battery. *J. Phys. Chem. C*, **2010**, 114, 10999-11008.
128. M. Nie, D. Chalasani, D. P. Abraham, Y. Chen, A. Bose and B. L. Lucht, Lithium Ion Battery Graphite Solid Electrolyte Interphase Revealed by Microscopy and Spectroscopy. *J. Phys. Chem. C*, **2013**, 117, 1257-1267.

129. M. Nie, D. P. Abraham, Y. Chen, A. Bose and B. L. Lucht, Silicon Solid Electrolyte Interphase (SEI) of Lithium Ion Battery Characterized by Microscopy and Spectroscopy. *J. Phys. Chem. C*, **2013**, 117, 13403-13412.
130. S.-H. Kang, D. P. Abraham, W.-S. Yoon, K.-W. Nam and X.-Q. Yang, First-cycle irreversibility of layered Li–Ni–Co–Mn oxide cathode in Li-ion batteries. *Electrochim. Acta*, **2008**, 54, 684-689.
131. S.-H. Kang, W.-S. Yoon, K.-W. Nam, X.-Q. Yang and D. P. Abraham, Investigating the first-cycle irreversibility of lithium metal oxide cathodes for Li batteries. *J. Mater. Sci.*, **2008**, 43, 4701-4706.
132. I. Buchberger, S. Seidlmayer, A. Pokharel, M. Piana, J. Hattendorff, P. Kudejova, R. Gilles and H. A. Gasteiger, Aging Analysis of Graphite/$LiNi_{1/3}Mn_{1/3}Co_{1/3}O_2$ Cells Using XRD, PGAA, and AC Impedance. *J. Electrochem. Soc.*, **2015**, 162, A2737-A2746.
133. L. Y. Beaulieu, K. W. Eberman, R. L. Turner, L. J. Krause and J. R. Dahn, Colossal reversible volume changes in lithium alloys. *Electrochem. Solid-State Lett.*, **2001**, 4, A137-A140.
134. X.-G. Yang, Y. Leng, G. Zhang, S. Ge and C.-Y. Wang, Modeling of lithium plating induced aging of lithium-ion batteries: Transition from linear to nonlinear aging. *J. Power Sources*, **2017**, 360, 28-40.
135. J. A. Gilbert, J. Bareño, T. Spila, S. E. Trask, D. J. Miller, B. J. Polzin, A. N. Jansen and D. P. Abraham, Cycling Behavior of NCM523/Graphite Lithium-Ion Cells in the 3–4.4 V Range: Diagnostic Studies of Full Cells and Harvested Electrodes. *J. Electrochem. Soc.*, **2017**, 164, A6054-A6065.
136. D. Aurbach, K. Gamolsky, B. Markovsky, Y. Gofer, M. Schmidt and U. Heider, On the use of vinylene carbonate (VC) as an additive to electrolyte solutions for Li-ion batteries. *Electrochim. Acta*, **2002**, 47, 1423-1439.
137. K. Xu, Electrolytes and Interphases in Li-Ion Batteries and Beyond. *Chem. Rev. (Washington, DC, U. S.)*, **2014**, 114, 11503-11618.
138. L. Ma, D. Y. Wang, L. E. Downie, J. Xia, K. J. Nelson, N. N. Sinha and J. R. Dahn, Ternary and Quaternary Electrolyte Additive Mixtures for Li-Ion Cells That Promote Long Lifetime, High Discharge Rate and Better Safety. *J. Electrochem. Soc.*, **2014**, 161, A1261-A1265.
139. D. Y. Wang, N. N. Sinha, R. Petibon, J. C. Burns and J. R. Dahn, A systematic study of well-known electrolyte additives in LiCoO2/graphite pouch cells. *J. Power Sources*, **2014**, 251, 311-318.
140. T. Waldmann, M. Wilka, M. Kasper, M. Fleischhammer and M. Wohlfahrt-Mehrens, Temperature dependent ageing mechanisms in Lithium-ion batteries - A Post-Mortem study. *J. Power Sources*, **2014**, 262, 129-135.
141. P. Arora, R. E. White and M. Doyle, Capacity Fade Mechanisms and Side Reactions in Lithium-Ion Batteries. *J. Electrochem. Soc.*, **1998**, 145, 3647-3667.
142. J. Wandt, C. Marino, H. A. Gasteiger, P. Jakes, R.-A. Eichel and J. Granwehr, Operando electron paramagnetic resonance spectroscopy - formation of mossy lithium on lithium anodes during charge-discharge cycling. *Energ. Environ. Sci.*, **2015**, 8, 1358-1367.
143. M. C. Smart and B. V. Ratnakumar, Effects of Electrolyte Composition on Lithium Plating in Lithium-Ion Cells. *J. Electrochem. Soc.*, **2011**, 158, A379-A389.
144. Z. Li, J. Huang, B. Yann Liaw, V. Metzler and J. Zhang, A review of lithium deposition in lithium-ion and lithium metal secondary batteries. *J. Power Sources*, **2014**, 254, 168-182.

145. J. Wandt, Operando Characterization of Fundamental Reaction Mechanisms and Degradation Processes in Lithium-Ion and Lithium-Oxygen Batteries, *PhD Thesis*, Technical University Munich, **2017**.
146. A. O. Kondrakov, A. Schmidt, J. Xu, H. Geßwein, R. Mönig, P. Hartmann, H. Sommer, T. Brezesinski and J. Janek, Anisotropic Lattice Strain and Mechanical Degradation of High- and Low-Nickel NCM Cathode Materials for Li-Ion Batteries. *J. Phys. Chem. C*, **2017**, 121, 3286-3294.
147. R. Jung, M. Metzger, F. Maglia, C. Stinner and H. A. Gasteiger, Chemical versus Electrochemical Electrolyte Oxidation on NMC111, NMC622, NMC811, LNMO, and Conductive Carbon. *J. Phys. Chem. Lett.*, **2017**, 4820-4825.
148. D. P. Abraham, R. D. Twesten, M. Balasubramanian, I. Petrov, J. McBreen and K. Amine, Surface changes on $LiNi_{0.8}Co_{0.2}O_2$ particles during testing of high-power lithium-ion cells. *Electrochem. Commun.*, **2002**, 4, 620-625.
149. D. P. Abraham, R. D. Twesten, M. Balasubramanian, J. Kropf, D. Fischer, J. McBreen, I. Petrov and K. Amine, Microscopy and Spectroscopy of Lithium Nickel Oxide-Based Particles Used in High Power Lithium-Ion Cells. *J. Electrochem. Soc.*, **2003**, 150, A1450-A1456.
150. S. Muto, Y. Sasano, K. Tatsumi, T. Sasaki, K. Horibuchi, Y. Takeuchi and Y. Ukyo, Capacity-Fading Mechanisms of $LiNiO_2$-Based Lithium-Ion Batteries: II. Diagnostic Analysis by Electron Microscopy and Spectroscopy. *J. Electrochem. Soc.*, **2009**, 156, A371-A377.
151. S. Hwang, W. Chang, S. M. Kim, D. Su, D. H. Kim, J. Y. Lee, K. Y. Chung and E. A. Stach, Investigation of Changes in the Surface Structure of $Li_xNi_{0.8}Co_{0.15}Al_{0.05}O_2$ Cathode Materials Induced by the Initial Charge. *Chem. Mater.*, **2014**, 26, 1084-1092.
152. J. Wandt, A. Freiberg, R. Thomas, Y. Gorlin, A. Siebel, R. Jung, H. A. Gasteiger and M. Tromp, Transition metal dissolution and deposition in Li-ion batteries investigated by operando X-ray absorption spectroscopy. *J. Mater. Chem. A*, **2016**, 4, 18300-18305.
153. D. R. Gallus, R. Schmitz, R. Wagner, B. Hoffmann, S. Nowak, I. Cekic-Laskovic, R. W. Schmitz and M. Winter, The influence of different conducting salts on the metal dissolution and capacity fading of NCM cathode material. *Electrochim. Acta*, **2014**, 134, 393-398.
154. H. Zheng, Q. Sun, G. Liu, X. Song and V. S. Battaglia, Correlation between dissolution behavior and electrochemical cycling performance for $LiNi_{1/3}Co_{1/3}Mn_{1/3}O_2$-based cells. *J. Power Sources*, **2012**, 207, 134-140.
155. W. Choi and A. Manthiram, Comparison of Metal Ion Dissolutions from Lithium Ion Battery Cathodes. *J. Electrochem. Soc.*, **2006**, 153, A1760-A1764.
156. L. E. Downie, S. R. Hyatt and J. R. Dahn, The Impact of Electrolyte Composition on Parasitic Reactions in Lithium Ion Cells Charged to 4.7 V Determined Using Isothermal Microcalorimetry. *J. Electrochem. Soc.*, **2016**, 163, A35-A42.
157. M. Metzger, C. Marino, J. Sicklinger, D. Haering and H. A. Gasteiger, Anodic Oxidation of Conductive Carbon and Ethylene Carbonate in High-Voltage Li-Ion Batteries Quantified by On-Line Electrochemical Mass Spectrometry. *J. Electrochem. Soc.*, **2015**, 162, A1123-A1134.
158. L. de Biasi, A. O. Kondrakov, H. Geßwein, T. Brezesinski, P. Hartmann and J. Janek, Between Scylla and Charybdis: Balancing Among Structural Stability and Energy Density of Layered NCM Cathode Materials for Advanced Lithium-Ion Batteries. *The Journal of Physical Chemistry C*, **2017**.
159. J. Choi and A. Manthiram, Role of chemical and structural stabilities on the electrochemical properties of layered $LiNi_{1/3}Mn_{1/3}Co_{1/3}O_2$ cathodes. *J. Electrochem. Soc.*, **2005**, 152, A1714-A1718.

160. L. Giordano, P. Karayaylali, Y. Yu, Y. Katayama, F. Maglia, S. Lux and Y. Shao-Horn, Chemical Reactivity Descriptor for the Oxide-Electrolyte Interface in Li-Ion Batteries. *J. Phys. Chem. Lett.*, **2017**, 8, 3881-3887.
161. M. Gauthier, T. J. Carney, A. Grimaud, L. Giordano, N. Pour, H.-H. Chang, D. P. Fenning, S. F. Lux, O. Paschos, C. Bauer, F. Maglia, S. Lupart, P. Lamp and Y. Shao-Horn, Electrode-Electrolyte Interface in Li-Ion Batteries: Current Understanding and New Insights. *J. Phys. Chem. Lett.*, **2015**, 6, 4653-4672.
162. D. Aurbach, B. Markovsky, G. Salitra, E. Markevich, Y. Talyossef, M. Koltypin, L. Nazar, B. Ellis and D. Kovacheva, Review on electrode-electrolyte solution interactions, related to cathode materials for Li-ion batteries. *J. Power Sources*, **2007**, 165, 491-499.
163. N. Yabuuchi, Y.-T. Kim, H. H. Li and Y. Shao-Horn, Thermal Instability of Cycled $Li_xNi_{0.5}Mn_{0.5}O_2$ Electrodes: An in Situ Synchrotron X-ray Powder Diffraction Study. *Chem. Mater.*, **2008**, 20, 4936-4951.
164. L. Wang, T. Maxisch and G. Ceder, A First-Principles Approach to Studying the Thermal Stability of Oxide Cathode Materials. *Chem. Mater.*, **2007**, 19, 543-552.
165. R. Jung, P. Strobl, F. Maglia, C. Stinner and H. A. Gasteiger, Temperature Dependence of Oxygen Release from $LiNi_{0.6}Mn_{0.2}Co_{0.2}O_2$ (NMC622) Cathode Materials for Li-Ion Batteries. *J. Electrochem. Soc.*, **2018**, 165, A2869-A2879.
166. S.-K. Jung, H. Gwon, J. Hong, K.-Y. Park, D.-H. Seo, H. Kim, J. Hyun, W. Yang and K. Kang, Understanding the Degradation Mechanisms of $LiNi_{0.5}Co_{0.2}Mn_{0.3}O_2$ Cathode Material in Lithium Ion Batteries. *Adv. Energy Mater.*, **2014**, 4, 1300787.
167. J. Wandt, A. Freiberg, A. Ogrodnik and H. A. Gasteiger, Singlet oxygen evolution from layered transition metal oxide cathode materials and its implications for lithium-ion batteries. *Materials Today*, **2018**, in press.
168. B. Strehle, K. Kleiner, R. Jung, F. Chesneau, M. Mendez, H. A. Gasteiger and M. Piana, The Role of Oxygen Release from Li- and Mn-Rich Layered Oxides during the First Cycles Investigated by On-Line Electrochemical Mass Spectrometry. *J. Electrochem. Soc.*, **2017**, 164, A400-A406.
169. M. G. S. R. Thomas, P. G. Bruce and J. B. Goodenough, AC Impedance Analysis of Polycrystalline Insertion Electrodes: Application to $Li_{1-x}CoO_2$. *J. Electrochem. Soc.*, **1985**, 132, 1521-1528.
170. C. H. Chen, J. Liu and K. Amine, Symmetric cell approach and impedance spectroscopy of high power lithium-ion batteries. *J. Power Sources*, **2001**, 96, 321-328.
171. K. J. Nelson, G. L. d'Eon, A. T. B. Wright, L. Ma, J. Xia and J. R. Dahn, Studies of the Effect of High Voltage on the Impedance and Cycling Performance of $Li[Ni_{0.4}Mn_{0.4}Co_{0.2}]O_2$/Graphite Lithium-Ion Pouch Cells. *J. Electrochem. Soc.*, **2015**, 162, A1046-A1054.
172. K. J. Nelson, D. W. Abarbanel, J. Xia, Z. Lu and J. R. Dahn, Effects of Upper Cutoff Potential on $LaPO_4$-Coated and Uncoated $Li[Ni_{0.42}Mn_{0.42}Co_{0.16}]O_2$/Graphite Pouch Cells. *J. Electrochem. Soc.*, **2016**, 163, A272-A280.
173. D. W. Abarbanel, K. J. Nelson and J. R. Dahn, Exploring Impedance Growth in High Voltage NMC/Graphite Li-Ion Cells Using a Transmission Line Model. *J. Electrochem. Soc.*, **2016**, 163, A522-A529.
174. K. Edström, T. Gustafsson and J. O. Thomas, The cathode–electrolyte interface in the Li-ion battery. *Electrochim. Acta*, **2004**, 50, 397-403.
175. M. Metzger, B. Strehle, S. Solchenbach and H. A. Gasteiger, Origin of H_2 Evolution in LIBs: H_2O Reduction vs. Electrolyte Oxidation. *J. Electrochem. Soc.*, **2016**, 163, A798-A809.

176. S. Solchenbach, G. Hong, A. Freiberg, R. Jung and H. A. Gasteiger, Investigating Electrolyte and SEI Decomposition Reactions by Transition Metal Ions with On-line Electrochemical Mass Spectrometry. *J. Electrochem. Soc.*, **2018**, in press.
177. M. Jiang, B. Key, Y. S. Meng and C. P. Grey, Electrochemical and Structural Study of the Layered, "Li-Excess" Lithium-Ion Battery Electrode Material $Li[Li_{1/9}Ni_{1/3}Mn_{5/9}]O_2$. *Chem. Mater.*, **2009**, 21, 2733-2745.
178. S. Meini, S. Solchenbach, M. Piana and H. A. Gasteiger, The Role of Electrolyte Solvent Stability and Electrolyte Impurities in the Electrooxidation of Li_2O_2 in Li-O_2 Batteries. *J. Electrochem. Soc.*, **2014**, 161, A1306-A1314.
179. A. E. Gebala and M. M. Jones, The acid catalyzed hydrolysis of hexafluorophosphate. *J. Inorg. Nuc. Chem.*, **1969**, 31, 771-776.
180. L. Terborg, S. Nowak, S. Passerini, M. Winter, U. Karst, P. R. Haddad and P. N. Nesterenko, Ion chromatographic determination of hydrolysis products of hexafluorophosphate salts in aqueous solution. *Analytica Chimica Acta*, **2012**, 714, 121-126.
181. A. V. Plakhotnyk, L. Ernst and R. Schmutzler, Hydrolysis in the system $LiPF_6$—propylene carbonate—dimethyl carbonate—H_2O. *J. Fluorine Chem.*, **2005**, 126, 27-31.
182. S. Solchenbach, M. Metzger, M. Egawa, H. Beyer and H. A. Gasteiger, Quantification of PF_5 and POF_3 from Side Reactions of $LiPF_6$ in Li-Ion Batteries. *J. Electrochem. Soc.*, **2018**, 165, A3022-A3028.
183. N. Tsiouvaras, S. Meini, I. Buchberger and H. A. Gasteiger, A novel on-line mass spectrometer design for the study of multiple charging cycles of a Li-O_2 battery. *J. Electrochem. Soc.*, **2013**, 160, A471-A477.
184. M. Metzger, J. Sicklinger, D. Haering, C. Kavakli, C. Stinner, C. Marino and H. A. Gasteiger, Carbon Coating Stability on High-Voltage Cathode Materials in H_2O-Free and H_2O-Containing Electrolyte. *J. Electrochem. Soc.*, **2015**, 162, A1227-A1235.
185. M. P. Seah and W. A. Dench, Quantitative electron spectroscopy of surfaces: A standard data base for electron inelastic mean free paths in solids. *Surface and Interface Analysis*, **1979**, 1, 2-11.
186. Y. Gorlin, A. Siebel, M. Piana, T. Huthwelker, H. Jha, G. Monsch, F. Kraus, H. A. Gasteiger and M. Tromp, Operando Characterization of Intermediates Produced in a Lithium-Sulfur Battery. *J. Electrochem. Soc.*, **2015**, 162, A1146-A1155.
187. R. Jung, R. Morasch, P. Karayaylali, K. Phillips, F. Maglia, C. Stinner, Y. Shao-Horn and H. A. Gasteiger, Effect of Ambient Storage on the Degradation of Ni-Rich Positive Electrode Materials (NMC811) for Li-Ion Batteries. *J. Electrochem. Soc.*, **2018**, 165, A132-A141.
188. N. Yabuuchi, K. Yoshii, S.-T. Myung, I. Nakai and S. Komaba, Detailed studies of a high-capacity electrode material for rechargeable batteries, Li_2MnO_3-$LiCo_{1/3}Ni_{1/3}Mn_{1/3}O_2$. *J. Am. Chem. Soc.*, **2011**, 133, 4404-4419.
189. H. Yu, H. Kim, Y. Wang, P. He, D. Asakura, Y. Nakamura and H. Zhou, High-energy 'composite' layered manganese-rich cathode materials via controlling Li_2MnO_3 phase activation for lithium-ion batteries. *Phys. Chem. Chem. Phys.*, **2012**, 14, 6584-6595.
190. A. R. Armstrong, M. Holzapfel, P. Novak, C. S. Johnson, S.-H. Kang, M. M. Thackeray and P. G. Bruce, Demonstrating Oxygen Loss and Associated Structural Reorganization in the Lithium Battery Cathode $Li[Ni_{0.2}Li_{0.2}Mn_{0.6}]O_2$. *J. Am. Chem. Soc.*, **2006**, 128, 8694-8698.
191. F. La Mantia, F. Rosciano, N. Tran and P. Novak, Direct evidence of oxygen evolution from $Li_{1+x}(Ni_{1/3}Mn_{1/3}Co_{1/3})_{1-x}O_2$ at high potentials. *J. Appl. Electrochem.*, **2008**, 38, 893-896.

192. D. Streich, A. Guéguen, M. Mendez, F. Chesneau, P. Novák and E. J. Berg, Online Electrochemical Mass Spectrometry of High Energy Lithium Nickel Cobalt Manganese Oxide/Graphite Half- and Full-Cells with Ethylene Carbonate and Fluoroethylene Carbonate Based Electrolytes. *J. Electrochem. Soc.*, **2016**, 163, A964-A970.
193. Z. Lu and J. R. Dahn, Understanding the Anomalous Capacity of Li / Li[$Ni_xLi_{(1/3-2x/3)}Mn_{(2/3-x/3)}$]$O_2$ Cells Using In Situ X-Ray Diffraction and Electrochemical Studies. *J. Electrochem. Soc.*, **2002**, 149, A815-A822.
194. N. Tran, L. Croguennec, M. Ménétrier, F. Weill, P. Biensan, C. Jordy and C. Delmas, Mechanisms Associated with the "Plateau" Observed at High Voltage for the Overlithiated $Li_{1.12}(Ni_{0.425}Mn_{0.425}Co_{0.15})_{0.88}O_2$ System. *Chem. Mater.*, **2008**, 20, 4815-4825.
195. A. Boulineau, L. Simonin, J.-F. Colin, C. Bourbon and S. Patoux, First Evidence of Manganese-Nickel Segregation and Densification upon Cycling in Li-Rich Layered Oxides for Lithium Batteries. *Nano Lett.*, **2013**, 13, 3857-3863.
196. C. Genevois, H. Koga, L. Croguennec, M. Menetrier, C. Delmas and F. Weill, Insight into the Atomic Structure of Cycled Lithium-Rich Layered Oxide $Li_{1.20}Mn_{0.54}Co_{0.13}Ni_{0.13}O_2$ Using HAADF STEM and Electron Nanodiffraction. *J. Phys. Chem. C*, **2015**, 119, 75-83.
197. A. Boulineau, L. Simonin, J.-F. Colin, E. Canévet, L. Daniel and S. Patoux, Evolutions of $Li_{1.2}Mn_{0.61}Ni_{0.18}Mg_{0.01}O_2$ during the Initial Charge/Discharge Cycle Studied by Advanced Electron Microscopy. *Chem. Mater.*, **2012**, 24, 3558-3566.
198. T. Teufl, B. Strehle, P. Müller, H. A. Gasteiger and M. A. Mendez, Oxygen Release and Surface Degradation of Li- and Mn-Rich Layered Oxides in Variation of the Li_2MnO_3 Content. *J. Electrochem. Soc.*, **2018**, 165, A2718-A2731.
199. H. Arai, S. Okada, Y. Sakurai and J.-i. Yamaki, Thermal behavior of $Li_{1-y}NiO_2$ and the decomposition mechanism. *Solid State Ionics*, **1998**, 109, 295-302.
200. S.-T. Myung, K.-S. Lee, C. S. Yoon, Y.-K. Sun, K. Amine and H. Yashiro, Effect of AlF_3 Coating on Thermal Behavior of Chemically Delithiated $Li_{0.35}[Ni_{1/3}Co_{1/3}Mn_{1/3}]O2$. *J. Phys. Chem. C*, **2010**, 114, 4710-4718.
201. P. Lanz, H. Sommer, M. Schulz-Dobrick and P. Novak, Oxygen release from high-energy $xLi_2MnO_3 \cdot (1-x)LiMO_2$ (M = Mn, Ni, Co): Electrochemical, differential electrochemical mass spectrometric, in situ pressure, and in situ temperature characterization. *Electrochim. Acta*, **2013**, 93, 114-119.
202. K. Luo, M. R. Roberts, R. Hao, N. Guerrini, D. M. Pickup, Y.-S. Liu, K. Edström, J. Guo, A. V. Chadwick, L. C. Duda and P. G. Bruce, Charge-compensation in 3d-transition-metal-oxide intercalation cathodes through the generation of localized electron holes on oxygen. *Nat. Chem.*, **2016**, 8, 684–691.
203. A. Guéguen, D. Streich, M. He, M. Mendez, F. F. Chesneau, P. Novák and E. J. Berg, Decomposition of $LiPF_6$ in High Energy Lithium-Ion Batteries Studied with Online Electrochemical Mass Spectrometry. *J. Electrochem. Soc.*, **2016**, 163, A1095-A1100.
204. R. Imhof and P. Novak, Oxidative electrolyte solvent degradation in lithium-ion batteries. An in situ differential electrochemical mass spectrometry investigation. *J. Electrochem. Soc.*, **1999**, 146, 1702-1706.
205. R. Bernhard, M. Metzger and H. A. Gasteiger, Gas Evolution at Graphite Anodes Depending on Electrolyte Water Content and SEI Quality Studied by On-Line Electrochemical Mass Spectrometry. *J. Electrochem. Soc.*, **2015**, 162, A1984-A1989.
206. D. Streich, C. Erk, A. Guéguen, P. Müller, F.-F. Chesneau and E. J. Berg, Operando Monitoring of Early Ni-mediated Surface Reconstruction in Layered Lithiated Ni–Co–Mn Oxides. *J. Phys. Chem. C*, **2017**, 121, 13481-13486.

207. J. Paulsen and J. H. Kim, High Nickel Cathode Material Having Low Soluble Base Content. US0054495A1, **2012**.
208. D. Aurbach, Review of selected electrode-solution interactions which determine the performance of Li and Li ion batteries. *J. Power Sources*, **2000**, 89, 206-218.
209. D. Aurbach, K. Gamolsky, B. Markovsky, G. Salitra, Y. Gofer, U. Heider, R. Oesten and M. Schmidt, The Study of Surface Phenomena Related to Electrochemical Lithium Intercalation into Li_xMO_y Host Materials (M = Ni, Mn). *J. Electrochem. Soc.*, **2000**, 147, 1322-1331.
210. K. Matsumoto, R. Kuzuo, K. Takeya and A. Yamanaka, Effects of CO_2 in air on Li deintercalation from $LiNi_{1-x-y}Co_xAl_yO_2$. *J. Power Sources*, **1999**, 81–82, 558-561.
211. K. Shizuka, C. Kiyohara, K. Shima and Y. Takeda, Effect of CO_2 on layered $Li_{1+z}Ni_{1-x-y}Co_xM_yO_2$ (M = Al, Mn) cathode materials for lithium ion batteries. *J. Power Sources*, **2007**, 166, 233-238.
212. H. S. Liu, Z. R. Zhang, Z. L. Gong and Y. Yang, Origin of deterioration for $LiNiO_2$ cathode material during storage in air. *Electrochem. Solid-State Lett.*, **2004**, 7, A190-A193.
213. S. Komaba, N. Kumagai and Y. Kataoka, Influence of manganese(II), cobalt(II), and nickel(II) additives in electrolyte on performance of graphite anode for lithium-ion batteries. *Electrochim. Acta*, **2002**, 47, 1229-1239.
214. S. R. Gowda, K. G. Gallagher, J. R. Croy, M. Bettge, M. M. Thackeray and M. Balasubramanian, Oxidation state of cross-over manganese species on the graphite electrode of lithium-ion cells. *Phys. Chem. Chem. Phys.*, **2014**, 16, 6898-6902.
215. X. Xiao, Z. Liu, L. Baggetto, G. M. Veith, K. L. More and R. R. Unocic, Unraveling manganese dissolution/deposition mechanisms on the negative electrode in lithium ion batteries. *Phys. Chem. Chem. Phys.*, **2014**, 16, 10398-10402.
216. C. Zhan, J. Lu, A. J. Kropf, T. Wu, A. N. Jansen, Y.-K. Sun, X. Qiu and K. Amine, Mn(II) deposition on anodes and its effects on capacity fade in spinel lithium manganate-carbon systems. *Nat. Commun.*, **2013**, 4, 3437, 8 pp.
217. Z. Li, A. D. Pauric, G. R. Goward, T. J. Fuller, J. M. Ziegelbauer, M. P. Balogh and I. C. Halalay, Manganese sequestration and improved high-temperature cycling of Li-ion batteries by polymeric aza-15-crown-5. *J. Power Sources*, **2014**, 272, 1134-1141.
218. S. Komaba, T. Itabashi, T. Ohtsuka, H. Groult, N. Kumagai, B. Kaplan and H. Yashiro, Impact of 2-Vinylpyridine as Electrolyte Additive on Surface and Electrochemistry of Graphite for C/$LiMn_2O_4$ Li-Ion Cells. *J. Electrochem. Soc.*, **2005**, 152, A937-A946.
219. L. Yang, M. Takahashi and B. Wang, A study on capacity fading of lithium-ion battery with manganese spinel positive electrode during cycling. *Electrochim. Acta*, **2006**, 51, 3228-3234.
220. C. Delacourt, A. Kwong, X. Liu, R. Qiao, W. L. Yang, P. Lu, S. J. Harris and V. Srinivasan, Effect of manganese contamination on the solid-electrolyte-interphase properties in Li-ion batteries. *J. Electrochem. Soc.*, **2013**, 160, A1099-A1107.
221. I. A. Shkrob, A. J. Kropf, T. W. Marin, Y. Li, O. G. Poluektov, J. Niklas and D. P. Abraham, Manganese in Graphite Anode and Capacity Fade in Li Ion Batteries. *J. Phys. Chem. C*, **2014**, 118, 24335-24348.
222. E. Markevich, G. Salitra, K. Fridman, R. Sharabi, G. Gershinsky, A. Garsuch, G. Semrau, M. A. Schmidt and D. Aurbach, Fluoroethylene Carbonate as an Important Component in Electrolyte Solutions for High-Voltage Lithium Batteries: Role of Surface Chemistry on the Cathode. *Langmuir*, **2014**, 30, 7414-7424.
223. M. E. Spahr, T. Palladino, H. Wilhelm, A. Wuersig, D. Goers, H. Buqa, M. Holzapfel and P. Novak, Exfoliation of Graphite during Electrochemical Lithium Insertion in

Ethylene Carbonate-Containing Electrolytes. *J. Electrochem. Soc.*, **2004**, 151, A1383-A1395.

224. B. Zhang, M. Metzger, S. Solchenbach, M. Payne, S. Meini, H. A. Gasteiger, A. Garsuch and B. L. Lucht, Role of 1,3-Propane Sultone and Vinylene Carbonate in Solid Electrolyte Interface Formation and Gas Generation. *J. Phys. Chem. C*, **2015**, 119, 11337-11348.
225. D. Aurbach, Y. Gofer, M. Ben-Zion and P. Aped, The behavior of lithium electrodes in propylene and ethylene carbonate: the major factors that influence lithium cycling efficiency. *J. Electroanal. Chem.*, **1992**, 339, 451-471.
226. S. Geier, R. Jung, K. Peters, H. A. Gasteiger, D. Fattakhova-Rohlfing and T. F. Fassler, A wet-chemical route for macroporous inverse opal Ge anodes for lithium ion batteries with high capacity retention. *Sustainable Energy & Fuels*, **2017**, 2, 85-90.

CV

Roland Jung

* 8th December 1989

PROFESSIONAL EXPERIENCE

since 12/2017 **Specialist battery cell technology**

BMW Group

- Development of innovative materials for the next generation of Li-ion batteries.

12/2014 – 11/2017 **PhD student**

Chair of Technical Electrochemistry (Prof. H. A. Gasteiger),

Technische Universität München and

Research Battery Technology, *BMW Group*

- Thesis: "Degradation Mechanisms of High-Energy Electrode Materials for Lithium-Ion Batteries"

09/2016 – 12/2016 **Visiting PhD student**

Electrochemical Energy Laboratory (Prof. Y. Shao-Horn),

Massachusetts Institute of Technology

- Investigation of the decomposition of Ni-rich cathode materials upon storage at ambient air.

08/2013 – 09/2013 **Intern**

BMW Group

- Development of electrode slurries with novel and innovative materials. Assembly of battery test cells for material testing and evaluation as well as interpretation of the test results.

03/2010 – 04/2010 **Intern**

Dr. Holger Bengs Biotech Consulting (nowadays: BCNP Consultants GmbH)

- Development of an expert report on nanotechnology with a focus on technological chances and risks as well as the market opportunities.

EDUCATION

10/2012 – 11/2014 **Master of Science (M.Sc.) in Advanced Materials Science**

Technische Universität München, Ludwigs-Maximilians Universität München, Universität Augsburg

- Final grade: 1.0
- Master thesis: "Characterization of Silicon Anodes for Lithium Ion Batteries", Chair of Technical Electrochemistry (Prof. H. A. Gasteiger), *Technische Universität München* (grade: 1.0)

10/2009 – 09/2012 **Bachelor of Science (B.Sc.) in Chemistry**

Technische Universität München

- Final grade: 1.3
- Bachelor thesis: "Stabilization of inorganic nanoparticles in aqueous solution using amphiphilic copolymers", *Max Planck Institute for Polymer Research* (Prof. K. Müllen) (grade: 1.0)

2009 **Abitur**

Adolf-Reichwein Gymnasium Heusenstamm

- Final grade: 1.2

SCHOLARSHIPS

05/2017 – 06/2017 DAAD Travel grant to the 231th ECS Meeting, New Orleans, USA

2011 – 2014 Scholarship "Max-Weber Programm Bayern"

LANGUAGE SKILLS

German native language

English fluently

Munich, October 10, 2018

List of scientific publications

Published:

1. **R. Jung**, M. Metzger, D. Haering, S. Solchenbach, C. Marino, N. Tsiouvaras, C. Stinner, and H. A. Gasteiger, Consumption of Fluoroethylene Carbonate (FEC) on Si-C Composite Electrodes for Li-Ion Batteries. *J. Electrochem. Soc.*, **2016**, 163, A1705-A1716.
2. J. Wandt, A. Freiberg, R. Thomas, Y. Gorlin, A. Siebel, **R. Jung**, H. A. Gasteiger, and M. Tromp, Transition metal dissolution and deposition in Li-ion batteries investigated by operando X-ray absorption spectroscopy. *J. Mater. Chem. A*, **2016**, 4, 18300-18305.
3. B. Strehle, K. Kleiner, **R. Jung**, F. Chesneau, M. Mendez, H. A. Gasteiger, and M. Piana, The Role of Oxygen Release from Li- and Mn-Rich Layered Oxides during the First Cycles Investigated by On-Line Electrochemical Mass Spectrometry. *J. Electrochem. Soc.*, **2017**, 164, A400-A406.
4. **R. Jung**, M. Metzger, F. Maglia, C. Stinner and H. A. Gasteiger, Oxygen Release and Its Effect on the Cycling Stability of $LiNi_xMn_yCo_zO_2$ (NMC) Cathode Materials for Li-Ion Batteries. *J. Electrochem. Soc.*, **2017**, 164, A1361-A1377.
5. **R. Jung**, M. Metzger, F. Maglia, C. Stinner and H. A. Gasteiger, Chemical vs. Electrochemical Electrolyte Oxidation on NMC111, NMC622, NMC811, LNMO, and Conductive Carbon. *J. Phys. Chem. Lett.*, **2017**, 8, 4820-4825.
6. M. Wetjen, D. Pritzl, **R. Jung**, S. Solchenbach, R. Ghadimib, and H. A. Gasteiger, Differentiating the Degradation Phenomena in Silicon-Graphite Electrodes for Lithium-Ion Batteries. *J. Electrochem. Soc.*, **2017**, 164, A2840-2852.
7. S. Geier, **R. Jung**, K. Peters, H. A. Gasteiger, D. Fattakhova-Rohlfing, and T. F. Fässler, A wet-chemical route for macroporous inverse opal Ge anodes for lithium ion batteries with high capacity retention. *Sustainable Energy Fuels*, **2018**, 2, 85-90.
8. **R. Jung**, R. Morasch, P. Karayaylali, K. Phillips, F. Maglia, C. Stinner, Y. Shao-Horn, and H. A. Gasteiger, Effect of Ambient Storage on the Degradation of Ni-rich Positive Electrode Materials (NMC811) for Li-Ion Batteries. *J. Electrochem. Soc.*, **2018**, 165, A132-141.
9. **R. Jung**, P. Strobl, F. Maglia, C. Stinner and H. A. Gasteiger, Temperature Dependence of Oxygen Release from $LiNi_{0.6}Mn_{0.2}Co_{0.2}O_2$ (NMC622) Cathode Materials for Li-Ion Batteries. *J. Electrochem. Soc.*, **2018**, 165, A2869-2879.

In preparation:

10. **R. Jung**, F. Linsenmann, R. Thomas, J. Wandt, S. Solchenbach, F. Maglia, C. Stinner, M. Tromp, and H. A. Gasteiger, Nickel, Manganese, and Cobalt Dissolution from Ni-rich NMC and Their Effects on NMC622-graphite cells. in preparation.

List of conference presentations

1. Consumption of Fluoroethylene Carbonate (FEC) on Si-C Composite Electrodes for Li-Ion Batteries, 230th Meeting of The Electrochemical Society, (October 2 – 7, 2016) in Honolulu, Abstract Number: # 284.
2. Oxygen Release and Its Effect on the Cycling Stability of $LiNi_xMn_yCo_zO_2$ (NMC) Cathode Materials for Li-Ion Batteries, 231st Meeting of The Electrochemical Society, (May 28- June 1, 2017) in New Orleans, Abstract Number: # 39.
3. Effect of Ambient Storage on the Degradation of Ni-rich Positive Electrode Materials (NMC811) for Li-Ion Batteries, 232nd Meeting of The Electrochemical Society, (October 1-5, 2017) in National Harbor, Abstract Number: # 216.
4. Oxygen Release and Its Effect on the Cycling Stability of $LiNi_xMn_yCo_zO_2$ (NMC) Cathode Materials for Li-Ion Batteries, Munich Battery Discussions, (February 19-20, 2018) in Munich.